UNIVERSITÉ DE STRASBOURG

ÉCOLE DOCTORALE DES SCIENCES DE LA VIE ET DE LA SANTÉ

&

Institut de Génétique et de Biologie Moléculaire et Cellulaire (IGBMC)

CNRS UMR 7104 – INSERM U1258

THÈSE présentée par :

Elizabeth RAMOS MORALES

soutenue le : **10 septembre 2021**

pour obtenir le grade de : **Docteur de l'université de Strasbourg**

Discipline/ Spécialité : Science de la vie et la santé

Biochemical, biophysical and structural studies of proteins associated to human diseases: tcDAC2 and the ADAT complex

THÈSE dirigée par :

M. ROMIER Christophe	Directeur de recherche, Institut de génétique et de biologie moléculaire et cellulaire (IGBMC), Illkirch, France

RAPPORTEURS :

Mme. SCHMITT Emmanuelle	Directrice de recherche, Institut Polytechnique de Paris, Palaiseau, France
M. KADLEC Jan	Chargé de recherche, Institut de Biologie Structurale (IBS), Grenoble, France

AUTRES MEMBRES DU JURY :

M. BECKER Hubert	Professeur, Génétique Moléculaire, Génomique, Microbiologie (GMGM), Strasbourg, France

MEMBRES INVITÉS :

Mme. GODIN Juliette	Chargée de recherche, Institut de génétique et de biologie moléculaire et cellulaire (IGBMC), Illkirch, France

Acknowledgement

I thank my thesis supervisor Christophe Romier and the jury members Emmanuelle Schmitt, Jan Kadlec, Hubert Becker and Juliette Godin. TcDAC2 and ADAT project collaborators Laurence Drouard, Thalia Salinas Giegé, Drouard's lab and Juliette's lab. Christophe's lab members for all their support: Martin Marek, Tajith Shaik, Sylvie Duclaud, Régis Back, Natalia Aleksandrova, Marie-Laure Durand, Pierre Antony, Edouard Troesch, Pernelle Klein, Pauline Landwerlin and Marina Vitoria Gomes.

Content

Figures list

Introduction

During my PhD thesis I worked on enzymes associated to human diseases: tcDAC2 and ADAT. TcDAC2 is an essential protein of the parasite *Trypanosoma cruzi* that causes Chagas disease. TcDAC2 is an epigenetic enzyme, belonging to the histone deacetylase family. Thus, targeting the *T. cruzi* epigenome, by inhibiting tcDAC2, represents a potential treatment for Chagas disease. In this project I solved the structure of tcDAC2 to guide the development of potent and specific tcDAC2 inhibitors. In my second project, I investigated the mechanism by which a mutation in the ADAT complex, formed of two subunits ADAT2 and ADAT3, triggers a neurodevelopmental disorder characterized by intellectual disability, microcephaly, strabismus and epilepsy. ADAT is an enzyme that transforms the adenosine at position 34 of tRNAs into inosine, therefore ADAT is an enzyme belonging to the epitranscriptomic field.

The worlds of epigenetics and epitranscriptomics

Epigenetics and epitranscriptomics are two fields characterized by the reversibility of chemical modifications in two different substrates: (i) the DNA and the histone proteins and (ii) RNAs, respectively. These two fields participate in the regulation of gene expression and different signaling pathways in the nucleus in the case of epigenetic and in both the nucleus and the cytoplasm compartments in the case of epitranscriptomics. If the field of epigenetics is now well established, the field of epitranscriptomics is receiving more and more attention. The effectors in these two fields control cell differentiation and development, and their deregulation cause numerous diseases including cancer, neurologic, cardiovascular, immune and metabolic disorders. These fields are therefore attracting a lot of attention to develop novel therapeutic approaches. During my PhD, I have developed scientific research projects in these two fields, gaining significant insights in both of them as reported in this manuscript.

First chapter: Epigenetics

1 Epigenetic mechanisms, associated diseases and epigenetic drugs

In order to fit within the eukaryotic nucleus, the genome of eukaryotes is compacted into a specific structure called chromatin. The basic unit of the chromatin is the nucleosome which is composed of two H2A/H2B and two H3/H4 histone pairs that arrange into a histone octamer, wrapping ~147 bp pairs of DNA (Luger et al. 1997). Nucleosomes can further interact with each other to form compacter structures which range from the 30 nm fiber to chromatin loops, up to the highest compaction in the mitotic chromosomes (Baldi, Korber, and Becker 2020).

The chromatin structure forms a barrier and a regulatory element for the other nuclear effectors to access the genetic information. Regulation of the chromatin structure through epigenetic mechanisms further provides a way to the cells to regulate the nuclear mechanisms, with direct implication on cellular homeostasis, development, but also on disease (Allis and Jenuwein 2016). Notably, epigenetic mechanisms play a major role in the regulation of gene expression through changes in chromatin structure (Day and Sweatt 2011; Goldberg, Allis, and Bernstein 2007).

Cells use five major epigenetic mechanisms to modulate the chromatin structure. These include: (i) histone variants and their associated chaperones, (ii) ATP-dependent chromatin-remodeling complexes, (iii) long non-coding RNA-mediated regulation (iv) DNA methylation and (v) histone modifications (Kouzarides 2007).

1.1 Histone variant and chaperones

Canonical histones are composed of H4, H3, H2A and H2B. The genes encoding these histones are present as multiple copies in the human genome where they form a cluster. These genes are intronless and are synthesized only in the S phase of the cell cycle and deposited onto newly replicated DNA (Sauer et al. 2018). Therefore, canonical histone deposition in nucleosomes is known to be replication dependent. In contrast, histone variants genes are present as a single or double copy in the genome, they are located outside the canonical histone cluster, they have introns, and their expression and deposition in the chromatin is not regulated by the cell cycle (Martire and Banaszynski 2020; Mendiratta, Gatto, and Almouzni

2018). Variants have been identified for each histone type, but most of them are found in the H3 and H2A histone families. Outside the chromatin, histones are generally bound to histone chaperones as canonical or variant histone pairs. Histone chaperones are responsible of the shuttling of the histones between the cytoplasm and the nucleus and within the nucleus (Martire and Banaszynski 2020).

Canonical histone H3 is composed of two isoforms H3.1 and H3.2. These isoforms differ by one amino acid: H3.1 has a cysteine and H3.2 has a serine at position 96. Histone H3 has two major variants: H3.3 and CENP-A. H3.3 differs by five residues from canonical histone H3.1. The Ala87-Ala88-Ile89-Gly90 sequence constitutes a motif that allows histone chaperones to distinguish H3.3 from canonical H3 histones. Furthermore, canonical H3 Ala31 in the histone tail is replaced in H3.3 variant by Ser31, which can be phosphorylated (Hake et al. 2005). Canonical histone H3 is deposited into DNA by CAF1 chaperone, while other chaperones oversee H3 histone variants (Smith and Stillman 1989; Tagami et al. 2004; Loyola et al. 2009; Quivy et al. 2004). Two chaperones, the HIRA and DAXX/ATRX complexes, deposit H3.3 in different genomic regions (Goldberg et al. 2010). The HIRA complex, formed by three subunits (HIRA, UBN1(or UBN2) and CABIN1) deposits H3.3 in active chromatin such as enhancers, promoters and gene bodies (C. Xiong et al. 2018, 1; Daniel Ricketts et al. 2015; Tagami et al. 2004). The DAXX/ATRX complex deposits H3.3 at repetitive heterochromatic regions: pericentromeric chromatin and telomeres repeats, endogenous retroviral elements and imprinted genes (Figure 1) (Goldberg et al. 2010; Lewis et al. 2010; L. H. Wong et al. 2010; Drané et al. 2010; Q. He et al. 2015; Elsässer et al. 2015). Furthermore, CENP-A, the other H3 variant, which is much more divergent from canonical H3, is deposited at the centromere by its chaperone HJURP (Sullivan, Hechenberger, and Masri 1994; Dunleavy et al. 2009; Foltz et al. 2009; H. Hu et al. 2011). CENP-A has two roles, it maintains centromere identity across mitosis and meiosis and directs assembly of the kinetochore (Figure 1) (Black and Cleveland 2011; Musacchio and Desai 2017).

Among the H2A variants, the best studied are H2AX, H2AZ and macroH2A. H2AX differs from canonical H2A by a C-terminal additional motif formed by Ser140, Gln141, Glu142, and Tyr143 residues. H2A.X phosphorylated at Ser140 marks dsDNA break in chromatin (Piquet et al. 2018). H2AZ shares 60% similarity with H2A. Human H2AZ has three isoforms: H2AZ1, H2AZ2.1 and H2AZ2.2 (Dryhurst et al. 2009; Matsuda et al. 2010). H2AZ, when compared to canonical H2A, has an extended acidic patch at the C-terminal tail which potentially decreases its interaction with DNA. Therefore, H2AZ has been associated with

transcriptional activation. Acetylated H2AZ is enriched at transcriptional start sites (TSS), enhancers and promoters of active genes (Creyghton et al. 2008; M. M. Wong, Cox, and Chrivia 2007; Luk et al. 2010; Bagchi et al. 2020; Jin et al. 2009). However, H2AZ is also associated to gene silencing since it participates in pericentromeric formation. In addition, H2AZ is present in bivalent chromatin domains in embryonic stem cells (Ku et al. 2012). Two chaperones incorporate H2AZ in the nucleosome that are both ATP-dependent chromatin remodeler complexes: p400-TIP60 and SRCAP (Ruhl et al. 2006; Xiaoping Liang et al. 2016). TIP60 also has a lysine acetyltransferase activity that modifies H2AZ (and canonical H2A). Furthermore, both complexes p400-TIP60 and SCARP can act as reader of histone PTMs through their GAS41 subunit. For instance, recognition of acetylated H3 by GAS41 directs H2AZ deposition. Eviction of H2AZ from nucleosomes is mediated by two chaperone complexes: the INO80 remodeler and ANP32E (Papamichos-Chronakis et al. 2011; Mao et al. 2014; Obri et al. 2014). Both complexes evict H2AZ from DNA damage sites, and ANP32E also removes H2AZ from the TSS, enhancers and insulators (Figure 1) (Obri et al. 2014; Mao et al. 2014).

MacroH2A is composed of an H2A-like domain, a lysine-rich linker and, at its C-terminus, a macrodomain protrudes from the nucleosome. There are three human isoforms of macroH2A: macroH2A1.1, macroH2A1.2 and macroH2A2 (Z. Sun and Bernstein 2019). MacroH2A is associated with transcriptional repression and heterochromatin formation since macroH2A is enriched in the inactive X chromosome, at PCR2-mediated facultative heterochromatin, in senescence-associated heterochromatin foci, on repetitive DNA sequences and at inactive genes (Kozlowski et al. 2018; Buschbeck et al. 2009; Douet et al. 2017). Furthermore, macroH2A colocalizes with H3K27me3 and H3K9me3 (Douet et al. 2017). No specific chaperone has been found for macroH2A. However co-transcriptional eviction of macroH2A2 is mediated by the FACT (Facilitates Chromatin Transcription) complex, a general H2A chaperone, and ATRX excludes macroH2A from subtelomeric regions (Figure 1) (Z. Sun et al. 2018). Finally, it has been shown that MacroH2A1.1 can bind ADP-ribose and poly(ADP-ribose) (Karras et al. 2005; Kustatscher et al. 2005; Timinszky et al. 2009). For instance, PARP1 ADP-ribosylated is bound by MacroH2A1.1 causing inhibition of PARP1 activity.

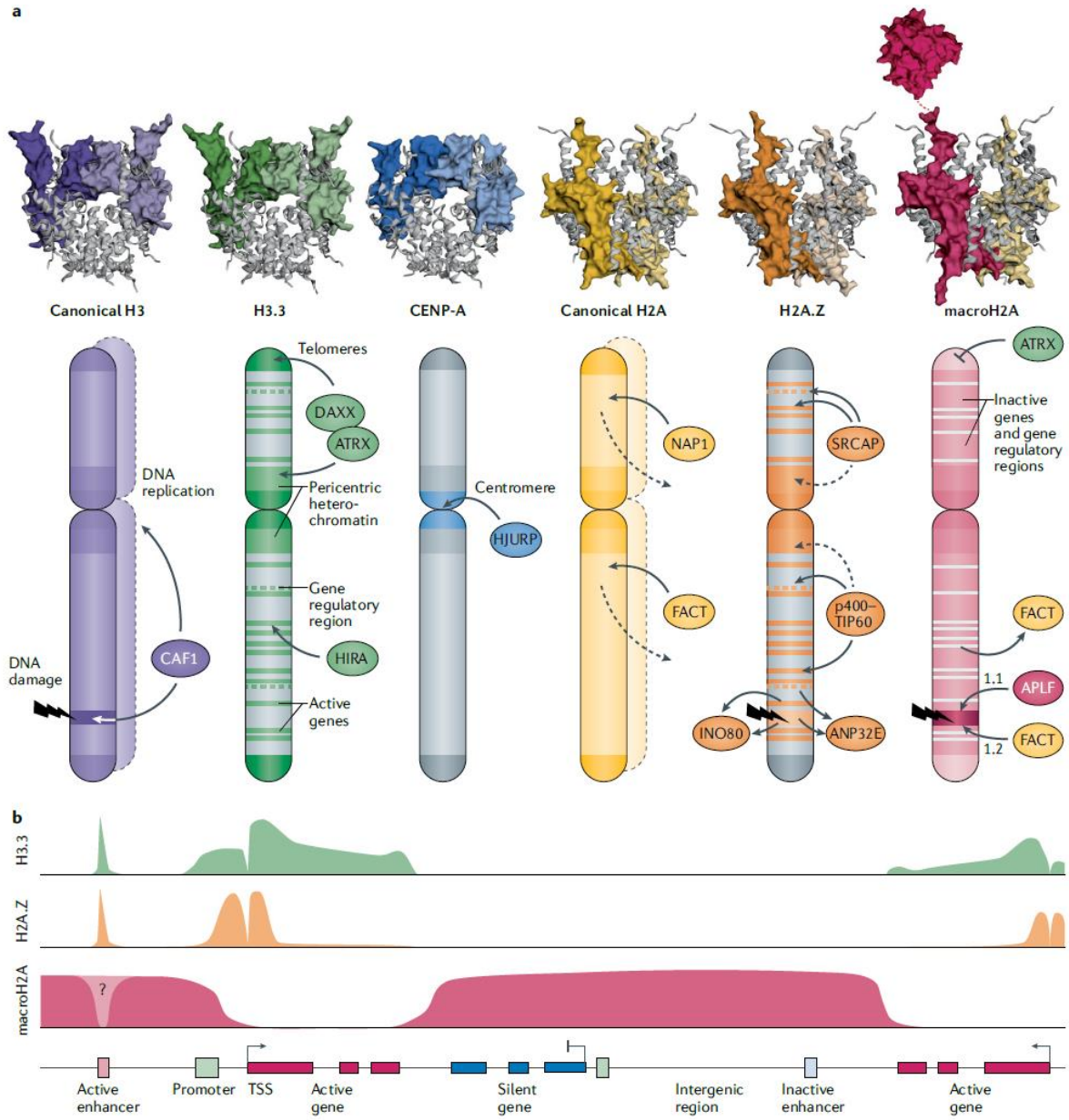

Figure 1. Histone variants, their chaperones and genomic distribution

a. Structures of canonical and histone variants show their similarities, except for macroH2A that contains a C-terminal macrodomain. Histone chaperones deposit histone variants at different genomic locations. CAF1 deposits canonical H3 during DNA replication and repair. HIRA complex deposits H3.3 at active genes and gene regulatory regions. In contrast, DAXX/ATRX deposits H3.3 at pericentric heterochromatic and subtelomeric regions. CENP-A is deposited at the centromere by HJURP. H2A deposition by NAP1 and FACT counterbalances (dashed lines) its continuous turnover. H2AZ is deposited at actives genes and regulatory elements by SRCAP and p400-TIP60; H2AZ is also observed at pericentromeric heterochromatin, but the mechanism is not clear. INO80 remodeler and ANP32E exchange H2AZ for H2A at active genes, regulatory elements and DNA damage sites. APLF and FACT promotes enrichment of macroH2A1.1 and macroH2A1.2 respectively. ATRX and FACT impedes deposition of macroH2A in telomeric and transcribed genes respectively. b. Gene-level distribution of histone variants. H3.3 and H2AZ are enriched at enhancers and promoters of actives genes. H3.3 is also present in transcribed gene bodies and transcription stop sites. MacroH2A are present in large domains but not in transcribed regions. Adapted from (Ghiraldini, Filipescu, and Bernstein 2021)

Incorporation of histone variants affects nucleosome structure and stability. For instance, homotypic H2AZ nucleosomes (containing two H2AZ/H2B pairs) are more stable than heterotypic nucleosomes (containing one canonical H2A/H2B pair and one H2AZ/H2B pair) due to their extended acidic patches (Y.-J. Park et al. 2004; J. Y. Fan et al. 2002). H2AZ and heterochromatin-associated Histone 3 lysine 9 trimethylation (H3K9me3) recruit heterochromatin protein 1α (HP1α), which promotes heterochromatin formation and gene silencing (Ryan and Tremethick 2018). However, nucleosomes containing heterotypic H2AZ and H2A histones show instability because of the steric hindrance produced by the H2A and H2AZ different L1 loops conformation (Suto et al. 2000). Additionally, H2AZ and H3.3 confers high instability to the nucleosome due to H2AZ C-terminal domain that reduces interactions with H3 (Jin et al. 2009; Jin and Felsenfeld 2007). This is in agreement with the enrichment of nucleosomes containing both H2AZ and H3.3 at enhancers and promoters, which gives transcription factors accessibility to the DNA (G. Hu et al. 2013; Iwafuchi-Doi et al. 2016). Furthermore, H3.3 deposition on centromeric regions during S phase represents a place holder for CENP-A, which is deposited at the end of mitosis (Dunleavy, Almouzni, and Karpen 2011). CENP-A has two extra amino acids (Arg80 and Gly81) in its L1 loop region, which represents a binding site for trans-acting factors, thereby providing nucleosome stability (Tachiwana et al. 2011).

The chromatin state is also affected by histone variants. For instance, phosphorylation of H3.3 at S31 on the N-terminal tail of H3.3 promotes an active chromatin state through acetylation of enhancer and promoters (Sitbon et al. 2020). For instance, phosphorylated S31, increases histone acetyl transferase p300-mediated H3K27ac, thereby activating new transcriptional programs at developmental genes in differentiated ES cells (Martire et al. 2019). In addition, in lipopolysaccharide-stimulated macrophages, phosphorylation of H3.3 at S31 recruits the histone methyltransferase SETD2 to stimulation-responsive genes where SETD2 catalyzes H3.3K36me3, which causes rapid gene induction (Armache et al. 2020). In addition, phosphorylated H3.3 at S31 inhibits binding of the transcription repressor ZMYND11 to H3.3K36me3 marks; thus H3.3 is proposed to play a role in rapid signal-mediated gene activation (R. Guo et al. 2014, 69; Wen et al. 2014).

Depending on H2AZ genomic location, H2AZ is differently modified. For instance, in regulatory elements H2AZ is acetylated promoting an open chromatin and transcription machinery binding to the DNA (Semer et al. 2019; Valdés-Mora et al. 2012; Ku et al. 2012; G. Hu et al. 2013). In contrast, in facultative heterochromatic regions, H2AZ is

monoubiquitylated by PRC1 and promotes deposition of H3K27me3 mediated by PRC2 (Yan Wang et al. 2018, 3; Sarcinella et al. 2007; Draker, Sarcinella, and Cheung 2011). Furthermore, H2AZ1 in combination with H4 acetylation promotes recruitment of the bromodomain BRD2 leading to transcription activation (Semer et al. 2019). Histone variant chaperones can also stimulate chromatin states, for instance H3.3 chaperone DAXX/ATRX recruits the corepressor complex KAP1 and methyltransferase SETDB1 which catalyzes H3K9me3 (Q. He et al. 2015; Elsässer et al. 2015; Hoelper et al. 2017; Udugama et al. 2015).

Deregulation of the expression of most histone variants and chaperones is associated to several adult cancer types. In contrast, specific mutations in H3.3 are associated with pediatric cancers (Figure 2). H2AZ is upregulated and promotes cell proliferation in several cancer types. For instance, H2AZ is upregulated in melanoma, hepatocellular carcinoma, breast and prostate cancer (Vardabasso et al. 2015; Hua et al. 2008; H. D. Yang et al. 2016; Valdés-Mora et al. 2017). Upregulation of components of the chaperone complex SRCAP has been identified in prostate and lung cancers (Slupianek et al. 2010; Hsu et al. 2018). In contrast, the TIP60 subunit of the p400-TIP60 complex, act as a tumor-suppressor, and TIP60 is downregulated in colorectal cancer (Mattera et al. 2009; Chevillard-Briet et al. 2014). MacroH2A1.1 also acts as a tumor suppressor since it is downregulated in several cancer types (Sporn et al. 2009; Novikov et al. 2011). The role of other isoforms of macroH2A is context dependent.

Specifically, missense mutations in H3.3 genes, encoding for either H3.3-K27M or H3.3-G34R/V have been identified in pediatric gliomas and the H3.3-K36M mutation in pediatric chondroblastoma (Schwartzentruber et al. 2012; Behjati et al. 2013). These substitutions hamper Lys27 and Lys36 methylations (Lu et al. 2016; Lewis et al. 2013; D. Fang et al. 2016). Mutations in the DAXX/ATRX chaperone complex have been identified in tumors of neural crest origin such as pancreatic neuroendocrine tumors, gliomas and neuroblastoma (Schwartzentruber et al. 2012; Heaphy et al. 2011; Y. Jiao et al. 2011). Furthermore, both CENP-A and HJURP are upregulated in several tumors, including gliomas, lung cancer, hepatocellular carcinoma, breast cancer, ovarian cancer (Yongmei Li et al. 2011; B. Hu et al. 2017; Q. Wu et al. 2012; Kato et al. 2007; Valente et al. 2013; de Tayrac et al. 2013; Stangeland et al. 2015; McGovern et al. 2012; Montes de Oca et al. 2015; Qiu et al. 2013; Lin Li et al. 2018).

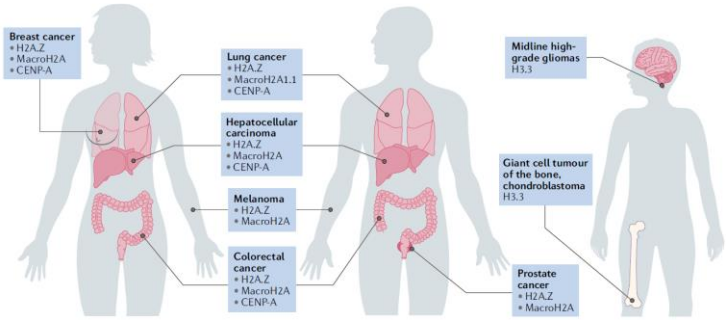

Figure 2. Histone variants altered expression in several cancer types

H2A variants (H2AZ and macroH2A) and histone H3 variants are commonly dysregulated in several adult cancer. In contrast, H3.3 is dysregulated in pediatric cancers. Adapted from (Ghiraldini, Filipescu, and Bernstein 2021)

1.2 ATP-dependent chromatin-remodeling complexes

ATP-dependent chromatin-remodeling complexes, also known as remodelers, are proteins or protein complexes that use the energy of ATP to act on nucleosomes (Bartholomew 2014). The structural changes associated with ATP hydrolysis enable the remodelers to act in several ways on the nucleosomes and modulate the chromatin compaction by performing three functions: (i) chromatin assembly and organization, where remodelers regulate the proper density and spacing of nucleosomes, (ii) chromatin access, where remodelers move or eject nucleosomes to create nucleosome free regions, for instance to enable transcription factors binding to DNA, and (iii) nucleosome editing, where remodelers exchange canonical histone pairs with histone variant pairs (Figure 3a) (Hargreaves and Crabtree 2011; Narlikar, Sundaramoorthy, and Owen-Hughes 2013). Remodelers are further divided into four subfamilies, based on their specific domains: ISWI (initiation of switch), chromodomain helicase DNA-binding (CHD), SWI/SNF and INO80 (Figure 3b) (Cedric R. Clapier and Cairns 2009; Becker and Workman 2013).

Most remodelers translocate the DNA, i.e. the movement of DNA over the histone surface. DNA translocation triggers the weakening or breakage of DNA and histones interactions. The catalytic subunits of remodelers have an ATPase domain that is split in two RecA-like lobes (lobe 1 and lobe 2) to perform DNA translocation through ATP binding and hydrolysis. Both lobes sequentially bind and release the same DNA strand like “two gloves”, 1bp of DNA is translocated per 1 ATP hydrolysis. The DNA movement occurs in one direction from 3’-to-5’ (Figure 3c). Remodelers have adapted and evolved this basic mechanism of DNA translocation to achieve their specific functions.

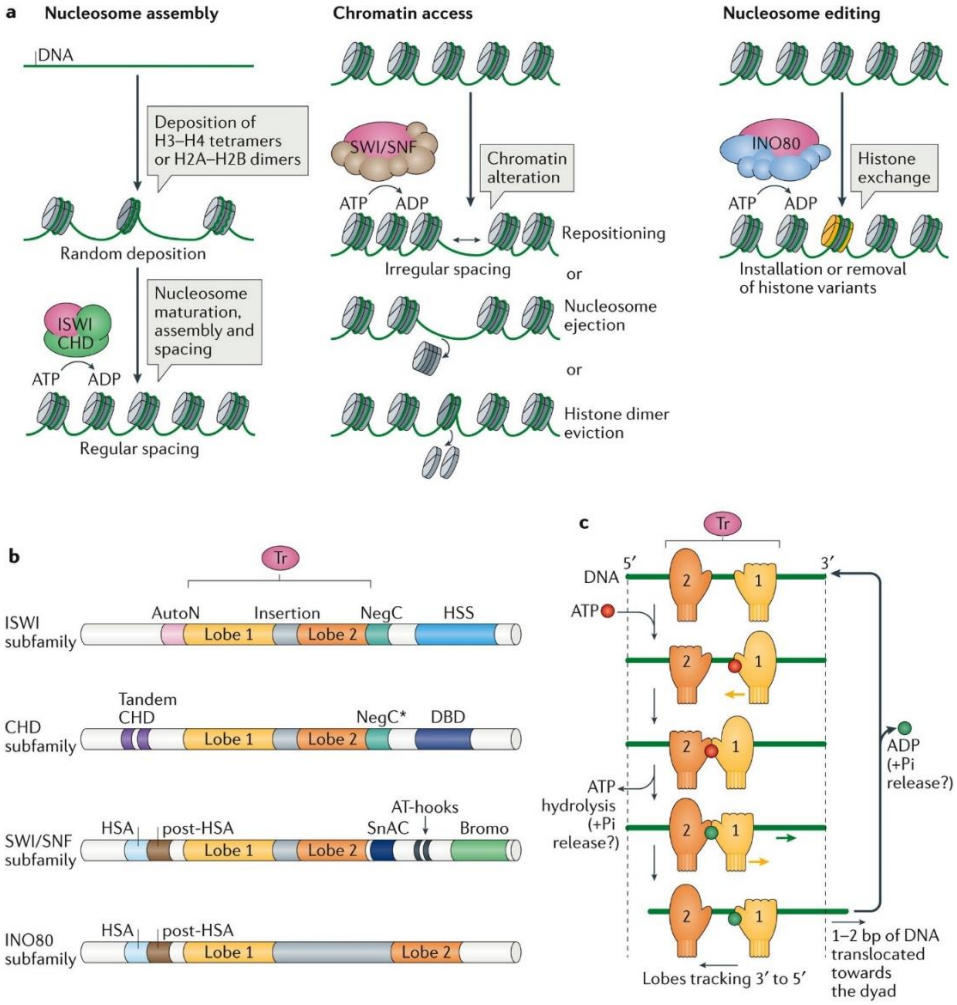

Figure 3. Chromatin remodelers functions and domain organization

a. Functional classification of remodelers. ATPase domain are shown in pink and additional subunits are represented in other colors: green (ISWI, CHD), brown (SWI/SNF) and blue (INO80). **b.** Remodelers classification into four subfamilies is based on their specific domains. The ATPase-translocase domain (Tr) is composed of two RecA-like lobes separated by a short or long insertion. **c.** Schematic view of the "inchworming" mechanism of DNA translocation by remodelers. The RecA-like lobe 1 and lobe 2 are depicted as gloves. Adapted from (Cedric R. Clapier et al. 2017)

Chromatin assembly and organization, takes place after DNA replication, where canonical histones are used for assembling new nucleosomes, and during transcription and other nuclear processes, where both variant and canonical histones are inserted in the nucleosomes, depending on their location in the genome and the role they are assigned to. Histone chaperones bring the histones proteins as H3-H4 tetramers and H2A-H2B dimers to the assembly locations (Gurard-Levin, Quivy, and Almouzni 2014). Next, ISWI and CHD assembles these histones-DNA complexes into the mature octameric nucleosomes that they also space at regular fixed distances (Figure 4) (Torigoe et al. 2011; Fei et al. 2015; Corona et al. 1999; T. Ito et al. 1997).

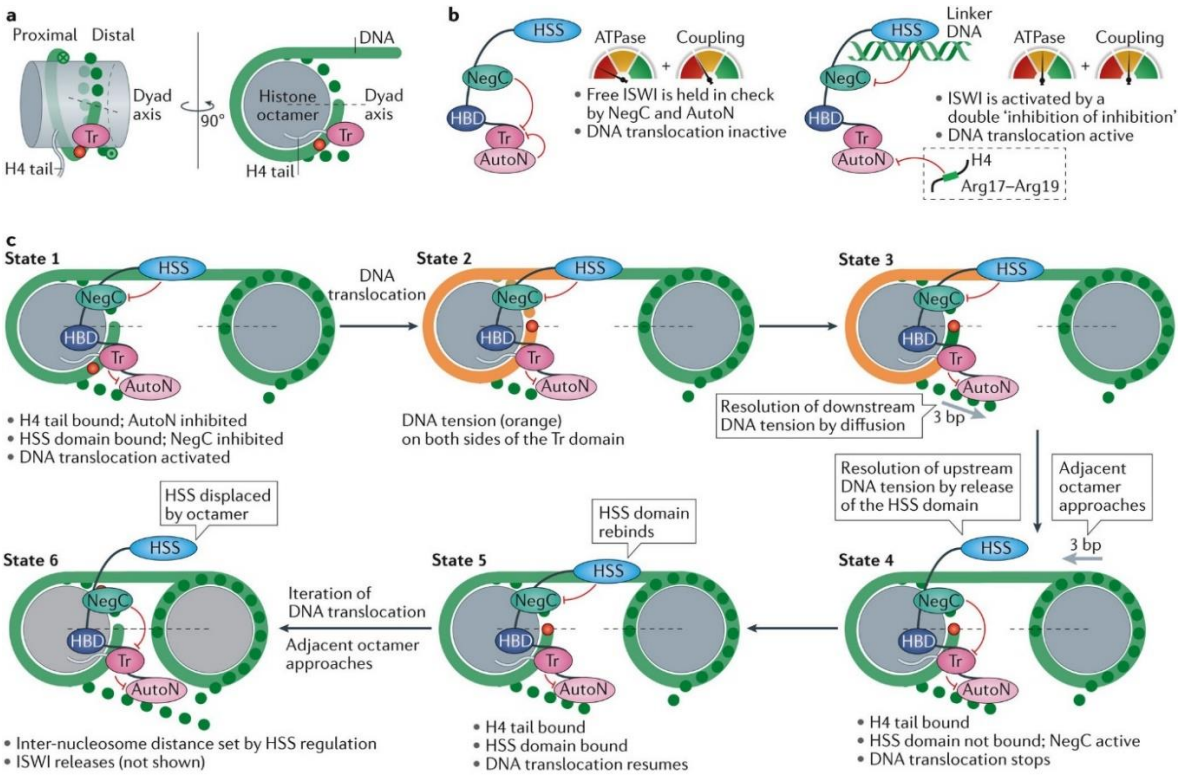

Figure 4. Model of nucleosome spacing by the ISWI complex

a. the ATPase-translocation (Tr) domain (pink) binds the nucleosome. The red circle is a reference to track DNA translocation. **b.** (left) Domain organization of *D. melanogaster* ISWI, the autoinhibitory-N-terminal (AutoN) and the negative regulator of coupling (NegC) domains inhibits the ATPase activity and coupling of the translocase domain respectively, thereby inactivating DNA translocation. (right) ISWI is activated by a double mechanism: the H4 tail and linker DNA antagonizes AutoN and NegC, respectively, promoting the ATPse activity and coupling. **c.** State 1: ISWI is anchored to the octameric histone by its histone binding domain (HBD) domain. Upon interaction between the H4 tail and ISWI, the AutoN domain inhibition is released. Meanwhile the HAND-SANT-SLIDE (HSS) domain binds the linker DNA, which releases NegC inhibition, which then promotes DNA translocation. DNA is translocated by 3 bp, which generate a DNA tension (orange) on both the proximal and distal side of the Tr domain (state 2). On the distal side, the tension is resolved by diffusion of the 3bp (state 2 to 3). On the proximal side, the HSS releases the linker DNA, then 3bp DNA enters the nucleosome which resolves the DNA tension (state 3 to 4). Therefore, the proximal nucleosome approaches by 3bp (state 4) and the HSS domain binds again the linker DNA (state 5). This mechanism of DNA translocation is reiterated resulting in the progressive approach of the adjacent nucleosome (state 5 to 6). At some point, the adjacent nucleosome is close enough and hampers HSS re-binding to the linker DNA, which causes inhibition of NegC. Thus, the inhibition of translocation and the release of the ISWI remodeler from the nucleosome occur. These mechanism sets a precise inter-nucleosome spacing (Cedric R. Clapier et al. 2017).

Chromatin access is mediated mainly by SWI/SNF. Chromatin access consists in sliding nucleosomes on the DNA, eviction of histone dimers or ejection of a complete histone octamer. These roles are performed mainly by the SWI/SNF remodeler and are required to expose DNA binding sites on promoter and enhancer regions to co-activators and co-repressors complexes, as well as to DNA repair and recombination factors (Figure 5) (Boeger et al. 2004).

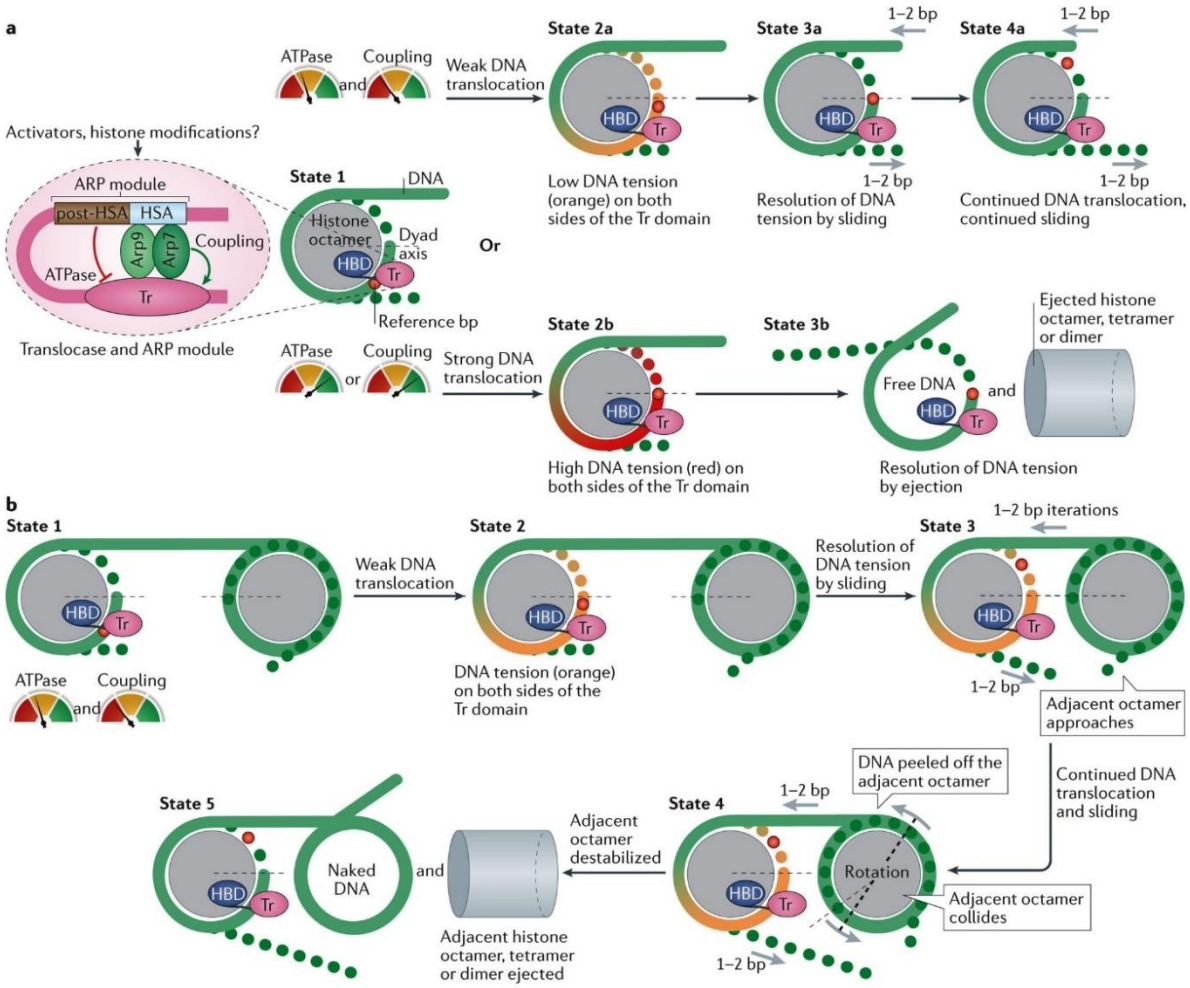

Figure 5. Model of SWI/SNF mechanism causing histone ejection

a.The actin-related protein ARP9 and ARP7 regulates both the ATPase and coupling activities of the ATPase-translocase domain (Tr). The Tr interacts with two helical turns away from the nucleosome dyad and anchors the octamer with its histone-binding domain (HBD). The Tr translocates 1-2 bp of DNA through the surface of the nucleosome which causes DNA tension on both sides of the Tr domain. Low ATPase activity and low coupling generates weak DNA tension that is resolved by sliding. However, high ATPase activity (mediated by the Post-has domain) and high coupling (mediated by the ARP-HAS interaction) mediate strong translocation. This causes high DNA tension and rupture of the histone-DNA interactions leading to the ejection of the histone octamer. b. Alternatively, the iterated process of low-to-moderate DNA translocation leads to the approaching of the adjacent nucleosome and collision with the remodeler-bound nucleosome which causes DNA peeling and histone ejection by "spooling" of the adjacent nucleosome (Cedric R. Clapier et al. 2017).

Nucleosome editing allows the deposition or removal of histone variants, it is carried out by remodelers of the INO80 subfamily in a replication-independent manner. For instance, the INO80C subtype replaces the histone variant H2AZ-H2B dimer for the canonical H2A-H2B dimer (Watanabe et al. 2015). The DNA tension of both sides of the Translocase domain is resolved by the destabilization of DNA contacts to the adjacent H2A-H2B dimer. After exchange with the H2AZ-H2B dimer, the DNA rewraps onto the histone octamer. The resulting nucleosome remains at the same position (Figure 6).

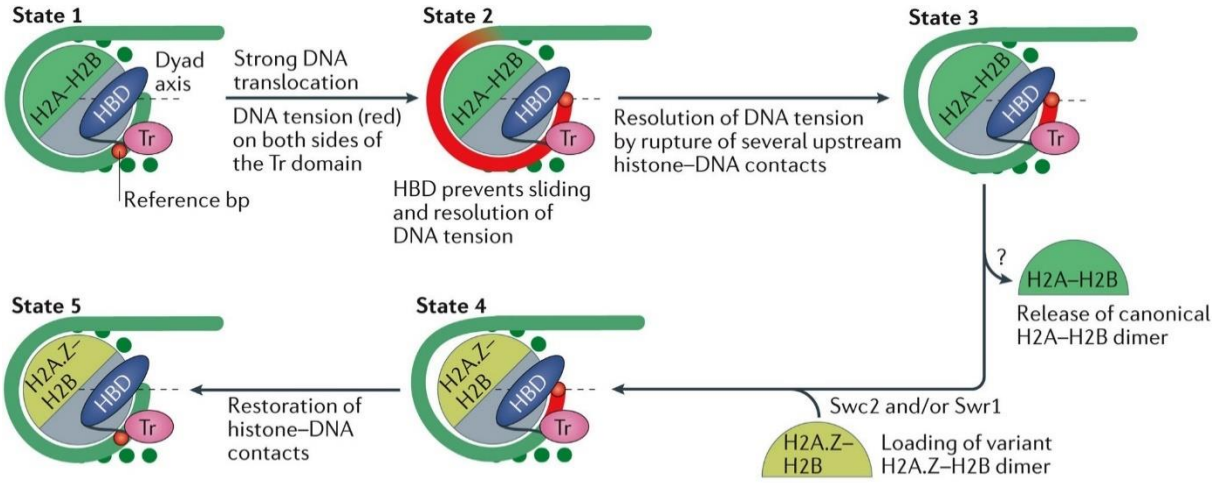

Figure 6. Model of nucleosome editing by INO80

The ATPase translocase domain (Tr) of yeast INO80 subfamily SWR1C interacts with the nucleosome two helical turns away from the dyad. INO80 is anchored to the surface of the octameric histone by the histone binding domain (HBD) (state 1). INO80 translocates 1-2 bp of DNA on the histone octamer surface, which generates DNA tension (red) on both sides of the Tr domain (state 2). On the proximal side, the DNA tension is resolved by disruption of upstream histone-DNA interactions (state 3), which leads to the release of one canonical H2A-H2B dimer and the loading of one variant H2AZ-H2B dimer by histone chaperones (state 3 to 4). After histone exchange, histone-DNA interactions are reconstituted (Cedric R. Clapier et al. 2017).

Importantly, remodelers select nucleosomes that have a particular histone modification (or histone variant) through specific domains (Suganuma and Workman 2011). These modifications can affect either positively or negatively the remodeler activity. For instance, the ISWI subfamily has a plant homeodomain (PHD) and a Pro-Trp-Trp-Asp (PWWD) domain which target methylated histones, H3K4me3 and H3K36me3 (Haitao Li et al. 2006; Santos-Rosa et al. 2003; Wysocka et al. 2006; Smolle et al. 2012). In addition, nucleosomes containing the H2AZ variant stimulates ISWI remodeling activity (Goldman, Garlick, and Kingston 2010). H4 tail stimulates the remodeling activity of ISWI; while, H4 tail acetylation weakens ISWI activity (C. R. Clapier et al. 2001; Hamiche et al. 2001; Cedric R. Clapier, Nightingale, and Becker 2002). The CHD subfamily has chromodomains that bind histone methylations (Sims et al. 2005). The SWI/SNF remodeler has a bromodomain that targets nucleosomes acetylated on H3 (Chatterjee et al. 2011). In addition, specific H3 acetylations, like H3K56ac, enhance SWI/SNF remodeling activity (Neumann et al. 2009). In the INO80 subfamily, bromodomains of SWR1C promote deposition of H2AZ on nucleosomes containing an acetylated H4 or H2A (Altaf et al. 2010). Furthermore, H3K56ac enhances the activity of the INO80C but affects nucleosome discrimination of SWR1C between H2A and H2AZ-containing nucleosomes (Watanabe et al. 2013).

1.3 Chromatin regulation by long non-coding RNAs

Long non-coding RNAs (lncRNAs) are defined as RNAs having longer than 200 nucleotides that do not encode for a protein. They are transcribed by RNA polymerase II (Pol II) or other polymerases, they have an m^7G cap at the 5'-UTR, are polyadenylated at the 3'-UTR and also undergo splicing (Statello et al. 2021a).

Gene expression can be regulated by the opening and closing of chromatin which is mediated by long non-coding RNAs. lncRNAs can recruit chromatin modifying enzymes to gene promoters to activate or repress transcription in cis or trans (Yap et al. 2010; Holdt et al. 2013). For instance, lncRNA *HOTTIP* regulates the gene cluster *HOXA*. *HOTTIP* interacts to the 5' region of the *HOXA* gene cluster through chromatin looping. *HOTTIP* recruits the methyltransferase complex WDR5/MLL to the *HOXA* gene cluster promoters, where WDR5/MLL mediates H3K4me3, which promotes gene expression (Figure 7a) (Luo et al. 2019; K. C. Wang et al. 2011). Furthermore, lncRNAs can acts as decoys of chromatin modifiers, through sequestration of chromatin modifiers from promoters of target genes. For instance, p53-regulated and embryonic stem cell-specific lncRNA, *lncPRESS1*, sequesters SIRT6 from promoter of pluripotency genes (Jain et al. 2016). Thereby, promoters of pluripotency genes maintain their acetylation state at Histone 3 lysine 56 (H3K56) and Histone 3 lysine 9 (H3K9), leading to pluripotency genes expression. However, when *lncPRESS1* is depleted, SIRT6 removes acetylated marks H3K56ac and H3K9ac from promoters of pluripotency genes, which represses pluripotency genes, therefore leading to differentiation (Figure 7b) (Jain et al. 2016).

lncRNAs can interacts directly with DNA, thus forming an R-loop structure, which is recognized by chromatin modifiers that activates or inhibits gene transcription (Beckedorff et al. 2013; Gibbons et al. 2018). R-loops can also be recognized by transcription factors (Boque-Sastre et al. 2015). The lncRNA TCF21 antisense inducing demethylation, lnc*TARID*, forms a R loop at the promoter of transcription factor 21 (*TCF21*) gene (Arab et al. 2019). The R loop is recognized by GADD45A, which recruits the DNA demethylase TET1 to the promoter of *TCF21*, thereby inducing transcriptional activation of *TCF21* (Figure 7c) (Arab et al. 2019).

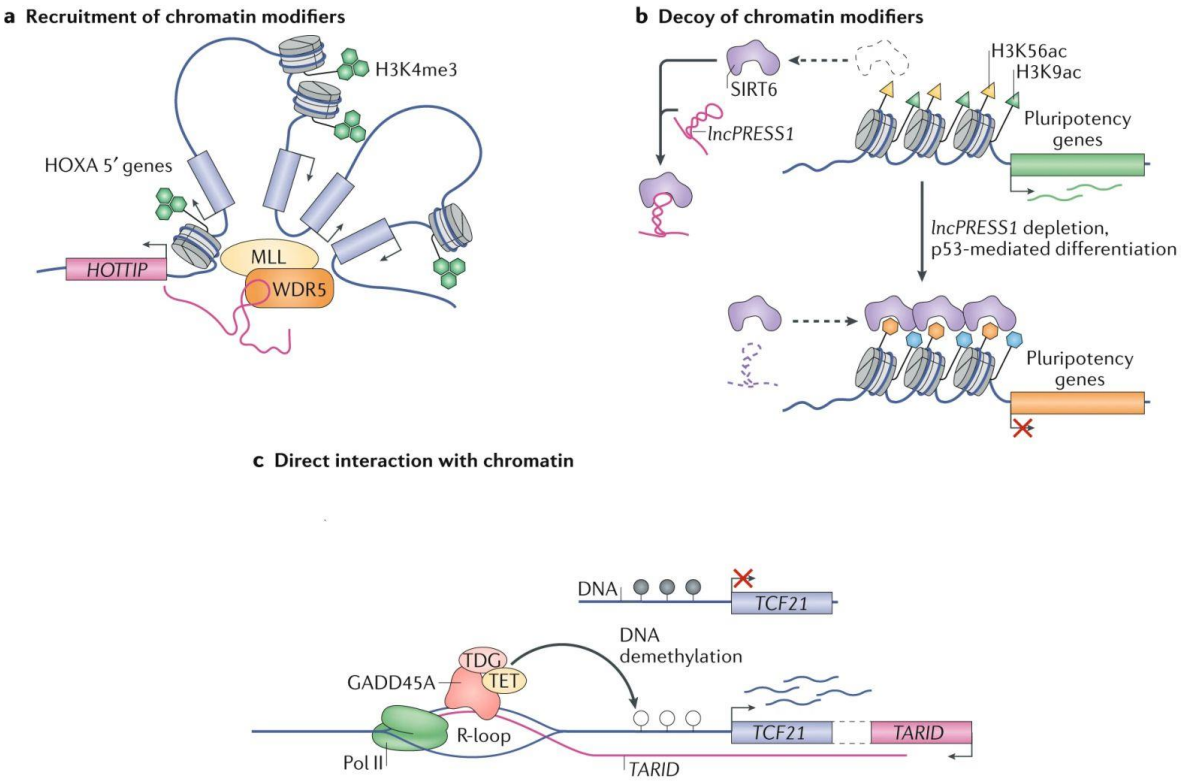

Figure 7. Chromatin regulation by non-coding RNAs

a.The long non-coding RNA (lncRNA) *HOTTIP*, interacts through chromatin looping with the *HOXA* gene cluster. *HOTTIP* recruits the WDR5-MLL methyltransferase, which mediates H3K4me3 at the promoter of *HOXA* genes, thus promoting gene expression. **b.** The *lncPRESS1* sequesters SIRT6 from promoters of pluripotency genes to maintain active gene markers H3K56ac and H3K9ac, thus favoring pluripotency. Upon p53-mediated differentiation or depletion of *lncPRESS1*, SIRT6 is free to remove acetylated marks, thus favoring differentiation. **c.** The lnc*TARID* forms an R-loop through its co-transcriptional interaction with DNA. This R-loop is placed upstream of its target gene *TCF1* and is recognized by GADD45A, which recruits TDG and the TET1 demethylase to remove DNA methylation from the promoter of the *TCF1* gene (Statello et al. 2021a).

Long non-coding RNAs can also regulate transcription. lncRNAs inhibit transcription in a transcript-dependent or -independent manner. For instance, in mouse extra-embryonal tissues, transcription of antisense from IGF2R non-protein coding RNA (*Airn*) causes steric hindrance and displacement of RNA polymerase II from the transcription start site (TSS) of *IGF2R*, leading to promoter methylation and silencing of *IGF2R* (Latos et al. 2012). Furthermore, *Airn* functions in trans as well since *Airn* interacts with the promoters of two imprinted distal genes, *Slc22a2* and *Slc22a3*, through a 3D chromosome conformation (Sleutels, Zwart, and Barlow 2002). Then, *Airn* recruits PRC2 which catalyzes H3K27me3 leading to gene silencing (Figure 8a) (Schertzer et al. 2019).

lncRNAs and enhancer RNAs (eRNAs) promotes expression of protein coding genes (PCGs) that are close to their enhancer through a preformed chromatin looping structure, recruiting activating chromatin complexes to the promoters of PCGs (Figure 8b) (Grossi et al. 2020; Melo et al. 2013). For instance, the lncRNA *SWINGN* (SWI/SNF interacting GAS6 enhancer non-coding RNA), recruits the SWI/SNF chromatin remodeling complex to the transcription start site of *GAS6* (Grossi et al. 2020). Furthermore, eRNAs and lncRNAs regulate transcription of distant genes by promoting chromatin looping through their interaction with the scaffold proteins Mediator and Cohesin (Kagey et al. 2010). Thereby enhancer and promoters separated megabases apart from each other can interact (W. Jiao et al. 2018). For instance, upon oestrogen receptor (ER) transcription activation, *NRIP1* enhancer (e*NRIP1*) is transcribed bidirectionally (W. Li et al. 2013). *eNRIP1* recruits Cohesin, causing formation of chromatin loops which mediates interaction between NRIP1 enhancer and promoters of NRIP1 and TFF1 (Figure 8c) (W. Li et al. 2013).

lncRNAs also promotes gene expression in a transcript-independent manner (Dao et al. 2017; Paralkar et al. 2016). Transcription of lncRNA *bendr* activates an enhancer element (e) embedded into its locus. The enhancer element promotes an active chromatin state, characterized by H3K4me3 mark, at the promoter of the proximal gene *Bend4* (Figure 8d) (Engreitz et al. 2016). Furthermore, lncRNAs *Uhn* and *Hdn* regulate *Hand2* expression (K. M. Anderson et al. 2016; Ritter et al. 2019). An enhancer element embedded in *Uhn* promotes transcription of the proximal gene *Hand2* when the lncRNA *Uhn* is transcribed (K. M. Anderson et al. 2016). In contrast, chromatin looping mediated by CTCF is required for spatial proximity between *Hdn* promoter and *Hand2* regulatory elements. During transcription of *Hdn*, enhancers of *Hand2* became unavailable for activation of *Hand2* promoters, causing inhibition of *Hand2* expression (Ritter et al. 2019). Therefore, removal of *Hnd* or decreased transcription of *Hnd* induces increased expression of *Hand2* (Figure 8e) (Ritter et al. 2019).

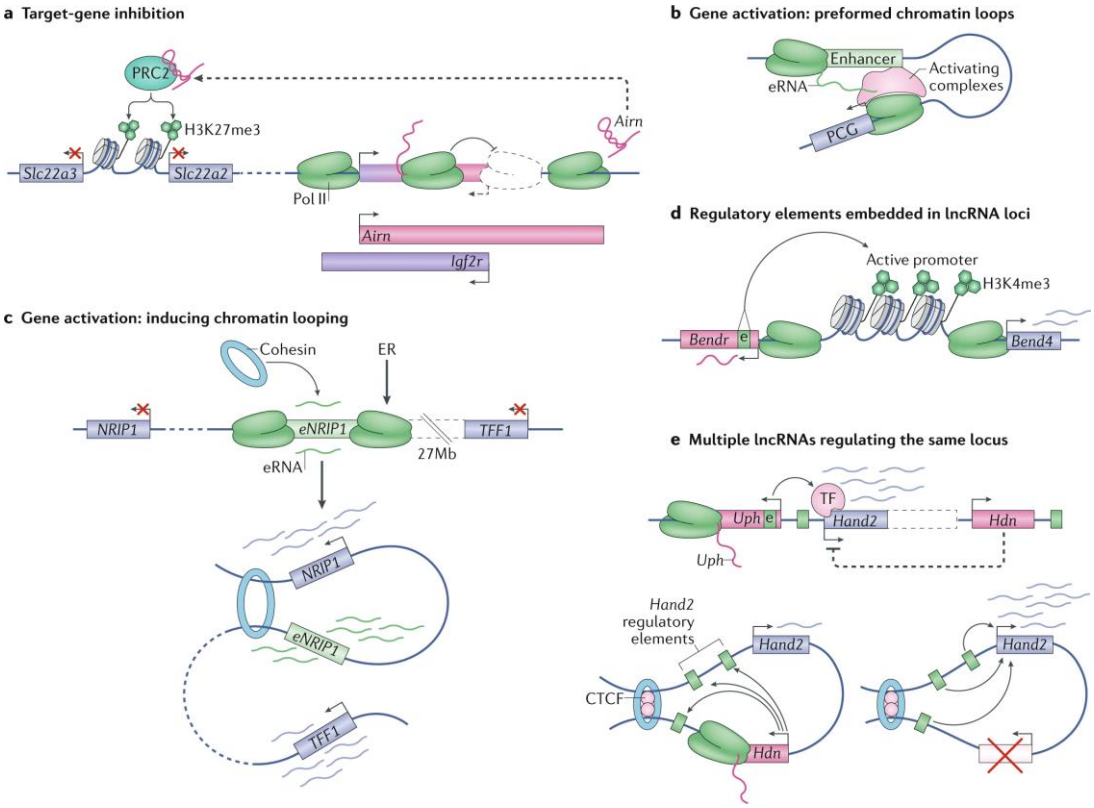

Figure 8. Transcription regulation by long non-coding RNAs

a.The lncRNA *Airn* regulates the promoters of two distal genes *Slc22a2* and *Slc22a3*. Airn recruits at these promoters the PCR2 complex, which mediates the trimethylation of H3K27, causing gene silencing. Furthermore, *Airn* and the insulin-like growth factor receptor 2 (*Igfr2*) genes overlaps; thus, *Airn* transcription causes steric hindrance for pol II at the transcription start site of *Igfr2*, which causes *Igfr2* silencing. **b.** lcnRNA and enhancer RNA (eRNA) that are in close proximity, through preformed chromatin loops, to protein coding genes (PCGs), recruit chromatin-activating complexes to promoters of PCGs to activates their expression. **c.** lncRNAs and eRNAs can also regulate distal genes, through chromatin looping. Upon estrogen receptor (ER) transcription activation, the *eNRIP1* is transcribed bidirectionally into eRNA which recruits cohesin. Cohesin promotes formation of chromatin loops, which mediates interaction between e*NRIP*1 and promoters of *NRIP1* and *TFF1* genes. **d.** Transcription of the lncRNA *Bendr* activates enhancer elements (e) placed within the *Bendr* locus, which promotes deposition of the active histone mark H3K4me3 at the promoter of the *Bend4* gene. **e.** lncRNAs *Uph* and *Hdn* regulate the *Hand2* gene. During transcription of *Uph*, an enhancer element is activated, which promotes *Hand2* transcription. Through chromatin looping, *Hdn* promoter comes in spatial proximity to enhancer elements of *Hand2*. During *Hdn* transcription, enhancer elements of *Hand2* become unavailable for *Hand2* promoter activation, and *Hand2* expression is inhibited. Decreased *Hdn* transcription promotes *Hand2* expression. (Statello et al. 2021a).

Deregulation of lncRNAs have been associated with neurodegenerative diseases, for instance *BACE1-AS* (antisense) promotes *BACE1* mRNA stability, which increases amyloid plaques in the brain of patients affected by Alzheimer disease (C.-W. Wei et al. 2018; Faghihi et al. 2010). LncRNAs are also associated with cancer, they are transcriptionally regulated by oncogenic or tumor-suppressor transcription factors. For instance, upon DNA damage, p53 regulates transcription of *lincRNA-p21*. *lincRNA-p21* recruits heterogeneous nuclear

ribonucleoprotein K (hnRNPK) leading to repression in trans of target genes (Huarte et al. 2010). However, *lincRNA-p21* regulates gene expression in a transcript-independent manner as well, since enhancer elements within the *lincRNA-p21* locus activates *in cis* target genes e.g. *CDKN1A* (Groff et al. 2016). The lncRNA *PANDA* is induced in a p53 dependent manner, *PANDA* sequesters the transcription factor NF-YA, thereby reducing apoptosis and senescence (Hung et al. 2011). lncRNA *DINO* interacts and promotes tetramerization of p53; DINO and P53 co-localize at promoters of target genes e.g. *CDKN1A* (Schmitt et al. 2016)

1.4 DNA methylation

The mammalian genome exhibits high levels of methylation of the fifth carbon of cytosines (5-methylcitosine (5mC)) in the context of CpG dinucleotides. In contrast, several eukaryotic lineages including animals have lost CpG methylations; for instance, *D. melanogaster, C. elegans*, fission yeast and baker's yeast do not present any m5C (Raddatz et al. 2013; Zemach and Zilberman 2010).

There are three phases of DNA methylation: establishment (de novo DNA methylation), maintenance and demethylation. De novo methylation can occur in any DNA sequence and is carried out by the two writer proteins: DNA Methyl Transferase 3A (DNMT3A) and DNA Methyl Transferase 3B (DNMT3B), which at their C-terminus have the DNA Methyl Transferase domain (MTase domain) (Okano, Xie, and Li 1998; Okano et al. 1999). At their N-terminus these enzymes have the chromatin reading domains ADD (ATRX (Alpha talassaemia/mental retardation syndrome X-linked homologue)- DNMT3- DNMT3L (DNA Methyl Trnasferase 3L)) and PWWP. The inactive DNMT3L protein binds to and regulates the function of both DNMT3A and DNMT3B (Ooi et al. 2007; Bourc'his et al. 2001). The ADD domain recognizes H3K4 and allows the MTase domain to methylate the DNA (Figure 9a, right). The CpG rich regions of promoters of actively transcribed genes are excluded of methylation because these promoters are enriched in H3K4me3; the ADD domain is repelled by methylation in H3K4 (Figure 9a, left) (Piunti and Shilatifard 2016; Yingying Zhang et al. 2010). In addition, when the ADD does not bind the methylated H3K4, it binds the MTase domain causing an auto-inhibition of DNMT3 readers (X. Guo et al. 2015). In contrast, the body of actively transcribed genes are enriched in DNA methylation (Lister et al. 2009). While transcription takes place, the methyltransferase SETD2 catalyzes H3K36m3, this histone mark is recognized by PWWP domain of DNMT3; next, the MTase domain methylates the DNA (Figure 9b) (Krogan et al. 2003; X.-J. Sun et al. 2005; Dhayalan et al. 2010).

Maintenance of DNA methylation occurs during DNA replication. It is performed by the DNMT1 reader, which work in concert with UHRF1. DNMT1 has a MTase domain and a RFTS domain. DNMT1 by itself exists in an autoinhibitory form, where the RFTS domain inhibits the MTase domain (Song et al. 2011; Takeshita et al. 2011; Ishiyama et al. 2017). UHRF1 has four domains: UBL, TTD, SRA and RING domains. During replication, UHRF1 brings DNMT1 to the DNA through its UBL domain, which binds the RFTS domain of DNMT1. UHRF1 recognizes the hemimethylated CpG dinucleotide through its SRA domain at the replication fork and binds to H3K9me2 or H3K9me3 marks by its TTD domain (Bostick et al. 2007; Sharif et al. 2007). This is followed by the ubiquitylation of H3 tail by the RING domain and the release of UHRF1 from the DNA. Then, the RFTS domain of DNMT1 binds the ubiquitylated H3 tail, which releases the autoinhibition of DNMT1 and MTase domain catalyzes the CpG methylation in the daughter strand (Figure 9c) (Nishiyama et al. 2013; Qin et al. 2015).

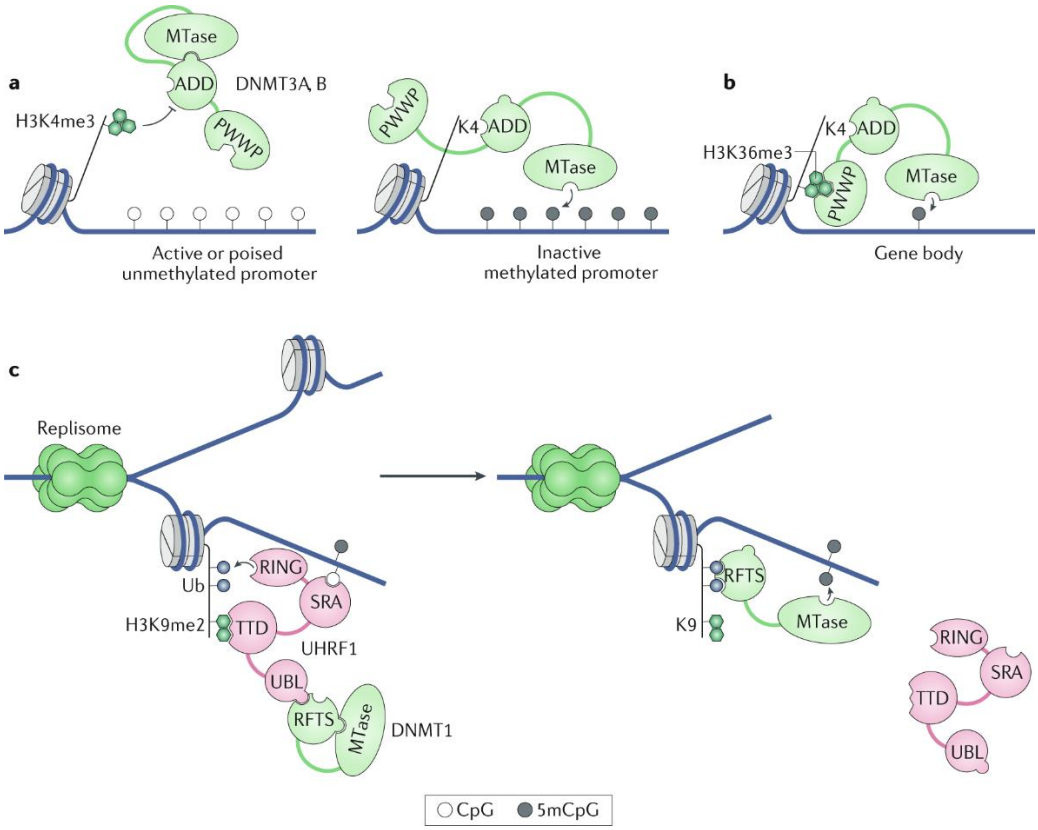

Figure 9. Two mechanisms (de novo and maintenance) of DNA methylation

a-b. *De novo* DNA methylation carried out by DNMT3A and DNMT3B. **c**. Maintenance of DNA methylation mediated by DNMT1 that works in concert with UHRF1. Adapted from (Greenberg and Bourc'his 2019)

Active DNA demethylation is performed by Ten-Eleven Translocation (TET) methylcytosine dioxygenase enzymes. These enzymes transform 5-methylcytosine (5mC) to 5-hydroxylmethylcytosine (5hmC), this later is further transformed in 5-formylcytosine (5fC) which is then converted into 5-carboxylcytosine (5caC) (S. Ito et al. 2011; Kriaucionis and Heintz 2009; Tahiliani et al. 2009). Demethylation of 5fC and 5caC can also occurs trough base removal by the thymine DNA glycosylase (TDG) enzyme, which is followed by the base excision repair pathway(Y.-F. He et al. 2011; Maiti and Drohat 2011; A. R. Weber et al. 2016). Methylated CpG readers are composed of methyl-CpG-binding domain (MBD) proteins. There are five MBD proteins in mammals: MBD1-4 and MeCP2 (methyl-CpG-binding protein 2) (Baubec et al. 2013; Nan et al. 1998).

DNA methylation is frequently associated to transcription repression but in some cases can activate transcription. DNA-methylation of CpG dinucleotides at promoters impedes binding of transcription factors, thereby repressing transcription (M. Weber et al. 2007; Yin et al. 2017). In addition, DNA methylation contribute to heterochromatin formation and gene silencing by recruiting chromatin remodelers and modifiers through DNMT or MBD proteins. For instance, DNMT3 works in complex with chromatin remodeling lymphocyte-specific helicase, H3K9 methyltransferases and histone deacetylases to promote heterochromatin formation (Tao et al. 2011; Myant et al. 2011; Dennis et al. 2001; Fuks et al. 2001). Furthermore, MBDs works in complex with chromatin remodeling and histone deacetylases complexes causing gene silencing (H.-H. Ng et al. 1999; Nan et al. 1998).

However, DNA methylation can also promote transcription activation in two ways. First, some transcription factors can bind specific methylated sequences, these transcription factors include cell pluripotency factors KLF4 and OCT4, the homeobox proteins HOXB13, KNX neural patterning factors and C/EBPα (important for differentiation of keratinocytes)(Yin et al. 2017; S. Hu et al. 2013; Rishi et al. 2010). For instance, C/EBPα and KLF4 recruit the demethylase TET2 to enhancers during cell-type reprogramming resulting in transcription activation (Figure 10a) (Sardina et al. 2018). Second, genes repressed by H3K27me3 mark, deposited by PRC2 (polycomb repressive complex 2), does not exhibit methylated CpGs (Yuanyuan Li et al. 2018; Statham et al. 2012). However, binding of DNMT3 to these genes repels the PRC2 complex, thereby H3K27me3 is lost leading to transcription activation (Figure 10b) (H. Wu et al. 2010; Ziller et al. 2018). For instance, human FOXA gene is regulated in that fashion during endoderm development (Bahar Halpern, Vana, and Walker 2014). Similarly, in mice *Zdbf2,* gene is activated by PRC2-DNA methylation switch during

development, otherwise *Zdbf2* gene remains inactivated forever causing reduced body size (Greenberg et al. 2017).

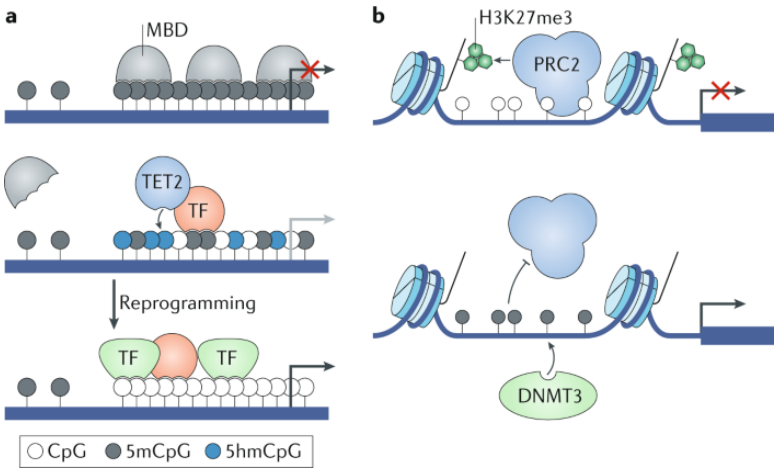

Figure 10. CpG DNA methylation promotes transcription.

a. Recruitment of some transcription factors to DNA methylated regulatory regions activates transcription. **b.** DNA methylation-mediated eviction of PRC2 from regulatory regions activates transcription. Adapted from (Greenberg and Bourc'his 2019)

The mammalian genome is CpG poor. However, over two-thirds of promoters contains CpG islands (CGI) (Larsen et al. 1992). Most inactive CGI promoters contains H3K27 methylation mediated by PRC2 (Marasca, Bodega, and Orlando 2018). However, there are three classes of genes that are life-long silenced by DNA methylation: genes on the X-inactive chromosome, imprinted genes and germline-specific genes. X-chromosome inactivation (XCI) is randomly selected and silenced by the non-coding RNA X-inactive specific transcript (Xist) (Grant, Zuccotti, and Monk 1992). SMCHD1 is required to condense the chromatin that undergoes silencing (Blewitt et al. 2008). Next methylation of the associated CpG island by DNMT3B (in mice) locks the XCI (Figure 11a) (Gendrel et al. 2012).

Parental germlines contain imprinting control regions (ICRs) (Proudhon et al. 2012). In the oocyte, ICRs are genomic regions enriched in CpGs, they bear the sequence motif TGCCGC and they are methylated (Quenneville et al. 2011). During oocyte growth, DNA methylation of gene bodies and intergenic CGIs, is accomplished by DNMT3A/DNMT3L in a transcription dependent manner. During early embryogenesis there is a global DNA methylation erasure and re-establishment, but ICRs withstand DNA methylation reprogramming and force mono-allelic expression of neighboring genes. Methylated ICRs is recognized by ZFP57 which recruits KAP1, DNMTs and other silencing factors to maintain allele-specific methylation post-fertilization (Figure 11b) (Messerschmidt et al. 2012).

Methylation of CGI-containing promoters of germline specific genes promotes their repression. It is proposed that a Polycomb repressive complex 1 (PRC1) variant PRC1.6 is recruited to these promoters to repress them (Stielow et al. 2018; Endoh et al. 2017). PCR1.6 recruits GLP/G9A complex that catalyzes H3K9me2 mark. Next, PRC1.6 is released. The H3K9me2 histone mark promotes the recruitment of DNMT3B that performs DNA methylation at the onset of somatic differentiation (Figure 11c) (Velasco et al. 2010).

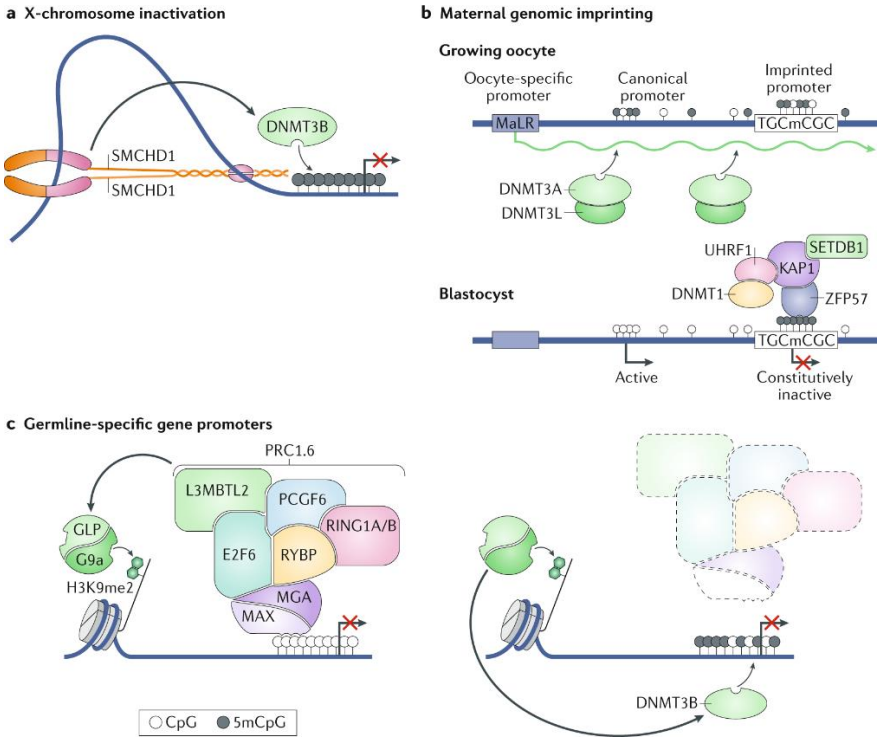

Figure 11. Methylation of CpG island (CGI)-containing promoters.

a. X chromosome inactivation (XCI) by XIST RNA requires SMCHD1. Lastly methylation of a linked CpG island by DNMT3B locks the XCI. **b.** In the oocyte, imprinted control regions (ICRs) are methylated and recruits ZFP57, KAP1 and another silencing factor. Thereby methylated ICRs withstand DNA methylation reprograming during early embryogenesis **c**. Model of repression of germline-specific genes by CGI DNA methylation at their promoters. Adapted from (Greenberg and Bourc'his 2019)

The main targets of mammalian DNA methylation are retrotransposons to silence them (Yoder, Walsh, and Bestor 1997). In mice, DNMT3C is a de novo methylation enzyme that is expressed in male fetal germ cells (Barau et al. 2016). DNMT3C methylates promoters of transposable elements in concert work with piwi interacting RNAs, thereby causing their transcriptional repression (Aravin et al. 2008). DNA methylation is also observed in gene bodies. Two hypothesis have been proposed about its function. First, it facilitates transcriptional elongation and co-transcriptional splicing (Shukla et al. 2011; Gelfman et al. 2013; Maunakea et al. 2013). Second, it represses intragenic cryptic promoters (Neri et al. 2017; Maunakea et al. 2010).

DNA methylation has been observed to change during development (Figure 12). Post fertilization, the zygote (one-cell stage embryo) losses gamete-specific DNA methylation patterns as it progresses to pluripotency, this is achieved in two phases. First, from fertilization to the two-cell stage, an active demethylation, primarily of the paternal genome, is mediated by TET3 (Iqbal et al. 2011; Gu et al. 2011). Second, from the two-cell stage to the blastocyst stage, the two parental genomes are passively demethylated, i.e. DNA methylation is diluted in a DNA replication dependent manner, since the DNMT1 is excluded from the nucleus (Howell et al. 2001). However, imprinted control regions (ICR) and transposable elements retain the inherited DNA methylation (Lu Wang et al. 2014). During post blastocyst implantation, levels of CpG methylation increases due to DNMT3A, DNMT3B and DNMTL. In the epiblast, some cells specialize to primordial germ cells (PGCs), they undergo a two-step demethylation. First a passive demethylation (Guibert, Forné, and Weber 2012; Vincent et al. 2013). Second, an active demethylation mediated by TET1 and TET2 which affects mainly germline-specific genes and imprinted control regions (ICR) as a prerequisite for male and female germline differentiation (Hackett et al. 2013). However, retrotransposons still retain inherited DNA methylation (Lane et al. 2003). Finally, the male gamete become highly methylated (80% of CpG methylation) before birth due to DNMT3A and DNMT3L (Lu Wang et al. 2014). The genome oocyte reaches 50% of CpG methylation (mostly at gene bodies) post meiosis and before ovulation through DNMT3A (Smallwood et al. 2011; Kobayashi et al. 2012). The hypomethylation in oocytes is associated with the sequestration of DNMT1 in the cytoplasm (Yingfeng Li et al. 2018).

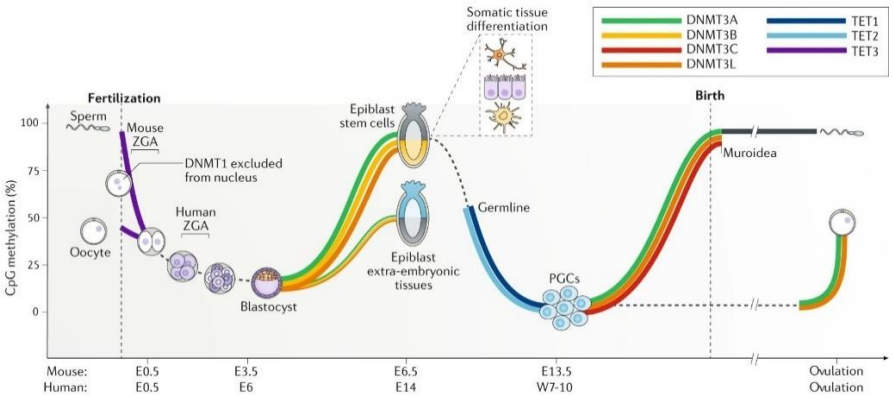

Figure 12. DNA methylation erasure and establishment in development

Two phases (passive and active) of global DNA demethylation are undergone by the zygote and cells acquiring germline identity. The active phase in the zygote is mediated by TET3, while in germline specification is mediated by TE1 and TET2. The blastocyst (post implantation) and primordial germ cells (PGCs) undergoes reimplantation of DNA methylation mediated by DNMT3. Adapted from (Greenberg and Bourc'his 2019)

Several diseases are associated to mutations in writers and TET2 eraser of DNA methylation. For instance, heterozygous mutations in *DNMT1* have been identified in autosomal-dominant forms of progressive cognitive and behavioral deterioration, which include: hereditary sensory autonomic neuropathy 1E (HSAN1E) and autosomal-dominant cerebellar ataxia, deafness and narcolepsy (ADAC-DN) (Klein et al. 2011; Winkelmann et al. 2012). In HSAN1E mutations cluster in the N-terminal and middle part of the RSTF domain of DNMT1 (Klein et al. 2011). While in ADAC-DN, mutations cluster in the C-terminal part of the RFTS domain (Winkelmann et al. 2012).

Recessive mutations in *DNMT3B*, that reduces its catalytic activity, causes the immunodeficiency, centromeric instability and facial abnormalities (ICF) syndrome. A hallmark of ICF is hypomethylation of centromeric repeats (Ueda et al. 2006). Heterozygous, germlines mutations of *DNMT3A* are associated with growth abnormalities. Missense, gain-of-function mutations in the PWWP domain of DNMT3A is associated with microcephaly and dwarfism (Heyn et al. 2019). These mutations affect the interaction of DNMT3A with histone mark H3K36me3. In contrast, heterozygous, haploinsufficiency mutations of *DNMT3A* causes Tatton-Brown-Rahman syndrome (TBRS also known as overgrowth syndrome); it is characterized by macrocephaly and intellectual disability (Tatton-Brown et al. 2014). Furthermore, loss-of-function missense mutation (R882) in the MTase domain of DNMT3A is observed in 15~35% of acute myeloid leukemia (Russler-Germain et al. 2014). Mutations in TET2 are common in hematological malignances, including acute myeloid leukemia, chronic myelomonocytic leukemia, lymphomas and myeloproliferative neoplasms (Langemeijer et al. 2009; M. Ko et al. 2010; Rasmussen et al. 2015).

1.5 Histone modifications

The amino-terminal tail of histones is mainly targeted by modifications including methylation, phosphorylation, acetylation and others. Histone acetylation is generally associated with transcriptional activation; in contrast, depending on the position of the lysine methylated, histone methylation associates with different chromatin states. Histone modification either favors or impedes the recruitment of effector proteins.

1.5.1 Histone methylation

The most studied histone methylations occur at histone H3 and H4, they include methylation at position H3K4, H3K9, H3K27, H3K36, H3K79 and H4K20. Di and trimethylations of H3K4, H3K36 and H3K79 are associated to gene activation. H3K4me3 marks gene promoters

and H3K36m2/m3 and H3K79m2/m3 methylation mark gene bodies (Z. Wang et al. 2008; Bannister et al. 2005; Barski et al. 2007). H3K4me1 is an activating mark of enhancers (Heintzman et al. 2007). H3K9 and H3K27 methylations are repressive marks (Bernstein et al. 2005). H3K9me3 is characteristic of heterochromatin, while H3K9me2 is present in silent or lowly expressed genes (Peters et al. 2003; J. C. Rice et al. 2003).

There are several writers of histone lysine methylations. H3K4 methylations is catalyzed by the COMPASS family (Krogan et al. 2002; Miller et al. 2001). Conserved subunits of each COMPASS complex important for their assembly include WDR5, RBBP5, ASH2L and DPY30 proteins (Ali and Tyagi 2017; Ernst and Vakoc 2012). The catalytic subunit of each member of the COMPASS family contains a SET domain. Several catalytic subunits have been identified, leading to the formation of different COMPASS complexes (Cenik and Shilatifard 2021). The subunit SET1A and SET1B catalyze demethylation and trimethylation of H3K4 (H3K4me2 and H3K4me3) throughout the genome (J.-H. Lee and Skalnik 2005; J.-H. Lee et al. 2007). MLL1/MLL2-COMPASS family catalyzes H3K4 methylations at promoters of developmental genes. They differ from the set-COMPASS complexes by the presence of Menin in place of Wdr82. MLL1-COMPASS mediates H3K4me2 at CpG islands and catalyzes H3K4me3 at promoters of developmental genes, e.g. the *Hox* cluster (P. Wang et al. 2009; Rickels et al. 2016). MLL2-COMPASS complex catalyzes H3K4me3 at bivalent promoters (D. Hu, Garruss, et al. 2013). Bivalent chromatin state exhibit both the activating and repressing histone marks H3K4me3 and H3K27me3, respectively (Bernstein et al. 2006). The bivalent chromatin state maintains chromatin in a poised state, which is important for proliferation, this state being resolved during differentiation (Mikkelsen et al. 2007). The MLL3/4-COMPASS family monomethylates H3K4 (H3K4me1) at enhancers (D. Hu, Gao, et al. 2013). These complexes have four more subunits compared to the rest of COMPASS complexes: UTX (demethylase of H3K27), PTIP, PA1 and NCOA6 (Schuettengruber et al. 2017). Active enhancers exhibits both histone marks H3K4me1 and H3K27ac, while poised enhancers contain H3K4me1 marks (D. Hu, Gao, et al. 2013). It is believed that UTX may facilitate the transition from a poised to an active enhancer through demethylation of H3K27me3 which then can be acetylated. MLL1, MLL2 and CXXC1 (from the SET1A- and SET1B-COMPAS complexes) contains the CXXC1 domain that mediates their interactions to non-methylated CpG islands (Lu Wang et al. 2017). Furthermore, the transcription factor OCT4 can recruits the SET1A-COMPASS complex and RNA polymerase II recruits the MLL1-COMPASS complex (L. Fang et al. 2016, 4; Muntean et al. 2010). Furthermore,

H4K16ac catalyzed by the MOF acetyltransferase, mediates the recruitment of the MLL4 complex to chromatin (Yi Zhang et al. 2019). Histone variant H2A.Z recruits methyltransferases complexes containing MLL1, MLL2, MLL3 and MLL4 (G. Hu et al. 2013).

Polycomb repressive complex 2 (PRC2) mediates the monomethylation, dimethylation and trimethylation of histone 3 at lysine 27 (H3K27me1, H3K27me2, H3K27me3). PRC2 core subunit is formed by four subunits: EED, SUZ12, EZH1 or EZH2 (they form the catalytic component of PRC2) and the RB binding protein 4 (RBBP4) or RBBP7 (R. Cao and Zhang 2004; Pasini et al. 2004; Piunti and Shilatifard 2016). Additional components such as JARID2, PCL1, PCL2 and PCL3 can join the core subunit which lead to formation of PRC2 variants, the additional components modulating the recruitment of PCR2 to and its activity on chromatin (van Mierlo et al. 2019). New additional components of the PRC2 complex have been identified including EPOP, PALI1, PALI2 and CATACOMB (Alekseyenko et al. 2014; Grijzenhout et al. 2016; Pajtler et al. 2018; Piunti et al. 2019). PCL proteins contain a Tudor domain that recognizes H3K36me3. It is believed that demethylases removed this mark upon PRC2 recruitment. That would explain why H3K36me3 is absent at PRC2 binding sites (Brien et al. 2012; Ballaré et al. 2012). Furthermore, PCL proteins contains at their N-terminus a region that is important for the binding of PRC2 to unmethylated CpGs (Haojie Li et al. 2017). There are two variants of PRC2 complex, the PRC2.1 and PRC2.2. The PRC2.1 has two mutually exclusive variants: the EPOP-containing PRC2.1 and the PALI-containing PRC2.1 variants; the PRC2.2 contains the JARID2 and AEBP2 subunits (Piunti and Shilatifard 2021). PRC2 core subunits are required for mammalian development, mice depleted in each of these genes encoding PRC2 core subunits die around the gastrulation state (Schumacher, Faust, and Magnuson 1996; O'Carroll et al. 2001; Pasini et al. 2004).

H3K9me3 is mediated by SUV39H1 and SUV39H2 at pericentromeric heterochromatin, while H3K9me1 and H3K9me2 are mediated by Ga9 and GLP in euchromatin (Peters et al. 2001; J. C. Rice et al. 2003). H3K79 methylation is catalyzed by DOT1 (van Leeuwen, Gafken, and Gottschling 2002). The SET domain bears the catalytic activity of these methyltransferases, however DOT1 does not present a SET domain (Q. Feng et al. 2002). Erasers of lysine methylations containing a LSD1 domain catalyze the removal of mono- and di-methylated H3K4 and H3K9 (Y. Shi et al. 2004; Metzger et al. 2005). Demethylases containing a jumonji domain demethylates mono-, di- and trimethylated lysines (Tsukada et al. 2006; Whetstine et al. 2006; Klose et al. 2006). Lysine methylation is recognized by

several domains including: chromodomain, MTB, PWWP, Tudor domain, plant homeodomain (PHD), zinc-finger and WD-repeat domain (Peña et al. 2006).

Histone methylations can play different roles. During cell differentiation and lineage specification, cells lose one histone mark in specific regions, which causes gene activation or repression. For instance, during neuronal differentiation, H3K27me3 is lost from neuronal gene promoters, while in mouse embryonic fibroblast H3K27me3 is retained and H3K4me3 is lost (Mikkelsen et al. 2007; Bernstein et al. 2006). MLL1 is important for *HoxA* and *HoxC* expression, anteroposterior skeletal patterning, and hematopoiesis (P. Wang et al. 2009; Terranova et al. 2006; Hanson et al. 1999). MLL2 has been shown to be important *HoxB* cluster expression and for development of male and female germ cells (Glaser et al. 2006; 2009; Andreu-Vieyra et al. 2010). Inactivating mutations of MLL3 and MLL4 in mice show defects in adipogenesis and myogenesis (J.-E. Lee et al. 2013). Furthemore, facultative heterochromatin is regulated by polycomb proteins, which silences genes encoding developmental regulators (Piunti and Shilatifard 2021). Constitutive heterochromatin regulates telomers, pericentromeres, transposable elements and virus-derived sequences (Allshire and Madhani 2018; Grewal and Jia 2007). Heterochromatin is characterized by the presence of H3K9 methylation and the absence of lysine acetylation (Allshire and Madhani 2018; Grewal and Jia 2007). In addition, heterochromatin associates with transcriptional silencing: H3K9me3 and HP1 participates in the formation of higher-order chromatin structure through liquid-liquid phase-separated compartments formation (Sanulli et al. 2019; Liang Wang et al. 2019).

Mutations in methylation writer proteins are associated to neurologic disorders. Mutations in components of the COMPASS family are associated to neurodevelopmental disorders (NDDs) characterized by intellectual disabilities, epileptic seizures and schizophrenic disorders. Loss of function mutation in SET1A is associated to schizophrenia (Takata et al. 2014). Mutations in SET1B are associated to intellectual disability, epilepsy (Hiraide et al. 2018). The Kabuky syndrome characterized by intellectual disability, skeletal and dental defects is caused by mutations in MLL4 (S. B. Ng et al. 2010, 2; Cocciadiferro et al. 2018). Mutations in MLL3 have been identified in autism spectrum disorders and the Kleesfstra syndrome, which is characterized by intellectual disability (Kleefstra et al. 2012; De Rubeis et al. 2014). MLL1 mutations causes the Wiedemann-Steiner syndrome characterized by intellectual disability, short stature and hypotonia (Strom et al. 2014). Mutations in PRC2

subunits causes the Weaver syndrome, which is characterized by pediatric overgrow and intellectual disability (Tatton-Brown et al. 2013).

Mutations in methylation writer proteins are associated to cancer as well. Mutations in MLL2 has been identified in patients with childhood-onset dystonia (E. Meyer et al. 2017, 2). MLL1 fusion proteins, produced from chromosomal translocations, has been identified in 10% of leukemias (Mohan et al. 2010; Rowley 1998). Loss of function mutations in MLL2, MLL3 and MLL4 are associated to cancer. Mutations in MLL2 has been identified in breast and colorectal cancers. MLL4 mutations is associated to lymphomas (Morin et al. 2011). MLL3 mutations has been observed in bladder and lung cancers (Lawrence et al. 2014). In follicular germinal center B cell lymphomas, an activating mutation of EZH2 increases the H3K27me2 and H3K27me3 activity of the PRC2 complex (Morin et al. 2010; Sneeringer et al. 2010). Diffuse intrinsic pontine gliomas show low levels of H3K27me3, these cells express CATACOMB which is an inhibitor of PRC2 complex (Pratt et al. 2020). CATACOMB is also expressed in posterior fossa type A (PFA) ependimomas (Pajtler et al. 2018; Bayliss et al. 2016). PRC2 subunits also act as tumor suppressors, for instance in malignant peripheral nerve sheath tumors (MPNST) which is characterized by absence of H3K27me2 and H3K27me3 (W. Lee et al. 2014).

1.5.2 Histone acetylation

Lysine acetylation levels are regulated by the interplay between both lysine acetyltransferases (KATs) and histone deacetylases (HDACs). KATs deposit acetylation marks in the ε-amino moiety of lysine residues, therefore known as acetyl writer. HDACs remove the acetyl mark, therefore known as acetyl eraser.

1.5.2.1 Lysine acetyltransferases (KATs)

KATs transfers the acetyl moiety from an acetyl-CoA molecule to a lysine residue on histone and non-histone proteins (Figure 13a). 37 human proteins have been reported to have histone acetyltransferase activity. They are classified into different families, the best studied KAT families being the MYST, p300/CBP and GCN5/PCAF families. Other KATs that do not belong to this families are: ATAT1, which acetylates α-tubulin, and ESCO1 and ESCO2 which acetylate the SMC3 subunit of the cohesin complex (Hou and Zou 2005; Shida et al. 2010). KATs are part of complexes, for instance the MOZ/KAT6B-ING5, HBO1-JADE, TIP60/p400, MOF-NSL, MOF-MLS, GCN5/ PCAF-SAGA and GCN5/PCAF-ATAC complexes (Figure 13b-h).

Acetylation at specific positions of histones in promoters, enhancer and the gene body have been shown to promote transcription. Promoters of actively transcribed genes are enriched in histone acetylation: H3K9ac, H2AK9ac, and H3K56ac (Z. Wang et al. 2008; Rajagopal et al. 2014). Accordingly, MOF, GCN5 and MOZ-ING5 complexes co-localize to promoters and activate transcription (Figure 14) (Ravens et al. 2014; Govind et al. 2007; Voss et al. 2012). Interactions between promoters and enhancers regulate transcription, active enhancer-promoter pairs being enriched in H3K27ac (Heintzman et al. 2009). Furthermore, p300 and CBP locate to active enhancers (Hnisz et al. 2013; Visel et al. 2009). These two KATs do not belong to defined complexes. It is believed that transcription factors recruit p300 and CBP to enhancer and promoters (Tang et al. 2013; Mujtaba et al. 2004). In addition, enhancer RNAs (eRNAs) have been shown to increase the activity of CBP leading to the deposition of H3K18ac and H3K27ac, thereby establishing an active enhancer state (Figure 14) (Bose et al. 2017). To allow the passage of Pol-II, the main body of genes are maintained in an open, transcriptionally permissive state through histones acetylation: H2AK5ac, H2BK5ac, H3K14ac and H3K23ac (Rajagopal et al. 2014). The GCN5-SAGA complex has been shown to acetylate H3 in gene bodies and the HBO1 complex mediates acetylation of H3K14ac (Figure 14) (Govind et al. 2007; Z. Wang et al. 2008; Kueh et al. 2011; Saksouk et al. 2009).

KATs work in collaboration with other chromatin modifying complexes. This crosstalk is mediated by domains found in chromatin complexes that can read different histone marks. For instance, the H3K4 methylation is catalyzed by the MLL family proteins that are associated with promoters of actively transcribed genes. KAT complexes (MOZ, KAT6B, HBO1, MOF-NLS, TIP60, GCN5 and PCAF) contains chromodomains and Tudor domains that can bind demethylated and trimethylated H3K4 (H3K4me2 and H3K4me3) histone marks. In hematopoietic progenitor cells, MLL mediates the recruitment of MOZ to *HOX* loci, leading to increased expression of *HOX* genes (Paggetti et al. 2010). In fibroblasts, MLL and MOF interact and regulate the expression of *Hoxa9*. (Dou et al. 2005). Furthermore, the YEATS domain is another example that mediates a crosstalk between chromatin complexes. TIP60 complex has the YEATS4 domain that can recognize acetylated H3 residues: H3K14ac, H3K27ac, H3K27ac-H3K18ac and H3K27ac-H3K23ac pairs (H. J. Cho et al. 2018; Hsu et al. 2018).

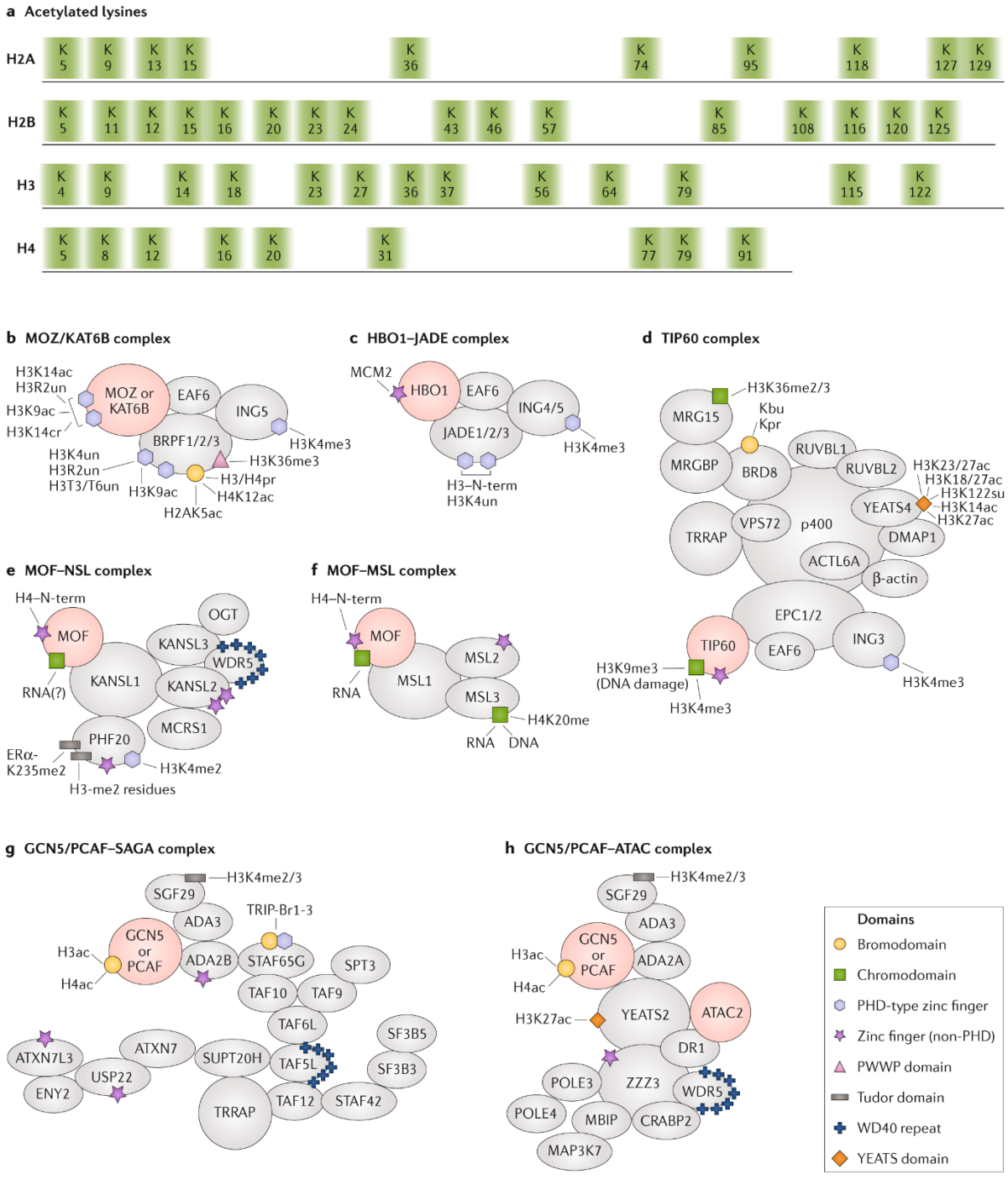

Figure 13.Acetylated positions in histones and major lysine acetyltransferases (KATs)

a. Acetylation sites on canonical histones (H2A, H2B, H3 and H4). **b-h.** Depiction of major lysine acetyltransferase (KAT) complexes: **b.** MOZ/KAT6B-ING5, **c.** HBO1-JADE, **d.** TIP60, **e.** MOF-NSL, **f.** MOF-MSL, **g.** GCN5/PCAF-SAGA, and **h.** GCN5/PCAF-ATAC. Different domains for protein interaction and crosstalk between complexes are depicted: bromodomains, chromodomains, zinc-finger, PWWP, Tudor, WD40 and YEATS domains. Ac, acetylated; bu, butyrylated; cr, crotonylated; Erα, estrogen receptor alpha; MCM2, mini-chromosome maintenance protein 2; me, methylated; N-term, amino-terminal; pr, propionylated; su, succinylated; TRIP-Br, transcriptional regulator interacting with the PHD-bromodomain proteins; un, unmodified (Sheikh and Akhtar 2019).

KATs activate transcription in a context- and cell type-specific manner. For instance, the MOZ complex regulates heart development by activating the expression of transcription factors Tbx1 and Tbx5 (Voss et al. 2012). During B cell development, MOZ maintains the proliferation of progenitor cells by activating the expression of *Meis1* and *Hoxa9*. (Sheikh et al. 2015). MOZ regulates T cell functions as well by acetylating the CD8 locus and CD8 enhancer (Newman et al. 2016). Depletion of GCN5-SAGA and MOF causes abnormalities in the anterior-posterior patterning in the developing embryo (W. Lin et al. 2008; Voss et al. 2009). GCN5 and retinoic acid stablish a correct pattern of the diencephalon (Wilde et al. 2017).

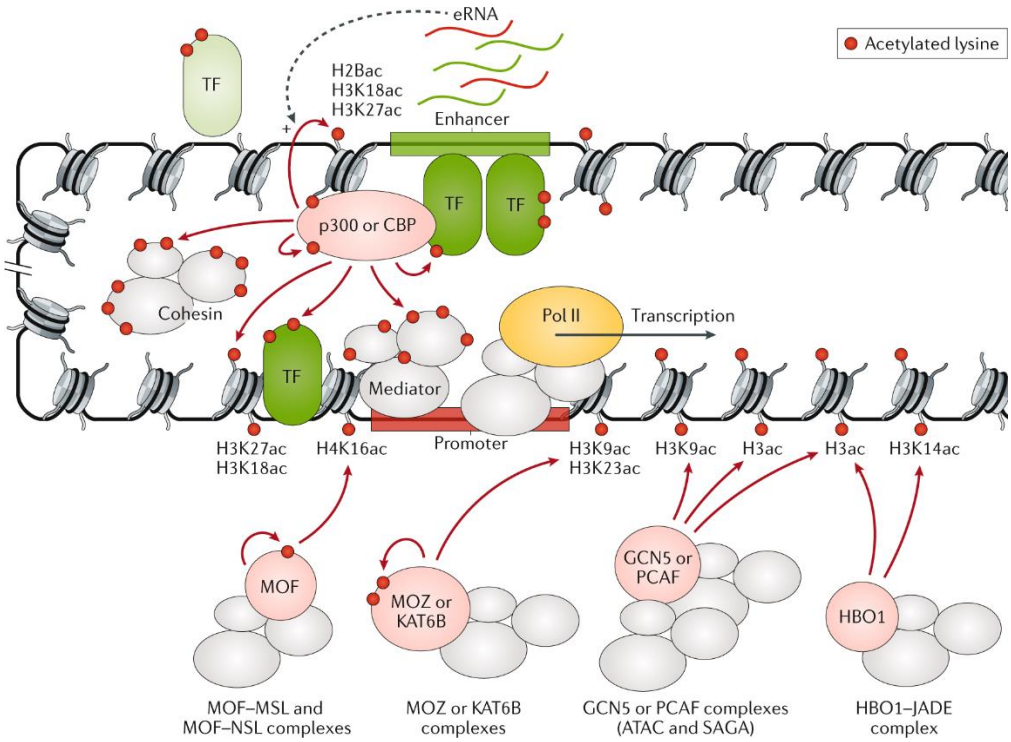

Figure 14.Histone acetylated in promoters, enhancers and gene bodies

Main lysine acetyltransferases and their substrates. P300 and CBP acetylates H2B, H3K18 and H3K27 at active enhancers and promoters. Transcription of enhancer RNAs enhances CBP acetylation activity. MOF acetylates H4K16 at promoters. MOZ and KAT6B are thought to acetylate H3K9 and H3K23, while GCN5 and PCAF acetylates H3K9 at promoters of active genes. In gene bodies, GCN5 and PCAF are thought to acetylate H3, and HBO1 acetylates H3K14. KATs also acetylates transcription factors, transcription initiation complexes (like the mediator) and chromatin remodelers (Sheikh and Akhtar 2019).

There is an interplay between acetylation and metabolism. Acetyl-CoA is produced from the breakdown of dietary energy sources. Therefore, levels of acetyl-CoA changes depending on nutrient availability (Mariño et al. 2014; Pietrocola et al. 2015). Acetyl-CoA can be produced in mitochondria, cytoplasm and the nucleus (Sadoul et al. 2011). In mitochondria, acetyl-CoA

is produced from the breakdown of fatty acids and amino acids. Furthermore, pyruvate (derived from glucose) and acetate are converted into Acetyl-CoA by the enzymes Pyruvate Dehydrogenase Complex (PDC) and Acetyl-CoA Synthetase Short Chain 1 (ACSS1) respectively (Sutendra et al. 2014; Fujino et al. 2001). In the cytoplasm, acetate and citrate (an intermediate product from the Tricarboxylic (TCA) cycle that takes place in mitochondria) can be converted into acetyl -CoA by ACSS2 and the ATP Citrate Lyase (ACL) respectively (Schug et al. 2015; Zaidi, Swinnen, and Smans 2012). The three major precursors of Acetyl-CoA (pyruvate, acetate and citrate) can diffuse into the nucleus and can be processed into Acetyl-CoA by the enzymes PDC, ACSS2 and ACL (Wellen et al. 2009; Sutendra et al. 2014; Mews et al. 2017; Comerford et al. 2014). High levels of acetyl-CoA triggers increased acetylation of mitochondrial, cytoplasmic and nuclear proteins. Increased acetylation activates genes associated to growth and energy storage in lipids, whereas genes associated with autophagy are repressed (Wan et al. 2017). However, under starvation conditions, global levels of acetylation are decreased, which leads to reduced protein acetylation and activation of NAD+ dependent lysine deacetylases known as Sirtuins (SIRT) (Mariño et al. 2014).

Transcription factors regulating metabolic pathways, such as C/EBPα, CRTC2, PGC1α and FXR, are regulated by acetylation (Zaini et al. 2018; Yi Liu et al. 2008; Lerin et al. 2006; Kemper et al. 2009). High concentration of glucoses triggers acetylation of C/EBPα by p300; in contrast, in low glucose concentration C/EBPα is deacetylated by SIRT1 (Zaini et al. 2018). Deacetylation of C/EBPα induces expression of genes involved in mitochondrial biogenesis, which leads to increase in ATP production in conditions of low glucose levels (Zaini et al. 2018). In fed conditions, GCN5 acetylates PGC1α, which inhibits PGC1α activity (Lerin et al. 2006).

KATs can also use other acyl-CoA molecules (propionyl-CoA, crotonyl-CoA, butyryl-CoA and succinyl-CoA) to modify ε-lysine residues (Figure 15). CBP and p300 can catalyze propionyalation, chrotonylation and butyrylation, though with reduced efficiency compared to acetylation (Y. Chen et al. 2007; Xiaoguang Liu et al. 2017; Sabari et al. 2015). MOF can catalyze propionylation and crotonylation (Xiaoguang Liu et al. 2017; Han et al. 2018). GCN5 can catalyze succinylation (Yugang Wang et al. 2017). MOZ, HBO1 and PCAF catalyze propionylation (Leemhuis et al. 2008; Han et al. 2018). Furthermore, acylated lysine residues can also be detected by readers domain. For instance, PHD finger domain of MOZ can bind crotonylated H3K14 (X. Xiong et al. 2016).

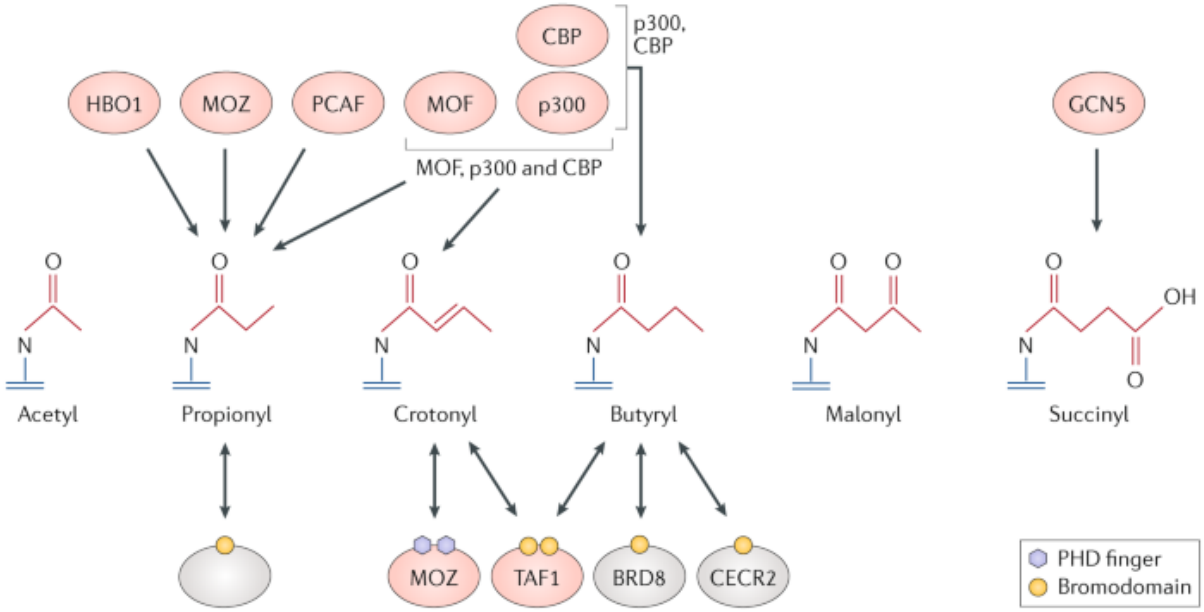

Figure 15. Acylations mediated by KATs

Different acyl-chain modification of lysines are mediated by KATs. CBP and p300 mediates propionylation, crotonylation and butyrylation. MOF mediates propionylation and crotonylation. GCN5 catalyzes succinylation, while HBO1, MOZ and PCAF mediates propionylation. The PHD finger domain of MOZ has affinity for crotonylated H3K14. Bromodomains have affinity for propionylated lysines. Bromodomains of TAF1, BRD8 and CERC2 have affinity for butyrylated lysines; the second bromodomain of TAF1 binds crotonylated lysines (Sheikh and Akhtar 2019).

Mutations in genes encoding KATs such as *CBP*, *EP300*, *MOZ*, *KAT6B*, and *ESCO2*, lead to developmental disorders, characterized by intellectual disabilities and developmental delay (Petrif et al. 1995; Roelfsema et al. 2005; Tham et al. 2015; Clayton-Smith et al. 2011; Vega et al. 2005). In addition, several other symptoms are also present like cardiac, craniofacial, genital and behavioral disorders. Furthermore, KATs can act as a tumor suppressor or oncogene, it depends on the type of cancer and KAT mutation. Translocations involving one or more KATs are pro-tumorigenic (Largeot et al. 2016; Huntly et al. 2004). Furthermore, MOZ is amplified in several cancer types (Zack et al. 2013). It is proposed EP300, CBP and TIP60 act as tumor suppressors (Mullighan et al. 2011; Gorrini et al. 2007; Peifer et al. 2012). In addition, MOF is expressed at low levels in different cancer types such as breast, ovarian, colorectal, renal, gastric and hepatocellular cancers (Pfister et al. 2008; Cai et al. 2015; L. Cao et al. 2014; Zhu et al. 2015; J. Zhang et al. 2014).

1.5.2.2 Histone deacetylases (HDACs and Sirtuins)

18 HDACs have been identified in mammalian cells. They are divided into four classes (I-IV): Class I (HDAC 1, 2, 3, 8), class IIa (HDAC 4, 5, 7, 9), class IIb (HDAC 6 and 10), class

III (Sirtuin 1-7) and class IV (HDAC 11). HDACs can be further divided into two families based on the deacetylase domain and cofactor dependence: The histone deacetylase family and the Sirtuin family. Class I, II and IV form the Histone deacetylase family that is dependent on a Zn^{2+} ion for their catalytic activity. Class III forms the Sirtuin family that depend on NAD^{+} for their catalytic activity (Figure 16) (Gregoretti, Lee, and Goodson 2004).

Class I HDACs are ubiquitously expressed and predominantly located in the nucleus. HDAC1 and HDAC2 are part of repressor complexes: SIN3, MiDAC, NuRD, and CoREST (Laherty et al. 1997; Xue et al. 1998; Ballas et al. 2001; Bantscheff et al. 2011). HDAC3 forms part of co-repressor complexes: NCOR1 and SMRT1 (Matthew G. Guenther et al. 2000; M. G. Guenther, Barak, and Lazar 2001). In contrast, HDAC8 is not part of a complex (Gregoretti, Lee, and Goodson 2004). Class II HDACs are found mainly in the cytoplasm and their deacetylase domain is located at their C-terminus. Class IIa HDACs have at their N-terminus a binding site for the DNA-binding transcription factor MEF2. They also have phosphorylation sites for 14-3-3 proteins binding (X.-J. Yang and Grégoire 2005; Parra and Verdin 2010). Class IIa HDACs form part of the of NCOR1 and SMRT1 co-repressor complex as well (Fischle et al. 2002). Because of a substitution in Class IIa HDACs of the catalytic tyrosine into histidine, these HDACs exhibit very low catalytic activity, and are rather thought to have a scaffolding role (Fischle et al. 2002). Class IIb HDACs have retained a catalytic tyrosine and exhibit an extension at their C terminus known as tail domain. Furthermore, HDAC6 shows two deacetylase domains and a C-terminal zinc finger ubiquitin-binding domain, which is important for transport of misfolded proteins to the aggresome (Kawaguchi et al. 2003). HDAC10 exhibits one deacetylase domain and a leucine rich repeat domain at its C-terminus, HDAC10 is an acetylspermidine deacetylase (Hai et al. 2017). Class IV HDACs, is composed by HDAC11 which has a defatty-acylase activity (Gao et al. 2002; J. Cao et al. 2019).

The class III KDACs are Sirtuins that are localized in different compartments, such as the nucleolus (SIRT7), the nucleus (SIRT1 and SIRT6), the cytoplasm (SIRT2) and in mitochondria (SIRT3, SIRT4 and SIRT5) (Houtkooper, Pirinen, and Auwerx 2012). SIRT4, SIRT5 and SIRT6 have a deacylation rather than a deacetylation activity. SIRT4 removes acyl moieties from methylglutaryl-, hydroxymethylglutaryl- and 3-methylglutaconyl-lysine (K. A. Anderson et al. 2017). SIRT5 is a desuccinylase, demalonylase and deglutarylase (C. Peng et al. 2011; J. Park et al. 2013; M. Tan et al. 2014). SIRT6 removes long-fatty acid acyl group from lysine residues (Jiang et al. 2013).

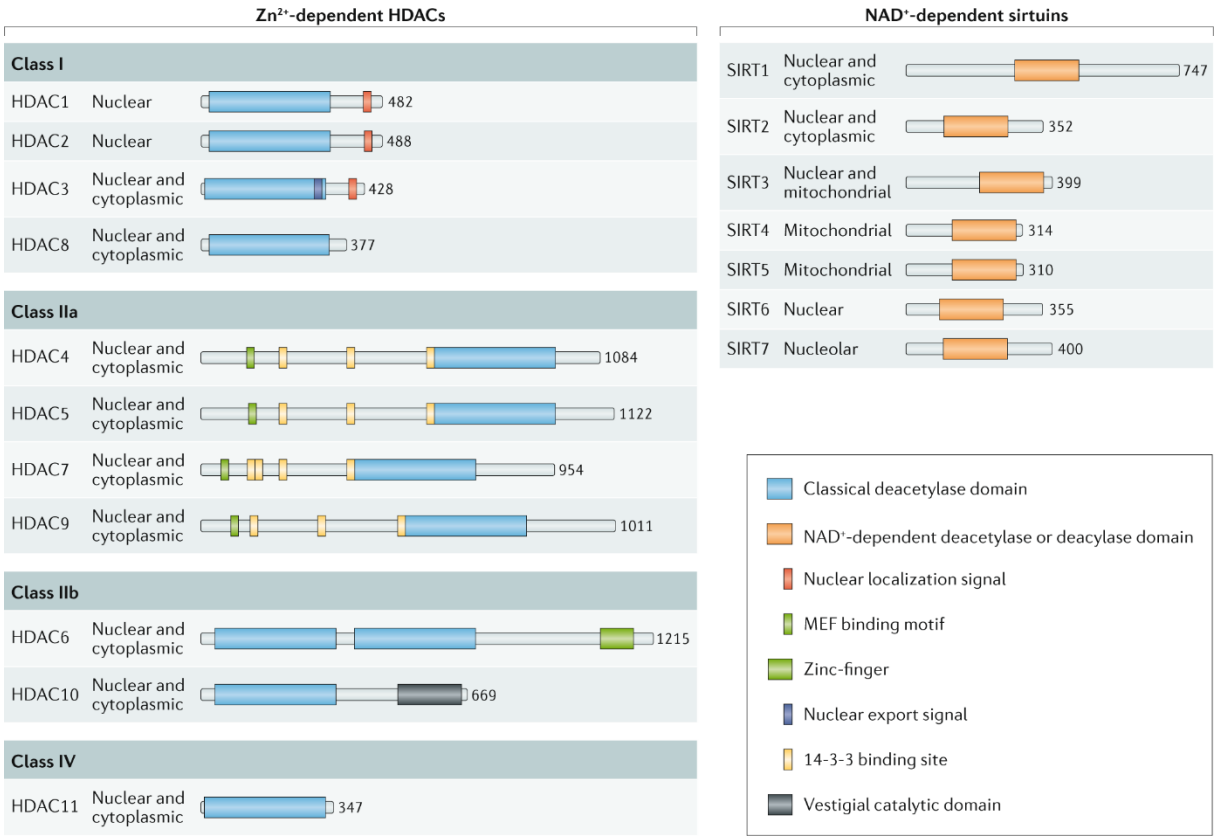

Figure 16. Histone deacetylases (HDACs) classification

Schematic representation of human HDACs. Mammalian class I, II and IV are Zn^{+}-dependent HDACs; while Class III are NAD^{+}-dependent HDACs called Sirtuins. Class I, HDAC1 and HDAC2 are catalytic subunits of the SIN3, MIDAC, NuRD, CoREST co-regulator complexes. HDAC3 is the catalytic subunit of the NCOR1 and SMRT complexes. HDAC3 associates with class IIa HDACs proteins. HDAC8 does not form part of a complex. Class II HDACs contains binding sites for MEF and 14-3-3 proteins, they have a role in nuclear-cytoplasmic transport. HDAC6 contains a zinc-finger motif, which is used for the transport of misfolded proteins. Class IV, HDAC11 interacts with HDAC6. Within class III HDACs, SIRT1, SIRT6 and SIRT7 are nuclear proteins. SIRT3, SIRT4 and SIRT5 have mitochondrial and SIRT2 cytoplasmic localization. SIRT3, SIRT4 and SIRT5 have deacylase activity rather than deacetylase activity (Ellmeier and Seiser 2018)

1.6 Zn-dependent HDAC catalytic mechanism

The proposed HDAC catalytic mechanism is based on HDAC8 structural and biochemical studies. Within HDAC8 active site a catalytic Zn^{2+} ion is coordinated by one histidine (H180), two aspartates (D178 and D267) and two water molecules (Vannini et al. 2004; Somoza et al. 2004). Upon substrate binding, the acetylated moiety of the acetylated lysine substrate replaces one water molecule, coordinates to Zn^{2+} and accepts a hydrogen bond from the catalytic tyrosine (Y306) (Vannini et al. 2007). The Y306 might undergo a conformational change from an out- conformation to an in-conformation to accommodate the substrate binding (Decroos et al. 2015). Histidine 143 (H143) acts as a general base, to assists the Zn^{2+}

in activating the water molecule; while His142 remains protonated throughout the catalytic cycle (Gantt et al. 2016). Both H142 and His143 hydrogen bond the zinc-bound water molecule to correctly position the zinc-bound water molecule for nucleophilic attack. Next, the carbonyl group of the acetylated lysine undergoes a nucleophilic attack by the zinc-bound water molecule, leading to the formation of a tetrahedral intermediate (Porter and Christianson 2017). Upon proton transfer from H143 (acting as a general acid) to the leaving amino group, the tetrahedral intermediate collapses yielding a lysine and acetate (Figure 17) (Gantt et al. 2016).

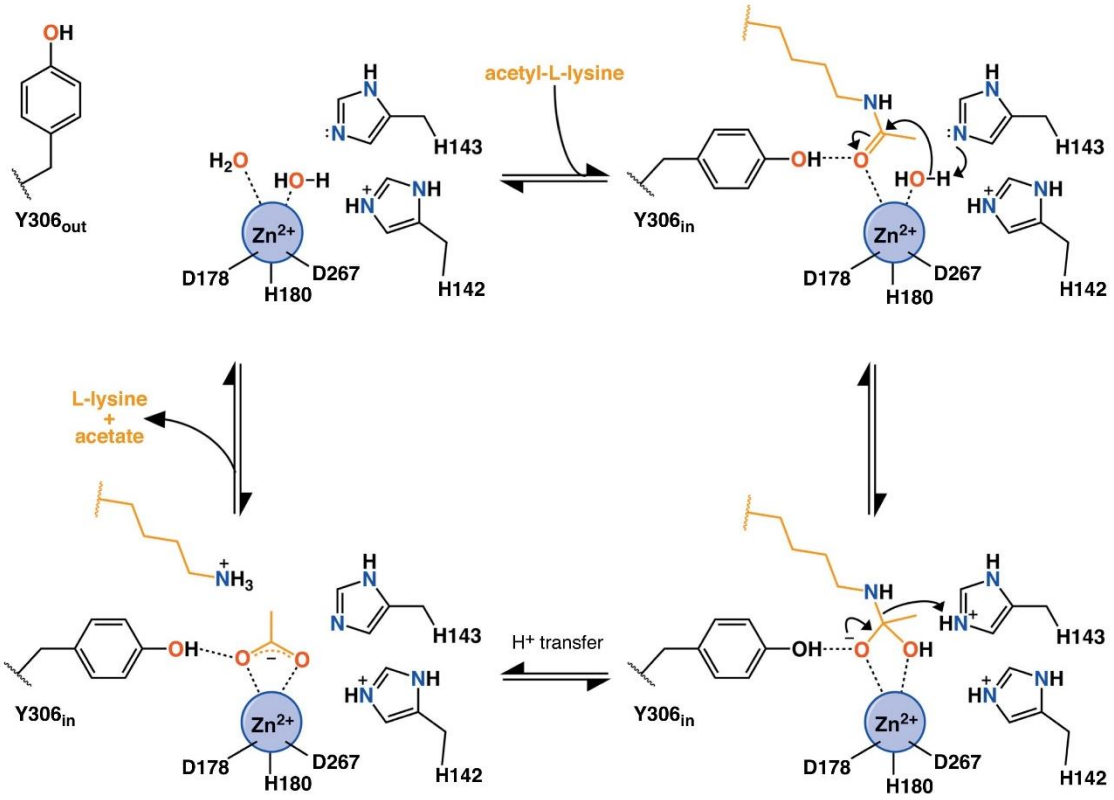

Figure 17. Catalytic mechanism of Zn-dependent HDACs

Catalytic mechanism of acetyl lysine hydrolysis as proposed for HDAC8. In the active site of HDAC8, the zinc ion is coordinated by D178, H180 and D267 and two water molecules. Upon entrance of the acetyl-lysine substrate, the acetyl group replaces one water molecule and hydrogen bonds to Tyr306 hydroxyl. H143 activates the remaining water molecule, which then performs a nucleophilic attack on the carbonyl of the acetylated lysine, leading to formation of a tetrahedral intermediate. Upon proton transfer from H143 to the leaving amino group, the tetrahedral intermediate collapses and yields lysine and acetate (Porter and Christianson 2019).

1.7 Roles of acetylation

Transcription factors, transcriptional co-activators and nuclear receptors are acetylated. For instance, p53 acetylation is important for its binding to DNA, interactions with other proteins

and activation of p53-regulated genes (Reed and Quelle 2015). Acetylation regulates several cell cycle regulators including cohesin. Acetylation of cohesin by ESCO1 and ESCO2, in the smc3 subunit, is required to lock the cohesin complex around the sister chromatids during DNA replication until mitosis (Ben-Shahar et al. 2008; Ünal et al. 2008). Deacetylation of smc3 by HDAC8 is required for release of the cohesin complex (Deardorff et al. 2012) (Figure 18a).

Acetylation regulates DNA repair. For instance, acetylation of histones H4K16 and H2AK15 by TIP60 acetyltransferase and acetylation of 53BP1 by CBP inhibits recruitment of 53BP1 to DNA double-stranded break, thereby promoting homology directed repair (HDR) pathway (Figure 18b). Acetylation regulates proteins involved in the DNA repair pathways BER (Base excision repair) and NER (Nucleotide excision repair) (Yamamori et al. 2010; W. Fan and Luo 2010; M. Zhao et al. 2017).

Cellular signaling is also regulated by acetylation. CNK1 acetylation triggers its membrane localization and interaction to RAF, which phosphorylates and activates ERK signaling, which in turn promotes cell proliferation and migration (Fischer et al. 2017, 1). SIRT2-mediated deacetylation of IRS2 triggers phosphorylation and activation of ERK signaling (Ying Li et al. 2008, 1). Levels of PIP3 are regulated by PI3K and PTEN. CBP-mediated acetylation of PTEN promotes its interaction with MAGI2, which enhances PTEN activity (Hopkins et al. 2014). PCAF- and p300-mediated acetylation of kinases AKT and PDK1 impedes their localization to the cell membrane and activity. while SIRT1-mediated deacetylation of AKT and PDK1 promotes their PIP3 binding and kinase activity (Sundaresan et al. 2011). p300-mediated acetylation of mTORC2 subunit RICTOR increases mTORC2 phosphorylation activity of AKT, which promotes cell proliferation and survival (Figure 18c).

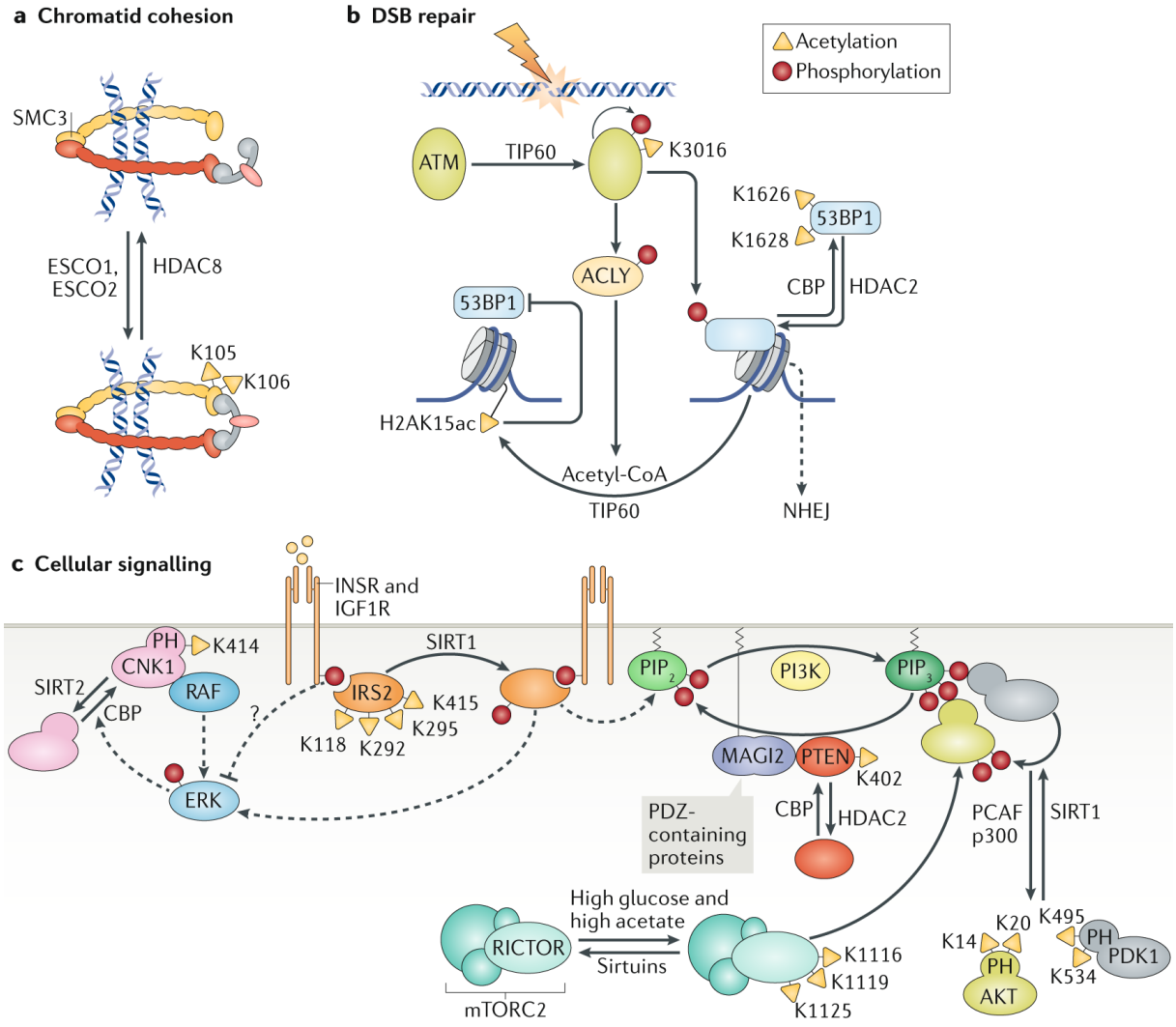

Figure 18. Roles of non-histone acetylation

a.The closure and efficient release from DNA of the cohesin ring complex is regulated respectively by acetylation and deacetylation of its smc3 subunit. **b.** In DNA double-strand breaks (DSBs), Tip60 acetylates the ATM kinase, causing its autophosphorylation. Active ATM phosphorylates 53BP1 and ACLY. Acetylation and deacetylation of 53BP1 respectively inhibits and promotes 53BP1 binding to damaged DNA. 53BP1 binding to chromatin promotes NHEJ-dependent DNA repair. However, deacetylated 53BP1 cannot bind to chromatin if H2AK15 is acetylated. ACLY produces Ac-CoA, which promotes Tip60-dependent acetylation of histones. **c**. Acetylation regulates signaling pathways. Acetylation regulates membrane localization of CNK1, which interacts with the RAF kinase and activates ERK signaling. Deacetylation of the insulin receptor substrate 2 (IRS2) promotes its phosphorylation and activation of ERK signaling. Acetylated PTEN interacts with MAGI2, which enhances PTEN activity. Acetylation of PDK1 and AKT inhibits their recruitment by PIP_3. Acetylation of RICTOR, a subunit of mTORC2, enhances its kinase activity towards AKT (Narita, Weinert, and Choudhary 2019).

Acetylation regulates cytoskeleton organization. α-tubulin is acetylated and deacetylated at Lys40 by TAT1 and HDAC6 respectively in the cytoplasm (Hubbert et al. 2002; Akella et al. 2010). Acetylation of microtubules inhibits their breakage thereby allowing long-lived microtubules (Xu et al. 2017) (Figure 19a). Cortactin can shuttle between the nucleus and the

cytoplasm. Cortactin is acetylated by CBP and p300 in the nucleus. Cortactin deacetylation, mediated by SIRT1, SIRT2 or HDAC6, is required for its interaction to KEAP, which keeps cortactin in the cellular cortex. Cortactin binds to F-actin, thereby promoting actin cellular organization and cell migration (X. Zhang et al. 2007; A. Ito et al. 2015; Y. Zhang et al. 2009, 1) (Figure 19b).

Acetylation also modulates protein aggregation. Acetylation of TDP43 inhibits its binding to RNA, and promotes aggregation of phosphorylated TDP43, which constitute a hallmark of Amyotrophic lateral sclerosis (Cohen et al. 2015) (Figure 19c). Acetylation of Tau at different sites modulates its activity. Acetylation of Tau in the microtubule-binding site K280 prevents its binding to the microtubule and leads to aggregation of acetylated Tau, which is observed in Alzheimer's disease and corticobasal degeneration (Cohen et al. 2011). However, acetylation of Tau at K259 and K353 prevents Tau phosphorylation at Ser262 and Ser356, thereby inhibiting aggregation of hyperphosphorylated Tau (Cook et al. 2014) (Figure 19d). RNA processing is also regulated by acetylation. CBP-mediated acetylation of both cleavage factor Im 25KDa (CFIm25), which is part of the CFIm complex, and poly(A) polymerase (PAP) complex inhibits polyadenylation of mRNAs. Interaction of cleavage factor CFIm25 to PAP is affected by their acetylation. Furthermore, the acetylated PAP complex is exported to the cytoplasm (Shimazu, Horinouchi, and Yoshida 2007). Acetylation also promotes RNA decay. The CCR4-associated factor 1 (CAF1, also known as CNOT7), the catalytic subunit of the CCR4-NOT deadenylase complex, is activated by CBP- or p300-mediated acetylation, thereby triggering RNA decay (Sharma et al. 2016) (Figure 19e).

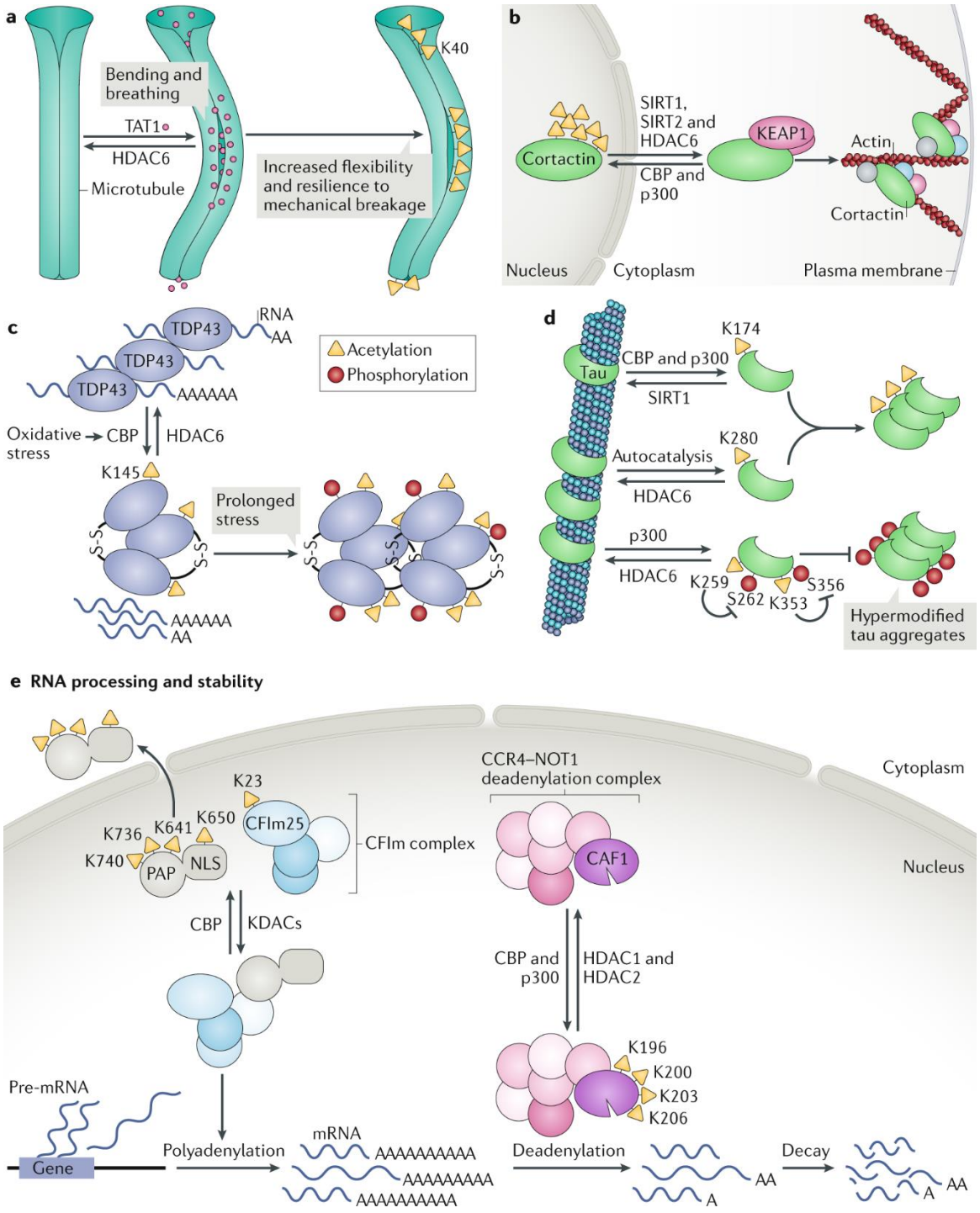

Figure 19. Roles of non-histone protein acetylation

a.Acetylation of α-tubulin increases microtubule resistance to breakage. **b.** Deacetylated cortactin binds to the KEAP1 protein, which promotes cortactin localization in the cellular cortex. Cortactin binds to F-actin and promotes actin cytoskeleton reorganization and cell migration. **c.** CBP-dependent acetylation of TDP43 causes TDP43 dissociation from RNA and TDP43 aggregation. Under continuous stress, TDP43 accumulates in a hyperphosphorylated form. **d.** Acetylation of the Tau protein at Lys174 and Lys280 promotes it aggregation. Tau acetylation at Lys259 and Lys353 prevents Tau phosphorylation at Ser262 and Ser356 respectively and its aggregation. **e.** Acetylation of CFIm25 and polyA polymerase (PAP) inhibits their interaction and promotes PAP nuclear export. Acetylation of CAF1, the catalytic component of the deadenylase complex CCR4-NOT1, promotes mRNA decay (Narita, Weinert, and Choudhary 2019).

Acetylation regulates Autophagy. During nutrient-rich condition, mTORC1 phosphorylates and activates p300 acetyltransferase, which promotes lipogenesis and inhibits autophagy (Wan et al. 2017). p300-mediated acetylation of LC3, ATG5, ATG7 and ATG12 inhibits the formation of autophagosomes (I. H. Lee and Finkel 2009). Furthermore, p300-mediated acetylation of beclin1 promotes recruitment of Rubicon to the UVRAG complex, thereby inhibiting autophagosome maturation, by inhibiting fusion of autophagosomes and lysosomes (T. Sun et al. 2015, 1; Funderburk, Wang, and Yue 2010). During nutrient starvation conditions, the kinase GSK3 phosphorylates and activates TIP60 acetyltransferase (S.-Y. Lin et al. 2012). TIP60 acetylates the kinase ULK1, which activates autophagy by phosphorylating and activating the complex that converts phosphatidylinositol in phospathydilinositol-3-posphate in autophagosome biogenesis-related membrane (Zhong et al. 2009; Obara et al. 2008). SIRT1-mediated deacetylated LC3 can interact to DOR, which causes LC3 export to the cytoplasm (R. Huang et al. 2015). SIRT-mediated deacetylated ATG5, ATG7 and ATG12 transfer LC3 to the autophagosome membrane (I. H. Lee et al. 2008, 1). Thus, deacetylation of ATG proteins and beclin1 promotes autophagosome formation (Figure 20).

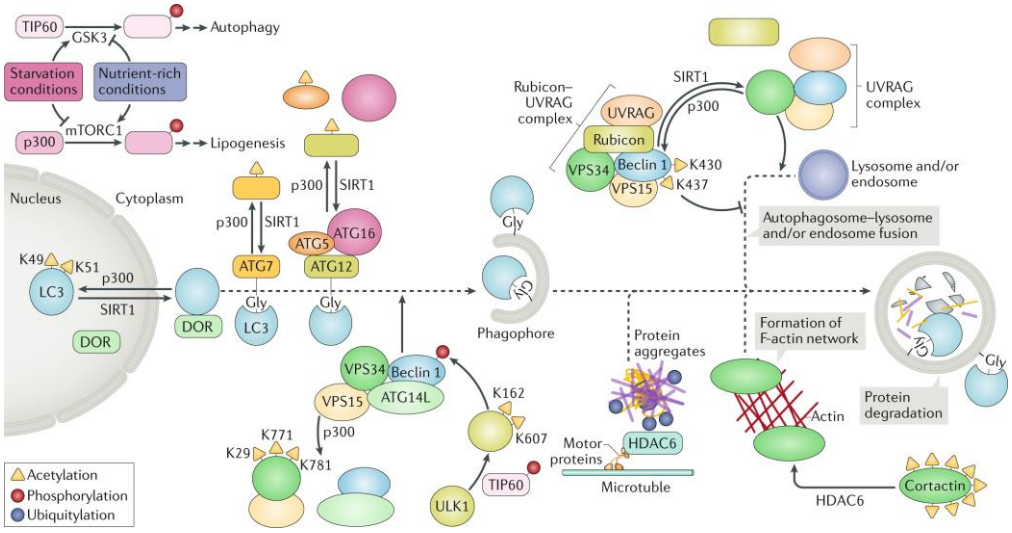

Figure 20. Role of acetylation in autophagy

During starvation, the GSK3 kinase phosphorylates TIP60. Phosphorylated TIP60 promotes autophagy by acetylating the ULK1 kinase. Furthermore, deacetylation of LC3 allows its interaction with DOR and its cytoplasmic localization. Thereby, Deacetylation of LC3 and ATG (ATG5, ATG7, ATG12) proteins promotes formation of autophagosomes. Likewise, deacetylation of beclin 1 promotes maturation of autophagosomes. HDAC6 facilitates transport of protein aggregates to autophagosomes. In nutrient-rich condition, mTORC1 phosphorylates p300, which promotes lipogenesis and inhibits autophagy. p300 acetylates beclin 1, vacuolar protein sorting 34 (VPS34), VPS15, LC3 and ATG proteins. Acetylation of beclin 1 promotes binding of rubicon to the UVRAG complex and inhibits maturation of autophagosomes. Acetylation of LC3 and ATG proteins inhibits the formation of autophagosomes (Narita, Weinert, and Choudhary 2019).

Acetylation can inhibit the catalytic activity of enzymes, for instance, AcetylCoA synthase 1 (ASCC1) and ASCC2 are enzymes that catalyze formation of AcetylCoA in the cytoplasm and mitochondria respectively. Acetylation of ASCC1 and ASCC2 inhibits their activity, while their deacetylation by SIRT1 and SIRT3, respectively, restores their activity (figure 21a, left) (Schwer et al. 2006; Hallows, Lee, and Denu 2006). KAT9-mediated acetylation of G6DP inhibits its dimerization and activity. However, G6DP deacetylation by SIRT2 restore its function (Y.-P. Wang et al. 2014) (Figure 21a, right). Acetylation of cell-cycle regulating kinases CDK1, CDK2 and CDK5 at a lysine important for ATP binding, prevents ATP binding and inhibits their catalytic activity (Mateo et al. 2009).

On the other hand, acetylation can enhance the activity of enzymes. For instance, autoacetylation of acetyltransferases p300, PCAF and MOF is known to enhance their catalytic activity (Figure 21b) (McCullough and Marmorstein 2016; Thompson et al. 2004). Liposaccharide-mediated activation of macrophages causes p300-mediated acetylation of MKP1 phosphatase which enhances its activity and interaction to p38 (W. Cao et al. 2008). However, acetylation of p38 in its ATP binding site enhances its binding to ATP and its catalytic activity (Pillai et al. 2011). Furthermore, acetylation causes change in target specificity. For instance, MDM2 acetylation by p300 causes its stabilization and recruitment of UPS7, thereby MDM2 can perform ubiquitylation of p53 causing p53 degradation and inhibition of apoptosis. However, deacetylation of MDM2 causes its auto-ubiquitylation and degradation (Nihira et al. 2017) (Figure 21c).

Acetylation regulates protein degradation. For instance, p300 acetylation of SMAD7, prevents its ubiquitylation by SMURF1, which prevents SMAD7 degradation (Grönroos et al. 2002). Tip60-mediated acetylation of DNMT1 triggers its ubiquitylation by UHRF1, thereby causing proteasome-dependent DNMT1 degradation (Z. Du et al. 2010) (Figure 21d). Acetylation can promote or inhibit protein-protein interactions. For instance, acetylation of the transcription factor TWIST and of H4 are recognized by two bromodomains of BRD4. Then, BRD4 recruits positive transcription elongation factor (P-TEFb), which phosphorylates the C-terminal domain of RNA Pol II at the enhancer and promoter of WTN5, thereby activating transcription (J. Shi et al. 2014, 4) (Figure 21e).

Acetylation also regulates the localization of proteins: for instance, IFI16 is a sensor of viral DNA, IFI16 is mainly localized in the nucleus, however its acetylation in its nuclear localization signal (NLS) triggers its cytoplasmic retention (T. Li et al. 2012, 16) (Figure 21f).

CBP-mediated acetylation of HNF4 causes its nuclear retention, while deacetylated HNF4 is exported to the cytoplasm (Soutoglou, Katrakili, and Talianidis 2000). Upon activation of monocytes and macrophages HMG protein B1 (HMGB1) is acetylated, which causes cytoplasmic relocalization and extracellular secretion of HMGB1. In contrast deacetylated HMGB1 is localized in the nucleus and bound to chromatin (Bonaldi et al. 2003). Acetylation regulates protein localization to the cell membrane, for instance, SIRT1-mediated deacetylation of a cardiac-specific voltage-gated sodium channel subunit α (Nav1.5) triggers its localization to the cell membrane. Lack of SIRT1 causes decreased level of Nav1.5 in cardiomyocyte cell membrane, which produces cardiac conduction defects (Vikram et al. 2017).

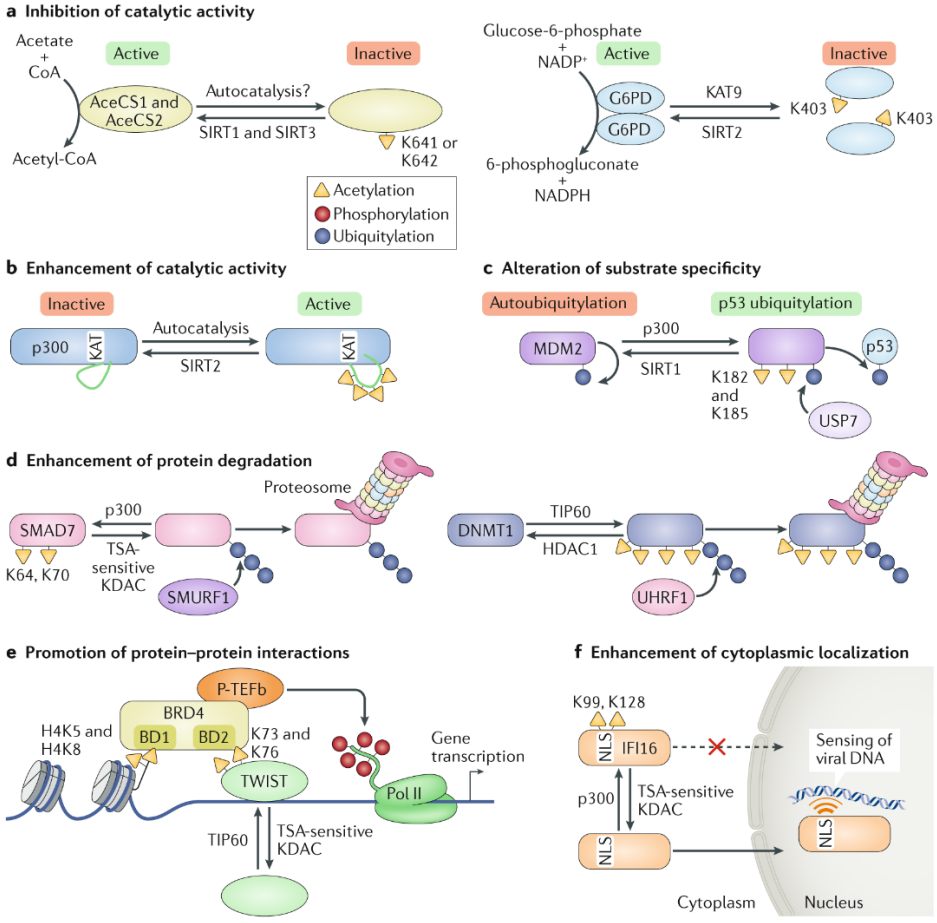

Figure 21. Roles of acetylation in non-histone proteins

a.SIRT1- and SIRT3-dependent deacetylation of respectively acetyl-CoA synthetase 1 (AceCS1) and AceCS2 activates them, while AceCS1 and AceCS2 acetylation causes their inactivation. Deacetylated G6PD can homodimerize and became an active enzyme. KAT9-dependent acetylation of Glucose 6-phosphate (G6PD) inhibits its dimerization and causes its inactivation. **b.** Autoacetylation of p300 activation loop removes this loop from p300 KAT domain causing p300 increased activity. **c.** Deacetylated MDM2, an E3 ubiquitin-protein ligase, ubiquitylates itself. In contrast, acetylated MDM2 is deubiquitylated by USP7, thereby MDM2 can ubiquitylates its substrate p53. **d.** p300-dependent acetylation of SMAD7 inhibits its ubiquitylation by SMURF and proteasomal degradation

as well. In case of DNMT1, TIP60-mediated DNMT1 acetylation promotes its ubiquitylation by UHRF1 and proteasomal degradation. **e.** BDR4 is recruited through its first bromodomain (BD1) to chromatin acetylated at H4K5 and H4K8, while the BD2 of BDR4 interacts with the acetylated transcription factor TWIST. BDR4 recruits positive transcription elongation factor b (P-TEFb), which phosphorylates the C-terminal domain of Pol II, thereby triggering transcription activation. **f.** Viral infection trigger acetylation of viral-DNA sensor γ-interferon inducible-protein 16 (IFI16), which inhibits IFI16 nuclear import; thus, IFI16 cannot recognize viral DNA in the nucleus (Narita, Weinert, and Choudhary 2019).

1.8 HDAC inhibitors

Lysine acetylation is associated to neurological disorders, cancer, cardiovascular diseases (P. Li, Ge, and Li 2020; Falkenberg and Johnstone 2014). Several histone deacetylaces inhibitors (HDACi) have been FDA-approved for the treatment of cancer (Cappellacci et al. 2020). Vorinostat (Saha), Romidepsin are used for the treatment of cutaneous T-cell lymphoma (Duvic et al. 2018; Marks and Breslow 2007). Belinostat and Chidamide (approved in China) for the treatment of peripheral T-cell lymphoma (Poole 2014; Chan, Tse, and Kwong 2017). Panobinostat, a non-selective inhibitor (pan-inhibitor), for the treatment of multiple myeloma (Prince, Bishton, and Johnstone 2009). In addition, two HDACi are FDA-approved for the treatment of neurologic disorders: the valproic acid and sodium butyrate. Vorinostat, Belinostat and Panobinostat have a hydroxamic acid war head that chelates the Zn^{2+} in HDACs (Richon 2006; Cappellacci et al. 2020). Romidepsin is a cyclic depsipeptide that, in the reduced form, have a thiol group that coordinates the Zn^{2+} (Nakajima et al. 1998).

1.9 Treatment of neglected diseases, smHDAC8

Schistosomiasis is an infectious disease caused by parasitic flatworms of the genus Schistosoma. Around 240 million people are infected worldwide, and schistosomiasis causes 300 000 deaths per year. The only drug available for treatment, Praziquantel, is used for mass treatment, which raises the possibility of resistance (Doenhoff et al. 2002). Therefore, it is the development of new drugs against schistosomiasis is urgently required. The *Schistosoma mansoni* genome have three HDACs of class I, which are orthologues of the mammalian HDACs: HDAC1, HDAC3 and HDAC8 (Oger et al. 2008). mRNAs of these three HDACs are expressed in all life-cycle stages of *S. mansoni*, but smHDAC8 is the most abundant transcript among class I HDACs in all life stages. In contrast, in human tissues HDAC8 is the lowest transcript expressed from the class I HDACs (E. Hu et al. 2000). Therefore, it is suggested smHDAC8 must have vital functions for *S.mansoni*. smHDAC8 thus constitute a potential target for drug development to treat schistosomiasis.

Given that the development of new drugs is a long an expensive process, a strategy called Piggyback was applied by my host team in collaboration with many other European and Brazilian groups within two large FP7 European projects (SETTReND, Schistosoma Epigenetics - Targets, Regulation, New Drugs, and A-ParaDDisE, Anti-Parasitic Drug Discovery in Epigenetics). This strategy implies the modification of FDA-approved HDAC inhibitors (epidrugs) used in the treatments against cancer (Falkenberg and Johnstone 2014) to be used in the treatment of infectious diseases. These epidrugs serve as scaffolds for the development of specific inhibitors targeting the smHDAC8 enzyme.

The piggyback strategy combines a high throughput and structure-based drug design methods. This latter to tackle the selectivity issue raised, since human HDAC and schistosome HDAC8 enzymes have similarities in the active site which could cause off-target effects when trying to inhibit the schistosome HDAC8. Therefore, a structure-based drug design has the objective to make a drug as specific as possible for the Schistosome enzyme. The structure of smHDAC8 showed that it has some differences to human HDACs (Marek et al. 2013). For instance, smHDAC8 has a wider active site pocket compared to its orthologue human HDAC8, which is due to the flipped-out conformation of residue F152 in smHDAC8. Furthermore, M274 in human HDAC8 is replaced by H292 in smHDAC8. These specific features of smHDAC8 have been used for the development of smHDAC8 inhibitors (Marek et al. 2015).

A virtual screening using a library of half-million of zinc-chelating compounds and the structure of smHDAC8 was conducted, resulting in the identification of two linkerless compounds J1038 and J1075 (Kannan et al. 2014). In vitro testing of inhibition activity showed these compounds have selectivity for HDAC8 enzymes (smHDAC8 and hHDAC8) over other HDACs (HDAC1, HDAC2, HDAC3 and HDAC6) compared to the commercial HDAC drug Voristonat, which inhibits with no selectivity all class I HDACs (HDAC1, HDAC2, HDAC3 and HDAC8) and class IIb HDAC6 (Marek et al. 2013). The J1038 was selected for a hit for optimization since it is a bulkier compound in accordance with the wider active site of smHDAC8. Based on the hit J1038, several compounds were developed. In vitro testing of their inhibitory capacity against smHDAC8 and human HDAC8 showed that these compounds have an IC_{50} value in the low nanomolar range and some of these compounds are also selective for the schistosome HDAC8 over its human counterpart (Heimburg et al. 2016).

Nevertheless, this study revealed the difficulty of designing drugs showing selectivity only for parasitic HDACs when these are similar to their human counterparts, raising the question of

how to improve selectivity. On the other hand, this proof of concept that the epigenetic machinery of pathogens can be targeted by the piggyback strategy opened new avenues to target other infectious diseases where the pathogens have HDACs that show significant divergence from the human HDACs. During my PhD, I have addressed these two questions by (i) participating to the precise molecular characterization of HDAC8 selective inhibition (Article 1) and (ii) investigating the selective inhibition of divergent parasitic HDACs, notably DAC2 from *Trypanosoma cruzi* (tcDAC2) (see below; Article 2).

Second chapter: Epitranscriptomics

2 The RNA world and the epitranscriptome

For decades, our view of the world of ribonucleic acids (RNA) has been mostly restricted to messenger RNA (mRNA), the photocopy of our genes, ribosomal RNA (rRNA), the structuring nucleic acid component of the ribosomes, and transfer RNA (tRNA), the adaptor molecule between the RNA and protein worlds. Since a few decades, however, this initial view of the RNA world has become much more complex, with the discovery of many more RNA species, such as small nuclear RNA (snRNA), small nucleolar RNA (snoRNA), long non-coding RNA (lncRNA), microRNA (miRNA), enhancer RNA (eRNA), vault RNA (VTRNA), and circular RNA (circRNA) (Statello et al. 2021b). These different RNA species functionally participate, together with mRNAs, rRNAs, tRNAs and the other cellular effectors, to the development and homeostasis of cells and organisms (Cech and Steitz 2014).

Beside the large variety of RNA species, it has been shown that most of these species can undergo a large number of modifications (X. Li, Xiong, and Yi 2017). More than a hundred of RNA modifications have being identified so far in all types of RNA molecules, including modifications in the ribose and nucleobases (Boccaletto et al. 2018). The discovery that some of these RNA modifications are deposited, read, and removed in response to internal or external cellular stimuli, showing that RNA modifications can be reversible and dynamic, as observed in the epigenetic field, has given rise to the emerging field of Epitranscriptomics that mirrors the established field of epigenetics (McMahon, Forester, and Buffenstein 2021; Livneh et al. 2020; Wiener and Schwartz 2021; Barbieri and Kouzarides 2020).

Notably, RNA modifications can regulate gene expression, thus modulating a large set of cellular processes, cellular homeostasis and development (Roundtree, Evans, et al. 2017; Frye et al. 2018; Barbieri and Kouzarides 2020; Chujo and Tomizawa 2021). It is therefore not surprising that dysregulation of RNA modifications are involved in various diseases. Notably, mutations in half of the RNA modification enzymes are associated with human diseases (Tsutomu Suzuki 2021; Jonkhout et al. 2017). These include cancer, cardiovascular, immune, metabolic, mitochondrial-related, and neurological diseases. Intriguingly, the most frequent diseases associated with RNA modification dysregulation is represented by neurological disorders, which agrees with the fact that many RNA modifications are enriched in the brain (Jonkhout et al. 2017; Chi and Delgado-Olguín 2013).

Among the RNA species, tRNAs are the most modified RNA macromolecules, containing about 120 different modifications. Each tRNA molecule contains on average 13 modifications located in its various arms where they play very different roles in tRNA folding, stabilization and decoding (Paul F. Agris et al. 2018; Tsutomu Suzuki 2021; Schimmel 2018; Kirchner and Ignatova 2014). Here again, mutations in and altered expression of 72% of the tRNA modification enzymes are associated with human diseases, 50% of these diseases being neurological disorders, notably neurodevelopmental disorders (NDDs) (Chujo and Tomizawa 2021).

There is therefore a strong growing interest to understand in molecular details the RNA modification pathways, the biological roles of these modifications, and how the dysregulation of these pathways (i) leads to modifications imbalance, (ii) influences RNA metabolism, gene expression, and (iii) how these perturbations lead to disease. Specifically, the large implication of tRNAs in brain development, as assessed by the dysregulations of its modifications causing NDDs, is providing a strong renewed interest in these essential effector molecules.

In the next paragraphs, I will detail some of the most widespread and well-studied RNA modifications, describing the enzymes mediating these modifications, the roles of these modifications, and different diseases associated with their dysregulation. Later, I will more precisely focus on tRNA modifications, their roles and their associated neurological disorders, as an introduction to my work on the tRNA wobble adenosine-to-inosine modification by the ADAT complex and its implication in intellectual disability, microcephaly and epilepsy.

2.1 RNA modifications: their modification enzymes, their roles and their implication in diseases

2.1.1 N^6-methyladenosine (m^6A)

The m^6A modification is the most frequent modification identified in mRNAs. m^6A is also observed in long non-coding RNAs (lncRNAs) (Patil et al. 2016), primary-microRNAs (pri-miRNAs) (Alarcón et al. 2015), spliceosomal small nuclear RNA (snRNA) (Pendleton et al. 2017), chromosome-associated regulatory RNAs (carRNAs) (including promoter-associated RNAs, enhancer RNAs and repeat RNA) (Jun Liu et al. 2020), circular RNA (circRNA) (C. Zhou et al. 2017), and ribosomal RNAs (rRNAs) (B. E. H. Maden 1988; B. E. Maden 1986), demonstrating of its ubiquitous importance. Specifically, in mRNAs, m^6A is located both within the 5' and 3' untranslated regions (5' and 3' UTRs) and within the coding region of

mRNAs. m^6A deposition seems restricted to the sequence motif DRACH (D=A, G or U; R=A or G; H=A, C or U) (Dominissini et al. 2012; K. D. Meyer et al. 2012).

The m^6A modification enzyme (writer) is different depending on the RNA species to be modified. In mRNAs, lncRNAs, miRNAs and carRNAs, the core complex writing the m^6A modification is the complex METTL3/METTL14/WTAP (Jianzhao Liu et al. 2014; Schöller et al. 2018). A group of partner proteins (VIRMA, ZC3H13, RBM15 and CBLL1) associates to the core complex to regulate m^6A deposition on specific transcripts, however their mechanisms of actions is not clear yet (Livneh et al. 2020). In U6 snRNA and in *MAT2a* (which codes for the SAM synthetase), the modification is catalyzed by METTL16 (Pendleton et al. 2017), while for the 18S and 28S rRNAs, the m^6A methylation is carried out by the METTL5/TRMT12 complex and ZCCHC4, respectively (van Tran et al. 2019; H. Ma et al. 2019; Ren et al. 2019).

Depending on the type of recognition of the m^6A mark, direct or indirect, two groups of m^6A readers can be distinguished. The first group of readers contains the YTH domain family, which includes YTHDF1 (Xiao Wang et al. 2015), YTHDF2 (Xiao Wang et al. 2014), YTHDF3 (H. Shi et al. 2017), YTHDC1(Roundtree, Luo, et al. 2017; Xiao et al. 2016) and YTHDC2 (Kretschmer et al. 2018). These proteins recognize m^6A-modified transcripts, either in the nucleus (YTHDC1/2) or in the cytoplasm (YTHDF1/2/3 and YTHDC2), directly through their YTH domain. In addition, other proteins can also recognize m^6A directly but do not have a YTH domain: the IGF2 mRNA-binding proteins (IGF2BPs) and the eukaryotic translation initiation factor 3 (eIF3).

The second group of m^6A readers recognizes this modification through the m^6A-switch effect, which consists of exposing a buried motif of the RNA upon its m^6A methylation. The exposed motif is then bound by readers such as HNRNPC and HNRNPG (N. Liu et al. 2015; K. I. Zhou et al. 2019). The m^6A modification can also cause repulsion to some proteins, known as anti-readers, *e.g.* the Ras-GTPase protein-binding proteins 1 and 2 (G3BP1, G3BP2), which preferentially bind the unmethylated RNA. Finally, two enzymes, FTO (Jia et al. 2011) and ALKBH5 (Zheng et al. 2013), dependent respectively on Fe^{2+} and α-ketoglutarate, remove the m^6A mark from mRNAs in the nucleus (FTO and ALKBH5) and cytoplasm (FTO).

m^6A plays many important roles by regulating gene expression through the modulation of RNA alternative splicing, nuclear export, stabilization, translation, and degradation (Huilin Huang, Weng, and Chen 2020). m^6A regulates alternative splicing through its nuclear reader

YTHDC1 and splicing factor SR proteins, SRSF3 and SRSF10. An m^6A-methylated exon is recognized by YTHDC1, which in turn recruits SRSF3, thus promoting exon inclusion. But in absence of the m^6A mark, it is SRSF10 which binds to the unmethylated transcript causing exon skipping (Figure 22a) (Xiao et al. 2016).

In addition, in case of nuclear export, YTHDC1 recognizes m^6A-marked transcripts and recruits SRSF3. This later protein in turn interacts with NXF1 that promotes export of these transcripts to the cytoplasm (Figure 22b) (Roundtree, Luo, et al. 2017). The m^6A modification also regulates the stability and degradation of transcripts. Each of these processes depends on the type of reader protein recognizing the m^6A mark. For instance, if m^6A is read by YTHDF2, which recruits the CCR4-NOT deadenylase complex, the transcript is degraded (Figure 22c) (Xiao Wang et al. 2014). On the other hand, if the m^6A-methylated transcript is bound by IGF2BPs, the transcripts is stabilized and is not degraded (Figure 22c).

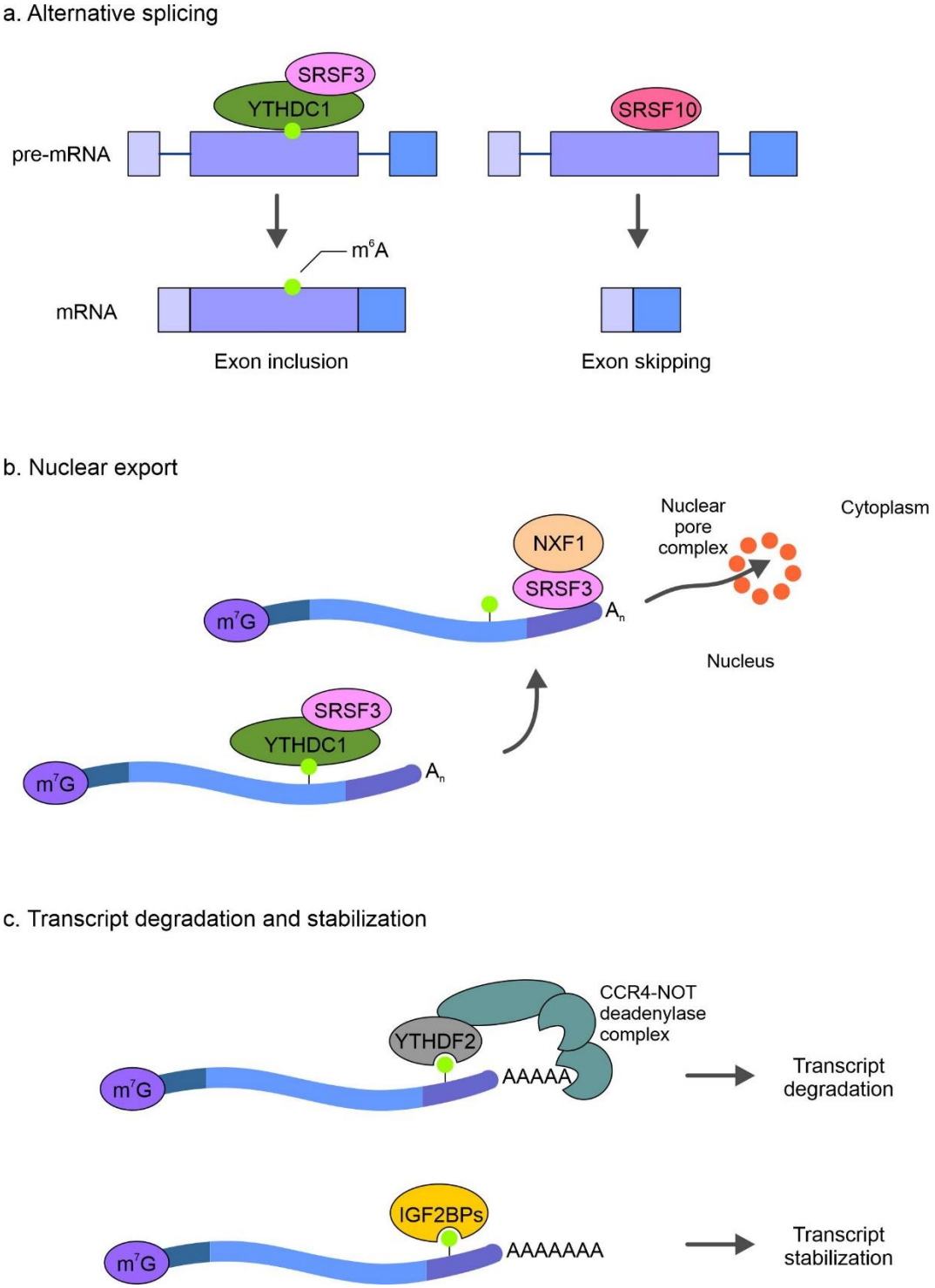

Figure 22. m^{6}A roles in mRNA metabolism

a. m^{6}A regulates alternative splicing. YTHDC1/SRSF3 bound to an m^{6}A mark in a pre-mRNA causes exon inclusion. In absence of the m^{6}A mark the pre-mRNA is bound by SRSF10, leading to exon skipping. **b.** m^{6}A promotes nuclear export of transcripts through interaction of YTHDC1 with SRSF3 and the export factor NXF1. **c.** m^{6}A causes transcript degradation through YTHDF2 which recruits the CCR4-NOT deadenylase complex that degrades the m^{6}A marked transcript. If IGF2BPs bind m^{6}A marked transcripts, it protects them from degradation. Based on (Livneh et al. 2020; Huilin Huang, Weng, and Chen 2020)

m^{6}A also regulates translation depending on its location within the mRNA. m^{6}A located within the 5'-UTR promotes cap-independent translation: briefly, m^{6}A in the 5'-UTR is recognized directly by the translation initiation factor eIF3, which recruits the 43S ribosomal complex to initiate translation, thus m^{6}A promotes translation initiation in absence of the usual cap-binding proteins (Figure 23a) (K. D. Meyer et al. 2015). In contrast, m^{6}A located within the 3'-UTR enhances translation initiation, but in a cap-dependent manner. This process is mediated through m^{6}A-bound YTHDF1/3 and their interaction to eIF3 (Xiao Wang et al. 2015). It is proposed that YTHDF1/3 bound to eIF3 interacts to the translation machinery through a loop structure mediated by eIF4G (Figure 23b) (Xiao Wang et al. 2015). However, if m^{6}A is located within the coding sequence, it disrupts the selection of cognate tRNAs by the ribosome, thus affecting the rate of translation elongation (Figure 23c) (Choi et al. 2016).

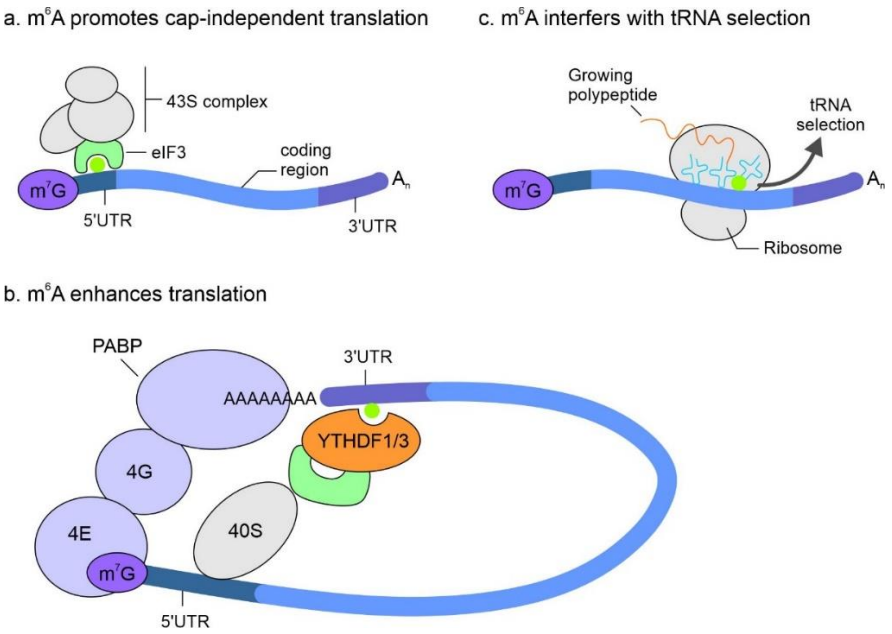

Figure 23. m^{6}A regulates translation

a. m^{6}A in the 5'-UTR promotes cap-independent translation through its interaction with eIF3, which recruits the 43S initiation complex. **b.** m^{6}A in the 3'-UTR enhances translation initiation in a cap-dependent manner through YTHDF1/3 binding to eIF3. It is proposed that the 40S complex binds eIF3 through a loop structure formed by eIF4G that brings closer the 5'- and 3'-UTR. **c.** m^{6}A in the coding sequence disrupts the selection of cognate tRNAs, thus affecting translation elongation. Based on (Livneh et al. 2020; K. D. Meyer et al. 2015; Xiao Wang et al. 2015)

Interestingly, m^{6}A has been shown to act in cortical and cerebellar development during the embryonic stages and postnatally, respectively (K.-J. Yoon et al. 2017; C. Ma et al. 2018; Livneh et al. 2020). Notably, m^{6}A regulates neurogenesis, gliogenesis and axonal guidance. During the embryonic stage, differentiation of Neural Progenitor Cells (NPCs) into neurons

and glial cells requires that transcripts important for self-renewal and pluripotency are m^{6}A-marked. In that way, these transcripts are degraded and differentiation transcripts expressed (Figure 24a) (Geula et al. 2015). Guidance of growing axons to reach their targets is mediated by m^{6}A as well (Zhuang et al. 2019). For instance, midline crossing of commissural axons involves YTHDF1-dependent translation of m^{6}A methylated R*obo3.1* transcripts in the soma of both pre-crossing and crossing axons. However, in post-crossing axons both YTHDF1 and m^{6}A-methylated R*obo3.1* are depleted, which causes R*obo3.1* degradation (Stoeckli 2018; Zhuang et al. 2019).

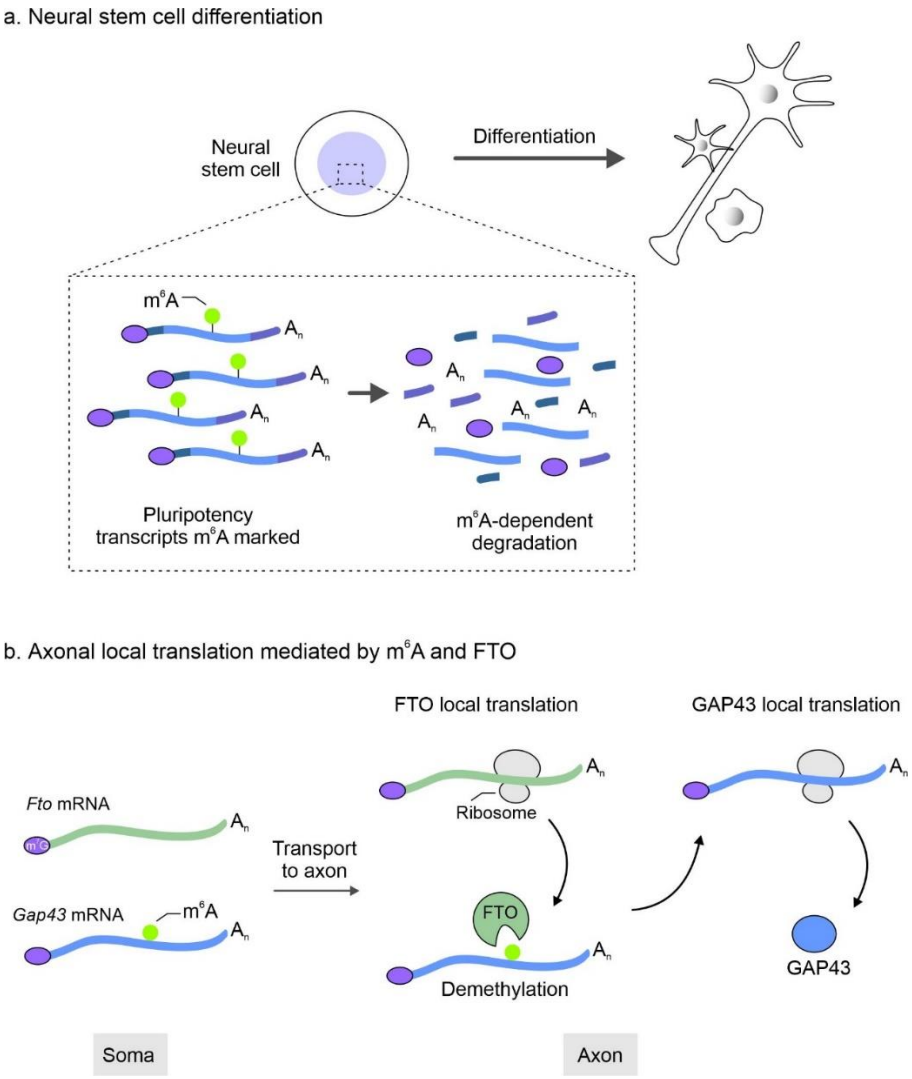

Figure 24. m^{6}A roles in neurodevelopment

a. m^{6}A regulates differentiation of neural stem cells (NSCs) into neurons and glial cells. Transcripts promoting pluripotency are m^{6}A marked and degraded, which allows the expression of differentiation transcripts. **b.** Local translation, in the axon, is mediated by m^{6}A and FTO. *Fto* and m^{6}A-marked *Gap43* transcripts are transported to the axon. In the axon, *Fto* transcript is translated, then the FTO protein removes the m^{6}A mark from *Gap43*. Next, the unmethylated *Gap43* can be translated. Local translation of *Gap43* is important for axon elongation during development. Based on (Livneh et al. 2020; J. Yu et al. 2018)

Postnatally, METTL3 is important for cerebellar development; loss of m6A by depletion of METTL3 in cerebellar granular cells (CGCs), increases the half-live of transcripts associated with cerebellar development and apoptosis. In addition, loss of m^6A affects *Grin1* splicing, causing excessive calcium influx in CGCs and their apoptosis (C.-X. Wang et al. 2018). Furthermore, during adult neurogenesis, located in the hippocampus, FTO plays a key role. FTO regulates the expression of methylated transcripts that are part of the brain-derived neurotrophic factor (BDNF) pathway, which controls the proliferation and differentiation of adult neural stem cells (aNSC) into neurons and glial cells, as well as learning and memory. Loss of FTO in mice shows decreased brain size, reduced proliferation and differentiation of aNSC and defects in learning and memory (Liping Li et al. 2017).

Finally, stimuli-dependent synapse transmission is important for learning and memory requires local translation at the pre-synaptic and post-synaptic compartments. Similarly, guidance of axonal growth and post-injury axon regeneration require local translation, in the axon. The local translation in the axon is regulated by m^6A and its eraser enzyme FTO (Figure 24b). Transcripts that need to be translated in the axon are first m^6A-marked and then transported to the axon; *Fto* transcript is also transported to the axon but in its unmethylated form. Once all those transcripts arrive to the axon, *Fto* is translated and demethylates the m^6A-marked transcripts, those transcript without the m^6A mark can now be translated locally (J. Yu et al. 2018).

Components of the m^6A machinery have been associated to neurologic diseases. For instance, mutations in YTHDC2 has been identified as a risk factor for autism spectrum disorder (Xiaoxi Liu et al. 2016). Inactivity of FTO has been associated to Parkinson's disease (PD). Inactivation of FTO causes both increased levels of m^6A and reduced translation of transcripts (*Drd3, Girk2, Grin1*), participating in the dopaminergic signaling (Hess et al. 2013). Furthermore, 6-hydroxydopamine (OHDA)-induced PD in cells and rat model caused decreased levels of m^6A. Therefore, to further investigate the role of m6A in PD, decreased m^6A levels was induced in dopaminergic cells by overexpressing FTO or treatment with m^6A inhibitor, the results showed an increased expression of the NMDA receptor, an ion channel which caused increase of Ca^{2+} influx into dopaminergic cells leading to apoptosis (Xuechai Chen et al. 2019). FTO overexpression is also associated to Alzheimer's disease (AD). In mice, it was shown that overexpression of FTO increases levels of Tau phosphorylation, which is a hallmark of AD. In addition, knockdown of FTO caused reduction of Tau phosphorylation levels in an mTOR-dependent manner (Huajie Li et al. 2018). Furthermore,

genetic variants of FTO and ALKBH5 are associated with Major Depressive Disorder (MDD) (T. Du et al. 2015).

Many writers, erasers and readers of the m^6A modification, including METTL3, METTL14, ALKBH5 and YTHDF2 also act as oncogenes or as tumor suppressor in several cancer types. In addition, WTAP, VIRMA, FTO, YTHDF1/3, YTHDC2 and IGF2BPs1-3 act as oncogenes in different cancer (Huilin Huang, Weng, and Chen 2020). m^6A is also associated to cardiovascular diseases such as heart failure, cardiac hypertrophy and ischemic heart disease. For instance, overexpression of METTL3 triggers cardiomyocyte hypertrophy, and decreased levels of FTO is observed in heart failure and hypoxic cardiomyocytes (Dorn Lisa E. et al. 2019; Mathiyalagan Prabhu et al. 2019).

2.1.2 5-methylcytosine (m^5C)

m^5C has been identified in rRNAs, tRNAs, and was also recently observed in mRNAs, at the 5'- and 3'-UTR, next to the translation start site and in coding regions (Amort et al. 2017; X. Yang et al. 2017). m^5C has also been detected in non-coding RNAs, for instance in vault RNAs (VTRNAs) (Hussain et al. 2013) and enhancer RNAs (eRNAs) (Aguilo et al. 2016).

The enzymes catalyzing the formation of m^5C on RNAs are part of the NOL1/NOP2/Sun (NSUN) family (NSUN1-7) and DNMT2 (DNA methyl transferase 2). NSUN1 catalyzes the formation of m^5C in human 28S rRNA at position 4447. NSUN2 methylates VTRNAs1.1 and VTRNA1.3 (Hussain et al. 2013). NSUN4, performs the m^5C methylation of the 12S (at C911) and 16S human mitochondrial rRNAs (Cámara et al. 2011; Yakubovskaya et al. 2012; Metodiev et al. 2014). NSUN5 mediates the m^5C modification of the human 28S rRNA at position 3782 (Heissenberger et al. 2019). NSUN7 mediates the m^5C methylation of eRNAs associated with PGC1α target genes, which are involved in metabolism: 6-phosphofructokinase, sirtuin 5, isocitrate dehydrogenase and heme deaoxygenase (Aguilo et al. 2016). Two m^5C readers have been identified so far: ALYREF (in the nucleus) and YBX1 (in the cytoplasm) (X. Yang et al. 2017; Xin Chen et al. 2019). The m^5C eraser Ten-eleven translocation 2 (TET2) enzyme oxidizes m^5C to 5-hydroxymethylcytosine (hm5C) in RNAs (Shen et al. 2018). Proteins mediating m^5C in tRNAs will be described in the section "tRNA modifications".

Biological roles of the m^5C modification include mRNA nuclear export, mRNA stabilization, ribosomal biogenesis, and translation. Nuclear export of m^5C methylated transcripts is mediated by the recognition of the m^5C mark by ALYREF (X. Yang et al. 2017). mRNA

stabilization is mediated by the binding of YBX1 to m^5C methylated transcripts (Xin Chen et al. 2019; Y. Yang et al. 2019). For instance, during maternal to zygotic transition in zebra fish, YBX1 has been shown to stabilize m^5C methylated maternal transcripts to prevent their decay (Y. Yang et al. 2019). In drosophila, YBX1 promotes germ line stem cells (GSC) maintenance, proliferation and differentiation in an m^5C dependent manner, since YBX1 mutated in residues recognizing the m^5C mark affected GSC development (Zou et al. 2020). Furthermore, human cells contain four VTRNAs, two of them are m^5C-modified, VTRNA1.1 and VTRNA1.3. It has been shown that SRSF2 binds the unmethylated VTRNA1.1 to protect it from processing. Otherwise, once the VTRNA1.1 is m^5C methylated by NSUN2, it is processed into small RNA fragments producing small vault RNA4 (svRNA4). The presence of svRN4 maintains epidermal cells in un undifferentiated stage (Hussain et al. 2013; Sajini et al. 2019).

Yeast 25S rRNA contains two m^5C modifications at positions 2278 and 2870. m^5C modification at position 2278 (intersubunit bridge) is important for maintaining the 25S rRNA structure and translational fidelity. Loss of the m^5C modification at position 2870 (peptidyltransferase center) affects ribosome biogenesis (Sharma 2013, Schosserer 2015). Similarly, lack of m^5C methylation at C911 in mitochondrial ribosomes by NSUN4 depletion affects both assembly of mitochondrial ribosome subunits and mitochondrial translation (Metodiev et al. 2014). In human 28S rRNA, loss of m^5C methylation at position 3782 affects global protein synthesis (Heissenberger et al. 2019; Janin et al. 2019).

Overexpression of NSUN1 and NSUN2 are associated with cancer and mutations in NSUN2 and lack of NSUN5 are associated to neurodevelopmental diseases. For instance, NSUN1 is overexpressed in lung and prostate cancer (Saijo et al. 2001; Bantis et al. 2004). In urothelial carcinoma of the bladder (UCB), an increase of NSUN2-mediated m^5C methylation compared to normal tissue has been identified in several transcripts. These hypermethylated transcripts are involved in oncogenic pathways. Moreover, both the m^5C writer NSUN2 and the m^5C reader YBX1 are overexpressed in UCB, where they promote invasiveness and metastasis of cancer cells (Xin Chen et al. 2019).

Mutations in *NSUN2* have been identified in patients affected by neurodevelopmental disorders. Notably, homozygous mutation of *NSUN2* in patients, that affects NSUN2 functions, causes intellectual disability (Abbasi-Moheb et al. 2012; Khan et al. 2012; Martinez et al. 2012). Specifically, a homozygous missense mutation in *NSUN2* generating

the G679R mutation, which causes intellectual disability, was shown to affect the nuclear localization of NSUN2 (Khan et al. 2012). In addition, homozygous splicing mutation in NSUN2 detected in patients was associated with the Dubowitz syndrome, which is characterized by intellectual disability, mild microcephaly and growth retardation (Martinez et al. 2012). Finally, NSUN5 deletion is detected in patients affected by the Williams-Beuren Syndrome (WBS), a multisystemic disorder characterized by cognitive impairment, cardiac, endocrine and gastrointestinal symptoms (Pober 2010).

2.1.3 Internal 7-methylguanosine (m^7G)

A methyl group at position 7 of the guanosine base, the m^7G modification, can be found at two locations. First, at the 5'-end of mRNAs, where it is known as m^7G cap. Second, m^7G can be located within the RNA molecule, known as internal m^7G. The m^7G cap has been extensively reviewed elsewhere (Ramanathan, Robb, and Chan 2016). In this part, I will focus on the internal m^7G modification that has been identified in rRNAs, tRNAs, mRNAs (at the coding sequence and 3'-UTR), in pri-miRNAs and miRNAs (Sloan et al. 2017; Tomikawa 2018; L.-S. Zhang et al. 2019; Pandolfini et al. 2019).

Enzymes catalyzing the internal m^7G modification depend on the type of RNA substrate. In tRNAs, mRNAs and pri-miRNAs, m^7G is mediated by the METTL1/WDR4 complex (Alexandrov, Martzen, and Phizicky 2002; S. Lin et al. 2018; L.-S. Zhang et al. 2019; Pandolfini et al. 2019). In rRNAs, WBSCRC22 protein catalyzes the m^7G mark at position G1639 in the 18S rRNA (Haag, Kretschmer, and Bohnsack 2015).

Two roles for the internal m^7G mark have been identified. First, in mRNAs, internal m^7G promotes translation efficiency. For instance, upon METTL1 depletion, mRNA levels decrease in polysome fractions for transcripts known to have internal m^7G (L.-S. Zhang et al. 2019). Furthermore, m^7G in the 3'-UTR of PCNA increases translation of a reporter gene compared to that of a mutant reporter where the guanosine in the 3'-UTR of PCNA, target of methylation, is mutated into adenosine (Malbec et al. 2019).

Second, m^7G promotes miRNA biogenesis. m^7G prevents formation of hoogsteen base pairing between guanosines. Otherwise, four unmethylated guanosines would form a G-quadruplex structure that, when present in pri-miRNA, affects its processing. For instance, m^7G marks have been identified in pri-miRNAs promoting cell migration, including in pri-miR-let7e. Unmethylated pri-miR let7e bears a G-quadruplex structure that hampers its cleavage by Drosha. Thus, by inhibiting the G-quadruplex structure formation, m^7G favors

pri-mi-let7e processing into mature let7e miRNA. miR-let7e targets a transcript that promotes cell migration, high mobility group AT-hook 2 (*HMGA2*). Accordingly, METTL1 depletion causes cell migration by decreasing miR-let7e formation, which promotes expression of *HMGA2* (Figure 25) (Pandolfini et al. 2019).

Consequently, METTL1 has been shown to be depleted in patients-derived colon cancer cells compared to normal cells. In addition, overexpression of METTL1 triggers inhibition of cell proliferation and migration by reducing *HMGA2* transcript expression through the miR-let7e targeting (Yang Liu et al. 2020). In addition, METTL1 also acts as an oncogene in some cancer types. For instance, in glioblastoma (Ping et al. 2015), and hepatocellular carcinoma (Tian et al. 2019).

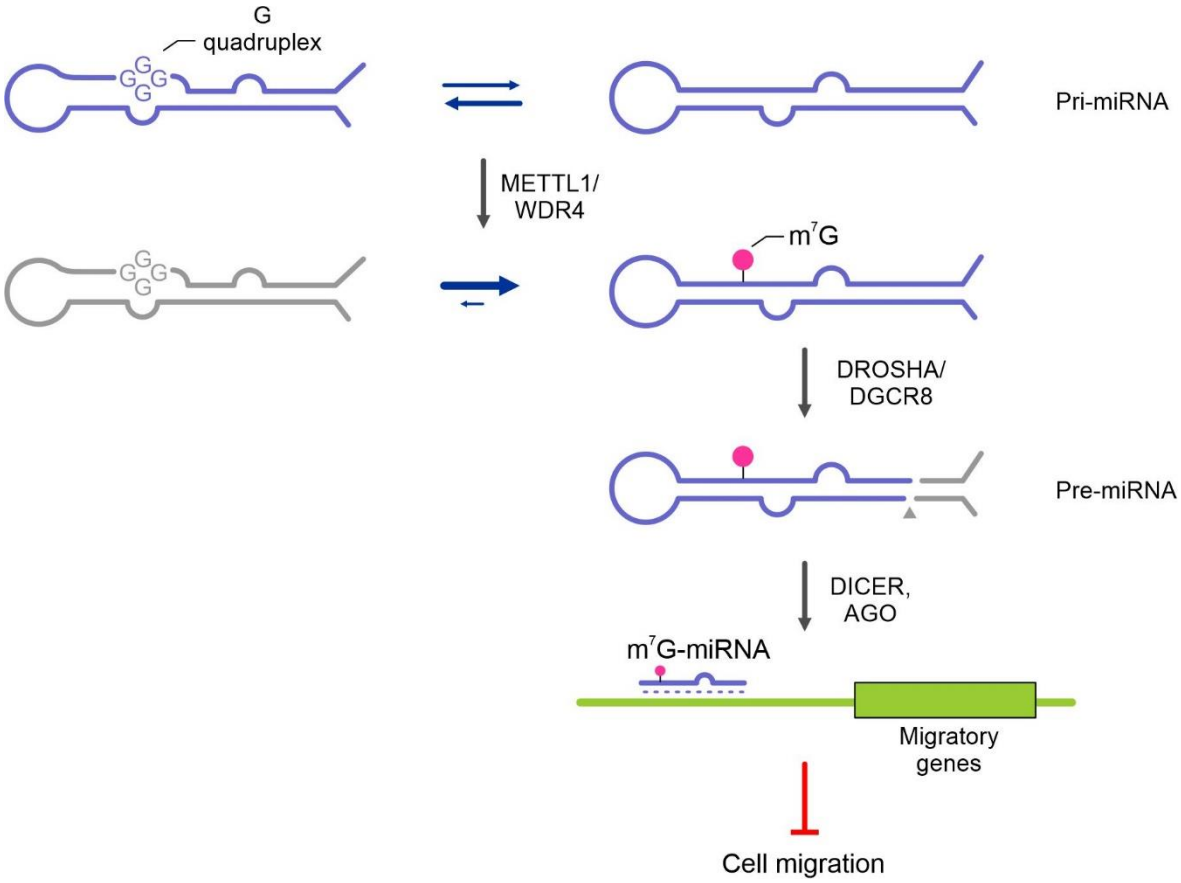

Figure 25. m^7G role in miRNA biogenesis

Presence of guanosines (G) in pri-miRNAs leads to formation of a G-quadruplex structure that affects the processing of pri-mi-RNAs. The METTL1/WDR4 complex methylates these guanosines at position 7 (m^7G), which prevents formation of G-quadruplex structures. m^7G modified pri-miRNAs promotes correct processing of pri-miRNAs into mature miRNA. For instance, modification of miR-let7e, which target migratory genes transcripts, leads to inhibition of cell migration. Based on (Pandolfini et al. 2019).

2.1.4 Pseudouridine (Ψ)

Pseudouridine (Ψ), produced by an isomerization of uridine, is found in most RNA types: rRNA, tRNA, mRNA, and other non-coding RNAs (Penzo et al. 2017).

Pseudouridine formation occurs in two manners: RNA-independent and RNA-dependent. In the first case, enzymes belonging to the Pseudouridine synthase (PUS) family perform the isomerization reaction. PUS targets include tRNAs, snRNAs and mRNAs (Penzo et al. 2017; Zoysa et al. 2018; Rintala-Dempsey and Kothe 2017). In the second case, a ribonucleoprotein complex, called H/ACA snoRNP, is required for pseudouridine formation (Figure 26a). The H/ACA snoRNA guides the complex to the position where the isomerization reaction takes place, which is performed by the Diskeryn (DKC1) protein, its catalytically active component. H/ACA targets are rRNAs, snRNAs, snoRNAs and the telomerase RNA component (TERC) (Penzo and Montanaro 2018; Schwartz et al. 2014). Neither readers nor erasers of pseudouridines have been identified so far. In addition, the role of Pseudouridine in mRNAs is poorly understood (Barbieri and Kouzarides 2020). Pseudouridine in tRNAs will be described in the last part of the introduction.

The ribosome has 95 Ψ modifications which are present in all rRNAs (28S, 18S, 5.8S and 5S). Upon ribosome formation, these Ψ are found mostly located at functionally sites: the tRNA binding site, the mRNA channel, the peptidyl transferase center, the decoding center and the intersubunit bridge. In yeast, it has been shown that pseudouridines in rRNAs are important for ribosome biogenesis, assembly and translation (Xue-hai Liang, Liu, and Fournier 2007; 2009; King et al. 2003; Piekna-Przybylska et al. 2008). Ψ of snRNA is also important for efficient splicing of mRNAs (Bohnsack and Sloan 2018).

In melanoma cells and breast cancer cells, the PUS1-mediated pseudouridilation of ncRNA steroid receptor activator 1 (SRA1) allows its interaction with nuclear receptors like retinoic acid receptor γ and oestrogen receptors, which enhances transcription in these cancer cells (X. Zhao et al. 2004). In addition, mutations in DKC1 causes Dyskeratosis congenita, which affects proliferating tissues (skin, mucosae, bone marrow) and promotes cancer (Figure 26b) (Kirwan and Dokal 2008; Ghanim et al. 2021). Inactivating mutations of DKC1 in mice caused decrease of pseudouridines in the 28S rRNA and translation dysregulation of IRES-containing mRNAs (A. Yoon et al. 2006). Specifically, translation of some of these mRNAs is decreased such as those coding for (i) tumor-promoting Bcl-xL and XIAP, which inhibit apoptosis, and (ii) tumor suppressor p27 and p53 (A. Yoon et al. 2006; Bellodi et al. 2010;

Montanaro et al. 2010). In contrast, translation of others IRES-containing mRNAs such as VEGF and heat shock 70 was increased (Rocchi et al. 2013). Furthermore, DKC1 overexpression is associated with prostate cancer and lung cancer (Sieron et al. 2009; Penzo et al. 2015).

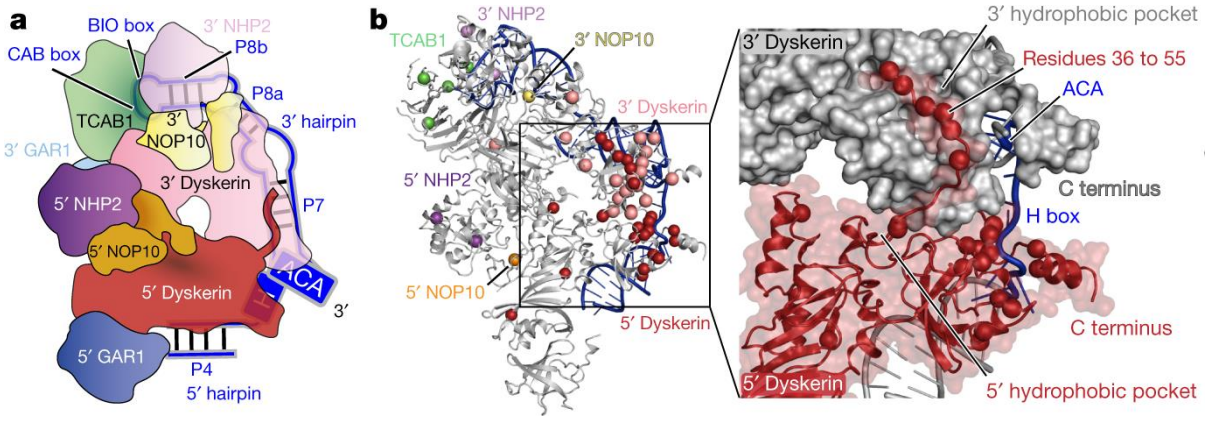

Figure 26. Structure of H/ACA ribonucleoprotein and mutations associated with disease

a. Schematic representation of the H/ACA RNA and its associated proteins. The H/ACA RNA is composed of two hairpins: the 5' hairpin (P4) and the 3' hairpin (P7, P8). Each hairpin binds a tetrameric protein complex including dyskerin, GAR1, NOP10 and NHP2. **b.** Structure of the H/ACA RNP, highlighting mutations (spheres) in its associated proteins that cause Dyskeratosis congenita. Inset and close-up view show a hotspot of disease mutations at the interface of both dyskerin subunits. Adapted from (Ghanim et al. 2021).

2.1.5 Adenosine to Inosine modification

Adenosine to Inosine (A-to-I) editing has been identified mainly in double stranded RNAs formed by inverted Alu repetitive elements (Alu dsRNA) located in introns and untranslated regions. A-to-I editing is detected also in primary miRNA, mRNA coding regions and tRNAs (H. Chung et al. 2018; Levanon et al. 2004). The enzymes performing the A-to-I editing on tRNAs are known as ADATs and will be described in the last part of the introduction.

A-to-I editing in the non tRNA molecules is mediated by the Adenosine Deaminases Acting on RNA (ADAR) family, which in vertebrates is composed of three proteins: ADAR1, ADAR2 and ADAR3 (Nishikura 2010). ADAR1 is expressed ubiquitously and ADAR2 mostly in the brain but also in some other tissues. In contrast, ADAR3 expression is restricted to the brain (Lonsdale et al. 2013). ADAR1 has two isoforms, ADAR1p100 and ADAR1p150; the first one is mainly present in the nucleus and the second one in the cytoplasm. ADAR2 and ADAR3 are mainly observed in the nucleus (Maas and Gommans 2009). All three ADAR proteins have dsRNA-binding domains and at their C-terminal regions a catalytic deaminase domain. ADAR1 and ADAR2 homodimerization is required to

exert their A-to-I editing activity (Figure 27). In contrast, ADAR3 cannot homodimerize and does not exhibit enzymatic activity (Nishikura 2010; M. H. Tan et al. 2017).

Two proteins recognizing the inosine modification have been identified: $p54^{nbr}$ (Z. Zhang and Carmichael 2001) and vigilin (Q. Wang et al. 2005). In addition, one enzyme, endonuclease V, has been identified as a ribonuclease cleaving inosine-containing RNAs at the second phosphodiester bond 3' to the inosine modification (Morita et al. 2013; J. Wu et al. 2019). Importantly, the A-to-I modification is involved in many different functional processes.

A-to-I editing causes recoding, *i.e.* editing in the coding regions of pre-mRNAs. Since the translational machinery recognizes inosine as guanosine, recoding produces a change in the amino acid composition of proteins. Some transcripts coding for neurotransmitter receptors and ion channels undergo this recoding-type editing, which affects their functions. For instance, the G protein-coupled serotonin receptor $5\text{-}HT_{2C}R$ (Burns et al. 1997), the potassium channel $K_V1.1$ (Bhalla et al. 2004), the calcium channel $Ca_V1.3$ (Hua Huang et al. 2012), the α3 subunit of $GABA_A$ receptor (Ohlson et al. 2007) and the GluR2 receptor. In case of this latter receptor, A-to-I editing in the *GluR2* transcript will change a glutamine residue, located in the channel pore of the GluR2 receptor, into arginine. The edited site is called the Q/R site. The unedited receptor is permeable to Ca^{++}, but the edited GluR2 receptor becomes impermeable to this ion. Specifically, ADAR2 deletion in mice cause seizures and death because of excessive Ca^{++} permeability (Higuchi et al. 1993; Konen et al. 2020).

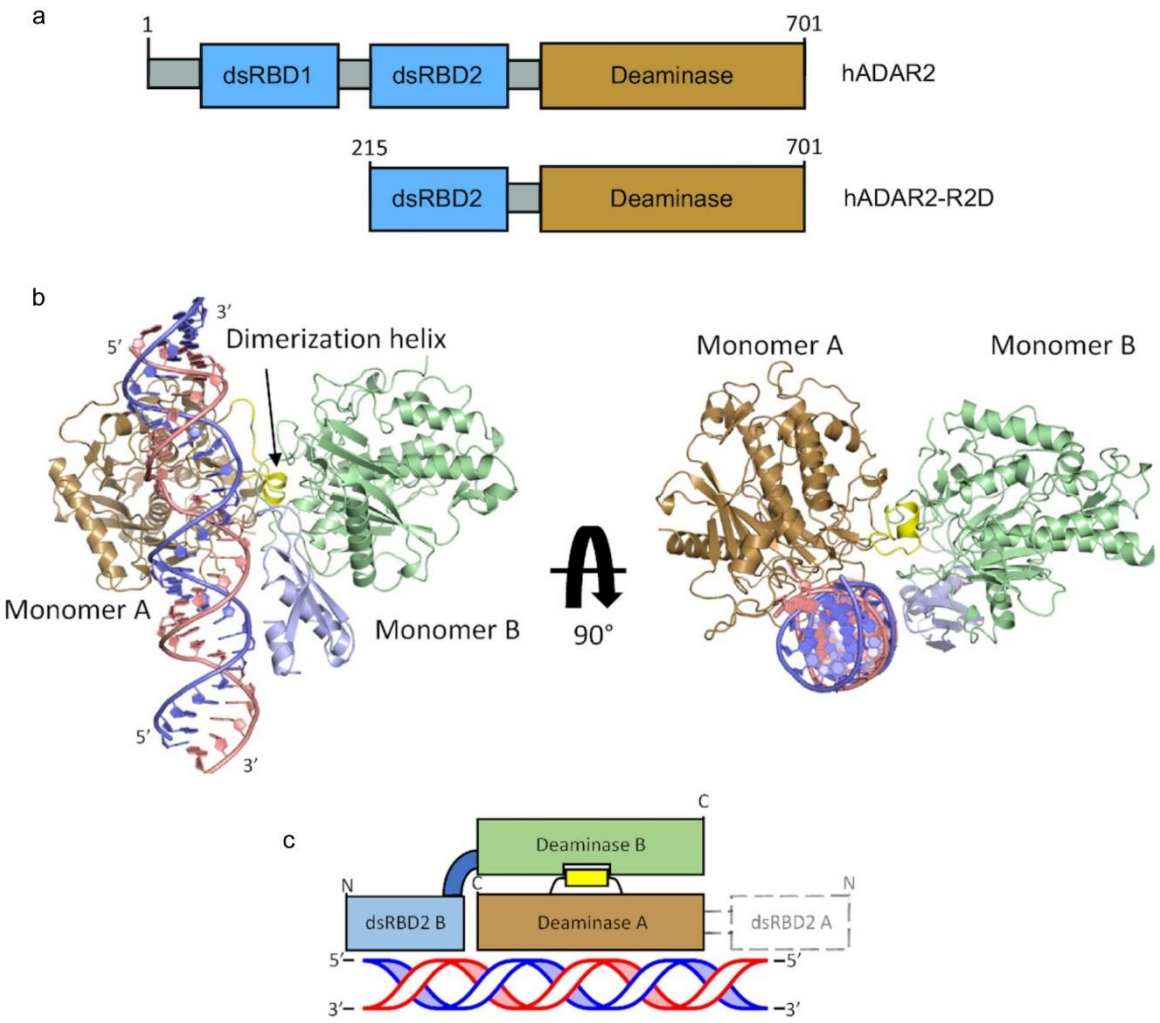

Figure 27. Structure of ADAR2 bound to dsRNA

a. Schematic representation of human ADAR2 (hADAR2) showing that it is composed of two dsRNA binding domains (dsRBDs) and one deaminase domain. ADAR2 construct bearing the second dsRBD and the deaminase domain (hADAR2-R2D) was revealed to be an active enzyme and was used for crystallization. **b.** Structure of hADAR2-R2D bound to a dsRNA. This structure shows a homodimerization of ADAR2 through its deaminase domain upon dsRNA binding. Curiously, ADAR2 binds to the dsRNA through the deaminase domain of one monomer and the dsRBD2 domain of the other monomer. **c.** Schematic representation of ADAR2 interaction with dsRNA. Adapted from (Thuy-Boun et al. 2020).

The A-to-I modification also plays a role in gene silencing. dsRNA containing several inosine modifications are recognized by Vigilin, which forms a complex with the RNA helicase A (RHA) and the KU86-70 proteins (Q. Wang et al. 2005). Vigilin also recruits the histone methyltransferase SUV39H1, which methylates histone H3 on Lys9. H3K9m is then recognized by heterochromatin protein 1(HP1), thus causing gene silencing (J. Zhou et al. 2008; Kondo and Issa 2003; Farooq et al. 2019).

The A-to-I modification has also been shown to play a role in RNA-nuclear retention. mRNAs containing, at their 3'-UTRs, A-to-I edited Alu dsRNA are retained in the nucleus in paraspeckles. Both, the inosine-specific dsRNA binding protein $p54^{nrb}$ and the long non-coding RNA NEAT1 (nuclear paraspeckle assembly transcript 1) are required to retain these mRNAs (Z. Zhang and Carmichael 2001; L.-L. Chen and Carmichael 2009). However, under stress condition these mRNAs are cleaved at their 3'-UTR and released to the cytoplasm for their translation. For instance, mCAT2, membrane receptor controlling uptake of Arginine, which is used for the biosynthesis of nitric oxide, is induced through this mechanism under cellular stress (Prasanth et al. 2005).

The A-to-I modification plays a role in splicing. A-to-I editing can create new 5' donor (GU) and 3' acceptor (AG) splicing sites. For instance, the AU-to-IU and the AA-to-AI editing will be read as a new 5' donor and 3' acceptor sites respectively by the spliceosome, which recognizes inosine as guanosines. Thus, A-to-I modification of Alu dsRNAs located within introns triggers the Alu exonization (Y. Feng et al. 2006; Lev-Maor et al. 2007).

Lastly, the A-to-I modification regulates RNA interference. A-to-I editing of long non-coding dsRNAs is performed by the ADAR1 homodimer and the A-to-I editing of primary miRNAs (pri-miRNA) by either ADAR1 or ADAR2 homodimers (W. Yang et al. 2006; D.-S. C. Cho et al. 2003). The presence of inosine in pri-miRNAs affects each step of their processing by RNA interference enzymes. Briefly, pri-miR are recognized and cleaved by the DROSHA/DGR8 complex, which leads to the formation of precursor-miRNA (pre-miRNA). Pre-miRNAs are further cleaved by the Dicer/TRBP complex to produce a miRNA which is loaded onto the RISC (RNA-induced silencing complex) complex. One of the miRNA strands, called the guide strand, directs the RISC complex to the target mRNA which causes translation inhibition or mRNA decay.

Specifically, A-to-I editing of some pri-miRNAs increases or decreases their cleavage by DROSHA/DGR8 complex. For instance, editing of pri-miR-142 (W. Yang et al. 2006), pri-miR-33, pri-miR-132a2, pri-miR-379 (Kawahara et al. 2008) and pri-miR-455 (Shoshan et al. 2015) decreases their cleavage by Drosha/DGR8. However, editing of pri-miR-197 and pri-miR-203 increases their cleavage by Drosha/DGR8 (W. Yang et al. 2006). In addition, A-to-I editing of pri-miR-151 affects the cleavage of its pre-miRNA by Dicer/TRBP complex (Kawahara, Zinshteyn, Chendrimada, et al. 2007), whereas A-to-I editing of pri-miR-BART6 from EBV (Epstein-Barr virus) affects the loading of the miR-BART6-5p onto RISC

complex, thus affecting its function. Otherwise, unedited pri-mi-BART6 causes production of miR-BART6-5p which targets the human Dicer mRNA, causing inhibition of the human RNAi (Iizasa et al. 2010). Thus, A-to-I editing of long dsRNA and pri-miRNAs causes less production of siRNAs and miRNAs.

However, ADAR1 can stimulate the miRNA processing in an enzymatic-independent manner. ADAR1 heterodimerization with Dicer triggers both a fourfold increase of the pre-miRNA cleavage rate by Dicer and promotes the miRNA loading onto RISC complex (Ota et al. 2013). Finally, A-to-I editing of miRNAs also affects the recognition of their target mRNA. For instance, edited miR376-5p targets a different mRNA, compared to that targeted by the unedited miR376-5p (Kawahara, Zinshteyn, Sethupathy, et al. 2007).

Importantly, the A-to-I modification has an essential role in the immune system. ADAR1p150 mediates the A-to-I editing of endogenous long dsRNA containing Alu repeats, which are located within introns and the 3'-UTR. A-to-I editing of these endogenous dsRNAs prevents their cytoplasmic sensing by antiviral sensing molecules, through three mechanisms, which lead to the inactivation of the interferon (INF) I signaling pathway, translation inhibition and apoptosis. First, in ADAR1-deficient cells, endogenous dsRNA activates RNA sensor molecules MDA5 and RIG-I (Schneider, Chevillotte, and Rice 2014; Rehwinkel and Gack 2020). Their activation causes expression of interferon I, which in turn leads to the activation of the interferon I signaling pathway and expression of interferon stimulated genes (ISGs), thus causing inflammation. Therefore, A-to-I editing of endogenous dsRNA allows their recognition as self to prevent auto-immune reaction (Pestal et al. 2015; Liddicoat et al. 2015; H. Chung et al. 2018). Second, in ADAR1-deficient cells and IFN type I induction, endogenous dsRNAs cause the activation of PKR (protein kinase R). PKR phosphorylates the eukaryotic initiation factor 2α (eIF2α), which affects the delivery of Met-tRNAi to the ribosome, leading to translation initiation inhibition (H. Chung et al. 2018). Third, in ADAR1-deficient cells and IFN type I induction, endogenous dsRNAs causes the activation of RNaseL, which cleaves endogenous RNAs, inhibits translation and promotes apoptosis (Figure 28) (Yize Li et al. 2017).

In agreement with its many different roles, A-to-I editing by ADARs is associated to several diseases including immune diseases, cancer, and neurological and neurodegenerative disorders.

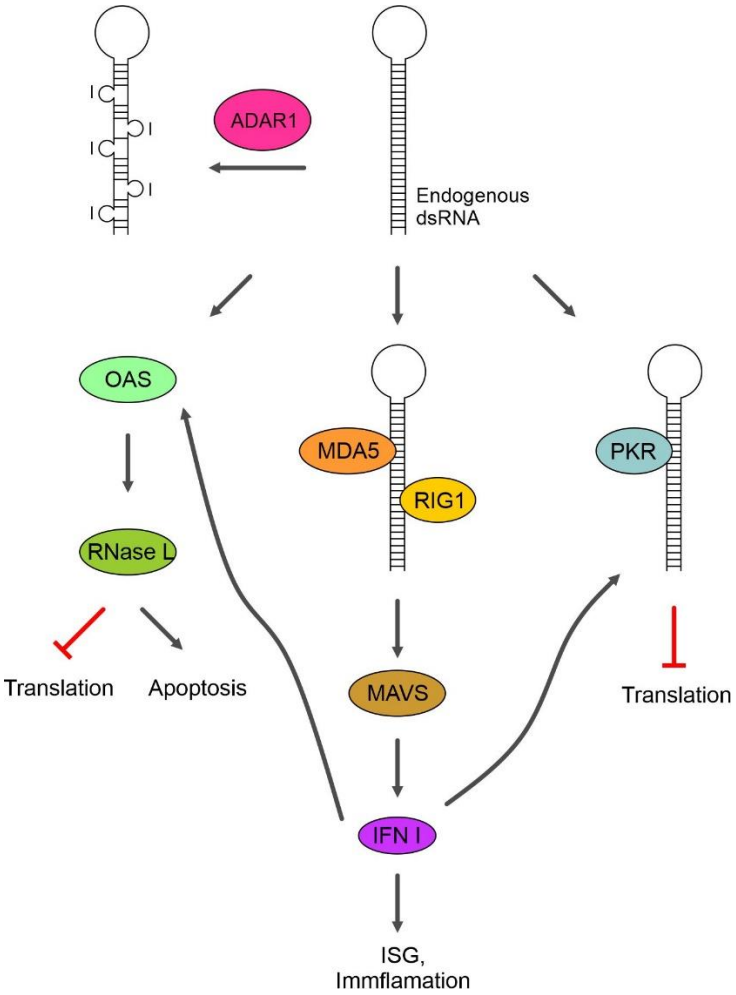

Figure 28. ADAR1 role in preventing an autoimune reaction

A-to-I editing of endogenous dsRNAs by ADAR1 prevents recognition of these dsRNAs as "non-self" by viral sensor molecules that otherwise would lead to an autoimmune reaction. Unedited endogenous dsRNAs causes inflammation, translation inhibition and apoptosis through three mechanisms. First, unedited dsRNAs are recognized by MDA5 and RIG1 which activates the interferon type I response, leading to inflammation. Second, unedited dsRNAs activates the oligoadenylate synthetase (OAS)/RNaseL pathway which causes translation inhibition and apoptosis. Third, unedited dsRNAs activates protein kinase R (PKR), which phosphorylates eIF2α leading to translational inhibition. Based on (Yize Li et al. 2017; H. Chung et al. 2018; Nishikura 2016)

Mutations in ADAR1, which affects the editing of endogenous dsRNAs, also causes the autoimmune Aicardi-Goutières syndrome (AGS). This syndrome is characterized by an increased interferon alpha expression characteristic of an excessive immune response (G. I. Rice et al. 2012). Overexpression of ADAR1p150 is associated with rheumatoid arthritis (RA) through the editing-dependent stabilization of Catepsin S transcript (Vlachogiannis et al. 2020). ADAR1p150 overexpression is also associated to systemic lupus erythematosus, through the editing of the alpha regulatory subunit of type I protein kinase A (Laxminarayana, Khan, and Kammer 2002).

Both ADAR1 and ADAR2 are implicated in cancer. ADAR1 act as an oncogene in different types of cancer, for instance in chronic myeloid leukaemia (Zipeto et al. 2016), cutaneous carcinoma (Herbert 2019), hepatocellular carcinoma (L. Chen et al. 2013) and lung cancer (Amin et al. 2017). In contrast, ADAR2 has been shown to acts as a tumor suppressor in glioblastoma. ADAR2 activity is impaired in this type of cancer, which causes both a decrease in A-to-I editing of the GluR2 Q/R receptor (Oakes et al. 2017; J. Wei et al. 2014; Cenci et al. 2008) and an altered editing of miRNAs in the most severe grades of glioblastoma (Paul et al. 2017). For instance, unedited form of miR-376a-5p and miR-589 target tumors suppressors transcripts, thus promoting glioblastoma cell proliferation and migration (Choudhury et al. 2012; Cesarini et al. 2018).

In Amyotrophic Lateral Sclerosis (ALS), it has been shown that deficient A-to-I editing of the GluA2 receptor, due to ADAR2 deletion, downregulation or mislocalization, causes increased of Ca^{++} influx in motor neurons, which activates the calpain protease that cleaves TDP-43 protein. Fragments of TDP-43 accumulates in the cytoplasm of affected neurons, which is a hallmark of ASL (Yamashita et al. 2012). In patients affected by the Alzheimer disease, it was shown a decreased editing of A-to-I sites in the hippocampus region (Khermesh et al. 2016). In adult rats, forebrain ischemia triggered decreased expression of ADAR2 in neurons of the hippocampus, which caused a reduction of A-to-I editing at the GluR2 Q/R. In addition, induced expression of ADAR2 lead to survival of these neurons (P. L. Peng et al. 2006).

2.2 tRNA modifications, their roles and their implication in neurological diseases

tRNAs are the most modified RNA macromolecules (Tsutomu Suzuki 2021). Modifications can concern the sugar or the base of the nucleosides and are distributed at various locations along the tRNA. These include the acceptor stem, the D stem loop, the anticodon stem loop (ASL), the variable loop (VL) and the T stem loop (Figure 29).

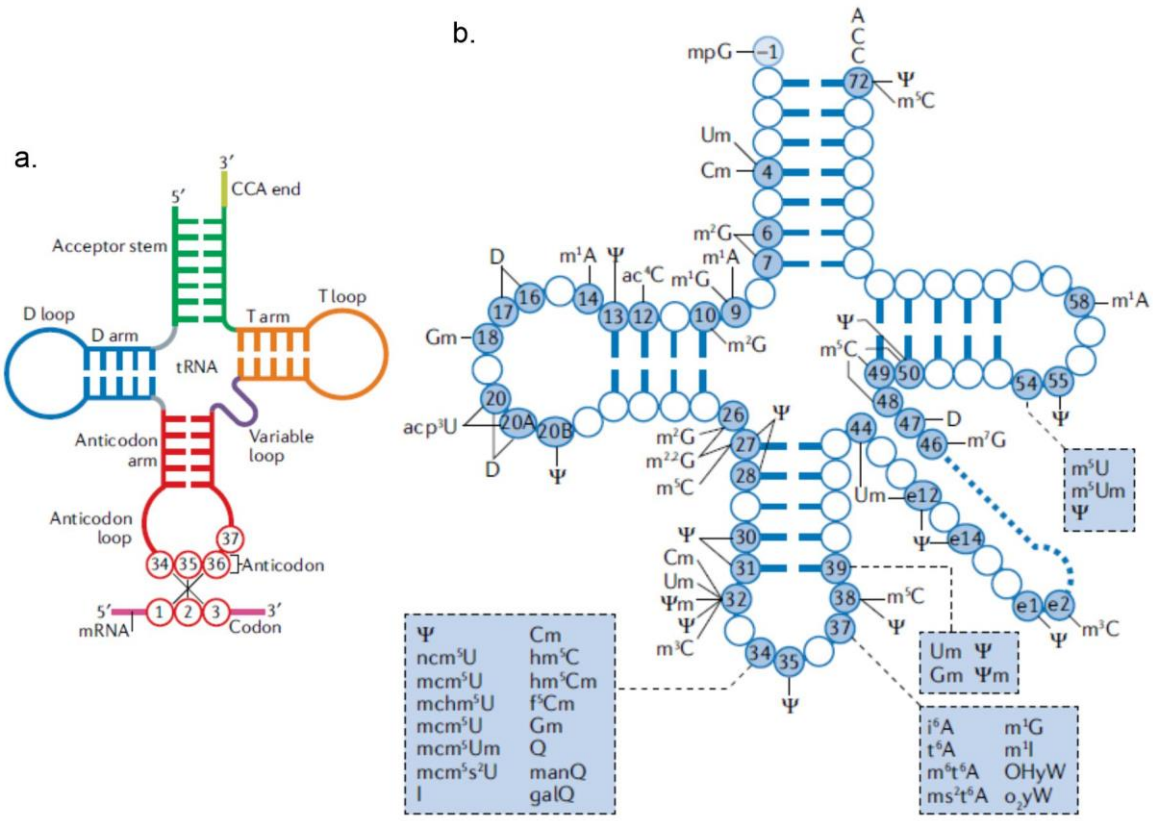

Figure 29. tRNA cloverleaf structure and modifications

a. Cloverleaf structure of the tRNA. The tRNA has five parts including: the acceptor stem, the dihydrouridine stem loop (DSL), the anticodon stem loop (ASL), the variable loop (VL) and the T stem loop (TSL). Nucleosides 34, 35 and 36 represent the anticodon, which recognizes by hydrogen bonding the three nucleobases of the codon of an mRNA in the ribosome. **b.** Modifications in the human cytoplasmic tRNA (Tsutomu Suzuki 2021).

Modifications have different roles including tRNA folding, structural stabilization and flexibility. In additions, some modifications are determinants for correct aminoacylation, while others can prevent tRNA enzymatic cleavage (Tsutomu Suzuki 2021). Furthermore, tRNA modifications within the ASL are important for correct decoding and maintenance of the reading frame. Importantly, mutations in tRNA modifying enzymes have been associated to several diseases, the most frequent being neurological disorders, revealing the importance of these modifications and reviving our interest for tRNAs as effector molecules (Chujo and Tomizawa 2021). A summary of neurological disorders and their associated tRNA modifications, including position and modification enzymes, is shown in Table 1.

Table 1. Human neurological disorders associated to aberrant tRNA modifications

Abbreviations: ID (intellectual disability), ASD (autism spectrum disorder), ASL (amyotrophic lateral sclerosis). Adapted from (Tsutomu Suzuki 2021; Chujo and Tomizawa 2021)

Neurological disorder	Gene	tRNA modification
Microcephaly, intellectual disability (ID), autism spectrum disorder (ASD), aggressive behavior, short stature	*PUS7*	Ψ (8, 13)
Microcephaly, ID, diabetes, short stature	*TRMT10A*	m^1G (9)
Lactic acidosis, hypotonia, polymicrogyria, deafness, early death	*TRMT10C*	m^1G, m^1A (9m)
Neurodegeneration, cardiomyopathy, early death	*HSD17B10* Partner protein of TRMT10C	m^1G, m^1A (9m)
Microcephaly, ID	*TRMT1*	$m^2{}_2G$ (26, 26m)
ID	*FTSJ1*	Nm (32, 34)
ID, Dubowitz-like syndrome, short stature, breast cancer	*NSUN2*	m^5C (34, 48, 49, 50, 48m, 49m, 50m)
ID, strabismus, microcephaly, epilepsy, speech delay	*ADAT3*	I (34)
Familial dysautonomia, male infertility, skin cancer (high expression)	*ELP1*	ncm^5U (34)
ID, ASD	*ELP2*	ncm^5U (34)
Amyotrophic lateral sclerosis (ALS), skin/breast cancers	*ELP3*	ncm^5U (34)
ID, ASD	*ELP4*	ncm^5U (34)
ID, bladder cancer	*ALKBH8*	$mchm^5U$ (34)
Microcephaly, ID, nephropathy, ambiguous genitalia, short stature, skin/breast cancers, early death	*CTU2*	2’ thiolation: mcm^5s^2U (34)
Hypertrophic cardiomyopathy, lactic acidosis, ID, short stature, early death	*MTO1*	tm^5U (34m)
MELAS, ID, hearing loss, short stature, early death	*GTPBP3*	tm^5U (34m)
Leigh syndrome, hepatopathy, lactic acidosis, hearing loss, early death	*MTU1*	tm^5s^2U (34m)
Microcephaly, seizure, lactic acidosis, muscle weakness, short stature, 5-AZA-resistant leukemia	*NSUN3*	f^5C (34m)
Demyelinating neuropathy, cardiomyopathy, lactic acidosis, renal tubulopathy, cirrhosis, short stature	*TRMT5*	m^1G (37, 37m), OHyW (37)
ALS	*TUW3*	OHyW (37)
Microcephaly, nephropathy, short stature, liver cancer (high expression), early death	*YRDC*	t^6A (37, 37m)
Microcephaly, nephropathy, short stature, early death	*OSGEP*	t^6A (37)
Microcephaly, nephropathy, short stature, early death	*TP53RK*	t^6A (37)
Microcephaly, nephropathy, short stature, early death	*TPRKB*	t^6A (37)
Microcephaly, nephropathy, short stature, early death	*LAGE3*	t6A (37)
Microcephaly, nephropathy	*GON7*	t6A (37)
Microcephaly, ID, cardiomyopathy, lung cancer (low expression), short stature	*TRIT1*	i^6A (37, 37m)
Microcephaly, ID, nephropathy, short stature	*PUS3*	Ψ (38, 39)
Partial epilepsy with pericentral spikes	*TRMT44*	Um (44)
Multiple sclerosis	*METTL1*	m^7G (46)
Microcephaly, ID, nephropathy, short stature	*WDR4*	m^7G (46)

2.2.1 Roles of modifications in the tRNA body

tRNA modifications can induce local or global structural changes in tRNAs. Local structural changes are mediated notably by sugar 2’-O-methylation, base methylations, pseudouridine (Ψ), and dihydrourine modifications (Figure 30).

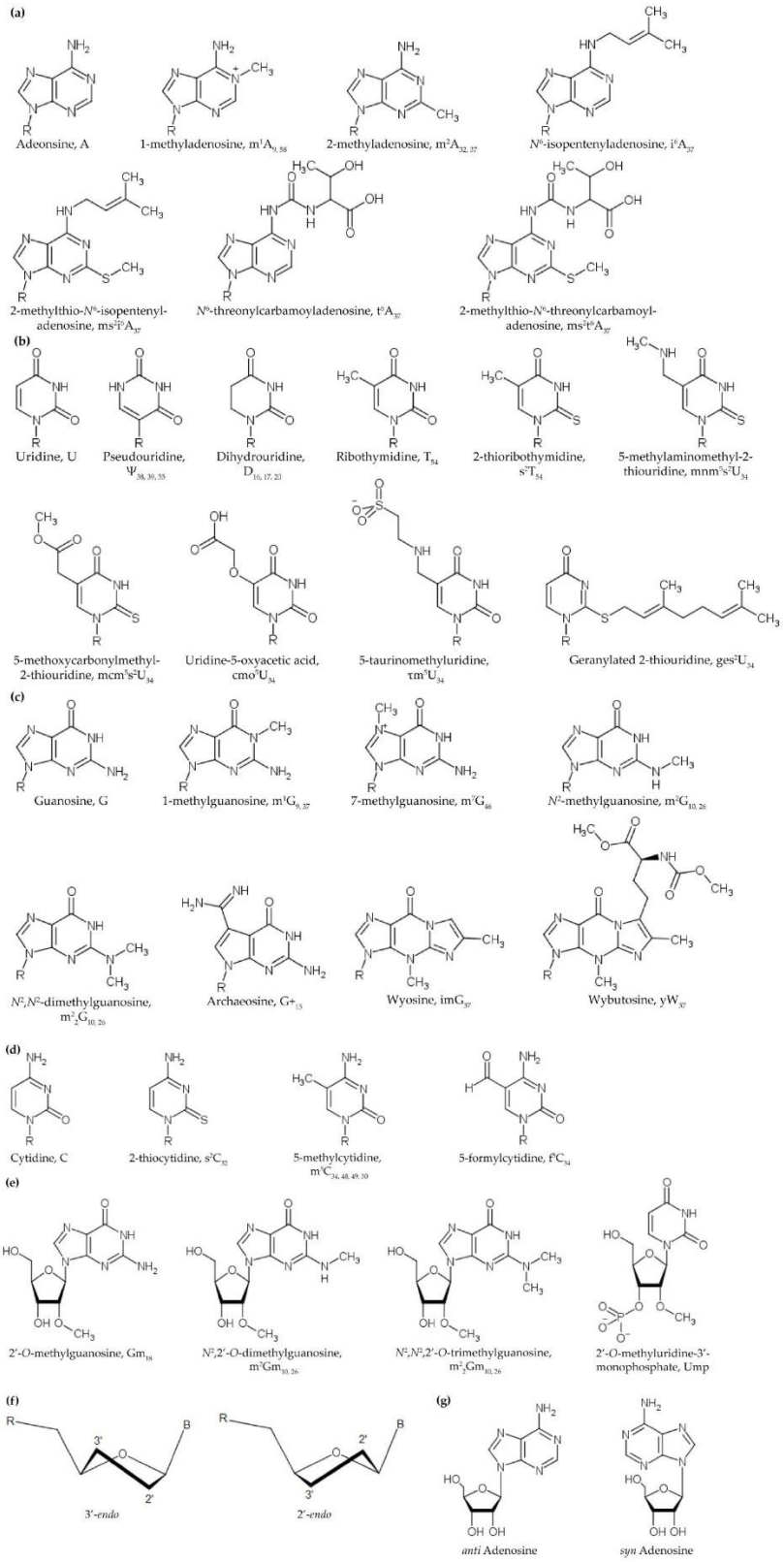

Figure 30. Nucleoside modifications and ribose conformation

a. Adenosine **b.** Uridine **c.** Guanosine **d.** Cytidine and their corresponding modifications (R=ribose) **e.** 2'-O-methylated nucleosides **f.** Ribose puckering: C3' endo and C2' endo conformations (R= phosphate, B= base) **g.** *anti* adenosine and *syn* Adenosine (Väre et al. 2017).

Sugar modifications also play a role. 2'-O- methylation is found in tRNAs at different positions (4, 6, 18, 32, 34, 39, 44, 54 and 56) (Hori 2014). The 2'-O methylation of ribose prevents a nucleophilic attack made by the unmodified 2'-OH, that otherwise would degrade the tRNA molecule (Soukup and Breaker 1999). Furthermore, 2'-O methylation favors the 3' endo sugar conformation that stabilizes an A-type helical region of tRNAs (Darrell R. Davis 1998; Kawai et al. 1992). For instance, Gm18 and Gm56 (at the TΨC loop) stabilize the tertiary interaction with G19 (at the D loop).

5-methylcitosine (m^5C) in tRNAs is identified at several positions: in the ASL at positions 34 and 38, at the junction between the variable loop and the TΨC stem-loop at positions 48, 49 and 50 and at the acceptor stem at position 72. Different NSUN proteins are responsible of these modification at different position and not all m^5C are present in one tRNA species. For instance, NSUN2 modifies tRNAs at positions 48-50 and $tRNA^{Leu}$ at position 34 (Khoddami and Cairns 2013; Blanco et al. 2014; Tuorto et al. 2012). DNMT2 mediates formation of m^5C at position 38 on $tRNAs^{Val}$, $tRNA^{Gly}$ and $tRNA^{Asp}$ (Goll et al. 2006; Schaefer et al. 2010; Tuorto et al. 2012). NSUN6 mediates methylation of C72 on $tRNA^{Cys}$ and $tRNA^{Thr}$ (Haag et al. 2015). NSUN3 modifies the C34 of mitocondrial $tRNA^{Met}$ (Van Haute et al. 2016; Nakano et al. 2016).

Since the 5-methyl group it is not located on the Watson-Crick interface, it does not affect canonical base pairing. C48 interacts with G15, known as 'Levitt-pair'. This non-canonical G15○C48 interaction brings together the D and variable loops important to keep the tRNA L-shape (Levitt 1969). The m^5C48 has a higher hydrophobic character compared to the unmodified cytosine, which is believed to favor stacking interactions. Furthermore, methylation of position 46 (m^7G) and 58 (m^1A) stabilize their ternary (C13●G22○m^7G46) and binary (U54○ m^1A) pairing interactions, respectively (P. F. Agris, Sierzputowska-Gracz, and Smith 1986).

Ψ is found at different positions in the tRNA depending on the isoaceptor, organism and organelle (Spenkuch, Motorin, and Helm 2014). Pseudouridine stabilizes local tRNA structure by three means. First, Ψ has an increased hydrophobic character compared to uridine, which favors stacking interactions (D. R. Davis 1995; Cs et al. 1999). Second, Ψ favors the C3' endo sugar conformation of its neighbors, which confers rigidity (Darrell R. Davis 1998). Third, pseudouridine has an additional hydrogen bond donor N1 compared to uridine. For instance, Ψ55 (located in the TΨC loop) form a tertiary interaction with G18

(within the D loop) (S. H. Kim et al. 1974). Ψ13 (at the end of the D stem) interaction with nucleoside 22 (U, G, C or A) is more stable than that involving U13, thereby contributing to the stabilization of the D stem (Kierzek et al. 2014).

In contrast to the modifications mentioned above, which confer structural stability, Dihydrouridine (D) gives flexibility to the tRNA molecule by two means. First, since D is a non-aromatic base, it is no planar but puckered (F. Yu et al. 2011; Rohrer and Sundaralingam 1970). Thereby, D does not form stacking interactions with aromatic bases. Second, the saturation of the C5=C6 double bond causes a C2' endo conformation of its ribose and in that of the 5' neighboring nucleoside, which destabilizes the tRNA local structure (Dalluge et al. 1996).

tRNA modifications can also have more global effects. Global structural effects on tRNA are mediated by modifications at position 9, 10 and 26. For instance, methylation at position 9 (N^1-methyladenosine (m^1A9) or N^1-methylguanosine (m^1G9)) is necessary for correct folding of mitochondrial tRNAs (Helm et al. 1998). The m^1A9 modification prevents misfolding by disrupting the Watson-Crick pairing between A9 and U64. In absence of m^1A9 mitochondrial, tRNA-Lys adopts a rod-like structure, which is functional neither for aminoacylation by lysil-tRNA synthetase nor for translation at ribosome (Helm, Giegé, and Florentz 1999).

N^2,N^2 dimethylguanosine ($m^2{}_2G$) at position 10 and 26 has been shown to be important for correct tRNA folding of thermophilic organisms and of some human cytoplasmic tRNAs. The modified $m^2{}_2G$ eliminates one hydrogen bond donor in the Watson-Crick interface of the precursor guanosine, thereby preventing its base pairing with C, but promoting pairing with G or A. For instance, in *Pyrococcus abissy* tRNA-Pro, the modified $m^2{}_2G10$ is important to wobble pair with U25, lack of this modification causing an extended D-arm (Urbonavicius, Armengaud, and Grosjean 2006). Furthermore, in *P. abissy* tRNA-Asp, $m^2{}_2G10$ prevents its pairing with C27, lack of $m^2{}_2G10$ producing an extended D-loop (Urbonavicius, Armengaud, and Grosjean 2006). In *Haloferax volcanii* tRNA-Lys $m^2{}_2G$ at position 26 prevents base pairing of C25-G45 and C26-G44, lack of this modification producing an extended anticodon stem and shortened D stem (Steinberg and Cedergren 1995). Moreover, human cytoplasmic tRNA-Asn has a $m^2{}_2G$ modification at position 26, which prevents its pairing with C11, but promotes its pairing with A44 at the beginning of the anticodon stem, which further promotes a correct tRNA structure (Steinberg and Cedergren 1995).

2.2.2 Roles of modifications in the tRNA anticodon loop

A functional anticodon loop should form a stable codon-anticodon pairing in the ribosome, which is absolutely required for efficient translation. The functional anticodon loop is characterized by a U-turn structure which is mediated by modifications at position 37. A modified position 37 prevents base pairing of nucleosides 32-38 and 33-37, which promotes an open seven-member anticodon loop for correct recognition of the codon in the ribosome decoding center (Cabello-Villegas, Winkler, and Nikonowicz 2002; Olejniczak and Uhlenbeck 2006; Stuart et al. 2000). Furthermore, the hydrophobic character of the modified base at position 37 improves stacking interactions which stabilize the anticodon loop (Durant et al. 2005; Stuart et al. 2000). Furthermore, modified position 37 maintains the reading frame by supporting correct first base pairing between the third anticodon base and the first codon base, which is mediated by van der waals and hydrophobic interactions (P. F. Agris 1996). For instance, the absence of 2-methylthio N^6-(cis-hydroxyisopentenyl) adenosine 37 (ms^2io^6A) or N1-methylguanosine 37 (m^1G37) triggers a +1 frameshinfting (Urbonavicius et al. 2003). Similarly, lack of wybotusine 37 (yW37) in tRNA-Phe causes +1 and -1 frameshifting (Waas et al. 2007).

Another essential position in the anticodon loop is position 34, also known as the wobble position ((Crick 1966; Paul F. Agris et al. 2018); see below). Modifications at position 34 have been shown to contribute to the maintenance of the reading frame. For instance, absence of Q34 for tRNAs coding for His, Tyr, Asn and Asp produces +1 frameshifting (Urbonavicius et al. 2003). Absence of mnm^5s^2U34 in *E.coli* tRNAs for Lys, Gln, Glu, Arg and Leu produces +1 frameshifting (Urbonavicius et al. 2003).

Upon stress, some human cytoplasmic tRNAs are cleaved at the anticodon by the endoribonuclease angiogenin (Yamasaki et al. 2009). Some modifications prevent angiogenin cleavage, for instance 2'-O methylation at C34 (Cm34), Queuosine 34 (Q34) and m^5C (Xiaoyun Wang et al. 2018). Specifically, in Cm34, the 2'-O-methylation modification is proposed to prevent deprotonation of 2'-OH, which is required for angiogenin activity (Vitali and Kiss 2019). m^5C also prevents binding of angiogenin, but it is not known which m^5C modified position (34, 48, 49, 50) contributes to prevent that cleavage (Blanco et al. 2014).

2.2.3 Roles of modifications in the wobble position

The genetic code has 61 codons that encode 22 amino acids, the remaining three codons (TAA, TAG, TGA) being used as stop codons. This means that some amino acids are encoded

by more than one codon, which is known as the degeneracy of the genetic code ((M. Nirenberg et al. 1965; Crick et al. 1961; M. W. Nirenberg and Matthaei 1961; Paul F. Agris et al. 2018). For instance, amino acids encoded by four different codons are known as amino acids belonging to a fourfold degenerate codon box; where the first two bases of the codon are conserved, and the third base of the codon are different and can be G, A, C or U (Paul F. Agris, Vendeix, and Graham 2007).

Furthermore, the 61 codons are decoded by a smaller number of tRNAs (40-50 depending on the organism), which means that a single tRNA should recognize more than one codon. For instance, a tRNA recognizing a fourfold degenerate codon box forms canonical Watson-Crick pairing between bases 36 and 35 of the anticodon and the first two bases of the codon. However, the base at position 34 (known as wobble position) of the anticodon, must recognize four different bases at the third position of the codon. This recognition is made in a non-canonical manner, known as wobble pairing, and generally requires modifications of the nucleoside 34. Therefore, modifications at the wobble position of tRNAs often expand its decoding capacity. However, in some cases, modifications of the wobble position rather restrict its decoding capacity for accurate decoding (Paul F. Agris et al. 2018).

2.2.3.1 Wobble modifications that restrict decoding capacity

Isoleucine and methionine share the same fourfold codon box, where AUC, AUU and AUA code for isoleucine and AUG for methionine. In bacteria, tRNA-Ile-GAU decodes AUC and AUU. An additional tRNA-Ile-k^2CAU which has a lysidine (k^2C) modification at position 34 is required to decode AUA as isoleucine but does not decode AUG (Henri Grosjean and Björk 2004). Therefore, lysidine allows recognition of A and prevents recognition of G at the third position of the codon (Muramatsu et al. 1988). Lysidine is a modified cytidine containing a lysine at position 2. Lysidine can exists in two tautomeric forms, and it is predicted that one of them allows recognition of A, while both tautomers do not recognize G (Paul F. Agris et al. 2018). Furthermore, lysidine is a determinant for correct amino acid charging by Isoleucyl-synthetase (IleRS), thus IleRS can discriminate tRNA-Ile- k^2CAU from tRNA-Met-CAU.

In yeast and archea lysidine's function is rather accomplished by pseudouridine and agmatidine (agm^{2}C34), respectively (Mandal et al. 2010; Senger et al. 1997). Agmatidine is a modified cytidine containing a decarboxy-arginine at position 2. The structure of the tRNA-Ile- agm^{2}CAU bound to the AUA codon in the ribosome, shows a single hydrogen bond between the agm^{2}C34 and the A at the third position of the codon (A3); in addition, the

terminal amine of agmatidine hydrogen bonds the O'4 of the ribose of a downstream nucleoside (Voorhees et al. 2013). Since agmatidine and lysidine are chemically similar, the interactions made by agmatidine might represent a conserve mode recognition and stabilization of the AUA codon (Voorhees et al. 2013).

2.2.3.2 Wobble modifications that expand decoding capacity

There are six amino acids (Ala, Gly, Pro, Ser, Thr and Val) that are encoded by at least one fourfold degenerated codon boxes. For each of these amino acids, the first two bases of the codon are conserved but the third base of the codon is different, and bears a U, C, G or A (reviewed by Paul F. Agris et al. 2018). In prokaryotes, for each of those amino acids, there are several tRNAs but among them one can decode all four codons of the degenerate codon box. This tRNA has the 5-oxyacetic acid (cmo^5) modification at position U34, which enables recognition of all U, C, G and A at the third position of the codon (Nasvall, Chen, and Bjork 2004; Näsvall, Chen, and Björk 2007).

For instance, in *E. coli*, the cmo^5U34 "pre-structures" the ASL of tRNA-Val-UAC by two means, to enhance its pairing capacity to near cognate codons of the GUN valine codons. First, the 3'-OH adopts a 3' endo conformation which provides stability (Weixlbaumer et al. 2007; Kawai et al. 1992; 1991). Second, a hydrogen bond is formed between the 2'-OH of U33 and the O5 of the cmo^5 modification, which constrains the U34 (Weixlbaumer et al. 2007). Thereby, the modification of tRNA-Val-cmo^5UAC can recognize U and C ending codons. Furthermore, U34 must be modified to pair with G at the third position of the codon. But, the cmo^5U34-G3 pair is no longer a wobble interaction, instead they interact by three hydrogen bonds thanks to the enol form of the cmo^5U34, as a reminiscence of a C-G pair (Weixlbaumer et al. 2007).

Furthermore, *E. coli* tRNA-Val-cmo^5U34AC contains another modification, m^6A at position 37. This later modification prevents intraloop hydrogen bond formation within the ASL and promotes base stacking, thereby forcing the ASL to adopt an open loop structure which is required for codon-anticodon pairing within the ribosome (Paul F. Agris, Vendeix, and Graham 2007). The ASL of tRNA-Val-UAC with neither cmo^5 at U34 nor m^6 at A37 binds weakly to the GUA codon and does not bind either to GUG, GUU and GUC codons within the 30S ribosome (Vendeix et al. 2008). This shows the importance of modifications in the ASL for expanding the decoding capacity.

Amino acids Asp, Asn, His and Tyr are represented by twofold degenerated codon box. For each of these amino acids, the first two bases are conserved and the third base of the codon bears either a G or a U. tRNAs decoding these codons have a Queuosine (Q) or its glycosylated derivatives at position 34 to be able to recognize both G and U ending codons (Morris, Brown, and Elliott 1999). Furthermore, position 37 of these tRNAs are modified, bearing often a Wyosine which enhances anticodon-codon pairing by stacking interactions. In addition, Wyosine pre-structures the ASL by preventing formation of hydrogen between bases 32 and 37 (de Crécy-Lagard et al. 2010). In mitochondria, Wyosine is replaced by i^6A or by methylated purines at position 37 (Takeo Suzuki and Suzuki 2014).

Lysine is coded by AAG and AAA codons. In mammals, tRNA-Lys-CUU decodes the AAG codon and tRNA-Lys-UUU can decode both lysine codons. However, this later tRNA is modified at U34 to xm^5s^2U34 or derivatives thereof, to be able to recognize both codons and for translocation on the ribosome (Phelps et al. 2004). In bacteria, the xm^5s^2U34 modification is mnm^5s^2U34. This modification adopts keto-enol tautomeric forms, one tautomer can pair with A and the other with G (Murphy et al. 2004; Paul F. Agris et al. 2018). Additionally, tRNA-Lys-UUU has a modification at position 37, t^6A, which inhibits formation of intraloop hydrogen bonds that would otherwise condensate the ASL (Murphy et al. 2004).

In mitochondria 5-formylcytidine (f^5C) modification at position 34 in tRNA-Met is important for recognition of both AUG and AUA codons as methionine (Takemoto et al. 2009). f^5C modification is catalyzed by both the methyltransferase NSUN3 and the dioxygenase ALKBH1 (Nakano et al. 2016; Haag et al. 2016).

Finally, Adenosine at position 34 pairs with U at the third position of the codon. However, when Adenosine is converted to Inosine, the I34 can recognize U, C and A bases at the third position of the codon (Crick 1966). Thus, A-to-I editing of the anticodon, expands its decoding capacity. For instance, in bacteria the ASL-Arg-ACG must be modified to ASL-Arg-ICG to be able to bind CGU, CGC and CGA Arg codons in the A site of the ribosome (Murphy and Ramakrishnan 2004; Cantara et al. 2012). The unmodified ASL-Arg-ACG binds only to the CGU codon and does not bind the two other codons CGC and CGA (Cantara et al. 2012).

2.3 A-to-I editing of tRNA-Arg(ACG) wobble adenosine in prokaryotes by the TadA homodimer

In bacteria, an homodimer of the TadA protein catalyzes the hydrolytic deamination reaction that converts A34 into I34 in one tRNA isotype, tRNA-Arg(ACG) (Wolf, Gerber, and Keller 2002). TadA belongs to the larger family of cytidine deaminases (CDA) (A. P. Gerber and Keller 2001). TadA has an overall fold formed of a central β-sheet flanked by α-helices. Helices α1, α5 are opposite to the dimer interface while helices α2-to-α4 are located at the dimer interface (Figure 31a) (J. Kim et al. 2006; Kuratani et al. 2005; Losey, Ruthenburg, and Verdine 2006). Helices α2-α4 and their loops form the active site of Tad, each monomer contributing however to both active sites of the complex. The active site of TadA contains a zinc ion which is coordinated by His53, Cys83, Cys86 and a water molecule that participate in catalysis (Losey, Ruthenburg, and Verdine 2006). In addition, a conserved Glu55 mediates proton transfer during catalysis, mutation of this conserved Glu into Ala producing a catalytically inactive enzyme (Elias and Huang 2005). The catalytic mechanism of A-to-I editing is proposed to be similar to that of cytidine deaminases (Betts et al. 1994; S. J. Chung, Fromme, and Verdine 2005). Glu55 acts as a proton shuttle, which both abstracts a proton from the zinc-bond water molecule to produce a hydroxide ion; and protonates the N^1 of the adenosine 34. Thereby, Glu55 reduces the double bond between N^1 and C^6 of adenosine, which renders the C^6 more susceptible to the hydroxide ion attack to form the tetrahedral intermediate. Next, the C^6-$NH_2{}^6$ bond cleavage is mediated by transfer of proton from OH^6 to $NH_2{}^6$, this proton is then abstracted by Glu55. The tetrahedral intermediate collapses after abstraction of this proton by Glu55 and delivery of this proton to the leaving amine to produce the inosine and ammonia (Figure 31b). (Wilson, Rudolph, and Quiocho 1991; Kinoshita et al. 2003; Hall et al. 2011; T.-P. Ko et al. 2003; Sh et al. 2004).

The structure of TadA in complex with the ASL of its substrate, tRNA-Arg-ACG, showed that, at the entrance of the TadA active site, several pockets are formed by the two TadA monomers and that interact with the ASL, notably the anticodon loop. These pockets accommodate bases 33 to 37; there is no pockets for the base pair 32-38, but this pair interacts with Tad A as well (Losey, Ruthenburg, and Verdine 2006). Residues at the C-terminal alpha helix of TadA have been proposed to interact the tRNA; in addition, mutations of these residues have been shown to affect TadA activity (Elias and Huang 2005). Indeed, the structure of TadA/ASL shows that residues forming the C-terminal helix of TadA interacts with the ASL. For instance, F144 and F145 form stacking interactions with C35 and G36

respectively, R149 interacts to the phosphate of U33 and forms two hydrogens bonds to the G36 base (Losey, Ruthenburg, and Verdine 2006). Interestingly, in absence of a substrate, this alpha helix is only partially observed or is not present at all in the electron density, showing that it can adapt to recognize TadA ASL substrate (Elias and Huang 2005).

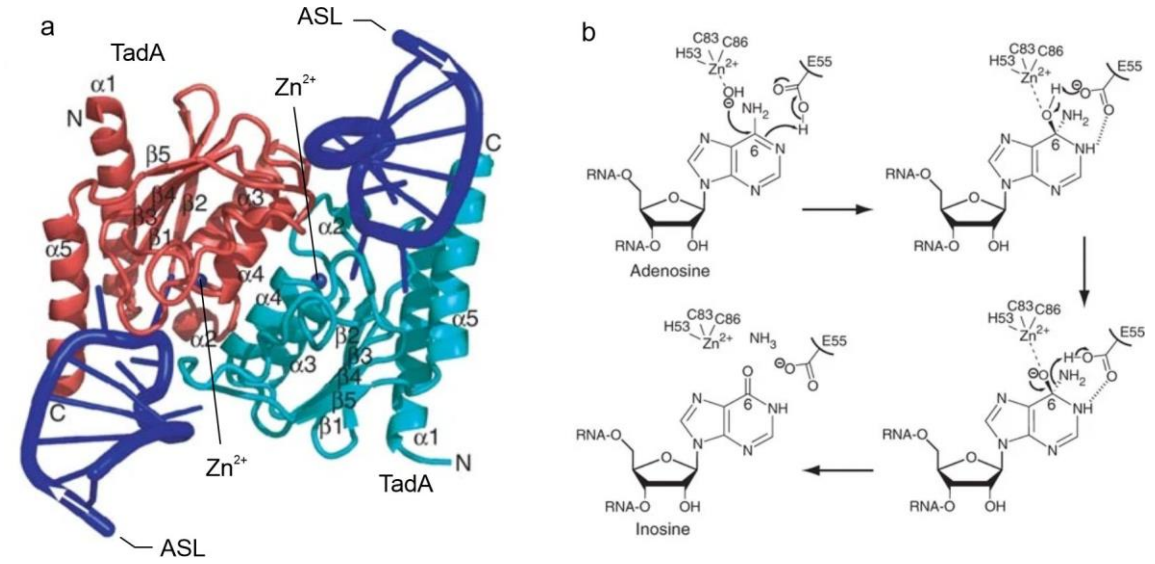

Figure 31.TadA structure and catalytic mechanism

a.Structure of *Staphylococcus aureus* TadA in complex with the anticodon stem loop (ASL) of tRNA-Arg. TadA has an overall fold composed of a central β-sheet surrounded of α-helices. Homodimerization of TadA (TadA monomers are colored red and cyan) have two zinc binding sites corresponding to each monomer, where the ASL is bound. **b.** Proposed catalytic mechanism of deamination. In the active site of TadA, the zinc ion is coordinated by H53, C83, C86 and a water molecule. The E55 abstract one proton from the zinc-bound water molecule to produce a hydroxide ion. E55 also protonates the N^1 of the incoming adenosine 34, which reduces the double bound between N^1 and C^6 of adenosine rendering the C^6 more susceptible to the hydroxide ion attack to form the tetrahedral intermediate. The C^6-$NH_2{}^6$ bond cleavage is mediated by transfer of proton from OH^6 to $NH_2{}^6$, this proton is then abstracted by Glu55. The tetrahedral intermediate collapses after abstraction of this proton by Glu55 and delivery of the proton to the leaving amine yields inosine and ammonia (Losey, Ruthenburg, and Verdine 2006).

2.4 A-to-I editing of tRNA wobble position in eukaryotes by the ADAT heterodimer

The A-to-I editing in eukaryotes is mediated by the Adenosine Deaminase Acting on tRNAs (ADATs). There are three types of ADATs: ADAT1, ADAT2 and ADAT3, all of them also have a deaminase domain that is similar to that of cytidine deaminases (Schaub and Keller 2002). ADAT1 mediates the A-to-I editing at position 37 in tRNA-Ala and at position 57 in archaeal tRNAs (H. Grosjean et al. 1996; A. Gerber et al. 1998). ADAT2 and ADAT3

(ADAT2/3) form a complex in the nucleus to perform A-to-I editing at position 34 on tRNAs (Torres et al. 2015). In contrast to the single substrate of the prokaryotic Tad A, eukaryotic ADAT2/3 complex have up to eight tRNAs isotypes as substrates. These substrates contain an adenosine at position 34 and include: tRNA-Ala-**A**GC, -Pro-**A**GG, -Thr-**A**GT, -Val-**A**AC, -Ser-**A**GA, -Arg-**A**CG, -Ile-**A**AT and Leu- **A**AG.

Amino acids Ala, Pro, Thr and Val are encoded by four different codons, i.e. fourfold degenerate. Ile is encoded by three different codons, threefold degenerate. Arg, Ser and Leu are sixfold degenerate (M. Nirenberg et al. 1965; Paul F. Agris, Vendeix, and Graham 2007). In contrast to the bacterial protein TadA which is able to deaminate A34 from an ASL alone, the ADAT2/3 complex requires a full length tRNA to deaminate A34 (Auxilien et al. 1996; Roura Frigolé et al. 2019). ADAT2/3 substrates do not require a 5' leader, 3' trailer, the 3'CCA, or a previous modification in another base within the tRNA for A-to-I editing (Torres et al. 2015; Roura Frigolé et al. 2019).

Although both ADAT2 and ADAT3 have a deaminase domain, only ADAT2 is the active subunit. ADAT3 has been proposed to be inactive since the conserved glutamate participating in catalysis by proton shuttling is mutated into valine (A. P. Gerber and Keller 1999). Nevertheless, ADAT2 requires the presence of ADAT3 to perform the deamination reaction. How ADAT3 contributes to A-to-I editing is however unknown. Sequence comparison of TadA and mouse ADAT2/3 show that mouse ADAT2 has 49.7% sequence similarity with *E. coli* TadA. Surprisingly, when comparing TadA and ADAT3, it is observed that only the C-terminal part of ADAT3 (residues 177- 349) has 45% of sequence similarity with *E. coli* TadA. The N-terminal domain of ADAT3 is an additional domain, characteristic of ADAT3, that is neither present in *E. coli* TadA, nor in eukaryotic ADAT2.

2.5 ADAT mutations and disease association

Several mutations in ADAT3 gene have been identified in patients affected by a neurological syndrome. This syndrome is characterized by intellectual disability (ID), strabismus, microcephaly, epilepsy, hypotonia, speech delay and grow failure. Forty one patients have been shown to carry the homozygous missense c.382G > A mutation in *ADAT3* gene, which leads to the replacement of valine 128 into methionine in the ADAT3 protein (Sharkia et al. 2019; Alazami et al. 2013; El-Hattab et al. 2016). Two other patients were shown to carry a compound heterozygous missense mutation of *ADAT3*, where each allele encodes a different ADAT3 variant, i.e. Val196Ala and Val196Leu (Thomas et al. 2019). Furthermore, one

patient presented a homozygous 8bp duplication in *ADAT3* gene leading to a N-terminal truncation in ADAT3 (Salehi Chaleshtori et al. 2018).

2.6 Questions associated

If the mechanism and tRNA recognition properties of prokaryotic TadA have been thoroughly addressed, much remains to be investigated on ADAT. Notably, several questions remain unanswered. First, what is the role of ADAT3 in ADAT? Second, what is the role of the specific N-terminal domain of ADAT3? Third, in contrast to prokaryotes where a TadA homodimer is sufficient for A-to-I editing, why do eukaryotes need a heterodimeric complex to accomplish the same purpose? Fourth, how does ADAT2/3 achieves recognition of tRNAs containing A34? Fifth, how does ADAT2/3 disease mutant affect the inosine levels of tRNAs? Sixth, is the affinity of ADAT2/3 disease-mutant to tRNAs decreased compared to that of the wild type (WT) complex? Finally, seventh, is the activity of ADAT2/3 disease-mutants decreased compared to that of the WT complex?

Thesis objectives

My major interest lies in the understanding of human diseases and how these can be cured. The two main projects that I have conducted during my PhD have addressed these questions, looking at the mechanistic of proteins and protein complexes involved in essential processes and that could be targeted to gain insights into therapeutic interventions, diagnostic and patient-care. Notably, my projects have tackled projects in the dynamic fields of epigenetics and epitranscriptomics, where many effectors are known to be involved in the onset and/or progression of diseases.

My thesis objectives have therefore matched my scientific interests and addressed the following questions:

Concerning tcDAC2:

- Solve the structure of tcDAC2 to determine its features that differentiate it from human HDACs.
- Solve the structure of tcDAC2 in complex with inhibitors to understand how to develop new anti-parasitic drugs.

Concerning the ADAT2/ADAT3 complex:

- Solve the structure of mouse ADAT2/ADAT3 WT and disease-mutant complexes to study the mechanism by which the most common mutation V128M in ADAT3 trigger the disease phenotype.
- Study the role of ADAT3, and ADAT3-Nter domain.
- Characterize the activity and binding affinities of ADAT2/3 WT and disease-mutant complexes.

Results

Article 1

Characterization of Histone Deacetylase 8 (HDAC8) Selective Inhibition Reveals Specific Active Site Structural and Functional Determinants (published)

HDAC8 has been shown to be upregulated in different tumors including neuroblastoma, and treatment of a neuroblastoma cell model with selective HDAC8 inhibitors resulted in cell differentiation and growth arrest. Nevertheless, the mode of binding of these HDAC8 specific inhibitors is not known. Furthermore, since human HDAC8 specific inhibitors PCI-34051 and NCC-149 (hereafter termed PCI and NCC) also inhibit in vitro and in vivo schistosome HDAC8, to study the structural determinants of PCI and NCC selective inhibition of HDAC8 enzymes, smHDAC8 was used as a model. Furthermore, several compounds targeting selectively smHDAC8 over human HDACs were developed previously in collaborators' teams to fight schistosomiasis. Therefore, to know the mode of binding of these different selective HDAC8 inhibitors, my team has co- crystallized them in complex with the smHDAC8 enzyme.

The structure of smHDAC8 in complex with these HDAC8 selective inhibitors showed the hydroxamic part of the inhibitors coordinates the catalytic zinc and hydrogen bonds with Tyr341, H141 and H142. Furthermore, the L shape of these inhibitors allow their capping group to interact with Tyr341 and residues of the L6 loop (P291 and H292). Thereby we could determine a specific pocket in HDAC8 enzymes where HDAC8-specific inhibitors bind. This pocket is formed by residues of different loops. The base of the pocket is formed by Tyr 341 (L7 loop) that participates in catalysis, while the walls of the pocket are formed by residues of the L1 and L6 loops. The capping group of HDAC8-specific inhibitors lays over and interacts with the catalytic tyrosine. Other HDACs do not present this pocket. For instance, in HDAC1, 2, 3,6 and10 this pocket is covered by residues of the L1 and L6 loops forming a L1-L6 lock. In class IIa HDACs, the pocket does not exist since the catalytic tyrosine is replaced by a histidine.

Further mutational experiments showed that the replacement of hHDAC8 L6 loops by those of human HDAC1 L6 loop did not change the overall conformation of this loop, as observed in HDAC8, but resulted in decreased activity of HDAC8 and increased IC_{50} values of PCI and

NCC against HDAC8. These results demonstrated the importance of the specific HDAC8 pocket for binding of HDAC8 selective inhibitors. On one hand, we could determine why homemade inhibitors are potent and are selective inhibitors for smHDAC8 over human HDACs, and how these inhibitors can be used as drug leads for further development to fight schistosomiasis. On the other hand, the discovery of the HDAC8 selective pocket will guide the development of more potent and selective human HDAC8 inhibitors for the treatment of cancer.

I joined this project as a master student and have been realizing the structural analysis of the human HDAC8 where its L6 loop was replaced by that of human HDAC1. I have notably solved the structure of this mutant of human HDAC in complex with the pan-HDAC inhibitor Quisinostat(QSN).

Journal of Medicinal Chemistry

Article

Cite This: J. Med. Chem. XXXX, XXX, XXX−XXX

pubs.acs.org/jmc

Characterization of Histone Deacetylase 8 (HDAC8) Selective Inhibition Reveals Specific Active Site Structural and Functional Determinants

Martin Marek,[*,†,◆,◇] Tajith B. Shaik,[†,◇] Tino Heimburg,[‡] Alokta Chakrabarti,[§] Julien Lancelot,[∥] Elizabeth Ramos-Morales,[†] Cyrielle Da Veiga,[⊥] Dmitrii Kalinin,[#] Jelena Melesina,[‡] Dina Robaa,[‡] Karin Schmidtkunz,[§] Takayoshi Suzuki,[▽,○] Ralph Holl,[¶] Eric Ennifar,[⊥] Raymond J. Pierce,[∥] Manfred Jung,[§] Wolfgang Sippl,[‡] and Christophe Romier[*,†]

[†]Institut de Génétique et Biologie Moléculaire et Cellulaire (IGBMC), Département de Biologie Structurale Intégrative, Université de Strasbourg, Centre National de la Recherche Scientifique (CNRS UMR7104), Institut National de la Santé et de la Recherche Médicale (INSERM U1258), 1 rue Laurent Fries, 67404 Illkirch Cedex, France

[‡]Institute of Pharmacy, Martin-Luther-Universität Halle-Wittenberg, Wolfgang-Langenbeck-Straße 4, 06120 Halle/Saale, Germany

[§]Institute of Pharmaceutical Sciences, Albert-Ludwigs-Universität Freiburg, Albertstraße 25, 79104 Freiburg, Germany

[∥]CNRS, Inserm, CHU Lille, Institut Pasteur de Lille, U1019−UMR 8204−CIIL−Centre d'Infection et d'Immunité de Lille, Université de Lille, F-59000 Lille, France

[⊥]Architecture et Réactivité de l'ARN, Institut de Biologie Moléculaire et Cellulaire (IBMC), UPR 9004 du CNRS, Université de Strasbourg, 15 Rue René Descartes, 67084 Strasbourg Cedex, France

[#]Institute of Pharmaceutical and Medicinal Chemistry, University of Münster, Corrensstraße 48, 48149 Münster, Germany

[▽]Graduate School of Medical Science, Kyoto Prefectural University of Medicine, 1-5 Shimogamohangi-Cho, Sakyo-Ku, 606-0823 Kyoto, Japan

[○]CREST, Japan Science and Technology Agency (JST), 4-1-8 Honcho Kawaguchi, 332-0012 Saitama, Japan

[¶]Department of Chemistry, Institute of Organic Chemistry, University of Hamburg, Martin-Luther-King-Platz 6, 20146 Hamburg, Germany

Supporting Information

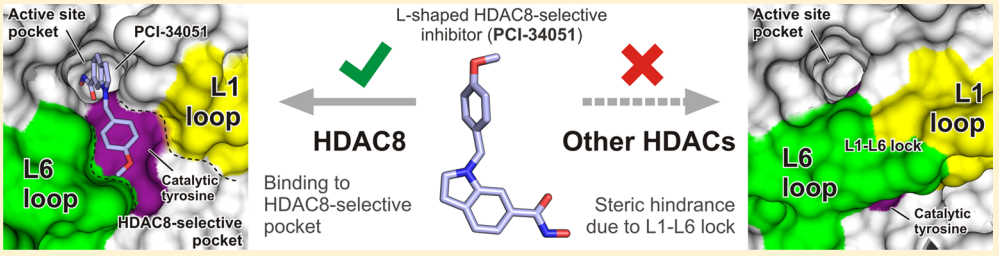

ABSTRACT: Metal-dependent histone deacetylases (HDACs) are key epigenetic regulators that represent promising therapeutic targets for the treatment of numerous human diseases. Yet the currently FDA-approved HDAC inhibitors nonspecifically target at least several of the 11 structurally similar but functionally different HDAC isozymes, which hampers their broad usage in clinical settings. Selective inhibitors targeting single HDAC isozymes are being developed, but precise understanding in molecular terms of their selectivity remains sparse. Here, we show that HDAC8-selective inhibitors adopt a L-shaped conformation required for their binding to a HDAC8-specific pocket formed by HDAC8 catalytic tyrosine and HDAC8 L1 and L6 loops. In other HDAC isozymes, a L1−L6 lock sterically prevents L-shaped inhibitor binding. Shielding of the HDAC8-specific pocket by protein engineering decreases potency of HDAC8-selective inhibitors and affects catalytic activity. Collectively, our results unravel key HDAC8 active site structural and functional determinants important for the design of next-generation chemical probes and epigenetic drugs.

INTRODUCTION

Acetylation of lysine residues in proteins is a major signaling mark that impacts most cellular processes.[1−3] In the cell nucleus, acetylation of histones has been shown to be essential for modulating chromatin structure and for acting in epigenetic signaling that drives and regulates nuclear mechanisms, cellular processes, and development.[1,3,4] Protein lysine acetylation is a

Received: July 11, 2018
Published: October 22, 2018

DOI: 10.1021/acs.jmedchem.8b01087
J. Med. Chem. XXXX, XXX, XXX−XXX

A

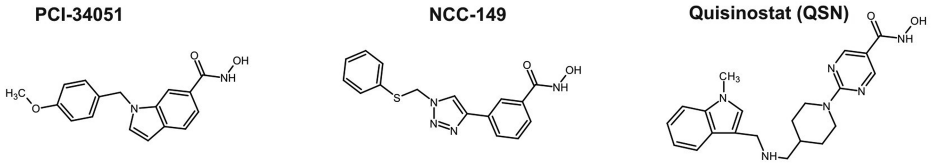

B

Enzyme	Inhibitor	IC_{50} (nM)	Kd (nM)	ΔG (kcal/mol)	ΔH (kcal/mol)	-TΔS (kcal/mol)
hHDAC8	**PCI-34051**	77.7 ± 18.1	75.1 ± 6.9	-9.7	-11.0	1.3
hHDAC8	**NCC-149**	44 ± 4.9	89.6 ± 18.4	-9.6	-10.3	0.7
hHDAC8	**QSN**	64.4 ± 3.4	22.7 ± 3.7	-10.4	-12.7	2.3
smHDAC8	**PCI-34051**	435.8 ± 61	367 ± 40.7	-8.8	-9.1	-0.3
smHDAC8	**NCC-149**	95.4 ± 9.3	81.7 ± 7.0	-9.7	-9.5	-0.15
smHDAC8	**QSN**	303.4 ± 39	28.4 ± 3.3	-10.3	-8.8	-1.5

Figure 1. HDAC8 inhibition and binding by inhibitors **PCI-34051**, **NCC-149**, and **QSN**. (A) Chemical structures of **PCI-34051**, **NCC-149**, and **Quisinostat** (**QSN**). (B) IC_{50} values and binding affinities/thermodynamic parameters of **PCI-34051**, **NCC-149**, and **QSN** for human HDAC8 (hHDAC8) and *Schistosoma mansoni* HDAC8 (smHDAC8).

reversible process relying on the opposing effects of acetyltransferases and deacetylases.[3,5,6] In addition, the acetylation marks on lysines are recognized by epigenetic readers harboring structural modules (e.g., bromodomains) that enable the recruitment of cellular effectors to specific subcellular and genomic loci.[5,7]

Because of the functional importance of acetylation mechanisms, their deregulation has been linked with multiple human diseases, including cancer.[4,8−11] The reversibility of acetylation and the possibility of modulating recognition of acetylated lysines by bromodomains provide a way to pharmacologically modulate acetylation pathways. Thus, epigenetic regulators involved in these pathways represent important therapeutic targets.[4,8−10,12,13]

Accordingly, among the currently approved epigenetic drugs, a majority (Vorinostat (SAHA), Romidepsin, Belinostat, Panobinostat, and Chidamide) target lysine deacetylases.[13−15] The family of lysine deacetylases has been divided into four classes depending on their folds and their sequence similarities. Classes I, II (IIa and IIb), and IV adopt an arginase-deacetylase α/β fold and rely on a zinc ion for activity (thereafter referred to as histone deacetylases or HDACs).[6] Class III deacetylases are referred to as sirtuins and adopt a Rossmann fold, relying on NAD^+ for activity.[6] Eleven HDACs and seven sirtuins are found in humans.

The currently approved drugs against lysine deacetylases target only proteins from the HDAC family. However, these drugs show poor selectivity against single members of the structurally similar but functionally different human HDAC isozymes, targeting at least two and generally more than two HDAC isozymes, thus hampering their broad therapeutic usage.[13,15] Several small-molecule inhibitors exhibiting selectivity for specific HDACs have been developed. **PCI-34051** and **NCC-149** were among the first HDAC isozyme-selective inhibitors discovered.[16−18] These two aromatic hydroxamate derivatives show high selectivity for human HDAC8 (hHDAC8), an HDAC isozyme that has been shown to be overexpressed in several cancers[19−21] and whose mutations can lead to the Cornelia de Lange syndrome.[22−24]

Specifically, **PCI-34051**, which is an indole-based derivative, is currently among the most selective HDAC8 inhibitors with a selectivity index of 290 and 400 for HDAC6 and HDAC1, respectively, making it a strong chemical tool for studying the biological role of HDAC8 in vivo.[16,25−28] In addition, our work on HDAC8 from the human-pathogenic flatworm *Schistosoma mansoni* (smHDAC8) has led to the design of new selective HDAC8 inhibitors targeting both the human and schistosome enzymes or, for some of them, showing selectivity toward schistosome HDAC8.[29,30]

To date, the experimental structural and mechanistic bases underlying HDAC8 selective inhibition by **PCI-34051**, **NCC-149**, and other related selective compounds remain poorly understood. Structural work on HDAC8 and computational studies have suggested that selective inhibitors target specific structural features of HDAC8 active site, potentially making use of the malleability of this active site.[17,18,31−34] Yet, no clear experimental evidence has been provided so far. To address this issue, we have dissected the molecular basis of HDAC8-selective inhibition by combining biochemical, biophysical, and crystallographic studies on hHDAC8 and smHDAC8.

Our results reveal that HDAC8-selective inhibitors bind into a specific HDAC8-selective pocket formed by the active site catalytic tyrosine and by residues from the L1 and L6 loops. This specific enzyme−ligand recognition is favored by the constrained L-shaped conformation of HDAC8-selective inhibitors. This selective binding relies on a specific conformation of the HDAC8 L6 loop and a shorter L1 loop that are not observed in any other HDAC isozyme. Our mutational studies further reveal HDAC8 structural determinants that support HDAC8 selective inhibition and function. Collectively, our results highlight the structural/functional similarities and dissimilarities between the various HDAC isozymes and pave the way for the development of new HDAC isozyme-selective chemical probes for cell biological research and inhibitors to treat human diseases.

RESULTS

In Vitro and in Vivo Effects of PCI-34051 and NCC-149. **PCI-34051** and **NCC-149** have been developed to target human HDAC8 (hHDAC8) selectively.[16−18] To investigate whether these inhibitors also target *Schistosoma mansoni* HDAC8 (smHDAC8), we have looked at their inhibition

DOI: 10.1021/acs.jmedchem.8b01087
J. Med. Chem. XXXX, XXX, XXX−XXX

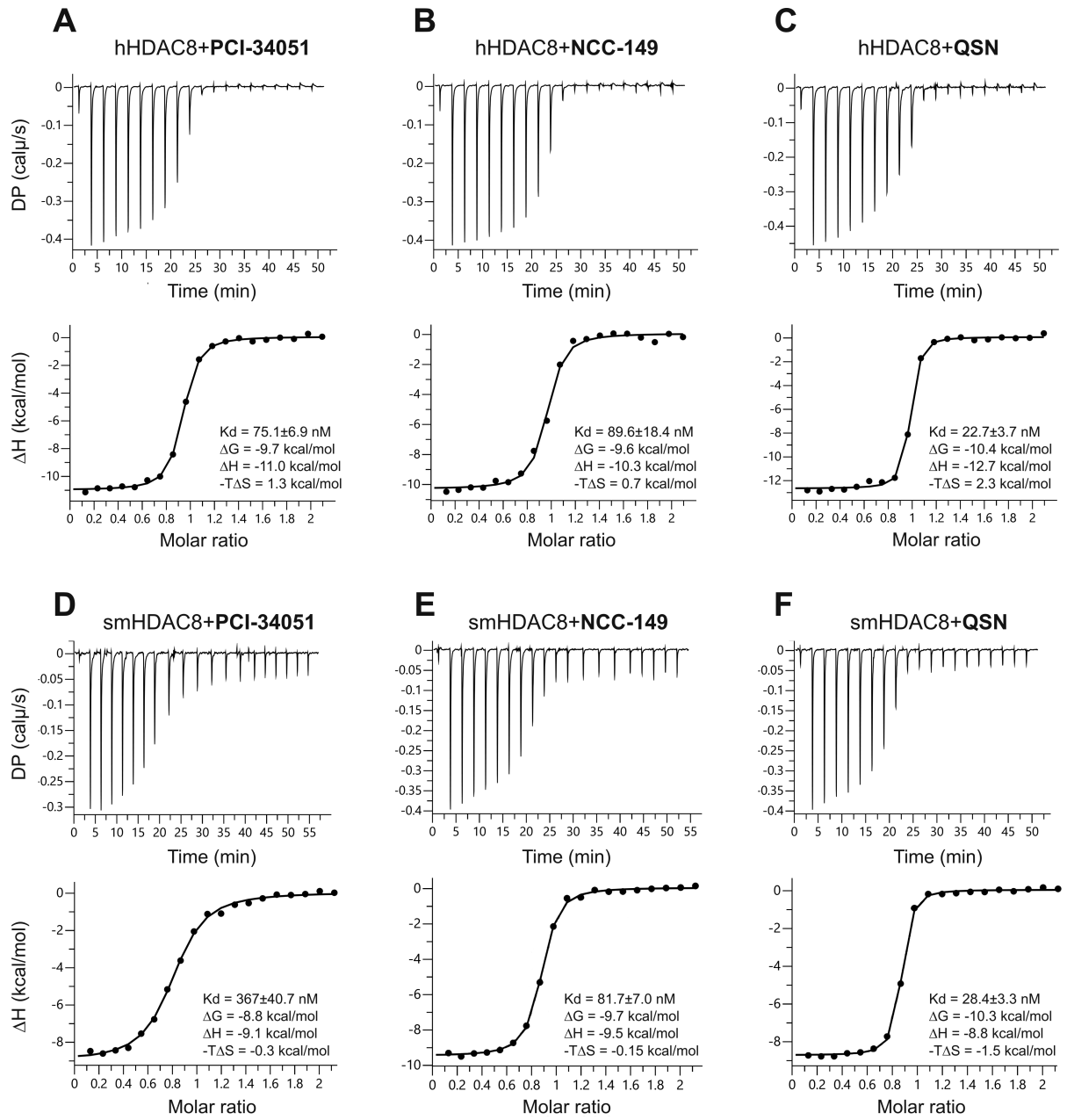

Figure 2. ITC measured affinities and thermodynamic signatures of **PCI-34051**, **NCC-149**, and **Quisinostat** (**QSN**) binding to hHDAC8 and smHDAC8. ITC profiles of the titration of hHDAC8 (A−C) and smHDAC8 (D−F) with **PCI-34051** (A,D), **NCC-149** (B,E), and **QSN** (C,F). Top panels: titration data of the enzymes into the corresponding inhibitor solution. DP: Differential power. Bottom panels: integrated heat measurements for the titration enzyme with the corresponding inhibitor.

and binding to smHDAC8. As a comparison, we have used the highly potent but nonselective HDAC inhibitor **Quisinostat** (**QSN**) which is in phase II clinical trials.[35,36]

Measurements of the half-maximal inhibitory concentration (IC_{50}) showed that all three inhibitors possess activity in the submicromolar range against hHDAC8 and smHDAC8. **NCC-149** showed the most potent inhibition, followed by **QSN** and **PCI-34051** (Figure 1). Measurement of the thermodynamic parameters using isothermal titration calorimetry (ITC) confirmed the inhibition results obtained, the equilibrium dissociation constant (K_d) values determined being in the same range as the corresponding IC_{50} values, with the exception of **QSN** that showed a lower K_d value for smHDAC8 (Figures 1 and 2).

The biological effects, especially the anticancer properties of **PCI-34051** and **NCC-149** in various cell types, have been characterized,[16−18,25−28] and we have previously shown that pan-HDAC inhibitors affect schistosome pathogens.[30,37] We therefore asked whether **PCI-34051** and **NCC-149** could also have an antiparasitic effect on schistosomes. Our various biological assays confirmed that **PCI-34051** and **NCC-149** affect the pathogens, triggering their apoptosis (Supporting Information, Figure S1). These results demonstrate that both hHDAC8 and smHDAC8 can be used for studying HDAC8 inhibition by **PCI-34051** and **NCC-149**.

So far, few structures of HDACs in complex with selective inhibitors have been solved. Moreover, in many HDAC/inhibitor structures, the active site of the HDAC and the

DOI: 10.1021/acs.jmedchem.8b01087
J. Med. Chem. XXXX, XXX, XXX−XXX

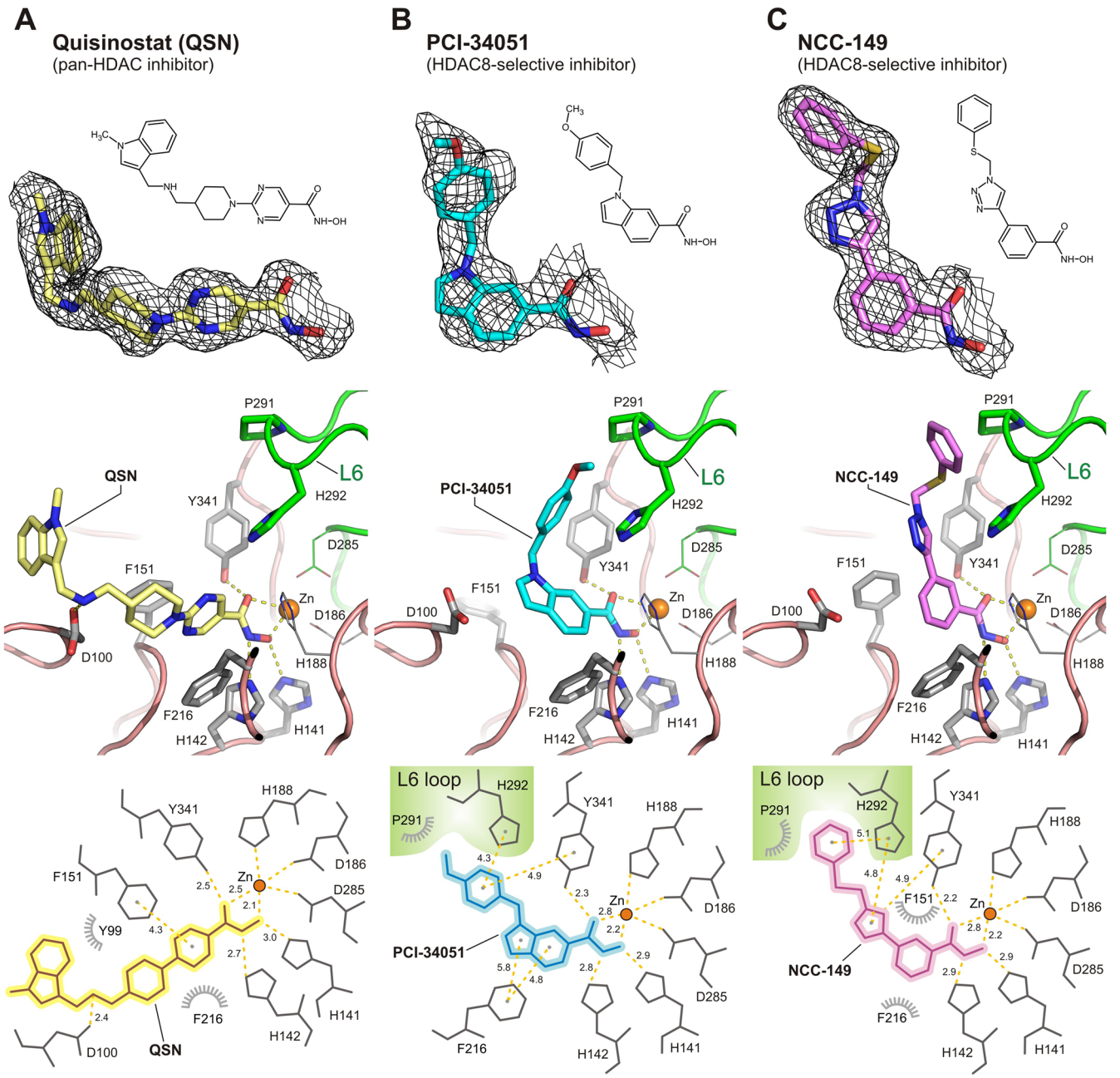

Figure 3. Structural characterization of **QSN**, **PCI-34051**, and **NCC-149** binding to smHDAC8 (PDBs 6HSH, 6HQY, 6HRQ) (A–C). Binding modes of **QSN** (A), **PCI-34051** (B), and **NCC-149** (C) to smHDAC8. Upper panels: Simulated annealing omit electron density map contoured at 2σ for the inhibitors when bound to smHDAC8. Middle panels: Binding mode of **QSN**, **PCI-34051**, and **NCC-149** in the active site of smHDAC8. The inhibitors and important residues are shown as sticks. smHDAC8 L6 loop is colored green. The catalytic zinc ion is shown as orange sphere. Zinc coordination and hydrogen bonds are shown as dashed lines. Only HDAC8-selective inhibitors **PCI-34051** and **NCC-149** adopt an L-shaped conformation and interact with the catalytic tyrosine and the L6 loop. Lower panels: Two dimensional illustrations of binding. Zinc coordination, hydrogen bonds, and aromatic interactions are shown as dashed lines. The corresponding distances between the atoms and/or chemical groups are given in Å. Hydrophobic contacts are shown by gray arcs with spokes radiating toward the atoms involved.

bound inhibitor are involved in extensive crystal packing contacts. This complicates the delineation between biologically relevant and crystal packing-driven conformations and interactions of the HDAC active site loops and the inhibitors. Therefore, in addition to the cocrystallization attempts of hHDAC8 with inhibitors, we have used the possibility offered by our apo smHDAC8 crystals to look at HDAC8/inhibitor interactions in a crystal lattice-open environment.[30]

Despite intensive efforts, we were not able to obtain well-diffracting crystals of hHDAC8 in complex with **PCI-34051**, **NCC-149**, and **QSN**. In contrast, soaking experiments of apo smHDAC8 crystals with all three inhibitors were successful and yielded high resolution complex structures (Figure 3; Supporting Information, Table S1).

Binding Mode of QSN to smHDAC8. Analysis of the smHDAC8/**QSN** structure revealed that **QSN** adopts a straight conformation as its piperidine-pyrimidine linker allows limited conformational flexibility (Figure 3A). The **QSN** hydroxamate warhead coordinates the catalytic zinc and simultaneously interacts via hydrogen bonding with the

DOI: 10.1021/acs.jmedchem.8b01087
J. Med. Chem. XXXX, XXX, XXX–XXX

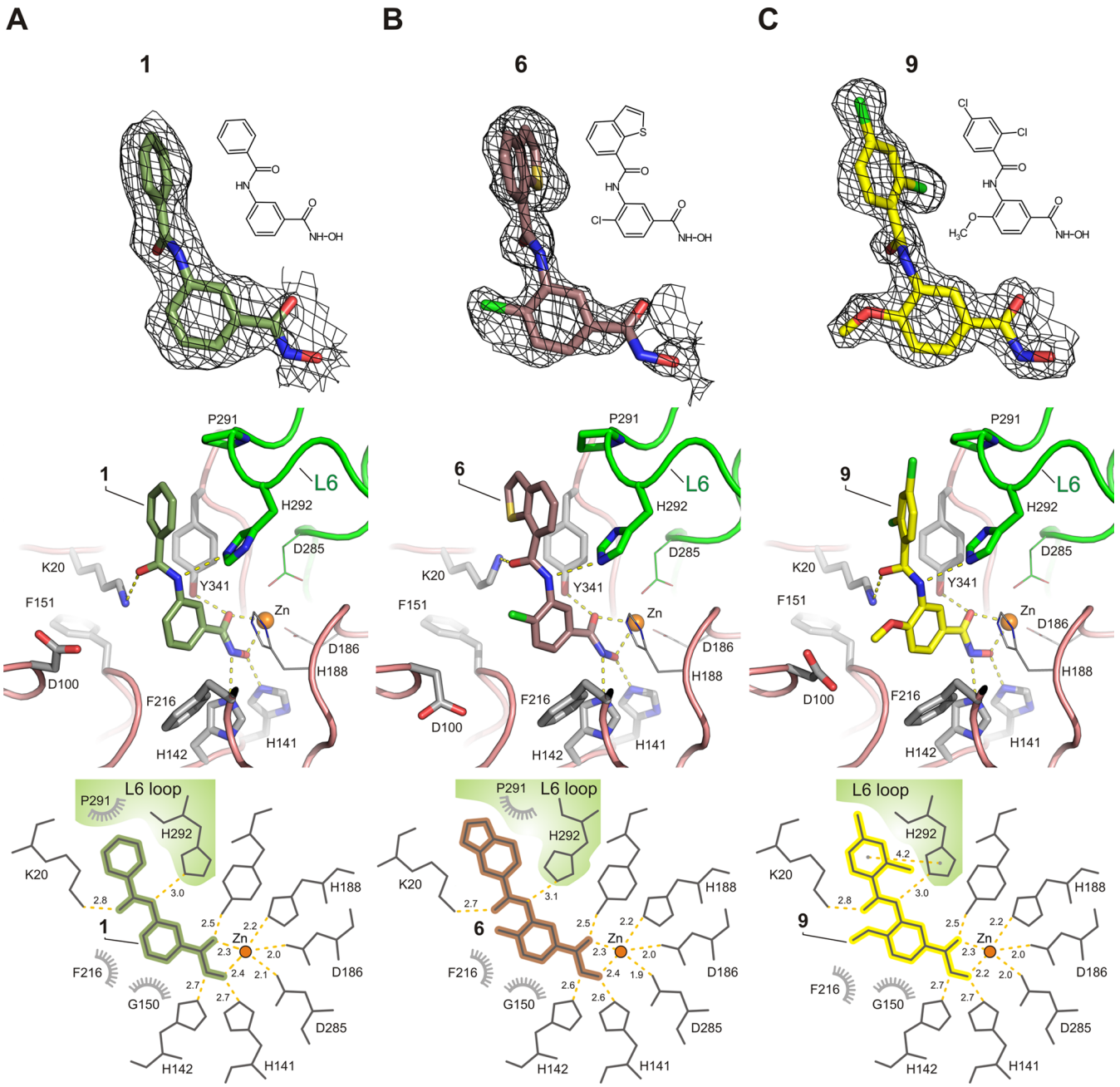

Figure 4. Structural characterization of **1**, **6**, and **9** HDAC8-selective inhibitors binding to smHDAC8 (PDBs 5FUE, 6HTI, 6HU0). (A–C) Binding modes of compounds **1** (A), **6** (B), and **9** (C) to smHDAC8. Upper panels: Simulated annealing omit electron density map contoured at 2σ for **1**, **6**, and **9** when bound to smHDAC8. Middle panels: Binding mode of **1**, **6**, and **9** in the active site of smHDAC8. Lower panels: Two dimensional illustrations of binding. Representations, coloring and display of interactions are as in Figure 3.

histidine dyad, H141 and H142 (hHDAC8 H142 and H143) and with the catalytic tyrosine Y341 (hHDAC8 Y306) hydroxyl, as commonly observed for most other hydroxamate-containing HDAC inhibitors. Furthermore, the **QSN** piperidine-pyrimidine linker is sandwiched between the side chains of smHDAC8 F151 (hHDAC8 F152) and F216 (hHDAC8 F208), where it forms planar π–π stacking and nonpolar contacts.

Specifically, the **QSN** piperidine ring adopts a chair conformation, which allows the **QSN** methylamino-methyl linker to form a hydrogen bond (2.4 Å) with the carboxyl group of smHDAC8 D100 (hHDAC8 D101), a conserved class I HDAC residue that has been shown to interact with the backbone of incoming acetylated peptides.[33,38] Finally, the **QSN** capping methyl-indole group is solvent exposed, making minimal nonpolar contacts with Y99 (hHDAC8 Y100). Interestingly, we previously observed a very similar binding mode to smHDAC8 for another pan-HDAC inhibitor, M344, including an interaction between D100 and the M344 internal amide group.[30] The M344 conformation is less constrained by its linker, which suggests that this binding mode is common to and favored by many pan-HDAC inhibitors. In agreement, a similar binding mode was also observed upon SAHA binding to human HDAC2 in a crystal lattice-free environment.[39]

Binding Mode of PCI-34051 to smHDAC8. The **PCI-34051** hydroxamate warhead interacts with the catalytic zinc

DOI: 10.1021/acs.jmedchem.8b01087
J. Med. Chem. XXXX, XXX, XXX–XXX

and active site residues as observed for **QSN** (Figure 3B). However, in contrast to **QSN**, the hinge connecting the central indole-based spacer and the methoxyphenyl group of **PCI-34051** favors binding of its capping group onto the side chain of smHDAC8 Y341 (hHDAC8 Y306). This tyrosine, together with the catalytic zinc, has been shown in hHDAC8 to be involved in catalysis by polarizing the leaving acetyl group of the incoming acetylated lysine.[33] Here, the methoxyphenyl capping group is perpendicularly (86°) oriented over the aromatic ring of this tyrosine, which favors T-shaped $\pi-\pi$ stacking (4.9 Å). Thus, the binding of **PCI-34051** onto Y341 is favored by the L-shape of this inhibitor.

The methoxyphenyl capping group of **PCI-34051** is positioned in close vicinity to the smHDAC8 L6 loop, being inserted in a small pocket shaped by the side chains of P291 and H292 (hHDAC8 P273 and M274). While the methoxy group forms nonpolar contacts with the pyrrolidine ring of P291, the phenyl ring of the inhibitor interacts (4.3 Å) via either $\pi-\pi$ or cation$-\pi$ interaction with H292, depending upon the protonation state of the histidine (Figure 3B).

The smHDAC8 and hHDAC8 differ by one residue in their active sites, where hHDAC8 M274 is replaced by smHDAC8 H292. Because this latter residue is involved in inhibitor binding, we asked whether the smHDAC8-H292M mutant binds **PCI-34051** in the same way as the wild-type (WT) enzyme. The crystal structure of **PCI-34051** bound to the "humanized" smHDAC8-H292M mutant reveals that **PCI-34051** still adopts a L-shaped conformation when bound to the smHDAC8-H292M mutant, but this conformation is slightly different from the one adopted with the WT enzyme (Supporting Information, Table S1, Figure S2A−C).

Specifically, **PCI-34051** still lies over Y341 catalytic tyrosine but appears more centered in the pocket created by smHDAC8 Y341, F151, and the L6 loop. In contrast to the WT enzyme, the central indole group of **PCI-34051** is axially rotated by an angle of ∼20°, which favors the positioning of the capping methoxyphenyl group over the aromatic ring of Y341 (4.8 Å), effecting nearly parallel (8.9°) $\pi-\pi$ stacking. As a consequence, the **PCI-34051** capping group interacts differently with the L6 loop than is observed with the WT enzyme but still making close nonpolar contacts with the aliphatic ring of P291 and the side chain of M292 in this loop (Supporting Information, Figure S2A).

Binding Mode of NCC-149 to smHDAC8. **NCC-149** hydroxamate also binds in a canonical way to the catalytic zinc and active site residues, and the rest of the L-shaped inhibitor is turned toward and interacts with Y341 and the smHDAC8 L6 loop (Figure 3C). Specifically, the 1,2,3-triazole ring of the linker is oriented in a position (4.9 Å) that is slightly off perpendicular (∼83°) to the aromatic ring of Y341, indicating their $\pi-\pi$ contacts. At the same time, the 1,2,3-triazole ring packs against L6 loop H292, which allows their mutual T-shaped (∼67°) aromatic interactions. In addition, and as observed for **PCI-34051**, the phenylthiomethyl capping group of **NCC-149** is inserted in the small subpocket of the HDAC8 L6 loop, where it effects both upright (∼76°) $\pi-\pi$ stacking with H292 and hydrophobic contacts (3.6 Å) with P291.

We also solved the structure of **NCC-149** bound to the smHDAC8-H292M mutant. Here, the hydroxamate and linker of **NCC-149** bind very similarly to the smHDAC8-H292M mutant and to the WT enzyme and show fewer conformational changes than observed with **PCI-34051**. Interestingly, the 1,2,3-triazole ring is closer to the L6 loop, where it interacts with M292 via a sulfur−aromatic interaction (3.7 Å), suggesting a similar interaction with hHDAC8 (Supporting Information, Figure S2D−F). This binding mode still favors T-shaped (82°) $\pi-\pi$ stacking between the 1,2,3-triazole and Y341 (4.7 Å), as well as hydrophobic contacts between the internal benzene ring and the two phenylalanines, F151 and F216. However, the terminal phenylthiomethyl capping group of the inhibitor changes its position and is turned away from the L6 loop, lying in another binding subpocket formed by smHDAC8 K20 and F21 (L1 loop) and Y341 and F343 (L7 loop), whose hydrophobic character is conserved in hHDAC8 (Supporting Information, Figure S2D).

The conformational adaptation of **NCC-149** to the smHDAC8-H292M selective pocket is eased by the intrinsically higher conformational flexibility of this inhibitor that allows the repositioning of its capping group. In the case of **PCI-34051**, which is more rigid as it contains only a one-atom hinge, a major part of the inhibitor had to be repositioned. Yet, these changes do not affect the major interaction of HDAC8-selective inhibitors with the uncovered aromatic ring of the catalytic tyrosine and with residues of the L6 loop, showing the importance of these elements as key binding surfaces for these selective inhibitors.

Selective Inhibition of smHDAC8 over Other Human HDACs. Previous work on the selective inhibition of smHDAC8 has yielded the development of an inhibitor series of 3-benzamido-benzohydroxamates that show strong selectivity for smHDAC8 and hHDAC8 over other human HDACs.[29] The structure of smHDAC8 with the simplest inhibitor of this series (**1**) revealed that the capping benzamido moiety lays over Y341 (3.9 Å), its benzene ring capping group further making nonpolar contacts with the smHDAC8 L6 loop, notably with P291 (3.6 Å) (Figure 4A). This inhibitor also exploits smHDAC8-specific interactions with residues K20 and H292 (hHDAC8 K33 and M274).[29]

Many of the 3-benzamido-benzohydroxamate inhibitors that were subsequently developed displayed higher potency than **1** in inhibiting smHDAC8.[29] To understand the molecular basis of these observations, we have further solved the structures of smHDAC8 bound to several of these inhibitors (compounds **2**−**11**) (Figure 4; Supporting Information, Figure S3, Table S2, Table S3).

All of these compounds showed a similar mode of binding to smHDAC8 as **1**. Yet, slight differences in chemical composition impacted specific interactions, potentially relating to the differences in the IC_{50} values observed. Compounds **2**−**4** only have different substituents at the *para* position of the benzohydroxamate moiety compared to **1**. These compounds bind very similarly to smHDAC8 as **1** (Supporting Information, Figure S3). Their lower IC_{50} values most likely stem from the additional contacts of their substituent groups with F216, as well as the possible stabilization by these groups of the noncanonical geometry of the amide group of these inhibitors.

In the case of **5** and **6**, which have respectively larger biphenyl and benzothiophene capping groups, these latter form more extensive hydrophobic contacts (3.5 Å) with P291 (Figure 4B; Supporting Information, Figure S3). In the case of **7**, which only has an inverted internal amide compared to **1**, the orientation and the length of the hydrogen bonds between **7** and smHDAC8 K20 and H292 appear more favorable for interaction (Supporting Information, Figure S3).

DOI: 10.1021/acs.jmedchem.8b01087
J. Med. Chem. XXXX, XXX, XXX−XXX

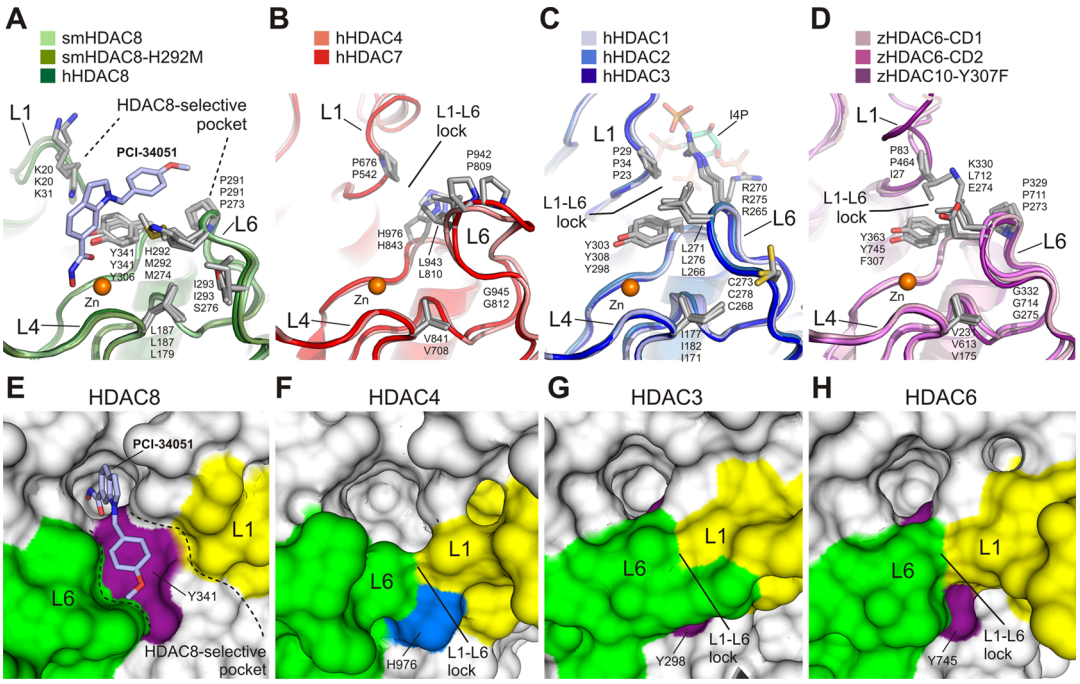

Figure 5. Structural delineation of HDAC8 selective inhibition. (A–D) Close-up views shown as ribbon and sticks of the superposed structures of (A) smHDAC8, smHDAC8-H292M and hHDAC8 (PDBs 6HQY, 6HSF, 1T67), (B) hHDAC4 and hHDAC7 (PDBs 5A2S, 3C0Z), (C) hHDAC1, hHDAC2, and hHDAC3 (PDBs 4BKX, 4LXZ, 4A69), and (D) zebrafish zHDAC6-(catalytic domain1)CD1 and zHDAC6-CD2, and zHDAC10 (PDBs 5G0J, 5TD7). The catalytic zinc is shown as orange sphere. HDAC8-selective inhibitor **PCI-34051** is shown in (A) as light-blue sticks when bound in HDAC8-selective pocket. In the other HDACs, this pocket is not formed because residues from L1 and L6 loops are protruding and forming a lock over the catalytic tyrosine (other class I and class IIb HDACs) or its replacement histidine (class IIa HDACs). (E) Surface representation of the pocket accommodating the linker and capping groups of the HDAC8-selective inhibitors. The **PCI-34051** inhibitor is represented as sticks and lays on the catalytic tyrosine (purple). The pocket walls are formed by residues from the L1 (yellow) and L6 (green) loops. (F,G,H) Surface representation of the same region in hHDAC4 (PDB 5A2S) (F), hHDAC3 (PDB 4A69) (G), and hHDAC6-CD2 (PDB 5EDU) (H) using the same color code as in (E). In these latter HDACs, L1 and L6 loop residues interact and form a L1-L6 lock over the pocket.

Compounds **8**–**10** are particularly interesting because they also show a higher selectivity for smHDAC8 over hHDAC8 (3-, 4.5-, and 6-fold, respectively) (Figure 4C; Supporting Information, Figure S3, Table S2). **8** has one additional methylene group between the internal amide and the phenyl capping group compared to **1**. Compound **8** appears to bind less deeply in the pocket to maximize its interactions with Y341 and the L6 loop. This change is compatible with the presence of smHDAC8 H292 but would be sterically unfavorable with hHDAC8 M274, which possibly explains the weaker inhibition observed for the human enzyme.

Compounds **9** and **10** both have a dichlorophenyl rather than a phenyl capping group and bind perfectly into the pocket formed by smHDAC8 Y341 and the L1 and L6 loops (Figure 4C; Supporting Information, Figure S3). The presence of the halogen atoms in the capping group of **9**/**10** forces the inhibitor to be slightly tilted toward the L6 loop, where it forms cation–π interaction (4.3 Å) with smHDAC8 H292. The bulkier character of the dichlorophenyl capping group may complicate the adaptation of **9**/**10** to the active site of hHDAC8.

Indeed, the predicted docking poses of **9** and **10** in hHDAC8 show that their dichlorophenyl capping groups are turned around 180° in comparison to their position in smHDAC8 and effects van der Waals interactions with the hydrophobic residues of the L6 loop P273 and M274 (Supporting Information, Figure S4). When comparing the obtained IC_{50} values of compounds **9**/**10** bearing a dichlorophenyl capping group with their parent counterparts **3**/**4**, which have a phenyl capping group, it becomes clear that the observed selectivity of the former compounds for smHDAC8 over hHDAC8 arises from a significantly decreased inhibitory activity toward hHDAC8. Compared to compounds **3**/**4**, compounds **9** and **10** show a 7–10-fold decrease in their inhibitory activities toward hHDAC8 (Supporting Information, Table S2). To further explain the selectivity of the dichlorophenyl derivatives, we carried out 100 ns molecular dynamics (MD) simulations for smHDAC8/**10** and hHDAC8/**10** complexes, as well as for smHDAC8/**4** and hHDAC8/**4** complexes for comparison.

MD simulations of smHDAC8/**4** crystal structure (Supporting Information, Figure S5A) reveal a relatively stable binding mode, where the phenyl capping group is placed parallel to Y341 in the side pocket, forming π–π stacking interactions, in addition to cation–π interactions with H292. During the MD simulation of smHDAC8/**10** crystal structure (Supporting Information, Figure S5B), the dichlorophenyl capping group similarly remains in the side pocket. Despite the loss of the π–π stacking interactions with Y341, compound **10** is still able to form strong cation–π interactions with H292, which are stable throughout MD. This might explain why the dichlorophenyl derivative only shows a slight decrease in inhibitory activity as compared to compound **4**.

Similarly, MD simulations of the hHDAC8/**4** docking complex (Supporting Information, Figure S5C) show that the phenyl capping group mostly remains stable in the side pocket, where it is placed perpendicular to Y306 of the side pocket, showing strong π–π stacking interactions besides van

DOI: 10.1021/acs.jmedchem.8b01087
J. Med. Chem. XXXX, XXX, XXX–XXX

der Waals interactions with M274. In contrast, our MD simulation of hHDAC8/**10** structure indicates that the predicted binding mode of the dichlorophenyl derivative **10**, where the capping phenyl ring is situated parallel to Y306, is not stable. Within less than 1 ns of the MD simulation time, the capping group flips by 90° and is placed perpendicular to Y306, with the *o*-chloro substituent pointing toward the side chain of Y306. (Supporting Information, Figure S5D). The $\pi-\pi$ stacking interactions with Y306, observed with compound **4**, are thus lost. Thus, a possible explanation for the decreased inhibitory activity of **10** for hHDAC8 as compared to compound **4** is that the dichlorophenyl capping group can only form weak van der Waals interactions between its *o*-chloro group and the side chain of Y306 and between its phenyl capping group and the side chain of M274.

We have used another benzohydroxamate inhibitor (**11**) which has an internal amine rather than an internal amide in its linker and shows a low nM IC_{50} for hHDAC8 but only a low μM IC_{50} for smHDAC8 (Supporting Information, Table S2). The smHDAC8/**11** structure reveals that this inhibitor does not form any strong interaction with K20 and H292, and its capping group interacts less extensively with the L6 loop (Supporting Information, Figure S3, Figure S6). The inhibitor binds centrally into the pocket, where it forms hydrophobic contacts with F216 (3.4 Å) and Y341 (3.7 Å), in a conformation identical to that observed for **PCI-34051** when bound to the smHDAC8-H292M mutant (Supporting Information, Figure S6). This suggests that HDAC8-selective inhibitors bind more centrally in this pocket in hHDAC8 than in smHDAC8 due to the slight different physicochemical properties of the active sites of these two proteins.

Finally, an unrelated compound, **12**, which has a triazole linker, binds similarly to smHDAC8, interacting with Y341 and the L6 loop (Supporting Information, Figure S3). This compound also adopts an L-shaped conformation to bind to the enzyme. **12** does not make direct contacts to K20 and H292, which might explain its higher IC_{50} value for smHDAC8 (Supporting Information, Table S2). This compound displays, however, a 4-fold higher potency for smHDAC8 over hHDAC8. Collectively, our results highlight how small chemical variations may be used to influence inhibition potency.

Structural Specificity of the HDAC8-Selective Pocket. Our findings show an HDAC8 selective inhibition relying on the binding of the selective inhibitors to a pocket that forms a shallow groove and that we have termed HDAC8-selective pocket. This pocket is defined by the catalytic tyrosine side chain (L7 loop), which forms the pocket bottom and residues from the L6 loop and, to a lesser extent, of the L1 loop of HDAC8 that both form the sides of the pocket.

The HDAC8-selective pocket is highly specific to this enzyme. Indeed, in class IIa HDACs, the catalytic tyrosine is replaced by a histidine whose side chain is turned away from the active site and cannot provide the same interaction surface as HDAC8 catalytic tyrosine (Figure 5). The situation is different for HDAC isozymes 1, 2, 3, 6, and 10 (thereafter called HDAC1−3,6,10) that all have retained a catalytic tyrosine at the same position. Specifically, these isozymes have a L6 loop that displays a similar conformation to that observed in HDAC8 (Figure 5). L6 loops in HDAC1−3,6,10, however, protrude slightly more over the catalytic tyrosine side chain than in the case of HDAC8 and could sterically perturb the binding of HDAC8-selective inhibitors (Figure 5).

Yet, our results with the smHDAC8-H292M mutant show that HDAC8-selective inhibitors can adapt to small changes within the HDAC8-selective pocket and could potentially overcome a more protrusive L6 loop. However, another specific and conserved feature of HDAC1−3,6,10 is a larger L1 loop that extends toward the L6 loop. Notably, at the tip of the HDAC1−3,6,10 L1 loop, a proline (or an isoleucine residue in HDAC10) is present that forms hydrophobic interactions with L6 loop residues and the catalytic tyrosine, thus forming a lock over the catalytic tyrosine and preventing the formation of a pocket similar to the HDAC8-selective pocket (Figure 5).

In HDAC8, the L1 and L2 loops have been shown to display flexibility, being able to change their conformation to adapt to different inhibitors such as the large largazole inhibitor and its analogues (Supporting Information, Figure S7).[40,41] This raises the question of whether the same L1 loop flexibility might exist in HDAC1−3,6,10. Current structural data on HDAC1−3,6,10, however, show that their L1 loops make much more extensive contacts with the rest of the enzyme, which most likely explains this lack of flexibility. Notably, the recent work on HDAC6/inhibitor complexes demonstrate that L1 loop conformational stability is important for the interactions of L1 loop residues with inhibitors capping groups to achieve HDAC6 selective inhibition.[42−46]

These major structural differences between HDAC8 and the other HDAC isozymes would explain how HDAC8 selective inhibition is achieved by inhibitors such as **PCI-34051** and **NCC-149**. This is supported by docking studies of **PCI-34051** and **NCC-149** with other HDAC isozymes (Supporting Information, Figure S8). These studies show that in case of HDAC1−3 and HDAC10, these inhibitors cannot reach properly and chelate the catalytic zinc ion. This is not as clear for the HDAC6 isozyme. Therefore, to assess the stability of the predicted docking poses and to further study the selectivity of **PCI-34051** and **NCC-149** toward HDAC8, we performed comparative 100 ns MD simulations on human HDAC6 and HDAC8 isoforms complexed with both inhibitors (Supporting Information, Figures S9 and S10). In hHDAC8, **PCI-34051** shows stable binding with an RMSD at ∼2 Å compared to the predicted docking pose. The capping group shows little deviation and remains in the side pocket throughout the 100 ns MD simulation (Supporting Information, Figure S9A). The same is observed for **NCC-149**, which displays a stable RMSD at ∼2 Å compared to the docking pose, except for a short increase in RMSD at 65−70 ns, with the capping group mostly remaining in the side pocket (Supporting Information, Figure S10A).

In smHDAC8, **PCI-34051** shows higher RMSD deviation at ∼3−4 Å compared to the crystal structure. The high RMSD arises from the movement of the capping group, which however remains in the side pocket throughout the simulation time (Supporting Information, Figure S9B). The MD simulation of the smHDAC8/**NCC-149** crystal structure yielded similar results as observed for the smHDAC8/**PCI-34051** complex (Supporting Information, Figure S10B).

In contrast, MD simulations of hHDAC6/**PCI-34051** and hHDAC6/**NCC-149** complexes, as predicted by docking, show high RMSD deviations for both ligands with RMSD values at ∼5 and up to 7 Å, respectively (Supporting Information, Figures S9C and S10C). Throughout the 100 ns simulation, the ligands maintain their chelation to the catalytic zinc ion. Meanwhile, the capping group of both ligands does not show any preferred conformation and remain

DOI: 10.1021/acs.jmedchem.8b01087
J. Med. Chem. XXXX, XXX, XXX−XXX

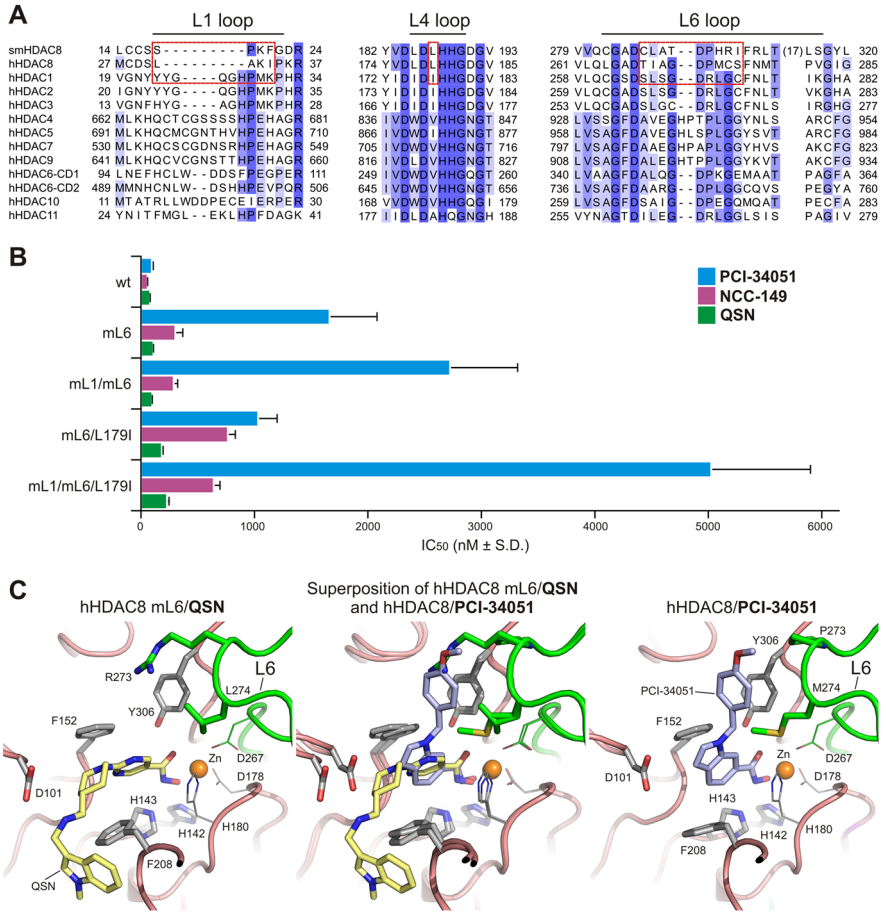

Figure 6. HDAC8 mutants inhibition by **PCI-34051**, **NCC-149**, and **QSN**, and structure of the human HDAC8 mL6/**QSN** complex. (A) Structure-based sequence alignment of L1, L4, and L6 loop sequences from various HDACs. Red boxes show the regions that have been swapped between HDAC1 and HDAC8 in the mutational analysis. (B) IC_{50} values for **PCI-34051**, **NCC-149**, and **QSN** on human HDAC8 WT and mutants. Assays were done in triplicate. Error bars represent the SD. (C) Close-up view of the hHDAC8-selective pocket in the human HDAC8 mL6/**QSN** complex (left panel: PDB 6HSK) compared to WT hHDAC8 bound to **PCI-34051** (right panel: model based on PDBs 1T67 and 6HSF) and the superposition of the two structures (middle panel). The side chain of the arginine R273 (from the hHDAC8 mL6/**QSN** complex) replacing P273 (from WT hHDAC8) binds into the HDAC8-selective pocket where **PCI-34051** (and the other HDAC8-selective inhibitors) were shown to bind. This mutation, which is the only common mutation to all mutants used, is most likely responsible for the general decrease of activity observed for these mutants.

surface exposed throughout the MD simulation, showing little interactions with the surrounding protein residues (Supporting Information, Figures S9C and S10C). Collectively, the MD simulations confirm the hypothesis made upon docking and are in agreement with the biochemical, biophysical, and crystallographic results obtained.

Essential Roles of L1 and L6 Loops in HDAC8 Catalysis and Inhibition. To further question the importance of HDAC8 L1 and L6 loops conformation in catalysis and inhibitor binding, we have performed a mutational analysis of these loops in HDAC8 and studied the effect of these mutations by biochemical, biophysical, and structural means. Despite an identical number of residues, the HDAC8 L6 loop has a conformation that is slightly different from that adopted by the corresponding loops in HDAC1−3,6,10. This slight conformational change prevents L6 loop residues from protruding over the catalytic tyrosine (Figure 5).

Sequence and structural comparisons highlighted two residues that could, at first sight, be responsible for this specific conformation of HDAC8 L6 loop: hHDAC8 P273/smHDAC8 P291 and hHDAC8 C275/smHDAC8 R293. However, we could not exclude the possibility that larger rearrangements are required, and we therefore created several different mutants for both hHDAC8 and smHDAC8 (Figure 6A; Supporting Information, Table S4).

First, specific point mutants (hHDAC8 P273R and P273R/C275G and smHDAC8 P291R and P291R/R293G) were made, where the residues were replaced by their HDAC1 counterparts. Second, we created mutants where we exchanged the HDAC8 L6 loop completely with that of HDAC1. We also constructed mutants where not only the L6 loop but also the L1 loop had been exchanged. Finally, triple mutants were also generated where a leucine (hHDAC8 L179/smHDAC8 L187) was replaced by an isoleucine, as observed in HDAC1, because this mutation could possibly facilitate an L6 loop conformational change (Figure 6A; Supporting Information, Table S4).

Except for the point mutants, all smHDAC8 mutants turned out to be insoluble. In contrast, all hHDAC8 mutants were soluble. Surprisingly, activity assays showed that all mutants had drastically reduced activity (Supporting Information, Table S4). While smHDAC8 single point mutants lost around one-third of their activity, hHDAC8 point mutants or L6 loop replacement mutants showed around 10-fold activity loss. Mutants of hHDAC8 combining L6 loop replacement with

DOI: 10.1021/acs.jmedchem.8b01087
J. Med. Chem. XXXX, XXX, XXX−XXX

either L1 loop replacement or the L179I point mutation showed a 50-fold loss of activity, and the triple mutant displayed almost no activity.

We used thermal shift assay experiments to assess whether the mutations affect the stability of the various mutants. All mutants only showed a decreased T_m of about 5 °C compared to the WT enzymes but did not indicate partial or complete unfolding of the proteins (Supporting Information, Table S4). Because of the residual activity of the mutants, we next measured the IC_{50} values for **PCI-34051**, **NCC-149**, and **QSN** for all mutants. All inhibitors showed significantly higher IC_{50} values indicative of a poorer inhibition capacity (Figure 6B; Supporting Information, Table S5). This was most pronounced for inhibitor **PCI-34051**, with a more than 64-fold increase of the IC_{50} value for the triple HDAC8 mutant. The IC_{50} values for **NCC-149** were also significantly increased but not as much as for **PCI-34051**. **QSN** also displayed decreased inhibition, albeit to a much lesser extent, possibly mirroring only the slight stability decrease of the mutants but supporting our conclusions on the crucial role of L1 and L6 loops for HDAC8 selective inhibition.

To investigate the molecular basis of conformational changes of the L1 and L6 loops following mutations, we attempted to solve the structures of the different HDAC8 mutants in complex with **PCI-34051**, **NCC-149**, and **QSN**. Although different mutants gave crystals in the presence of some of these inhibitors, only the crystals obtained with the human HDAC8 mL6/**QSN** complex led to exploitable structural data (Supporting Information, Table S6). To our knowledge, this is the first structure of compound **QSN** bound to human HDAC8. Here again the capping group of the inhibitor is extensively involved in crystal packing and it is impossible to understand whether the binding conformation of **QSN**, which is different from that observed when bound to smHDAC8, represents a favored binding conformation in solution to hHDAC8 (Supporting Information, Figure S11). Strikingly, the structure of this complex revealed that, despite the complete exchange of the L6 loop, the conformation of this loop remains as observed in hHDAC8 WT (Figure 6C). The hHDAC8 P273R replacement, however, leads to the partial occupation of the HDAC8-selective pocket by the side chain of the arginine replacing the proline (Figure 6). In fact, the only mutation common to all our smHDAC8 and hHDAC8 mutants is this proline to arginine change. In hHDAC1 and hHDAC3, this arginine is involved in inositol phosphate binding and is important for activity.[38,47,48] Our results therefore further highlight the importance of the L6 loop for class I HDACs activity and inhibitor binding and pinpoint differences between HDAC8 and the other members of this class that can be used for selective inhibition of the former enzyme.

DISCUSSION AND CONCLUSIONS

To date, HDAC8 is one of the most investigated HDAC for selective inhibition and numerous crystallographic studies have been performed on human HDAC8 in complex with, mostly, nonselective inhibitors to understand the molecular basis of the inhibition of this enzyme.[33,34,40,41,49−54] Many of these studies have revealed how HDAC8 active site residues and loops, notably the L1 and L2 loops, display flexibility, thus making the design of HDAC8 selective inhibitors a complicated task. In addition, in many structures, the bound inhibitor is involved in extensive crystallographic contacts, which makes it difficult to assess whether the observed conformations of the inhibitor, notably of its capping group, but also potentially of the active site loops, are biologically favored.

Yet, HDAC8 selective inhibitors have been designed, showing that selective inhibition of this enzyme can be achieved. One of the most potent and best known HDAC8 selective inhibitor is **PCI-34051**.[16] However, so far, the molecular basis for its selective inhibition remains poorly understood. We have previously shown that our smHDAC8 crystals can be used to look at inhibitor binding in a crystal lattice-unbiased manner.[29,30,55−58] Here, we have used this feature to look at HDAC8 selective inhibition using a large set of selective inhibitors of this enzyme, including **PCI-34051**.

Our results provide a comprehensive and detailed molecular view of HDAC8 selective inhibition, highlighting a specific HDAC8-selective pocket where selective inhibitors form preferential interactions with HDAC8 catalytic tyrosine and L6 loop residues. These results particularly emphasize the balance between chemical structure and inherent conformational flexibility of the inhibitors, with important implications for selective inhibition. In addition, the restricted conformation of HDAC8 L6 loop, compared to the more flexible character of the L1 loop, points out the importance of the L6 loop for selective inhibition. Moreover, the constrained conformation of the L7 loop that bears the catalytic tyrosine also appears as an essential feature of HDAC8 selective inhibition. Specifically, the position of the tyrosine side chain, which is locked by the interaction of its hydroxyl with the inhibitor's hydroxamate, most likely constrains the reported flexibility of the L7 loop.[59]

Interestingly, in class IIa HDACs the replacement of the catalytic tyrosine by a histidine creates a specific pocket at the position of the tyrosine side chain. This feature prevents HDAC8-selective inhibitors from binding to class IIa HDACs and has been exploited to design class IIa-selective inhibitors that cannot distinguish, however, between the different class IIa isozymes.[60]

In the case of HDAC1−3,6,10, although the catalytic tyrosine is conserved and the L6 loop is similar in these isozymes, the HDAC8-selective pocket is not present due to a larger L1 loop in HDAC1−3,6,10 that covers the catalytic tyrosine and forms a lock together with loop L6 over this selectivity pocket. The structures of HDAC6 in complex with HDAC6-selective inhibitors show that the capping group of these inhibitors interact with the proline at the tip of the L1 loop as well as with the preceding histidine residue. This mirrors the interaction observed between the HDAC8-selective inhibitors and the smHDAC8 L6 loop P291−H292 motif. Surprisingly, these inhibitors are selective for HDAC6 although the same motif is conserved in HDAC1−3 L1 loops that show similar conformations as HDAC6 L1 loop. Selective inhibition appears to rely on small structural differences between HDAC1−3 and HDAC6 and on small thermodynamic differences in selective inhibitor binding.[42−46] This parallels our study that demonstrate how selective inhibition can be affected by small changes in protein conformation and inhibitor composition.

Interestingly, the HDAC8-selective pocket can adapt to bulkier inhibitors that can also interact with the back of the pocket, as observed for compound **NCC-149** when bound to the smHDAC8-H292M mutant, thus potentially paving the way for the design of more potent HDAC8-selective inhibitors. Of note, the reduced conformational flexibility of compound

DOI: 10.1021/acs.jmedchem.8b01087
J. Med. Chem. XXXX, XXX, XXX−XXX

PCI-34051, if it prevents this inhibitor from easily adapting to small changes within the HDAC8 active site, might also explain why this inhibitor is so selective for this enzyme.

The existence of a unique selective specific pocket in HDAC8 and the effects observed on activity when this pocket is partially occupied indicate that it might also be essential for the recognition of specific targets. Collectively, our results unravel the structural determinants underlying HDAC8 selective inhibition and pave the way toward the design of more potent HDAC selective inhibitors, the development of novel epigenetic drugs, and the delineation of HDACs specific biological role through chemical biology approaches.

EXPERIMENTAL SECTION

Small-Molecule Inhibitors. The inhibitors **PCI-34051** and **Quisinostat** (**QSN**) were purchased from Selleck Chemicals (USA). The **NCC-149** inhibitor was purchased from the Tokyo Chemical Company (Japan). The smHDAC8-selective inhibitors were synthesized and characterized as described previously[29,56] unless stated below.

Compound **6** (3-(benzthiophene-7-carboxamido)-4-chlorobenzohydroxamate) was synthesized as follows (Supporting Information, Figure S12A): Procedure. (a) Benzthiophene-7-carboxylic acid (1.4 mmol) was cooled to 0 °C and then thionyl chloride (3 mmol) was added dropwise. The mixture was heated under reflux for 30 min. After evaporating the excess of thionyl chloride under vacuum, the obtained acid chloride was dissolved in dry THF (50 mL) and added to a solution of methyl 3-amino-4-chlorobenzoate (1.4 mmol) and DIPEA (3 mmol) in THF. The reaction was monitored by TLC. Subsequently, the solvent was evaporated under vacuum and the mixture was dissolved in ethyl acetate (50 mL) and washed with aq sodium hydroxide solution. The organic layer was evaporated under reduced pressure, and the product was purified by column chromatography (chloroform/methanol, 99:1), yield 88.8%. (b) The obtained amide was dissolved in methanol (25 mL) and 1 M aq sodium hydroxide solution (10 mL) and heated to 50 °C for 2 h. The reaction was monitored by TLC. Subsequently, the solvent was evaporated under reduced pressure and the product was dissolved in ethyl acetate and washed with 1 M HCl solution, the organic layer was finally evaporated under reduced pressure, yield 85.0%. (c) The substituted benzoic acid derivative (1 mmol) was dissolved in dry THF (50 mL), and PyBOP (1.2 mmol) was added. To the activated acid, a mixture of NH_2OTHP (1.5 mmol) and DIPEA (2.5 mmol) in dry THF (5 mL) was added, and the reaction mixture was stirred overnight at room temperature. The solvent was evaporated under reduced pressure, and the mixture was dissolved in ethyl acetate (50 mL) and washed with aq potassium hydrogen carbonate solution and brine. The organic layer was evaporated under reduced pressure, and the product was purified by column chromatography (chloroform/methanol/TEA, 99.5:0.45:0.05). The obtained product was dissolved in THF, and a catalytic amount of diluted HCl was added and was stirred at room temperature. The reaction was controlled by TLC. After that, the solvent was evaporated under reduced pressure and the mixture was dissolved in ethyl acetate (50 mL) and washed with brine. The organic layer was evaporated under reduced pressure, and the product was purified by column chromatography (chloroform/methanol/formic acid, 95:4.95:0.05). Yield: 35%. Analytical data MS m/z: 345.23 (Cl^{35}), 347.24 (Cl^{37}) $[M - H]^-$. ^1H NMR (400 MHz, DMSO-d_6) δ 11.37 (s, 1H), 10.42 (s, 1H), 9.14 (s, 1H), 8.22 (d, J = 7.3 Hz, 1H), 8.15 (d, J = 7.7 Hz, 1H), 8.02 (s, 1H), 7.85 (d, J = 5.2 Hz, 1H), 7.74−7.63 (m, 2H), 7.59 (t, J = 7.5 Hz, 1H), 7.53 (d, J = 5.2 Hz, 1H). HRMS m/z: 369.0072 $[M + Na]^+$ calculated, $C_{16}H_{11}N_2O_3ClSNa^+$ 369.0071. HPLC: rt 10.68 min (99.65%). Yield: 120 mg; 0.35 mmol; 25%.

Compound **12** (1-[5-chloro-2-(4-fluorophenoxy)phenyl]-*N*-hydroxy-1*H*-1,2,3-triazole-4-carboxamide) was synthesized as follows (Supporting Information, Figure S12B). Procedure: (a) 2-Amino-4-chlorophenol (7.0 mmol) was dissolved in 1 M HCl (20 mL). At −5 °C, a solution of sodium nitrite (8.4 mmol) in water (2 mL) was added dropwise over a period of 5 min. After stirring additional 5 min, urea (50 mg) was added. Then the mixture was added to a cold solution of sodium azide (14 mmol) and sodium acetate (0.06 mmol) in water (10 mL). The resulting mixture was stirred for 2 h at −5 °C. Then it was extracted with diethyl ether (3×). The combined organic layers were dried (Na_2SO_4), filtered, and the solvent removed under reduced pressure. The residue was purified by flash column chromatography (cyclohexane/ethyl acetate = 10/1), yield 86%. (b) The obtained azide (3.0 mmol) was dissolved in a 1:1 mixture of water and *tert*-butyl alcohol (15 mL). Methyl propiolate (4.0 mmol), sodium ascorbate (0.20 mmol), and copper(II) sulfate pentahydrate (0.04 mmol) were added, and the mixture was stirred for 18 h at room temperature. Then water was added, and the mixture was extracted with ethyl acetate (3×). The combined organic layers were dried (Na_2SO_4), filtered, and the solvent removed under reduced pressure. The residue was purified by flash column chromatography (cyclohexane/ethyl acetate = 2/1), yield 89%. (c) A 100 mL round-bottom flask was charged with the obtained triazole (0.59 mmol), $Cu(OAc)_2$ (0.59 mmol), 4-fluorophenylboronic acid (0.71 mmol), and powdered 4 Å molecular sieves. Then dichloromethane (4.5 mL) was added. After the addition of triethylamine (2.9 mmol), the reaction mixture was stirred at ambient temperature overnight. Then the suspension was filtered and the filtrate diluted with water and extracted with ethyl acetate (3×). The combined organic layers were dried (Na_2SO_4), filtered, and the solvent removed under reduced pressure. The residue was purified by flash column chromatography (cyclohexane/ethyl acetate = 9/1 → 3/1), yield 13%. (d) A 5.4 M solution of sodium methoxide in methanol (1.1 mmol) was added to a solution of the obtained diphenyl ether (0.11 mmol) and hydroxylamine hydrochloride (0.55 mmol) in dry methanol (3 mL). The mixture was stirred at ambient temperature overnight. Then the solvent was removed under reduced pressure and the residue was purified by automatic flash column chromatography using a Biotage purification apparatus (5% → 50% ACN in H_2O, Biotage SNAP KP-C18-HS 12 g). Fractions containing the desired product were combined, dried from acetonitrile under reduced pressure, and then subjected to lyophilization; yield 95%. Analytical data: ^1H NMR (DMSO-d_6) δ 7.02−7.06 (m, 1H), 7.15−7.20 (m, 2H), 7.22−7.28 (m, 2H), 7.53−7.57 (m, 1H), 7.87−7.90 (m, 1H), 8.31 (s, 1H). ^{13}C NMR (DMSO-d_6) δ 116.9 (d, J = 23.7 Hz, 2C), 120.4 (1C), 121.1 (d, J = 8.7 Hz, 2C), 123.1 (1C), 125.7 (1C), 127.4 (1C), 128.8 (1C), 130.2 (1C), 147.1 (1C), 148.4 (1C), 151.3 (d, J = 2.4 Hz, 1C), 158.3 (1C), 158.8 (d, J = 241 Hz, 1C). HRMS (m/z): $[M + H]^+$ calculated for $C_{15}H_{11}ClFN_4O_3$ 349.0498, found 349.0522. HPLC: t_R = 16.0 min, purity 95.7%.

Purity of Chemicals. The purity of all compounds used was assessed by HPLC. All synthesized compounds have a purity higher than 95%. The purity for the **PCI-34051** and **Quisinostat** (**QSN**) compounds purchased from Selleck Chemicals is 99.01% and 99.62%, respectively, as stated by the manufacturer (see HPLC data in the following webpages: http://www.selleckchem.com/products/pci-34051.html and http://www.selleckchem.com/products/JNJ-26481585.html). The purity for the NCC-149 compound purchased from the Tokyo Chemical Company is 96.00% as stated by the manufacturer (see http://www.tcichemicals.com/eshop/en/sg/commodity/H1340/). The HPLC traces for all other compounds are provided in Supporting Information, Figure S13A−L).

Cloning, Expression and Purification of HDAC8 Proteins. The full-length cDNA constructs (WT and mutants) for hHDAC8 and smHDAC8 were amplified by polymerase-chain reaction (PCR) and cloned into bacterial expression vectors. The hHDAC8 (WT and mutant) gene was inserted between the *Nde*I and *Bam*HI restriction sites of the pnEA-3HT expression vector,[61] where it is in frame with a sequence coding for a N-terminal poly histidine affinity purification tag followed by thioredoxin and a protease 3C cleavage site. The smHDAC8 (WT and mutant) gene was cloned between the *Nde*I and *Bam*HI restriction sites of the pnEA-tH expression vector[61] and is in frame with a sequence coding for a C-terminal thrombin cleavage site followed by a poly histidine affinity purification tag.

DOI: 10.1021/acs.jmedchem.8b01087
J. Med. Chem. XXXX, XXX, XXX−XXX

For wild-type smHDAC8 overproduction, a modified protocol was used compared to that published previously. Expression was carried out in BL21(DE3) cells in 2 × LB medium. Cultures were grown and induced at 37 °C with 0.7 mM IPTG in the presence of 100 μM $ZnCl_2$. After overnight incubation at 37 °C, cells were harvested and resuspended in lysis buffer A (150 mM NaCl, 50 mM Tris pH 8.0). Lysis was done by sonication, the lysate was clarified by centrifugation. The supernatant was loaded onto Talon Superflow Metal Affinity Resin (Clontech) pre-equilibrated with the lysis buffer A. The his-tagged protein was released from the Talon resin by thrombin protease treatment in buffer B (50 mM KCl, 10 mM Tris pH 8.0) and subsequently loaded onto a 16/60 Superdex 200 gel filtration column (GE Healthcare) pre-equilibrated with buffer C (50 mM KCl, 10 mM Tris-HCl pH 8.0 and 2 mM DTT). Peak fractions were concentrated with an Amicon Ultra centrifugal filter unit. This protocol yielded three times more protein for the wild type enzyme. smHDAC8 mutants could not be purified using this protocol and their overproduction was carried out as described initially.[30,62]

hHDAC8 overproduction was carried out in *Escherichia coli* BL21(DE3) cells in 2 × LB medium. Culture induction was done at 23 °C by adding 0.5 mM final isopropyl-1-thio-β-D-galactopyranoside (IPTG, Euromedex), in the presence of 100 μM $ZnCl_2$. Harvested bacteria were resuspended in lysis buffer (50 mM KCl, 10 mM Tris-HCl pH 8.0) and lysed by sonication. The lysate was clarified by centrifugation (17500 rpm, 50 min, 4 °C, Sorvall Lynx 6000 Thermo Scientific). The supernatant was loaded onto Talon Superflow Metal Affinity Resin (Clontech) pre-equilibrated with lysis buffer. The his-thioredoxin-tagged protein was released from the Talon resin by 3C protease treatment and subsequently loaded onto a 16/60 Superdex 200 gel filtration column (GE Healthcare) pre-equilibrated with the purification buffer (50 mM KCl, 10 mM Tris-HCl pH 8.0, and 0.5 mM TCEP). The recombinant protein was concentrated with an Amicon Ultra centrifugal filter unit.

Mutagenesis Experiments. The mutant constructs were generated using standard PCR-based nested protocols and inserted into the corresponding expression vectors. The L1 and L6 loops exchange mutants were designed based on structural comparison. The hHDAC1 L6 sequence S_{265}LSGDRLGC was introduced instead of the T_{268}IAGDPMCS sequence in hHDAC8, to create the hHDAC8 mL6 mutant. In the second step, the hHDAC1 L1 sequence Y_{23}YGQGHPMK was introduced instead of the L_{31}AKI sequence in hHDAC8 mL6, to create the double hHDAC8 mL1/mL6 mutant. Finally, the triple mutant hHDAC8 mL1/mL6/L179I was generated by the introduction of an isoleucine residue in the L179 position, using the double hHDAC8 mL1/mL6 mutant as a template. smHDAC8 mutants were produced as described for hHDAC8 mutants. Sequences replaced in smHDAC8 were the same as the ones replaced in hHDAC8.

Crystallization and X-ray Data Collection. Diffraction-quality crystals of the native smHDAC8 enzyme were obtained at 17 °C after 3 days by mixing equal volumes of smHDAC8 (2.5 mg/mL) with reservoir solution composed of 21% PEG 3350 (Fluka) and 0.05 M Na^+/K^+ L-tartrate, and crystallized using the hanging-drop vapor diffusion technique. After 3 days, grown crystals were soaked for 20 h in mother liquor supplemented with the corresponding inhibitor (10 mM final concentration of the inhibitor, preparation from a 100 mM stock in N,N-dimethylformamide (DMF) or DMSO). Crystals used for X-ray data collection were briefly transferred in reservoir solution supplemented with 22% glycerol and flash-frozen in liquid nitrogen.

Co-crystallization of hHDAC8 mL6 together with **QSN** (**Quisinostat**) inhibitor was performed using the hanging-drop vapor diffusion technique. The hHDAC8 mL6/**QSN** complex was formed by incubating the hHDAC8 mL6 mutant protein (5 mg/mL) with **QSN** (5 mM resuspended in DMF) at 4 °C for 1 h. Diffraction-quality crystals were obtained at 20 °C after 3−4 days by mixing equal volumes of the hHDAC8 mL6/**QSN** complex with reservoir solution composed of 20% polyethylene glycol 3350 (Fluka), 0.2 M KNO_3 and 0.1 M Bis-tris propane pH 7.5. Crystals used for X-ray data collection were briefly transferred in reservoir solution supplemented with 22% glycerol and flash-frozen in liquid nitrogen. Crystallographic data obtained in this project were collected at 100 K on SOLEIL beamline PROXIMA1, ESRF beamlines ID30b, ID29 and ID23 and SLS PX beamlines.

Structure Determination, Model Building, and Refinement. The crystallographic data were processed and scaled using HKL2000[63] or XDS.[64] Phases for smHDAC8/inhibitor complexes were obtained by molecular replacement followed by rigid body refinement against smHDAC8 native structure as a model (4BZ5). The initial models were refined through several cycles of manual building using Coot[65] and automated refinement with Phenix.[66] The structure of hHDAC8 mL6 complexed with **QSN** was solved by molecular replacement with Phenix[66] using the hHDAC8 structure (PDB 1T67) as a search model. The final models were validated using tools provided in Coot[65] and Molprobity.[67] Visualization of structural data was done with Pymol (The PyMOL Molecular Graphics System, version 2.0; Schrödinger, LLC), and two-dimensional diagrams summarizing molecular interaction between inhibitors and HDAC8 enzymes were prepared with the help of the LigPlot program.[68] Atomic coordinates and structure factors of the smHDAC8 and hHDAC8 mL6 complexes were deposited in the Protein Data Bank under the PDB codes 6HQY, 6HRQ, 6HSH, 6HSF, 6HSG, 6HSZ, 6HT8, 6HTG, 6HTH, 6HTI, 6HTT, 6HTZ, 6HU0, 6HU1, 6HU2, 6HU3, and 6HSK.

HDAC Activity and Inhibition Assays. Catalytic activity and inhibition assays of smHDAC8 and hHDAC8 were performed as described earlier.[30] Briefly, the hHDAC8 and smHDAC8 activity testing was carried out with the HDAC8 Fluorimetric Drug Discovery Kit (Fluor de Lys(R)- HDAC8, BML-KI178) from Enzo Life Sciences, according to the manufacturer's instructions with a substrate concentration of 50 μM. Fluorescence was measured in a plate reader (BMG Polarstar) with excitation at λ = 390 nm and emission at λ = 460 nm. IC_{50} values were determined with OriginPro (version 9.0.0, Northampton, Massachusetts).

Studies on *Schistosoma mansoni* in Culture. The effects of **PCI-34051** and **NCC-149** compounds on the viability of *S. mansoni* schistosomula (Puerto Rican strain) were tested using a microscopy-based assay, as described previously.[69] In brief, schistosomula (2000 per well), prepared by standard mechanical transformation from cercaria,[70] were maintained in 6-well plates in M199 medium kept at pH 7.4 with 10 mM HEPES and supplemented at 37 °C in a humid atmosphere containing 5% CO_2. Three different concentrations of inhibitors (25, 50, and 100 μM) were tested, the inhibitors were dissolved in DMSO, and the culture medium was refreshed each day. The assessment of parasite mortality was carried out after microscopic examination, based on three criteria: a granular appearance, tegumental defects and the absence of motility. At least 300 schistosomula were observed at each time point for each condition and results were expressed as a percentage of viable larvae remaining. Three biological replicates (different batches of larvae) were examined in duplicate for each condition.

The stability of adult worm pairs and egg production were assayed as previously described.[70] Adult worm pairs were obtained from infected golden hamsters (*Mesocricetus auratus)* by perfusion, washed in M199 medium and ten pairs placed in 2 mL of M199 buffered complete medium (as for schistosomula above) in each well of a 6-well culture plate. Worms were maintained in culture for 5 days at 37 °C (humid atmosphere, 5% CO_2) before the addition of HDAC8-selective inhibitors, the application of DMSO alone served as a negative control experiment. Both the culture medium and the inhibitors were refreshed daily. The number of couples remaining as pairs was determined daily by microscopy and the medium of each well containing eggs laid by the couples was recovered and centrifuged to allow eggs to be counted under the microscope. Three biological replicate experiments were performed in triplicate.

TUNEL Assay. Detection of DNA strand breaks in inhibitor-treated *S. mansoni* schistosomula was done using the terminal deoxynucleotidyl transferase dUTP nick-end labeling (TUNEL) method using the In Situ Cell Death Detection Kit TMR Red (Roche). The method designed for cell suspensions was followed as described in the manufacturer's instructions with few modifications.

DOI: 10.1021/acs.jmedchem.8b01087
J. Med. Chem. XXXX, XXX, XXX−XXX

Briefly, 2000 schistosomula were treated with 100 μM **PCI-34051** or **NCC-149** for 96 h, in 6-well plates containing 2 mL of complete medium. The treatment with DMSO alone served as negative control experiment. After 96 h incubation, culture media were removed and the schistosomula were centrifuged (1,000 rpm, 2 min), washed three times in PBS buffer, and then fixed in 2% formaldehyde for 60 min. Schistosomula were afterward washed once more in PBS and permeabilization solution (0.1% Triton X-100, 0.1% sodium citrate) was added for 10 min on ice. Labeling of schistosomula with 4′,6-diamidino-2-phenylindole (DAPI) and TMR Red dUTP was performed according to the manufacturer's instructions and TUNEL-positive parasites were observed by fluorescence using an AxioImager Z1-Apotome microscope (Zeiss).

Isothermal Titration Calorimetry (ITC). ITC experiments were done at 25 °C using a PEAQ microcalorimeter (Malvern Instruments). All protein samples were purified in the same ITC buffer (50 mM KCl, 10 mM Tris pH = 8.0 and 0.5 mM TCEP). In a typical experiment, aliquots of 2.0 μL of HDAC8 protein sample at 200 μM were injected into an inhibitor solution at 20 μM placed in the ITC cell. Blank experiments were used to retrieve signal due to solvent (DMSO or DMF) dilution into ITC buffer. Data were analyzed with PEAQ-ITC Analysis Software (Malvern Instruments) and with Affinimeter (Software 4 Science Developments).

Differential Scanning Fluorimetry. Thermal stability of HDAC8 proteins was analyzed by a label-free differential scanning fluorimetry (DSF) approach using a Prometheus NT.48 instument (NanoTemper Technologies). Briefly, the shift of intrinsic tryptophan fluorescence of HDAC8 proteins upon gradual temperature-triggered unfolding (temperature gradient 20−95 °C) was monitored by detecting the emission fluorescence at 330 and 350 nm. The measurements were carried out nanoDSF-grade high sensitivity glass capillaries (NanoTemper Technologies) at a heating rate of 1 °C/min. Protein melting points (T_m) were inferred from the first derivative of the ratio of tryptophan emission intensities at 330 and 350 nm. Finally, the ΔT_m value of an HDAC8 protein for a particular inhibitor was calculated as the difference between the Tm values of the inhibitor-bound and inhibitor-free proteins. All the assays were done in triplicate.

Docking Experiments. Crystal structures of hHDAC1−3, hHDAC8, and hHDAC6-CD2 for docking as well as zHDAC10 for homology modeling of hHDAC10 were downloaded from Protein Data Bank (corresponding PDBs 4BKX, 4LXZ, 4A69, 2V5X, 5EDU, 5TD7). Also the zHDAC6 CD1−2 structure with Nexturastat A (PDB 5G0J) was downloaded from PDB in order to retrieve conserved water molecules for docking to hHDAC6-CD2. Specifically, water molecule W2141 coordinating the zinc ion was extracted from zHDAC6 and inserted in the superimposed structure of hHDAC6-CD2. This water molecule was used to stabilize the monodentate coordination of the zinc ion by the inhibitor, as is observed for hydroxamic acids with bulky aromatic linkers in HDAC6 X-ray structures. The homology model of human HDAC10 was built on zebrafish HDAC10 structure[71] using MODELER version 9.11.[72] Structures of inhibitors were generated in MOE version 2014.09 (Molecular Operating Environment (MOE), 2014.09; Chemical Computing Group Inc., 1010 Sherbooke St. West, Suite 910, Montreal, QC, Canada, H3A 2R7, 2014).

Protein and inhibitor structures were further prepared for docking in Schrödinger Suite (Schrödinger Suite 2014-2, Maestro version 9.8; Protein Preparation Wizard; Epik version 2.8; Glide version 9.8; Schrödinger, LLC, New York, NY, 2041, UA4). Human HDAC1−3,6,10 were prepared using the Protein Preparation Wizard tool. Hydrogen atoms and missing amino acid residues side chains were added. Solvent molecules were removed except for two conserved water molecules: one near the catalytic zinc ion and another above the zinc coordinating histidine residue (H180, hHDAC8 numbering). Next, hydrogen bond networks and amino acid residues protonation states and tautomers were optimized. Finally, protein models were subjected to energy minimization using OPLS-2005 force field with default settings. Inhibitor structures were prepared with LigPrep and ConfGen tools. Namely, the tautomeric forms and stereoisomers were created and energy minimization was performed with OPLS force field using Ligprep. Conformers were generated with default settings (fast) and energy minimization of the output conformations was performed using ConfGen.

Molecular docking was performed using Glide from the Schrödinger Suite. Receptor grids were generated using default settings. The Standard Precision docking protocol with default settings without any constraints was used, except the number of docking poses for postdocking minimization per ligand was increased to 20 and the maximal number of output poses per ligand was increased to 2.

Molecular Dynamics Simulations. Initial coordinates of the smHDAC8/inhibitor complexes were taken from the newly resolved crystal structures of smHDAC8 in complex with **PCI-34051**, **NCC-149**, and compounds **4** and **10**. Coordinates of **PCI-34051**, **NCC-149**, and compounds **4** and **10** in complex with hHDAC8, as well as **PCI-34051** and **NCC-149** in complex with HDAC6 were taken from the obtained docking poses described above. All ligands were generated in the negatively charged hydroxamate form, and the protein residues were charged at pH 7, where the His residue coordinating the negatively charged O atom of the hydroxamate was assigned a positive charge (HIP residue). Water molecules and K^+ ions were kept.

MD simulations were performed using Amber16 package (AMBER 2016, UCSF, San Francisco, California, USA, 2016). Force field parameters for all ligands were assigned using the Antechamber package and AM1-BCC atomic charges.[73,74] The TLEaP module of Amber16, the ff03 force field[75] and the General Amber Force Field (GAFF)[76] were applied to the protein residues and ligand, respectively, and the 12−6−4 LJ-type nonbonded model parameters[77] for divalent ions in SPC/E water model was used for the catalytic Zn^{2+} ion. The complex structures were solvated in an octahedral periodic box of SPC/E water molecules[78] at a margin of 10 Å and the system was neutralized using Na^+ counterions.

The system was first subjected to consecutive steps of minimization. The first step encompassed 3000 iterations (first 1000 steepest descent and then 2000 conjugate gradient), where only solvent atoms were minimized, while restraining the protein and ligand atoms as well as the Zn^{2+} ion to their initial coordinates with a force constant of 10 kcal·mol^{-1}·Å^{-2}. In the second step, the whole system was minimized with no restraints using 4000 iterations (first 2000 steepest descent and then 2000 conjugate gradient). The system was then heated to the production temperature of 300 K through 100 ps of MD, while keeping the complex atoms (protein, ligand, and zinc ion) restrained with a force constant of 10 kcal·mol^{-1}·Å^{-2} to prevent large structural deviations. Constant volume periodic boundary was set to equilibrate the temperature of the system by Langevin thermostat using a collision frequency of 2 ps^{-1}. The system was subsequently subjected to a pressure equilibration routine for 100 ps at 300 K, where a constant pressure of 1 bar was applied.

Finally, a production run of 100 ns was simulated at constant temperature (300 K) using the Langevin thermostat with a collision frequency of 2 ps^{-1}. Constant pressure periodic boundary was used to maintain the pressure of the system at 1 bar using isotropic position scaling with a relaxation time of 2 ps. During the temperature equilibration and MD routines a nonbonded cutoff distance of 10.0 Å was used by applying the Particle Mesh Ewald (PME) method[79] for long-range electrostatic interactions. The SHAKE algorithm[80] was applied to constrain all bonds involving hydrogen. A time step of 2 fs was used for equilibration and the production of MD. All simulations were run using PMEMD.cuda implementation from AMBER16 on CUDA-enabled NVIDIA graphics processing units (GPUs).

The trajectories were analyzed using the CPPTRAJ module of AMBER and visualized using VMD. Plots were generated using the R package, and the pictures using PYMOL.

PAINS Filter. All the herein described compounds were filtered for pan-assay interference compounds (PAINS). For this purpose, PAINS1, PAINS2, and PAINS3 filters, as implemented in Schrödinger's Canvas module (Schrödinger Suite 2014−2, Canvas

DOI: 10.1021/acs.jmedchem.8b01087
J. Med. Chem. XXXX, XXX, XXX−XXX

version 2.0), were employed. None of the compounds was flagged as PAINS.

■ ASSOCIATED CONTENT

Supporting Information

The Supporting Information is available free of charge on the ACS Publications website at DOI: 10.1021/acs.jmedchem.8b01087.

Fitness analysis of schistosomes treated with inhibitors **PCI-34051** and **NCC-149**; structures of **PCI-34051** and **NCC-149** bound to the smHDAC8-H292M mutant; close-up view of HDAC8-selective inhibitors bound to smHDAC8; docking results of compounds **9** and **10** bound to human HDAC8; snapshots and RMSD plots of MD simulations of smHDAC8/**4**, smHDAC8/**10**, hHDAC8/**4**, and hHDAC8/**10** complexes; comparison of the binding modes of compound **11** and **PCI-34051** to smHDAC8; structural plasticity and flexibility of human HDAC8 L1 and L2 loops; docking poses of **PCI-34051** and **NCC-149** in different HDAC isozymes; snapshots and RMSD plots of MD simulations of HDAC/**PCI-34051** complexes; snapshots and RMSD plots of MD simulations of HDAC/**NCC-149** complexes; binding mode of **Quisinostat** (**QSN**) in the structure of the human HDAC8 mL6/**QSN** complex; synthesis pathways; HPLC traces of compounds **1**−**12**; data collection and refinement statistics for the structures of smHDAC8 WT and H292M mutant bound to **PCI-34051**, **NCC-149**, and **Quisinostat**; IC_{50} values for HDAC8-selective inhibitors on different HDACs; data collection and refinement statistics for the structures of smHDAC8 bound to compounds **1**−**12**; HDAC8 mutants and activity measurements; IC_{50} values for hHDAC8 mutants with **PCI-34051**, **NCC-149**, and **Quisinostat** (**QSN**); data collection and refinement statistics for the structure of human HDAC8 mL6/**Quisinostat** (**QSN**) complex (PDF)

HM-hHDAC10 (PDB)

Molecular formula strings (CSV)

Accession Codes

Atomic coordinates and structure factors of the smHDAC8 and hHDAC8 mL6 complexes were deposited in the Protein Data Bank under the PDB ID codes 6HQY, 6HRQ, 6HSH, 6HSF, 6HSG, 6HSZ, 6HT8, 6HTG, 6HTH, 6HTI, 6HTT, 6HTZ, 6HU0, 6HU1, 6HU2, 6HU3, and 6HSK. Authors will release the atomic coordinates and experimental data upon article publication.

■ AUTHOR INFORMATION

Corresponding Authors

*For C.R.: phone, (+33) 3-69-48-52-94; E-mail, romier@igbmc.fr.

*For M.M.: E-mail, martin.marek@recetox.muni.cz.

ORCID

Martin Marek: 0000-0001-7220-5644

Takayoshi Suzuki: 0000-0003-2439-879X

Manfred Jung: 0000-0002-6361-7716

Wolfgang Sippl: 0000-0002-5985-9261

Christophe Romier: 0000-0002-3680-935X

Present Address

◆For M.M.: Loschmidt Laboratories, Department of Experimental Biology & RECETOX, Faculty of Science, Masaryk University, Kamenice 5/A13, 625 00 Brno, Czech Republic.

Author Contributions

◇M.M. and T.B.S. contributed equally to this work. M.M., T.B.S., E.R.M., and C.R. solved the HDAC8-inhibitor crystal structures, constructed and biophysically characterized the HDAC8 mutants. J.L. and R.J.P. performed antiparasitic studies. C.D.V., M.M., and E.E. performed and interpreted the ITC experiments. T.S. synthesized the **NCC-149** inhibitor. D.K. and R.H synthesized inhibitor **12**. T.H., J.M., and D.R. carried out docking studies, synthesized and characterized smHDAC8 inhibitors. A.C., K.S., and M.J. performed enzymatic activity and inhibition assays. M.M., R.J.P, M.J., W.S., and C.R. designed experiments, analyzed data and wrote the paper. All authors have given approval to the final version of the manuscript.

Notes

The authors declare no competing financial interest.

■ ACKNOWLEDGMENTS

This work and the authors of this paper have been supported by funding from the European Union's Seventh Framework Programme for research, technological development, and demonstration under grant agreements nos. 241865 (SEt-TReND) and 602080 (A-ParaDDisE) as well as the German Research Foundation (DFG) to W.S. (Si868/13-1) and M.J. (Ju295/13-1). This study was supported by the grant ANR-10-LABX-0030-INRT, a French State fund managed by the Agence Nationale de la Recherche under the frame program Investissements d'Avenir ANR-10-IDEX-0002-02. C.R., M.M., T.B.S., E.R.M., and R.J.P. are supported by institutional funds from the Centre National de la Recherche Scientifique (CNRS), the Institut National de la Santé et de la Recherche Médicale (INSERM), the Université de Strasbourg, the Institut Pasteur de Lille and the Université de Lille. W.S. was supported by the European Regional Development Fund of the European Commission. We acknowledge the support and the use of resources of the French Infrastructure for Integrated Structural Biology FRISBI ANR-10-INBS-05 and of Instruct-ERIC. We thank members of the ESRF-EMBL joint structural biology groups, the SOLEIL, and the Swiss Light Source (SLS) synchrotrons for the use of their beamline facilities and for help during data collection. We are grateful to Alastair McEwen (IGBMC) for his kind assistance during X-ray data collections.

■ ABBREVIATIONS USED

HDAC,histone deacetylase; HDAC1−3,6,10,HDAC1, HDAC2, HDAC3, HDAC6, and HDAC10.

■ REFERENCES

(1) Choudhary, C.; Weinert, B. T.; Nishida, Y.; Verdin, E.; Mann, M. The growing landscape of lysine acetylation links metabolism and cell signalling. *Nat. Rev. Mol. Cell Biol.* **2014**, *15*, 536−550.

(2) Drazic, A.; Myklebust, L. M.; Ree, R.; Arnesen, T. The world of protein acetylation. *Biochim. Biophys. Acta, Proteins Proteomics* **2016**, *1864*, 1372−1401.

(3) Verdin, E.; Ott, M. 50 years of protein acetylation: from gene regulation to epigenetics, metabolism and beyond. *Nat. Rev. Mol. Cell Biol.* **2015**, *16*, 258−264.

DOI: 10.1021/acs.jmedchem.8b01087
J. Med. Chem. XXXX, XXX, XXX−XXX

(4) Haberland, M.; Montgomery, R. L.; Olson, E. N. The many roles of histone deacetylases in development and physiology: implications for disease and therapy. *Nat. Rev. Genet.* **2009**, *10*, 32−42.
(5) Marmorstein, R.; Zhou, M. M. Writers and readers of histone acetylation: structure, mechanism, and inhibition. *Cold Spring Harbor Perspect. Biol.* **2014**, *6*, a018762.
(6) Seto, E.; Yoshida, M. Erasers of histone acetylation: the histone deacetylase enzymes. *Cold Spring Harbor Perspect. Biol.* **2014**, *6*, a018713.
(7) Musselman, C. A.; Lalonde, M. E.; Cote, J.; Kutateladze, T. G. Perceiving the epigenetic landscape through histone readers. *Nat. Struct. Mol. Biol.* **2012**, *19*, 1218−1227.
(8) Arrowsmith, C. H.; Bountra, C.; Fish, P. V.; Lee, K.; Schapira, M. Epigenetic protein families: a new frontier for drug discovery. *Nat. Rev. Drug Discovery* **2012**, *11*, 384−400.
(9) Campbell, R. M.; Tummino, P. J. Cancer epigenetics drug discovery and development: the challenge of hitting the mark. *J. Clin. Invest.* **2014**, *124*, 64−69.
(10) Dawson, M. A.; Kouzarides, T. Cancer epigenetics: from mechanism to therapy. *Cell* **2012**, *150*, 12−27.
(11) Falkenberg, K. J.; Johnstone, R. W. Histone deacetylases and their inhibitors in cancer, neurological diseases and immune disorders. *Nat. Rev. Drug Discovery* **2014**, *13*, 673−691.
(12) Jones, P. A.; Issa, J. P.; Baylin, S. Targeting the cancer epigenome for therapy. *Nat. Rev. Genet.* **2016**, *17*, 630−641.
(13) West, A. C.; Johnstone, R. W. New and emerging HDAC inhibitors for cancer treatment. *J. Clin. Invest.* **2014**, *124*, 30−39.
(14) Chan, T. S.; Tse, E.; Kwong, Y. L. Chidamide in the treatment of peripheral T-cell lymphoma. *OncoTargets Ther.* **2017**, *10*, 347−352.
(15) Maolanon, A. R.; Madsen, A. S.; Olsen, C. A. Innovative strategies for selective inhibition of histone deacetylases. *Cell Chem. Biol.* **2016**, *23*, 759−768.
(16) Balasubramanian, S.; Ramos, J.; Luo, W.; Sirisawad, M.; Verner, E.; Buggy, J. J. A novel histone deacetylase 8 (HDAC8)-specific inhibitor PCI-34051 induces apoptosis in T-cell lymphomas. *Leukemia* **2008**, *22*, 1026−1034.
(17) Suzuki, T.; Muto, N.; Bando, M.; Itoh, Y.; Masaki, A.; Ri, M.; Ota, Y.; Nakagawa, H.; Iida, S.; Shirahige, K.; Miyata, N. Design, synthesis, and biological activity of NCC149 derivatives as histone deacetylase 8-selective inhibitors. *ChemMedChem* **2014**, *9*, 657−664.
(18) Suzuki, T.; Ota, Y.; Ri, M.; Bando, M.; Gotoh, A.; Itoh, Y.; Tsumoto, H.; Tatum, P. R.; Mizukami, T.; Nakagawa, H.; Iida, S.; Ueda, R.; Shirahige, K.; Miyata, N. Rapid discovery of highly potent and selective inhibitors of histone deacetylase 8 using click chemistry to generate candidate libraries. *J. Med. Chem.* **2012**, *55*, 9562−9575.
(19) Chakrabarti, A.; Melesina, J.; Kolbinger, F. R.; Oehme, I.; Senger, J.; Witt, O.; Sippl, W.; Jung, M. Targeting histone deacetylase 8 as a therapeutic approach to cancer and neurodegenerative diseases. *Future Med. Chem.* **2016**, *8*, 1609−1634.
(20) Chakrabarti, A.; Oehme, I.; Witt, O.; Oliveira, G.; Sippl, W.; Romier, C.; Pierce, R. J.; Jung, M. HDAC8: a multifaceted target for therapeutic interventions. *Trends Pharmacol. Sci.* **2015**, *36*, 481−492.
(21) Ramos, T. L.; Sanchez-Abarca, L. I.; Redondo, A.; Hernandez-Hernandez, A.; Almeida, A. M.; Puig, N.; Rodriguez, C.; Ortega, R.; Preciado, S.; Rico, A.; Muntion, S.; Porras, J. R. G.; Del Canizo, C.; Sanchez-Guijo, F. HDAC8 overexpression in mesenchymal stromal cells from JAK2+ myeloproliferative neoplasms: a new therapeutic target? *Oncotarget* **2017**, *8*, 28187−28202.
(22) Deardorff, M. A.; Bando, M.; Nakato, R.; Watrin, E.; Itoh, T.; Minamino, M.; Saitoh, K.; Komata, M.; Katou, Y.; Clark, D.; Cole, K. E.; De Baere, E.; Decroos, C.; Di Donato, N.; Ernst, S.; Francey, L. J.; Gyftodimou, Y.; Hirashima, K.; Hullings, M.; Ishikawa, Y.; Jaulin, C.; Kaur, M.; Kiyono, T.; Lombardi, P. M.; Magnaghi-Jaulin, L.; Mortier, G. R.; Nozaki, N.; Petersen, M. B.; Seimiya, H.; Siu, V. M.; Suzuki, Y.; Takagaki, K.; Wilde, J. J.; Willems, P. J.; Prigent, C.; Gillessen-Kaesbach, G.; Christianson, D. W.; Kaiser, F. J.; Jackson, L. G.; Hirota, T.; Krantz, I. D.; Shirahige, K. HDAC8 mutations in Cornelia de Lange syndrome affect the cohesin acetylation cycle. *Nature* **2012**, *489*, 313−317.
(23) Deardorff, M. A.; Porter, N. J.; Christianson, D. W. Structural aspects of HDAC8 mechanism and dysfunction in Cornelia de Lange syndrome spectrum disorders. *Protein Sci.* **2016**, *25*, 1965−1976.
(24) Kaiser, F. J.; Ansari, M.; Braunholz, D.; Gil-Rodriguez, M. C.; Decroos, C.; Wilde, J. J.; Fincher, C. T.; Kaur, M.; Bando, M.; Amor, D. J.; Atwal, P. S.; Bahlo, M.; Bowman, C. M.; Bradley, J. J.; Brunner, H. G.; Clark, D.; Del Campo, M.; Di Donato, N.; Diakumis, P.; Dubbs, H.; Dyment, D. A.; Eckhold, J.; Ernst, S.; Ferreira, J. C.; Francey, L. J.; Gehlken, U.; Guillen-Navarro, E.; Gyftodimou, Y.; Hall, B. D.; Hennekam, R.; Hudgins, L.; Hullings, M.; Hunter, J. M.; Yntema, H.; Innes, A. M.; Kline, A. D.; Krumina, Z.; Lee, H.; Leppig, K.; Lynch, S. A.; Mallozzi, M. B.; Mannini, L.; McKee, S.; Mehta, S. G.; Micule, I.; Mohammed, S.; Moran, E.; Mortier, G. R.; Moser, J. A.; Noon, S. E.; Nozaki, N.; Nunes, L.; Pappas, J. G.; Penney, L. S.; Perez-Aytes, A.; Petersen, M. B.; Puisac, B.; Revencu, N.; Roeder, E.; Saitta, S.; Scheuerle, A. E.; Schindeler, K. L.; Siu, V. M.; Stark, Z.; Strom, S. P.; Thiese, H.; Vater, I.; Willems, P.; Williamson, K.; Wilson, L. C.; Hakonarson, H.; Quintero-Rivera, F.; Wierzba, J.; Musio, A.; Gillessen-Kaesbach, G.; Ramos, F. J.; Jackson, L. G.; Shirahige, K.; Pie, J.; Christianson, D. W.; Krantz, I. D.; Fitzpatrick, D. R.; Deardorff, M. A. Loss-of-function HDAC8 mutations cause a phenotypic spectrum of Cornelia de Lange syndrome-like features, ocular hypertelorism, large fontanelle and X-linked inheritance. *Hum. Mol. Genet.* **2014**, *23*, 2888−2900.
(25) Dasgupta, T.; Antony, J.; Braithwaite, A. W.; Horsfield, J. A. HDAC8 inhibition blocks SMC3 deacetylation and delays cell cycle progression without affecting cohesin-dependent transcription in MCF7 cancer cells. *J. Biol. Chem.* **2016**, *291*, 12761−12770.
(26) Hsieh, C. L.; Ma, H. P.; Su, C. M.; Chang, Y. J.; Hung, W. Y.; Ho, Y. S.; Huang, W. J.; Lin, R. K. Alterations in histone deacetylase 8 lead to cell migration and poor prognosis in breast cancer. *Life Sci.* **2016**, *151*, 7−14.
(27) Lopez, G.; Bill, K. L.; Bid, H. K.; Braggio, D.; Constantino, D.; Prudner, B.; Zewdu, A.; Batte, K.; Lev, D.; Pollock, R. E. HDAC8, A potential therapeutic target for the treatment of malignant peripheral nerve sheath tumors (MPNST). *PLoS One* **2015**, *10*, e0133302.
(28) Zhang, K.; Lu, Y.; Jiang, C.; Liu, W.; Shu, J.; Chen, X.; Shi, Y.; Wang, E.; Wang, L.; Hu, Q.; Dai, Y.; Xiong, B. HDAC8 functions in spindle assembly during mouse oocyte meiosis. *Oncotarget* **2017**, *8*, 20092−20102.
(29) Heimburg, T.; Chakrabarti, A.; Lancelot, J.; Marek, M.; Melesina, J.; Hauser, A. T.; Shaik, T. B.; Duclaud, S.; Robaa, D.; Erdmann, F.; Schmidt, M.; Romier, C.; Pierce, R. J.; Jung, M.; Sippl, W. Structure-based design and synthesis of novel inhibitors targeting HDAC8 from Schistosoma mansoni for the treatment of schistosomiasis. *J. Med. Chem.* **2016**, *59*, 2423−2435.
(30) Marek, M.; Kannan, S.; Hauser, A. T.; Moraes Mourao, M.; Caby, S.; Cura, V.; Stolfa, D. A.; Schmidtkunz, K.; Lancelot, J.; Andrade, L.; Renaud, J. P.; Oliveira, G.; Sippl, W.; Jung, M.; Cavarelli, J.; Pierce, R. J.; Romier, C. Structural basis for the inhibition of histone deacetylase 8 (HDAC8), a key epigenetic player in the blood fluke Schistosoma mansoni. *PLoS Pathog.* **2013**, *9*, e1003645.
(31) Estiu, G.; West, N.; Mazitschek, R.; Greenberg, E.; Bradner, J. E.; Wiest, O. On the inhibition of histone deacetylase 8. *Bioorg. Med. Chem.* **2010**, *18*, 4103−4110.
(32) Krennhrubec, K.; Marshall, B. L.; Hedglin, M.; Verdin, E.; Ulrich, S. M. Design and evaluation of 'linkerless' hydroxamic acids as selective HDAC8 inhibitors. *Bioorg. Med. Chem. Lett.* **2007**, *17*, 2874−2878.
(33) Somoza, J. R.; Skene, R. J.; Katz, B. A.; Mol, C.; Ho, J. D.; Jennings, A. J.; Luong, C.; Arvai, A.; Buggy, J. J.; Chi, E.; Tang, J.; Sang, B. C.; Verner, E.; Wynands, R.; Leahy, E. M.; Dougan, D. R.; Snell, G.; Navre, M.; Knuth, M. W.; Swanson, R. V.; McRee, D. E.; Tari, L. W. Structural snapshots of human HDAC8 provide insights into the class I histone deacetylases. *Structure* **2004**, *12*, 1325−1334.
(34) Tabackman, A. A.; Frankson, R.; Marsan, E. S.; Perry, K.; Cole, K. E. Structure of 'linkerless' hydroxamic acid inhibitor-HDAC8 complex confirms the formation of an isoform-specific subpocket. *J. Struct. Biol.* **2016**, *195*, 373−378.

DOI: 10.1021/acs.jmedchem.8b01087
J. Med. Chem. XXXX, XXX, XXX−XXX

(35) Arts, J.; King, P.; Marien, A.; Floren, W.; Belien, A.; Janssen, L.; Pilatte, I.; Roux, B.; Decrane, L.; Gilissen, R.; Hickson, I.; Vreys, V.; Cox, E.; Bol, K.; Talloen, W.; Goris, I.; Andries, L.; Du Jardin, M.; Janicot, M.; Page, M.; van Emelen, K.; Angibaud, P. JNJ-26481585, a novel "second-generation" oral histone deacetylase inhibitor, shows broad-spectrum preclinical antitumoral activity. *Clin. Cancer Res.* **2009**, *15*, 6841−6851.
(36) Venugopal, B.; Baird, R.; Kristeleit, R. S.; Plummer, R.; Cowan, R.; Stewart, A.; Fourneau, N.; Hellemans, P.; Elsayed, Y.; McClue, S.; Smit, J. W.; Forslund, A.; Phelps, C.; Camm, J.; Evans, T. R.; de Bono, J. S.; Banerji, U. A phase I study of quisinostat (JNJ-26481585), an oral hydroxamate histone deacetylase inhibitor with evidence of target modulation and antitumor activity, in patients with advanced solid tumors. *Clin. Cancer Res.* **2013**, *19*, 4262−4272.
(37) Dubois, F.; Caby, S.; Oger, F.; Cosseau, C.; Capron, M.; Grunau, C.; Dissous, C.; Pierce, R. J. Histone deacetylase inhibitors induce apoptosis, histone hyperacetylation and up-regulation of gene transcription in Schistosoma mansoni. *Mol. Biochem. Parasitol.* **2009**, *168*, 7−15.
(38) Watson, P. J.; Millard, C. J.; Riley, A. M.; Robertson, N. S.; Wright, L. C.; Godage, H. Y.; Cowley, S. M.; Jamieson, A. G.; Potter, B. V.; Schwabe, J. W. Insights into the activation mechanism of class I HDAC complexes by inositol phosphates. *Nat. Commun.* **2016**, *7*, 11262.
(39) Lauffer, B. E.; Mintzer, R.; Fong, R.; Mukund, S.; Tam, C.; Zilberleyb, I.; Flicke, B.; Ritscher, A.; Fedorowicz, G.; Vallero, R.; Ortwine, D. F.; Gunzner, J.; Modrusan, Z.; Neumann, L.; Koth, C. M.; Lupardus, P. J.; Kaminker, J. S.; Heise, C. E.; Steiner, P. Histone deacetylase (HDAC) inhibitor kinetic rate constants correlate with cellular histone acetylation but not transcription and cell viability. *J. Biol. Chem.* **2013**, *288*, 26926−26943.
(40) Cole, K. E.; Dowling, D. P.; Boone, M. A.; Phillips, A. J.; Christianson, D. W. Structural basis of the antiproliferative activity of largazole, a depsipeptide inhibitor of the histone deacetylases. *J. Am. Chem. Soc.* **2011**, *133*, 12474−12477.
(41) Decroos, C.; Clausen, D. J.; Haines, B. E.; Wiest, O.; Williams, R. M.; Christianson, D. W. Variable active site loop conformations accommodate the binding of macrocyclic largazole analogues to HDAC8. *Biochemistry* **2015**, *54*, 2126−2135.
(42) Hai, Y.; Christianson, D. W. Histone deacetylase 6 structure and molecular basis of catalysis and inhibition. *Nat. Chem. Biol.* **2016**, *12*, 741−747.
(43) Porter, N. J.; Mahendran, A.; Breslow, R.; Christianson, D. W. Unusual zinc-binding mode of HDAC6-selective hydroxamate inhibitors. *Proc. Natl. Acad. Sci. U. S. A.* **2017**, *114*, 13459−13464.
(44) Miyake, Y.; Keusch, J. J.; Wang, L.; Saito, M.; Hess, D.; Wang, X.; Melancon, B. J.; Helquist, P.; Gut, H.; Matthias, P. Structural insights into HDAC6 tubulin deacetylation and its selective inhibition. *Nat. Chem. Biol.* **2016**, *12*, 748−754.
(45) Porter, N. J.; Osko, J. D.; Diedrich, D.; Kurz, T.; Hooker, J. M.; Hansen, F. K.; Christianson, D. W. Histone deacetylase 6-selective inhibitors and the influence of capping groups on hydroxamate-zinc denticity. *J. Med. Chem.* **2018**, *61*, 8054−8060.
(46) Porter, N. J.; Wagner, F. F.; Christianson, D. W. Entropy as a driver of selectivity for inhibitor binding to histone deacetylase 6. *Biochemistry* **2018**, *57*, 3916−3924.
(47) Millard, C. J.; Watson, P. J.; Celardo, I.; Gordiyenko, Y.; Cowley, S. M.; Robinson, C. V.; Fairall, L.; Schwabe, J. W. Class I HDACs share a common mechanism of regulation by inositol phosphates. *Mol. Cell* **2013**, *51*, 57−67.
(48) Watson, P. J.; Fairall, L.; Santos, G. M.; Schwabe, J. W. R. Structure of HDAC3 bound to co-repressor and inositol tetraphosphate. *Nature* **2012**, *481*, 335−340.
(49) Dowling, D. P.; Gantt, S. L.; Gattis, S. G.; Fierke, C. A.; Christianson, D. W. Structural studies of human histone deacetylase 8 and its site-specific variants complexed with substrate and inhibitors. *Biochemistry* **2008**, *47*, 13554−13563.
(50) Dowling, D. P.; Gattis, S. G.; Fierke, C. A.; Christianson, D. W. Structures of metal-substituted human histone deacetylase 8 provide mechanistic inferences on biological function. *Biochemistry* **2010**, *49*, 5048−5056.
(51) Gantt, S. M.; Decroos, C.; Lee, M. S.; Gullett, L. E.; Bowman, C. M.; Christianson, D. W.; Fierke, C. A. General base-general acid catalysis in human histone deacetylase 8. *Biochemistry* **2016**, *55*, 820−832.
(52) Vannini, A.; Volpari, C.; Filocamo, G.; Casavola, E. C.; Brunetti, M.; Renzoni, D.; Chakravarty, P.; Paolini, C.; De Francesco, R.; Gallinari, P.; Steinkuhler, C.; Di Marco, S. Crystal structure of a eukaryotic zinc-dependent histone deacetylase, human HDAC8, complexed with a hydroxamic acid inhibitor. *Proc. Natl. Acad. Sci. U. S. A.* **2004**, *101*, 15064−15069.
(53) Vannini, A.; Volpari, C.; Gallinari, P.; Jones, P.; Mattu, M.; Carfi, A.; De Francesco, R.; Steinkuhler, C.; Di Marco, S. Substrate binding to histone deacetylases as shown by the crystal structure of the HDAC8-substrate complex. *EMBO Rep.* **2007**, *8*, 879−884.
(54) Whitehead, L.; Dobler, M. R.; Radetich, B.; Zhu, Y.; Atadja, P. W.; Claiborne, T.; Grob, J. E.; McRiner, A.; Pancost, M. R.; Patnaik, A.; Shao, W.; Shultz, M.; Tichkule, R.; Tommasi, R. A.; Vash, B.; Wang, P.; Stams, T. Human HDAC isoform selectivity achieved via exploitation of the acetate release channel with structurally unique small molecule inhibitors. *Bioorg. Med. Chem.* **2011**, *19*, 4626−4934.
(55) Bayer, T.; Chakrabarti, A.; Lancelot, J.; Shaik, T. B.; Hausmann, K.; Melesina, J.; Schmidtkunz, K.; Marek, M.; Erdmann, F.; Schmidt, M.; Robaa, D.; Romier, C.; Pierce, R. J.; Jung, M.; Sippl, W. Synthesis, crystallization studies, and in vitro characterization of cinnamic acid derivatives as smhdac8 inhibitors for the treatment of schistosomiasis. *ChemMedChem* **2018**, *13*, 1517−1529.
(56) Heimburg, T.; Kolbinger, F. R.; Zeyen, P.; Ghazy, E.; Herp, D.; Schmidtkunz, K.; Melesina, J.; Shaik, T. B.; Erdmann, F.; Schmidt, M.; Romier, C.; Robaa, D.; Witt, O.; Oehme, I.; Jung, M.; Sippl, W. Structure-based design and biological characterization of selective histone deacetylase 8 (HDAC8) inhibitors with anti-neuroblastoma activity. *J. Med. Chem.* **2017**, *60*, 10188−10204.
(57) Simoben, C. V.; Robaa, D.; Chakrabarti, A.; Schmidtkunz, K.; Marek, M.; Lancelot, J.; Kannan, S.; Melesina, J.; Shaik, T. B.; Pierce, R. J.; Romier, C.; Jung, M.; Sippl, W. A novel class of Schistosoma mansoni histone deacetylase 8 (HDAC8) inhibitors identified by structure-based virtual screening and in vitro testing. *Molecules* **2018**, *23*, 566.
(58) Stolfa, D. A.; Marek, M.; Lancelot, J.; Hauser, A. T.; Walter, A.; Leproult, E.; Melesina, J.; Rumpf, T.; Wurtz, J. M.; Cavarelli, J.; Sippl, W.; Pierce, R. J.; Romier, C.; Jung, M. Molecular basis for the antiparasitic activity of a mercaptoacetamide derivative that inhibits histone deacetylase 8 (HDAC8) from the human pathogen Schistosoma mansoni. *J. Mol. Biol.* **2014**, *426*, 3442−3453.
(59) Porter, N. J.; Christianson, N. H.; Decroos, C.; Christianson, D. W. Structural and Functional Influence of the glycine-rich loop G(302)GGGY on the catalytic tyrosine of histone deacetylase 8. *Biochemistry* **2016**, *55*, 6718−6729.
(60) Burli, R. W.; Luckhurst, C. A.; Aziz, O.; Matthews, K. L.; Yates, D.; Lyons, K. A.; Beconi, M.; McAllister, G.; Breccia, P.; Stott, A. J.; Penrose, S. D.; Wall, M.; Lamers, M.; Leonard, P.; Muller, I.; Richardson, C. M.; Jarvis, R.; Stones, L.; Hughes, S.; Wishart, G.; Haughan, A. F.; O'Connell, C.; Mead, T.; McNeil, H.; Vann, J.; Mangette, J.; Maillard, M.; Beaumont, V.; Munoz-Sanjuan, I.; Dominguez, C. Design, synthesis, and biological evaluation of potent and selective class IIa histone deacetylase (HDAC) inhibitors as a potential therapy for Huntington's disease. *J. Med. Chem.* **2013**, *56*, 9934−9954.
(61) Diebold, M. L.; Fribourg, S.; Koch, M.; Metzger, T.; Romier, C. Deciphering correct strategies for multiprotein complex assembly by co-expression: application to complexes as large as the histone octamer. *J. Struct. Biol.* **2011**, *175*, 178−188.
(62) Marek, M.; Shaik, T. B.; Duclaud, S.; Pierce, R. J.; Romier, C. Large-scale overproduction and purification of recombinant histone deacetylase 8 (HDAC8) from the human-pathogenic flatworm Schistosoma mansoni. *Methods Mol. Biol.* **2016**, *1436*, 109−118.

DOI: 10.1021/acs.jmedchem.8b01087
J. Med. Chem. XXXX, XXX, XXX−XXX

(63) Otwinowski, Z.; Minor, W. Processing of x-ray diffraction data collected in oscillation mode. *Methods Enzymol.* **1997**, *276*, 307−326.
(64) Kabsch, W. Xds. *Acta Crystallogr., Sect. D: Biol. Crystallogr.* **2010**, *66*, 125−132.
(65) Emsley, P.; Cowtan, K. Coot: model-building tools for molecular graphics. *Acta Crystallogr., Sect. D: Biol. Crystallogr.* **2004**, *60*, 2126−2132.
(66) Adams, P. D.; Afonine, P. V.; Bunkoczi, G.; Chen, V. B.; Davis, I. W.; Echols, N.; Headd, J. J.; Hung, L. W.; Kapral, G. J.; Grosse-Kunstleve, R. W.; McCoy, A. J.; Moriarty, N. W.; Oeffner, R.; Read, R. J.; Richardson, D. C.; Richardson, J. S.; Terwilliger, T. C.; Zwart, P. H. PHENIX: a comprehensive Python-based system for macromolecular structure solution. *Acta Crystallogr., Sect. D: Biol. Crystallogr.* **2010**, *66*, 213−221.
(67) Chen, V. B.; Arendall, W. B., 3rd; Headd, J. J.; Keedy, D. A.; Immormino, R. M.; Kapral, G. J.; Murray, L. W.; Richardson, J. S.; Richardson, D. C. MolProbity: all-atom structure validation for macromolecular crystallography. *Acta Crystallogr., Sect. D: Biol. Crystallogr.* **2010**, *66*, 12−21.
(68) Wallace, A. C.; Laskowski, R. A.; Thornton, J. M. LIGPLOT: a program to generate schematic diagrams of protein-ligand interactions. *Protein Eng., Des. Sel.* **1995**, *8*, 127−134.
(69) Vanderstraete, M.; Gouignard, N.; Cailliau, K.; Morel, M.; Lancelot, J.; Bodart, J. F.; Dissous, C. Dual targeting of insulin and venus kinase Receptors of Schistosoma mansoni for novel anti-schistosome therapy. *PLoS Neglected Trop. Dis.* **2013**, *7*, e2226.
(70) Ramalho-Pinto, F. J.; Gazzinelli, G.; Howells, R. E.; Mota-Santos, T. A.; Figueiredo, E. A.; Pellegrino, J. Schistosoma mansoni: defined system for stepwise transformation of cercaria to schistosomule in vitro. *Exp. Parasitol.* **1974**, *36*, 360−372.
(71) Hai, Y.; Shinsky, S. A.; Porter, N. J.; Christianson, D. W. Histone deacetylase 10 structure and molecular function as a polyamine deacetylase. *Nat. Commun.* **2017**, *8*, 15368.
(72) Sali, A.; Blundell, T. L. Comparative protein modelling by satisfaction of spatial restraints. *J. Mol. Biol.* **1993**, *234*, 779−815.
(73) Jakalian, A.; Bush, B. L.; Jack, D. B.; Bayly, C. I. Fast, efficient generation of high-quality atomic charges. AM1-BCC model: I. method. *J. Comput. Chem.* **2000**, *21*, 132−146.
(74) Jakalian, A.; Jack, D. B.; Bayly, C. I. Fast, efficient generation of high-quality atomic charges. AM1-BCC model: II. parameterization and validation. *J. Comput. Chem.* **2002**, *23*, 1623−1641.
(75) Duan, Y.; Wu, C.; Chowdhury, S.; Lee, M. C.; Xiong, G.; Zhang, W.; Yang, R.; Cieplak, P.; Luo, R.; Lee, T.; Caldwell, J.; Wang, J.; Kollman, P. A point-charge force field for molecular mechanics simulations of proteins based on condensed-phase quantum mechanical calculations. *J. Comput. Chem.* **2003**, *24*, 1999−2012.
(76) Wang, J.; Wolf, R. M.; Caldwell, J. W.; Kollman, P. A.; Case, D. A. Development and testing of a general amber force field. *J. Comput. Chem.* **2004**, *25*, 1157−1174.
(77) Li, P.; Merz, K. M., Jr. Taking into account the ion-induced dipole interaction in the nonbonded model of ions. *J. Chem. Theory Comput.* **2014**, *10*, 289−297.
(78) Berendsen, H. J. C.; Grigera, J. R.; Straatsma, T. P. The missing term in effective pair potentials. *J. Phys. Chem.* **1987**, *91*, 6269−6271.
(79) Darden, T.; York, D.; Pedersen, L. Particle Mesh Ewald - an N.Log(N) method for Ewald sums in large systems. *J. Chem. Phys.* **1993**, *98*, 10089−10092.
(80) Ryckaert, J. P.; Ciccotti, G.; Berendsen, H. J. C. Numerical-integration of cartesian equations of motion of a system with constraints - molecular-dynamics of N-alkanes. *J. Comput. Phys.* **1977**, *23*, 327−341.

DOI: 10.1021/acs.jmedchem.8b01087
J. Med. Chem. XXXX, XXX, XXX−XXX

Supporting Information

Characterization of Histone Deacetylase 8 (HDAC8) Selective Inhibition Reveals Specific Active Site Structural and Functional Determinants

Martin Marek, Tajith B. Shaik, Tino Heimburg, Alokta Chakrabarti, Julien Lancelot, Elizabeth Ramos-Morales, Cyrielle Da Veiga, Dmitrii Kalinin, Jelena Melesina, Dina Robaa, Karin Schmidtkunz, Takayoshi Suzuki, Ralph Holl, Eric Ennifar, Raymond J. Pierce, Manfred Jung, Wolfgang Sippl & Christophe Romier

Table of contents

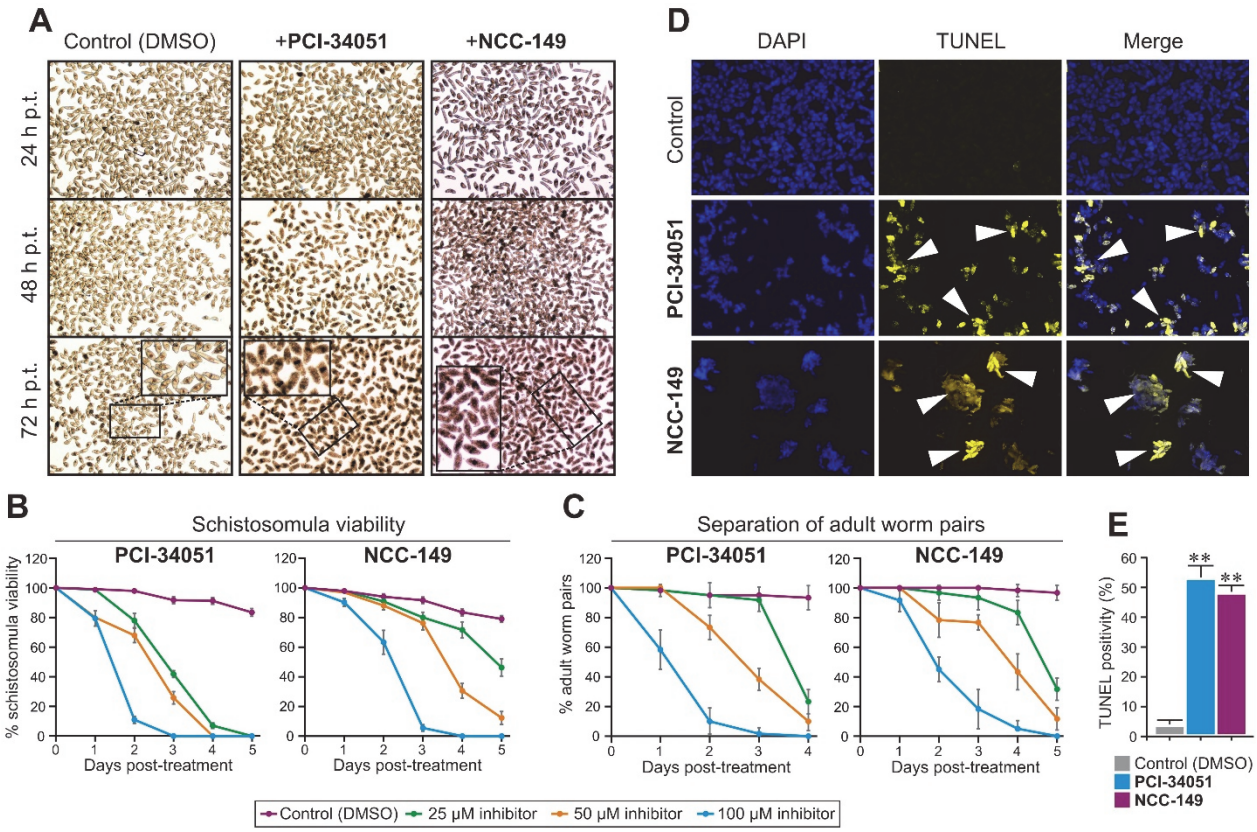

Figure S1. Fitness analysis of schistosomes treated with inhibitors **PCI-34051** and **NCC-149**. (**A**) Time-course analysis of schistosomula viability. *S. mansoni* schistosomula were cultivated in the presence of **PCI-34051** or **NCC-149**, and their viability was assessed by microscopic observations at the indicated time points post treatment (p.t.). Schistosomula cultivated in the DMSO alone served as a control. (**B**) Dose- and time-dependent mortality of schistosomula induced by **PCI-34051** and **NCC-149**. *S. mansoni* schistosomula (1000 per well) were incubated in 1 mL of culture medium with varying quantities of inhibitors or the solvent (DMSO). Both inhibitors have a dose-dependent effect on larval viability, with **PCI-34051** inducing a somewhat stronger phenotypic response than **NCC-149**. Assays were done in triplicate; error bars represent the SD. (**C**) Induction of separation of *S. mansoni* adult worm pairs. The paired status of male and female adult worms was assessed daily in the presence of varying quantities of **PCI-34051** and **NCC-149**. Both inhibitors have a dose-dependent effect on adult worm pairing. Assays were done in triplicate; error bars represent the SD. (**D**) TUNEL assays. Fluorescent microscopy of *S. mansoni* schistosomula incubated with DMSO alone (top panels), **PCI-34051** (middle panels), or **NCC-149** (bottom panels) for 96 h. DAPI (blue), TUNEL (yellow) and merged figures are presented. (**E**) Quantification of TUNEL positivity of schistosomula incubated for 96 h with **PCI-34051** or **NCC-149** (both at 100 µM), or with DMSO alone. Mortality of *in vitro* cultivated schistosomes treated with **PCI-34051** and **NCC-149** is due to the triggering of apoptosis. Assays were done in triplicate; error bars represent the SD.

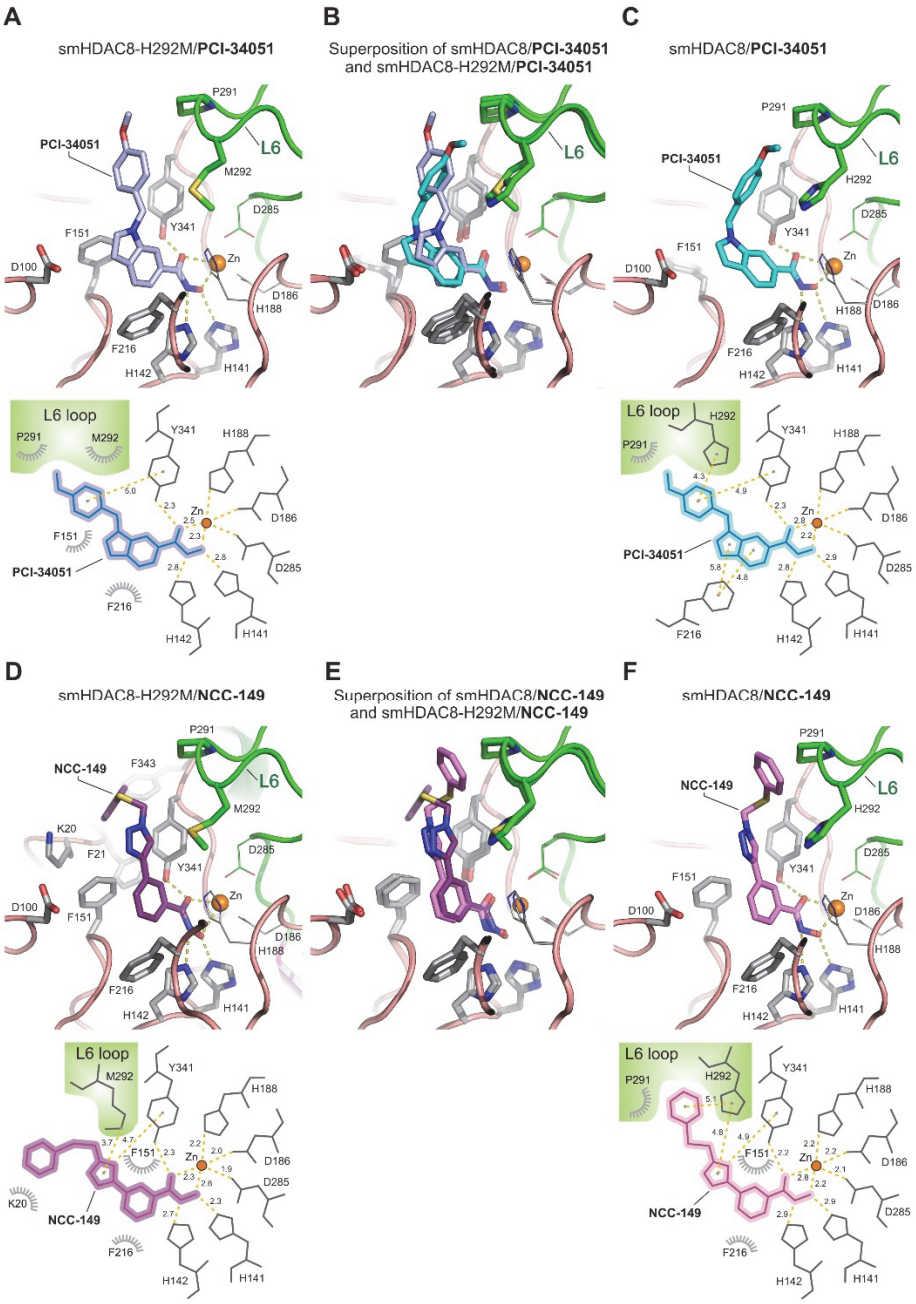

Figure S2. Structures of **PCI-34051** and **NCC-149** bound to the smHDAC8-H292M mutant. (**A**-**C**) Close-up view of HDAC8-selective inhibitor **PCI-34051** bound to smHDAC8 WT (**C**) and the smHDAC8 H292M mutant (**A**), and the superposition of the two structures (**B**). The upper panels show the structures and the lower panels provide a schematic view of the interaction. In the structures, the inhibitors and important residues are shown as sticks. The L6 loop is colored green. The catalytic zinc ion is shown as an orange sphere. Zinc coordination and hydrogen bonds are shown as dashed lines. In the schematic views, zinc coordination, hydrogen bonds and aromatic interactions are shown as dashed lines, and the corresponding distances are given in Å. Hydrophobic contacts are shown by grey arcs with spokes radiating toward the atoms involved. (**D**-**F**) Same as for (**A**-**C**) with the **NCC-149** selective inhibitor. (PDB IDs 6HYQ, 6HRQ, 6HSF, 6HSG).

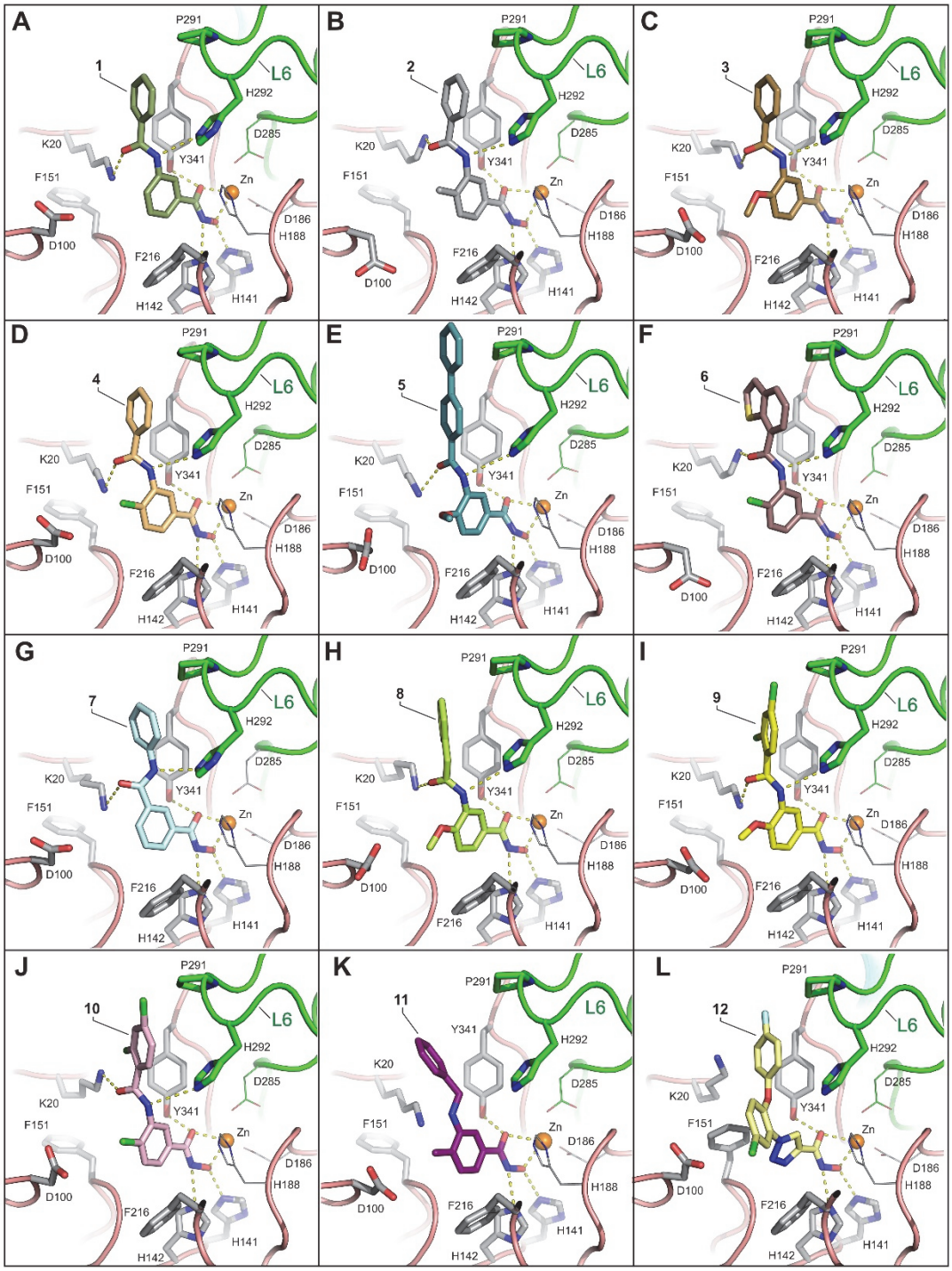

Figure S3. Close-up view of HDAC8-selective inhibitors bound to smHDAC8. (**A-K**) Close-up views of 3-benzamido-benzohydroxamates HDAC8-selective inhibitors **1-11** bound to smHDAC8. (**L**) Close-up view of the unrelated 1-[5-chloro-2-(4-fluorophenoxy)phenyl]-N-hydroxy-1H-1,2,3-triazole-4-carboxamide inhibitor **12** that also shows HDAC8-selective inhibition. All inhibitors bind into a HDAC8-specific pocket formed by catalytic tyrosine Y341 and residues from L1 and L6 loops. Inhibitors and important residues are shown as sticks. The L6 loop is colored green. The catalytic zinc ion is shown as an orange sphere. Zinc coordination and hydrogen bonds are shown as dashed lines. (PDB IDs 5FUE, 6HSZ, 6HT8, 6HTG, 6HTH, 6HTI, 6HTT, 6HTZ, 6HU0, 6HU1, 6HU2, 6HU3).

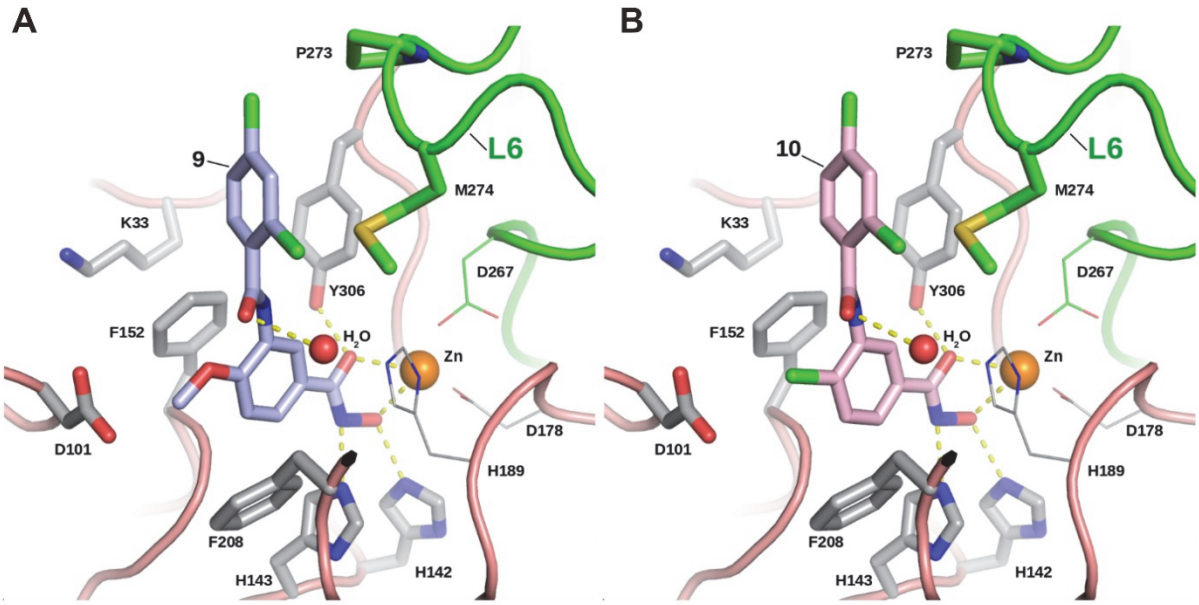

Figure S4. Docking results of compounds **9** and **10** bound to human HDAC8. Inhibitor **9** (**A**), pale blue colored sticks, and **10** (**B**), pale pink colored sticks, are shown at the human HDAC8 binding pocket. Protein backbone is represented as a pale salmon colored ribbon. Protein residues are shown as grey colored sticks and the zinc ion as an orange sphere. The ribbon and residues of the L6 loop are colored in green. Yellow dashed lines represent zinc coordination and hydrogen bonds. (PDB ID 2V5X for hHDAC8 structure used for docking).

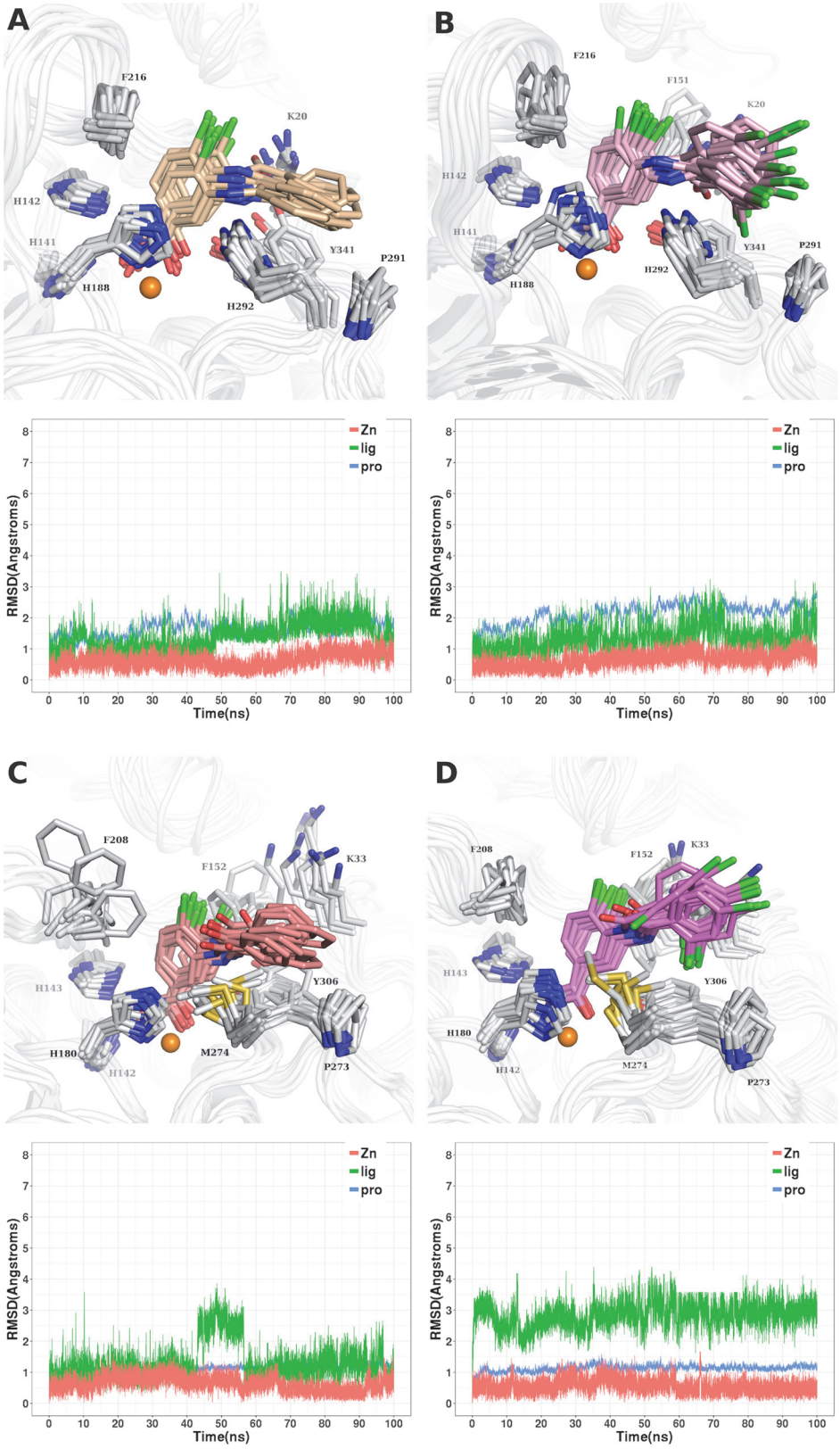

Figure S5. Snapshots and RMSD plots of 100 ns MD simulations of (**A**) crystal structure of smHDAC8/**4** (PDB ID 6HTG), (**B**) crystal structure of smHDAC8/**10** (PDB ID 6HU1), (**C**) docking pose of **4** in hHDAC8, (**D**) docking pose of **10** in hHDAC8. (PDB ID 2V5X for hHDAC8 structure used for docking).

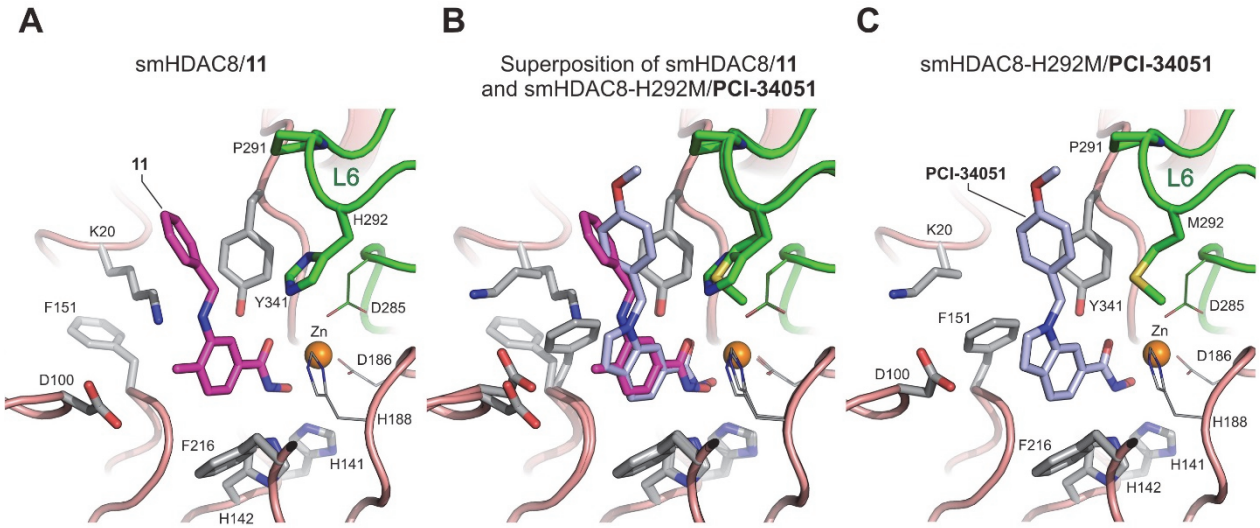

Figure S6. Comparison of the binding modes of compound **11** and **PCI-34051** to smHDAC8. Structures of compound **11** bound to smHDAC8 (**A**) and **PCI-34051** bound to the smHDAC8-H292M mutant (**C**), and the superposition of these two structures (**B**). Both inhibitors bind with a similar conformation to smHDAC8 that most likely mimics the binding of HDAC8-selective inhibitors to hHDAC8. Protein residues are shown as sticks, the catalytic zinc ion is shown as an orange sphere, and L6 loop residues are colored green. (PDB IDs 6HSF, 6HU2).

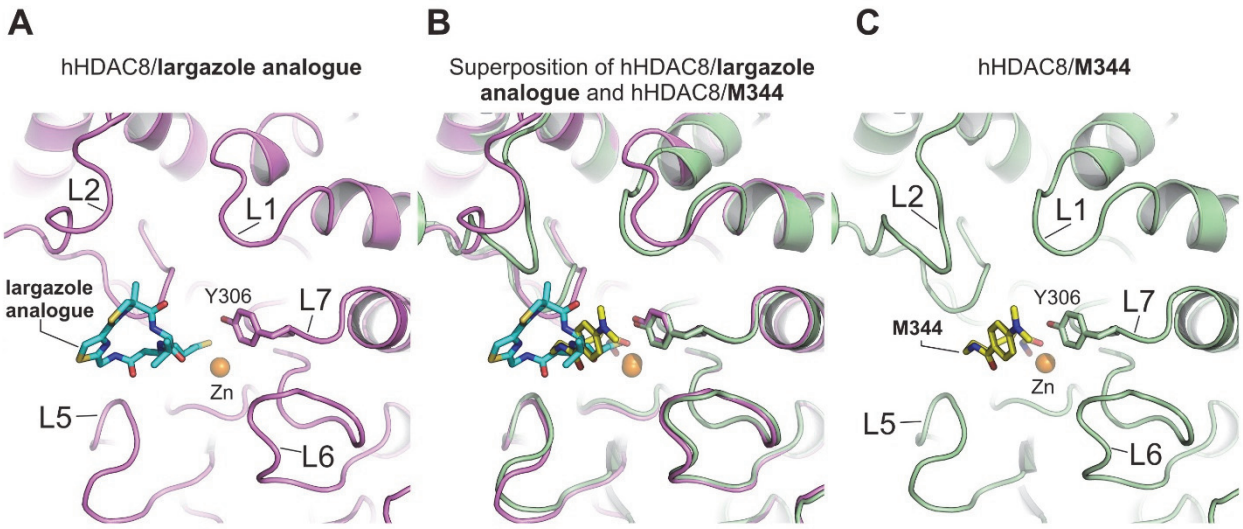

Figure S7. Structural plasticity and flexibility of human HDAC8 L1 and L2 loops. Structure of a largazole analog (PDB ID 4RNO) (**A**) and inhibitor M344 (PDB ID 1T67) (**C**) bound to human HDAC8, and the superposition of both structures (**B**). HDAC8 L1 and L2 loops show strong plasticity and flexibility to accommodate the inhibitors in their active sites. In contrast, L6 and L7 (containing the catalytic tyrosine 306) loop conformations are constrained, providing a stable unique surface for the interaction with HDAC8-selective inhibitors. The proteins are shown as ribbons and the inhibitors as sticks, the catalytic zinc ion is shown as an orange sphere.

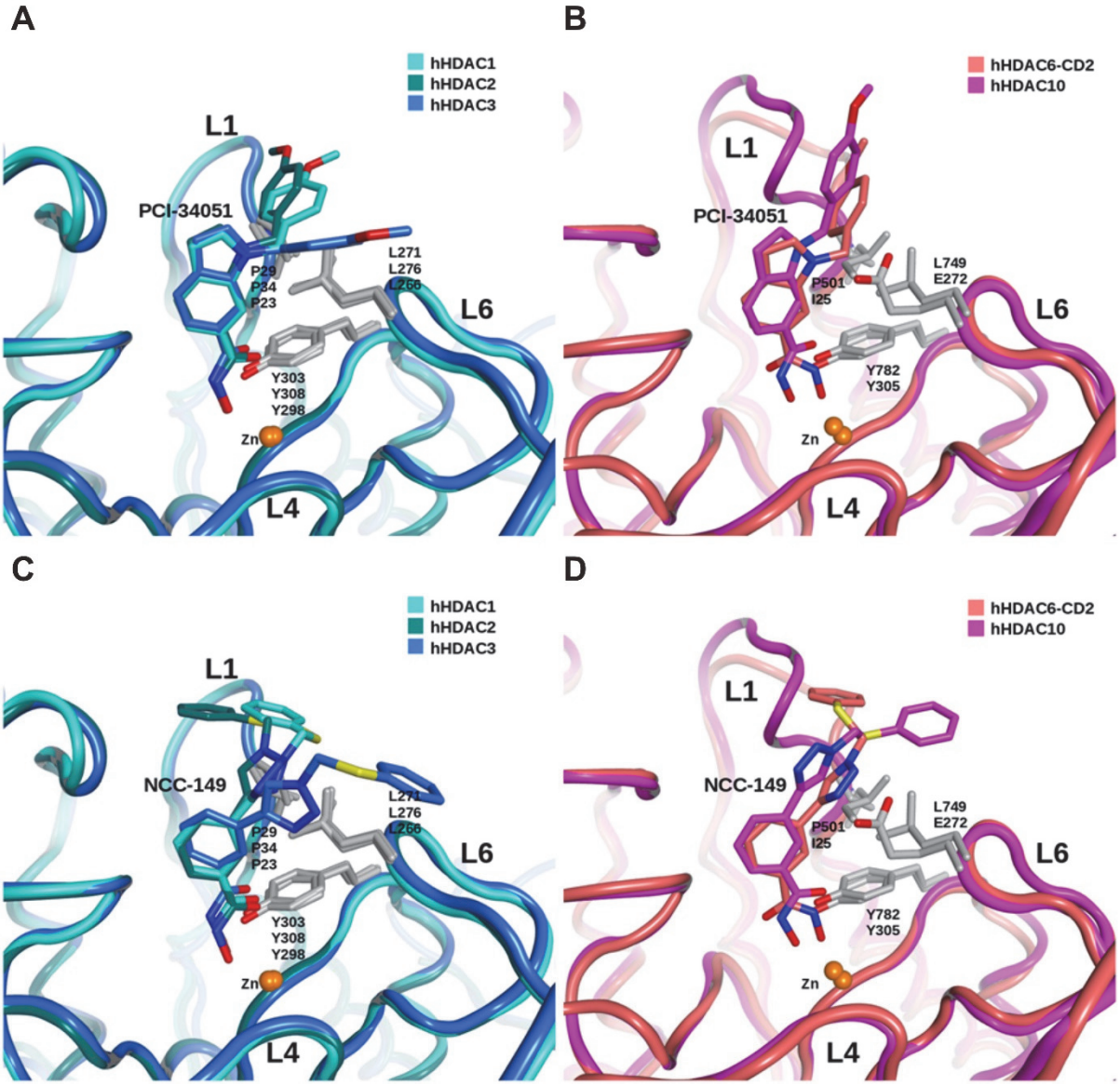

Figure S8. Docking poses of **PCI-34051** and **NCC-149** in different HDAC isozymes. Modelling of binding of HDAC8-selective inhibitors **PCI-34051** (**A**,**B**) and **NCC-149** (**C**,**D**) to hHDAC1-3 (PDB IDs 4BKX, 4LXZ, 4A69) (**A**,**C**), hHDAC6-CD2 (PDB ID 5EDU) and hHDAC10 (modelled from PDB ID 5TD7) (**B**,**D**). The hydroxamic acid group of both L-shaped HDAC8-selective inhibitors is not able to reach the catalytic zinc ion in HDAC1-3 and HDAC10 and to chelate it in a bidentate fashion. Meanwhile, in HDAC6, the hydroxamate group also shows a monodentate chelation of the zinc ion similar to that observed in the crystal structures of zHDAC6 with the benzohydroxamate derivatives Nexturastat A and HPOB (PDB IDs 5G0J, 5EF7). Moreover, the capping groups of both inhibitors are resting on the surface of the protein and cannot interact strongly with the catalytic tyrosine due to the lock imposed by residues from L1 and L6 loops of these different HDACs. As a result, inhibitors are more solvent-exposed, which most likely negatively influences their inhibitory activity. Protein backbone is represented as ribbon. Color codes for protein backbones and corresponding inhibitor docking poses are depicted in the figure. Protein residues (grey color) and inhibitors (see color codes in figure) are shown as sticks, the catalytic zinc ion as orange sphere.

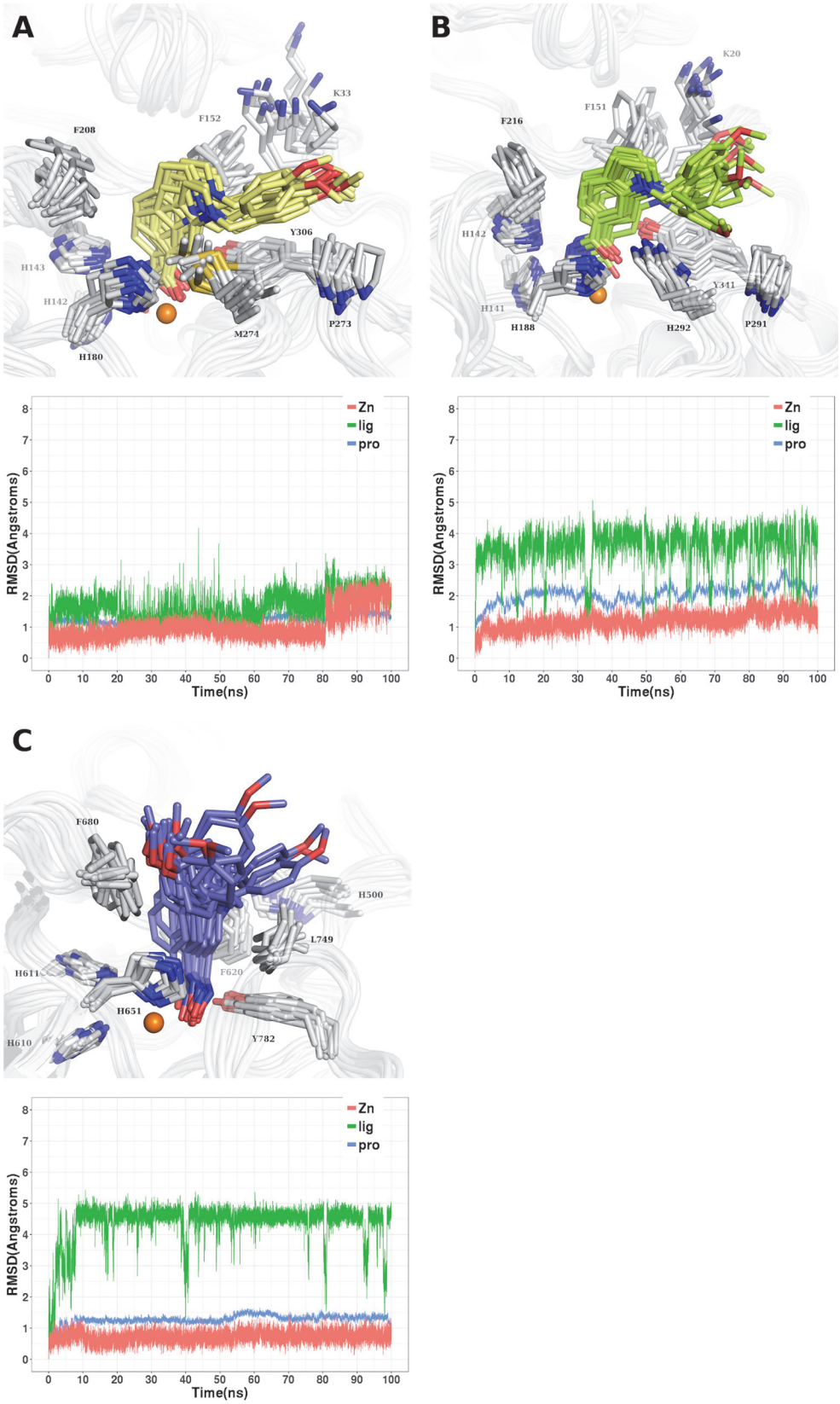

Figure S9. Snapshots and RMSD plots of 100 ns MD simulations of (**A**) docking pose of **PCI-34051** in hHDAC8, (**B**) crystal structure of **PCI-34051** in smHDAC8 (PDB ID 6HQY), (**C**) docking pose of **PCI-34051** in hHDAC6. Models of hHDAC8 and hHDAC6 established from PDB IDs 2V5X and 5EDU.

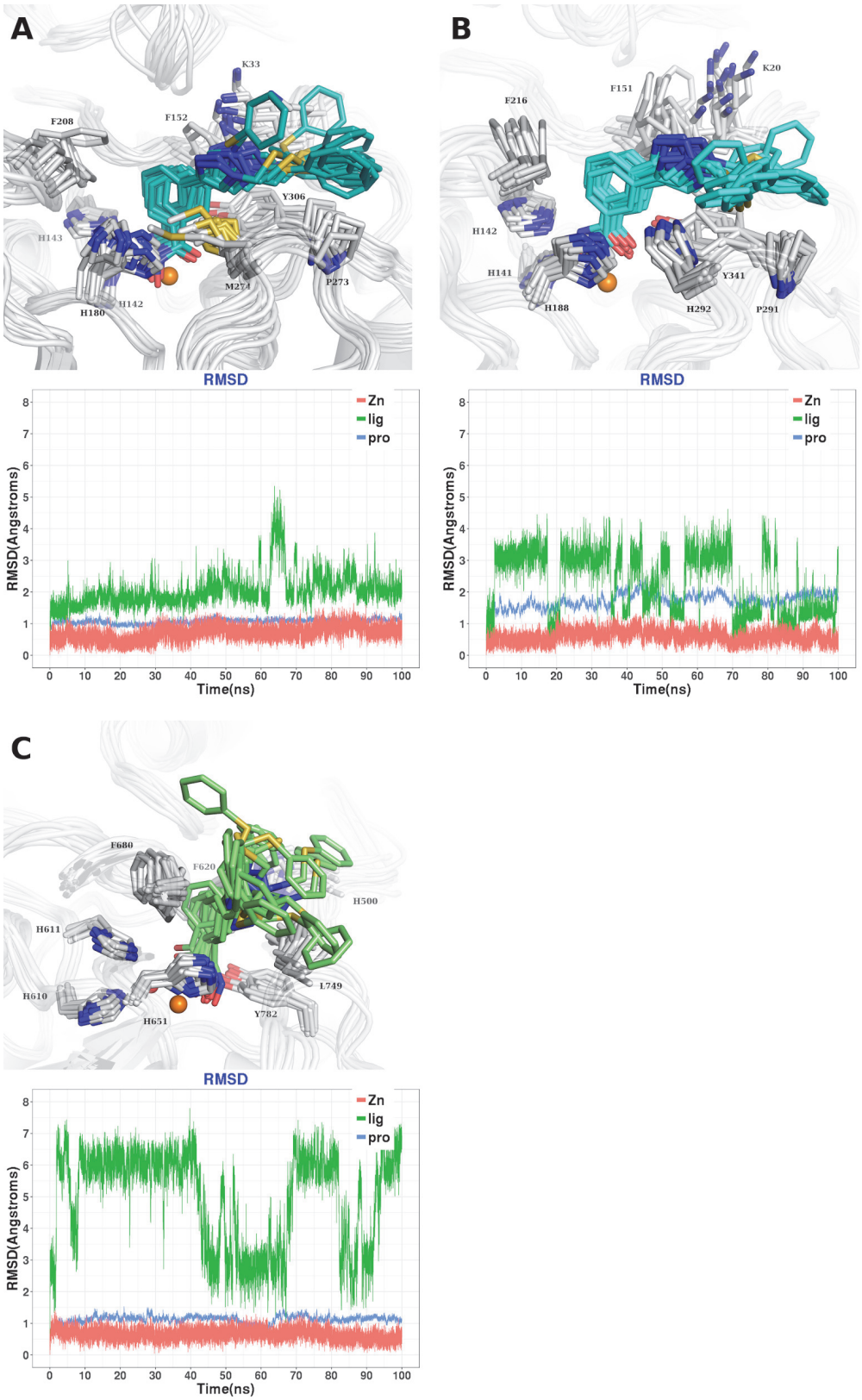

Figure S10. Snapshots and RMSD plots of 100 ns MD simulations of (**A**) docking pose of **NCC-149** in hHDAC8, (**B**) crystal structure of **NCC-149** in smHDAC8 (PDB ID 6HRQ), (**C**) docking pose of **NCC-149** in hHDAC6. Models of hHDAC8 and hHDAC6 established from PDB IDs 2V5X and 5EDU.

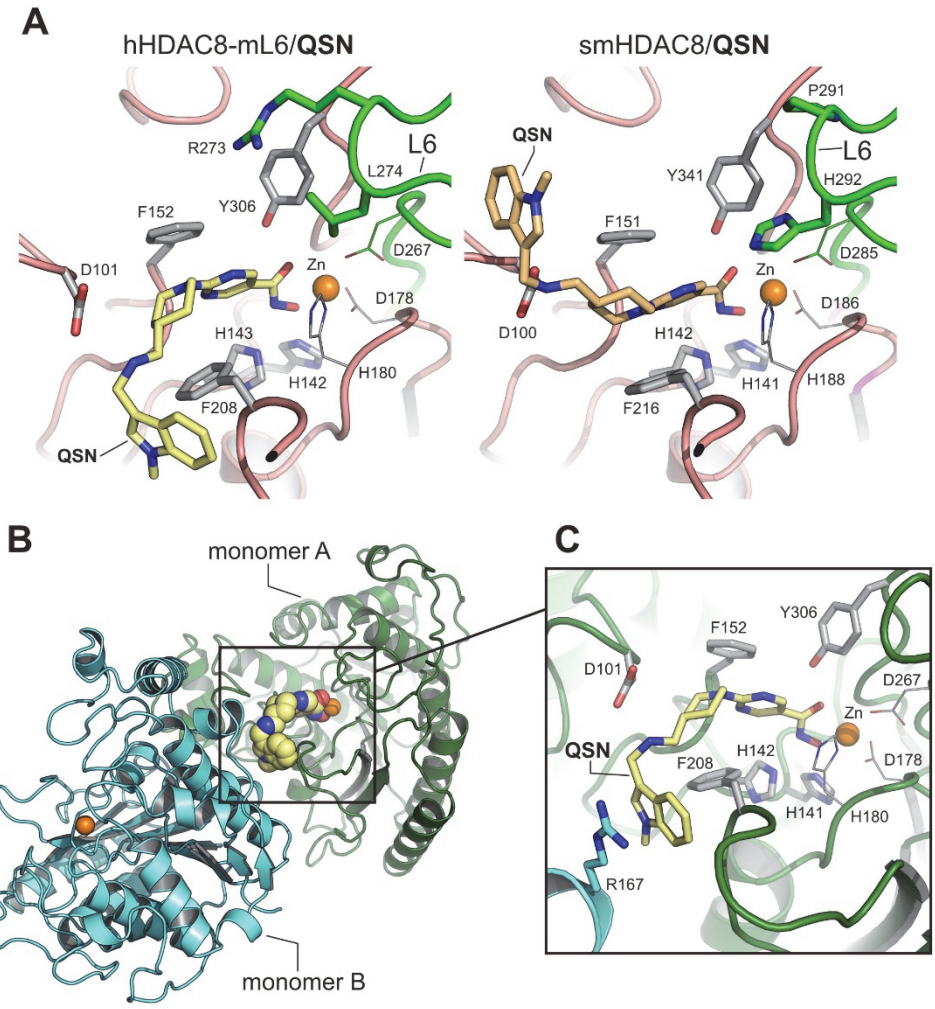

Figure S11. Binding mode of **Quisinostat** (**QSN**) in the structure of the human HDAC8 mL6/**QSN** complex. (**A**) Conformation of **QSN** bound to the human HDAC8 mL6 mutant (left panel) and to smHDAC8 (right panel) (PDB IDs 6HSH,6HSK). **QSN** does not interact with the L6 loop in either structure. The conformation difference observed most likely stems from the involvement of **QSN** in crystal packing in the hHDAC8 mL6/**QSN** complex. (**B**,**C**) Overall (**B**) and close-up (**C**) views of **QSN** involvement in crystal packing. **QSN** is absolutely required for crystallization.

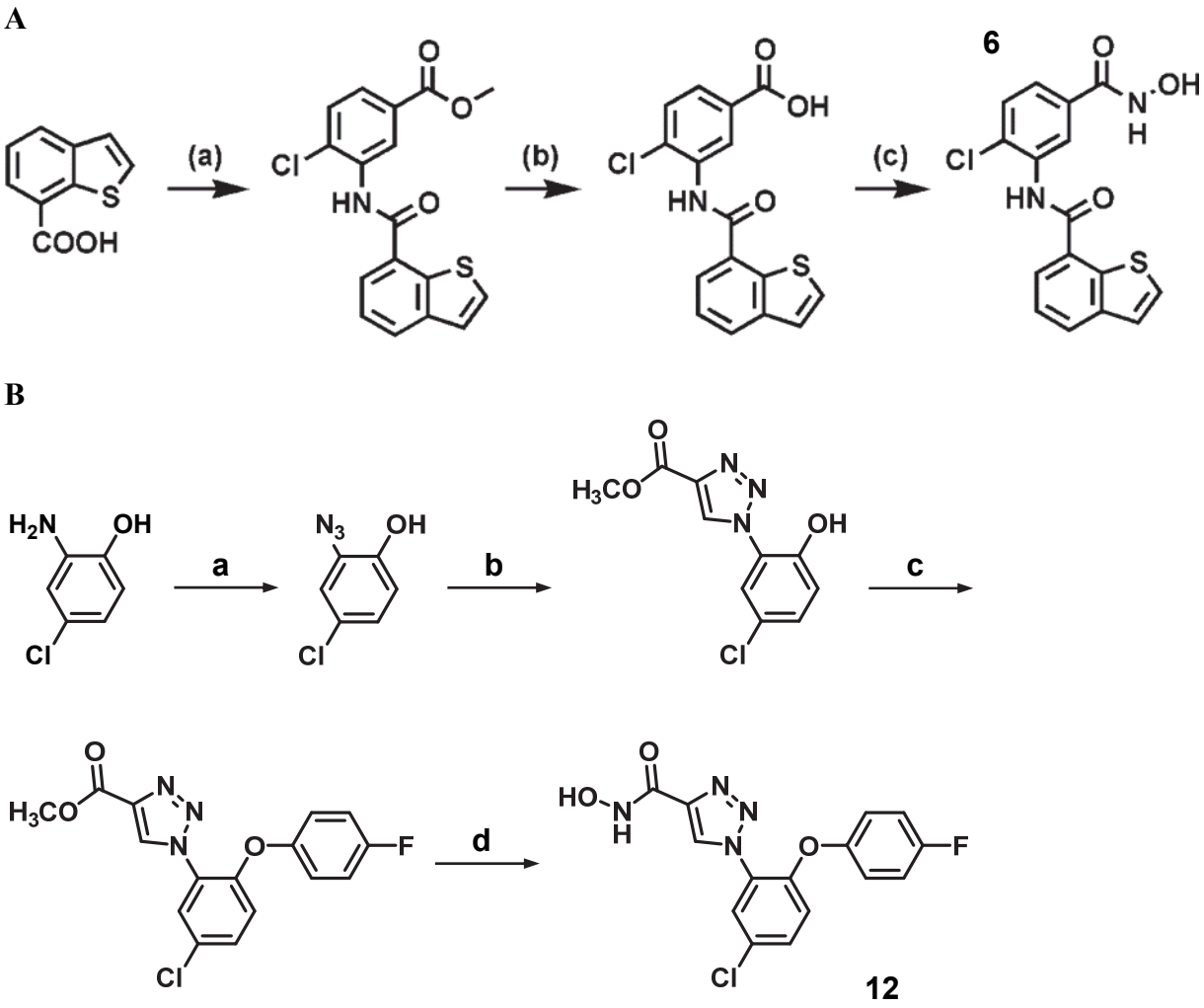

Figure S12. Synthesis pathways. Synthesis pathways for (**A**) the 3-(benzthiophene-7-carboxamido)-4-chlorobenzohydroxamate inhibitor (**6**) and (**B**) the 1-[5-chloro-2-(4-fluorophenoxy)phenyl]-N-hydroxy-1H-1,2,3-triazole-4-carboxamide inhibitor (**12**). The synthesis steps are described in detail in the experimental section of the manuscript.

Article 2

The atypical structure and active site modularity of the essential *Trypanosoma cruzi* histone deacetylase DAC2 as inhibition target (submitted)

Chagas disease is caused by an infection of the parasite *Trypanosome cruzi*. Around 7 million people are infected worldwide by this parasite that cause tens of thousands of deaths yearly. Treatment of the acute phase is efficient only in 70% of the case. In addition, the acute phase is not easily detected, leading to a chronic infection that cannot be treated by any drug so far. The chronic phase is characterized by complicated symptoms affecting the heart, brain and digestive system, no treatment is available at this stage and can cause a sudden death as well.

The histone deacetylase 2 of *Trypanosome cruzi* (tcDAC2) has been shown to be essential for the viability of *T. cruzi*. Therefore, tcDAC2 represents a target for drug development. The piggyback strategy, which combines high throughput screening and structure-based drug development, was already proved efficient to develop several inhibitors drug-leads to fight schistosomiasis. Therefore, to develop inhibitors targeting tcDAC2 the piggyback was also applied on this enzyme. I have joined this project as master student and continued it during my PhD. I have notably been involved in all the protein engineering and stabilization by inhibitor steps, prior to structure determination and further characterization of this enzyme. I have participated in the structure determination of the tcDAC2 in complex with the Quisinostat (QSN) inhibitor and have afterwards solved the structure of the tcDAC2 in complex with TB56 (inhibitor developed by our collaborators).

Specifically, I have rationalized inhibitor compounds to be used in complex with tcDAC2 for crystallization experiments, by performing thermal shift assays. These experiments showed that Quisinostat (QSN), TB56 and TB75 increased the thermal stability of tcDAC2. Therefore, these inhibitors were used for crystallization assays. I could crystallize and solve the structure of tcDAC2 in complex with two inhibitors, QSN and TB56 which revealed tcDAC2 specific features compared to human HDACs. Notably, most of the loops forming the catalytic site of tcDAC2 are like that of human HDAC8, but the loop 6 is like that of human HDAC1-3. These features cause a partial interaction between the L1 and L6 loops of tcDAC2, which is different from human HDACs.

Furthermore, tcDAC2 has a specific pocket next to its active site, this pocket, formed between the L5 and L6 loops is due to the replacement of bulkier residues Phe/Tyr and Lysine (in

human HDACs) by a smaller residues Ile266 and Ala261, respectively, in tcDAC2. Moreover, tcDAC2 presents a smaller foot pocket compared to human HDAC1-3 and the presence of the human HDAC8 foot pocket depends on the conformation of a W141. This latter residue is replaced by a Leu residue in HDAC1-3 and in tcDAC2 by R196, showing a different residue composition of the foot pockets. Therefore, many specific features of tcDAC2 can be exploited for the development of selective inhibitors targeting tcDAC2, combining a structure-based drug development and high-throughput strategies. This latter strategy has been applied by using the European Lead Factory (ELF) program that enabled us to have tcDAC2 tested with half a million compounds from 7 large pharmaceutical companies. The results of this screen are still further used for selective drug design against tcDAC2.

Species-selective epigenetic targeting of pathogens revealed by the atypical structure and active site of *Trypanosoma cruzi* histone deacetylase DAC2

Marek, M.[1,2,3,§], Ramos-Morales, E.[1,2,§], Picchi-Constante, G.F.A.[4,§], Bayer, T.[5], Norström, C.[6], Herp, D.[7], Sales-Junior, P.A.[8], Guerra-Slompo, E.P.[4], Hausmann, K.[5], Chakrabarti, A.[7], Shaik, T.B.[1,2], Merz, A.[7], Troesch, E.[1,2], Schmidtkunz, K.[7], Goldenberg, S.[4], Pierce, R.J.[9], Mourão, M.M.[8], Jung, M.[7], Schultz, J.[6], Sippl, W.[5], Zanchin, N.I.T.[4,*] and Romier, C.[1,2,*]

[1]Université de Strasbourg, CNRS, INSERM, Institut de Génétique et de Biologie Moléculaire et Cellulaire, UMR 7104, U 1258, 67400, Illkirch, France.

[2]IGBMC, Department of Integrated Structural Biology, 1 rue Laurent Fries, B.P. 10142, 67404 Illkirch Cedex, France.

[3]Current address: Loschmidt Laboratories, Department of Experimental Biology & RECETOX, Faculty of Science, Masaryk University, Kamenice 5/C13, 625 00 Brno, Czech Republic.

[4]Instituto Carlos Chagas, Fiocruz Paraná, Curitiba, Paraná 81350-010, Brazil.

[5]Institute of Pharmacy, Martin-Luther-Universität Halle-Wittenberg, Wolfgang-Langenbeck-Straße 4, 06120 Halle/Saale, Germany.

[6]Kancera AB, Nanna Svartz Väg 4, SE-17165 Solna, Sweden.

[7]Institute of Pharmaceutical Sciences, Albert-Ludwigs-Universität Freiburg, Albertstraße 25, 79104 Freiburg, Germany.

[8]Instituto René Rachou, Fundação Oswaldo Cruz, Avenida Augusto de Lima, 1715, 30190-002, Belo Horizonte, Brazil.

[9]Université de Lille, CNRS, Inserm, CHU Lille, Institut Pasteur de Lille, U1019 - UMR 9017 - CIIL -Centre d'Infection et d'Immunité de Lille, 59000 Lille, France.

[§]These authors have contributed equally to this work.

[*]Correspondence should be addressed to Nilson Zanchin (nilson.zanchin@fiocruz.br) and Christophe Romier (romier@igbmc.fr).

Keywords: Epigenetics, Histone deacetylases, Eukaryotic parasites, *Trypanosoma cruzi*, Functional essentiality, Atypical three-dimensional structure, Chemical inhibition.

Short title: Epigenetic targeting of essential *T. cruzi* histone deacetylase DAC2

Abstract

Epigenetics plays a prominent role in the phenotypic plasticity and antigenic variation of eukaryotic pathogens. Targeting pathogens epigenetic machineries thus represents a valid approach to fight parasitic diseases. Yet, identification of *bona fide* targets in parasites and the development of selective anti-parasitic drugs still represent major bottlenecks. Here, we show that the zinc-dependent histone deacetylases (HDACs) of the flagellate protozoan parasite *Trypanosoma cruzi* are key epigenetic regulators that have significantly diverged from their human counterparts. Depletion of the *T. cruzi* class I HDACs (tcDAC1 or tcDAC2) compromises cell cycle progression and division and leads to cell death. Notably, tcDAC2 displays an acetyl-lysine deacetylase activity essential to the parasite and shows major structural differences with human HDACs. Specifically, tcDAC2 harbours a modular active site that defines a unique subpocket that can be targeted by inhibitors that show substantial anti-parasitic effects *in cellulo* and *in vivo*. Our study reveals that the targeting of the many atypical histone deacetylases in pathogens pave the way to anti-parasitic selective epigenetic chemical impairment.

Introduction

High phenotypic plasticity and antigenic variation is the hallmark of eukaryotic parasites that enable them to adapt to their different hosts and escape their immune surveillance. Cumulative evidence shows that epigenetic processes play a prominent role in these transformations. Epigenetic effectors in pathogens thus represent important potential drug targets, and repurposing of epigenetic drugs has been identified as an effective strategy to reduce the time and financial costs associated with anti-parasitic drug development (Andrews et al., 2012b, Andrews et al., 2012a, Andrews et al., 2014, Wang et al., 2015, Hailu et al., 2017, Schiedel and Conway, 2018, Fioravanti et al., 2020). Combining repurposing with a piggyback strategy, where the chemical scaffolds of the repurposed drugs are modified, can further foster the design of parasite-selective compounds with little or no cross-reactivity with human enzymes.

Currently, most approved epigenetic drugs target zinc-dependent histone lysine deacetylases (HDACs) (Eckschlager et al., 2017, Falkenberg and Johnstone, 2014, Li and Seto, 2016). This explains why repurposing of HDAC inhibitors to fight neglected diseases is receiving considerable attention (Andrews et al., 2012b, Andrews et al., 2012a, Andrews et al., 2014, Wang et al., 2015, Hailu et al., 2017, Fioravanti et al., 2020). Acetylation of lysines in eukaryotes is a major reversible post-translational modification that links metabolism to cell signalling and plays a critical role in the regulation of key cellular processes (Choudhary et al., 2009, Choudhary et al., 2014, Drazic et al., 2016, Marmorstein and Zhou, 2014, Seto and Yoshida, 2014, Verdin and Ott, 2015, Narita et al., 2019). In humans, the dysregulation of acetylation mechanisms is implicated in the onset and progression of numerous diseases (Eckschlager et al., 2017, Falkenberg and Johnstone, 2014, Fujisawa and Filippakopoulos, 2017, Li and Seto, 2016). Nevertheless, the reversible nature of acetylation can be used to pharmacologically modulate eukaryotic acetylation pathways (Eckschlager et al., 2017, Falkenberg and Johnstone, 2014, Li and Seto, 2016, Schiedel and Conway, 2018).

HDACs are generally named according to their similarity with the 11 human HDAC isozymes which have been divided into four classes: class I (HDAC1, 2, 3, 8), class IIa (HDAC4, 5, 7, 9), class IIb (HDAC6, 10) and class IV (HDAC11) (Porter and Christianson, 2019, Seto and Yoshida, 2014). Specifically, class IIa HDACs have lost their essential catalytic tyrosine, replaced by a histidine, and are thought to play a scaffolding role in macromolecular complexes (Desravines et al., 2017, Hudson et al., 2015, Park et al., 2018). Not only histones but also other non-histone proteins are targeted by the various active HDAC isozymes which can even display specific or dual deacetylation and deacylation activities (Sabari et al., 2017, Narita et al., 2019).

We have previously used repurposing and piggyback strategies, combining structure-based and high-throughput screening approaches, on smHDAC8, the homolog of human class I HDAC8 from the parasitic flatworm *Schistosoma mansoni* that causes schistosomiasis. Our studies have led to the design of smHDAC8-selective inhibitors but have also enabled the characterization of the structure/function relationships of HDAC8 enzymes to help with the development of selective anti-cancer drugs (Bayer et al., 2018, Heimburg et al., 2016, Heimburg et al., 2017, Marek et al., 2013, Marek et al., 2015, Marek et al., 2018). This work has highlighted the challenge in developing selective anti-parasitic drugs targeting HDACs, notably due to the high structural similarity of the active sites of smHDAC8 and human HDACs. However, HDACs from other parasites show stronger phylogenetic differences with human HDAC enzymes, suggesting that the selectivity issue might be easier to overcome in these parasites (Scholte et al., 2017, Wang et al., 2015).

This is the case of the HDACs of *Trypanosoma brucei* and *Trypanosoma cruzi* that are responsible for African trypanosomiasis (Sleeping sickness (Büscher et al., 2017)) and American trypanosomiasis (Chagas disease (Perez-Molina and Molina, 2018)), respectively. While the fight against human African trypanosomiasis has made significant progress, with only a few tens of thousands of people infected and a continuous decrease of new cases each year, Chagas disease remains a major threat with millions of people infected and tens of thousands of yearly deaths (Büscher et al., 2017, Perez-Molina and Molina, 2018, Varikuti et al., 2018). Notably, the side effects and the acute phase-restricted efficacy of the drugs Benznidazole and Nifurtimox currently used to treat Chagas disease are major issues and call for the development of new drugs (Scarim et al., 2018, Varikuti et al., 2018).

Four HDACs are found in *T. cruzi* and *T. brucei* that show restricted phylogenetic resemblance to human HDACs and that have been attributed to HDAC class I (tcDAC1/tbDAC1 and tcDAC2/tbDAC2) and class IIb (tcDAC3/tbDAC3 and tcDAC4/tbDAC4) (Scholte et al., 2017). So far, functional characterization of these HDACs has predominantly been performed in *T. brucei*, showing that tbDAC1 and tbDAC3, but not tbDAC2 and tbDAC4, are essential and act in helping the parasite to evade the host immune response (Ingram and Horn, 2002, Wang et al., 2010). In contrast, little is known about *T. cruzi* HDACs. Importantly, protein acetylation patterns in both pathogenic species are different, even for histone proteins, suggesting substantial functional divergences in the acetylation pathways of these flagellate parasites (Mandava et al., 2007, Moretti et al., 2018, Picchi et al., 2017).

Treatments of both *T. brucei* and *T. cruzi* parasites with HDAC inhibitors have identified molecules that could potentially target these protozoans, but direct repurposing was impaired due to toxicity problems. However, these studies suggested the presence of unique features within the trypanosome HDACs that could be exploited to develop selective inhibitors targeting these enzymes (Andrews et al.,

2012a, Campo, 2017, Carrillo et al., 2015, Engel et al., 2015, Hailu et al., 2017, Kelly et al., 2012, Scarim et al., 2018, Varikuti et al., 2018, Zuma and de Souza, 2018, Fioravanti et al., 2020).

Here we show that trypanosome HDACs harbour very specific features compared to human HDACs. Surprisingly, *T. cruzi* class I HDACs tcDAC1 and tcDAC2 are both functionally essential to the parasite, in contrast to *T. brucei* where only tbDAC1 is essential. Specifically, tcDAC2 has retained canonical functional determinants and displays an acetyl-lysine deacetylase activity that can be inhibited. The crystal structure of tcDAC2 bound to different inhibitors reveals a zinc-dependent deacetylase fold but with major differences in its overall structure as well as in its active site compared to the various human HDACs. Notably, tcDAC2 displays an atypical fold and the loops forming its active site show structural similarities either with loops of the HDAC1/HDAC2/HDAC3 (hereafter termed HDAC1-3) isozymes family or with loops of the HDAC8 isozyme, revealing the combinatorial modularity of histone deacetylase active sites. Importantly, tcDAC2 harbours a unique pocket in its active site that is targeted by one of the inhibitors used in our structural study. *In cellulo* and *in vivo*, parasitic infection is affected by this inhibitor, which thus represents a starting scaffold for designing more potent and more selective inhibitors targeting tcDAC2. Collectively, our results reveal the atypical nature of the *Trypanosoma cruzi* DAC2 lysine deacetylase which extends to other parasitic HDACs and pave the way to the rational design of selective inhibitors to fight Chagas and potentially other parasitic diseases.

Results

Trypanosome HDACs are atypical

Phylogenetic analyses have suggested that DAC1 enzymes are more related to the HDAC1-3 isozymes family, but DAC2, DAC3 and DAC4 enzymes could not be specifically assigned to a precise isozyme family (Ingram and Horn, 2002, Scholte et al., 2017). We have extended sequence analyses to better understand the divergences observed. Specifically, two contiguous residues at the tip of HDAC active site L6 loop inform on HDAC isozyme family, partners and substrates (Millard et al., 2013, Watson et al., 2012, Watson et al., 2016, Hai and Christianson, 2016, Miyake et al., 2016, Hai et al., 2017, Porter and Christianson, 2019, Marek et al., 2018). In DAC1 enzymes, an arginine-leucine (RL) motif is found (Supplementary Figure 1A) which is typical of HDAC1-3 isozymes, where the arginine plays an essential role for recruiting partners and for activity (Millard et al., 2013, Watson et al., 2012, Watson et al., 2016).

In contrast, in DAC2, a proline-leucine (PL; tcDAC2) or proline-tyrosine (PY; tbDAC2) motif is found, reminiscent of both class I HDAC8 proline-methionine (PM) and class II PL motifs (Figure 1; Supplementary Figure 1B). Surprisingly, in DAC3 a leucine-leucine (LL) motif is found which is not observed in any other trypanosome or human HDACs (Supplementary Figure 1C), while DAC4 displays

a canonical class II PL motif (Supplementary Figure 1D). Additional sequence analyses (Supplementary Figure 1) further show that DAC3 and DAC4 have a single catalytic domain, in contrast to the tandem domains observed in human class IIb HDACs. Compared to human HDACs, DAC2, DAC3 and DAC4 also contain small-to-medium size insertions in their catalytic domains whose roles are unknown. In addition, the DAC3 enzymes catalytic domain is split in its middle by a ~170 residue long insertion that should protrude from the HDAC core without affecting its structural integrity (Supplementary Figure 1C).

Further analyses of sequence identities/similarities between the catalytic domains of trypanosome and human HDACs show that all trypanosome HDACs have low identities (< 40%) compared to human HDACs, DAC2 and DAC4 showing the strongest divergence (identities < 30%) (Supplementary Figure 2A-B). Surprisingly, the identities/similarities are even lower when comparing the four parasitic isozymes between themselves, suggesting a strong functional divergence for each parasitic isozyme (Supplementary Figure 2C). Moreover, comparisons of the same isozymes from *T. brucei* and *T. cruzi* also reveal considerable divergence (Supplementary Figure 2C). While the DAC1 enzymes are strongly conserved (85% identity), DAC3 and DAC4 show intermediate conservation (64%), and the DAC2 enzymes have the lowest sequence identity (51%). These differences possibly relate to the changes in acetylation patterns observed in these two parasites (Mandava et al., 2007, Moretti et al., 2018, Picchi et al., 2017).

Strikingly, careful comparison of tbDAC2 and tcDAC2 sequences reveals major differences in their respective active sites. *T. brucei* DAC2, which has been shown to be non-essential (Ingram and Horn, 2002), has many active site residues involved in zinc coordination, acetyl-lysine binding and catalysis replaced by non-canonical amino acids, including the replacement of its catalytic tyrosine by an asparagine, thus questioning its function as a *bona fide* deacetylase. In contrast, *T. cruzi* DAC2 has retained all canonical active site residues and could therefore have a fully functional deacetylase activity (Figure 1; Supplementary Figure 1B). Collectively, our sequence analyses confirmed the atypical character of trypanosome HDACs, suggesting that they could represent potential drug targets. These results also highlighted the unexpected difference between *T. brucei* and *T. cruzi* class I DAC2 enzymes, which prompted us to further characterize trypanosome class I HDACs, notably tcDAC2.

T. cruzi DAC1 and DAC2 are both essential to the parasite

We first investigated *in vivo* the essential character of *T. cruzi* class I HDACs. Gene targeted deletion experiments by homologous recombination showed that both tcDAC1 and tcDAC2 are essential to *T. cruzi* since null parasites did not grow in culture and ended up dying over time. In addition, single and double allele knocked-out cells presented a lower proliferative rate than wild type parasites (Figure

2A-B) and DNA content quantification by flow cytometry revealed aberrant cell cycle progression (Figure 2C-D) that could be explained by the presence of several abnormal cells containing multiple nuclei/kinetoplasts (Figure 2E).

To further investigate the unexpected essential character tcDAC2 compared to tbDAC2, we complemented these results by generating null mutants with the CRISPR/Cas9 technology for *tcDAC2* using three different sgRNAs to direct Cas9 to distinct positions in the *tcDAC2* gene sequence. This strategy resulted in aberrant cells that were not able to divide, consistent with the phenotype expected for an essential gene. DNA content quantification by flow cytometry revealed abnormal cell cycle progression (Figure 2F) with defects ranging from cells without DNA to cells with several nuclei/kinetoplasts (Figure 2G).

We then used the essential character of tcDAC2 to further characterize this enzyme by complementation assays with different constructions and by using a *T. cruzi* cell line stably expressing Cas9. An initial construction with the original *tcDAC2* DNA sequence in the sgRNA target region and encoding wild type (WT) tcDAC2 (tcDAC2_sens) was used as negative control. After sgRNA transfection, the cells transfected with the tcDAC2_sens construct showed abnormal cell cycle and cell morphology along with reduced cell proliferation (Figure 2H-I; Supplementary Figure 3). In contrast, cells transfected with a construction of WT tcDAC2 but containing an altered sequence not recognized by the sgRNA (tcDAC2_res) restored the wild type phenotype (Figure 2H-I; Supplementary Figure 3), confirming that the depletion of tcDAC2 causes lethality.

HDACs where the catalytic tyrosine is replaced by a phenylalanine are known to be mostly inactive. We used the same complementation strategy with a catalytic Y371F mutant of tcDAC2 whose DNA sequence was not recognized by the sgRNA (tcDAC2_Y371F). Our results showed that the cells containing the tcDAC2_Y371F construct presented a deleterious phenotype, similar to tcDAC2 knocked out cells, as observed by alteration in cell cycle progression, cell proliferation and cell morphology (Figure 2H-I; Supplementary Figure 3), showing the importance of tyrosine 371 for tcDAC2 function.

We then used the same strategy to investigate the long and highly acidic tcDAC2 C-terminal tail (Figure 1) whose functional role is unknown. The complementation strategy using a construction deleted for this C-terminal tail (tcDAC2_ΔC) showed that, in contrast to the tcDAC2_Y371F mutant, cells expressing the tcDAC2_ΔC mutant did not present any detectable phenotype, showing that this tail is functionally dispensable *in vivo* (Figure 2H-I; Supplementary Figure 3).

T. cruzi DAC2 possesses an acetyl-lysine deacetylase activity that can be inhibited

We next characterized tcDAC2 biochemically and biophysically. During purification, the shorter C-terminal construct of tcDAC2 (tcDAC2_ΔC), which is sufficient for parasitic survival, showed a strong

increase in solubility compared to the WT enzyme and was subsequently used in our studies. Size exclusion chromatography and dynamic light scattering analyses showed that tcDAC2_ΔC is mostly monomeric, suggesting tcDAC2 similarity with HDAC8. However, thermal shift assays revealed its lower thermal stability compared to human and *S. mansoni* HDAC8 enzymes (Figure 3A).

Deacetylation assays showed that tcDAC2_ΔC possesses an acetyl-lysine deacetylase activity, slightly lower than human HDAC8 on the substrates used (Figure 3B). In agreement with our in vivo experiments, the Y371F mutant was completely inactive (Figure 3B), suggesting that tcDAC2 has a *bona fide* deacetylase activity relying on its canonical catalytic residues. Inhibition assays were then performed using pan-HDAC (SAHA (Vorinostat), Quisinostat), HDAC1-3-selective (Entinostat, Mocetinostat), HDAC8-selective (PCI-34051, NCC-149) inhibitors as well as a set of in-house available HDAC inhibitors (TB51, TB56, TB72 and TB75; chemical structures and synthesis provided in Supplementary Methods) that we developed during the work on smHDAC8. We identified these latter compounds as putative tcDAC2 inhibitors by *in silico* docking experiments with a tcDAC2 model established using human and *S. mansoni* HDAC8 as templates. Quisinostat (hereafter termed QSN) and the TB compounds had IC_{50} values in the low nM and μM range, respectively, showing that tcDAC2 deacetylase activity can be inhibited potently (Figure 3C; Supplementary Table 1). However, neither SAHA nor any of the HDAC1-3-selective and HDAC8-selective inhibitors showed strong inhibitory effects in these assays.

T. cruzi DAC2 stabilization and structure determination

Attempts to crystallize the tcDAC2_ΔC protein to permit structure determination yielded only unreproducible, poorly diffracting crystals. Since tcDAC2 contains several medium-sized insertions compared to human HDAC8 that could hamper crystallization (Insertions 1, 2 and 3; Figure 1), we hypothesized that removing some specific regions in these insertions could stabilize the enzyme, facilitating its crystallization. Protein engineering experiments on tcDAC2_ΔC showed that only partial deletions in insertion 2 can be tolerated in terms of solubility. Specifically, only one precise deletion in this insertion could lead to a construct (tcDAC2_ΔIns2; Figure 1) showing a significant increase in thermal (~10°C) and proteolytic stability compared to tcDAC2_ΔC (Figure 3A; Supplementary Figure 4A), suggesting that the part removed is a solvent exposed, possibly unstructured loop region. This tcDAC2_ΔIns2 construct also showed a moderately increased deacetylase activity compared to tcDAC2_ΔC (Figure 3B).

Importantly, the tcDAC2_ΔIns2 mutant could rescue the death phenotype of the tcDAC2 knockout *in vivo*, indicating that the part removed is not functionally essential for parasite survival (Supplementary Figure 4B). The tcDAC2_ΔIns2 protein could be reproducibly crystallized but the small crystals obtained

did not diffract. We therefore looked at inhibitor-induced tcDAC2_ΔIns2 thermal stabilisation using notably the most potent inhibitors characterized in our *in vitro* inhibition study. All inhibitors tested increased the thermal stability of the enzyme (Supplementary Figure 4C). Specifically, the highest increase was observed with the pan-HDAC inhibitor Quisinostat (QSN) that increased the stability of the enzyme by ~18°C, followed by the novel inhibitors TB56 and TB75 with ~13°C increase. Co-crystallization experiments with all tested inhibitors yielded crystals only in presence of QSN and TB56.

The crystals of both complexes showed good diffraction and complete crystallographic data sets could be collected in cryogenic conditions at 1.75 (QSN) and 2.3 (TB56) Å resolution at the synchrotron. Structure determination was performed by molecular replacement using our initial homology-model of tcDAC2 and both tcDAC2/QSN and tcDAC2/TB56 structures were refined through manual building and automated refinement, the final models showing good data collection and refinement statistics (Supplementary Table 2).

T. cruzi DAC2 has an atypical class I HDAC structure

Our structures showed that tcDAC2_ΔIns2 (hereafter termed tcDAC2 for simplicity) possesses a classical arginase/HDAC fold composed of a central β-sheet sandwiched between several α-helices (Figure 4A). Search with DALI (Holm, 2020) showed unambiguous similarity of tcDAC2 with class I HDACs, notably HDAC8. Precise comparison revealed however that although a large N-terminal part of tcDAC2 superposes well with human class I HDACs, the majority of the C-terminal part of tcDAC2 turns out to be structurally divergent (Figure 4B). This was surprising since all human class I enzymes (HDAC1-3 and HDAC8) show a high similarity in their overall structures, differences being mostly observed at the amino acid level and for the conformation of some active site loops (Figure 4B).

The differences observed between tcDAC2 and class I human HDACs start from the end of tcDAC2 α8-helix, which is longer than its human counterparts. Following this helix, Insertion 3 is fully visible in our two tcDAC2 structures and packs tightly against the tcDAC2 core, forming specific interactions (Figure 4B). Interestingly, many of the aforementioned small sequence insertions found in tcDAC2 compared to human HDAC1-3 and HDAC8 (Figure 1; Supplementary Figure 1B) appear to form small extended loops in the vicinity of Insertion 3, defining a specific surface on tcDAC2. Similarly, Insertion 1, which is only partially seen in density in our structures, is also found in the close vicinity of Insertion 3, packing against tcDAC2 core, also participating in this tcDAC2-specific surface (Figure 4B).

Following Insertion 3, the only structurally similar part between tcDAC2 C-terminal region and the same region in human HDAC1-3 and HDAC8 concerns the region spanning the 3_{10}-helix η10 that adopts a common fold and is similarly positioned in all these enzymes (Figure 1 and 4B). However, tcDAC2 again diverges structurally from human class I HDACs immediately after this region. Specifically,

whereas human class I HDACs have a short straight stretch of residues (LC loop) that links the η10 region to their αC-helix, the tcDAC2 LC loop harbours additional residues that form a bulge extending toward the active site. This tcDAC2 extended LC loop lies over the active site L6 loop, with the side chain of arginine R439 forming a bidentate interaction with L6 loop main chain carbonyls (Figure 4C).

This longer LC loop of tcDAC2 ends up at the same position where human HDAC αC-helices start, these latter human helices packing tightly against their HDAC cores through multiple hydrophobic interactions. Surprisingly, an αC-helix in tcDAC2 is only observed for the tcDAC2/TB56 complex, but not for the tcDAC2/QSN complex, where no electron density is observed for this helix. In addition, the tcDAC2 αC-helix does not pack against the HDAC core but, instead, projects away from this core and is involved in crystal packing (Supplementary Figure 5A).

We have tentatively modelled the binding of the tcDAC2 αC-helix as observed in human HDAC1 and HDAC8. An interaction similar to the one observed in the human HDACs appears impossible in tcDAC2, several hydrophobic residues being replaced by charged residues at the end of its αC-helix and both surfaces displaying a positive charge (Supplementary Figure 5A). In fact, as seen in our two tcDAC2 structures, a few residues preceding and starting the tcDAC2 αC-helix form specific hydrophobic interactions with the tcDAC2 core and position the start of the tcDAC2 αC-helix differently, further explaining the difference observed with human class I HDACs (Supplementary Figure 5B). Therefore, the fact that this helix is not observed in the tcDAC2/QSN structure, although our two structures otherwise superpose very well, suggests that this region is disordered and could only fold and adopt its specific position upon interaction with a partner and/or a substrate.

Finally, we have shown that part of tcDAC2 Insertion 2 could be removed for crystallization. The remaining part of Insertion 2 mostly interacts with the tcDAC2 core, whereas our structures show that the part removed for crystallization would most likely bulge out of the structure without making strong contacts with the rest of the protein, in agreement with our deletion experiments (Figure 4A). Interestingly, superposition of tcDAC2 with the hsHDAC1/MTA1 (PDB code 4bkx) and hsHDAC3/NCOR (PDB code 4a69) complexes shows that Insertion 2, but also Insertion 1, would both clash with the binding of either MTA1 or NCOR homologs (Figure 4D). This latter feature, in addition to the absence of an arginine in the tcDAC2 L6 loop and the observed monomeric form of this enzyme, further supports the functional difference between tcDAC2 and the isozymes of the HDAC1-3 family.

T. cruzi DAC2 active site displays HDAC1-3 and HDAC8 features

As expected from our sequence analyses, tcDAC2 has a zinc ion at the bottom of its active site which is coordinated canonically by the two aspartates, D237 and D328, and one histidine, H239 (hsHDAC8 D178, D267 and H180). Similarly, the catalytic tyrosine Y371 (hsHDAC8 Y306) is perfectly positioned to

play a role in catalysis as well as the histidine dyad H197 and H198 (hsHDAC8 H142 and H143) (Figure 5A). In addition, phenylalanines F207 and F267 (hsHDAC8 F152 and F208) form the hydrophobic tunnel that normally accommodates the aliphatic part of the incoming acetylated lysine. Finally, glutamate E156 is present at the position where hsHDAC8 D101 is positioned to interact with the main chain of the incoming acetylated lysine substrate (Figure 5A). Mutation of this glutamate to alanine (E156A) causes the reduction by half of tcDAC2 deacetylase activity (Figure 3B). Thus, tcDAC2 has a *bona fide* deacetylase active site also observed in other human class I enzymes (Figure 5A).

We next looked at the conformations of the loops forming the tcDAC2 active site and compared them to those of active site loops from human class I HDACs. Similar to what is observed between the different human HDACs, the loops forming the bottom of the tcDAC2 active site (L3, L4 and L7 loops) show no strong conformational changes compared to their human counterparts. Looking at the loops forming the upper part of the tcDAC2 active site pocket, we observe that the tcDAC2 L1 loop is very similar to the hsHDAC8 L1 loop, this loop being much shorter than that of the hsHDAC1-3 isozymes family (Figure 5B). Likewise, a strong structural similarity is observed between tcDAC2 and hsHDAC8 L2 loops, while those of hsHDAC1-3 adopt a slightly different conformation. The same similarity applies for tcDAC2 and hsHDAC8 L5 loops when compared with those of hsHDAC1-3 (Figure 5B).

Surprisingly, however, this is not the case for the tcDAC2 L6 loop that adopts a *bona fide* hsHDAC1-3 L6 loop conformation, markedly different from that of the hsHDAC8 L6 loop (Figure 5B). A conformational change of this loop in tcDAC2 appears highly unlikely since it is covered and appears kept in position by the LC loop of tcDAC2, notably R439 (Figure 4C). This is in agreement with our previous observation of the high conformational stability of the hsHDAC8 L6 loop despite its full replacement by that of hsHDAC1 (Marek et al., 2018).

T. cruzi DAC2 contains a unique active site pocket that can be targeted by inhibitors

The presence of both HDAC1-3- and HDAC8-specific loops in the tcDAC2 active site clearly confers an atypical and specific character to the active site of this this parasite enzyme. We previously showed that HDAC8 enzymes have a unique pocket in their active site, which we termed the HDAC8-selective pocket, that can specifically accommodate HDAC8-selective inhibitors and could also be employed for specific substrate recognition (Marek et al., 2018). This pocket is composed of the catalytic tyrosine side chain at its bottom and its walls are made up of residues from HDAC8 L1 and L6 loops.

Notably, we showed that the HDAC8 active site L6 loop composition, specific conformation and rigidity are critical for the design of HDAC8-selective inhibitors but also for the activity of this enzyme, mirroring the functional importance of this loop in other HDACs (Millard et al., 2013, Porter and Christianson, 2019, Watson et al., 2012, Watson et al., 2016, Marek et al., 2018, Hai and Christianson,

2016, Miyake et al., 2016, Hai et al., 2017). The HDAC8-selective pocket only exists in HDAC8, being filled in by hydrophobic residues from the L1 and L6 loops (L1-L6 lock) in other human HDACs (Marek et al., 2018). Due to the HDAC8 character of the tcDAC2 L1 loop and the HDAC1-3 character of the tcDAC2 L6 loop, this pocket is also partially filled in tcDAC2, causing a partial L1-L6 lock (Figure 5C), thus explaining that HDAC8-selective inhibitors cannot strongly inhibit tcDAC2 (Figure 3D).

Careful analysis of the tcDAC2 active site reveals, however, the presence of a unique pocket in this enzyme, not observed in the structures of other human HDACs (Figure 5C). This pocket is located between tcDAC2 L5 and L6 loops. The unique character of this pocket is due to the replacement of a bulky phenylalanine/tyrosine residue, observed in all human HDAC structures solved so far, by a smaller isoleucine residue (I266) in the tcDAC2 L5 loop (Figures 1 and 5D; Supplementary Figure 1B). In addition, the back of the pocket is freed by a short alanine residue (A261) replacing longer arginine or lysine residues in human HDAC structures, and overlooked on the side opposite to the active site zinc by a long glutamate residue replacing generally shorter residues in human HDACs (Figure 1 and 5D; Supplementary Figure 1B).

Since our two tcDAC2 structures were solved in presence of the HDAC inhibitors QSN and TB56, we analysed the binding mode of these inhibitors to tcDAC2. We observe that both inhibitors bind in the tcDAC2 active site with their hydroxamate warhead coordinating the catalytic zinc, interacting with the hydroxyl group of Y371 catalytic tyrosine and both histidines H197 and H198 (Figure 6), as observed in many HDAC/hydroxamate inhibitor-containing structures. The rigid linker of QSN binds into the hydrophobic channel formed by F207, F267 and L6 loop L335, its capping group stacking on top of the L5 loop, notably F267 (Figure 6A). However, QSN does not interact with residues of the tcDAC2-unique pocket. This is different for TB56 whose dibenzofuran moiety also binds into the pocket formed by F207, F267 and L6 loop L335 but also occupies the entrance of the tcDAC2-unique pocket (Figure 6B). This demonstrates that the tcDAC2-unique pocket can be targeted to develop novel inhibitors that could be selective for this trypanosome enzyme.

Finally, not only the active site but also the foot pocket at the base of HDAC active sites can be targeted by inhibitors. In hsHDAC1-3, this pocket is reduced in size due to various hydrophobic residues that fill it in, while in hsHDAC8 its size can change according to the conformations adopted by tyrosine Y111 and tryptophan W141. Interestingly, in tcDAC2 an arginine (R196) is found in replacement of hydrophobic hsHDAC8 W141, and the equivalent leucine in hsHDAC1-3, thus increasing the charged character of this foot pocket that could also be used to selectively target tcDAC2. The unique character of the tcDAC2 foot pocket could also explain why the benzamide-based HDAC1-3-selective inhibitors (Mocetinostat, Entinostat), which bind selectively into the foot pocket, also perform poorly in our inhibition studies.

Anti-parasitic effects of inhibitors

We next investigated the effects of QSN and the tcDAC2 specific pocket-targeting compound TB56, together with the anti-trypanosome drug Benznidazole (hereafter termed BZN), in *in cellulo* infection models using two previously validated protocols using different cell lines and two different *T. cruzi* strains (Buckner et al., 1996, MacLean et al., 2018, Romanha et al., 2010). Specifically, these protocols made use (i) of the *T. cruzi* Tulahuen strain infecting L929 cells with an indirect readout determining the β-galactosidase activity and (ii) of the *T. cruzi* Dm28c strain infecting Vero cells using a direct high-content image-based readout. Cytotoxicity assays were performed at different time points for both protocols and revealed that BZN has no effect on L929 cells and only very little toxicity on Vero cells, as previously reported (Araujo-Lima et al., 2018, MacLean et al., 2018, Martin-Escolano et al., 2018) (Figure 7A-B). In contrast, QSN showed significant cytotoxicity (CC_{50} in the range 0.01-0.09 µM) for both cell lines, in agreement with recently reported cytotoxicity assays for different cell lines (Morales Torres et al., 2020). TB56 showed a lower cytotoxicity than QSN, with CC_{50} values ranging between 4.3 and 9.9 µM, depending on the cell line (Figure 7A-B).

We next tested the effect of the three compounds on the *T. cruzi* parasite in infected cells, using three readout time points (24, 48 and 72h) (Figure 7C-D; Supplementary Figure 6). Later time points were not used since the infected cells start to be lysed by the parasites after 72h. In these assays, BZN showed EC_{50} values between 2.1 and 15.2 µM for both *T. cruzi* strains. Similarly, TB56 showed EC_{50} values in the range 1.7-6.6 µM on both *T. cruzi* strains. Importantly, we observed in our high-content image-based experiments that TB56 is more toxic to the parasite than to the cells when kept at sufficiently low concentration (3.3 µM; Supplementary Figure 6D-E). These assays therefore indicated that TB56 represents a potentially promising anti-parasitic lead compound.

In contrast to BZN and TB56, the EC_{50} values measured for QSN were different depending on the protocol used, with values in the range 2.5-115.7 µM for the Tulahuen strain and 0.05-0.18 µM for the Dm28c strain (Figure 7C-D). Further contrasting with the two other compounds, even when the EC_{50} values of QSN were close to the CC_{50} for the infection of Vero cells by the Dm28c strain, our high-content image-based assays showed that QSN is more toxic to the cells than to the *T. cruzi* strain (Supplementary Figure 6C,E). Therefore, in contrast to its potential use for treating cancer cells reported recently (Morales Torres et al., 2020), QSN appears less well-suited as potential anti-Chagas disease agent.

The positive results obtained with TB56 prompted us to investigate further this compound in a mouse infection model in comparison with BZN. We first carried out a pharmacokinetic study to assess the TB56 dose to be used. 50 mg/kg TB56 was administered to two male mice intravenously (i.v.) and to two male mice orally by gavage (p.o.). The doses were well tolerated and we observed during the first hour a high TB56 plasma concentration with i.v. administration and a moderate TB56 plasma concentration with p.o. administration (Figure 7E). However, the plasma concentrations decreased

rapidly to below 1 µM at 3 hours post-administration. A TB56 dose of 50 mg/kg/day was chosen for the mouse infection model.

While the mice treated with Benznidazole recovered fully at 9 days post infection (dpi), the mice treated with TB56 showed a significant reduction in parasite load at 7 dpi compared to the control group, but much less at 9 dpi, showing that TB56 had an effect but could not fully stop the infection (Figure 7F-G). The TB56 plasma concentration decrease observed during the pharmacokinetic study could explain the milder effect of TB56 in these *in vivo* assays. Nevertheless, although TB56 does not reach the same level of *in vivo* efficacy as observed with the drug Benznidazole, it shows a potential as a starting lead compound for the development of new drugs against *T. cruzi* and paves the way for the design of inhibitors binding into the tcDAC2-unique pocket.

Discussion

The fight against eukaryotic parasites remains a major health issue when no vaccine and only a few drugs are available to treat them. We have previously shown that targeting the epigenetic machinery of eukaryotic pathogens through repurposing and piggyback strategies represent a valid strategy to tackle this issue, although selectivity has to be addressed (Bayer et al., 2018, Heimburg et al., 2016, Heimburg et al., 2017, Marek et al., 2013, Marek et al., 2015, Marek et al., 2018, Schiedel et al., 2015, Monaldi et al., 2019). Here we have used a similar approach to target histone deacetylases (HDACs) from the eukaryotic flagellate *Trypanosoma cruzi* that causes tens of thousands of deaths yearly. Our study shows that trypanosome HDACs could be bona fide anti-parasitic drug targets as they have evolved specific features that should facilitate addressing the selectivity issue.

Specifically, our structure of tcDAC2 shows major changes in its C-terminal part that distinguish this enzyme from human HDACs and define specific structural elements at its surface that could be used by tcDAC2 to interact with specific partners and targets. This specificity is reinforced by tcDAC2 insertions 1 and 2, and the absence of an arginine in its L6 loop, which prevent interactions to be made with partners as observed for the human HDAC1/MTA1 and HDAC3/NCoR complexes (Millard et al., 2013, Watson et al., 2012, Watson et al., 2016), or the unique positioning of the tcDAC2 αC-helix. Thus, the atypical character of tcDAC2 suggested by the initial phylogenetic analyses is confirmed at the structural level.

The specific character of tcDAC2 is also found in the organization of its active site. While most of the loops that form the tcDAC2 active site adopt a conformation close to that of HDAC8 loops, the L6 loop conformation is highly similar to that observed for the HDAC1-3 isozyme family. However, in contrast to the tcDAC2 C-terminal half whose structure has evolved novel features, tcDAC2 active site loops still retain canonical structural features as observed in human HDACs, only the combination of the loops being different and creating specificity. This modularity of the tcDAC2 active site raises the question of

target recognition by tcDAC2, one possibility being that tcDAC2 deacetylates targets that are normally processed by different HDACs in humans.

Another non-mutually exclusive possibility would be that the combination of these different loops creates a surface that recognizes a completely different sequence motif specific to *T. cruzi* proteins. Accordingly, we observe the presence in the tcDAC2 active site of a unique pocket that potentially does not exist in human HDACs. This pocket recalls the unique pocket found in HDAC8 that appears important for HDAC8 activity (Marek et al., 2018). Importantly, reminiscent of the HDAC8-selective pocket, the tcDAC2-unique pocket could be used to develop selective inhibitors to fight Chagas disease.

Specifically, we show that one inhibitor used in our study can partially occupy this pocket and shows anti-parasitic effects in *in cellulo* and *in vivo* models of infection. Although the *in vivo* effects are surpassed by the Chagas disease-approved drug Benznidazole, the fact that our compound has potency in the low micromolar range and is rapidly degraded *in vivo* leaves room for the development of novel stable drug candidates. The fact that it does not make use of the full interaction potential of the tcDAC2-unique pocket potentially explains its reduced selectivity and provides a clear path for structure-guided improvement. Other hydroxamic acid-based HDAC inhibitors are approved for therapy of human diseases, which shows that the pharmacokinetic weakness can be overcome in this class of inhibitors.

Thus, tcDAC2 represents a novel target to develop new drugs against *T. cruzi* since this enzyme is functionally essential to the parasite in contrast to the *T. brucei* tbDAC2 homolog. Importantly, analysis of the conservation of active site residues in different trypanosome species shows that most of them have a DAC2 enzyme which resembles tcDAC2 and not tbDAC2 (Supplementary Table 3). DAC2 therefore also represent a potential therapeutic target in these other trypanosome species. More generally, our results show that the different trypanosome HDACs, due to their atypical character, could also be used as drug targets. Most importantly, this also applies to the other major pathogens causing leishmaniosis and malaria that also harbour evolutionarily distinct zinc-dependent histone deacetylases (Scholte et al., 2017) but whose structures still remain unknown. Therefore, our work opens new avenues toward the species-specific epigenetic targeting of eukaryotic pathogens.

STAR Material and Methods

Sequence comparisons

For sequence comparisons, only the deacetylase domains were considered. Those of human HDACs were chosen based on available structural data. For those of trypanosome HDACs, the boundaries of these domains were defined based on inter-parasitic sequence conservation, sequence conservation between the parasitic and human HDACs, secondary structure predictions and disorder predictions.

These analyses revealed the existence of a large, almost 200 residues long and potentially disordered region in the centre of the trypanosome DAC3 enzymes. Sequence similarities and identities were calculated on the identified deacetylase domains (excluding the DAC3 insertion) using the global EMBOSS-Needle alignment program (Madeira et al., 2019). Multiple sequence alignments were done with MAFFT (Katoh et al., 2019).

Parasite culture

Infective trypomastigote forms from *T. Cruzi* Tulahuen strain were obtained through culture in monolayers of mouse L929 fibroblasts (NTCT clone 929 (ATCC CCL 1)) in RPMI-1640 medium (Gibco BRL), containing 10% FBS (Gibco) and 2 mM glutamine (Gibco) at 37 °C in a humid 5% CO2 environment (Romanha et al., 2010). *T. cruzi* Dm28c (Contreras et al., 1988) epimastigotes were cultured in liver infusion tryptose (LIT) medium (Camargo, 1964) supplemented with 10% fetal bovine serum (FBS) without agitation at 28 °C.

Gene targeted deletion by homologous recombination

Gene targeted deletion was achieved by homologous recombination. The flanking sequences of the tcDAC1 and tcDAC2 genes were initially amplified by PCR from *T. cruzi* Dm28c genomic DNA, using specific primers. Neomycin phosphotransferase or hygromycin phosphotransferase B containing cassettes were amplified from pTc2KO-neo and pTc2KO-hyg (Pavani et al., 2016), respectively. Complete knockout cassettes were obtained by fusion PCR using the individual fragments and external primers.

Single and double knock out strains for both tcDAC1 and tcDAC2 were obtained as previously described (de Souza et al., 2010). Briefly, epimastigote forms of *T. cruzi* Dm28c were transfected with 20 μg of 5'flank-hyg-3'flank cassette DNA and selected in LIT medium supplemented with hygromycin B (500 μg/ml). The hygromycin resistant population was subsequently transfected with 20 μg of 5'flank-neo-3'flank cassette DNA and selected in LIT medium supplemented with hygromycin B (500 μg/ml) and G418 (500 μg/ml). The selected population was used for further analyses.

Gene targeted deletion mediated by CRISPR-Cas9

Null mutants were also obtained by the CRISPR/Cas9 methodology using a *T. cruzi* Cas9-GFP expressing strain (Romagnoli et al., 2018). For this purpose, sgRNA sequences were designed using the Eukaryotic Pathogen CRISPR guide RNA/DNA Design Tool (Peng and Tarleton, 2015). DNA templates were generated by using PCR to amplify the sgRNA scaffold sequence from plasmid pX330 (Peng and Tarleton, 2015) with specific forward primers that contain the T7 promoter and a 20-bp target-specific sequence (Supplementary Figure 7). The sgRNA was obtained by in vitro transcription using the MEGAshortscript T7 kit (Ambion) according to the manufacturer's instructions.

CRISPR-Cas9 mediated knock out was obtained by transfection of 5 x 10^6 Cas9-GFP expressing cells with 20 μg of specific sgRNA using the U-033 program in an Amaxa Nucleofector device as previously

described (Romagnoli et al., 2018). All the analyses were carried out between 1- and 3-days post-transfection.

tcDAC2 complementation assays

Next, we designed a genetic complementation strategy to investigate specific mutations on tcDAC2 which are relevant for its functional characterization. The experimental strategy is based on the CRISPR-Cas9 technology combined with two variants of the tcDAC2 gene sequences, one sensitive and another resistant to a specific sgRNA. The sensitive variant (tcDAC2_sens) serves as a negative control (knock out phenotype) since it has no alteration in the original tcDAC2 sequence (Supplementary Figure 7A) being cleaved by Cas9 at the same time as the genomic tcDAC2 copy, while the resistant versions contain silent mutations at the sgRNA recognition site, so that the sequence is not cleaved by Cas9 as it is not recognized by the sgRNA (Supplementary Figure 7B).

Thus, DNA templates designed to be resistant to Cas9 cleavage allow gene replacement by specific mutants of the tcDAC2 gene to test for complementation of genomic knockout (tcDAC2_res, tcDAC2_Y371F and tcDAC2_ΔC). Briefly, tcDAC2_res corresponds to the positive control of the complementation assay, since it contains no change outside the sgRNA recognition site, and tcDAC2_Y371F and tcDAC2_ΔC are the test molecules, since they contain, respectively, a substitution of the catalytic residue and a deletion of a C-terminal domain.

All four different DNA templates were obtained by site-directed mutagenesis from previously obtained plasmids followed by fusion PCR and cloning of the resulting PCR products into pGEM-T-Easy (Promega). In addition, a blasticidin S resistance cassette digested from pTc2KO-bsd (derived from pTc2KO-hyg (Pavani et al., 2016)) was cloned into all plasmids and the complete constructs were confirmed by DNA sequencing.

Cas9-expressing *T. cruzi* cells were independently transfected with 30 μg of each construct (ptcDAC2_res, ptcDAC2_Y371F, ptcDAC2_ΔC and ptcDAC2_sens; Supplementary Figure 7C) and the four resulting populations were stably maintained under selection marker pressure (12.5 μg/ml blasticidin) (Supplementary Figure 7C). For the complementation assays, the blasticidin-selected populations were transfected with a tcDAC2 specific sgRNA to knockout the endogenous tcDAC2 gene (Supplementary Figure 7C). All the analyses were performed between 1- and 10-days post-transfection.

Cell cycle analysis

Cell cycle analyses were performed in a FACSAria II (Becton-Dickinson) cytometer. A total of 1 x 106 cells were harvested (3000 x g, 5 minutes), suspended in 100 μl of PBS and mixed with 100 μl of propidium iodide staining solution (3.4 mM Tris-HCl pH 7.4, 0.1% NP40, 10 μg/ml RNAse A, 10 mM NaCl, 30 μg/ml propidium iodide). Propidium iodide was excited by a 488 nm laser and emitted light

was collected using a 616/23 bandpass filter (PE-Texas Red channel). Single cells were gated based on pulse area versus pulse width of the PE-Texas Red channel, excluding cell aggregates and debris. DNA content of gated cell population was analysed (Nunez, 2001) using FlowJo V10.1r7.

Morphological characterization

Morphological characterization was obtained as previous described (Romagnoli et al., 2018). Briefly, a total of 1-10 x 10^5 cells were deposited on a glass slide, allowed to dry and fixed in methanol. After drying, samples were clarified for 4 min with 5 M HCl and washed 5 times with water. After a second drying step, the samples were stained with Panotico (Laborclin). Parasites were observed by light microscopy using a Nikon Eclipse E600 or a Leica DMi8 microscope.

Cell proliferation analysis

For cell proliferation analysis, epimastigote cultures were established at a density of 0.5 - 1 × 10^6 cells/ml and population growth was monitored during four days, by cell counting in a Z series Coulter counter (Beckman Coulter).

Molecular cloning and mutagenesis

The *tcDAC2* wild-type gene and its mutants were PCR-amplified and cloned between the *NdeI* and *BamHI* restriction sites of the pnEA/3CH vector that encodes a C-terminal His-tag preceded by a protease 3C site (Diebold et al., 2011, Vincentelli and Romier, 2016). *E. coli* DH5α cells were used for cloning and re-amplification of plasmid vectors, whereas *E. coli* BL21 (DE3) cells were used for recombinant production of tcDAC2. The *tcDAC2* gene mutants were generated by fusion PCR or rolling circle strategies, gel-purified and ligated into the plasmid pnEA/3CH. All clones were verified by DNA sequencing.

Large-scale overproduction and purification of tcDAC2

E. coli BL21 (DE3) cells were transformed with the plasmid coding for the various tcDAC2 constructs of interest using 100 µg/ml ampicillin for plasmid selection. Ampicillin-resistant colonies were inoculated in large agar plates (15 cm) which were then incubated overnight at 37°C. Film-forming *E. coli* cells were suspended in 10 ml 2xLB medium per large agar plate (15 cm). The bacterial suspension was used to inoculate 5-L Erlenmeyer flasks (1 L 2xLB medium, ampicillin 100 µg/ml) where cells grew (200 rpm, 37°C, and 6 h) until reaching OD_{600} of 0.8. Induction was done at 22°C by adding 0.7 mM isopropyl-1-thio-β-D-galactopyranoside (IPTG) (Euromedex). Harvested bacteria were suspended in lysis buffer (50 mM KCl, 10 mM Tris-HCl pH 8.0) and lysed by sonication. The lysate was clarified by centrifugation (17,000 rpm, 55 min, 4°C, Sorvall Lynx 6000 Thermo Scientific). The supernatant was loaded onto Talon Superflow Metal Affinity Resin (Clontech) pre-equilibrated with the lysis buffer. The His-tagged proteins were released from the Talon resin by protease 3C (home-made) treatment and subsequently loaded onto 16/60 Superdex 200 gel filtration column (GE Healthcare) pre-equilibrated with the lysis buffer supplemented with 0.5 mM TCEP (pH 7.0).

TB compounds synthesis

Synthesis of the TB compounds as well as analytical characterization are described in Supplementary methods, including the synthesis schemes.

tcDAC2 activity and inhibition assays

Upon initial purification of the tcDAC2 enzyme, several assays were investigated to measure tcDAC2 activity. Two assays have been shown to measure reproducibly tcDAC2 deacetylase activity and have been used subsequently for our mutational and inhibition studies. First, tcDAC2 activity tests were carried out with the Ac-Leu-Gly-(TFA)Lys-AMC substrate (Sigma), according to the manufacturer's instructions with a substrate concentration of 50 μM. Fluorescence was measured in a plate reader (BMG Polarstar) with excitation at λ =390 nm and emission at λ = 460 nm. IC_{50} values were determined with OriginPro (version 9.0.0, Northampton, Massachusetts). Second, tcDAC2 activity tests were carried out with the fluorogenic substrate ZMTFAL (Z-(F3Ac)Lys-AMC) (Heltweg et al., 2004) in 1/2 AreaPlate-96 F microplates (PerkinElmer). The total assay volume of 30 μL contains 12.5 μL assay buffer (15 mM Tris, pH 7.5, 50 mM KH_2PO_4, 3 mM $MgSO_4 \cdot 7\ H_2O$ and 10 mM KCl), 10 μL of enzyme solution in assay buffer, 2.5 μL of increasing concentrations of inhibitors in DMSO and 5 μL of the fluorogenic substrate ZMTFAL (Z-(F3Ac)Lys-AMC) in assay buffer (25 μM). After incubation (90 min, 37 °C) 30 μL of stop solution, containing 2.5 μL Trichostatin A (TSA) (33 μM) and 5 μL trypsin (6 mg/mL) in trypsin buffer (50 mM Tris-HCl, pH 8.0, 100 mM NaCl), were added. After incubation (30 min, 37 °C), the fluorescence signal (λ_{ex} = 390 nm, λ_{em} = 460 nm) was measured on a BMG LABTECH POLARstar OPTIMA plate reader (BMG Labtechnologies, Germany).

hHDAC1/6 activity and inhibition assays

Commercially available human recombinant HDAC1 (BPS Bioscience, catalog no. 50051) and human recombinant HDAC6 (BPS Bioscience, catalog no. 50006) were used. Activity assays were performed as described before (Heltweg et al., 2005). Total amount of assay volume (60 μL), containing 52 μL of enzyme solution in incubation buffer (50 mM Tris-HCl, pH 8.0, 137 mM NaCl, 2.7 mM KCl, 1 mM $MgCl_2$, and 1 mg/mL bovine serum albumin), 3 μL of increasing concentrations of inhibitors in DMSO and 5 μL of the fluorogenic substrate ZMAL (Z-(Ac)Lys-AMC, 126 μM), were pipetted into OptiPlateTM-96 F black microplates (PerkinElmer). Followed by an incubation step (90 min, 37 °C). Stop solution (60 μL), containing 5 μL Trichostatin A (TSA, 33 μM) and 10 μL trypsin (6 mg/mL) in trypsin buffer (Tris-HCl 50 mM, pH 8.0, NaCl 100 mM), were added. After incubation (30 min, 37 °C) the fluorescence signal signal (λ_{ex} = 390 nm, λ_{em} = 460 nm) was measured on a BMG LABTECH POLARstar OPTIMA plate reader (BMG Labtechnologies, Germany).

hsHDAC8 activity and inhibition assays

For HDAC8 activity testing the commercially available Fluor-de-Lys (FDL) drug discovery kit (Enzo Life Sciences, BML-KI178) was used. The assay was performed according to the manufacturer's instructions. Enzyme solution (15 μL), inhibitor in increasing concentrations (10 μL) and FDL substrate solution (25 μL) were pipetted into 1/2 AreaPlate-96 F microplates (PerkinElmer) and the assay was incubated for 90 min at 37 °C. Developer solution (50 μL) was added. After incubation (45 min, 30 °C) the fluorescence signal signal (λ_{ex} = 390 nm, λ_{em} = 460 nm) was measured on a BMG LABTECH POLARstar OPTIMA plate reader (BMG Labtechnologies, Germany).

Dynamic light scattering

The dynamic light scattering (DLS) experiments were conducted with tcDAC2 protein solutions (2mg/ml) in a buffer containing 50 mM KCl, 10 mM Tris-HCl (pH=8.0) and 0.5 mM TCEP using a DynaPro NanoStar instrument (Wyatt). Protein solutions were centrifuged at 13,000 rpm for 10 min prior to DLS measurement in order to remove impurities. Before measurement the temperature was equilibrated to 20°C.

Differential scanning fluorimetry measurements

Thermal stability of tcDAC2 was measured by a label-free differential scanning fluorimetry (DSF) approach using a Prometheus NT.48 instrument (NanoTemper Technologies). Briefly, the shift of intrinsic tryptophan fluorescence of tcDAC2 proteins upon gradual temperature-triggered unfolding (temperature gradient 20°C to 95°C) was monitored by detecting the emission fluorescence at 330 and 350 nm. The measurements were carried out in nanoDSF-grade high sensitivity glass capillaries (NanoTemper Technologies) at a heating rate of 1°C/min. Protein melting points (Tm) were inferred from the first derivative of the ratio of tryptophan emission intensities at 330 and 350 nm. All the assays were done in triplicate.

Limited proteolysis assay

Limited proteolysis reactions contained 20 μl reaction buffer (50 mM KCl, 10 mM Tris-HCl pH 8.0), 7 μl protein (6.5 mg/ml) and 3 μl serially diluted trypsin protease (0.1 to 0.000001 mg/ml). The reactions were incubated at 4°C for 1h, and then stopped by addition of 15 μl Laemmli buffer. Limited proteolysis products were analysed by SDS-PAGE and visualised by Coomassie Brilliant Blue staining.

Protein crystallization experiments and data collection

The tcDAC2 enzyme in complex with Quisinostat (QSN) or TB56 inhibitors was prepared for crystallization by mixing the purified protein (concentration of 0.12 mM to 0.3 mM) with a three or five-fold molar excess of the inhibitors and incubated for 1 h at 4°C. Crystallizations were performed in 96-, 48- or 24-well plates (MRC). Crystals of the tcDAC2/QSN complex were obtained in 5% PEG 6000 and 0.1 M Hepes pH 7.0 or pH 7.5. Crystals of the tcDAC2/TB56 complex were obtained in 8% PEG8000, 0.2 M $MgCl_2$, and 0.1 M Bis-tris or Bis-tris propane pH 6.5. Crystals used for X-ray data collection were

briefly transferred into reservoir solution supplemented with 22% glycerol or PEG200 and flash-frozen in liquid nitrogen. Crystallographic data were collected at 100 K on Swiss Light Source (SLS) beamline PX-III equipped with PILATUS 2M-F detector.

Structure determination, model building and refinement

Crystallographic data were processed and scaled using XDS (Kabsch, 2010). The structure of tcDAC2/QSN complex at 1.7 Å resolution was solved by molecular replacement with Phaser (McCoy et al., 2007) implemented in Phenix (Liebschner et al., 2019) using our tcDAC2 homology-derived model as a search model. The structure of the tcDAC2/TB56 complex at 2.3 Å resolution was solved by molecular replacement with Phaser (McCoy et al., 2007) implemented in Phenix (Liebschner et al., 2019) using the tcDAC2/QSN structure. The initial models were refined through several cycles of manual building using Coot (Emsley et al., 2010) and automated refinement with Phenix (Liebschner et al., 2019). The final models were validated using tools provided in Coot (Emsley et al., 2010) and Molprobity (Williams et al., 2018).

Determination of cytotoxicity on L929 cells

To assess the cytotoxicity over L929 cells, 4,000 L929 cells (NTCT clone 929 (ATCC CCL 1)) suspended in 200 µL of RPMI-1640 medium (Gibco BRL) plus 10% FBS (Gibco) and 2 mM glutamine (Gibco) were added to each well of a 96-well microtiter plate and was incubated for three days at 37 °C in a humid 5% CO_2 environment. The medium was then replaced, and the cells were exposed to compounds at eight different concentrations. After up to 72 h of incubation with the compounds, alamarBlue™ (Invitrogen) was added, incubated for 4-6 h, and the absorbance at 570 and 600 nm was assessed. Controls including untreated and 1% DMSO -treated cells were run in parallel. Four technical replicates were run in the same plate and the experiments were repeated at least in two biological replicates. The results were expressed as the percent difference in the reduction between treated (TC) and untreated cells (UT), using the equation: $\underline{((117{,}216)\ (Abs_{570}\ TC) - (80{,}586)\ (Abs_{600}\ TC))/(}\ (117{,}216)\ (Abs_{570}\ UT) - (80{,}586)\ (Abs_{600}\ UT)\underline{)} \times 100$. Dose-response curves were plotted using GraphPad Prism version 7.05. Non-linear regression was used to determine CC_{50} values.

L929 cell infection assays

The *in vitro* test of trypanocidal activity was performed as previously described (Romanha et al., 2010, Buckner et al., 1996), using the *T. cruzi* Tulahuen strain expressing the *Escherichia coli* β-galactosidase gene. Briefly, 4,000 L929 cells were added in 80 µL of supplemented medium, without phenol red, to each well of a 96-well microtiter plate. After an overnight incubation, 40,000 trypomastigotes suspended in 20 µL volume were added to the cells and incubated for 2h. Medium containing parasites that did not penetrate the cells was replaced with 200 µL of fresh medium and incubated for an additional 48h, allowing the establishment of infection. The medium was then replaced by compounds diluted at different concentrations in fresh medium (200 µL) and the plate was incubated for 96h at

37°C. After this period, 50 μL of 500 μM chlorophenol red β-D-galactopyranoside (Roche) in 0.5% Nonidet P40 (Sigma) was added to each well, followed by an incubation of 18 h at 37°C, after which the absorbance at 570 nm was measured. Controls included: uninfected cells, untreated infected cells, infected cells treated with 3.8 μM benznidazole (positive control) or cells exposed to 1% DMSO (Sigma). The results were expressed as the percentage of *T. cruzi* growth inhibition in compound-tested cells as compared to the infected cells and untreated cells. Quadruplicates were run in the same plate and the experiments were repeated at least in two biological replicates. Compounds and the reference drug benznidazole were serially diluted (1:4 ratio) in RPMI medium, to obtain eight-points (from 80 μM to 0.0025 μM). Dose-response curves were plotted using GraphPad Prism version 7.05 (GraphPad Software, San Diego CA, USA). Non-linear regression was used to determine the EC_{50} values.

Analysis of intracellular T. cruzi inhibition in infected Vero cells

Vero cells were cultured in DMEM low glucose medium (Gibco) supplemented with 10% FBS, 10 units/mL of penicillin and 10 μg/mL of streptomycin at 37 °C in a humid 5% CO_2 environment. Infective trypomastigote cells of *T. cruzi* Dm28c were obtained as previously described (Bonaldo et al., 1988) and stored under liquid nitrogen. Trypomastigotes from a frozen stock were amplified in Vero cells for one passage before starting the assays. For Vero cells infection assays, $3x10^3$ cells adhering to 96-well plates were infected with $6x10^4$ trypomastigotes in a MOI of 20:1 for 16h. After this time, the wells were washed twice with PBS to remove the parasite cells that remained free. TB56, Quisinostat (QSN) and the reference drug benznidazole were initially diluted in dimethylsulfoxide (DMSO) to obtain a ten-point serial dilution (1:3 ratio) from 18 mM to 0.905 μM. Subsequently, 1 μL of each dilution was added to 200 μL of culture medium to obtain final culture concentrations from 90 μM to 0.045 μM in 10 points of 1:3 factor each (final DMSO was 0.5% v/v). The medium containing the compounds was homogenized prior to addition to cells. Medium containing 0.5% DMSO (v/v) was administered to control wells of uninfected and untreated cells. Cultures were maintained under the same conditions for 24, 48 and 72h to determine EC_{50} and CC_{50} values. For image analysis, the cells were washed twice with PBS prior to and after fixation with 4% paraformaldehyde (PFA) for 15 min and stained with 0,001% Evans' blue and 1 μg/mL DAPI. Images of 25 fields per well were acquired on an Operetta Image System (PerkinElmer) and analysed using the Harmony software (PerkinElmer) to discriminate nucleus, cytoplasm and the spots delimited for the intracellular amastigotes. The number of cells and amastigotes per well were determined and dose-response curves were plotted using GraphPad Prism version 7.05. Non-linear regression was calculated to determine CC_{50} and EC_{50} for cells and parasites, respectively. The inhibition ratio (in %) was calculated based on the mean of cells or amastigotes from the infected untreated wells.

Pharmacokinetic study.

The TB56 pharmacokinetic study was performed using four NMRI mice (Charles River, Germany) where two mice were administered 50 mg/kg TB56 intravenously (i.v.) and two mice were administered 50 mg/kg TB56 orally by gavage (p.o.). The formulation of TB56 was: 5 mg/ml TB56 in 7% DMSO, 35% (w/v) HPβCD in DPBS, pH ca 7. The health status of the mice was followed and blood sampling took place at 15, 60 and 180 min (i.v.) and 30, 60 and 180 min (p.o.). Following the last blood sampling the animals were euthanized. The blood samples were immediately centrifuged and the plasma transferred and frozen. Bioanalysis of the plasma samples was performed by LC-MS/MS using an ACQUITY UPLC-TQD (Waters). Propranolol was used as an internal standard. Preparation of plasma samples: 20 µl of each plasma sample and the standard samples (prepared from TB56 DMSO stocks using inactive mouse plasma) were added to 100 µl (5 volumes) cold acetonitrile with 2 µM propranolol (internal standard) in a 96-well plate. The plate was left for 20 minutes equilibration on a shaker table. The plate was then centrifuged for 15 min at 2800 rpm, 4^{o}C and 50 µl of the supernatants were transferred to wells containing 100 µl distilled water in another 96-well plate. The plate was left to equilibrate on a shaker table for 10 minutes. The plate was sealed and the LC-MSMS experiments performed. The analysis of each sample was performed in duplicate. The quantification of the plasma concentrations was done with the eight point calibration curve obtained from the TB56 standard plasma samples ranging from 160 µM to 9.8 nM (R^2= 0.999).

Mouse infection assays

Mouse infection assays were performed with three groups of 5-week old Balb/C females infected by intraperitoneal injection with 2x10^5 *T. cruzi* Dm28c trypomastigotes expressing firefly luciferase (Henriques et al., 2014). One group comprised the untreated controls and a second group was treated with the reference drug benznidazole, while the third group received TB56. TB56 and benznidazole were prepared in 7% DMSO (v/v), 40 % (2-Hydroxypropyl)-β-cyclodextrin (v/w) in DPBS. Intraperitoneal injections were performed from day 4 to day 8 post-infection with 50 mg/kg/day of each compound. Mice from the control group were treated with vehicle only. Parasite load was determined by luminescence quantification using D-luciferin administered at 150 mg/kg 10-20 min before data acquisition using a IVIS Spectrum CT (Perkin-Elmer) on dorsal and ventral positions, on days 3, 7 and 9 post infection. Images were processed using the Living Image v.4.3 software. Regions of interest (ROI) were selected to the full body including tail. Background auto luminescence was calculated using the same ROI size where indicated. Total flux [photons/second] was considered for calculations and average radiance [photons/sec/cm^2/steradian] for image units. Statistical analysis was performed by using one-way ANOVA with spherical data and Tukey's multiple tests in GraphPad Prism v.7.

Acknowledgments

This work and the authors of this manuscript have been supported by funding from the European Union's Seventh Framework Programme for research, technological development and demonstration under grant agreement no. 602080 (A-ParaDDisE). CR, MM, ERM, and TBS were supported by institutional funds from the Centre National de la Recherche Scientifique (CNRS), the Institut National de la Santé et de la Recherche Médicale (INSERM) and the Université de Strasbourg. RJP was supported by institutional funds from the CNRS, the Institut Pasteur de Lille and Lille University. NITZ, GFAP, EGS, MMM were partially supported by the Brazilian National Research Council (CNPq), the Research Foundation from the state of Paraná (FapPR) and the INOVA research program from FIOCRUZ. The authors acknowledge the support and the use of resources of the French Infrastructure for Integrated Structural Biology FRISBI ANR-10-INBS-05 and of Instruct-ERIC. The authors thank the Program for Technological Development of Tools for Health-PDTIS-FIOCRUZ for the use of its facilities. W.S. and K.H. acknowledge the financial support by the European Regional Development Fund of the European Commission. MJ and AM were supported by the Deutsche Forschungsgemeinschaft - Project ID 192904750 - CRC 992 Medical Epigenetics. We wish to thank members of the Swiss Light Source (SLS) synchrotrons for the use of their beamline facilities and for help during data collection.

Author contributions

M.M., E.R.M. and G.F.A.P.-C. contributed equally to this work. M.M., E.R.M., T.B.S., E.T. and C.R. performed all the biochemical, biophysical and structural studies. G.F.A.P.-C., E.P.G.S. and N.T.Z. performed the *T. cruzi* gene deletion and genetic complementation studies, the *in cellulo* high-content image-based experiments and the mice infection assays. P.S.J and M.M.M performed the *in cellulo* assays based on indirect readout of β-galactosidase activity. T.B., K.H. and W.S. synthesized the tested inhibitors, did the analytical characterizations and carried out the docking studies. D.H., A.M., A.C., K.S. and M.J. performed the enzymatic activity and inhibition assays and analysed these data. C.N. and J.S. performed enzymatic activity assays and the pharmacokinetic study. M.M., G.F.A.P.-C., S.G., R.J.P., M.M.M., M.J., J.S., W.S, N.Z. and C.R. designed the experiments, analysed data and wrote the paper.

Competing interests

The authors declare no competing interests.

References

Andrews, K. T., Fisher, G. & Skinner-Adams, T. S. 2014. Drug Repurposing And Human Parasitic Protozoan Diseases. *Int J Parasitol Drugs Drug Resist,* 4**,** 95-111.

Andrews, K. T., Haque, A. & Jones, M. K. 2012a. Hdac Inhibitors In Parasitic Diseases. *Immunology And Cell Biology,* 90**,** 66-77.

Andrews, K. T., Tran, T. N. & Fairlie, D. P. 2012b. Towards Histone Deacetylase Inhibitors As New Antimalarial Drugs. *Curr Pharm Des,* 18**,** 3467-79.

Araujo-Lima, C. F., Peres, R. B., Silva, P. B., Batista, M. M., Aiub, C. A. F., Felzenszwalb, I. & Soeiro, M. N. C. 2018. Repurposing Strategy Of Atorvastatin Against Trypanosoma Cruzi: In Vitro Monotherapy And Combined Therapy With Benznidazole Exhibit Synergistic Trypanocidal Activity. *Antimicrob Agents Chemother,* 62.

Bayer, T., Chakrabarti, A., Lancelot, J., Shaik, T. B., Hausmann, K., Melesina, J., Schmidtkunz, K., Marek, M., Erdmann, F., Schmidt, M., Robaa, D., Romier, C., Pierce, R. J., Jung, M. & Sippl, W. 2018. Synthesis, Crystallization Studies, And In Vitro Characterization Of Cinnamic Acid Derivatives As Smhdac8 Inhibitors For The Treatment Of Schistosomiasis. *Chemmedchem*.

Bonaldo, M. C., Souto-Padron, T., De Souza, W. & Goldenberg, S. 1988. Cell-Substrate Adhesion During Trypanosoma Cruzi Differentiation. *J Cell Biol,* 106**,** 1349-58.

Buckner, F. S., Verlinde, C. L., La Flamme, A. C. & Van Voorhis, W. C. 1996. Efficient Technique For Screening Drugs For Activity Against Trypanosoma Cruzi Using Parasites Expressing Beta-Galactosidase. *Antimicrob Agents Chemother,* 40**,** 2592-7.

Büscher, P., Cecchi, G., Jamonneau, V. & Priotto, G. 2017. Human African Trypanosomiasis. *Lancet,* 390**,** 2397-2409.

Camargo, E. P. 1964. Growth And Differentiation In Trypanosoma Cruzi. I. Origin Of Metacyclic Trypanosomes In Liquid Media. *Rev Inst Med Trop Sao Paulo,* 6**,** 93-100.

Campo, V. A. 2017. Comparative Effects Of Histone Deacetylases Inhibitors And Resveratrol On Trypanosoma Cruzi Replication, Differentiation, Infectivity And Gene Expression. *Int J Parasitol Drugs Drug Resist,* 7**,** 23-33.

Carrillo, A. K., Guiguemde, W. A. & Guy, R. K. 2015. Evaluation Of Histone Deacetylase Inhibitors (Hdaci) As Therapeutic Leads For Human African Trypanosomiasis (Hat). *Bioorg Med Chem,* 23**,** 5151-5.

Choudhary, C., Kumar, C., Gnad, F., Nielsen, M. L., Rehman, M., Walther, T. C., Olsen, J. V. & Mann, M. 2009. Lysine Acetylation Targets Protein Complexes And Co-Regulates Major Cellular Functions. *Science,* 325**,** 834-40.

Choudhary, C., Weinert, B. T., Nishida, Y., Verdin, E. & Mann, M. 2014. The Growing Landscape Of Lysine Acetylation Links Metabolism And Cell Signalling. *Nat Rev Mol Cell Biol,* 15**,** 536-50.

Contreras, V. T., Araujo-Jorge, T. C., Bonaldo, M. C., Thomaz, N., Barbosa, H. S., Meirelles Mde, N. & Goldenberg, S. 1988. Biological Aspects Of The Dm 28c Clone Of Trypanosoma Cruzi After Metacyclogenesis In Chemically Defined Media. *Mem Inst Oswaldo Cruz,* 83**,** 123-33.

De Souza, F. S., Rampazzo Rde, C., Manhaes, L., Soares, M. J., Cavalcanti, D. P., Krieger, M. A., Goldenberg, S. & Fragoso, S. P. 2010. Knockout Of The Gene Encoding The Kinetoplast-Associated Protein 3 (Kap3) In Trypanosoma Cruzi: Effect On Kinetoplast Organization, Cell Proliferation And Differentiation. *Mol Biochem Parasitol,* 172**,** 90-8.

Desravines, D. C., Serna Martin, I., Schneider, R., Mas, P. J., Aleksandrova, N., Jensen, M. R., Blackledge, M. & Hart, D. J. 2017. Structural Characterization Of The Smrt Corepressor Interacting With Histone Deacetylase 7. *Sci Rep,* 7**,** 3678.

Diebold, M. L., Fribourg, S., Koch, M., Metzger, T. & Romier, C. 2011. Deciphering Correct Strategies For Multiprotein Complex Assembly By Co-Expression: Application To Complexes As Large As The Histone Octamer. *J Struct Biol,* 175**,** 178-88.

Drazic, A., Myklebust, L. M., Ree, R. & Arnesen, T. 2016. The World Of Protein Acetylation. *Biochim Biophys Acta,* 1864**,** 1372-401.

Eckschlager, T., Plch, J., Stiborova, M. & Hrabeta, J. 2017. Histone Deacetylase Inhibitors As Anticancer Drugs. *Int J Mol Sci,* 18.
Emsley, P., Lohkamp, B., Scott, W. G. & Cowtan, K. 2010. Features And Development Of Coot. *Acta Crystallographica Section D: Biological Crystallography,* 66**,** 486-501.
Engel, J. A., Jones, A. J., Avery, V. M., Sumanadasa, S. D., Ng, S. S., Fairlie, D. P., Skinner-Adams, T. & Andrews, K. T. 2015. Profiling The Anti-Protozoal Activity Of Anti-Cancer Hdac Inhibitors Against Plasmodium And Trypanosoma Parasites. *Int J Parasitol Drugs Drug Resist,* 5**,** 117-26.
Falkenberg, K. J. & Johnstone, R. W. 2014. Histone Deacetylases And Their Inhibitors In Cancer, Neurological Diseases And Immune Disorders. *Nat Rev Drug Discov,* 13**,** 673-91.
Fioravanti, R., Mautone, N., Rovere, A., Rotili, D. & Mai, A. 2020. Targeting Histone Acetylation/Deacetylation In Parasites: An Update (2017-2020). *Curr Opin Chem Biol,* 57**,** 65-74.
Fujisawa, T. & Filippakopoulos, P. 2017. Functions Of Bromodomain-Containing Proteins And Their Roles In Homeostasis And Cancer. *Nat Rev Mol Cell Biol,* 18**,** 246-262.
Hai, Y. & Christianson, D. W. 2016. Histone Deacetylase 6 Structure And Molecular Basis Of Catalysis And Inhibition. *Nat Chem Biol,* 12**,** 741-7.
Hai, Y., Shinsky, S. A., Porter, N. J. & Christianson, D. W. 2017. Histone Deacetylase 10 Structure And Molecular Function As A Polyamine Deacetylase. *Nat Commun,* 8**,** 15368.
Hailu, G. S., Robaa, D., Forgione, M., Sippl, W., Rotili, D. & Mai, A. 2017. Lysine Deacetylase Inhibitors In Parasites: Past, Present, And Future Perspectives. *J Med Chem,* 60**,** 4780-4804.
Heimburg, T., Chakrabarti, A., Lancelot, J., Marek, M., Melesina, J., Hauser, A. T., Shaik, T. B., Duclaud, S., Robaa, D., Erdmann, F., Schmidt, M., Romier, C., Pierce, R. J., Jung, M. & Sippl, W. 2016. Structure-Based Design And Synthesis Of Novel Inhibitors Targeting Hdac8 From Schistosoma Mansoni For The Treatment Of Schistosomiasis. *J Med Chem,* 59**,** 2423-35.
Heimburg, T., Kolbinger, F. R., Zeyen, P., Ghazy, E., Herp, D., Schmidtkunz, K., Melesina, J., Shaik, T. B., Erdmann, F., Schmidt, M., Romier, C., Robaa, D., Witt, O., Oehme, I., Jung, M. & Sippl, W. 2017. Structure-Based Design And Biological Characterization Of Selective Histone Deacetylase 8 (Hdac8) Inhibitors With Anti-Neuroblastoma Activity. *J Med Chem,* 60**,** 10188-10204.
Heltweg, B., Dequiedt, F., Marshall, B. L., Brauch, C., Yoshida, M., Nishino, N., Verdin, E. & Jung, M. 2004. Subtype Selective Substrates For Histone Deacetylases. *J Med Chem,* 47**,** 5235-43.
Heltweg, B., Trapp, J. & Jung, M. 2005. In Vitro Assays For The Determination Of Histone Deacetylase Activity. *Methods,* 36**,** 332-7.
Henriques, C., Henriques-Pons, A., Meuser-Batista, M., Ribeiro, A. S. & De Souza, W. 2014. In Vivo Imaging Of Mice Infected With Bioluminescent Trypanosoma Cruzi Unveils Novel Sites Of Infection. *Parasit Vectors,* 7**,** 89.
Holm, L. 2020. Dali And The Persistence Of Protein Shape. *Protein Sci,* 29**,** 128-140.
Hudson, G. M., Watson, P. J., Fairall, L., Jamieson, A. G. & Schwabe, J. W. 2015. Insights Into The Recruitment Of Class Iia Histone Deacetylases (Hdacs) To The Smrt/Ncor Transcriptional Repression Complex. *J Biol Chem,* 290**,** 18237-44.
Ingram, A. K. & Horn, D. 2002. Histone Deacetylases In Trypanosoma Brucei: Two Are Essential And Another Is Required For Normal Cell Cycle Progression. *Mol Microbiol,* 45**,** 89-97.
Kabsch, W. 2010. Xds. *Acta Crystallogr D Biol Crystallogr,* 66**,** 125-32.
Katoh, K., Rozewicki, J. & Yamada, K. D. 2019. Mafft Online Service: Multiple Sequence Alignment, Interactive Sequence Choice And Visualization. *Brief Bioinform,* 20**,** 1160-1166.
Kelly, J. M., Taylor, M. C., Horn, D., Loza, E., Kalvinsh, I. & Bjã¶Rkling, F. 2012. Inhibitors Of Human Histone Deacetylase With Potent Activity Against The African Trypanosome Trypanosoma Brucei. *Bioorganic And Medicinal Chemistry Letters,* 22**,** 1886-1890.
Li, Y. & Seto, E. 2016. Hdacs And Hdac Inhibitors In Cancer Development And Therapy. *Cold Spring Harb Perspect Med,* 6.

Liebschner, D., Afonine, P. V., Baker, M. L., Bunkoczi, G., Chen, V. B., Croll, T. I., Hintze, B., Hung, L. W., Jain, S., Mccoy, A. J., Moriarty, N. W., Oeffner, R. D., Poon, B. K., Prisant, M. G., Read, R. J., Richardson, J. S., Richardson, D. C., Sammito, M. D., Sobolev, O. V., Stockwell, D. H., Terwilliger, T. C., Urzhumtsev, A. G., Videau, L. L., Williams, C. J. & Adams, P. D. 2019. Macromolecular Structure Determination Using X-Rays, Neutrons And Electrons: Recent Developments In Phenix. *Acta Crystallogr D Struct Biol,* 75**,** 861-877.

Maclean, L. M., Thomas, J., Lewis, M. D., Cotillo, I., Gray, D. W. & De Rycker, M. 2018. Development Of Trypanosoma Cruzi In Vitro Assays To Identify Compounds Suitable For Progression In Chagas' Disease Drug Discovery. *Plos Negl Trop Dis,* 12**,** E0006612.

Madeira, F., Park, Y. M., Lee, J., Buso, N., Gur, T., Madhusoodanan, N., Basutkar, P., Tivey, A. R. N., Potter, S. C., Finn, R. D. & Lopez, R. 2019. The Embl-Ebi Search And Sequence Analysis Tools Apis In 2019. *Nucleic Acids Res,* 47**,** W636-W641.

Mandava, V., Fernandez, J. P., Deng, H., Janzen, C. J., Hake, S. B. & Cross, G. A. 2007. Histone Modifications In Trypanosoma Brucei. *Mol Biochem Parasitol,* 156**,** 41-50.

Marek, M., Kannan, S., Hauser, A. T., Moraes Mourao, M., Caby, S., Cura, V., Stolfa, D. A., Schmidtkunz, K., Lancelot, J., Andrade, L., Renaud, J. P., Oliveira, G., Sippl, W., Jung, M., Cavarelli, J., Pierce, R. J. & Romier, C. 2013. Structural Basis For The Inhibition Of Histone Deacetylase 8 (Hdac8), A Key Epigenetic Player In The Blood Fluke Schistosoma Mansoni. *Plos Pathog,* 9**,** E1003645.

Marek, M., Oliveira, G., Pierce, R. J., Jung, M., Sippl, W. & Romier, C. 2015. Drugging The Schistosome Zinc-Dependent Hdacs: Current Progress And Future Perspectives. *Future Med Chem,* 7**,** 783-800.

Marek, M., Shaik, T. B., Heimburg, T., Chakrabarti, A., Lancelot, J., Ramos-Morales, E., Da Veiga, C., Kalinin, D., Melesina, J., Robaa, D., Schmidtkunz, K., Suzuki, T., Holl, R., Ennifar, E., Pierce, R. J., Jung, M., Sippl, W. & Romier, C. 2018. Characterization Of Histone Deacetylase 8 (Hdac8) Selective Inhibition Reveals Specific Active Site Structural And Functional Determinants. *J Med Chem,* 61**,** 10000-10016.

Marmorstein, R. & Zhou, M. M. 2014. Writers And Readers Of Histone Acetylation: Structure, Mechanism, And Inhibition. *Cold Spring Harb Perspect Biol,* 6**,** A018762.

Martin-Escolano, R., Moreno-Viguri, E., Santivanez-Veliz, M., Martin-Montes, A., Medina-Carmona, E., Paucar, R., Marin, C., Azqueta, A., Cirauqui, N., Pey, A. L., Perez-Silanes, S. & Sanchez-Moreno, M. 2018. Second Generation Of Mannich Base-Type Derivatives With In Vivo Activity Against Trypanosoma Cruzi. *J Med Chem,* 61**,** 5643-5663.

Mccoy, A. J., Grosse-Kunstleve, R. W., Adams, P. D., Winn, M. D., Storoni, L. C. & Read, R. J. 2007. Phaser Crystallographic Software. *J Appl Crystallogr,* 40**,** 658-674.

Millard, C. J., Watson, P. J., Celardo, I., Gordiyenko, Y., Cowley, S. M., Robinson, C. V., Fairall, L. & Schwabe, J. W. 2013. Class I Hdacs Share A Common Mechanism Of Regulation By Inositol Phosphates. *Mol Cell,* 51**,** 57-67.

Miyake, Y., Keusch, J. J., Wang, L., Saito, M., Hess, D., Wang, X., Melancon, B. J., Helquist, P., Gut, H. & Matthias, P. 2016. Structural Insights Into Hdac6 Tubulin Deacetylation And Its Selective Inhibition. *Nat Chem Biol,* 12**,** 748-54.

Monaldi, D., Rotili, D., Lancelot, J., Marek, M., Wossner, N., Lucidi, A., Tomaselli, D., Ramos-Morales, E., Romier, C., Pierce, R. J., Mai, A. & Jung, M. 2019. Structure-Reactivity Relationships On Substrates And Inhibitors Of The Lysine Deacylase Sirtuin 2 From Schistosoma Mansoni (Smsirt2). *J Med Chem,* 62**,** 8733-8759.

Morales Torres, C., Wu, M. Y., Hobor, S., Wainwright, E. N., Martin, M. J., Patel, H., Grey, W., Gronroos, E., Howell, S., Carvalho, J., Snijders, A. P., Bustin, M., Bonnet, D., Smith, P. D., Swanton, C., Howell, M. & Scaffidi, P. 2020. Selective Inhibition Of Cancer Cell Self-Renewal Through A Quisinostat-Histone H1.0 Axis. *Nat Commun,* 11**,** 1792.

Moretti, N. S., Cestari, I., Anupama, A., Stuart, K. & Schenkman, S. 2018. Comparative Proteomic Analysis Of Lysine Acetylation In Trypanosomes. *J Proteome Res,* 17**,** 374-385.

Narita, T., Weinert, B. T. & Choudhary, C. 2019. Functions And Mechanisms Of Non-Histone Protein Acetylation. *Nat Rev Mol Cell Biol,* 20**,** 156-174.

Nunez, R. 2001. Dna Measurement And Cell Cycle Analysis By Flow Cytometry. *Curr Issues Mol Biol,* 3**,** 67-70.

Park, S. Y., Kim, G. S., Hwang, H. J., Nam, T. H., Park, H. S., Song, J., Jang, T. H., Lee, Y. C. & Kim, J. S. 2018. Structural Basis Of The Specific Interaction Of Smrt Corepressor With Histone Deacetylase 4. *Nucleic Acids Res,* 46**,** 11776-11788.

Pavani, R. S., Da Silva, M. S., Fernandes, C. A., Morini, F. S., Araujo, C. B., Fontes, M. R., Sant'anna, O. A., Machado, C. R., Cano, M. I., Fragoso, S. P. & Elias, M. C. 2016. Replication Protein A Presents Canonical Functions And Is Also Involved In The Differentiation Capacity Of Trypanosoma Cruzi. *Plos Negl Trop Dis,* 10**,** E0005181.

Peng, D. & Tarleton, R. 2015. Eupagdt: A Web Tool Tailored To Design Crispr Guide Rnas For Eukaryotic Pathogens. *Microb Genom,* 1**,** E000033.

Perez-Molina, J. A. & Molina, I. 2018. Chagas Disease. *Lancet,* 391**,** 82-94.

Picchi, G. F., Zulkievicz, V., Krieger, M. A., Zanchin, N. T., Goldenberg, S. & De Godoy, L. M. 2017. Post-Translational Modifications Of Trypanosoma Cruzi Canonical And Variant Histones. *J Proteome Res,* 16**,** 1167-1179.

Porter, N. J. & Christianson, D. W. 2019. Structure, Mechanism, And Inhibition Of The Zinc-Dependent Histone Deacetylases. *Curr Opin Struct Biol,* 59**,** 9-18.

Romagnoli, B. A. A., Picchi, G. F. A., Hiraiwa, P. M., Borges, B. S., Alves, L. R. & Goldenberg, S. 2018. Improvements In The Crispr/Cas9 System For High Efficiency Gene Disruption In Trypanosoma Cruzi. *Acta Trop,* 178**,** 190-195.

Romanha, A. J., Castro, S. L., Soeiro Mde, N., Lannes-Vieira, J., Ribeiro, I., Talvani, A., Bourdin, B., Blum, B., Olivieri, B., Zani, C., Spadafora, C., Chiari, E., Chatelain, E., Chaves, G., Calzada, J. E., Bustamante, J. M., Freitas-Junior, L. H., Romero, L. I., Bahia, M. T., Lotrowska, M., Soares, M., Andrade, S. G., Armstrong, T., Degrave, W. & Andrade Zde, A. 2010. In Vitro And In Vivo Experimental Models For Drug Screening And Development For Chagas Disease. *Mem Inst Oswaldo Cruz,* 105**,** 233-8.

Sabari, B. R., Zhang, D., Allis, C. D. & Zhao, Y. 2017. Metabolic Regulation Of Gene Expression Through Histone Acylations. *Nat Rev Mol Cell Biol,* 18**,** 90-101.

Scarim, C. B., Jornada, D. H., Chelucci, R. C., De Almeida, L., Dos Santos, J. L. & Chung, M. C. 2018. Current Advances In Drug Discovery For Chagas Disease. *Eur J Med Chem,* 155**,** 824-838.

Schiedel, M. & Conway, S. J. 2018. Small Molecules As Tools To Study The Chemical Epigenetics Of Lysine Acetylation. *Curr Opin Chem Biol,* 45**,** 166-178.

Schiedel, M., Marek, M., Lancelot, J., Karaman, B., Almlof, I., Schultz, J., Sippl, W., Pierce, R. J., Romier, C. & Jung, M. 2015. Fluorescence-Based Screening Assays For The Nad(+)-Dependent Histone Deacetylase Smsirt2 From Schistosoma Mansoni. *J Biomol Screen,* 20**,** 112-21.

Scholte, L. L. S., Mourao, M. M., Pais, F. S., Melesina, J., Robaa, D., Volpini, A. C., Sippl, W., Pierce, R. J., Oliveira, G. & Nahum, L. A. 2017. Evolutionary Relationships Among Protein Lysine Deacetylases Of Parasites Causing Neglected Diseases. *Infect Genet Evol,* 53**,** 175-188.

Seto, E. & Yoshida, M. 2014. Erasers Of Histone Acetylation: The Histone Deacetylase Enzymes. *Cold Spring Harb Perspect Biol,* 6**,** A018713.

Varikuti, S., Jha, B. K., Volpedo, G., Ryan, N. M., Halsey, G., Hamza, O. M., Mcgwire, B. S. & Satoskar, A. R. 2018. Host-Directed Drug Therapies For Neglected Tropical Diseases Caused By Protozoan Parasites. *Front Microbiol,* 9**,** 2655.

Verdin, E. & Ott, M. 2015. 50 Years Of Protein Acetylation: From Gene Regulation To Epigenetics, Metabolism And Beyond. *Nat Rev Mol Cell Biol,* 16**,** 258-64.

Vincentelli, R. & Romier, C. 2016. Complex Reconstitution And Characterization By Combining Co-Expression Techniques In Escherichia Coli With High-Throughput. *Adv Exp Med Biol,* 896**,** 43-58.

Wang, Q., Rosa, B. A., Nare, B., Powell, K., Valente, S., Rotili, D., Mai, A., Marshall, G. R. & Mitreva, M. 2015. Targeting Lysine Deacetylases (Kdacs) In Parasites. *Plos Negl Trop Dis,* 9**,** E0004026.

Wang, Q. P., Kawahara, T. & Horn, D. 2010. Histone Deacetylases Play Distinct Roles In Telomeric Vsg Expression Site Silencing In African Trypanosomes. *Mol Microbiol,* 77**,** 1237-45.

Watson, P. J., Fairall, L., Santos, G. M. & Schwabe, J. W. R. 2012. Structure Of Hdac3 Bound To Co-Repressor And Inositol Tetraphosphate. *Nature,* 481**,** 335-340.
Watson, P. J., Millard, C. J., Riley, A. M., Robertson, N. S., Wright, L. C., Godage, H. Y., Cowley, S. M., Jamieson, A. G., Potter, B. V. & Schwabe, J. W. 2016. Insights Into The Activation Mechanism Of Class I Hdac Complexes By Inositol Phosphates. *Nat Commun,* 7**,** 11262.
Williams, C. J., Headd, J. J., Moriarty, N. W., Prisant, M. G., Videau, L. L., Deis, L. N., Verma, V., Keedy, D. A., Hintze, B. J., Chen, V. B., Jain, S., Lewis, S. M., Arendall, W. B., 3rd, Snoeyink, J., Adams, P. D., Lovell, S. C., Richardson, J. S. & Richardson, D. C. 2018. Molprobity: More And Better Reference Data For Improved All-Atom Structure Validation. *Protein Sci,* 27**,** 293-315.
Zuma, A. A. & De Souza, W. 2018. Histone Deacetylases As Targets For Antitrypanosomal Drugs. *Future Sci Oa,* 4**,** Fso325.

Figure legends

***Figure 1. Trypanosoma cruzi* tcDAC2 has specific sequence features.**

Multiple sequence alignment of *Trypanosoma cruzi* (tc) DAC2 and human (hs) HDAC1 and HDAC8. Ends of sequences are indicated with a '*'. For clarity, the non-conserved HDAC1 C-terminus has been shortened, with the number of additional residues indicated. Sequence identity is indicated with red boxes and sequence similarity with red letters. Residues involved in zinc binding are shown with yellow stars, the catalytic tyrosine with a blue star. The yellow diamond marks the residue distinguishing the HDAC1-3 and HDAC11 isozyme families from the other human HDAC isozymes. The blue diamond marks the residue gatekeeping the HDAC active sites. The green diamond marks the arginine that caps the tcDAC2 L6 loop. Purple circles mark important residues forming the tcDAC2-unique pocket. Secondary structure elements (α, α-helices; β, β-strands; η, 3_{10}-helices) from tcDAC2 are shown above the alignment. Sequence insertions in tcDAC2 are boxed (orange) and the three largest ones are labelled (Ins. 1-3) below the alignment. The region removed for crystallization is shown in grey italics. Loops forming the active site are indicated and labelled blue under the alignment.

Figure 2.* Lack of class I deacetylases impacts cell cycle and proliferation of *T. cruzi.

(A,B) Growth curves showing that tcDAC1 and tcDAC2 knocked out cells (purple and orange curves, respectively) present lower proliferation rates when compared to wild type cells (light blue). **(C,D)** Cell cycle analyses show abnormal progression as determined by DNA content quantification. Blue: wild type cells; dark and light purple: single and double tcDAC1 knocked out cells; red and orange: single and double tcDAC2 knocked out cells. **(E)** Light microscopy images showing an increase in the number of nuclei/kinetoplasts in tcDAC1 and tcDAC2 knocked out cells. **(F)** Abnormal cell cycle progression observed for all three different sgRNAs used in tcDAC2 disruption using the CRISPR-Cas9 methodology. Cyan blue curve: wild-type cells; red line curves: null mutant cells. **(G)** Light microscopy images showing an increase in the number of nuclei/kinetoplasts in tcDAC2 knocked out cells using the CRISPR-Cas9 methodology. **(H)** Cell proliferation rates and **(I)** light microscopy images of parasites from tcDAC2 complementation assays. tcDAC2_sens: negative control (knockout phenotype); tcDAC2_res: positive control; tcDAC2_Y371F: substitution of the catalytic tyrosine residue by a phenylalanine; tcDAC2_ΔC: deletion of the glutamic acid-rich C-terminal region. n – nucleus, k – kinetoplast, dpt – days post-transfection.

Figure 3. tcDAC2 is a functional acetyl-lysine deacetylase that is inhibited by drug-like inhibitors.

(A) Thermal stability (°C) of human (h) HDAC8 (dark blue), *Schistosoma mansoni* (sm) HDAC8 (green), and the *Trypanosoma cruzi* (tc) DAC2_ΔC and DAC2_ΔIns2 constructs (cyan). The thermal stability of

tcDAC2 is lower than that of HDAC8 enzymes but can be increased by removing a small region of Insertion 2. **(B)** Measurements of the deacetylase activity of hHDAC8 and various tcDAC2 constructs. The deacetylase activity is increased upon removal of the small region of Insertion 2 that stabilizes the enzyme but is decreased by the mutation of important active site residues, as already observed in many HDACs. This demonstrates that tcDAC2 has a bona fide deacetylase activity. **(C)** Structures and IC_{50} values for tcDAC2 of various inhibitors. Detailed IC_{50} values, including for other human HDACs, are provided as supplementary information.

Figure 4. Atypical structure of tcDAC2.

(A) Ribbon representation of the tcDAC2 structure in different views as observed in the tcDAC2/TB56 complex. The zinc (orange) and potassium (purple) ions are shown as spheres, helices are coloured cyan and β-strands are coloured yellow. The largest insertions found in tcDAC2 compared to human HDACs are shown in orange. The C-terminal α9 helix of tcDAC2 which binds in a non-canonical position is labelled. **(B)** Ribbon representation of the tcDAC2-specific surface. Regions that diverge strongly at the sequence and structural level from the canonical sequences and folds observed in human class I HDACs are coloured red, revealing that they mostly concentrate on a single side of the enzyme, potentially defining a surface dedicated to specific interactions. **(C)** Close-up view of tcDAC2 LC loop (orange) that caps tcDAC2 active site L6 loop (green). Notably, LC loop arginine 439 interacts with L6 loop main chain carboxyl oxygens, firmly maintaining its capping position. **(D)** Positioning of tcDAC2 Insertions 1 and 2 that would interfere with partners binding as observed for human class I HDAC1 and HDAC3.

Figure 5. Unique nature of the tcDAC2 active site.

Comparison of active site features of tcDAC2 (middle panels), human HDAC1 (left panels) and human HDAC8 (right panels). **(A)** Positioning of important active site deacetylation residues. The conservation of these residues and of their positioning is in agreement with the observed deacetylation activity of tcDAC2. **(B)** Active site loops of the three enzymes showing that most tcDAC2 loops have a similar conformation as those of HDAC8, with the major exception of tcDAC2 L6 loop whose conformation is similar to that of HDAC1. **(C)** Surface representation of the active site of the three enzymes. The conformation of tcDAC2 L6 loop causes an L1-L6 lock that prevents the formation of a selective and functionally important pocket observed in HDAC8 (Marek et al., 2018). In contrast, tcDAC2 has a unique pocket formed between its L5 and L6 loops that does not exist in other human HDACs due to an L5-L6 lock. **(D)** Residues forming the tcDAC2 unique pocket. This pocket is created by the replacement by small residues in tcDAC2 of larger residues found in other HDACs.

Figure 6. Molecular basis of inhibition of tcDAC2 by QSN and TB56.

Binding of inhibitors in the tcDAC2 active site using residues (left panels), surface (middle panels) and pocket (right panels) views. **(A)** Binding of Quisinostat (QSN) to tcDAC2. The QSN inhibitor shows a canonical binding mode as observed for many pan-HDAC inhibitors bound to different HDACs. **(B)** Binding of TB56 to tcDAC2. TB56 occupies the entrance of the tcDAC2-unique pocket, demonstrating of the potential of this pocket to accommodate tcDAC2-selective inhibitors.

Figure 7. Inhibition of *T. cruzi* in cellular and in mice infection models.

(A) Dose-response curves obtained from L929 cells treated with Benznizadole (BZN), Quisinostat (QSN) and TB56 for 24 and 96h. BZN does not show toxicity to L929 cells with the concentrations used in these assays. The toxicity values (CC_{50}) for BZN, QSN and TB56 are indicated in the figure. **(B)** Dose-response curves obtained from Vero cells treated with BZN, QSN and TB56 for 24, 48 and 72h. The toxicity values (CC_{50}) for BZN, QSN and TB56 are indicated in the figure. BZN show very little toxicity, while TB56 show the same toxicity as for the L929 cells. QSN shows lower cytotoxicity as for the L929 cells. **(C)** Dose-response curves of *T. cruzi* Tulahuen strain inhibition obtained from infected L929 cell cultures treated with BZN, QSN and TB56 for 24, 48 and 72 hours. The respective EC_{50} values are indicated in the figure. **(D)** Dose-response curves obtained from Vero cell cultures infected by the *T. cruzi* Dm28c strain treated with BZN, QSN and TB56 for 24, 48 and 72h. The respective EC_{50} values are indicated in the figure. **(E)** Results of the pharmacokinetic study results showing the TB56 concentration versus time in mouse plasma samples after administration of 50 mg/kg TB56 p.o. (mouse 126 and 127) or i.v. (mouse 128 and 129). **(F)** Analysis of *T. cruzi* infection in a mice model. In vivo luminescence images of the untreated control group (left), the group treated with TB56 (center) and the group treated with Benznidazole (BZN; right) acquired at 3 days post infection, before the treatment started, and at 7 and 9 days post infection, respectively after 3 and 5 days of treatment with the indicated compounds. A visual reduction of luminescence levels can be observed both for TB56 and BZN treated mice. **(G)** Luminescence quantification of the images shown in graph in (F), confirming a significant inhibition of *T. cruzi* in TB56-treated mice relative to the control group at 7 dpi, albeit weaker than for the BZN-treated mice.

Figure 1

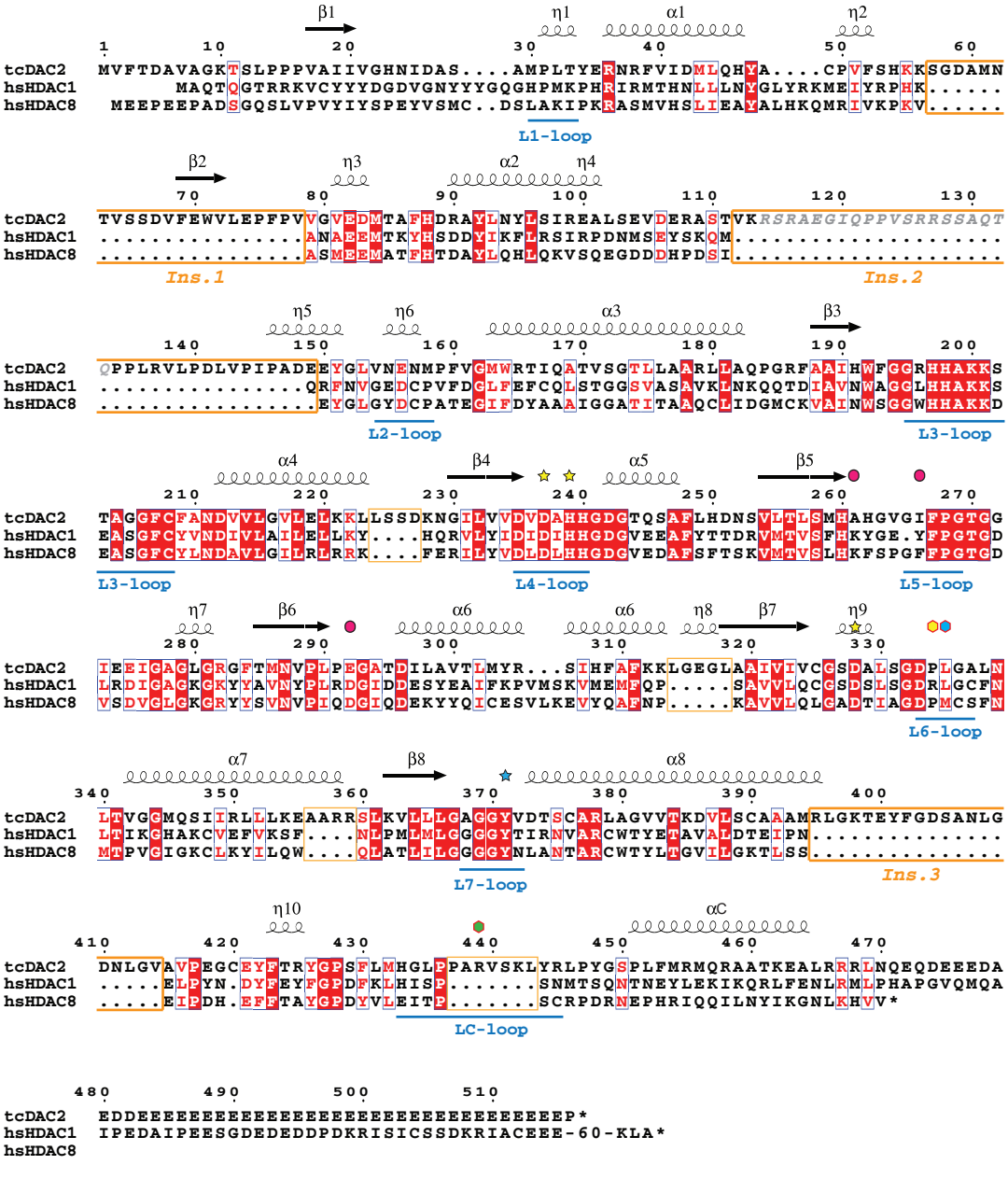
β1 η1 α1 η2
1 10 20 30 40 50 60
tcDAC2 MVFTDAVAGKTSLPPPVAIIVGHNIDAS....AMPLTYERNRFVIDMLQHYA....CPVFSHKKSGDAMN
hsHDAC1 MAQTQGTRRKVCYYYDGDVGNYYYGQGHPMKPHRIRMTHNLLLNYGLYRKMEIYRPHK......
hsHDAC8 MEEPEEPADSGQSLVPVYIYSPEYVSMC..DSLAKIPKRASMVHSLIEAYALHKQMRIVKPKV......
L1-loop
β2 η3 α2 η4
70 80 90 100 110 120 130
tcDAC2 TVSSDVFEWVLEPFPVVGVEDMTAFHDRAYLNYLSIREALSEVDERASTVKRSRAEGIQPPVSRRSSAQT
hsHDAC1 ..............ANAEEMTKYHSDDYIKFLRSIRPDNMSEYSKQM..................
hsHDAC8 ..............ASMEEMATFHTDAYLQHLQKVSQEGDDDHPDSI..................
Ins.1 Ins.2
η5 η6 α3 β3
140 150 160 170 180 190 200
tcDAC2 QPPLRVLPDLVPIPADEEYGLVNENMPFVCMWRTIQATVSGTLLAARLLAQPGRFAAIHWFGGRHHAKKS
hsHDAC1 ..............QRFNVGEDCPVFDGLFEFCQLSTGGSVASAVKLNKQQTDIAVNWAGGLHHAKKS
hsHDAC8 ..............EYGLGYDCPATEGIFDYAAAIGGATITAAQCLIDGMCKVAINWSGGWHHAKKD
L2-loop L3-loop
α4 β4 α5 β5
210 220 230 240 250 260 270
tcDAC2 TAGGFCFANDVVLGVLELLKKLLSSDKNGILVVDVDAHHGDGTQSAFLHDNSVLTLSMHAHGVGIFPGTGG
hsHDAC1 EASGFCYVNDIVLAILELLKY....HQRVLYIDIDIHHGDGVEEAFYTTDRVMTVSFHKYGE.YFPGTGD
hsHDAC8 EASGFCYLNDAVLGILRLRRK....FERILYVDLDLHHGDGVEDAFSFTSKVMTVSLHKFSPGFFPGTGD
L3-loop L4-loop L5-loop
η7 β6 α6 α6 η8 β7 η9
280 290 300 310 320 330
tcDAC2 IEEIGAGLGRGFTMNVPLPEGATDILAVTLMYR...SIHFAFKKLGEGLAAIVICGSDALSGDPLGALN
hsHDAC1 LRDIGAGKGKYYAVNYPLRDGIDDESYEAIFKPVMSKVMEMFQP.....SAVVLQCGSDSLSGDRLGCFN
hsHDAC8 VSDVGLGKGRYYSVNVPIQDGIQDEKYYQICESVLKEVYQAFNP.....KAVVLQLGADTIAGDPMCSFN
L6-loop
α7 β8 α8
340 350 360 370 380 390 400
tcDAC2 LTVGGMQSIIRLLLKEAARRSLKVLLLGAGGYVDTSCARLAGVVTKDVLSCAAAMRLGKTEYFGDSANLG
hsHDAC1 LTIKGHAKCVEFVKSF....NLPMLMLGGGGYTIRNVARCWTYETAVALDTEIPN..............
hsHDAC8 MTPVGIGKCLKYILQW....QLATLILGGGGYNLANTARCWTYLTGVILGKTLSS..............
L7-loop Ins.3
η10 αC
410 420 430 440 450 460 470
tcDAC2 DNLGVAVPEGCEYFTRYGPSFLMHGLPPARVSKLYRLPYGSPLFMRMQRAATKEALRRRLNQEQDEEEDA
hsHDAC1 .....ELPYN.DYFEYFGPDFKLHISP.......SNMTSQNTNEYLEKIKQRLFENLRMLPHAPGVQMQA
hsHDAC8 .....EIPDH.EFFTAYGPDYVLEITP.......SCRPDRNEPHRIQQILNYIKGNLKHVV*
LC-loop
480 490 500 510
tcDAC2 EDDEEEEEEEEEEEEEEEEEEEEEEEEEEEEEEEEEP*
hsHDAC1 IPEDAIPEESGDEDEDDPDKRISICSSDKRIACEEE-60-KLA*
hsHDAC8

Figure 2

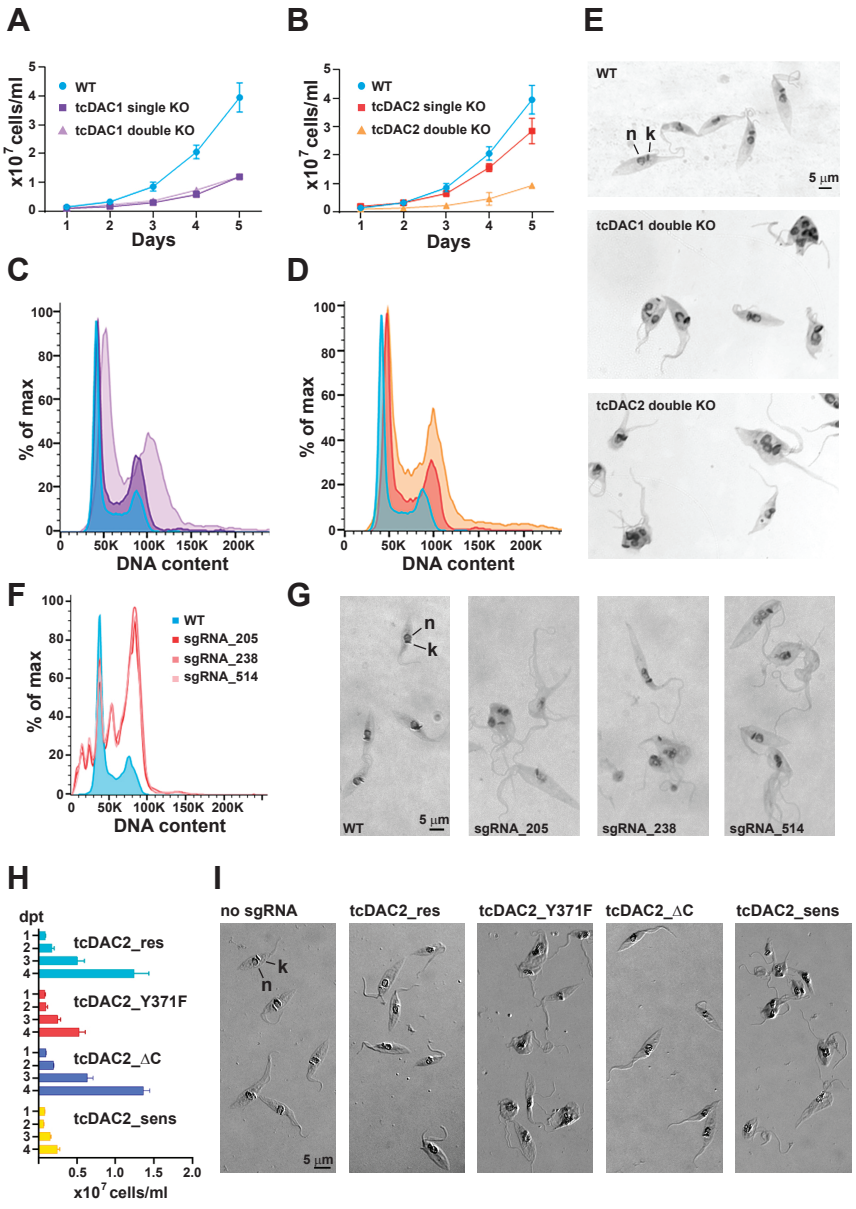
A
B
E
WT
tcDAC1 single KO
tcDAC1 double KO
tcDAC2 single KO
tcDAC2 double KO
x10^7 cells/ml
Days
n k
5 µm
tcDAC1 double KO
tcDAC2 double KO
C
D
% of max
DNA content
F
G
sgRNA_205
sgRNA_238
sgRNA_514
H
I
dpt
tcDAC2_res
tcDAC2_Y371F
tcDAC2_ΔC
tcDAC2_sens
no sgRNA

Figure 3

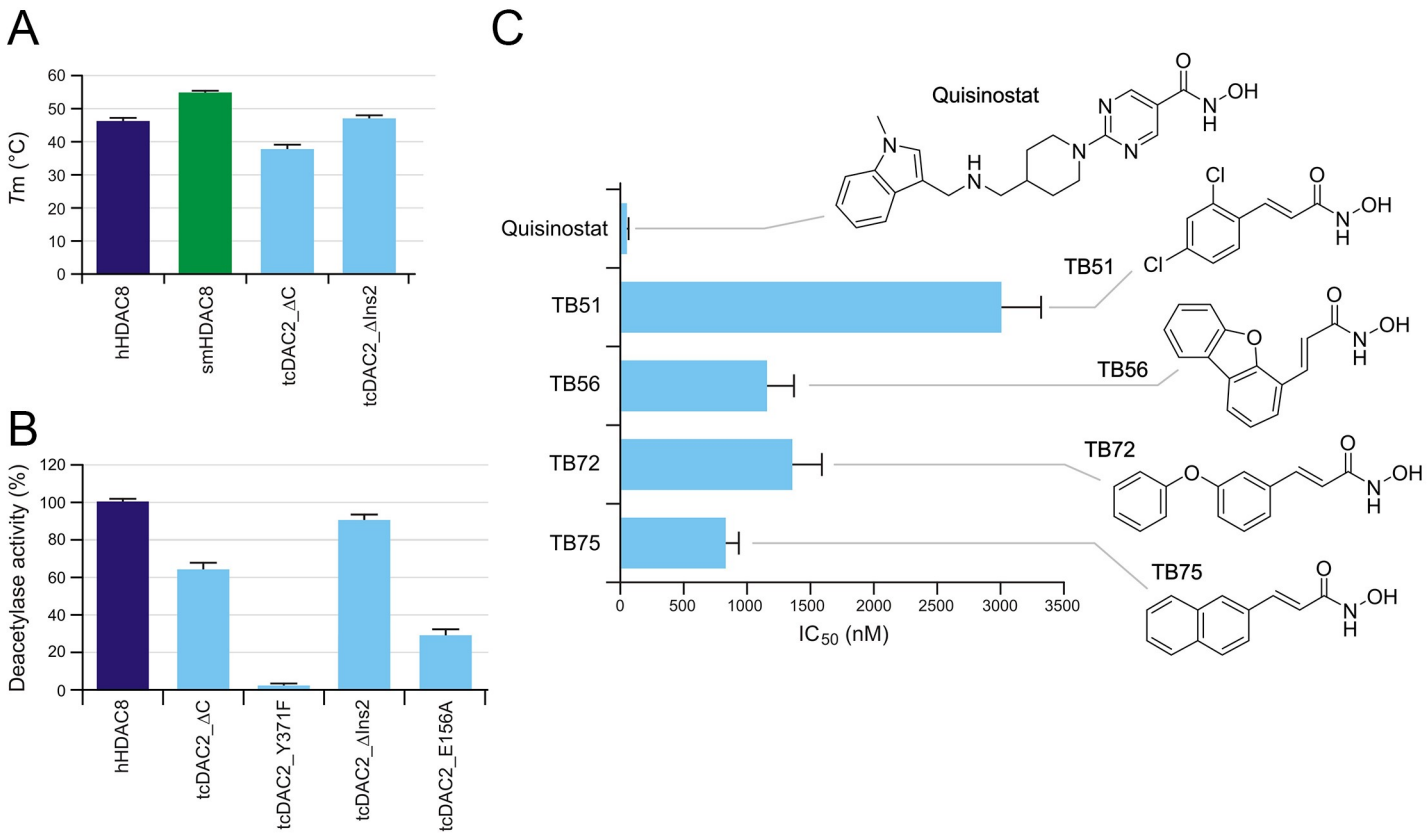
A
Tm (°C)
60
50
40
30
20
10
0
hHDAC8
smHDAC8
tcDAC2_ΔC
tcDAC2_ΔIns2
B
Deacetylase activity (%)
120
100
80
60
40
20
0
hHDAC8
tcDAC2_ΔC
tcDAC2_Y371F
tcDAC2_ΔIns2
tcDAC2_E156A
C
Quisinostat
TB51
TB56
TB72
TB75
0
500
1000
1500
2000
2500
3000
3500
IC50 (nM)
Quisinostat
TB51
TB56
TB72
TB75

Figure 4

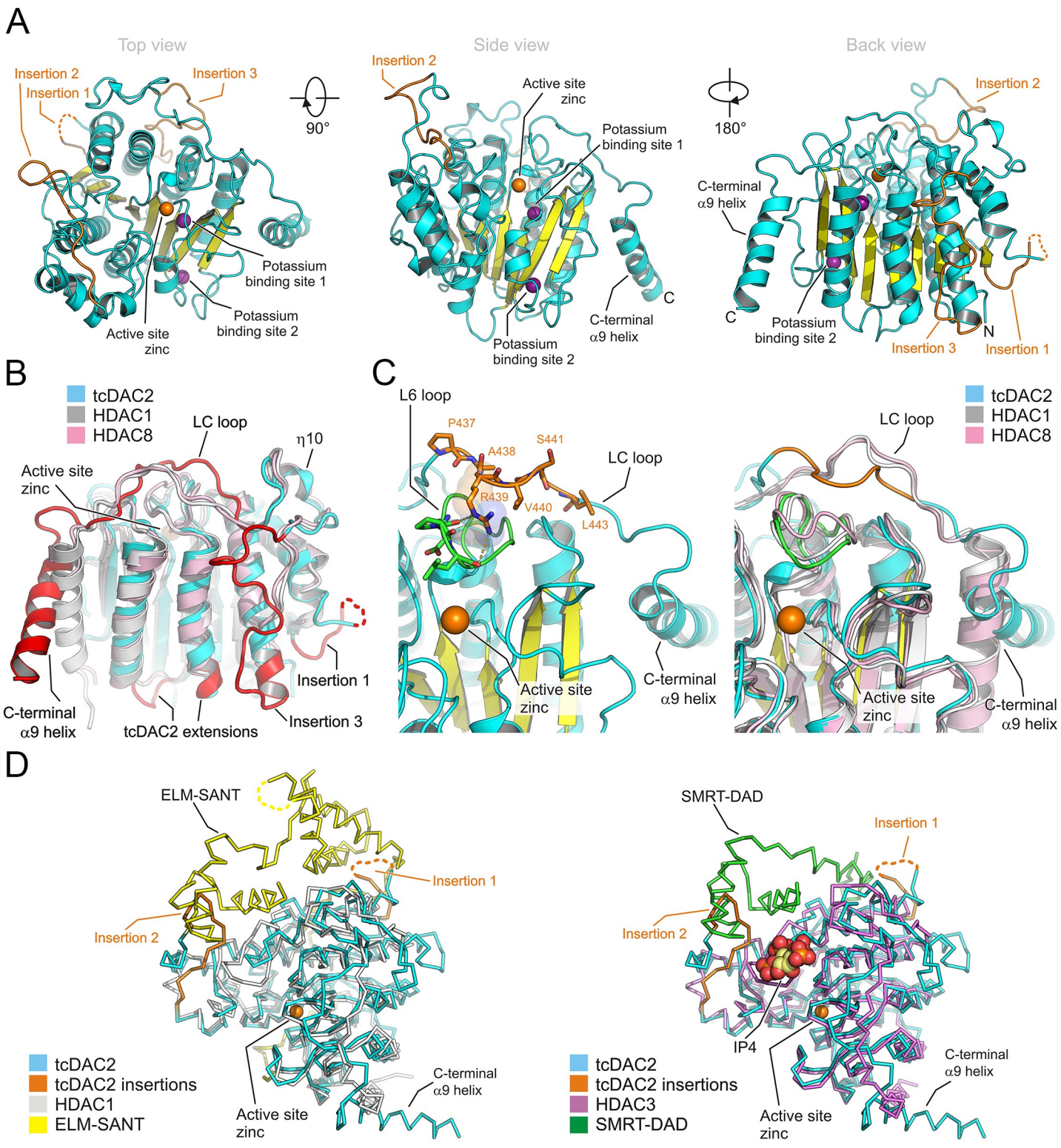
A
Top view
Insertion 2
Insertion 1
Insertion 3
90°
Potassium binding site 1
Potassium binding site 2
Active site zinc
Side view
Insertion 2
Active site zinc
Potassium binding site 1
C
C-terminal α9 helix
Potassium binding site 2
Back view
180°
Insertion 2
C-terminal α9 helix
C
Potassium binding site 2
N
Insertion 3
Insertion 1
B
tcDAC2
HDAC1
HDAC8
LC loop
η10
Active site zinc
Insertion 1
C-terminal α9 helix
tcDAC2 extensions
Insertion 3
C
L6 loop
P437
A438
S441
LC loop
R439
V440
L443
Active site zinc
C-terminal α9 helix
tcDAC2
HDAC1
HDAC8
LC loop
Active site zinc
C-terminal α9 helix
D
ELM-SANT
Insertion 1
Insertion 2
tcDAC2
tcDAC2 insertions
HDAC1
ELM-SANT
Active site zinc
C-terminal α9 helix
SMRT-DAD
Insertion 1
Insertion 2
IP4
tcDAC2
tcDAC2 insertions
HDAC3
SMRT-DAD
Active site zinc
C-terminal α9 helix

Figure 5

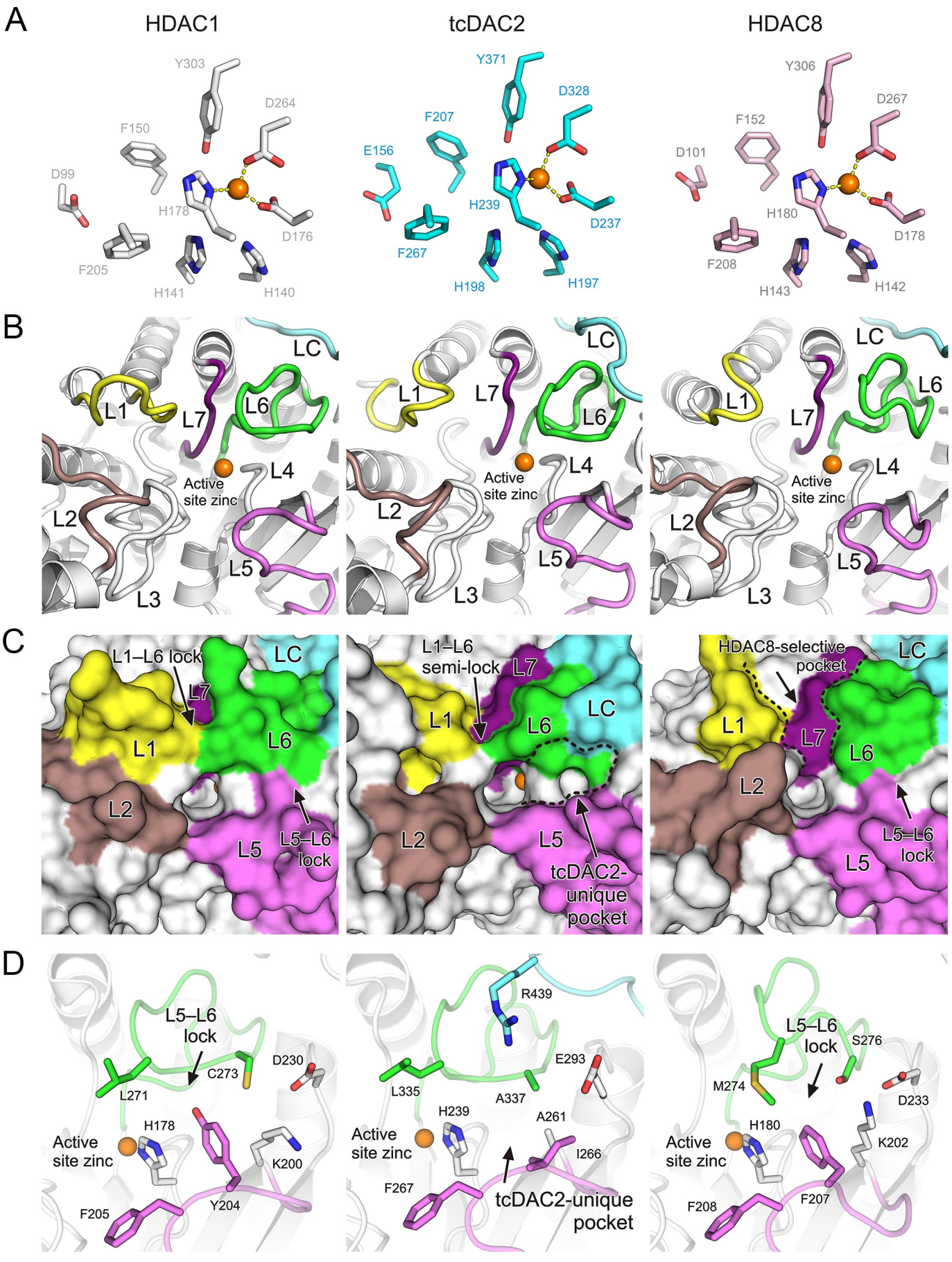
A
HDAC1
tcDAC2
HDAC8
Y303
D264
F150
D99
H178
D176
F205
H141
H140
Y371
D328
F207
E156
H239
D237
F267
H198
H197
Y306
D267
F152
D101
H180
D178
F208
H143
H142
B
LC
L1
L7
L6
L4
Active site zinc
L2
L5
L3
C
L1–L6 lock
L1–L6 semi-lock
HDAC8-selective pocket
L5–L6 lock
tcDAC2-unique pocket
D
L5–L6 lock
C273
D230
L271
H178
Active site zinc
K200
F205
Y204
R439
E293
L335
A337
H239
A261
I266
F267
tcDAC2-unique pocket
S276
M274
D233
H180
K202
F208
F207

Figure 6

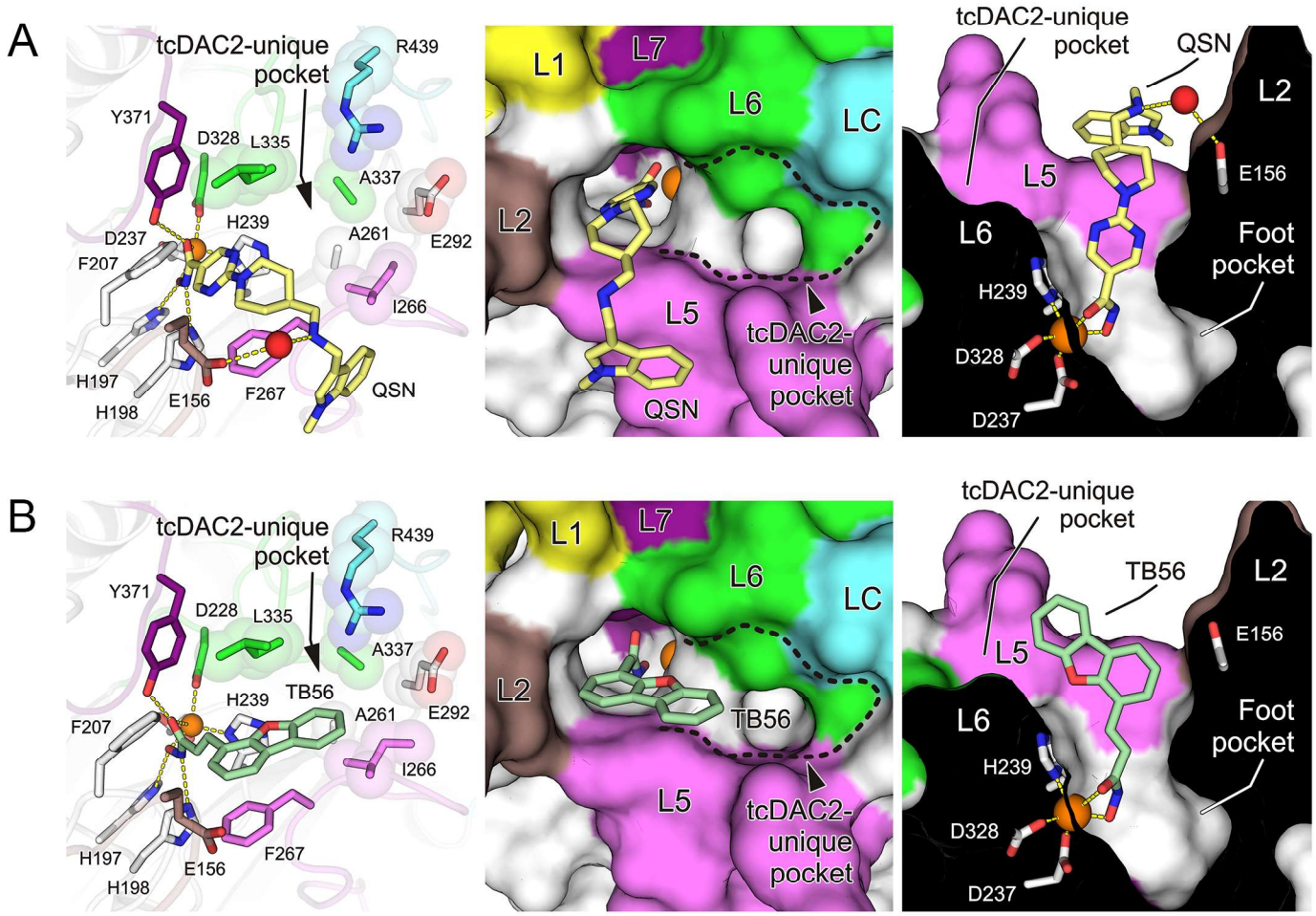
A
tcDAC2-unique pocket
R439
Y371
D328
L335
A337
H239
D237
A261
E292
F207
I266
H197
H198
E156
F267
QSN
L1
L7
L6
LC
L2
L5
tcDAC2-unique pocket
QSN
tcDAC2-unique pocket
QSN
L2
E156
L5
L6
Foot pocket
H239
D328
D237
B
tcDAC2-unique pocket
R439
Y371
D228
L335
A337
H239
TB56
A261
E292
F207
I266
H197
H198
E156
F267
L1
L7
L6
LC
L2
TB56
L5
tcDAC2-unique pocket
tcDAC2-unique pocket
TB56
L2
E156
L5
L6
Foot pocket
H239
D328
D237

Figure 7

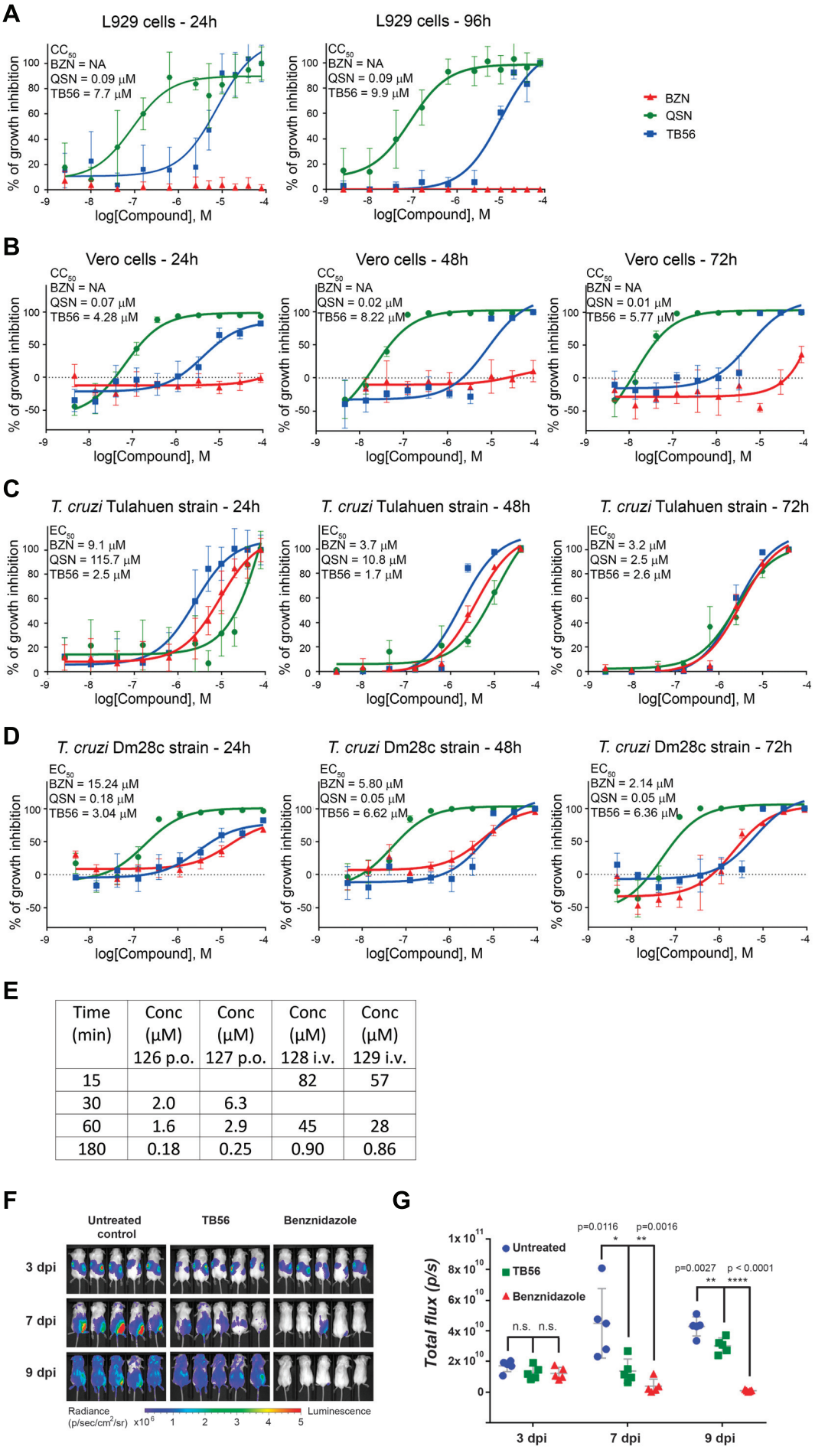

E

Time (min)	Conc (µM) 126 p.o.	Conc (µM) 127 p.o.	Conc (µM) 128 i.v.	Conc (µM) 129 i.v.
15			82	57
30	2.0	6.3		
60	1.6	2.9	45	28
180	0.18	0.25	0.90	0.86

Species-selective epigenetic targeting of pathogens revealed by the atypical structure and active site of *Trypanosoma cruzi* histone deacetylase DAC2

Marek, M., Ramos-Morales, E., Picchi-Constante, G.F.A., Bayer, T., Norström, C., Herp, D., Sales-Junior, P.A., Guerra-Slompo, E.P., Hausmann, K., Chakrabarti, A., Shaik, T.B., Merz, A., Troesch, E., Schmidtkunz, K., Goldenberg, S., Pierce, R.J., Mourão, M.M., Jung, M., Schultz, J., Sippl, W., Zanchin, N.I.T. and Romier, C.

Supplementary Information

A

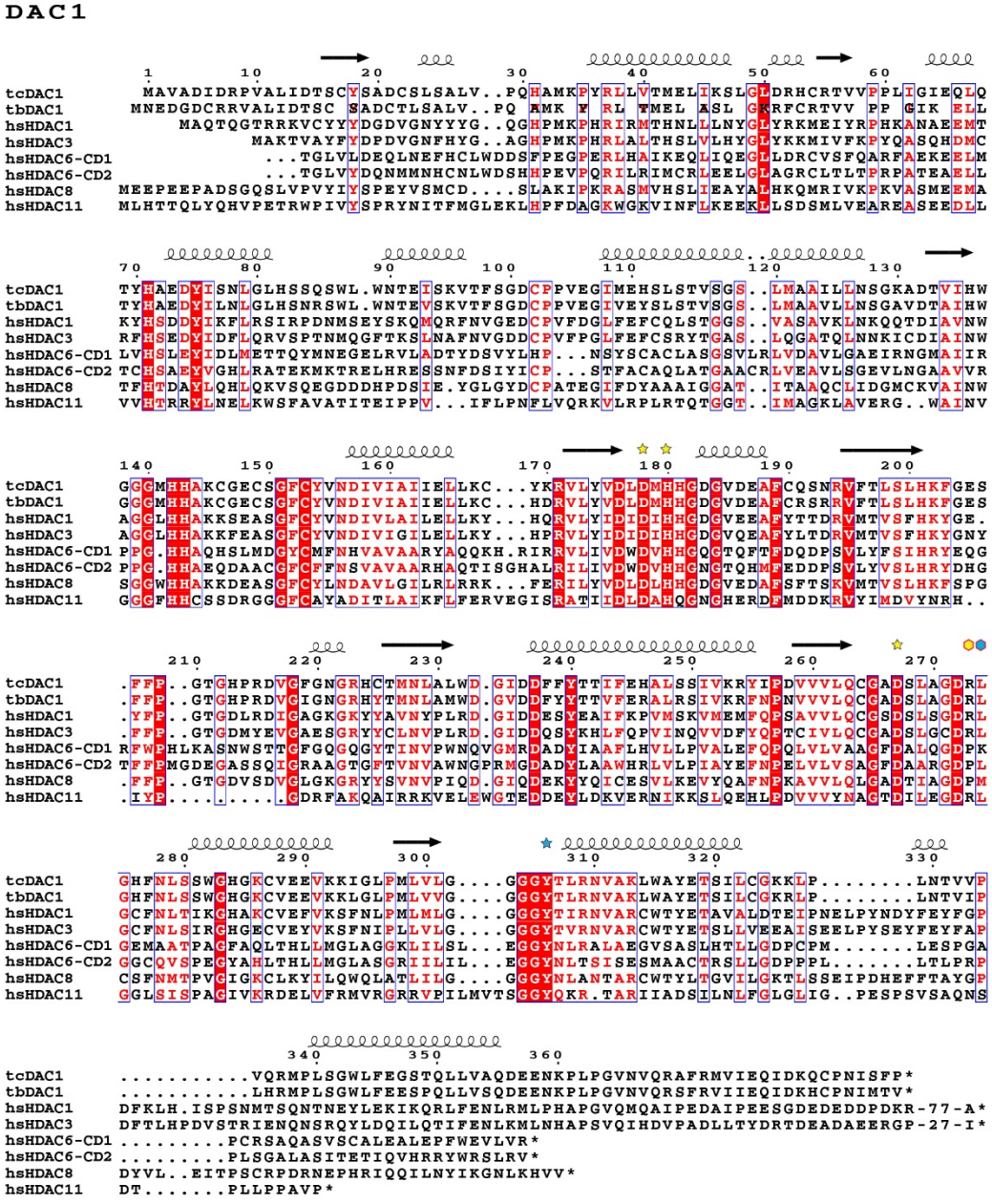
DAC1
tcDAC1
tbDAC1
hsHDAC1
hsHDAC3
hsHDAC6-CD1
hsHDAC6-CD2
hsHDAC8
hsHDAC11

B

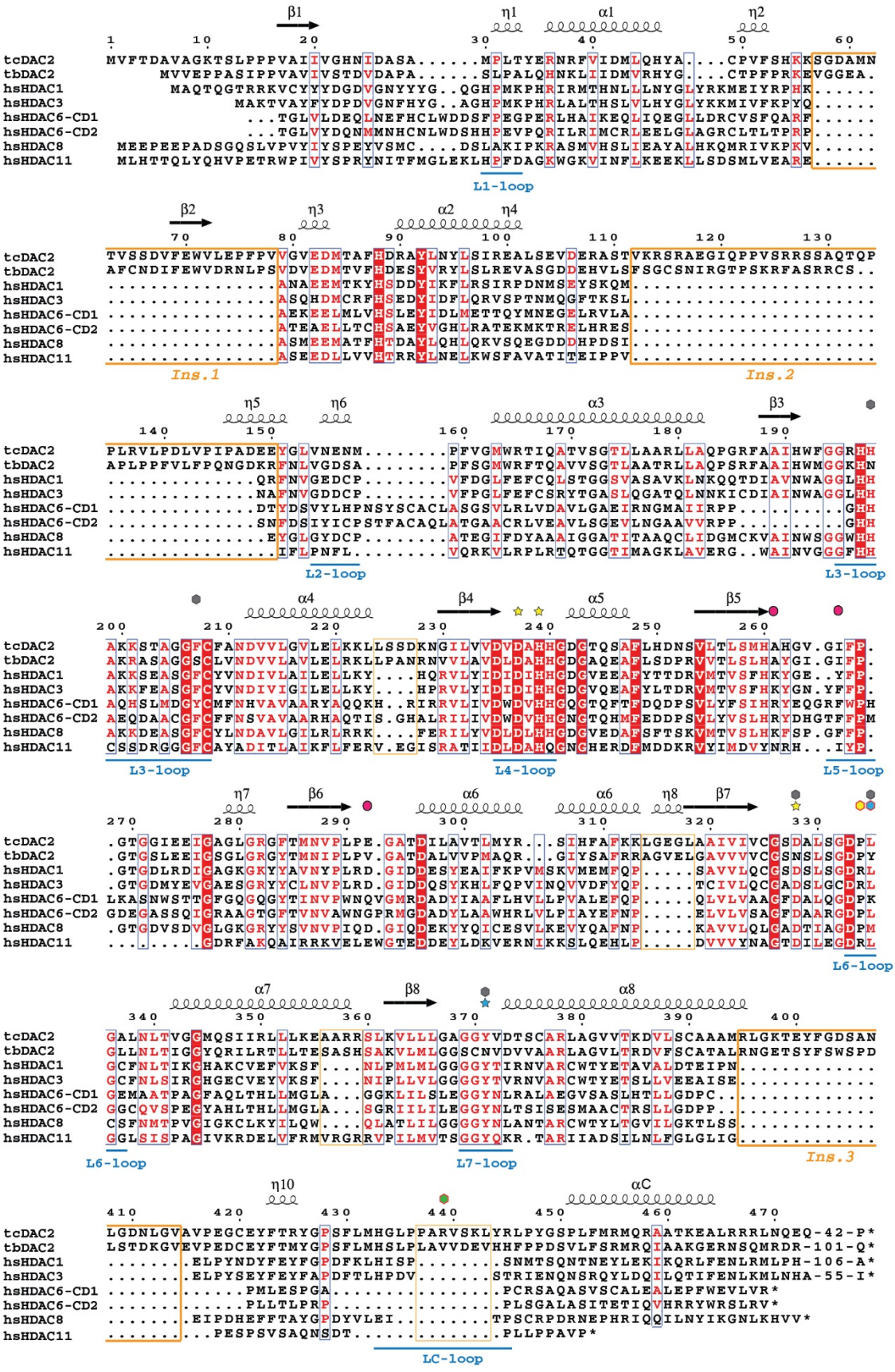
DAC2
tcDAC2
tbDAC2
hsHDAC1
hsHDAC3
hsHDAC6-CD1
hsHDAC6-CD2
hsHDAC8
hsHDAC11
L1-loop
Ins.1
Ins.2
L2-loop
L3-loop
L4-loop
L5-loop
L6-loop
L7-loop
Ins.3
LC-loop

C

DAC3

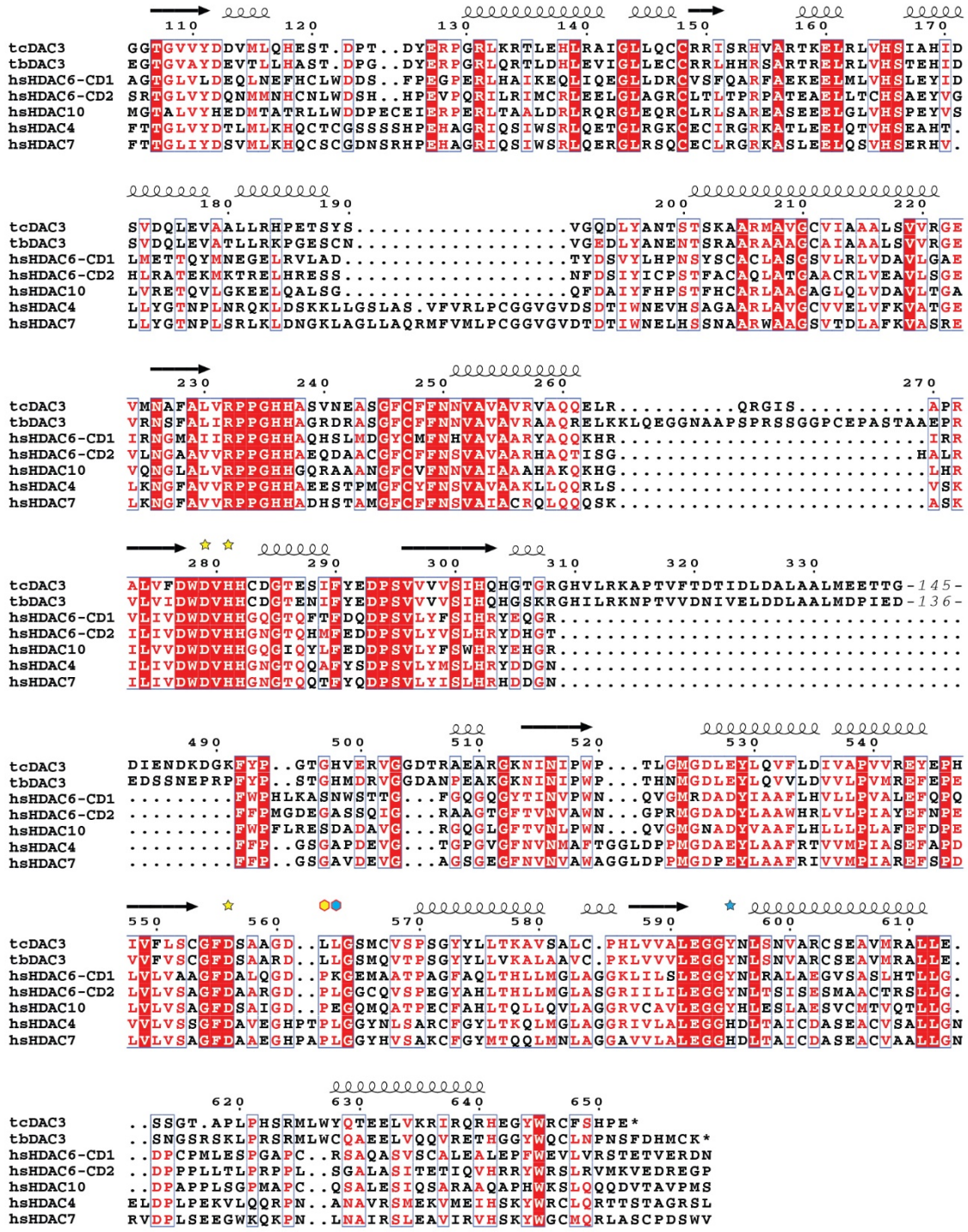
110 120 130 140 150 160 170
tcDAC3 GGTGVVYDDVMLQHEST.DPT..DYERPGRLKRTLEHLRAIGLLQCCRRISRHVARTKELRLVHSIAHID
tbDAC3 EGTGVAYDEVTLLHAST.DPG..DYERPGRLQRTLDHLEVIGLLECCRRLHHRSARTRELRLVHSTEHID
hsHDAC6-CD1 AGTGLVLDEQLNEFHCLWDDS..FPEGPERLHAIKEQLIQEGLLDRCVSFQARFAEKEELMLVHSLEYID
hsHDAC6-CD2 SRTGLVYDQNMMNHCNLWDSH..HPEVPQRILRIMCRLEELGLAGRCLTLTPRPATEAELLTCHSAEYVG
hsHDAC10 MGTALVYHEDMTATRLLWDDPECEIERPERLTAALDRLRQRGLEQRCLRLSARERASEEELGLVHSPEYVS
hsHDAC4 FTTGLVYDTLMLKHQCTCGSSSSHPEHAGRIQSIWSRLQETGLRGKCECIRGRKATLEELQTVHSEAHT.
hsHDAC7 FTTGLIYDSVMLKHQCSCGDNSRHPEHAGRIQSIWSRLQERGLRSQCECLRGRKASLEELQSVHSERHV.
180 190 200 210 220
tcDAC3 SVDQLEVAALLRHPETSYS.....VGQDLYANTSTSKAARMAVGCVIAAALSVVRGE
tbDAC3 SVDQLEVATLLRKPGESCN.....VGEDLYANENTSRAARAAAGCAIAAALSVVRGE
hsHDAC6-CD1 LMETTQYMNEGELRVLAD.....TYDSVYLHPNSYSCACLASGSVLRLVDAVLGAE
hsHDAC6-CD2 HLRATEKMKTRELHRESS.....NFDSIYICPSTFACAQLATGAACRLVEAVLSGE
hsHDAC10 LVRETQVLGKEELQALSG.....QFDAIYFHPSTFHCARLAAGAGLQLVDAVLTGA
hsHDAC4 LLYGTNPLNRQKLDSKKLLGSLAS.VFVRLPCGGVGVDSDTIWNEVHSAGAARLAVGCVVELVFKVATGE
hsHDAC7 LLYGTNPLSRLKLDNGKLAGLLAQRMFVMLPCGGVGVDTDTIWNELHSSNAARWAAGSVTDLAFKVASRE
230 240 250 260 270
tcDAC3 VMNAFALVRPPGHHASVNEASGFCFFNNVAVAVRVAQQELR.....QRGIS.....APR
tbDAC3 VRNSFALIRPPGHHAGRDRASGFCFFNNVAVAVRAAQRELKKLQEGGNAAPSPRSSGGPCEPASTAAEPR
hsHDAC6-CD1 IRNGMAIIRPPGHHAQHSLMDGYCMFNHVAVAARYAQQKHR.....IRR
hsHDAC6-CD2 VLNGAAVVRPPGHHAEQDAACGFCFFNSVAVAARHAQTISG.....HALR
hsHDAC10 VQNGLALVRPPGHHGQRAAANGFCVFNNVAIAAAHAKQKHG.....LHR
hsHDAC4 LKNGFAVVRPPGHHAEESTPMGFCYFNSVAVAAKLLQQRLS.....VSK
hsHDAC7 LKNGFAVVRPPGHHADHSTAMGFCFFNSVAIACRQLQQQSK.....ASK
280 290 300 310 320 330
tcDAC3 ALVFDWDVHHCDGTESIFYEDPSVVVVSIHQHGTGRGHVLRKAPTVFTDTIDLDALAALMEETTG-145-
tbDAC3 VLVIDWDVHHCDGTENIFYEDPSVVVVSIHQHGSKRGHILRKNPTVVDNIVELDDLAALMDPIED-136-
hsHDAC6-CD1 VLIVDWDVHHGQGTQFTFDQDPSVLYFSIHRYEQGR.....
hsHDAC6-CD2 ILIVDWDVHHGNGTQHMFEDDPSVLYVSLHRYDHGT.....
hsHDAC10 ILVVDWDVHHGQGIQYLFEDDPSVLYFSWHRYEHGR.....
hsHDAC4 ILIVDWDVHHGNGTQQAFYSDPSVLYMSLHRYDDGN.....
hsHDAC7 ILIVDWDVHHGNGTQQTFYQDPSVLYISLHRHDDGN.....
490 500 510 520 530 540
tcDAC3 DIENDKDGKFYP..GTGHVERVGGDTRAEARGKNINIPWP...TLGMGDLEYLQVFLDIVAPVVREYEPH
tbDAC3 EDSSNEPRPFYP..STGHMDRVGGDANPEAKGKNINIPWP...THNMGDLEYLQVVLDVVLPVMREFEPE
hsHDAC6-CD1 .....FWPHLKASNWSTTG...FGQGQGYTINVPWN...QVGMRDADYIAAFLHVLLPVALEFQPQ
hsHDAC6-CD2 .....FFPMGDEGASSQIG...RAAGTGFTVNVAWN...GPRMGDADYLAAWHRLVLPIAYEFNPE
hsHDAC10 .....FWPFLRESDADAVG...RGQGLGFTVNLPWN...QVGMGNADYVAAFLHLLLPLAFEFDPE
hsHDAC4 .....FFP..GSGAPDEVG...TGPGVGFNVNMAFTGGLDPPMGDAEYLAAFRTVVMPIASEFAPD
hsHDAC7 .....FFP..GSGAVDEVG...AGSGEGFNVNVAWAGGLDPPMGDPEYLAAFRIVVMPIAREFSPD
550 560 570 580 590 600 610
tcDAC3 IVFLSCGFDSAAGD..LLGSMCVSPSGYYLLTKAVSALC.PHLVVALEGGYNLSNVARCSEAVMRALLE.
tbDAC3 VVFVSCGFDSAARD..LLGSMQVTPSGYYLLVKALAAVC.PKLVVVLEGGYNLSNVARCSEAVMRALLE.
hsHDAC6-CD1 LVLVAAGFDALQGD..PKGEMAATPAGFAQLTHLLMGLAGGKLILSLEGGYNLRALAEGVSASLHTLLG.
hsHDAC6-CD2 LVLVSAGFDAARGD..PLGCQVSPEGYAHLTHLLMGLASGRIILILEGGYNLTSISESMAACTRSLLG.
hsHDAC10 LVLVSAGFDSAIGD..PEGQMQATPECFAHLTQLLQVLAGGRVCAVLEGGYHLESLAESVCMTVQTLLG.
hsHDAC4 VVLVSSGFDAVEGHPTPLGGYNLSARCFGYLTKQLMGLAGGRIVLALEGGHDLTAICDASEACVSALLGN
hsHDAC7 LVLVSAGFDAAEGHPAPLGGYHVSAKCFGYMTQQLMNLAGGAVVLALEGGHDLTAICDASEACVAALLGN
620 630 640 650
tcDAC3 ..SSGT.APLPHSRMLWYQTEELVKRIRQRHEGYWRCFSHPE*
tbDAC3 ..SNGSRSKLPRSRMLWCQAEELVQQVRETHGGYWQCLNPNSFDHMCK*
hsHDAC6-CD1 ..DPCPMLESPGAPC..RSAQASVSCALEALEPFWEVLVRSTETVERDN
hsHDAC6-CD2 ..DPPPLLTLPRPPL..SGALASITETIQVHRRYWRSLRVMKVEDREGP
hsHDAC10 ..DPAPPLSGPMAPC..QSALESIQSARAAQAPHWKSLQQDVTAVPMS
hsHDAC4 ELDPLPEKVLQQRPN..ANAVRSMEKVMEIHSKYWRCLQRTTSTAGRSL
hsHDAC7 RVDPLSEEGWKQKPN..LNAIRSLEAVIRVHSKYWGCMQRLASCPDSWV

D

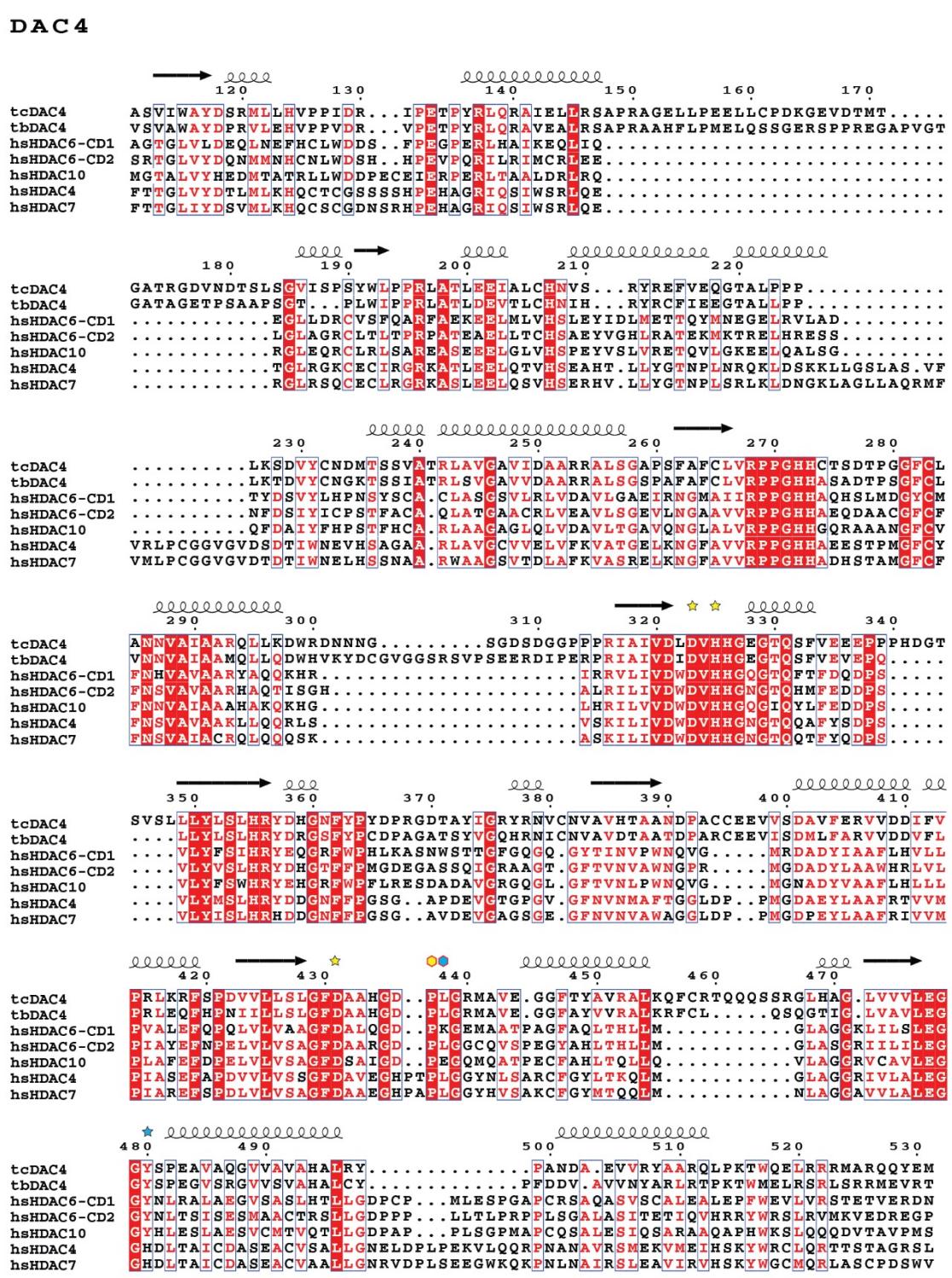
DAC4
tcDAC4
tbDAC4
hsHDAC6-CD1
hsHDAC6-CD2
hsHDAC10
hsHDAC4
hsHDAC7

Supplementary Figure 1. Multiple sequence alignments of the trypanosome HDACs.

(A) Multiple sequence alignment of trypanosome (tc, *Trypanosoma cruzi*; tb, *Trypanosoma brucei*) DAC1 enzymes with class I, class IIb and class IV human (hs) HDACs. Residues involved in zinc binding are shown with yellow stars, the catalytic tyrosine as blue star. The yellow diamond marks the residue in the active site L6 loop distinguishing the HDAC1-3 and HDAC11 isozymes subfamilies from the other human HDAC isozymes. The blue diamond marks the neighbouring residue in the L6 loop gatekeeping the HDAC active sites. Secondary structure elements from hsHDAC1 are shown above the alignment. The C-terminal sequences of some HDACs have been removed for clarity and the number of residues removed is indicated. '*' mark the end of the sequences. **(B)** Same as in (A) for DAC2 enzymes. Insertions specific to DAC2 enzymes are boxed and active site loops are indicated. The green diamond marks the arginine that caps tcDAC2 L6 loop. Purple circles mark important residues forming the tcDAC2-unique pocket. Grey diamonds mark non-conserved active site residues in tbDAC2. Secondary structure elements (α, α-helices; β, β-strands; η, 3_{10}-helices) are those observed in tcDAC2 structure. **(C)** Same as in (A) for DAC3 enzymes and human class IIa and IIb HDACs. For clarity, the large insertion in the middle of the DAC3 enzymes is only partially shown and the number of residues removed from the alignment is displayed. **(D)** Same as in (C) for DAC4 enzymes. The alignments were produced with Espript (Robert and Gouet, 2014).

A

	hHDAC1	hHDAC2	hHDAC3	hHDAC8	tbDAC1	tcDAC1	tbDAC2	tcDAC2
hHDAC1		92,6	63,0	39,5	39,1	39,1	26,1	25,5
hHDAC2	97,3		61,7	39,7	38,7	36,4	23,7	26,2
hHDAC3	82,0	80,7		39,8	37,7	39,6	26,2	25,2
hHDAC8	60,5	61,0	59,4		33,4	32,3	25,8	25,1
tbDAC1	55,3	55,4	50,4	52,10		85,6	25,4	25,1
tcDAC1	55,1	50,0	54,8	51,10	92,3		27,1	25,0
tbDAC2	41,7	37,1	38,4	41,70	37,2	38,1		51,0
tcDAC2	37,4	40,6	37,7	39,80	33,5	38,9	64,7	

Identities

Similarities

B

	hHDAC4	hHDAC7	hHDAC6CD1	hHDAC6CD2	hHDAC10CD1	tbDAC3	tcDAC3	tbDAC4	tcDAC4
hHDAC4		73,9	37,9	44,7	36,2	30,1	32,9	26,3	25,0
hHDAC7	85,3		36,8	43,0	36,6	32,6	33,0	23,2	28,3
hHDAC6CD1	52,6	51,9		47,0	54,0	30,2	31,8	24,5	26,0
hHDAC6CD2	57,8	54,1	63,9		50,8	32,5	33,9	26,3	28,0
hHDAC10CD1	52,4	51,1	70,9	64,9		33,2	33,3	23,2	28,0
tbDAC3	42,4	44,8	43,5	46,5	45,6		64,0	25,0	26,9
tcDAC3	47,6	46,0	45,0	47,9	47,1	74,5		27,8	26,9
tbDAC4	37,7	31,2	36,1	36,2	31,6	38,1	40,4		63,3
tcDAC4	33,4	38,7	37,8	39,0	39,3	40,7	39,2	74,4	

Identities

Similarities

C

	tbDAC1	tcDAC1	tbDAC2	tcDAC2	tbDAC3	tcDAC3	tbDAC4	tcDAC4
tbDAC1		85,6	25,4	21,5	23,2	24,9	18,7	18,6
tcDAC1	92,3		27,1	25,0	28,0	21,6	16,4	16,8
tbDAC2	37,2	38,1		51,0	18,0	18,6	18,8	21,9
tcDAC2	33,5	38,9	64,7		22,3	19,0	19,2	20,9
tbDAC3	36,0	34,9	28,4	34,3		64,0	25,0	26,9
tcDAC3	35,4	33,6	29,0	30,4	74,5		27,8	26,9
tbDAC4	31,1	27,6	28,9	32,4	38,1	40,4		63,3
tcDAC4	29,4	29,0	32,6	33,4	40,7	39,2	74,4	

Identities

Similarities

< 20%	20-30%	30-40%	40-50%	50-60%	60-70%	70-80%	80-90%	> 90%

Supplementary Figure 2. Sequence identities/similarities between human and trypanosome HDACs.

(A-C) Sequence identities (upper right part of the tables) and sequence similarities (lower left part of the tables) between (A) class I human and trypanosome HDACs, (B) class II human and trypanosome HDACs, and (C) trypanosome HDACs. The colour code is provided at the bottom of the figure. Sequence identities/similarities were calculated with the EMBOSS Needle program using only the catalytic domains of each HDAC as defined by structural data. Sequence boundaries of the catalytic domains for the trypanosome HDACs, except for the DAC2 enzymes, were defined based on their multiple sequence alignments. The large additional domain within DAC3 enzymes was removed for sequence identities/similarities calculations.

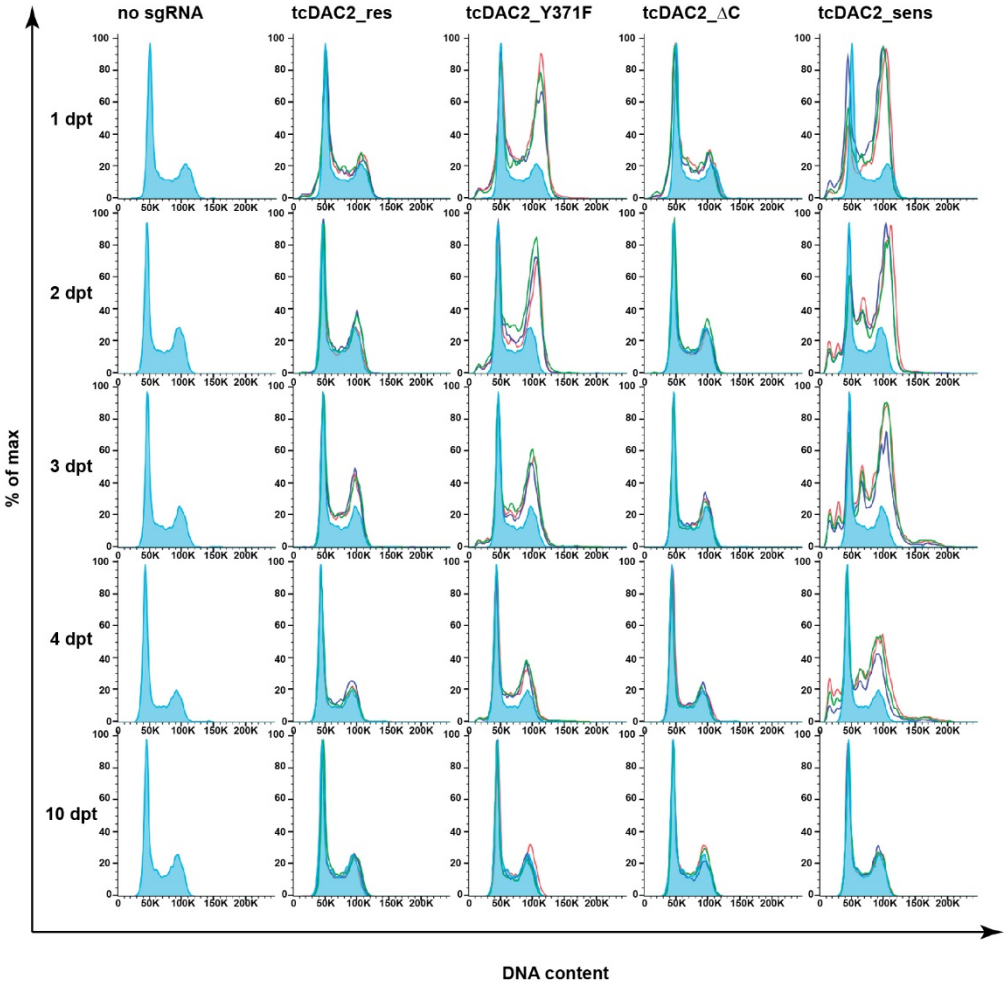

Supplementary Figure 3. tcDAC2 complementation assay shows lethal phenotype for the Y371F mutation but not for removal of the non-conserved acidic C-terminal tail.

The genetic complementation strategy is based on the CRISPR-Cas9 technology combined with two variants of the tcDAC2 gene sequences, one sensitive and another resistant to a specific sgRNA, as described in the Material and Methods Section. Cell cycle progression of the cell lines carrying the different genetic variants was analyzed at the indicated times after sgRNA transfection. Cyan curves show wild-type cell profiles. The red, blue and green line curves show mutant cell profiles done in triplicate. The tcDAC2_sens variant is the negative control (knockout phenotype) and the tcDAC2_res variant is the positive control for tcDAC2 complementation. The tcDAC2_Y371F and tcDAC2_ΔC variants contain, respectively, the substitution of the catalytic tyrosine residue by a phenylalanine and a deletion of the glutamic acid-rich C-terminal region. The tcDAC2_Y371F variant shows phenotype similar to the tcDAC2_sens variant which does not complement deletion of the genomic copy of tcDAC2. dpt – days post-transfection.

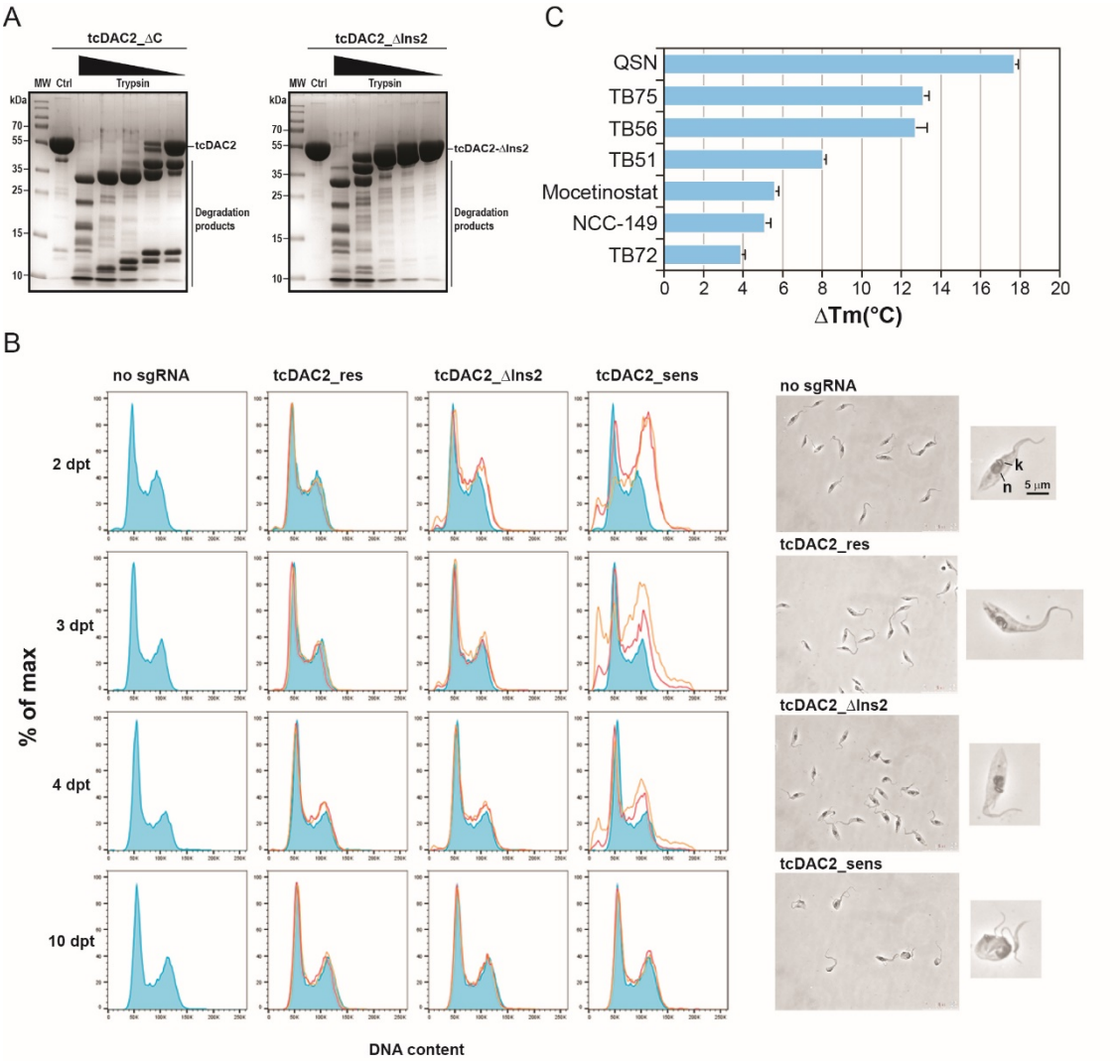

Supplementary Figure 4. Stabilization of tcDAC2 by protein engineering and inhibitors.

(A) Comparative limited proteolysis analysis of tcDAC2_ΔC and tcDAC2_ΔIns2. Removal of a part of Insertion2 in tcDAC2 has a strong protective effect on proteolysis, suggesting that Insertion2 is an accessible surface loop. **(B)** *T. cruzi* complementation assay with tcHDAC2_ΔIns2 shows no deleterious effect of this variant. Cell cycle progression (left) and light microscopy images (right) of parasites carrying the different genetic variants were analyzed at the indicated times after sgRNA transfection. Cyan curves show wild-type cell profiles. The red and yellow line curves show mutant cell profiles. tcHDAC2_sens: negative control (knockout phenotype); tcHDAC2-res: positive control for tcHDAC2 complementation; tcHDAC2_ΔIns2: loop deletion. The phenotype of cells carrying the tcHDAC2_ΔIns2 and tcDAC2_res variants is similar showing that tcHDAC2_ΔIns2 can efficiently complement tcDAC2 gene deletion. n – nucleus, k – kinetoplast, dpt – days post-transfection. **(C)** Thermal stability of tcDAC2_Δins2 in presence of various inhibitors. The values on the abscissa represent the gain in °C of melting temperature (ΔTm) of the inhibited enzyme compared to the enzyme alone.

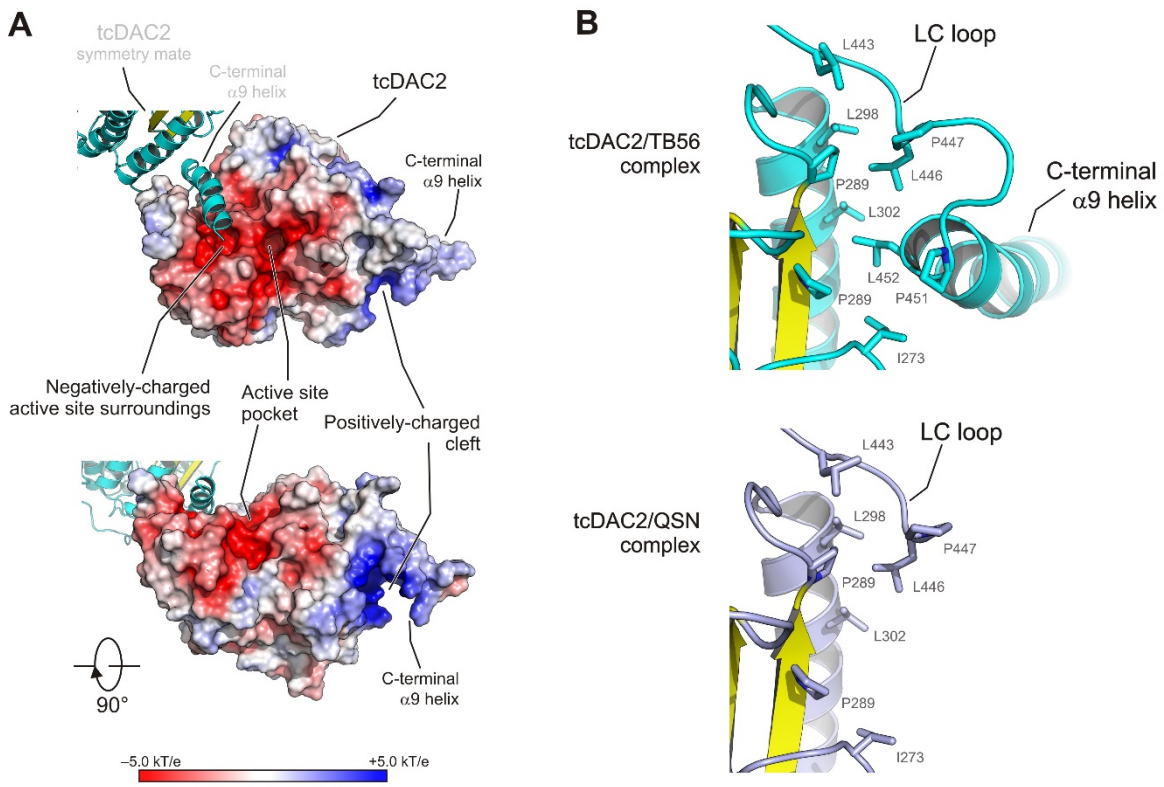

Supplementary Figure 5. Non-canonical nature of tcDAC2 C-terminal helix (α9).

(A) Crystallographic contacts made by tcDAC2 α9 C-terminal helix. The electrostatic potential (red, negative potential; blue, positive potential) is displayed at the surface of the crystallographic symmetric tcDAC2 monomer. This shows that both tcDAC2 α9 C-terminal helix and the region of tcDAC2 core, where HDACs normally interact with their C-terminal helices, are both positively charged. This explains that these two regions cannot interact with each other due to repulsive electrostatic contacts. **(B)** Hydrophobic interactions positioning differently the start of tcDAC2 αC-helix. These features are mostly conserved in both structures solved, showing that they cannot be due to the crystal packing observed in the tcDAC2/TB56 structure.

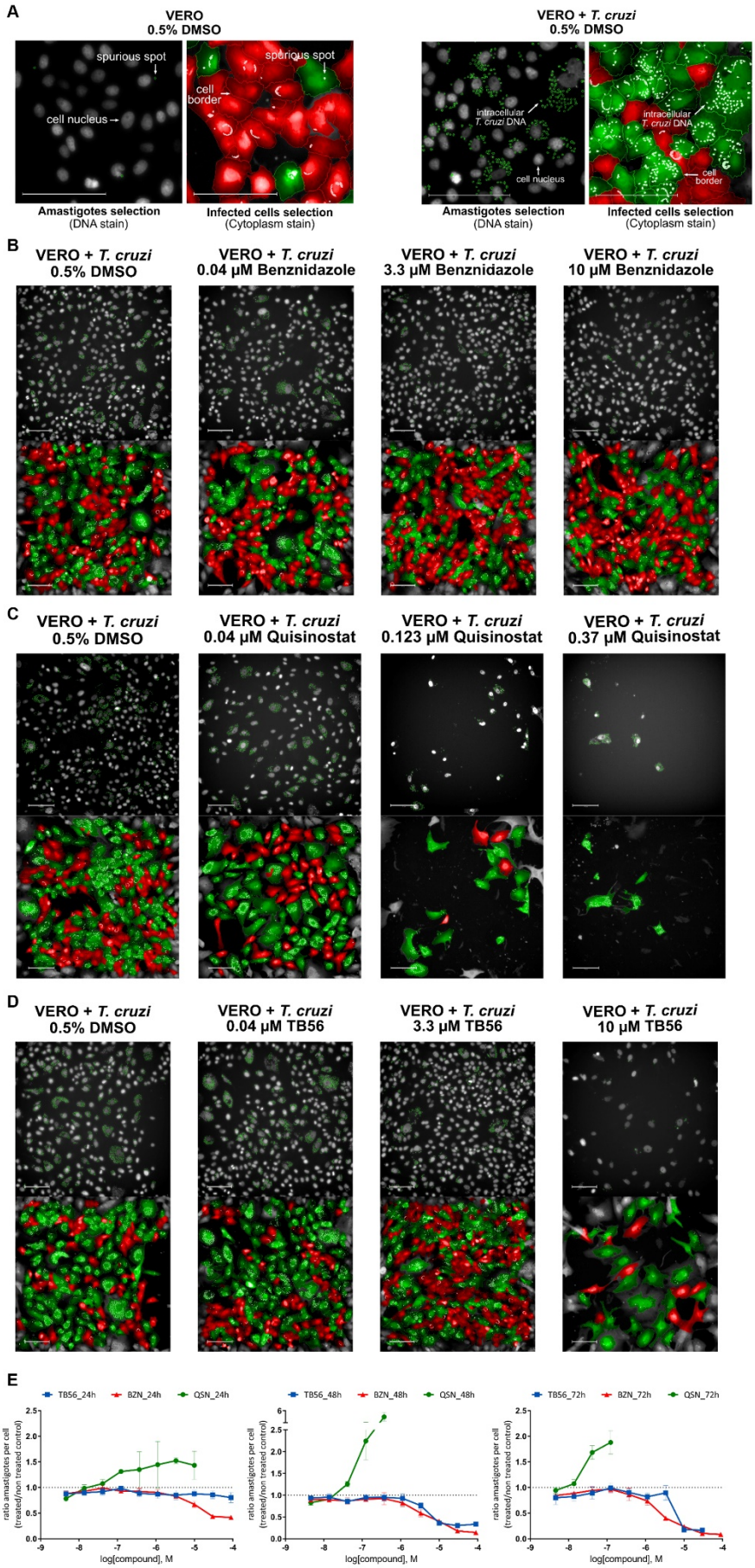
A
VERO
0.5% DMSO
spurious spot
cell nucleus
spurious spot
cell border
Amastigotes selection
(DNA stain)
Infected cells selection
(Cytoplasm stain)
VERO + T. cruzi
0.5% DMSO
intracellular T. cruzi DNA
cell nucleus
intracellular T. cruzi DNA
cell border
Amastigotes selection
(DNA stain)
Infected cells selection
(Cytoplasm stain)
B
VERO + T. cruzi
0.5% DMSO
VERO + T. cruzi
0.04 µM Benznidazole
VERO + T. cruzi
3.3 µM Benznidazole
VERO + T. cruzi
10 µM Benznidazole
C
VERO + T. cruzi
0.5% DMSO
VERO + T. cruzi
0.04 µM Quisinostat
VERO + T. cruzi
0.123 µM Quisinostat
VERO + T. cruzi
0.37 µM Quisinostat
D
VERO + T. cruzi
0.5% DMSO
VERO + T. cruzi
0.04 µM TB56
VERO + T. cruzi
3.3 µM TB56
VERO + T. cruzi
10 µM TB56
E
TB56_24h
BZN_24h
QSN_24h
TB56_48h
BZN_48h
QSN_48h
TB56_72h
BZN_72h
QSN_72h
ratio amastigotes per cell (treated/non treated control)
log[compound], M

Supplementary figure 6. Representative images from high-content image-based experiments for the determination of *T. cruzi* inhibition by Benznidazole (BZN), Quisinostat (QSN) and TB56 in Vero cells infection assays.

(A) Representative images of uninfected (left images) and infected (right images) control cells both treated with DMSO showing the relevant features for assay quantification. Nuclei from Vero cells and from intracellular *T. cruzi* amastigotes were visualized by staining the DNA with 1 µg/mL DAPI. The images of the left panels show the DNA-stained nuclei of Vero cells (grey) and *T. cruzi* amastigote spots (green). In the right panels, Vero cells border and *T. cruzi* amastigotes spots were determined using the Harmony software (PerkinElmer). In addition, the images on the right panels show overlays of the DNA-stained images with the images of the cell borders and *T. cruzi* amastigotes spots (white). The non-infected and infected Vero cells are shown in red and green, respectively. Irregularities in nuclei staining of non-infected Vero cells can be misidentified by the software and are labelled as spurious spots. Size bars = 100 µm. **(B)** Images from the assays performed to determine the inhibition effect of BZN on *T. cruzi* amastigotes in infected Vero cells. Sample images from the cells treated with DMSO and 0.04 µM, 3.3 µM and 10 µM of BZN are shown. **(C)** Images from the assays performed to determine the inhibition effect of QSN on *T. cruzi* amastigotes in infected Vero cells. Sample images from the cells treated with DMSO and the concentrations of 0.04 µM, 0.12 µM and 0.37 µM of QSN are shown. **(D)** Images from the assays performed to determine the inhibition effect of TB56 on *T. cruzi* amastigotes in infected Vero cells. Sample images from the cells treated with DMSO and 0.04 µM, 3.3 µM and 10 µM of TB56 are shown. The images shown in (B-D) are from the median 48h time point. Size bars are 100 µm for all images. **(E)** Determination of the ratio of the number of intracellular *T. cruzi* amastigotes that remain in Vero cell in cultures treated with BZN, QSN and TB56 for 24, 48 and 72 hours. For the QSN (green line) and TB56 (blue line) assays, only the concentration points with living Vero cells are shown in the graphs. As expected, the BZN (red line) treatment leads to a consistent reduction of intracellular amastigotes reaching nearly zero in the higher concentrations at the 48h and 72h time points. In the TB56 assay, the ratio of amastigotes per cell remains constant in the first 24h but decreases similarly to the BZN treatment in the 48h and 72h treatment times. In the case of QSN assay, the ratio of intracellular amastigotes increases. This indicates that the Vero cells die at a faster rate than the intracellular amastigotes.

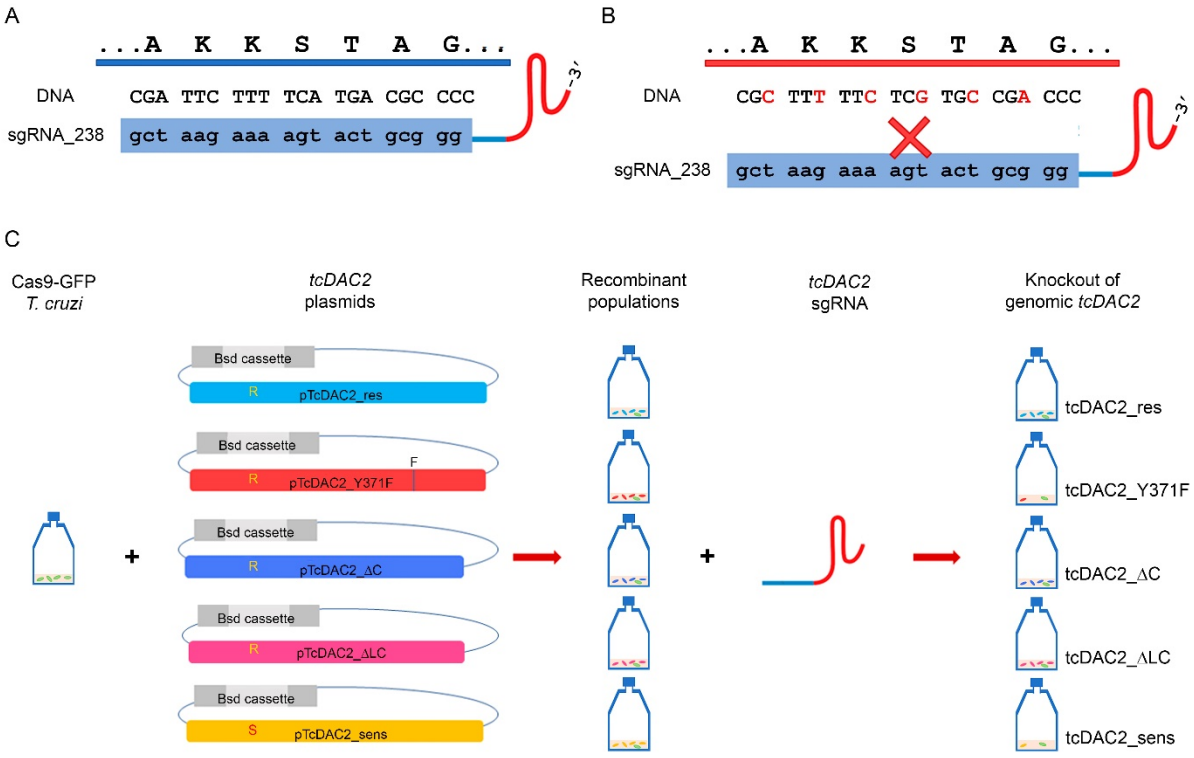

Supplementary Figure 7. Resistant Cas9-cleavage sequences and tcDAC2 complementation assays.

(A) Original tcDAC2 nucleotide sequence at the sgRNA_238 recognition site. This sequence was maintained unaltered in the Cas9 sensitive variant. The sensitive variant (tcDAC2_sens) serves as a control for the knockout phenotype. **(B)** tcDAC2 nucleotide sequence at the sgRNA_238 recognition site with altered nucleotides (indicated in red) to generate a Cas9-resistant variant but keeping the protein sequence unchanged. This resistant variant (tcDAC2_res) was combined with the catalytic site (tcDAC2_Y371F), C-terminal deletion (tcDAC2_ΔC) and loop/C-terminal deletion (tcHDAC2-ΔLC) mutants in *T. cruzi* expression plasmids (tcDAC2 plasmids) allowing for gene replacement to test for complementation of genomic tcDAC2 knockout by the plasmid-borne copy variants of tcDAC2. **(C)** Sequential steps of the complementation assay. Initially, tcDAC2 plasmids were transfected into Cas9-expressing *T. cruzi* cells (left panel). After selection of the five derivative *T. cruzi* transfectants (middle panel), the recombinant populations were transfected with the tcDAC2 sgRNA to knock out the genomic copies of tcDAC2 (right panel) for the phenotypical analyses.

Supplementary Table 1. Inhibitors IC_{50} values (nM resp. % inhibition at the given concentration) for tcDAC2 and selected human HDACs.

Compound	Chemical structure	tcDAC2	hsHDAC1	hsHDAC6	hsHDAC8
SAHA	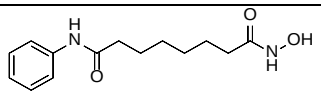	> 10,000	117 ± 6	104 ± 9	400 ± 100
Quisinostat	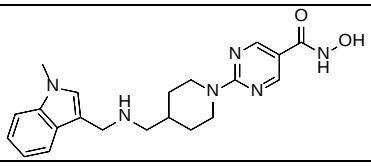	45 ± 5	3 ± 0.3	182 ± 22	65 ± 4
Mocetinostat	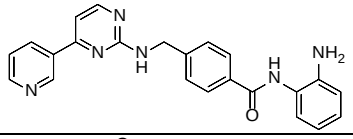	n.i.[a]	10[b] ± 1	68 % @ 20 μM	> 10,000
Entinostat	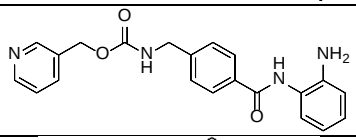	n.i.	519[b] ± 63	< 15 % @ 10 μM	> 10,000[b]
PCI-34051	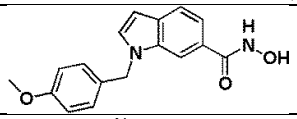	n.i.	> 10,000	> 10,000	92 ± 15
NCC-149	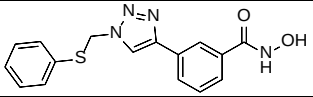	> 10,000	69 % @ 25 μM	96 % @ 25 μM	44 ± 5
TB51	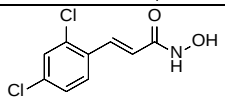	3000 ± 320	3630 ± 190	700 ± 320	420 ± 60
TB56	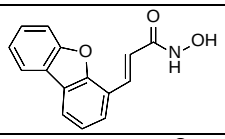	1150 ± 220	3450 ± 100	298 ± 2	770 ± 185
TB72	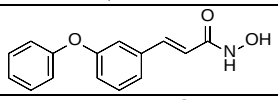	1350 ± 240	2200 ± 200	119 ± 10	113 ± 20
TB75	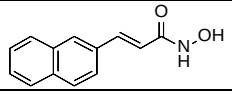	824 ± 111	2220 ± 60	80 ± 21	816 ± 198

[a] n.i., no inhibition observed.

[b] values already published (Hess-Stumpp et al., 2007, Krieger et al., 2019, Marson et al., 2015).

Supplementary Table 2. **Data collection and refinement data statistics**

Data collection*	**tcDAC2/QSN**	**tcDAC2/TB56**
Space group	I222	$P2_1$
Cell dimensions		
a, b, c (Å)	82.17, 93.58, 119.46	66.07, 95.35, 96.92
α, β, γ (°)	90.00, 90.00, 90.00	90.00, 103.50, 90.00
Resolution (Å)	50 – 1.70 (1.81 – 1.70)	50.0 – 2.3 (2.44 – 2.3)
Rsym or Rmerge	11.0 (238.7)	19.5 (168.7)
I / σI	14.2 (1.0)	7.76 (1.23)
Completeness (%)	99.9 (99.5)	99.7 (98.8)
Redundancy	13.3 (13.0)	7.00 (6.78)
CC(1/2)	99.9 (67.4)	99.5 (42.5)
Refinement		
Resolution (Å)	46.79 – 1.75	48.1 – 2.30
No. reflections	46459	51993
Rwork / Rfree	0.183 / 0.214	0.187 / 0.225
Number of atoms		
Protein	3042	6478
Ligand/ion	38	44
Water	226	230
B-factors		
Protein	40.88	45.78
Ligand/ion	42.49	43.87
Water	46.92	98.68
R.m.s. deviations		
Bond lengths (Å)	0.006	0.008
Bond angles (º)	0.776	0.967

** Values in parentheses are for the highest-resolution shell.*

Supplementary table 3. Sequence differences of major active site residues in Trypanosoma strains

Strain	E156 L2	H197 Ac Bind	H198 Ac Bind	F207 Channel	D237 Zn	H239 Zn	F267 Channel	D328 Zn	P334 L6	L335 L6	Y371 Cat
T. cruzi	E	H	H	F	D	H	F	D	P	L	Y
T. conorhini	D	H	H	F	D	H	F	D	P	L	Y
T. rangeli	D	N	H	F	D	H	F	D	P	L	Y
T. grayi	D	H	H	F	D	H	Y	D	P	I	Y
T. theileri	D	H	H	F	D	H	Y	D	P	L	Y
T. brucei	D	H	N	**S**	D	H	F	N	P	Y	**N**
T. equiperdum	D	H	N	**S**	D	H	F	N	P	Y	**N**
T. vivax	**I**	**S**	H	**S**	C	**R**	Y	D	P	D	**Q**

Residues diverging from canonical HDAC active site amino acids but potentially playing the same role are shown in red.
Residues potentially incompatible with a bona fide lysine deacetylase activity are shown in red and bold and are highlighted yellow.
Ac Binding: residue participating to acetyl group binding.
Channel: residue participating to the active site pocket channel accommodating the lysine side chain aliphatic part.
Zn: residue participating in zinc binding.
L2: residue of L2 loop normally interacting with the main chain of the incoming acetylated target.
L6: residue in L6 loop.

Supplementary Methods: TB compounds synthesis

Materials: All materials and reagents were purchased from Sigma– Aldrich Co. Ltd., abcr GmbH, ChemPUR GmbH, and Carbolution Chemicals. All solvents were analytically pure and dried before use. Thin-layer chromatography (TLC) was carried out on aluminum sheets coated with silica gel 60 F254 (Merck, Darmstadt, Germany). For column chromatography under atmospheric pressure, silica gel 60 (0.036–0.200 mm) was used. Medium-pressure liquid chromatography was used for more thorough purification of compounds that after gravity column chromatography had purities of <95%. As stationary phase, silica gel 60 (0.040–0.063 mm; Merck) was used. Filling of the columns was performed with the aid of a Cartriger C-670. The elution solvent was mixed and pumped through the column via two pumps (both Pump Module C-601) and the Pump Manager C615. Fractions were collected by a Fraction Collector C-660. All equipment mentioned above was acquired from the manufacturer Büchi. The eluent was also $CHCl_3$ with 0.25% formic acid and a MeOH gradient. For detection of the product a C-630 UV Monitor was used as well as TLC.

Purity: Final compounds were confirmed to be of >95% purity based on HPLC. Purity was measured by UV absorbance at 254 nm. HPLC instrumentation consisted of an XTerra RP18 column (3.5 mm 3.9x100 mm; Waters, Milford, MA, USA) two LC-10AD pumps, an SPD-M10A VP PDA detector, and an SIL-HT auto sampler all from the manufacturer Shimadzu (Kyoto, Japan). The mobile phase was in all cases a gradient of MeOH/H_2O (starting at 95% H_2O going to 5% H_2O).

Mass spectrometry analyses were performed with a Finnigan MAT 710C (Thermo Separation Products, San Jose, CA, USA) for ESI-MS spectra, and with a LTQ (linear ion trap)-Orbitrap XL hybrid mass spectrometer (Thermo Fisher Scientific, Bremen, Germany) for HRMS-ESI (high-resolution mass spectrometry) spectra. For HRMS analyses, the signal for the isotopes with the highest prevalence was given and calculated for ^{35}Cl and ^{79}Br.

1H and 13C NMR spectra were taken on a Varian Gemini 2000 and a Varian Inova 500 using $CDCl_3$ and DMSO-d_6 as solvents. Chemical shifts (δ, ppm) are referenced to the residual solvent signals.

General procedure for the synthesis of the cinnamic acid derivatives 2a-e:

To the respective aldehyde **1a-e** (1 eq) and malonic acid (1.2 eq) in pyridine was added piperidine (0.1 eq) and the mixture was stirred at 80°C until completion of reaction was confirmed by TLC. After that, ice and concentrated hydrochloric acid were added. The formed precipitate was collected by filtration, washed with water and dried under reduced pressure to afford the corresponding carboxylic acid **2a-e**.

General procedure for conversion of the carboxylic acid into the corresponding hydroxamic acid derivatives 4a-e: PyBOP (1.2 eq) was added to a solution of carboxylic acid **2a-e** (1.0 eq) and DIPEA (2.5 eq) in dry THF and the reaction mixture was stirred at RT. After 15 min H_2NOTHP (1.5 eq) was added and the resulting mixture was stirred at RT overnight. The mixture was concentrated and the residue was taken up in DCM and washed with 5% aqueous $NaHCO_3$. The organic layer was separated, dried over $MgSO_4$, filtered and evaporated. The crude residue was purified by column chromatography on silica gel (eluent: $CHCl_3$ with 0.25% Et_3N / MeOH). The THP-protected intermediate **3a-e** was dissolved in MeOH and a catalytic amount of 1M aqueous HCl was added. The reaction mixture was stirred at RT until completion of reaction was observed by TLC. The solvent was evaporated and the crude product was purified by column chromatography on silica gel (eluent: $CHCl_3$ with 0.25% HCOOH / MeOH) to obtain the hydroxamic acid **4a-e**.

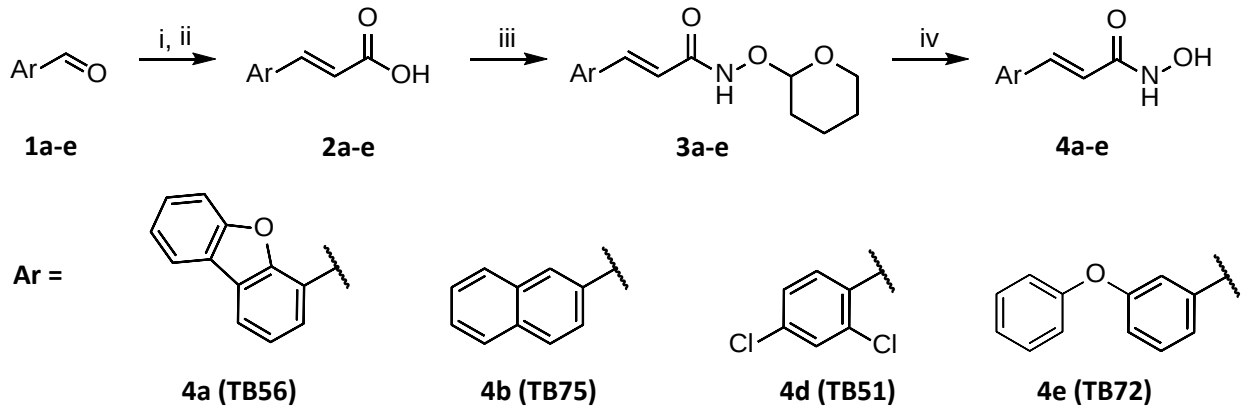

Scheme 1: Synthesis of hydroxamic acids **4a-e**: i) malonic acid, pyridine, piperidine, 3-6 h, 70-80°C; ii) HCl, 0°C, O/N, 4-8h; iii) PyBOP, DIPEA, H_2NOTHP, THF, rt, O/N; iv) HCl, MeOH, rt, 6-24h.

(2E)-3-(dibenzo[b,d]furan-4-yl)-N-hydroxyprop-2-enamide (4a, TB56): pale pink powder; yield: 26 %; ^{1}H NMR (400 MHz, DMSO-d6) δ 10.97 (s, 1H, NHO**H**), 9.11 (s, 1H, N**H**OH), 8.22 – 8.16 (m, 2H), 7.81 – 7.70 (m, 3H), 7.59 (ddd, J = 8.4, 7.4, 1.3 Hz, 1H), 7.45 (dd, J = 10.8, 4.3 Hz, 2H), 7.02 (d, J = 15.9 Hz, 1H, Hα); ^{13}C NMR (101 MHz, DMSO-d6) δ 162.71 (s), 155.35 (s), 153.26 (s), 132.60 (s), 127.95 (s), 127.67 (s), 124.24 (s), 123.50 (d, *J* = 6.4 Hz), 123.12 (s), 122.35 (s), 122.03 (s), 121.35 (s), 119.75 (s), 111.68 (s); MS (ESI-, MeOH) *m/z* (%): 252.34 (100) [*M*-H]$^-$; HRMS-ESI *m/z* [*M*+H]$^+$ calcd for $C_{15}H_{12}NO_3^+$: 254.0817, found: 254.0809. Purity is higher than 95% as assessed by HPLC.

(2E)-N-hydroxy-3-(naphthalen-2-yl)prop-2-enamide (4b, TB75): off-white powder; yield: 62 %; ^{1}H NMR (400 MHz, DMSO-d6) δ 10.80 (s, 1H, NHO**H**), 9.07 (s, 1H, N**H**OH), 8.07 (s, 1H, H1), 7.97 – 7.89 (m, 3H, H5, H6, H8), 7.71 (d, J = 8.7 Hz, 1H, H3), 7.62 (d, J = 15.8 Hz, 1H, Hβ), 7.54 (m, J = 6.3, 3.1 Hz, 2H, H4, H7), 6.60 (d, J = 15.8 Hz, 1H, Hα); MS (ESI-, MeOH) *m/z* (%): 212.28 (100) [*M*-H]$^-$; HRMS-ESI *m/z* [*M*+H]$^+$ calcd for $C_{13}H_{12}NO_2^+$: 214.0868, found: 214.0864. Purity is higher than 95% as assessed by HPLC.

(2E)-3-(2,4-dichlorophenyl)-N-hydroxyprop-2-enamide (4d,TB51): pale yellow powder**;** yield: 48 %; ^{1}H NMR (400 MHz, DMSO-d6) δ 10.88 (s, 1H, NHO**H**), 9.16 (s, 1H, N**H**OH), 7.72 (d, J = 8.8 Hz, 1H, H6), 7.70 (d, J = 2.1 Hz, 1H, H3), 7.67 (d, J = 15.9 Hz, 1H, Hβ), 7.48 (dd, J = 8.4, 1.8 Hz, 1H, H5), 6.53 (d, J = 15.7 Hz, 1H, Hα); MS (ESI-, MeOH) *m/z* (%): 230.17 (100) [*M*-H]$^-$; HRMS-ESI *m/z* [*M*+H]$^+$ calcd for $C_9H_8Cl_2NO_2^+$: 231.9932, found: 231.9928. Purity is higher than 95% as assessed by HPLC.

(2E)-N-hydroxy-3-(3-phenoxyphenyl)prop-2-enamide (4e, TB72): off-white powder; yield: 39 %; ^{1}H NMR (400 MHz, DMSO-d6) δ 10.72 (s, 1H, NHO**H**), 9.05 (s, 1H, N**H**OH), 7.47 – 7.36 (m, 4H, Hβ, H3', H4', H5'), 7.33 (d, J = 7.7 Hz, 1H, H6), 7.22 – 7.13 (m, 2H, H2, H5), 7.04 (dd, J = 8.6, 0.9 Hz, 2H, H2', H6'), 7.00 (dd, J = 8.0, 1.8 Hz, 1H, H4), 6.43 (d, J = 15.8 Hz, 1H, Hα); MS (ESI-, MeOH) *m/z* (%): 254.30 (100) [*M*-H]$^-$; HRMS-ESI *m/z* [*M*+H]$^+$ calcd for $C_{15}H_{14}NO_3^+$: 256.0974, found: 256.0969. Purity is higher than 95% as assessed by HPLC.

References

Hess-Stumpp, H., Bracker, T. U., Henderson, D. & Politz, O. 2007. Ms-275, A Potent Orally Available Inhibitor Of Histone Deacetylases--The Development Of An Anticancer Agent. *Int J Biochem Cell Biol,* 39**,** 1388-405.

Krieger, V., Hamacher, A., Cao, F., Stenzel, K., Gertzen, C. G. W., Schaker-Hubner, L., Kurz, T., Gohlke, H., Dekker, F. J., Kassack, M. U. & Hansen, F. K. 2019. Synthesis Of Peptoid-Based Class I-Selective Histone Deacetylase Inhibitors With Chemosensitizing Properties. *J Med Chem,* 62**,** 11260-11279.

Marson, C. M., Matthews, C. J., Atkinson, S. J., Lamadema, N. & Thomas, N. S. 2015. Potent And Selective Inhibitors Of Histone Deacetylase-3 Containing Chiral Oxazoline Capping Groups And A N-(2-Aminophenyl)-Benzamide Binding Unit. *J Med Chem,* 58**,** 6803-18.

Robert, X. & Gouet, P. 2014. Deciphering Key Features In Protein Structures With The New Endscript Server. *Nucleic Acids Res,* 42**,** W320-4.

Article 3

The structure of the mouse ADAT2/ADAT3 complex reveals the molecular basis for mammalian tRNA wobble adenosine-to-inosine deamination (Published)

Editing of adenosine into inosine (A-to-I) at position 34 in tRNAs is important to expand the decoding capacity of tRNAs, since inosine 34 can recognize the uridine, cytosine and adenosine at the third position of the codon, in contrast to adenosine 34 that can only pair with uridine at the third position of the codon. In prokaryotes A-to-I editing is performed by a homodimer protein TadA on its unique substrate tRNA-Arg. In eukaryotes A-to-I editing is carried out by the heterodimeric ADAT2/ADAT3 complex in up to eight tRNA isotypes, ADAT2 being the active subunit and ADAT3 being considered as the inactive subunit with unknown role. Moreover, sequence comparison of the prokaryotic TadA with the eukaryotic ADAT2 showed 50% of similarity and with ADAT3 C-terminal domain 45% of similarity. Interestingly, the N-terminal domain of ADAT3 is an extension sequence that is not present in the prokaryotic TadA. Furthermore, a mutation of valine 128 into methionine localized in the N-terminal domain of ADAT3 subunit causes a neurodevelopmental disorder characterized by intellectual disability, microcephaly, strabismus, epilepsy.

Several questions have been raised. For instance, why do eukaryotes require a heterodimeric complex for A-to-I editing of tRNAs? What is the role of the N-terminal domain of eukaryotic ADAT3 subunit? Why ADAT3 is the inactive subunit? Is the V128M mutant ADAT still able to bind tRNAs? To address these questions the structure of the mammalian ADAT complex was required. This project has represented a large part of my thesis work. I could purify, crystallize, and solve the structure of the first mammalian ADAT complex, which reveals important insights. First, the N-terminal domain of ADAT3 is essential for tRNA recognition, which I also confirmed by binding tests. Second, ADAT3 subunit is inactivated by the capping of its zinc-binding site by ADAT3 C-terminal residues, which would block the entry site for the incoming adenosine 34, which I also confirmed by enzymatic tests. Furthermore, the ADAT structure confirms that in the zinc binding site of ADAT3, V225 replaces a glutamate that participates in catalysis observed in ADAT2 active site. Third, the ADAT mutant V128M can bind tRNAs, however its catalytic activity is compromised compared to the wildtype enzyme. Therefore, I hypothesized that the reduced level of inosine in tRNAs in affected patients, might come from the incorrect presentation of the tRNA substrate by ADAT3 N-terminal domain to the active site of ADAT2, leading to a reduced catalytic activity.

Published online 31 May 2021

Nucleic Acids Research, 2021, Vol. 49, No. 11 ***6529–6548***
https://doi.org/10.1093/nar/gkab436

The structure of the mouse ADAT2/ADAT3 complex reveals the molecular basis for mammalian tRNA wobble adenosine-to-inosine deamination

Elizabeth Ramos-Morales[1], Efil Bayam[1,†], Jordi Del-Pozo-Rodríguez[1,†], Thalia Salinas-Giegé[2], Martin Marek[1], Peggy Tilly[1], Philippe Wolff[3], Edouard Troesch[1], Eric Ennifar[3], Laurence Drouard[2], Juliette D. Godin[1,*] and Christophe Romier[1,*]

[1]Université de Strasbourg, CNRS, INSERM, Institut de Génétique et de Biologie Moléculaire et Cellulaire (IGBMC), UMR 7104, U 1258, 1 rue Laurent Fries, B.P. 10142, 67404, Illkirch Cedex, France, [2]Institut de biologie moléculaire des plantes-CNRS, Université de Strasbourg, 12 rue du Général Zimmer, 67084 Strasbourg, France and [3]Université de Strasbourg, CNRS, Architecture et Réactivité de l'ARN, UPR 9002, 67000 Strasbourg, France

Received October 13, 2020; Revised April 28, 2021; Editorial Decision May 02, 2021; Accepted May 05, 2021

ABSTRACT

Post-transcriptional modification of tRNA wobble adenosine into inosine is crucial for decoding multiple mRNA codons by a single tRNA. The eukaryotic wobble adenosine-to-inosine modification is catalysed by the ADAT (ADAT2/ADAT3) complex that modifies up to eight tRNAs, requiring a full tRNA for activity. Yet, ADAT catalytic mechanism and its implication in neurodevelopmental disorders remain poorly understood. Here, we have characterized mouse ADAT and provide the molecular basis for tRNAs deamination by ADAT2 as well as ADAT3 inactivation by loss of catalytic and tRNA-binding determinants. We show that tRNA binding and deamination can vary depending on the cognate tRNA but absolutely rely on the eukaryote-specific ADAT3 N-terminal domain. This domain can rotate with respect to the ADAT catalytic domain to present and position the tRNA anticodon-stem-loop correctly in ADAT2 active site. A founder mutation in the ADAT3 N-terminal domain, which causes intellectual disability, does not affect tRNA binding despite the structural changes it induces but most likely hinders optimal presentation of the tRNA anticodon-stem-loop to ADAT2.

GRAPHICAL ABSTRACT

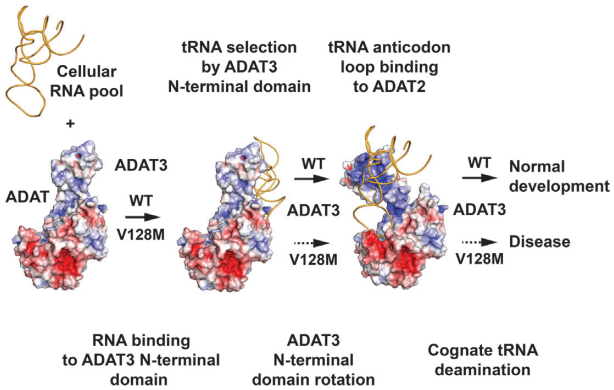

INTRODUCTION

All ribonucleic acid molecules undergo a large number of post-transcriptional covalent modifications (1). Transfer RNAs are among the most modified RNA species, where modifications play a role in tRNA folding, stabilization and decoding, but can also provide a checkpoint for the interaction between translation and other cellular processes and environmental cues (2–5). Mutations in genes coding for tRNA-modifying enzymes cause numerous diseases. Intriguingly, the vast majority of genetic disorders linked to these mutations are neurological disorders, particularly neurodevelopmental disorders (NDDs), highlighting the importance of tRNA editing for proper brain devel-

*To whom correspondence should be addressed. Tel: +33 3694 85294; Fax: +33 3886 53201; Email: romier@igbmc.fr
Correspondence may also be addressed to Juliette Godin. Email: godin@igbmc.fr
†The authors wish it to be known that, in their opinion, the second and third authors should be regarded as Joint Second Authors.
Present address: Martin Marek, Loschmidt Laboratories, Department of Experimental Biology and RECETOX, Faculty of Science, Masaryk University, Kamenice 5/A13, 625 00 Brno, Czech Republic.

opment (6–8). How dysregulation of tRNA modifications causes these diseases remains poorly understood.

Among the tRNA modifications, a large set is located in the anticodon-stem-loop (ASL) of tRNAs, playing notably a major role in decoding. This is particularly the case for the modifications of nucleoside 34 of the ASL, which faces the third base of mRNA codons during translation. Modification of adenosine into inosine (A-to-I) at position 34 led Crick to propose the wobble hypothesis, thereby providing an explanation to the degeneracy of the genetic code, inosine being able to pair with uridine, adenosine and cytosine in contrast to the typical Watson–Crick base pairing made by adenosine with uridine (9). Since this initial hypothesis, the number of modifications discovered for the wobble base at position 34 and in other nucleosides of the ASL has increased, enabling a better understanding of codon decoding by tRNAs (10).

Wobble A-to-I modification is conserved among prokaryotes and eukaryotes (10,11). Yet, whereas only $tRNA^{Arg}$(ACG) is modified in prokaryotes, up to eight tRNAs are inosine-modified in eukaryotes (Ala(AGC), Arg(ACG), Ile(AAU), Leu(AAG), Pro(AGG), Ser(AGA), Thr(AGU) and Val(AAC); Supplementary Table S1) (1). Wobble A-to-I modification occurs through a deamination reaction catalysed by enzymes that belong to the larger cytidine deaminase (CDA) family (12).

In prokaryotes, the essential homodimeric TadA enzyme is responsible for this reaction that only requires the ASL of the cognate $tRNA^{Arg}$(ACG) for activity (13). The structures of various prokaryotic TadA enzymes have been solved, showing that the fold and the coordination of the catalytic zinc ion through one histidine, two cysteines and a water molecule are conserved within the cytidine deaminase family, also including the catalytic glutamate proposed to shuttle a proton from the aforementioned water to the wobble adenine (14–16).

The structure of *Staphylococcus aureus* TadA in complex with an ASL containing Nebularine, a non-hydrolysable adenosine analogue, has further shed light on the recognition of prokaryotic $tRNA^{Arg}$(ACG) by TadA (17). Specifically, the ASL undergoes significant conformational changes upon binding to TadA, and five bases of the anticodon stem-loop are splayed and recognized within different pockets. Bases 32–38 of the ASL are sufficient for specific recognition of $tRNA^{Arg}$(ACG) by TadA.

In eukaryotes, the enzyme responsible for wobble adenosine 34 modification into inosine is the essential ADAT (ADAT2/ADAT3; Tad2p/Tad3p in yeast) heterodimeric complex (18–22). Both ADAT2 and the C-terminal domain of ADAT3 show sequence homology to the TadA enzyme (Figure 1). Yet, whereas ADAT2 appears to have conserved TadA residues required for activity, ADAT3 has been suggested to be inactive, the essential glutamate proposed to be involved in proton shuttling during catalysis being replaced by a valine in ADAT3 (18,22). In yeast, mutation of this valine into glutamate in Tad3p could not rescue the loss of activity of a Tad2p mutant where the equivalent glutamate was changed into alanine (18). Therefore, ADAT2 and ADAT3 play different roles in the deamination reaction by the ADAT complex. Additionally, in contrast to TadA, the ADAT heterodimeric complex requires a full tRNA to perform its deamination reaction. Specifically, both the tRNA tertiary structure and the tRNA strict positioning are essential for ADAT activity (14,23,24).

Another major difference with prokaryotic TadA is the presence in ADAT3 of an additional N-terminal domain (Figure 1) whose function has so far remained elusive. In humans, mutation of valine 128 into methionine (p.Val128Met) in this N-terminal domain causes intellectual disability, microcephaly, strabismus and several other neurodevelopmental abnormalities (25–28). In cell lines derived from affected individuals, the p.Val128Met mutation (mutant hereafter termed V128M; also described as p.Val144Met in a N-terminally 16 amino acids longer human transcript) is responsible for reducing the levels of inosine at the wobble position of cognate tRNAs (29). Mutant ADAT3 alone displays an increased propensity to aggregate and to associate with protein chaperones, but its heterodimerization with ADAT2 is not perturbed, only the tRNA deamination activity of the ADAT V128M mutant complex being affected (29).

Here we have solved the crystal structure of the mouse ADAT2/ADAT3 complex. Our structure and associated enzymatic and biophysical analyses reveal that while ADAT2 active site catalyses the deamination reaction, ADAT3 active site is inactivated by the replacement by a valine of the glutamate involved in proton shuttling during catalysis but also by the capping of its zinc-binding pocket and the loss of tRNA recognition determinants. Our results show that the ADAT3 N-terminal domain adopts a fold that shares similarity with the ferredoxin-like domains (FLD) of other tRNA-modifying enzymes, yet with an additional specific structural subdomain, containing V128, which forms a loose interface between ADAT3 N- and C-terminal domains. ADAT3 N-terminal domain is essential for tRNA binding and deamination by ADAT and can rotate with respect to the catalytic domain formed by ADAT2 and the ADAT3 C-terminal domain, without affecting the structure of this latter catalytic domain. Interestingly, binding and deamination levels are varying depending on the cognate tRNA, showing that each cognate tRNA interacts differently with ADAT.

In addition, we observe that the mouse ADAT2/ADAT3-V128M mutant can still bind tRNAs as strongly as the wild-type complex but shows a reduced deamination activity. Our data show that the V128M mutation perturbs but does not prevent the folding of the ADAT3 N-terminal domain. These changes most likely affect the optimal presentation of the ASL of the tRNAs to ADAT2 and lead to reduced deamination activity. *In vivo*, inactivation of ADAT2, removal of ADAT3 N-terminal domain and the ADAT3-V128M mutant cause similar defects in neuronal migration, confirming the catalytic role of ADAT2 and the functional importance of ADAT3 N-terminal domain. Collectively, our results provide the molecular basis for mammalian ADAT complex tRNAs wobble adenine to inosine deamination and shed light on the implication of ADAT in intellectual disability, microcephaly and other neurodevelopmental disorders.

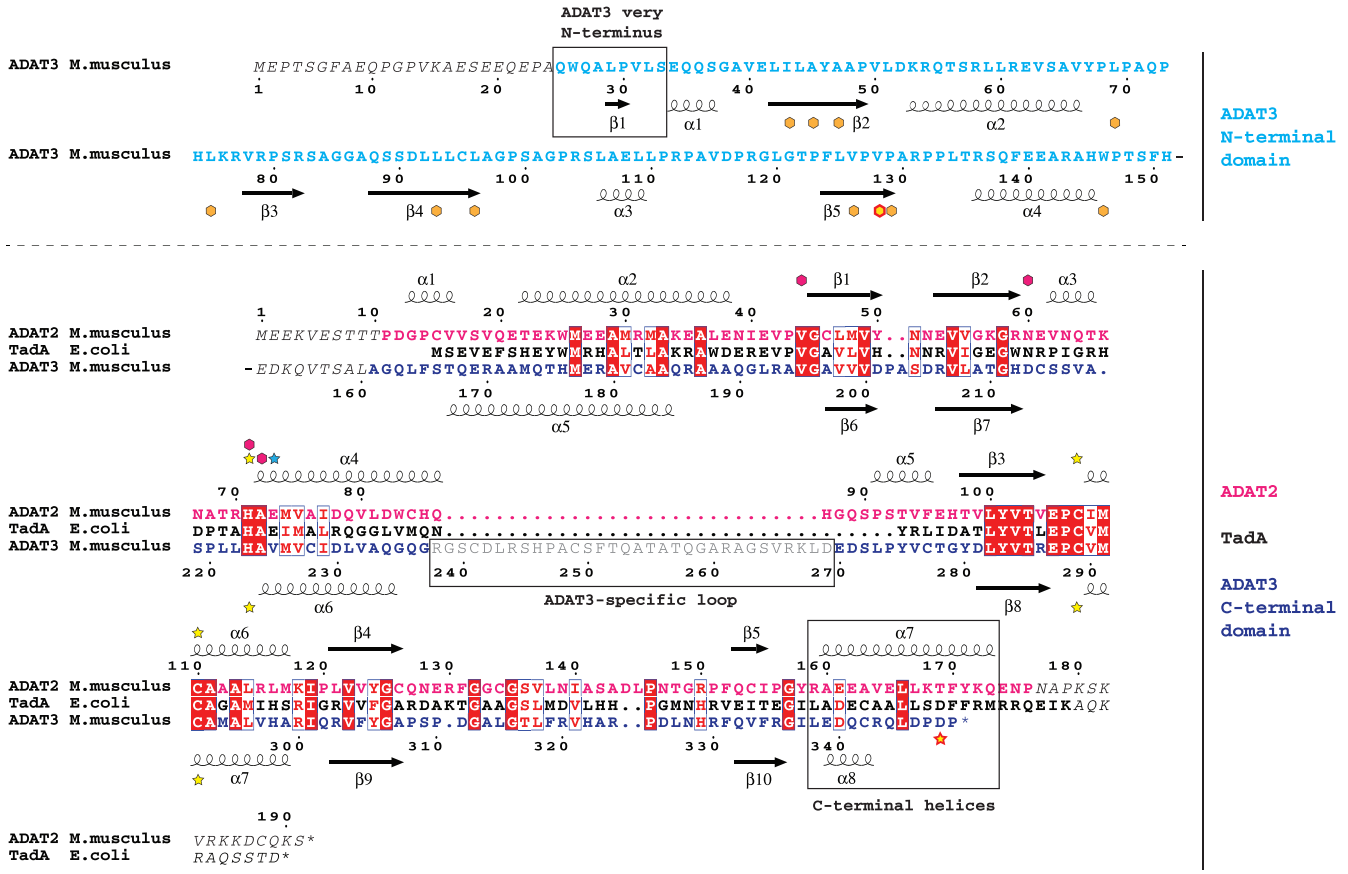

Figure 1. Sequence alignment of mouse ADAT2 and ADAT3 subunits and *Escherichia coli* TadA. The alignment of the sequences of mouse (M.musculus) ADAT2 (pink) and ADAT3 (N-terminal domain, cyan; C-terminal domain, blue) subunits and of *E. coli* TadA (black) shows an overall conservation of their deaminase domain (lower part of alignment) which extends to their secondary structure elements. ADAT3 has diverged from ADAT2 and TadA, including a specific N-terminal domain (cyan) and a shorter C-terminal α-helix (boxed). Residues not observed in density are italicized and the ADAT3-specific loop removed for crystallization is shown in grey and boxed. Numbering as well as secondary structure elements for mouse ADAT2 and ADAT3 are shown above and below the alignment, respectively. Yellow stars: zinc binding residues. The fourth zinc ligand in ADAT3 is represented by a red-framed yellow star. Blue star: TadA (and potentially ADAT2) glutamate involved in proton shuttling. Purple diamonds: TadA (and potentially ADAT2) residues involved in wobble adenine binding. Orange diamonds: ADAT3 residues participating in ADAT3 V128 (red circled yellow diamond) hydrophobic core. The sequence alignments were produced with Espript (48).

MATERIAL AND METHODS

Molecular cloning and mutagenesis

The genes encoding for full-length mouse ADAT2 and ADAT3 (NCBI reference sequences NM_025748.4 and NM_001100606) have been amplified by polymerase-chain reaction from E16.5 cortices and cloned into bacterial co-expression vectors (30,31) between NdeI and BamHI restriction sites. Mutants were made either by nested PCR or rolling circle and cloned in the same vectors. Specifically, the *adat2* gene was inserted in the pnCS vector that does not code for any fusion tag. The *adat3* gene was inserted in the pnEA-HT3 vector, in frame with a 5′-sequence coding for an N-terminal histidine-tag, thioredoxin and a protease 3C cleavage site.

For *in vivo* studies, wild-type and mutant mouse ADAT2 and ADAT3 were further subcloned into the pCAGGs-HA vector by restriction-ligation. pCAGGS-HA was obtained from the PCAGEN vector (addgene cat. number 11160) by restriction ligation (EcoRI and BglII enzymes) and addition of the HA sequence (5′-TACCCATACGATGTTCCAGA TTACGCT-3′).

Large-scale overproduction and purification of mADAT2/ADAT3 and *E. coli* TadA

ADAT2/ADAT3 WT and mutants were produced by co-expression in *Escherichia coli* BL21(DE3) cells in LB Broth medium. Culture induction was performed at 22°C by adding final concentration of 0.5 mM of isopropyl-1-thio-β-D-galactopyranoside (IPTG) in presence of 100 μM of $Zn(SO_4)_2$. Cells were harvested, resuspended and lysed in a buffer containing 10 mM Tris-HCl pH 8.0 and 200 mM NaCl and centrifuged at 17 500 rpm for 1 h at 4°C. The supernatant was incubated with Talon Affinity resin (Clonetech). To release the his-tagged complex from the Talon resin, the sample was treated with 3C protease overnight at 4°C. The next day, ion exchange chromatography was performed with a HiTrap Q HP column (GE Healthcare) using a gradient of NaCl from 50 mM to 1 M

NaCl to remove bound nucleic acids. The sample was then further purified by size exclusion chromatography in 10 mM Tris HCl pH 8.0, 200 mM NaCl and 0.5 mM TCEP on a 16/60 Superdex 200 gel filtration column (GE Healthcare). *Escherichia coli* TadA was produced and purified using the same protocol as for the ADAT complex.

Protein crystallization

For crystallization, WT and mutant ADAT2/ADAT3 complex at 12 mg/ml was mixed with an equal volume of reservoir reagent and crystallized using the sitting drop vapor diffusion technique at 4, 20 and 27°C. All crystals grew within one week. Crystals of ADAT2/ADAT3 that diffracted up to 3.0 Å resolution were obtained using a crystallization condition containing 0.1 M HEPES pH 7.0, 7% PEG 8000 and 8% ethylene glycol. The second crystal form of ADAT2/ADAT3 that diffracted up to 2.0 Å resolution was obtained using a crystallization solution containing 0.1 M Bis-Tris-Propane pH 7.5, 18–20% PEG 3350 and 0.2 M KSCN or NaBr.

Data collection, structure determination, model building and refinement

For data collection, the crystals were frozen in liquid nitrogen after their short transfer into a cryo-protectant solution composed of their crystallization conditions added with either 20% glycerol or 20% PEG200. Data collection was performed under cryogenic conditions on beamline PXIII at the Swiss Light Source synchrotron (SLS, Switzerland) using a 1 Å wavelength. Data sets collected were processed with XDS (32). Structure determination was made by collecting MAD data on ADAT zinc ions on the crystal form diffracting to 3.0 Å resolution. The phases obtained were sufficient to place the human ADAT2 homodimer (PDB code: 3hd1) in the electron density and to modify it by several cycles of manual building using Coot (33) and automated refinement using Phenix (34) to model mouse ADAT2 and the mouse ADAT3 C-terminal domain. The combined MAD and model phases were then used to build the ADAT3 N-terminal domain. The complete WT model was further refined by several cycles of manual building using Coot and automated refinement using Phenix. This first final model was used to solve the structures of the WT and V128L ADAT complexes in the second space group by molecular replacement, followed by several cycles of manual building using Coot and automated refinement using Phenix. All final models were validated using tools provided in Coot and Molprobity (35). Structures have been deposited in the Protein Data Bank under PDB IDs: 7nz7, 7nz8, 7nz9.

Mass spectrometry analyses

Prior mass spectrometry analysis, 100 ng of the nucleic acids-containing fractions were digested with 20 μl of 0.1 U/μl of RNase T1 during 4 h at 50°C or digested with 50 μl of 0.01 U/μl of RNase V1 during 3 h at 37°C. The samples were then desalted using ZipTip C18 (Millipore) by several washes with 200 mM ammonium acetate and eluted with 50% acetonitrile in milliQ water and dried under vacuum.

The pellets containing the RNase digestion products were resuspended in 3 μl of milliQ water and separated on an Acquity peptide BEH C18 column (130 Å, 1.7 μm, 75 μm x 200 mm) using a nanoAcquity system (Waters). The column was equilibrated in buffer A containing 7.5 mM TEAA (Triethylammonium acetate), 7.0 mM TEA (Triethyammonium) and 200 mM HFIP (Hexafluoroisopropanol) at a flow rate of 300 nl/min. Oligonucleotides were eluted using a gradient from 15% to 35% of buffer B (100% Methanol) for 2 min followed by elution with an increase of buffer B to 50% in 20 min. MS and MS/MS analyses were performed using a Q-Tof SYNAPT G2-S from Waters. All experiments were performed in negative mode with a capillary voltage set at 2.6 kV and a sample cone voltage set at 30 V. Source was heated to 130°C. The sample was analyzed over an m/z range from 500 to 1500 for the full scan, followed by fast data direct acquisition scan (Fast DDA).

tRNA were identified by specific RNase T1 digestion products (36). All RNase T1 and V1 CID (Collision Induced Decay) MS/MS spectra were deconvoluted using the MassLynx software from Waters and manually sequenced by following the y and/or c series (w ions were also useful when sequencing was difficult or in order to confirm the sequence). Experimental mass of parents and fragments were compared to the theoretical mass obtained by the Mongo Oligo Mass Calculator (https://mods.rna.albany.edu/masspec/Mongo-Oligo) (37). tRNA identification was done by comparisons with the genomic sequences obtained from GtRNAdb (http://gtrnadb.ucsc.edu/) (38). Information about nucleoside modifications were obtained from Modomics (1).

tRNA production and CY5-labelling

All tRNA genes used were synthesized as primers (Sigma) and inserted in the different vectors used. For *in vitro* expression, the tRNA sequences were cloned into the pUC19 vector between a T7 RNA polymerase promoter and a BstNI restriction site as previously described (39). The tRNAs were synthesized from the BstNI digested DNA by *in vitro* transcription using recombinant T7 RNA polymerase (40). After transcription, samples were treated with RQ1 RNAse-Free DNAse (Promega) and RNA transcripts were phenol-extracted and precipitated. Pelleted tRNAs were dissolved in water and loaded on 7 M Urea-15% acrylamide and 1 X TBE gels. After methylene blue staining, gel slices containing tRNA transcripts were cut from the gel. The tRNAs were eluted overnight at room temperature in 0.5 M ammonium acetate, 10 mM magnesium acetate, 0.1 mM EDTA and 0.1% SDS. After phenol extraction, tRNAs were ethanol precipitated and finally recovered in water. Their concentration was determined by absorbance measurements and by gel quantification. At this step, the final concentration varied between 400 and 700 ng/μl. The tRNAs were then used for deamination enzymatic assays and CY5-labelling.

For CY5-labelling, 25% DMSO (1 μl) was first added to the purified tRNA solution (3 μl), incubated 10 s at 100°C and immediately cooled on ice. The labelling reaction was performed in the presence of 10 units of Biolabs T4 RNA ligase (M0204), 1X supplied buffer, 1 mM ATP, 12% PEG6000, 0.1 mM hexamine cobalt chloride and 10

μM of pCp-CY5 (Jena Bioscience NU-1706-CY5). A ligase mixture was added to the tRNA-DMSO mix and ligation was performed in 10 μl overnight at 16°C. After labelling, unincorporated pCp-CY5 was trapped on a G-50 column. The CY5-labelled tRNAs were fractionated on 7 M Urea-15% acrylamide gel and scanned on a GE Healthcare Ettan DIGE imager system.

Microscale thermophoresis

A serial dilution of the mouse ADAT2/ADAT3 (WT and mutants) and TadA complexes (300 μM) was mixed with a constant concentration of CY5-labeled $tRNA^{Val}$(AAC), $tRNA^{Arg}$(ACG), $tRNA^{Ala}$(AGC) or $tRNA^{Gly}$(CCC) (5–20 nM). Samples were prepared in a buffer containing 10 mM Tris-HCl pH 8.0, 100 mM NaCl, 0.5 mM TCEP and 0.05% Tween. Samples were then filled into standard capillaries and measurements were performed using a NanoTemper Monolith NT115 instrument at 80% red LED power and 20% MST power with Laser-On time 30 s and Laser-Off time 5 s. All assays were performed in triplicate.

Enzymatic deamination assays

Deamination assays were done in deamination buffer (10 mM Tris-HCl pH 8.0, 100 mM NaCl, 1 mM $MgCl_2$, 2 mM dithiothreitol (DTT)) using 2 μM of tRNA transcript and 5.6, 0.56 or 0.056 μM of purified enzyme complex (tRNA:protein ratios of approximately 1:3, 1:0.3 and 1:0.03) in a final volume of 5 μl. The reaction was initiated when adding the purified enzyme complex to the reaction mixture and immediately incubated at 37°C during 10 min. After incubation, the reaction was immediately stopped by phenol-chloroform extraction. The supernatant was precipitated, and the pellet containing the tRNA transcript was dissolved in 20 μl of water. The cDNA was synthesized using the SuperScript™ IV Reverse Transcriptase (Invitrogen Cat.# 18090010) according to the manufacturer's instructions with 2 μl of the tRNA transcript solution and 0.1 μM of gene-specific complementary primer. The tRNAs were then amplified using the GoTaq® G2 Flexi (Promega Cat.# M7801) according to the manufacturer's instructions with 5 μl of cDNA, 2.5 mM of $MgCl_2$ and 1 μM of gene-specific primers. As PCR fragments were too small for direct sequencing, they were ligated using pGEM®-T Easy Vector System (Promega Cat.# A1360) according to the manufacturer's instructions. The ligated PCR products were then reamplified using the vector-specific primer and the tRNA-specific primer. The resulting PCR fragments were precipitated, redissolved and directly sequenced with the vector-specific primer. The A-to-I deamination analysis was done by measuring peak areas at the expected nucleotide position on the sequencing electropherograms. Deamination reaction was visualized by the presence of a guanosine peak at the adenosine peak position since reverse transcriptase incorporates a cytosine in the place of inosine. Due to inherent sequencing background, guanosine peaks with areas <5% of the total areas might not fully reflect a deamination activity. Therefore, a 5% threshold has been applied when displaying the results graphically. The forward primers used for PCR were as follows (5′→3′): $tRNA^{Val}$(AAC),GTTTCCGTAGTGTAGTGGTTATC; $tRNA^{Ala}$(AGC),GGGGAATTAGCTCAAATGGTA; $tRNA^{Arg}$(ACG),GGGCCAGTGGCGCAATGGA; $tRNA^{Gly}$(ACC),GCGCCGCTGGTGTAGTGG. The reverse primers used for RT-PCR were as follows: $tRNA^{Val}$(AAC),TGGTGTTTCCGCCCGGTTTC; $tRNA^{Ala}$(AGC),TGGAGAATGCGGGCATCGAT; $tRNA^{Arg}$(ACG),TGGCGAGCCAGCTAGGAGT; $tRNA^{Gly}$(ACC),TGGTGCGCCGCCCGGG. The forward primer for the pGEM®-T Easy Vector was as follows (5′→3′):GTAAAACGACGGCCAG.

Mice, *in utero* electroporation and brain processing and analysis

All animal studies were conducted in accordance with French regulations (EU Directive 86/609 – French Act Rural Code R 214–87 to 126) and all procedures were approved by the local ethics committee and the Research Ministry (APAFIS#15691-201806271458609). Mice were bred at the IGBMC animal facility under controlled light/dark cycles, stable temperature (19°C) and humidity (50%) conditions and were provided with food and water ad libitum.

Timed-pregnant wild-type (WT) CD1 (Charles River Laboratories) mice were anesthetized with isoflurane (2 l per min of oxygen, 4% isoflurane in the induction phase and 2% isoflurane during surgery operation; Tem Sega). The uterine horns were exposed, and a lateral ventricle of each embryo was injected using pulled glass capillaries (Harvard apparatus, 1.0OD*0.58ID*100 mml) with Fast Green (1 μg/μl; Sigma) combined with different amounts of DNA constructs using a micro injector (Eppendorf Femto Jet). We injected 0.02 μg/μl of WT or mutant pCAGGS-HA-ADAT3 constructs together with 1 μg/μl of empty NeuroD-IRES-GFP vector (41) and 0.02 μg/μl of WT or E73A pCAGGS-ADAT2 constructs at E14.5. pCAGGs-HA-empty was used as a control at 0.04 μg/μl. Plasmids were further electroporated into the neuronal progenitors adjacent to the ventricle by discharging five electric 40 volts pulses for 50 at 950 ms intervals using electrodes (diameter: 3 mm; Sonidel CUY650P3) and ECM-830 BTX square wave electroporator (VWR international). After electroporation, embryos were placed back in the abdominal cavity and the abdomen was sutured using surgical needle and thread. For E18.5 analysis, pregnant mice were sacrificed by cervical dislocation four days after surgery.

E18.5 animals were sacrificed by head sectioning and brains were fixed in 4% paraformaldehyde (PFA, Electron Microscopy Sciences) diluted in phosphate-buffered saline (PBS, HyClone) overnight at 4°C. Vibratome section were prepared as follows: after fixation, brains were washed and embedded in a 4% low-melting agarose solution (Bio-Rad) and cut at a thickness of 60 μm coronally using a vibrating-blade microtome (Leica VT1000S, Leica Microsystems). Sections were kept in PBS-azide 0.05% for short-term storage or in an antifreeze solution (30% ethyleneglycol, 20% glycerol, 30% DH2O, 20% PO4 buffer) for long-term storage. For immunolabelling, vibratome sections were permeabilized and blocked with blocking solution (5% Normal Donkey Serum (NDS, Dominic Dutscher), 0.1% Triton-X-

100 in PBS) for 1 h at room temperature (RT). Sections were then incubated with anti-GFP primary antibody (Abcam, ref GFP-1020) diluted in blocking solution overnight at 4°C and with A488-coupled secondary antibody (Thermofisher, ref A-11039) and DAPI (dilution 1/1000, 1 mg/ml Sigma) diluted in PBS 0,1% Triton for 1 h at RT. Slides were mounted using Aquapolymount mounting medium (Polysciences Inc).

Images were acquired using a TCS SP8 X (Leica microsystems) confocal microscope using a 20× DRY HC PL APO CS2 objective. For all experiments, a Z-stack of 1.50 μm was acquired. Image analysis was done using ImageJ software (NIH). Cell counting was performed in 4–11 different brain sections of at least four different embryos per condition. Only similarly electroporated regions were considered for further analysis. Cortical areas (upper cortical plate, lower cortical plate, intermediate zone, subventricular zone/ventricular zone) were delimited based on cell density (nuclei count with DAPI staining) using equivalent sized boxes. Number of GFP-positive cells was determined in each cortical area to establish the percentage of positive cells. Statistical analyses were performed using GraphPad Prism 6 (GraphPad) and are represented as mean ± S.E.M. The level of significance was set at $P<0.05$. Statistical tests used and n size numbers are shown in the figure legend.

Cell culture, transfections, protein extraction and western blot

N2A mouse neuroblastoma cells were cultured in Dulbecco's modified Eagle's medium (DMEM, GIBCO) with 10% foetal calf serum (FCS), penicillin 100 U/ml and streptomycin 100 μg/ml in a humidified atmosphere containing 5% CO_2 at 37°C. Cells were transfected using Lipofectamine 2000 (Invitrogen) with 1 μg of pCAGGs-HA-ADAT3 constructs together with 1 μg of pCAGGs-ADAT2 constructs. Forty-eight hours post-transfection expression, proteins were extracted as follows: cells were lysed in RIPA buffer (50 mM Tris pH 8.0, 150 mM NaCl, 5 mM EDTA pH 8.0, 1% Triton X-100, 0.5% sodium deoxycholate, 0.1% SDS) supplemented with EDTA-free protease inhibitors (cOmplete™, Roche) for 30 min, then cells debris were removed by high speed centrifugation at 4°C for 25 min. Protein concentration was measured by spectrophotometry using Bio-Rad Bradford protein assay reagent. Samples were denatured at 95°C for 10 min in Laemmli buffer (Bio-Rad) with 2% β-mercaptoethanol, then resolved by SDS–PAGE and transferred onto nitrocellulose membranes. Membranes were blocked in 5% milk in PBS buffer with 0.1% Tween (PBS-T) and incubated overnight at 4°C with the anti-HA (Merck, ref. 11867423001; 1:1000), anti-ADAT2 (Proteintech, 13621-1-AP) or α-tubulin (Sigma, T9026) primary antibody in blocking solution. Membranes were washed three times in PBS-T, incubated at room temperature for 1 h with HRP-coupled secondary antibodies (ThermoFisher Sc.) at 1:10 000 dilution in PBS-T, followed by three times PBS-T washes. Visualization was performed by quantitative chemiluminescence using SuperSignal West Pico PLUS Chemiluminescent Substrate (Sigma). All immunoblot experiments consisted of at least three independent replicates.

RESULTS

Crystallization and structure determination of the mouse ADAT complex

We have reconstituted mouse ADAT2/ADAT3 by producing the complex in *E. coli* using multi-expression (30,31). The complex could be readily produced and purified by combining affinity purification and size-exclusion chromatography. Crystallization attempts were successful but the crystals did not diffract at high resolution. The addition of an ion exchange chromatographic step enabled the separation of the complex from bound nucleic acids, but crystallization attempts to obtain well-diffracting crystals remained unsuccessful.

Multiple sequence alignment of ADAT2, TadA and ADAT3 revealed that ADAT3 contains a poorly conserved region which is neither present in ADAT2 nor TadA (ADAT3-specific loop; Figure 1; Supplementary Figure S1). Therefore, an ADAT3 mutant lacking this loop was created. The ADAT2/ADAT3-Δloop mutant complex could easily be produced and purified using the same experimental procedure developed for the wild-type (WT) complex, including the ion exchange chromatography step to remove the bound nucleic acids, and further crystallized.

Two crystal forms were obtained, diffracting up to 2.1 and 3.0 Å, respectively. The mouse ADAT2/ADAT3 complex structure was solved by performing MAD phasing on the zinc ions and positioning the structure of the human ADAT2 homodimeric complex (PDB code 3hd1) within the MAD density. The models for both structures were further built through several rounds of manual building and refinement. Both models show good data collection and refinement statistics (Supplementary Table S2).

Domain organization of the mouse ADAT complex

For ADAT2, only the first 10 and the last 15 residues are not seen in the electron density, while for ADAT3 the first 24 residues and residues 152–160 are not observed in the density (Figure 1). Our structures reveal that the ADAT2/ADAT3 complex harbours two semi-independent domains. The first domain (hereafter termed catalytic domain) comprises not only ADAT2 (residues 11–176) and the ADAT3 C-terminal domain (residues 161–349; hereafter termed ADAT3-C), but also ADAT3 very N-terminus (residues 25–33) that stably interacts with ADAT3-C by participating to its central β-sheet (Figures 1 and 2A).

The second ADAT domain comprises the ADAT3 N-terminal domain without the very N-terminus (residues 34–151; hereafter termed ADAT3-N) (Figure 2A). Surprisingly, the ADAT3-N domain is positioned differently in both structures with respect to the catalytic domain. Specifically, while the very N-terminus of ADAT3 interacts similarly with ADAT3-C in both structures, we observe a rotation of the ADAT3-N domains by around 90° with respect to each other (Figure 2B). This rotation is only due to the movement of residues 34–39, the rest of ADAT3-N superposing very well, and possibly of residues 152–160 that are not seen

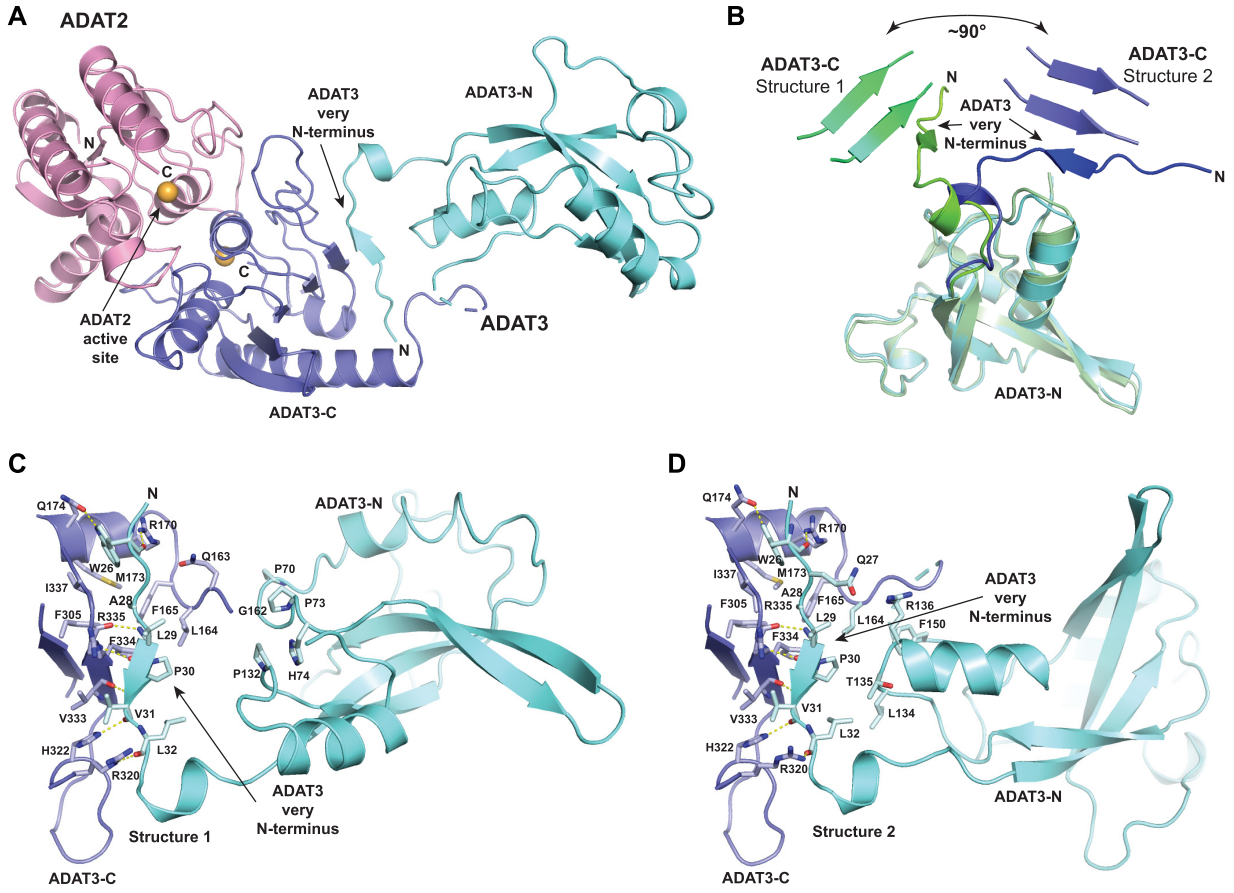

Figure 2. Structure of the mouse ADAT2/ADAT3 complex. (**A**) Ribbon representation of the 2.1 Å resolution structure of the mouse ADAT complex. ADAT2 is shown in pink, while ADAT3 N- and C-terminal domains are shown in cyan and blue, respectively, using the same colour code as in Figure 1. The zinc ions of both subunits are shown as orange spheres. ADAT2 active site and ADAT3 very N-terminus, which participates to the central β-sheet of ADAT3 C-terminal domain, are indicated. (**B**) Superposition of ADAT3 N-terminal domains from both structures. The different positioning of ADAT3 very N-terminus, which is linked to ADAT3 C-terminal domain, reveals that ADAT3 N- and C-terminal domains can rotate by at least 90° with respect to each other. (**C** and **D**) Close-ups of the ADAT3-N and ADAT3-C interfaces in both ADAT structures. The residues that participate in the loose interactions between the two domains are shown as sticks and labelled. Interactions between ADAT3 very N-terminus (residues 25–33) and ADAT3-C are shown, demonstrating the tight and stable interface between these two regions.

in the electron density. Thus, our structures reveal the ability of ADAT3-N to rotate with respect to the catalytic domain, even though it is doubly bound with this catalytic domain at its N- and C-termini. Yet, in both structures, ADAT3-N can still interact, albeit loosely, with the catalytic domain (Figure 2C and D).

Molecular basis of ADAT3 catalytic inactivity

ADAT3 has been suggested to be inactivated due to the replacement by a valine of the glutamate in its zinc-binding pocket that is usually involved in proton shuttling during catalysis (18). Our structure confirms this replacement since ADAT3 V225 is positioned precisely where the equivalent ADAT2 E73 is located, V255 side chain being however turned away from ADAT3 zinc-binding pocket (Figure 3A). Yet, a zinc ion is found in ADAT3 at the same position as in ADAT2, being coordinated by a canonical triad composed of one histidine (ADAT3 H223) and two cysteines (ADAT3 C289 and C292) (Figure 3A and B).

Strikingly, however, we observe that the fourth zinc coordination is not provided by a water molecule, which in TadA, and presumably in ADAT2, participates in the deamination reaction, but by the side chain carboxylate of D348, the before last residue of ADAT3 (Figure 3A and B). Specifically, D348 carboxylate is positioned where the catalytic water is located in TadA and ADAT2. In addition, the C-terminal carboxylate of the last ADAT3 residue, P349, forms a bidentate interaction with the side chain of ADAT3 R193. This latter interaction firmly positions the proline ring as a cap over the ADAT3 zinc binding site (Figure 3A and B).

These features are not observed in TadA where its long C-terminal α-helix (αC-helix), also observed in ADAT2 (α7), is not in close vicinity to the zinc ion but is essential for the binding of the ASL (Figures 1, 3A and 4A–C). In contrast, in ADAT3, the equivalent α-helix (α8) is much shorter and the last ADAT3 residues (343-349), which are not part of this helix, tightly pack in the vicinity and on top of the zinc-binding pocket (Figures 1, 3A and 4A–C).

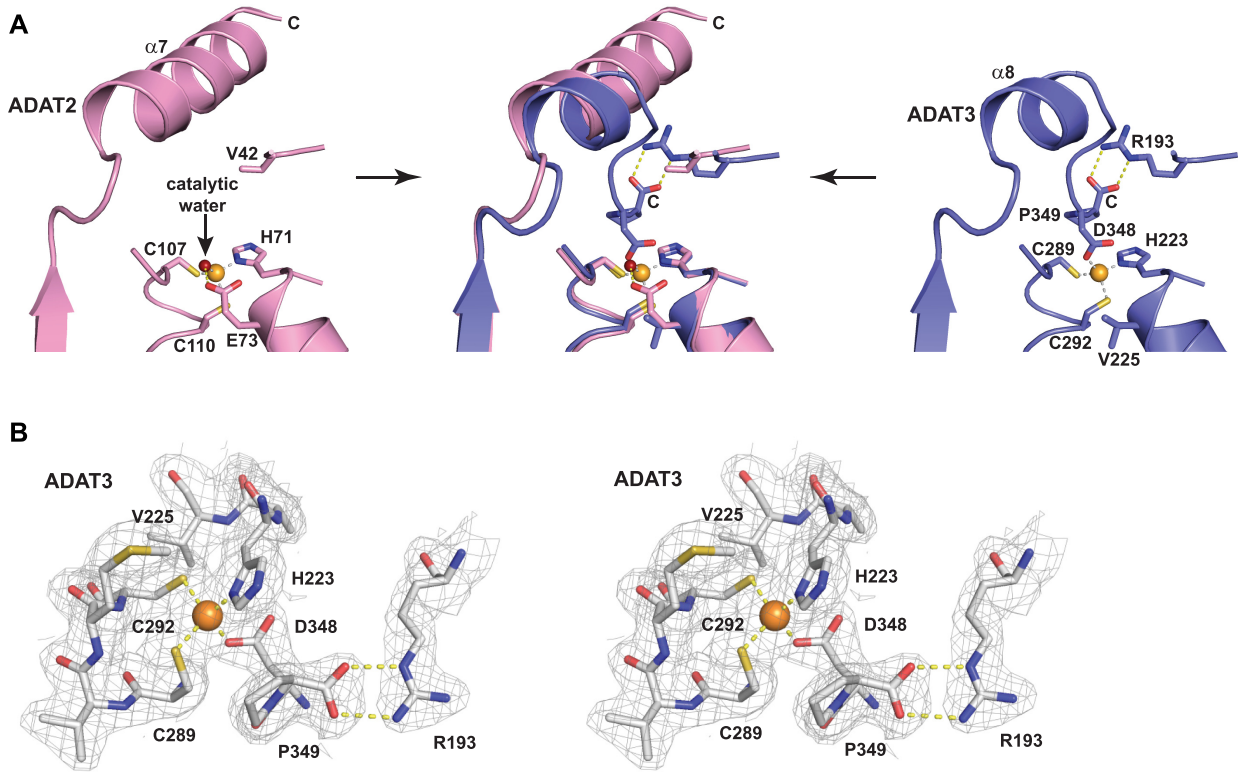

Figure 3. Molecular basis of ADAT3 inactivity. (**A**) Close-up view of the ADAT2 (left panel) and ADAT3 (right panel) zinc-binding pockets and their superpositions (middle panel). Zinc ions are shown as orange spheres. While ADAT2 (left panel) shows a canonical zinc coordination, including a catalytic water (red sphere), ADAT3 (right panel) has a fourth protein ligand (D348, the before last ADAT3 residue) that replaces the catalytic water. Capping of the zinc-binding pocket by the last ADAT3 residue, P349, as well as replacement of the catalytic glutamate by a valine (V225) in ADAT3 further provide the molecular basis of ADAT3 inactivation. These different interactions within the zinc-pocket of ADAT3 are allowed by the shortening of ADAT3 α8 helix compared to the longer α7 helix of ADAT2 (middle panel). (**B**) Wall-eye stereo view of ADAT3 zinc binding site. The 2Fo-Fc electron density is contoured at 1σ.

Since TadA has been shown to accommodate five anticodon loop bases in specific pockets (17), we have looked at the possible recognition of an ASL by ADAT3 by superposing its zinc-binding site onto the TadA/ASL active site (Figure 4A and B). As expected, we observe that ADAT3 could not accommodate an ASL due to the capping of the zinc binding site by C-terminal residues that closes the pocket where the wobble adenosine should be bound. Specifically, the ADAT3 D348 side chain overlaps partially with the position of the wobble adenine, and P349 occupies the position of the sugar moiety of the wobble adenosine in the TadA/ASL complex (Figure 4D and E).

In addition, the groove and the pockets accommodating the other bases of the anticodon loop are not found in ADAT3 and the shorter α8 C-terminal helix of ADAT3 cannot interact with an incoming ASL as observed for TadA C-terminal helix (Figure 4A and B; Supplementary Figure S2). In addition, the electrostatic potential at the surface of ADAT3 above its zinc binding pocket is negative and would be repulsive for an ASL (Supplementary Figure S2). Collectively, our results provide the molecular basis for ADAT3 catalytic inactivity.

ADAT2 active site can accommodate an ASL

In contrast, superposition of ADAT2 active site onto that of the TadA/ASL complex (17) shows that ADAT2 active site could accommodate an ASL (Figure 4A and C). In this model, the interactions with the sugar-phosphate backbone described in the TadA/ASL structure should be mostly conserved and a pocket is found in ADAT2 that can accommodate a wobble adenosine (Figure 4D and F). Importantly, ADAT2 and TadA have retained the same organization of this wobble adenosine binding pocket. Besides the conserved coordination of the zinc through ADAT2 histidine H71 (TadA H53) and cysteines C107 and C110 (TadA C83 and C86), the zinc ion is bound to a water molecule which is perfectly positioned to participate in the catalytic reaction, being also hydrogen bound to proton shuttling E73 (TadA E55). In addition, both nitrogens N1 and N3 of adenine 34 can accept hydrogen bonds from the backbone nitrogen of ADAT2 A72 (TadA A54) and the side chain of ADAT2 N60 (TadA N42). Further, ADAT2 H71 (TadA H53) and ADAT2 V44 (TadA I26) side chains can form stacking interactions with the adenine base (Figure 4D and F).

Even though pockets involved in the recognition of the other bases of the anticodon loop, as observed in the

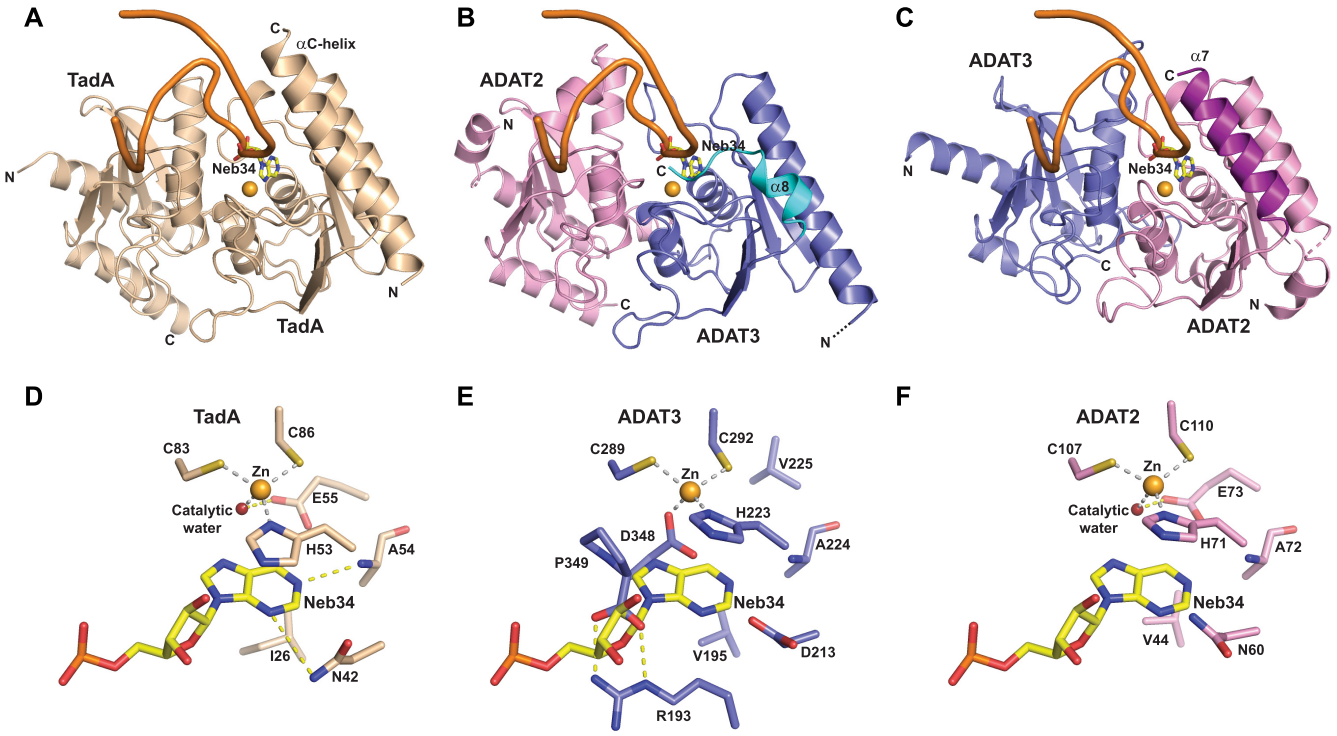

Figure 4. ADAT2 but not ADAT3 can accommodate an anticodon stem-loop in its active site. (**A**) Structure of an anticodon-stem-loop (ASL) bound to *S. aureus* TadA (PDB code: 2b3j) (17). The ASL is shown as an orange ribbon and the catalytic zinc as a light orange sphere. The non-hydrolysable adenine analog, nebularine, at the wobble position is shown as sticks and labeled (Neb34). The αC-helix of TadA is required for ASL binding. (**B**) Model based on our structures and the structure shown in (A) of an ASL binding to mouse ADAT in the ADAT3 zinc-binding pocket. The shorter α8 helix and the position of the ADAT3 C-terminus are incompatible with the ASL binding. (**C**) Same as in (B) but with the ASL binding in the ADAT2 active site. The ASL and the wobble adenosine could be recognized, provided minor conformational rearrangements of the ADAT complex. ADAT2 long α7 helix could participate in ASL binding. (**D**) Close-up from (A) of the interaction of wobble Nebularine within TadA. The zinc and catalytic water are shown as light orange and red spheres, respectively. (**E**) Close-up from (B) of the putative interaction of wobble Nebularine within ADAT3 zinc-binding pocket. Binding is incompatible with the position of ADAT3 C-terminus, notably aspartate 348 and C-terminal proline 349. (**F**) Close-up from (C) of the putative interaction of wobble Nebularine within ADAT2 active site. TadA and ADAT2 share the same recognition determinants of the wobble base.

TadA/ASL complex (17), are still present in the ADAT2 active site, the recognition determinants for these other bases appear to be changed or even partially lost between TadA and ADAT2 and even in ADAT3, since this latter protein also contributes significantly to these pockets (Supplementary Figure S3). Even if the recognition of the base pair formed by nucleosides 32 and 38 could still be carried out by ADAT2 R130 (TadA K106) and ADAT3 N328 (TadA N123), recognition of the nucleosides 33, 35, 36 and 37 by ADAT2 and ADAT3 seems to have evolved, only half of the recognition determinants of TadA being conserved in ADAT2 and ADAT3 (Supplementary Figure S3). This is however in agreement with the requirement that ADAT recognizes different ASLs with different anticodon loop sequences (Supplementary Table S1) and possibly different conformations.

ADAT3 N-terminal domain harbours a ferredoxin-like domain

To reduce the risk of ADAT recognizing and modifying a larger set of RNA molecules in the cell due to this loss of recognition determinants, our analysis suggests that this complex has developed additional mechanisms to ensure selective modification of tRNAs. In this view, the presence in ADAT3 of a eukaryote-specific N-terminal domain is intriguing. We have used the DALI server (42) to look for structural domains potentially similar to ADAT3-N. Among the top solutions, we found the structure of the tRNA-bound archeal Trm5 (guanine-37-N1-methyltransferase) enzyme, which modifies guanosines at position 37 of tRNAs into N1-methylguanosine (43). Interestingly, we could show that the ADAT3-N domain can superpose partially with the Trm5 N-terminal D1 domain that participates in tRNA binding (Figure 5A and B). Trm5-D1 can adopt different positions with respect to the Trm5 catalytic domain, reminiscent of what is observed for ADAT3-N. This movement of Trm5-D1 is required to correctly position this domain to interact with the incoming tRNA.

Our analyses further showed that Trm5-D1 adopts a ferredoxin-like domain (FLD) fold also found in other tRNA-modifying enzymes, such as archaeal CDAT8 (cytidine deaminase acting on tRNA base C8) and prokaryotic ThiI (4-thiouridine synthetase). These latter enzymes both use a tandem FLD-THUMP domain for interacting with tRNAs (Figure 5B and C) (44,45). ADAT3-N can also partially superpose with the FLDs of these tRNA-modifying

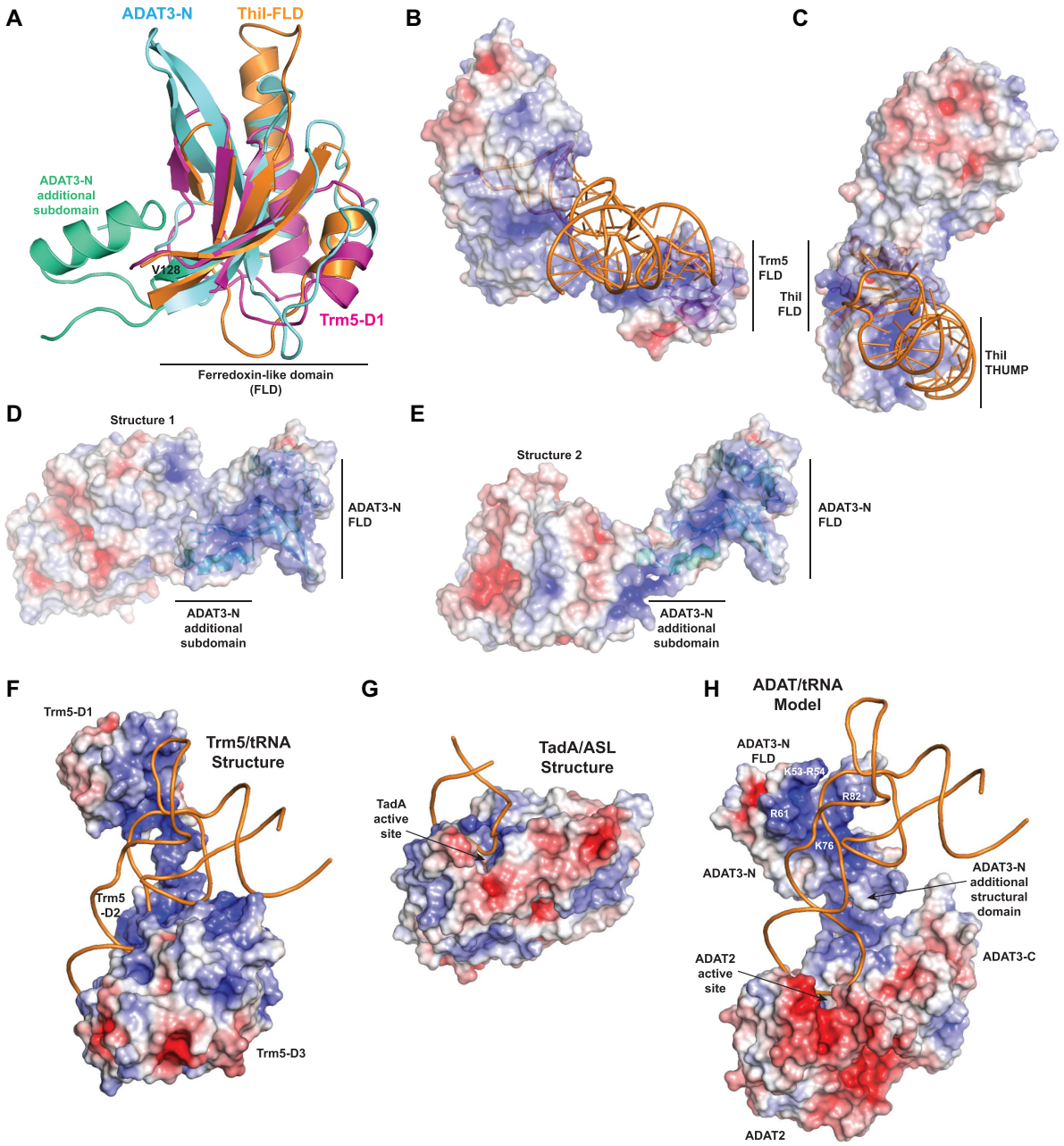

Figure 5. ADAT3-N harbours a ferredoxin-like domain (FLD) found in other tRNA-modifying enzymes. (**A**) Superposition of mammalian ADAT3-N, archeal Trm5-D1 (purple) and ThiI-FLD (ferredoxin-like domain; orange). All three domains adopt a FLD fold but show specific structural features. Specifically, ADAT3-N contains an additional structural subdomain (aquamarine) tightly bound to its FLD (cyan). This additional subdomain is mostly responsible for the loose interactions made between ADAT3-N and ADAT catalytic domain. (**B**) Cognate tRNA bound at the surface of Trm5. The electrostatic potential is displayed (blue, positively charged; red, negatively charged) at the surface of Trm5, showing that the tRNA interacts with the positive (blue) electrostatic patches in Trm5-FLD. (**C**) Same as in (b) for the ThiI/tRNA complex. (**D** and **E**) Electrostatic potential at the surface of the ADAT complex for both structures obtained, showing positive electrostatic patches that could interact with an incoming tRNA. For figures in (B–E), the FLDs are displayed as ribbons in the same orientation, after their superposition, showing that each FLD should interact with different surfaces with tRNAs. (**F**) Structure of archeal Trm5 bound to a cognate tRNA (PDB code: 2zzm). The electrostatic potential is represented at the surface of the Trm5 protein and the tRNA is shown as orange ribbon. The active site of Trm5 is not seen, being in the back of the enzyme. (**G**) Structure of the prokaryotic TadA/ASL complex (PDB code: 2b3j) with the same features as in (F). The orientation of the ASL is identical as in (F). The ASL makes a limited number of contacts with TadA, only nucleosides 32 to 38 interacting with the protein. (**H**) Model of an ADAT/tRNA complex based on the structures shown in (F and G), keeping the position of the ASL as in (F) and (G), and rotating slightly the position of the ADAT3-N domain from its observed position in the high resolution ADAT structure. The ASL might undergo conformational changes upon ADAT binding, as observed in the TadA/ASL complex (not included in the current model). The model shows that the ADAT3-N domain could participate to tRNA binding by interacting, notably through its FLD, with parts of the ASL stem, the D-arm and possibly, but to a lesser extent, with the variable arm of the incoming tRNAs. Basic residues changed to glutamates in ADAT3-acidic1 and ADAT3-acidic2 mutants are coloured white.

enzymes (Figure 5A). Yet, whereas Trm5, CDAT8 and ThiI FLDs form single structural domains, ADAT3-N harbours an additional structural subdomain composed of residues 37–42 and 128–151 that correspond to the N- and C-terminal extremities of ADAT3-N. Interestingly, this structural subdomain is tightly bound to ADAT3-N FLD (residues 43–127) through hydrophobic interactions and is mostly responsible for the loose interactions observed between ADAT3-N and the ADAT catalytic domain, forming a hinge between ADAT3-N FLD and ADAT catalytic domain (Figures 2C,D and 5D,E).

Analysis of the Trm5/tRNA and ThiI/tRNA structures shows that the surfaces of their FLDs which bind tRNA are different for both enzymes, the interactions being correlated with the positive electrostatic patches at the surface of their FLDs (Figure 5B and C) (43,44). This shows the functional plasticity of the FLDs in tRNA binding and suggests that ADAT3-N could also bind to tRNAs. Analysis of the electrostatic potential at the surface of ADAT3-N reveals that this domain also harbours large positive patches that could indeed be used to bind tRNAs (Figure 5D and E).

ADAT3 N-terminal domain is required for tRNA binding by ADAT

When establishing the purification protocol for the ADAT complex, we realized that the complex co-purifies with nucleic acids that we could remove by an additional ion exchange purification step (Supplementary Figure S4a). Analysis of the nucleic acid fraction on agarose gel showed that these nucleic acids had a molecular weight around 100 bp (Supplementary Figure S4b). We sequenced by mass spectrometry the nucleic acids fraction directly obtained from the ion-exchange column. Strikingly, these were exclusively composed of tRNAs from *E. coli*, the expression host used for the production of the ADAT complex. Specifically, tRNAs with >10 different anticodons could be unambiguously assigned (Supplementary Figure S4c). The reason why ADAT selected primarily this subset of tRNAs among all *E. coli* tRNAs is unknown and could be linked to many different parameters such as growth rate, tRNA abundance, tRNA modifications but also purification conditions, among others.

These results prompted us to purify *E. coli* TadA and check whether this enzyme could also co-purify with tRNAs. Ion exchange chromatography showed indeed two peaks containing nucleic acids that were co-purifying with *E. coli* TadA. Mass spectrometry revealed that both peaks contained TadA cognate $tRNA^{Arg}$(AGC). If the first peak was exclusively composed of this tRNA, the second peak also contained traces of degraded 16S ribosomal RNA. Strikingly, both mass spectrometry and sequencing showed that the co-purifying *E. coli* $tRNA^{Arg}$(AGC) was in fact fully modified with inosine at the wobble position, indicating that TadA can interact stably with its product (Supplementary Figure S4d). Surprisingly, among the other modifications observed, a methylated guanosine was also found at position 18, a modification not yet reported for this *E. coli* tRNA in the MODOMICS database (1).

The results on the ADAT complex suggested that this complex can recognize and bind stably to tRNAs that do not harbour the ASL of a cognate tRNA. We, therefore, investigated the importance of the additional N-terminal domain of ADAT3 in tRNA binding. We created a mutant of ADAT3 (ADAT3-ΔN) encompassing only ADAT3-C and co-expressed it with ADAT2. A stable ADAT2/ADAT3-ΔN mutant complex was obtained that could readily be purified. However, during complex purification, almost no nucleic acids co-purified with ADAT2/ADAT3-ΔN (Supplementary Figure S4a), suggesting that ADAT3-N is important for tRNA binding by ADAT.

Since these results had been obtained with prokaryotic tRNAs, we then looked at mouse tRNA binding by mouse ADAT using microscale thermophoresis. First, cognate mouse $tRNA^{Val}$(AAC) was produced, purified and CY5-labelled, and its binding by the ADAT complex was determined using microscale thermophoresis (MST). WT ADAT bound to $tRNA^{Val}$(AAC) with a K_d of 3.5 ± 0.2 μM. In contrast, the ADAT2/ADAT3-ΔN mutant had a K_d of 44.5 ± 4.4 μM for the same tRNA, >10 times higher than the WT complex (Supplementary Figure S5a). Interestingly, the same difference was observed using a non-cognate $tRNA^{Gly}$(CCC), with K_d values of 3.0 ± 0.2 μM for the WT complex and 35.8 ± 2.8 μM for the ADAT2/ADAT3-ΔN mutant (Supplementary Figure S5a). We then checked two other cognate tRNAs, $tRNA^{Arg}$(ACG) and $tRNA^{Ala}$(AGC). Whereas the former showed a similar K_d of 3.7 ± 0.3 μM for binding to WT ADAT, the latter had a slightly higher K_d of 8.0 ± 0.8 μM (Supplementary Figure S5b). Interestingly, TadA showed a K_d of 6.6 ± 1.1 μM for $tRNA^{Arg}$(ACG) (Supplementary Figure S5b). Collectively, our results demonstrated the importance of ADAT3-N for tRNA binding by ADAT but showed that this domain does not discriminate between cognate and non-cognate tRNAs.

We have tentatively modelled tRNA binding by ADAT by superposing onto the TadA/ASL complex (i) our two ADAT structures and (ii) the Trm5/tRNA complex. In the former case, the catalytic dimeric domains of TadA and ADAT2/ADAT3 were used for superposition, whereas in the latter case only the ASLs of the TadA/ASL and Trm5/tRNA structures were considered. This led to two ADAT/tRNA models, one for each ADAT structure, where the ADAT3-N domain had a different position related to the tRNA molecule. Inspection of the location of the positively charged surfaces of ADAT3-N with respect to the tRNA revealed that these surfaces are completely opposite to the tRNA in the low resolution ADAT structure.

In contrast, in the case of the high resolution structure, we observed that a slight rotation of ADAT3-N could bring its positively charged surfaces in close vicinity of the tRNA backbone. In this model, both ADAT3-N and the ADAT catalytic domain are positioned relative to each other so that the two flexible ADAT3 stretches (34-39 and 152–160) could accommodate the positioning of these two domains. The final model (Figure 5F–H) shows that ADAT3-N could make extensive interactions with the upper part of the stem of the ASL and with the tRNA D arm. Interactions with other parts of the tRNA, like the variable arm, could also occur.

Specifically, our model suggests that ADAT3-N FLD could be primarily responsible for the interaction with the

tRNA D arm and the upper part of the stem of the ASL, while ADAT3-N additional structural subdomain would play its role of hinge between the FLD and ADAT catalytic domain, still contributing to overall binding through its positive charge. Finally, as observed in TadA, ADAT2 active site would recognize the tRNA anticodon loop (Figure 5G and H).

ADAT deaminates differently its cognate tRNAs and partially discriminates non-cognate tRNAs

In order to characterize the structure/function relationships of ADAT, we next performed deamination assays. Using initially the WT complex and different ADAT:tRNA^{Val}(AAC) ratios, we observed decreasing amounts of inosine-modified tRNA for decreasing amount of ADAT complex for a fixed reaction time. Surprisingly, time-course experiments did not yield much higher tRNA modification for longer incubation times at a fixed ADAT concentration, although the enzyme appeared highly processive since most of the tRNA was modified within seconds in excess of ADAT. Since *E. coli* TadA can co-purify with its product, we reasoned that the ADAT product could also remain bound to this enzyme, at least to the ADAT3 N-terminal domain, perturbing time course assays by competing with unmodified tRNAs. We, therefore, proceeded using different ADAT:tRNA ratios and a fixed reaction time (Figure 6; Supplementary Table S3).

The three tRNA^{Val}(AAC), tRNA^{Arg}(ACG)and tRNA^{Ala}(AGC) were used for these assays. We not only first measured the deamination activity of the WT ADAT2/ADAT3 complex, but also tested the activity of, as assessed by size exclusion chromatography, the homodimeric ADAT2/ADAT2 complex, the monomeric ADAT3 protein and the homodimeric *E. coli* TadA. WT ADAT showed a robust deamination activity, while ADAT2/ADAT2 and ADAT3 were inactive (Figure 6A). TadA homodimer was active only in presence of tRNA^{Arg}(ACG), as previously shown (Figure 6A) (13). Decreasing ADAT:tRNA ratios revealed however that ADAT could more readily deaminate tRNA^{Ala}(AGC) than the two other cognate tRNAs used, possibly reflecting a higher turnover rate for tRNA^{Ala}(AGC) (Figure 6B; Supplementary Table S3).

We next analysed the importance of the ADAT3 N-terminal domain on activity. The ADAT2/ADAT3-ΔN mutant completely abolished deamination for the three tRNAs (Figure 6A). Since our ADAT/tRNA model suggested that incoming tRNAs could bind to positively charged patches on ADAT3-N FLD, we identified two sets of basic exposed residues that could participate in tRNA binding: K53-R54-R61 and K76-R82 (Figure 5H). We constructed two mutants where these residues were mutated into glutamates, one mutant modifying only the first set of residues (ADAT3-acidic1), the second mutant modifying both sets of residues (ADAT3-acidic2). Both complexes were unable to co-purify with *E. coli* tRNAs. Interestingly, while the ADAT-acidic1 mutant showed some residual deamination activity, notably for tRNA^{Ala}(AGC), the ADAT-acidic2 mutant completely lost its deamination activity, whatever the tRNA (Figure 6A and B; Supplementary Table S3). These results therefore reinforced our modelling studies and binding hypothesis.

We next investigated the two zinc binding sites of ADAT2 and ADAT3. An ADAT2-E73A/ADAT3 mutant, where the proton shuttling residue E73 was mutated into alanine, hardly retained any activity (Figure 6A). We then tested whether ADAT3 zinc binding pocket mutants could rescue the inactivity of the ADAT2-E73A mutant. Three ADAT3 mutants were constructed: ADAT3-V225E, ADAT3-ΔC, where the capping of the ADAT3 zinc binding site was prevented by removing the last five residues (345-349) of ADAT3, and ADAT3-V225E-ΔC. Only the first two mutants turned out to be soluble upon co-expression with ADAT2. Intriguingly, while the ADAT2-E73A/ADAT3-V225E mutant was completely inactive, the ADAT2-E73A/ADAT3-ΔC mutant was inactive for tRNA^{Val}(AAC) and tRNA^{Arg}(ACG) but showed significant deamination activity for tRNA^{Ala}(AGC), albeit only in presence of high amounts of ADAT (Figure 6A; Supplementary Table S3).

We also investigated the role of the ADAT3-specific loop that we removed for crystallization (Figure 1). Interestingly, the ADAT2/ADAT3-Δloop mutant showed a significant reduction of deamination activity, notably for tRNA^{Val}(AAC) and tRNA^{Arg}(ACG) (Figure 6A and B). We therefore tested the binding of this mutant to the three tRNAs by microscale thermophoresis. K_d values for the three complexes were very similar: 6.7 ± 0.7 μM (Val), 6.5 ± 0.2 μM (Arg) and 6.7 ± 0.3 μM (Ala). These values were slightly higher for tRNA^{Val}(AAC) and tRNA^{Arg}(ACG) but slightly lower for tRNA^{Ala}(AGC) when compared to the WT complex (Supplementary Figure S5c). These results showed that the ADAT3-specific loop, which is located in the ADAT3 C-terminal domain and is close to the ADAT2 active site, can influence positively or negatively tRNA binding into ADAT2 active site.

Finally, we have asked whether ADAT could deaminate a non-cognate tRNA having an adenosine at the wobble position. Since we previously showed that tRNA^{Gly}(CCC) was able to bind to ADAT, we created a mutant of this tRNA by replacing its wobble cytosine with an adenosine (tRNA^{Gly}(ACC)). The anticodon loop sequence of this mutant tRNA perfectly fitted the diversity of base recognition required by ADAT2 to recognize all ADAT cognate tRNAs (Supplementary Table S1). Interestingly, WT ADAT was able to modify the wobble adenosine into inosine of the pseudo-cognate tRNA^{Gly}(ACC), albeit much poorly as for a cognate tRNA (Figure 6A). This demonstrated that ADAT has still retained specificity determinants for its cognate tRNAs beside the recognition of the wobble adenine.

The V128M mutation enlarges ADAT3-N without precluding tRNA binding but affects ADAT deamination activity

Mutation of valine 128 into methionine (p.Val128Met) in human ADAT3-N has been shown to cause intellectual disability, microcephaly and other neurodevelopmental disorders (25–28). We observe that the equivalent valine 128 in mouse ADAT3 is part of a large hydrophobic core comprising I43, A45, A47, L69, L75, L93, L96, V126, P129 and W146 (Figures 1 and 7A). This hydrophobic core is located in the centre of ADAT3-N and is responsible for the

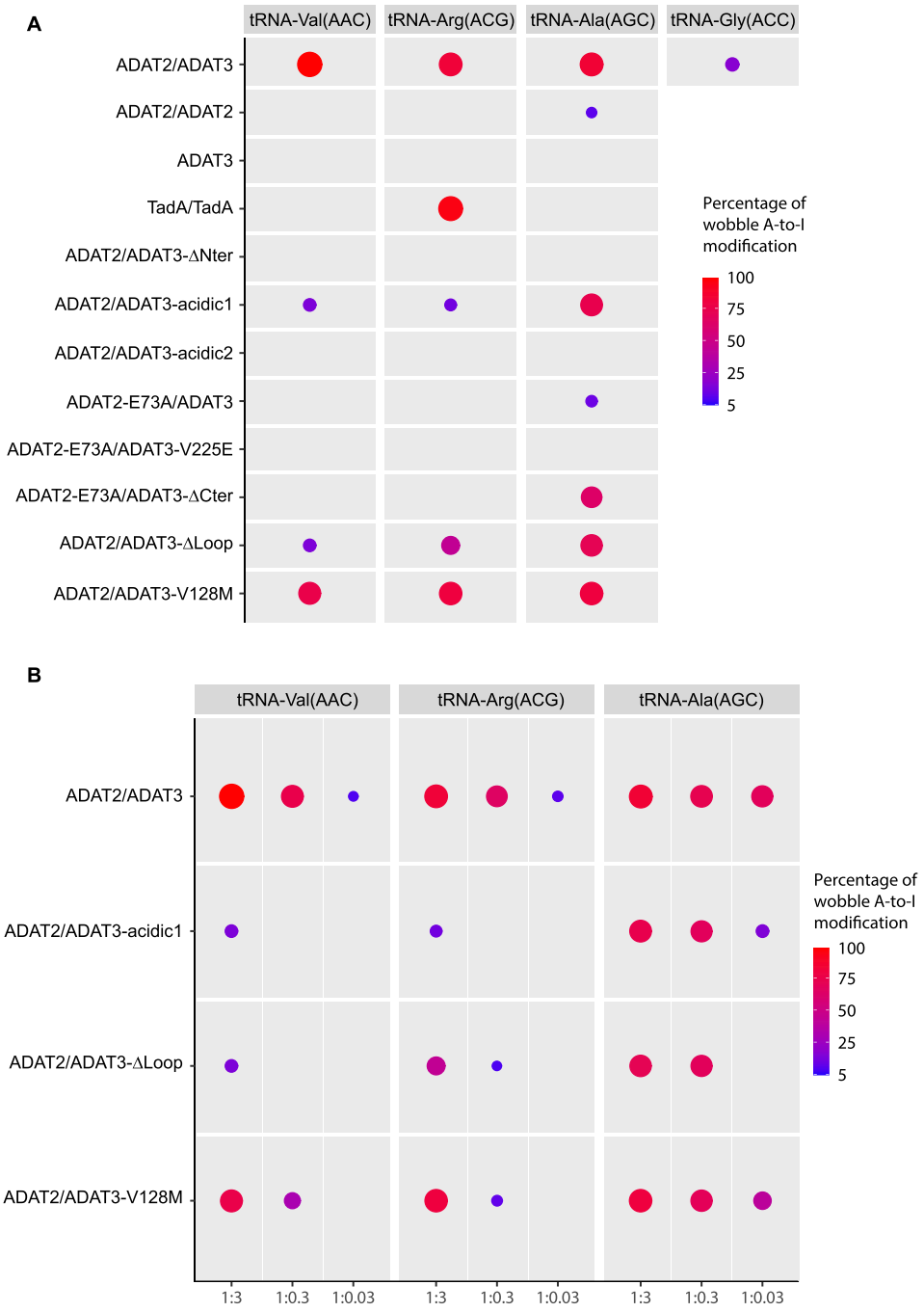

Figure 6. Deamination activity of ADAT, ADAT2, ADAT3 and TadA and various ADAT mutants. (**A** and **B**) The percentages of deamination activity of ADAT(ADAT2/ADAT3), ADAT2, ADAT3 and TadA and of various ADAT mutants on four different tRNAs (tRNA^{Val}(AAC), tRNA^{Arg}(ACG) and tRNA^{Ala}(AGC), and the pseudo-cognate mutant tRNA^{Gly}(ACC)) are shown as circles decreasing in size for a decreasing deamination activity. The threshold for activity has been set at 5%. The full data for all complexes is provided in Supplementary Table S3. Different tRNA:enzyme ratios (1:3, 1:0.3, 1:0.03) were used for the measurements. In (A) only the 1:3 ratio is shown for all complexes, while in (B) the three ratios are shown for a few complexes that did not appear to lose activity at high enzyme concentration but turn out to be less active when the ratio is decreasing. Only ADAT and TadA were shown to have a robust deamination activity. All enzyme mutants showed perturbation of the deamination activity, albeit to a lesser extent in the case of tRNA^{Ala}(AGC) that appears to bind slightly differently to ADAT, but still requires ADAT3-N. TadA only deaminates tRNA^{Arg}(ACG), and ADAT can partially deaminate a pseudo-cognate mutant tRNA^{Gly}(ACC), where the wobble cytosine has been replaced by an adenosine.

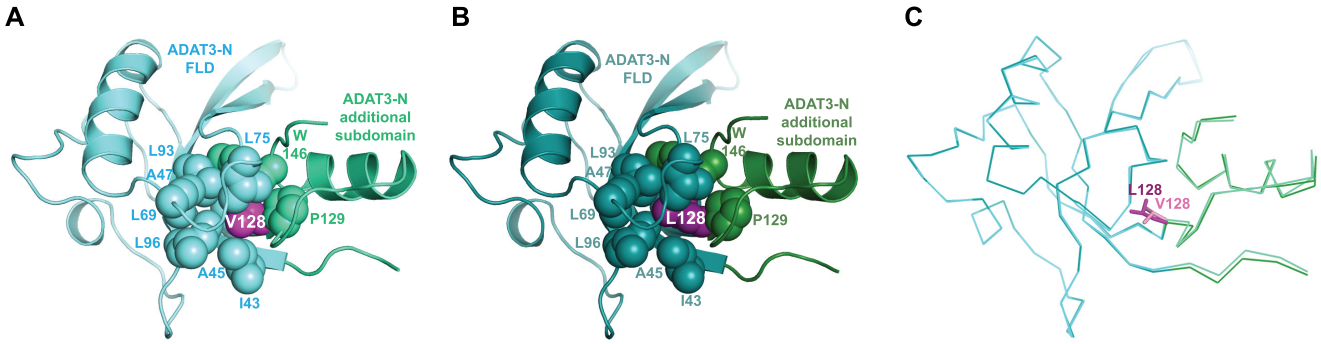

Figure 7. Position of V128 within ADAT3-N and effect of its mutation in leucine (V128L). (**A**) Ribbon structure of ADAT3-N with the residues forming its central V128 (purple) hydrophobic core shown as spheres. The residues are coloured according to the subdomain they belong to: FLD (cyan) and additional structural subdomain (aquamarine). (**B**) Same as (A) for the V128L mutant. The same colour code is used with slightly darker colours. (**C**) Superposition of the ADAT3-N WT and V128L domains shown as Cα ribbons. Slight changes are observed in the main chain position (movements of 0.3–0.9 Å) of residues from the V128 hydrophobic core and of neighbouring residues upon the V128L mutation. These movements propagate notably within the ADAT3-N specific structural subdomain but much less in the FLD. A V128M mutation is expected to exacerbate these changes.

tight interaction between the ADAT3-N FLD and the additional structural subdomain of ADAT3-N. This suggested that the V128M mutation would affect the overall folding of ADAT3-N. To test this hypothesis, we generated constructs bearing the V128M mutation but also the V128L or V128I mutations, those latter two substitutions having potentially a milder effect on ADAT3-N folding.

All three ADAT3 mutants could be co-expressed with ADAT2 and their complex purified to homogeneity following the same experimental protocol as for the WT enzyme. All mutant complexes co-purified with nucleic acids (Supplementary Figure S4a,b). We showed by mass spectrometry that these nucleic acids were also composed of diverse *E. coli* tRNAs, as for WT ADAT (Supplementary Figure S4c). Interestingly, all three mutants could be crystallized in similar conditions as for the WT complex, albeit with some decrease in crystallization propensity for the V128M mutant complex. The tendency of the crystals to aggregate, as already observed with the WT complex, was also observed with the mutants and hindered our structural analyses. Whereas the crystals with the V128I and V128M mutants, which showed stronger aggregation, did not diffract sufficiently, we were able to collect a full data set at 2.0 Å resolution for the V128L mutant. The structure of the ADAT-V128L complex was refined with good data collection and refinement statistics (Supplementary Table S2).

The same crystallographic space group and unit cell as well as the similar resolution obtained for both WT and V128L ADAT complexes allowed the precise analysis of the structural changes occurring upon the V128L mutation. Superposition of the complexes showed that both ADAT3-N and the ADAT catalytic domain are mostly unaffected by the mutation. In details, however, we observed that the main chain of residues involved in the V128 central hydrophobic core and of their neighbours is moving away from the core by about 0.3–0.9 Å (Figure 7A–C). We found that these movements are mainly propagated within the ADAT3-N specific structural subdomain but much less in the FLD, which displays a more stable fold due to its tighter packing (Figure 7C).

A bulkier methionine in place of the leucine at position 128 will have a more substantial effect on the ADAT3-N structure and we expect the movements observed in the case of the V128L mutation to be larger in the V128M mutant. Yet, since the ADAT-V128M complex can crystallize in conditions where the ADAT3-N domain participates in crystal packing, it appears unlikely that the movements induced by the V128M mutation would cause the complete unfolding of the ADAT3-N domain. We have assessed the enzymatic activity of the ADAT-V128M mutant and showed that it retains a significant activity. However, this occurs notably when the enzyme is in excess compared to the tRNA. In addition, this activity is always lower than that of the WT enzyme at the same concentration (Figure 6A,B; Supplementary Table S3). Of note, we did not observe that this mutant modified any other adenosines in these tRNAs, showing that, at least for the tRNAs considered, the V128M mutation does not cause a loss of specificity for the targeted adenosine.

Since the V128 mutants co-purified with *E. coli* tRNAs, we also looked by microscale thermophoresis at tRNA binding by the mutants to the cognate $tRNA^{Val}$(AAC). Our measurements gave K_d values of 3.3 ± 0.2, 4.2 ± 0.4 and 2.5 ± 0.1 μM for the V128I, V128L and V128M mutants, respectively (Supplementary Figure S5d). These quantitative results show minimal differences for tRNA binding compared to the WT, in agreement with the qualitative observations made with the *E. coli* tRNAs during complex purification. As such, loss of tRNA binding by the V128M cannot be considered as a major reason for the reported decrease of tRNA deamination observed *in vitro* (Figure 6A and B) and in patient cells (29), implying that this mutation perturbs other mechanisms.

Mutant ADAT complexes show impaired neuronal migration *in vivo*

To evaluate the functional impact of the ADAT3-N domain *in vivo* and considering the implication of the p.Val128Met variant in neurodevelopmental disorders,

we assessed the consequences of overexpressing mouse ADAT3 mutants together with ADAT2 *in vivo* in the mouse developing cortex using *in utero* electroporation (IUE) (Figure 8A). Since ADAT plays a crucial role in the regulation of migration of the projection neurons (Del-Pozo-Rodríguez, in preparation), we investigated the effects of the mutated constructs on neuronal positioning. In addition, since other mutants used in our study showed significant effects on tRNA binding and deamination, we extended our *in vivo* investigations to the most significant ones. We therefore considered seven mutants: ADAT2-E73A/ADAT3, ADAT2-E73A/ADAT3-ΔC, ADAT2/ADAT3-Δloop, ADAT2/ADAT3-ΔN, ADAT2/ADAT3-V128I, ADAT2/ADAT3-V128L and ADAT2/ADAT3-V128M.

We first verified by transfection experiments in a N2A neuroblastoma cell line that WT ADAT2 and ADAT3 as well as their mutants were similarly expressed (Figure 8B). We then expressed mouse WT or E73A ADAT2 and ADAT3 mutants using IUE of pCAGGS-ADAT2 and HA-tagged pCAGGS-ADAT3 constructs together with a NeuroD-IRES-GFP reporter plasmid, allowing the expression of GFP specifically in post mitotic neurons in WT mouse cortices at E14.5 (Figure 8A).

We then evaluated the effects of the mutants 4 days after IUE, when most of the GFP+ postmitotic neurons expressing full-length WT ADAT are reaching the cortical plate as in the control (Figure 8C). Interestingly, all neurons expressing the different variants accumulated in the intermediate zone, with a decrease of 15.7%, 9.3%, 10.8%, 12.7%, 18%, 14.8% and 18.4% of the cells reaching the upper cortical plate in the ADAT2-E73A/ADAT3, ADAT2-E73A/ADAT3-ΔC, ADAT2/ADAT3-Δloop, ADAT2/ADAT3-ΔN, ADAT2/ADAT3-V128I, ADAT2/ADAT3-V128L and ADAT2/ADAT3-V128M conditions, respectively (Figure 8D and E). These results demonstrated that the disease- and structure-based variants impede to similar extents the radial migration of projection neurons.

Interestingly, we observe no rescue of the catalytic ADAT2 inactivity phenotype by the ADAT2-E73A/ADAT3-ΔC mutant, reflecting the very partial rescue of the enzymatic activity of this mutant *in vitro*. In addition, these results further confirm the functional importance of the ADAT3-specific loop, whose deletion was required for the structural studies, as well as that of ADAT3 N-terminal domain. Thus, collectively, our *in vivo* results corroborate our *in vitro* analyses.

DISCUSSION

Our analysis of the mammalian ADAT complex reveals specific features that distinguish this complex from the prokaryotic TadA homodimeric complex. While ADAT2 has retained structural determinants for the recognition of cognate tRNAs anticodon loops and the deamination activity, ADAT3 has become inactive through amino acid changes, the capping of its zinc binding pocket by ADAT3 C-terminus, and the disappearance of binding pockets for the anticodon loop nucleosides. *In vitro*, removal of ADAT3 zinc binding site capping in the ADAT3-ΔC mutant is not sufficient to confer a full deamination activity to ADAT3 and, *in vivo*, the ADAT3-ΔC mutant fails to rescue the phenotype caused by ADAT2 inactivation. In addition, the homodimeric ADAT2/ADAT2 complex and ADAT3 alone do not show any robust deamination activity. Although this could be due to an inadequate buffer, our structural analysis shows that both ADAT2 and ADAT3 residues are participating to the formation of ADAT active site. Our results therefore reinforce the generally admitted idea that ADAT2/ADAT3 is the functional biological unit for mammalian tRNA wobble adenosine-to-inosine deamination and show that ADAT2 is the catalytic subunit of this complex but requires several ADAT3 residues to be active.

The requirement for ADAT to modify different tRNAs imposes that ADAT2, in contrast to TadA, has evolved a specific anticodon loop recognition strategy to adapt to the various tRNAs with different anticodon loop sequences and possibly with different ASL conformations. This is in agreement with the apparent loss of some recognition determinants observed in the ADAT2 anticodon loop bases recognition pockets. In turn, this has constrained the ADAT complex to change to recognize specifically tRNA macromolecules, in agreement with the fact that the full tRNA tertiary structure, and not only the ASL, is required for ADAT activity (14,23,24).

Our results demonstrate that the eukaryote-specific ADAT3 N-terminal domain is essential for the strong, albeit non-selective interaction between ADAT and tRNAs. An important result of our structural studies is the discovery of the inherent mobility of the ADAT3-N domain with respect to the catalytic domain. This positional mobility of ADAT3-N appears linked to the fact that the ADAT complex binds and modifies differently various tRNAs having variable compositions and tertiary structures. Thus, the capacity of movement of ADAT3-N should be essential to facilitate the binding of the tRNAs and the strict positioning of their anticodon loop into the ADAT2 active site. Thus, the differences that we and others (24) observe in the recognition and the processing of cognate tRNAs by ADAT could be explained by different binding of those tRNAs to the ADAT active site but also onto ADAT3-N.

The apparent non-selective nature of ADAT3-N raises the question of the specific recognition of cognate tRNAs by ADAT. As for TadA, which only recognizes the anticodon loop of its cognate tRNA, notably its wobble adenosine, the specific recognition of the wobble adenosine by ADAT2 could suffice, this subunit scanning the tRNAs bound to ADAT3-N for a wobble adenosine. In agreement, our deamination assays with a pseudo-cognate $tRNA^{Gly}$(ACC) mutant revealed that ADAT can deaminate *in vitro* a non-cognate tRNA which has an artificial adenosine at its wobble position, rendering its anticodon loop perfectly compatible with the recognition diversity required for deamination of all ADAT cognate tRNAs (Supplementary Table S1). However, the fact that the deamination level of this tRNA remains poor indicates that ADAT has also retained specific cognate tRNA recognition determinants but that these are possibly not only situated in ADAT2 anticodon loop binding pockets.

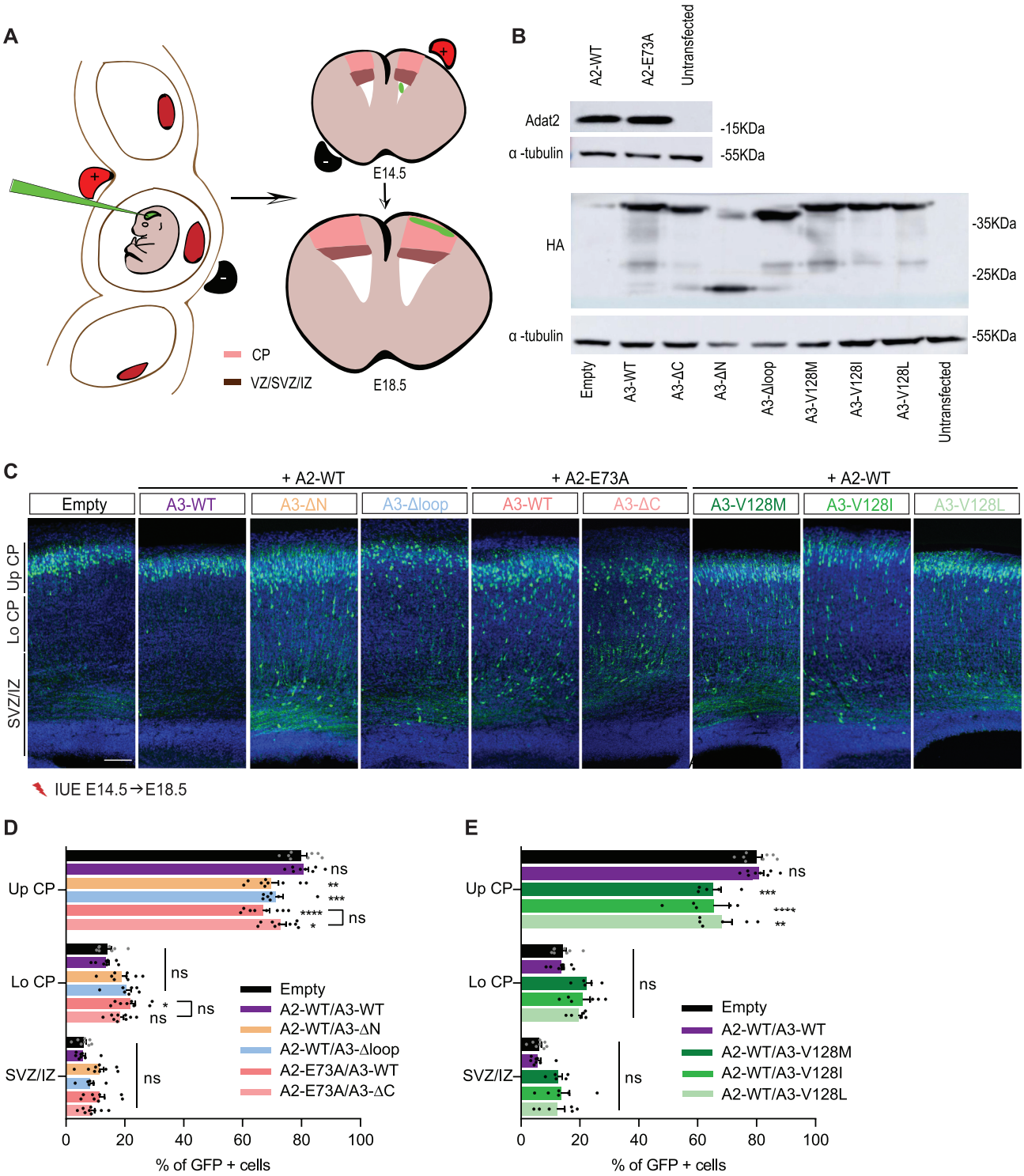

Figure 8. *In vivo* effects of mutant ADAT complexes. (**A**) Scheme representing the *in utero* electroporation procedure used to follow the migration of GFP+ neurons expressing WT and mutant ADAT2 and/or ADAT3. (**B**) Western blot of extract from N2A cells transfected with an empty vector or the indicated ADAT2 (upper panel) or HA-tagged ADAT3 (lower panel) constructs showing similar expression of WT and catalytically inactive ADAT2 (E73A) proteins and of WT, mutant and truncated ADAT3 proteins. α-Tubulin was used as a loading control. (**C**) Coronal sections of E18.5 cortices, 4 days after IUE with NeuroD-IRES-GFP and the indicated ADAT2 and ADAT3 constructs, showing impaired distribution of GFP-positive electroporated cells (green) in all conditions tested. Nuclei are stained with DAPI (blue); scale bar: 100 μm. (**D** and **E**) Histograms (means ± S.E.M) showing the distribution of GFP-positive neurons in different regions (Up CP, Upper cortical plate; Lo CP, Lower cortical plate; IZ, intermediate zone; SVZ, subventricular zone) for all conditions as indicated. Significance was calculated by two-way ANOVA (Bonferroni's multiple comparisons test). Number of embryos analysed: empty vector and A2-WT/A3-WT, $n = 8$; A2-WT/A3-V128L and A2-WT/A3-V128I, $n = 6$; A2-WT/A3-V128M, $n = 5$; A2-WT/A3-Δloop, A2-E73A/A3-WT and A2-E73A/A3-ΔC, $n = 8$; A2-WT/A3-ΔN, $n = 9$; ns, non-significant; $^{*}P < 0.05$; $^{**}P < 0.01$; $^{***}P < 0.001$; $^{****}P < 0.0001$. A2 and A3 stand for ADAT2 and ADAT3, respectively.

Whether these additional determinants are located at the level of ADAT3 N-terminal domain, in the ADAT3-specific loop, which we have shown to impact tRNA binding and ADAT enzymatic activity, or in other regions of ADAT2 and/or ADAT3, remains to be determined. We cannot exclude that all these domains contribute to various extents to specificity. Interestingly, our deamination experiments show that ADAT does not process equally its various cognate tRNAs. Notably, $tRNA^{Ala}$(AGC) appears less sensitive to ADAT perturbations, especially those affecting mildly ADAT3 N-terminal domain, and differences in the binding of $tRNA^{Arg}$(ACG) and $tRNA^{Ala}$(AGC) by ADAT have already been reported (24). In line with this, $tRNA^{Ala}$(AGC) interaction with ADAT shows a slightly higher K_d around 8 μM. This could suggest that ADAT interaction with $tRNA^{Ala}$(AGC) is different than with $tRNA^{Val}$(AAC) and $tRNA^{Arg}$(ACG). However, removal of ADAT3 N-terminal domain or mutating several basic residues in ADAT3-N FLD basic patches completely prevents deamination of $tRNA^{Ala}$(AGC), demonstrating that even $tRNA^{Ala}$(AGC) requires ADAT3-N for binding in regions far away from ADAT2 active site.

The V128M mutation in ADAT3-N is known to cause intellectual disability, microcephaly and other neurodevelopmental disorders in patients due to a decreased wobble A-to-I modification by the ADAT complex (25–29). It has been suggested that this decrease could be due to the instability of mutant ADAT3 and its interaction with chaperones (29). The central position of V128 in the hydrophobic core organizing ADAT3-N could indeed affect ADAT3-N folding *in vivo*, potentially leading to ADAT3 interaction with chaperones. Yet, the differences observed in A-to-I modification of various tRNAs by mutant ADAT observed *in cellulo* (29) imply that the V128M mutation also plays a role in a correctly folded ADAT V128M mutant complex. Our observations that ADAT3-V128M associates with ADAT2 and that the resulting ADAT mutant complex can bind as strongly as WT to tRNAs and retains some deamination activity demonstrate that this mutant still possesses the propensity to fold correctly and to be partially active. This raises the question of how the V128M mutation could affect the deamination reaction of ADAT.

Our data suggest that the structural enlargement of ADAT3-N by the V128M mutation could perturb (i) the positioning of the tRNAs onto the ADAT3-N domain, (ii) the rotation of this domain with respect to the catalytic domain and/or (iii) the stable interface between these latter two domains during catalysis. The results presented here favour the hypothesis that the V128M mutation does not significantly perturb tRNA binding by ADAT3-N FLD but rather affects ADAT3-N additional structural subdomain and its role of hinge between ADAT3-N and the ADAT catalytic domain. This would perturb the optimal anticodon loop presentation to ADAT2 and lead to a decreased A-to-I modification. Yet, considering that we observe that the V128M mutant effect on deamination is different depending on the cognate tRNA, it is most likely that the mode of binding of the tRNA onto ADAT3-N will also influence the catalytic reaction.

Collectively, our results shed light on the modification of tRNAs by the ADAT complex and its similarities and difference with TadA, suggesting a two-step mechanism for the eukaryotic complex (Figure 9). First, the tRNA, especially its tertiary structure, is recognized by the ADAT3 N-terminal domain, notably its FLD. This domain then rotates to maximize the interactions between the tRNA and the full ADAT complex, and presents the ASL correctly to ADAT2 that then modifies the wobble adenosine into inosine. This mechanism is perturbed by the V128M mutation, causing a decrease in A-to-I modification, leading to neurodevelopmental disorders (Figure 9).

While this manuscript was in revision, the yeast ADAT complex structure was published (46). Conclusions of the study on the yeast complex are similar to ours, notably on the role of ADAT3/Tad3p N-terminal domain for tRNA recognition and presentation to ADAT2/Tad2p active site, as well as the inactivation of ADAT3/Tad3p by capping of its zinc binding site. Both studies, however, show significant structural differences between the yeast and mouse ADAT complexes that could relate to function (Supplementary Figure S6). Specifically, the yeast Tad2p C-terminus is much longer than that of mammalian ADAT2 and wraps around its core domain, and the ADAT3/Tad3p specific loops appear to adopt different conformations. In addition, although both ADAT3/Tad3p N-terminal domains show a similar fold, they also show significant structural differences that could impact tRNA binding, and the V128 structural environment is different in both mouse ADAT3-N and yeast Tad3p-N (Supplementary Figure S6). Surprisingly, although both mouse ADAT3 and yeast Tad3p C-termini provide the fourth zinc-ligand to this subunit, the composition and conformation of these two C-termini are quite different in both ADAT3/Tad3p subunits in contrast to the rest of their structures. Finally, the V128M equivalent mutation in yeast Tad3p causes ∼90% loss of deamination activity in presence of $tRNA^{Ala}$. Our study shows that in similar experimental conditions (tRNA:enzyme ratio of 1:0.03), the effect of the ADAT3-V128M mutation can be more drastic, with a complete loss of activity, although we demonstrate that this effect is, in fact, varying depending on the tRNA bound. This latter aspect was not investigated in the yeast study that made use of a single tRNA species, leaving therefore open several questions on the similarities and dissimilarities of the yeast Tad2p/Tad3p mechanism compared to the vertebrate ADAT2/ADAT3 mechanism.

Thus, our study provides the molecular basis for further investigating the involvement of ADAT in diseases (25–29,47). However, the mechanisms affected by the loss of tRNA wobble A-to-I modification in disease remain to be characterized. Notably, whether faulty tRNA deamination impacts tRNAs stability, abundance, maturation and aminoacylation remains to be investigated. In addition, efficiency and/or accuracy of protein synthesis also remains to be determined. Notably, further study of actively-translated transcripts and translation rate by ribosome profiling would shed light on translational effects at the ribosome. Such studies would benefit from an analysis in the most relevant conditions, i.e. in diseased brains using knock-in or knock-out ADAT3 mouse models, to determine the consequences of ADAT variants on translation.

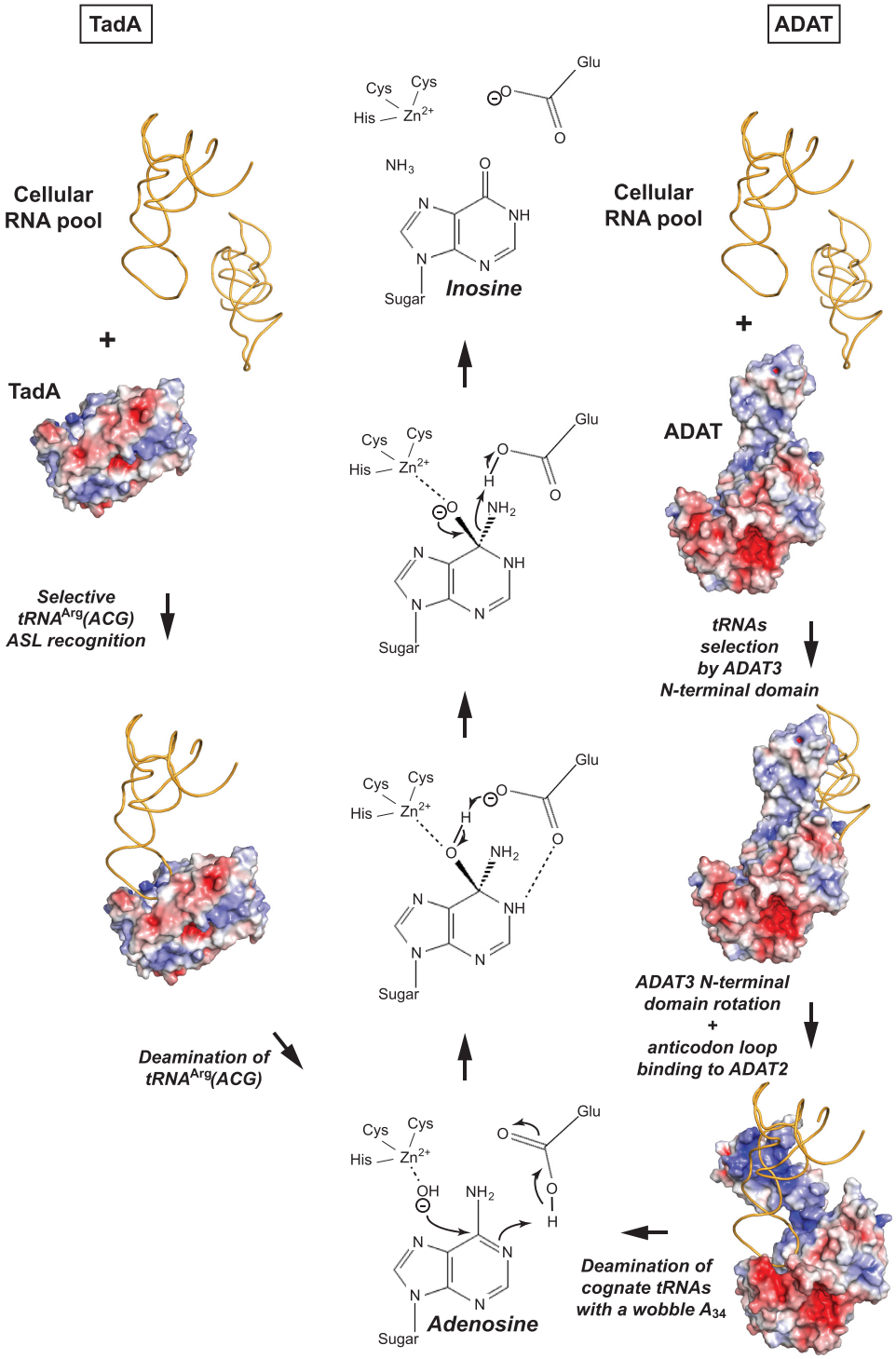

Figure 9. Proposed TadA and ADAT cognate tRNAs deamination mechanisms. The modes of tRNA binding and recognition for prokaryotic TadA (left) and ADAT (right) enzymes are indicated. While TadA can specifically and directly bind and recognize within its active site its cognate $tRNA^{Arg}(ACG)$ from the pool of cellular RNAs using the specific anticodon-stem-loop conformation and the anticodon loop base composition of $tRNA^{Arg}(ACG)$, ADAT appears to have evolved a two-step mechanism. ADAT first binds to tRNAs irrespective of their anticodon composition through its N-terminal domain, most likely upon recognizing the tRNAs specific three-dimensional structure. Upon rotation of ADAT3 N-terminal domain, the anticodon of the tRNAs is presented to the ADAT2 active site that recognizes its cognate tRNAs in a process requiring residues from both ADAT2 and ADAT3. Both TadA and ADAT2 deaminate the cognate tRNAs wobble adenosine into inosine using the same conserved mechanism (centre), requiring a catalytic water bound to their zinc ion as well as a proton shuttling glutamate residue.

DATA AVAILABILITY

The three crystallographic structures described in the manuscript have been deposited in the Protein Data Bank under the PDB IDs 7nz7, 7nz8, 7nz9.

SUPPLEMENTARY DATA

Supplementary Data are available at NAR Online.

ACKNOWLEDGEMENTS

We thank Catherine Birck and Philippe Dumas for MST data collection and analysis. We wish to thank members of the Swiss Light Source (SLS) synchrotrons, especially Vincent Olieric, for the use of their beamline facilities and for help during data collection and structure determination. We thank Gilles Laverny for his help with R. We thank Pierre Antony for critical reading of the manuscript.
Author Contributions: E.R.M., E.T. and M.M. performed all cloning, biochemical and biophysical analyses. E.R.M. and C.R. performed all structural analyses. P.T. performed the *in utero* electroporation experiments. E.B. and J.D.G. conceived the *in vivo* experiments. J.D.P.R. and E.B. performed the analyses on the mouse embryos. T.S.G. and L.D. conceived the *in vitro* deamination assays and T.S.G., E.R.M. and L.D. produced the tRNAs. P.W. and E.E. analysed the nucleic acid contents of co-purifying nucleic acids. J.D.G., L.D. and C.R. planned the experiments, analysed the results and wrote the manuscript.

FUNDING

Centre National de la Recherche Scientifique (CNRS); Institut National de la Santé et de la Recherche Médicale (Inserm); Université de Strasbourg; ATIP-Avenir program (to J.D.G.); Région Grand Est; Fondation Association pour la Recherche contre le Cancer (ARC) (to J.D.P.R.); Agence Nationale de la Recherche [ANR-10-IDEX-0002-02, ANR-10-LABX-0030-INRT to J.D.G., C.R.]; French Infrastructure for Integrated Structural Biology (FRISBI) [ANR-10-INBS-05 to J.D.G, C.R.]; Instruct-ERIC. Funding for open access charge: Team Funds.
Conflict of interest statement. None declared.

REFERENCES

1. Boccaletto,P., Machnicka,M.A., Purta,E., Piatkowski,P., Baginski,B., Wirecki,T.K., de Crecy-Lagard,V., Ross,R., Limbach,P.A., Kotter,A. *et al.* (2018) MODOMICS: a database of RNA modification pathways. 2017 update. *Nucleic Acids Res.*, **46**, D303–D307.
2. El Yacoubi,B., Bailly,M. and de Crecy-Lagard,V. (2012) Biosynthesis and function of posttranscriptional modifications of transfer RNAs. *Annu. Rev. Genet.*, **46**, 69–95.
3. Tuorto,F. and Lyko,F. (2016) Genome recoding by tRNA modifications. *Open Biol.*, **6**, 160287.
4. Kirchner,S. and Ignatova,Z. (2015) Emerging roles of tRNA in adaptive translation, signalling dynamics and disease. *Nat. Rev. Genet.*, **16**, 98–112.
5. Schimmel,P. (2018) The emerging complexity of the tRNA world: mammalian tRNAs beyond protein synthesis. *Nat. Rev. Mol. Cell Biol.*, **19**, 45–58.
6. de Crecy-Lagard,V., Boccaletto,P., Mangleburg,C.G., Sharma,P., Lowe,T.M., Leidel,S.A. and Bujnicki,J.M. (2019) Matching tRNA modifications in humans to their known and predicted enzymes. *Nucleic Acids Res.*, **47**, 2143–2159.
7. Chujo,T. and Tomizawa,K. (2021) Human transfer RNA modopathies: diseases caused by aberrations in transfer RNA modifications. *FEBS J.*, doi:10.1111/febs.15736.
8. Suzuki,T. (2021) The expanding world of tRNA modifications and their disease relevance. *Nat. Rev. Mol. Cell Biol.*, **22**, 375–392.
9. Crick,F.H. (1966) Codon–anticodon pairing: the wobble hypothesis. *J. Mol. Biol.*, **19**, 548–555.
10. Agris,P.F., Eruysal,E.R., Narendran,A., Vare,V.Y.P., Vangaveti,S. and Ranganathan,S.V. (2018) Celebrating wobble decoding: Half a century and still much is new. *RNA Biol.*, **15**, 537–553.
11. Torres,A.G., Pineyro,D., Filonava,L., Stracker,T.H., Batlle,E. and Ribas de Pouplana,L. (2014) A-to-I editing on tRNAs: biochemical, biological and evolutionary implications. *FEBS Lett.*, **588**, 4279–4286.
12. Gerber,A.P. and Keller,W. (2001) RNA editing by base deamination: more enzymes, more targets, new mysteries. *Trends Biochem. Sci.*, **26**, 376–384.
13. Wolf,J., Gerber,A.P. and Keller,W. (2002) tadA, an essential tRNA-specific adenosine deaminase from Escherichia coli. *EMBO J.*, **21**, 3841–3851.
14. Elias,Y. and Huang,R.H. (2005) Biochemical and structural studies of A-to-I editing by tRNA:A34 deaminases at the wobble position of transfer RNA. *Biochemistry*, **44**, 12057–12065.
15. Kuratani,M., Ishii,R., Bessho,Y., Fukunaga,R., Sengoku,T., Shirouzu,M., Sekine,S. and Yokoyama,S. (2005) Crystal structure of tRNA adenosine deaminase (TadA) from Aquifex aeolicus. *J. Biol. Chem.*, **280**, 16002–16008.
16. Kim,J., Malashkevich,V., Roday,S., Lisbin,M., Schramm,V.L. and Almo,S.C. (2006) Structural and kinetic characterization of Escherichia coli TadA, the wobble-specific tRNA deaminase. *Biochemistry*, **45**, 6407–6416.
17. Losey,H.C., Ruthenburg,A.J. and Verdine,G.L. (2006) Crystal structure of Staphylococcus aureus tRNA adenosine deaminase TadA in complex with RNA. *Nat. Struct. Mol. Biol.*, **13**, 153–159.
18. Gerber,A.P. and Keller,W. (1999) An adenosine deaminase that generates inosine at the wobble position of tRNAs. *Science*, **286**, 1146–1149.
19. Tsutsumi,S., Sugiura,R., Ma,Y., Tokuoka,H., Ohta,K., Ohte,R., Noma,A., Suzuki,T. and Kuno,T. (2007) Wobble inosine tRNA modification is essential to cell cycle progression in G(1)/S and G(2)/M transitions in fission yeast. *J. Biol. Chem.*, **282**, 33459–33465.
20. Ragone,F.L., Spears,J.L., Wohlgamuth-Benedum,J.M., Kreel,N., Papavasiliou,F.N. and Alfonzo,J.D. (2011) The C-terminal end of the Trypanosoma brucei editing deaminase plays a critical role in tRNA binding. *RNA*, **17**, 1296–1306.
21. Zhou,W., Karcher,D. and Bock,R. (2014) Identification of enzymes for adenosine-to-inosine editing and discovery of cytidine-to-uridine editing in nucleus-encoded transfer RNAs of Arabidopsis. *Plant Physiol.*, **166**, 1985–1997.
22. Torres,A.G., Pineyro,D., Rodriguez-Escriba,M., Camacho,N., Reina,O., Saint-Leger,A., Filonava,L., Batlle,E. and Ribas de Pouplana,L. (2015) Inosine modifications in human tRNAs are incorporated at the precursor tRNA level. *Nucleic Acids Res.*, **43**, 5145–5157.
23. Auxilien,S., Crain,P.F., Trewyn,R.W. and Grosjean,H. (1996) Mechanism, specificity and general properties of the yeast enzyme catalysing the formation of inosine 34 in the anticodon of transfer RNA. *J. Mol. Biol.*, **262**, 437–458.
24. Roura Frigole,H., Camacho,N., Castellvi Coma,M., Fernandez-Lozano,C., Garcia-Lema,J., Rafels-Ybern,A., Canals,A., Coll,M. and Ribas de Pouplana,L. (2019) tRNA deamination by ADAT requires substrate-specific recognition mechanisms and can be inhibited by tRFs. *RNA*, **25**, 607–619.
25. Alazami,A.M., Hijazi,H., Al-Dosari,M.S., Shaheen,R., Hashem,A., Aldahmesh,M.A., Mohamed,J.Y., Kentab,A., Salih,M.A., Awaji,A. *et al.* (2013) Mutation in ADAT3, encoding adenosine deaminase acting on transfer RNA, causes intellectual disability and strabismus. *J. Med. Genet.*, **50**, 425–430.
26. El-Hattab,A.W., Saleh,M.A., Hashem,A., Al-Owain,M., Asmari,A.A., Rabei,H., Abdelraouf,H., Hashem,M., Alazami,A.M., Patel,N. *et al.* (2016) ADAT3-related intellectual disability: Further delineation of the phenotype. *Am. J. Med. Genet. A*, **170A**, 1142–1147.

27. Sharkia,R., Zalan,A., Jabareen-Masri,A., Zahalka,H. and Mahajnah,M. (2019) A new case confirming and expanding the phenotype spectrum of ADAT3-related intellectual disability syndrome. *Eur. J. Med. Genet.*, **62**, 103549.
28. Hengel,H., Buchert,R., Sturm,M., Haack,T.B., Schelling,Y., Mahajnah,M., Sharkia,R., Azem,A., Balousha,G., Ghanem,Z. *et al.* (2020) First-line exome sequencing in Palestinian and Israeli Arabs with neurological disorders is efficient and facilitates disease gene discovery. *Eur. J. Hum. Genet.*, **28**, 1034–1043.
29. Ramos,J., Han,L., Li,Y., Hagelskamp,F., Kellner,S.M., Alkuraya,F.S., Phizicky,E.M. and Fu,D. (2019) Formation of tRNA wobble inosine in humans is disrupted by a millennia-old mutation causing intellectual disability. *Mol. Cell. Biol.*, **39**, e00203-19.
30. Diebold,M.L., Fribourg,S., Koch,M., Metzger,T. and Romier,C. (2011) Deciphering correct strategies for multiprotein complex assembly by co-expression: application to complexes as large as the histone octamer. *J. Struct. Biol.*, **175**, 178–188.
31. Vincentelli,R. and Romier,C. (2016) Complex Reconstitution and Characterization by Combining Co-expression Techniques in Escherichia coli with High-Throughput. *Adv. Exp. Med. Biol.*, **896**, 43–58.
32. Kabsch,W. (2010) Xds. *Acta Crystallogr. D. Biol. Crystallogr.*, **66**, 125–132.
33. Emsley,P., Lohkamp,B., Scott,W.G. and Cowtan,K. (2010) Features and development of Coot. *Acta Crystallogr. Sect. D: Biol. Crystallogr.*, **66**, 486–501.
34. Liebschner,D., Afonine,P.V., Baker,M.L., Bunkoczi,G., Chen,V.B., Croll,T.I., Hintze,B., Hung,L.W., Jain,S., McCoy,A.J. *et al.* (2019) Macromolecular structure determination using X-rays, neutrons and electrons: recent developments in Phenix. *Acta Crystallogr. D Struct. Biol.*, **75**, 861–877.
35. Williams,C.J., Headd,J.J., Moriarty,N.W., Prisant,M.G., Videau,L.L., Deis,L.N., Verma,V., Keedy,D.A., Hintze,B.J., Chen,V.B. *et al.* (2018) MolProbity: More and better reference data for improved all-atom structure validation. *Protein Sci.*, **27**, 293–315.
36. Hossain,M. and Limbach,P.A. (2007) Mass spectrometry-based detection of transfer RNAs by their signature endonuclease digestion products. *RNA*, **13**, 295–303.
37. Cantara,W.A., Crain,P.F., Rozenski,J., McCloskey,J.A., Harris,K.A., Zhang,X., Vendeix,F.A., Fabris,D. and Agris,P.F. (2011) The RNA Modification Database, RNAMDB: 2011 update. *Nucleic Acids Res.*, **39**, D195–D201.
38. Chan,P.P. and Lowe,T.M. (2016) GtRNAdb 2.0: an expanded database of transfer RNA genes identified in complete and draft genomes. *Nucleic Acids Res.*, **44**, D184–D189.
39. Carneiro,V.T., Dietrich,A., Marechal-Drouard,L., Cosset,A., Pelletier,G. and Small,I. (1994) Characterization of some major identity elements in plant alanine and phenylalanine transfer RNAs. *Plant Mol. Biol.*, **26**, 1843–1853.
40. Gross,L., Vicens,Q., Einhorn,E., Noireterre,A., Schaeffer,L., Kuhn,L., Imler,J.L., Eriani,G., Meignin,C. and Martin,F. (2017) The IRES5′UTR of the dicistrovirus cricket paralysis virus is a type III IRES containing an essential pseudoknot structure. *Nucleic Acids Res.*, **45**, 8993–9004.
41. Hand,R. and Polleux,F. (2011) Neurogenin2 regulates the initial axon guidance of cortical pyramidal neurons projecting medially to the corpus callosum. *Neural Dev.*, **6**, 30.
42. Holm,L. (2020) DALI and the persistence of protein shape. *Protein Sci.*, **29**, 128–140.
43. Goto-Ito,S., Ito,T., Kuratani,M., Bessho,Y. and Yokoyama,S. (2009) Tertiary structure checkpoint at anticodon loop modification in tRNA functional maturation. *Nat. Struct. Mol. Biol.*, **16**, 1109–1115.
44. Neumann,P., Lakomek,K., Naumann,P.T., Erwin,W.M., Lauhon,C.T. and Ficner,R. (2014) Crystal structure of a 4-thiouridine synthetase-RNA complex reveals specificity of tRNA U8 modification. *Nucleic Acids Res.*, **42**, 6673–6685.
45. Randau,L., Stanley,B.J., Kohlway,A., Mechta,S., Xiong,Y. and Soll,D. (2009) A cytidine deaminase edits C to U in transfer RNAs in Archaea. *Science*, **324**, 657–659.
46. Liu,X., Chen,R., Sun,Y., Chen,R., Zhou,J., Tian,Q., Tao,X., Zhang,Z., Luo,G.Z. and Xie,W. (2020) Crystal structure of the yeast heterodimeric ADAT2/3 deaminase. *BMC Biol.*, **18**, 189.
47. Ramos,J., Proven,M., Halvardson,J., Hagelskamp,F., Kuchinskaya,E., Phelan,B., Bell,R., Kellner,S.M., Feuk,L., Thuresson,A.C. *et al.* (2020) Identification and rescue of a tRNA wobble inosine deficiency causing intellectual disability disorder. *RNA*, **26**, 1654–1666.
48. Robert,X. and Gouet,P. (2014) Deciphering key features in protein structures with the new ENDscript server. *Nucleic Acids Res.*, **42**, W320–W324.

The structure of the mouse ADAT2/ADAT3 complex reveals the molecular basis for mammalian tRNA wobble adenosine-to-inosine deamination

Elizabeth Ramos-Morales, Efil Bayam, Jordi Del-Pozo-Rodríguez, Thalia Salinas-Giegé, Martin Marek, Peggy Tilly, Philippe Wolff, Edouard Troesch, Eric Ennifar, Laurence Drouard, Juliette D. Godin, Christophe Romier

Supplementary information

(a) ADAT2

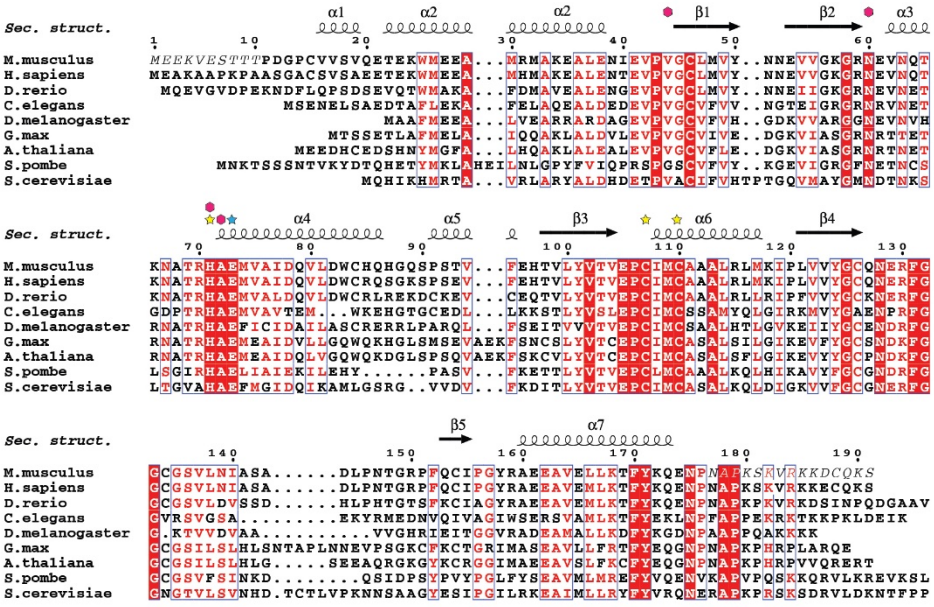

(b) ADAT3

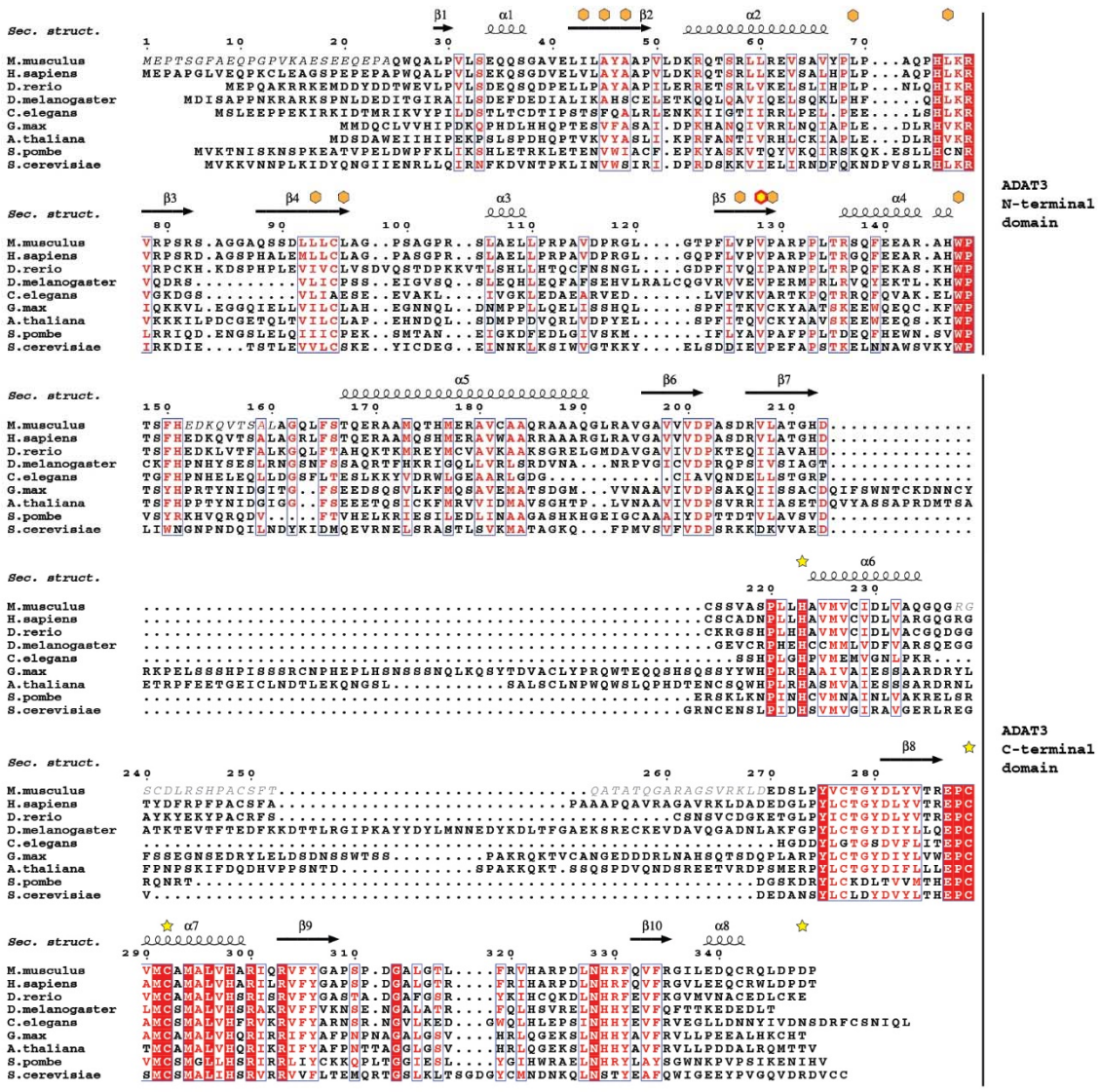

Supplementary Figure 1. Multiple sequence alignment of ADAT2 and ADAT3

(a,b) Multiple sequence alignment of (a) ADAT2 and (b) ADAT3 subunits from reference organisms. For clarity, in (a) the ADAT2 non-conserved N-terminal part of *S. pombe* and the non-conserved C-terminal parts of *D. rerio*, *S. pombe* and *S. cerevisiae* have been omitted. In (b), the ADAT3 N-terminal 16 amino acids longer part of *H. sapiens* (longer human transcript considered (NM_138422), the shorter human transcript (NM_001329533) being equivalent in length to the mouse transcript (NM_001100606)) has been omitted. Secondary structure elements (Sec. Struct.), as observed in the mouse ADAT2/ADAT3 structure, are indicated above the alignments. Residues not found in the electron density and missing in the final model are shown in italics. The ADAT3-specific loop removed for crystallization is shown in grey. Residues of ADAT2 and ADAT3 involved in zinc binding are indicated with yellow stars. ADAT2 glutamate potentially involved in proton shuttling is indicated with a blue star. ADAT2 residues potentially involved in wobble adenine recognition are shown with purple diamonds. Residues involved in the ADAT3 V128 (red circled yellow diamond) hydrophobic core are indicated with orange diamonds.

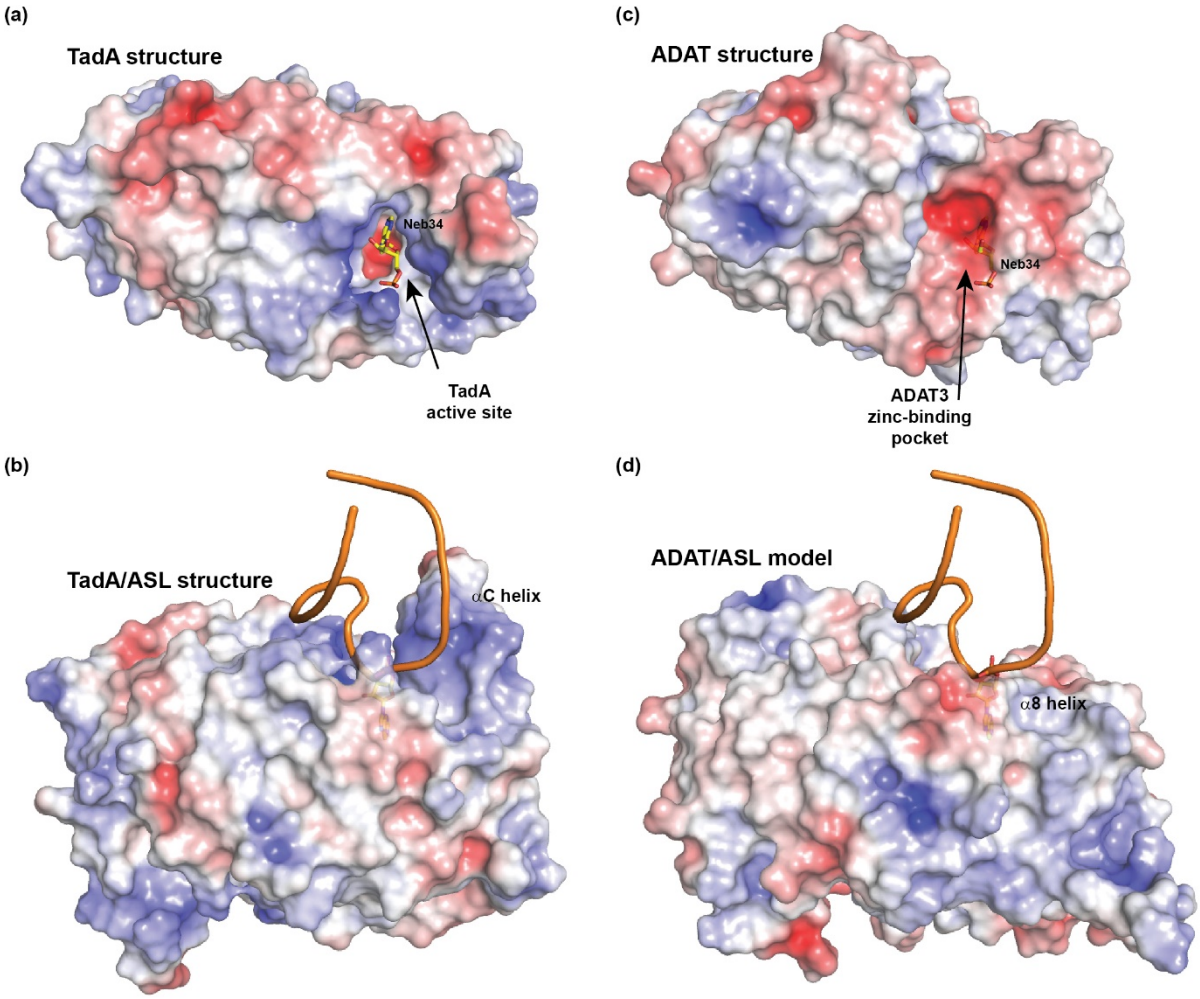

Supplementary Figure 2. ADAT3 active site cannot accommodate an anticodon stem-loop

(a) Binding of a wobble non-hydrolysable adenine analog, nebularine (Neb34), within the active site of *S.aureus* TadA (PDB code 2b3j). The electrostatic potential at the TadA homodimer surface is displayed (blue, positively charged; red, negatively charged). **(b)** Same as in (a) in a rotated view with the ASL shown as orange ribbon. The αC-helix of TadA participates to the formation of the groove that recognizes the ASL. **(c)** Model same as in (a) with the ADAT3 zinc-binding site of the ADAT complex. There is no pocket for the wobble nucleoside due to the capping of the zinc-binding site by ADAT3 C-terminus. In addition, the negative (red) electrostatic character of the ADAT3 surface would be repulsive for binding of an ASL. **(d)** Model same as in (b) with the ADAT complex and the ASL binding to ADAT3 zinc-binding site. The α8 helix of ADAT3 is too short to help form an ASL recognition groove as observed in TadA.

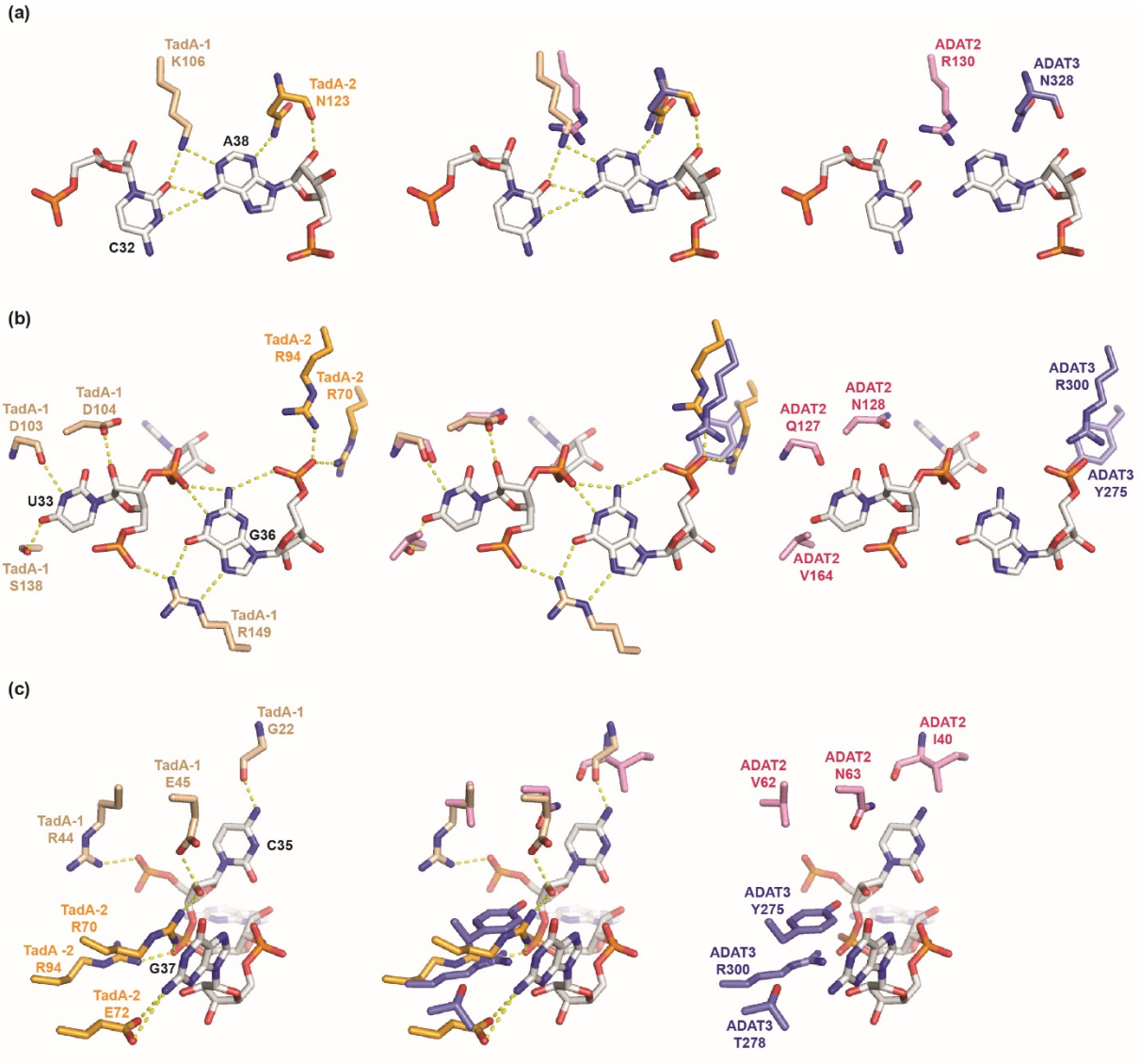

Supplementary Figure 3. ADAT anticodon loop recognition pockets diverge from those of TadA

(a-c) Anticodon loop recognition pockets of TadA active site (left panels) and of ADAT2 active site (right panels) and their superposition (middle panels). Residues involved in interactions are shown as sticks with different colours depending on whether they belong to TadA first monomer (TadA-1, coloured sand) or second monomer (TadA-2, coloured orange), or to ADAT2 (coloured pink) or ADAT3 (coloured blue). Some TadA-equivalent residues are not shown in the ADAT pockets due to their non-existence in the ADAT2 and ADAT3 proteins. While recognition of the 32-38 pair (a) appears conserved between TadA and ADAT, recognition of the 33 and 35 nucleosides has lost some determinants, the strongest loss of determinants concerning nucleosides 36 and 37 (b-c).

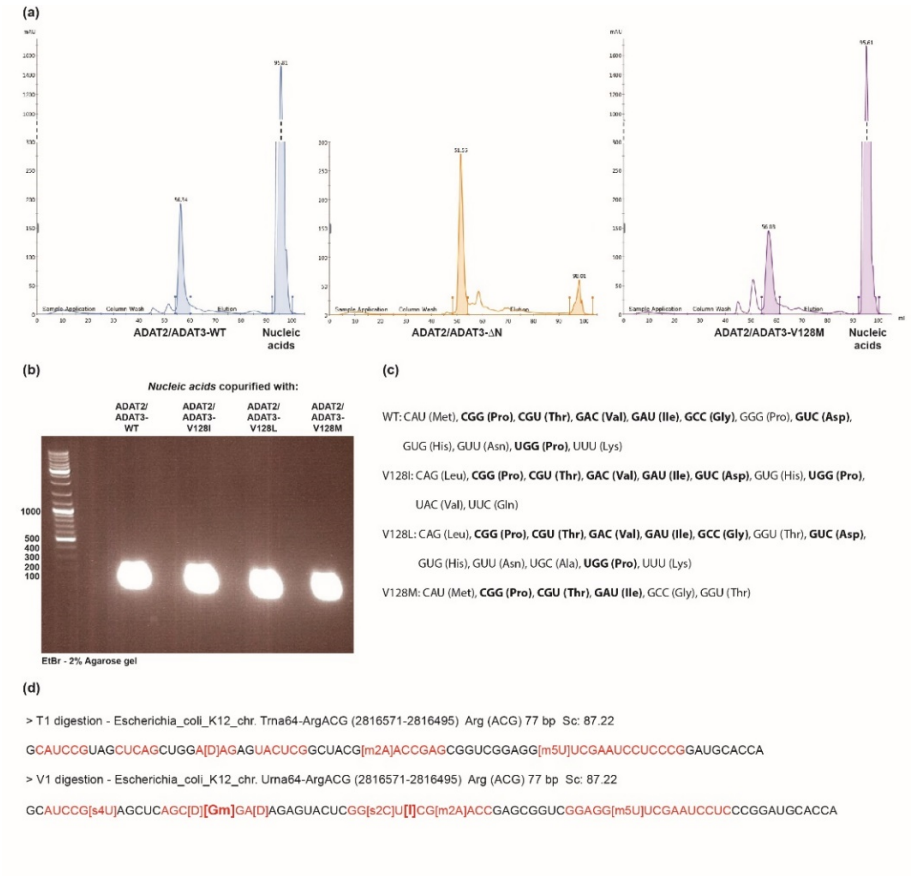

Supplementary Figure 4. **Mouse ADAT binds to various *E. coli* tRNAs and *E. coli* TadA co-purifies with *E. coli* tRNA^{Arg}(ICG) having an unexpected Gm$_{18}$ modification.**

(a) Ion exchange purification profiles for ADAT2/ADAT3 WT (left panel), ADAT2/ADAT3-ΔN (middle panel) and ADAT2/ADAT3-V128M (right panel). The ADAT2/ADAT3-V128I and ADAT2/ADAT3-V128L mutants purification profiles are not displayed but show the same profile as the WT or the V128M mutant. A large peak of nucleic acids is observed for both the WT and the V128M mutant (signal above 1500 mAU), whereas a residual peak (30 fold decrease in height) is observed for the ΔN mutant (signal below 100 mAU), demonstrating that ADAT3 N-terminal region is important for nucleic acid binding. **(b)** Analysis on agarose gel of the nucleic acids co-purifying with the ADAT2/ADAT3 WT, V128I, V128L and V128M mutants. All nucleic acids migrate around the 100 bp marker and have been shown by mass spectrometry analysis to be exclusively a mix of *E. coli* tRNAs. **(c)** Anticodons (and corresponding amino acids) of tRNAs unambiguously characterized in the mass spectrometry analysis. Anticodons found in at least three of the four samples are shown in bold. **(d)** Result of the mass spectrometry sequencing analysis of the *E. coli* tRNA^{Arg}(ACG) co-purifying with *E. coli* TadA after its digestion with RNAses T1 and V1. The red sequences indicate the identified regions. The methylated G$_{18}$ and the wobble inosine identified upon T1 digestion are indicated in bold. The full modification of the wobble adenosine into inosine of this tRNA was also observed by sequencing. Note that some modifications like pseudouridine cannot be detected due to equivalent mass with the non-modified base.

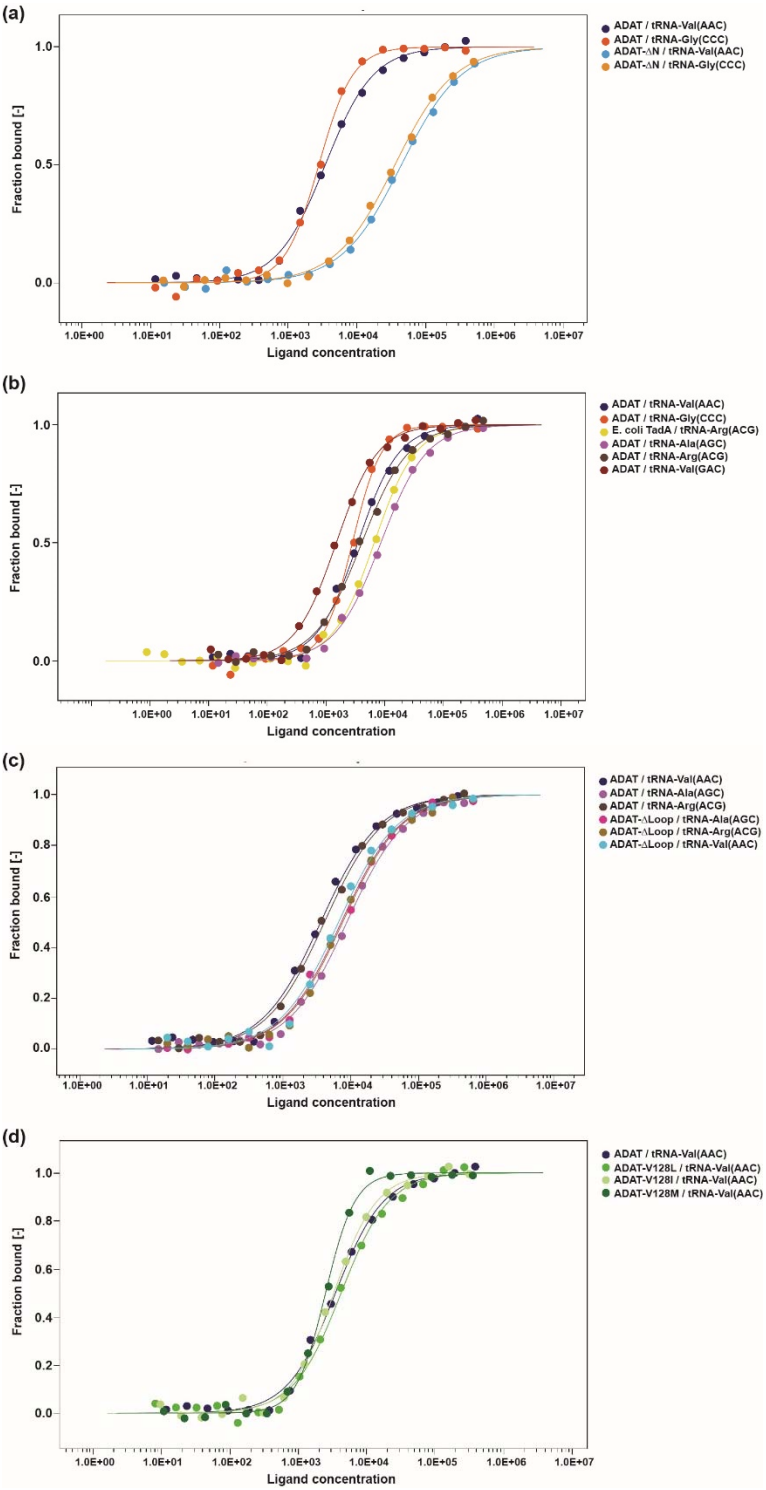

Supplementary Figure 5. **Assessment of tRNAs binding to ADAT and TadA**

(a,b,c,d) Measurements by Microscale Thermophoresis (MST) of the Kd of various tRNAs for mouse ADAT (both WT and mutants) and *E. coli* TadA. The Kd values can vary between the different tRNAs. ADAT can even bind to non-cognate tRNAs. Binding is dependent on ADAT3-specific loop, as assessed by the ΔLoop mutant, and notably on ADAT3 N-terminal domain, as assessed by the ΔN mutant. The disease-causing mutation V128 does not prevent tRNA binding.

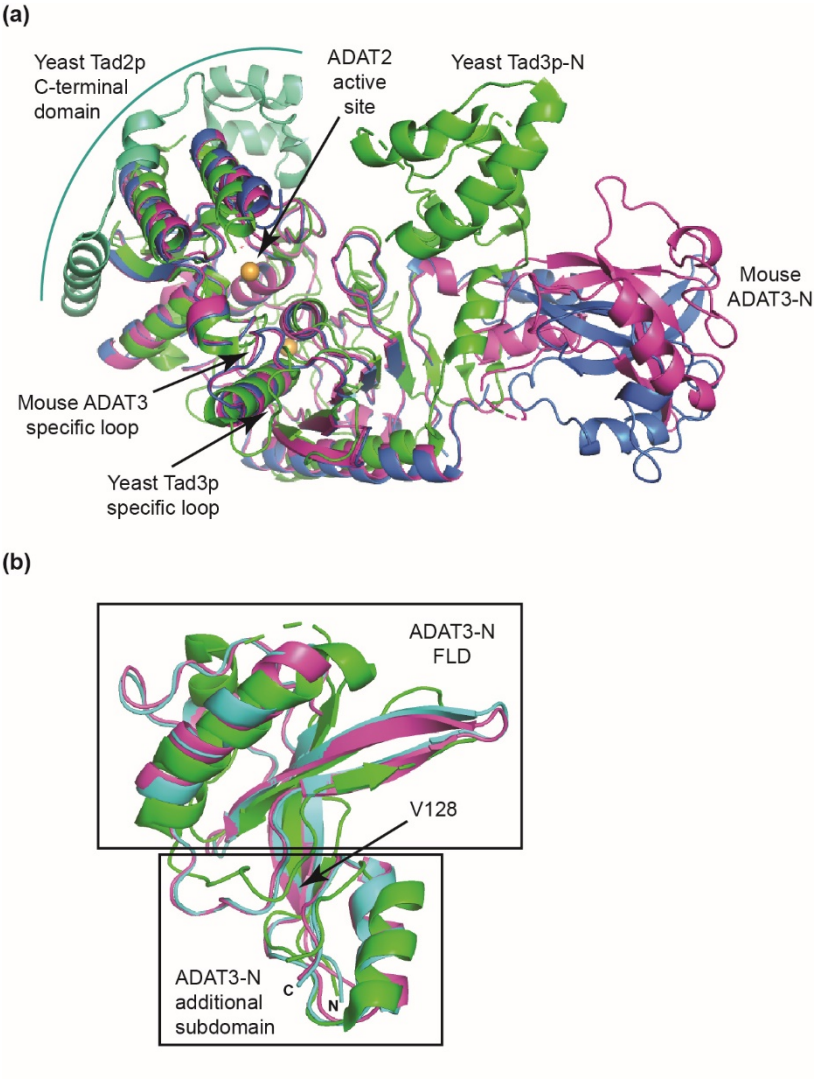

Supplementary Figure 6. **Comparison of mouse and yeast ADAT complexes.**

(a) Superposition of both mouse ADAT2/ADAT3 structures (blue and magenta) and yeast Tad2p/Tad3p structure (coloured green). The mouse and yeast complexes show structural similarities and dissimilarities. Specifically, yeast Tad2p has an additional C-terminal domain (green-cyan), not present in mouse ADAT2, whose function is unknown and that wraps around Tad2p deamination domain. Mouse ADAT3-N and yeast Tad3p-N domains are indicated with a significant difference in positioning, although their movement could bring them in similar positions compared to their respective catalytic domains. The position of mouse and yeast ADAT3 specific loops are indicated. The mouse loop is closer to ADAT2 active site, in agreement with a potential role in tRNA positioning for catalysis, as suggested by our deamination assays. **(b)** Superposition of the ADAT3-N domains of mouse and yeast ADAT complexes displayed from their tRNA binding sides. The colour code is the same as in (a). Despite a similar fold, significant structural differences are observed for both their FLDs and their additional structural subdomains. Specifically, the structural environment of mouse V128 is different in both complexes.

Supplementary Table 1. Anticodon loops recognized by human/mouse ADAT and E. coli TadA

tRNA	Position 32	Position 33	Position 34 (wobble)	Position 35	Position 36	Position 37	Position 38
Hs/Mm* ALA (AGC)	U	U	**A**	G	C	A	U
Hs/Mm ARG (ACG)	C	U	**A**	C	G	G	A
Hs/Mm ILE (AAU)	C	U	**A**	A	U	A	A
Hs/Mm LEU (AAG)	U	U	**A**	A	G	G	C
Hs/Mm PRO (AGG)	U	U	**A**	G	G	G	U
Hs/Mm SER (AGA)	C	U	**A**	G	A	A	A
Hs/Mm THR (AGU)	C	U	**A**	G	U	A	A
Hs/Mm VAL (AAC)	C	U	**A**	A	C	A	C
Hs/Mm All cognate tRNAs	C/U	U	**A**	A/C/G	A/C/G/U	A/G	A/C/U
Hs/Mm GLY (CCC)	*C/U*	*U*	***C***	*C*	*C*	*A*	*U*
E. coli ARG (AGC)	*C*	*U*	***A***	*C*	*G*	*A*	*A*

*Hs, Homo sapiens; Mm, Mus musculus.

Supplementary Table 2. Crystallographic table.

Data collection*	**mADAT WT Structure 1**	**mADAT WT Structure 2**	**mADAT V128L**
Space group	P 3_2 2 1	P 2 2_1 2_1	P 2 2_1 2_1
Cell dimensions			
a, b, c (Å)	105.47, 105.47, 187.08	52.29, 106.83, 130.58	51.98, 106.81, 129.67
α, β, γ (°)	90.0, 90.0, 120.0	90.0, 90.0, 90.0	90.0, 90.0, 90.0
Resolution (Å)	50. – 2.96 (3.13 – 2.96)	50. – 2.12 (2.25 – 2.12)	50. – 1.99 (2.11 – 1.99)
Rsym or Rmerge	9.2 (381.9)	18.0 (242.0)	13.6 (244.4)
I / σI	26.48 (1.02)	11.57 (1.05)	15.15 (1.05)
Completeness (%)	99.9 (99.9)	99.8 (99.1)	99.8 (99.1)
Redundancy	19.7 (19.7)	13.3 (13.3)	13.2 (12.4)
CC(1/2) (%)	100.0 (54.5)	99.8 (52.2)	99.9 (38.5)
Refinement			
Resolution (Å)	45.94 – 2.96	49.44 – 2.12	49.38 – 1.99
No. reflections	25868	42204	49990
Rwork / Rfree	0.195 / 0.233	0.201 / 0.233	0.189 / 0.218
Number of atoms			
Protein	3446	3437	3423
Ions	2	2	2
Waters	1	167	288
B-factors			
Protein	122.51	49.24	46.47
Ions	102.65	35.35	32.01
Waters	102.69	46.46	49.34
R.m.s. deviations			
Bond lengths (Å)	0.009	0.008	0.007
Bond angles (°)	1.065	0.880	0.857

* *Values in parentheses are for the highest-resolution shells.*

Supplementary Table 3. Deamination assays.

	tRNA-Val(AAC)			tRNA-Arg(ACG)			tRNA-Ala(AGC)			tRNA-Gly(ACC)		
	1:3[a]	*1:0.3*	*1:0.03*	*1:3*	*1:0.3*	*1:0.03*	*1:3*	*1:0.3*	*1:0.03*	*1:3*	*1:0.3*	*1:0.03*
ADAT2/ADAT3	98.0±1.4[b]	75.5±6.4	5.5±0.7	83.0±1.4	65.5±12.0	7.5±10.6	84.0±1.4	73.0±0	69.0±4.2	18.0±1.4	0	0
ADAT2/ADAT2	1.0±1.1	*n.d.*[c]	*n.d.*	0	*n.d.*	*n.d.*	7.5±0.7	*n.d.*	*n.d.*	*n.d.*	*n.d.*	*n.d.*
ADAT3	0	*n.d.*	*n.d.*	0	*n.d.*	*n.d.*	0	*n.d.*	*n.d.*	*n.d.*	*n.d.*	*n.d.*
TadA/TadA	0	*n.d.*	*n.d.*	94.5±4.9	36.0±9.9	0	0	*n.d.*	*n.d.*	*n.d.*	*n.d.*	*n.d.*
ADAT2/ADAT3-ΔNter	0	*n.d.*	*n.d.*	3.5±2.1	*n.d.*	*n.d.*	0	*n.d.*	*n.d.*	*n.d.*	*n.d.*	*n.d.*
ADAT2/ADAT3-Acidic1	15.0±8.5	0	0	12.0±0	1.0±1.1	1.0±1.1	74.5±0.7	68.5±3.5	15.5±21.9	*n.d.*	*n.d.*	*n.d.*
ADAT2/ADAT3-Acidic2	0	0	0	1.0±0	0	0	0	0	0	*n.d.*	*n.d.*	*n.d.*
ADAT2-E73A/ADAT3	0	*n.d.*	*n.d.*	2.0±1.4	*n.d.*	*n.d.*	11.0±0	3	0	*n.d.*	*n.d.*	*n.d.*
ADAT2-E73A/ADAT3-V225E	0.5±0.7	*n.d.*	*n.d.*	0	*n.d.*	*n.d.*	0	*n.d.*	*n.d.*	*n.d.*	*n.d.*	*n.d.*
ADAT2-E73A/ADAT3-ΔCter	2.0±2.8	*n.d.*	*n.d.*	2.5±3.5	*n.d.*	*n.d.*	64.0±1.4	0	0	*n.d.*	*n.d.*	*n.d.*
ADAT2/ADAT3-Δloop	15.0±0	3.5±2.1	0	44.0±1.4	5.0±4.2	0	71.5±0.7	69.0±2.8	3.5±4.9	*n.d.*	*n.d.*	*n.d.*
ADAT2/ADAT3-V128M	76.0±12.7	32.0±5.7	0	80.5±0.7	8.5±7.8	0	80.5±0.7	70.5±0.7	41.0±31.1	*n.d.*	*n.d.*	*n.d.*

[a] tRNA/enzyme ratio

[b] mean value ± standard deviation from duplicates

[c] n.d., not determined. For most samples, the dilution 1:0.3 and 1:0.03 were only tested once and not tested again if (i) no deamination was observed for these dilutions in the first measurement and (ii) the 1:3 dilution first measurement was close or equal to 0. These single measurements have been marked as not determined. The $tRNA^{Gly}$(ACC) was only tested with WT ADAT.

Conclusions and Perspectives

During my PhD thesis I worked on enzymes associated to human diseases: tcDAC2 and ADAT. TcDAC2 is an essential protein of the parasite *T. cruzi* that causes Chagas disease, therefore tcDAC2 represents a potential drug target for treatment. In my second project I investigated the mechanism by which a mutation in ADAT complex triggers a neurodevelopmental disorder characterized by intellectual disability, microcephaly, strabismus, epilepsy.

Several potent and specific inhibitor leads targeting smHDAC8, to treat schistosomiasis, have been developed previously in the team using the piggyback strategy, which combines high-throughput screening and structure-based drug design. The work in fighting schistosomiasis also allowed the discovery of a specific pocket in HDAC8 enzymes where HDAC8-specific inhibitors bind. The base of this pocket is formed by a catalytic tyrosine and the walls by the L1 and L6 loops. Such a pocket is not present in other HDACs, since it is blocked by interactions between residues of these two loops. The HDAC8 specific pocket will guide the development of more potent and specific human HDAC8 inhibitors for treatment of cancers, for instance neuroblastoma where HDAC8 is upregulated.

A similar strategy as the one used to target smHDAC8 was applied to target tcDAC2, since depletion of *tcDAC2* affects the viability of *T. cruzi*. During my PhD thesis I could solve the structure of tcDAC2 in complex with two non-specific inhibitors. These structures revealed specific features of tcDAC2. For instance, tcDAC2 harbors similar features of its orthologue hHDAC8 but also of other human HDACs (hHDAC1-3). Furthermore, tcDAC2 has a specific pocket next to its active site, which is not observed in human HDACs. Besides, tcDAC2 presents different residue composition in its foot pocket. Therefore, all these specific features of tcDAC2 will be used to guide the development of potent and specific tcDAC2 inhibitors combining high-throughput screening and structure-based drug design.

Regarding my second project, the ADAT complex is formed by two subunits, ADAT2 and ADAT3. I could determine the importance of ADAT3 N-terminal domain, characteristic of eukaryotes, in selecting and binding tRNA molecules. I could determine the first structure of the mammalian ADAT complex, which reveals that the capping of the ADAT3 zinc-binding site is covered by ADAT3 C-terminal residues, which contributes to ADAT3 inactivity by blocking the entrance of the tRNA-adenosine 34. *In vitro* enzymatic assay also confirmed the

inactivity of ADAT3. Furthermore, the disease mutant ADAT complex that contains the mutation V128M in the N-terminal domain of ADAT3 is still able to bind tRNAs. Therefore, I hypothesize that the decrease of inosine levels observed in tRNAs of patients carrying the ADAT V128M mutation might come from the incorrect presentation of the substrate tRNA by ADAT3 to the active site of ADAT2, thereby causing an inefficient ADAT activity on tRNAs.

My work on the ADAT complex enables a better understanding of the mechanism of this complex and the mechanism behind the neurodevelopmental disorder caused by the mutant ADAT. However, further studies are required to understand the implications of the ADAT complex on neurodevelopmental disorder. For instance, the structures of ADAT in complex with tRNAs in context of the wildtype and disease mutant ADAT will reveal the structural determinants that triggers the disease process. It will be also important to study ADAT with tRNAs bearing a long variable loop, since it seems that the mutant V128M have a lower affinity for these tRNAs.

Appendix

During my PhD and within the frame of the European project A-ParaDDisE, I have purified enzymes (notably HDAC8 and Sirtuin 2 from *Schistosoma mansoni*) for some other teams forming the consortium and for their collaborators. For this reason, I have been added as co-author of a couple of manuscripts. These two articles are provided in this appendix.

Article 4

Structure–Reactivity Relationships on Substrates and Inhibitors of the Lysine Deacylase Sirtuin 2 from Schistosoma mansoni (SmSirt2)

Journal of Medicinal Chemistry

Article

Cite This: J. Med. Chem. 2019, 62, 8733−8759

pubs.acs.org/jmc

Structure−Reactivity Relationships on Substrates and Inhibitors of the Lysine Deacylase Sirtuin 2 from *Schistosoma mansoni* (*Sm*Sirt2)

Daria Monaldi,[†] Dante Rotili,*[,‡] Julien Lancelot,[§] Martin Marek,[∥] Nathalie Wössner,[†] Alessia Lucidi,[‡] Daniela Tomaselli,[‡] Elizabeth Ramos-Morales,[∥] Christophe Romier,[∥] Raymond J. Pierce,[§] Antonello Mai,*[,‡] and Manfred Jung*[,†]

[†]Institute of Pharmaceutical Sciences, University of Freiburg, Albertstr. 25, 79104 Freiburg, Germany

[‡]Dipartimento di Chimica e Tecnologie del Farmaco, "Sapienza" Università di Roma, 00185 Rome, Italy

[§]Université de Lille, CNRS, Inserm, CHU Lille, Institut Pasteur de Lille, U1019—UMR 8204—CIIL—Centre d'Infection et d'Immunité de Lille, 59000 Lille, France

[∥]Département de Biologie Structurale Intégrative, Institut de Génétique et Biologie Moléculaire et Cellulaire (IGBMC), Université de Strasbourg (UDS), CNRS, INSERM, 67404 Illkirch Cedex, France

Supporting Information

ABSTRACT: The only drug currently available for treatment of the neglected disease Schistosomiasis is Praziquantel, and the possible emergence of resistance makes research on novel therapeutic agents necessary and urgent. To this end, the targeting of *Schistosoma mansoni* epigenetic enzymes, which regulate the parasitic life cycle, emerged as a promising approach. Due to the strong effects of human sirtuin inhibitors on parasite survival and reproduction, *Schistosoma* sirtuins were postulated as potential therapeutic targets. In vitro testing of synthetic substrates of *S. mansoni* sirtuin 2 (*Sm*Sirt2) and kinetic experiments on a myristoylated peptide demonstrated lysine long-chain deacylation as an intrinsic *Sm*Sirt2 activity in addition to its known deacetylase activity for the first time. Focused in vitro screening of the GSK Kinetobox library and structure−activity relationships of identified hits led to the first *Sm*Sirt2 inhibitors with activity in the low micromolar range. Several *Sm*Sirt2 inhibitors showed potency against both larval schistosomes (viability) and adult worms (pairing, egg laying) in culture without general toxicity to human cancer cells.

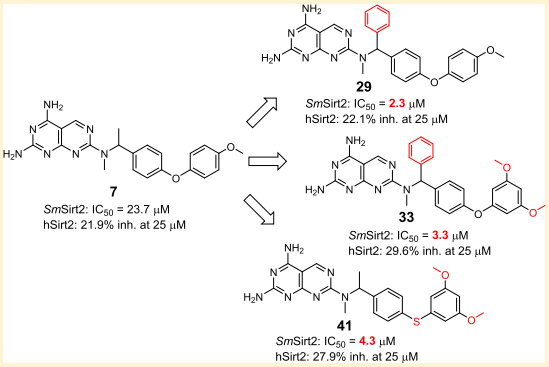

INTRODUCTION

Schistosomiasis is a neglected tropical disease, affecting millions of people in tropical and subtropical countries and causing more than 300 000 deaths per year.[1] One of its major causative agents is the blood fluke *Schistosoma mansoni*, characterized by a complex life cycle, where the parasite is developed through four morphologically distinct forms, with two of them, schistosomula and adult worms (AWs), present in the final human host. Praziquantel (PZQ) is so far the gold standard for the treatment of schistosomiasis, showing several positive features like low cost, high efficacy, and low toxicity,[2] which made possible its use in mass treatment campaigns.[3] Long-term mass treatment with Praziquantel has led to a reduction in mortality and morbidity in endemic areas,[4,5] as well as to a reduction in treatment efficacy and, in some cases, to the isolation of resistant strains.[6−9] This aspect, in association with the drug inactivity on larval stages and its unknown mechanism of action,[2,7] renders relying on only one drug inadequate in the long term and highlights the need for the development of novel therapeutic agents. Different approaches have been already studied, for example, the use of artemisinins[10] and benzodiazepines,[11] but none of them is similar to Praziquantel in terms of efficacy, safety, and cost.

The publication of the *S. mansoni* genome sequence[12] made the research and validation of novel therapeutic targets a particularly promising paradigm for the development of novel antischistosomal drugs. A drug repurposing approach,[13] based on targeting orthologues of proteins already targeted in other pathologies,[10] has demonstrated potential for developing compounds able to selectively inhibit parasitic enzymes without affecting the corresponding human isoforms. Moreover, since schistosomes can be considered similar to cancer cells in terms of intensive metabolic activity and invisibility to host immune system,[14] our interest is focused on histone deacetylase enzymes (HDACs), which are able to remove acetyl groups from lysine residues of histones and other proteins and are already known cancer drug targets with clinically approved drugs. The essentiality of several histone deacetylases for growth and survival has already been

Received: April 15, 2019
Published: September 8, 2019

DOI: 10.1021/acs.jmedchem.9b00638
J. Med. Chem. 2019, 62, 8733−8759

Scheme 1. Synthesis of 3a−g[a]

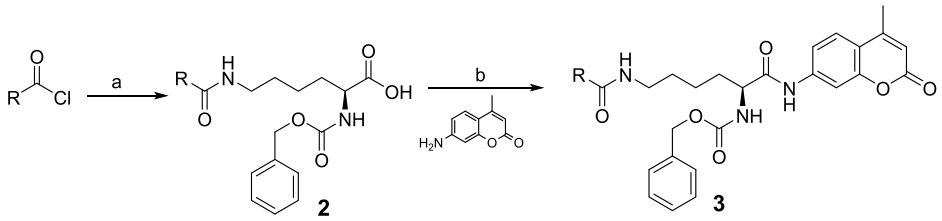

R = $(CH_2)_2CH_3$ (**a**), $(CH_2)_4CH_3$ (**b**), $(CH_2)_6CH_3$ (**c**), $(CH_2)_8CH_3$ (**d**), $(CH2)_{10}CH_3$ (**e**), $(CH_2)_{12}CH_3$ (**f**), $(CH_2)_{14}CH_3$ (**g**)

[a]Reagents and conditions: (a) (*Z*)-Lys-OH, 1 M sodium hydroxide, water, room temperature (rt), 20−45 min; (b) AMC (structure shown), phosphoryl chloride, dry pyridine, −15 °C, 40 min to 3 h.

demonstrated in a variety of parasite genera, including *Plasmodium*, *Leishmania*, *Trypanosoma*, and *Schistosoma*.[15] The complex life cycles of these parasites are subject to complex epigenetic regulation, and the selective inhibition of enzymes involved in these processes, including HDACs, represents a valid therapeutic strategy. For example, in the cases of *Plasmodium falciparum* and *Trypanosoma brucei*, several molecules display selective in vitro and in vivo inhibitory activity against parasitic Zn^{2+}-dependent HDACs (classes I and II).[15] This approach has also led to the development of selective inhibitors of *S. mansoni* HDAC8, including a mercaptoacetamide analogue of suberoylanilide hydroxamic acid,[16] alkylhydroxamates,[17] and benzoylhydroxamates,[18] characterized by submicromolar or nanomolar IC_{50} values for *Sm*HDAC8 with good selectivity over hHDAC1, hHDAC6, and, in some cases, also over hHDAC8. Some of these compounds also had low micromolar EC_{50} values for killing schistosome larvae and abolished pairing stability and egg laying in adult worms.[16−18]

The situation is different for NAD^+-dependent HDACs (class III, sirtuins), where, despite their evident potential as human anticancer and metabolic disease targets,[19] only one compound (Selisistat) has reached clinical trials so far as a potential treatment for Huntington's disease. In parasites, sirtuin isoforms have been identified in *P. falciparum* (*Pf*Sir2A and *Pf*Sir2B),[20,21] *Trypanosoma cruzi* (*Tc*Sir2rp1 and *Tc*Sir2rp3),[22,23] and *Leishmania* (*Lm*Sir2rp1 and *Li*-sir2rp1),[24,25] but most in vitro tested inhibitors showed modest activity and/or lack of selectivity.[15] An exception is provided by bisnaphthalimidopropyl derivatives that showed significant activity *in vitro* and in mice chronically infected with *Leishmania infantum*.[26]

In 2013, Lancelot et al. published the identification and characterization of five *S. mansoni* sirtuins (*Sm*Sirt1, *Sm*Sirt2, *Sm*Sirt5, *Sm*Sirt6, and *Sm*Sirt7) as orthologues of their respective mammalian counterpart isoforms.[27] Furthermore, it was demonstrated that Sirtinol and Salermide, known inhibitors of human sirtuin 1 and 2 (hSirt1 and hSirt2),[28−30] in addition to being inducers of selective apoptosis in cancer cell lines[29,31] and showing protective effects in a muscular dystrophy model in nematodes,[32] have proapoptotic effects in schistosome larvae (schistosomula), through DNA fragmentation, and markedly reduce pairing stability and egg production in adult worms. These features support the potential of *Schistosoma* sirtuins as drug targets for the development of novel and selective antischisosomal drugs.

Beyond their deacetylase activity, human sirtuins are also implicated in the removal of short, medium, and long fatty acyl groups from lysine residues of histone and nonhistone proteins.[33−38] Lysine acylation has been identified as a posttranslational modification, and it is strongly connected to regulation of metabolism. In fact, metabolic intermediates are used for this process, and enzymes implicated in energy pathways are, in many cases, subject to these modifications.[36,39,40] Although deacylation of acyl-lysine is a common feature for all mammalian sirtuins, each isoform is characterized by a different pattern of specificity and efficiency for deacylation that may be quite distinct from the deacetylase activity.[41] In parasites, studies regarding lysine deacylation are lacking so far with the exception of the medium and long fatty acyl chain removal by *Pf*Sir2A in *P. falciparum*.[42] In a previous study, we established a homogeneous in vitro assay for the determination of *Sm*Sirt2 deacetylase activity, which uses the readily available (*Z*)-(Ac)Lys-AMC (ZMAL, **1**) and represents an optimal tool for cost-efficient high-throughput campaigns.[43] To further characterize the function of *Sm*Sirt2, we performed and reported here the analysis of *Sm*Sirt2 lysine deacylation activity by the use of both lysine-derived small-molecule and oligopeptidic substrates.

Moreover, with the aim of finding novel and selective druglike inhibitors of *Sm*Sirt2, we present an extensive structure−activity relationship (SAR) study concerning novel hits identified by an in vitro screening of the Kinetobox library,[44] provided by GSK. This library is constituted by compounds that were shown to be potent and specific inhibitors of growth of *Leishmania donovani*, *T. cruzi*, and *T. brucei* with low human cellular cytotoxicity.[44] The kinetoplastid parasites *Leishmania* sp. and *Trypanosoma* sp. are characterized by complex morphological changes and an involvement of epigenetic regulation during their life cycle, and we postulated that the screening of this diverse library would be a good starting point for our study on *S. mansoni* aimed at identifying novel chemical entities able to interfere with parasite growth. *S. mansoni* is phylogenetically very distant from kinetoplastids, but has similar dynamic phenotypic changes through the different life stages, some of them implying epigenetic modifications.[45] This inhibitor collection is freely available and provides a set of 592 compounds with diverse structural features, potentially providing novel chemical space for chemically yet uncharted targets. Here we present new hits for *Sm*Sirt2 (as well as hSirt2) and present initial SAR to further characterize ligand affinity and specificity to *Sm*Sirt2. In particular, we can show for the first time that *Sm*Sirt2 is a druggable target with selectivity over hSirt2. Moreover, several of the characterized *Sm*Sirt2 inhibitors were active against both schistosomula larvae and adult worms in culture. Some of the

DOI: 10.1021/acs.jmedchem.9b00638
J. Med. Chem. 2019, 62, 8733−8759

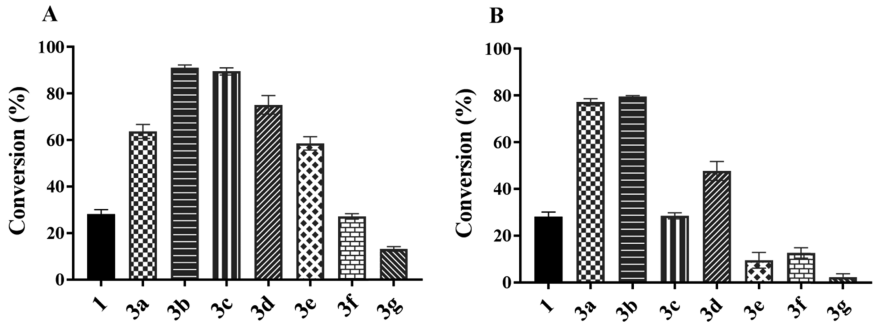

Figure 1. In vitro conversion of **1** (acetyl) and **3a−g** (see Scheme 1) by *Sm*Sirt2 (A) and hSirt2 (B). A pure AMC sample is measured to simulate a (hypothetical) conversion of 100% for comparison. The errors are represented as standard deviation (SD) of the mean (SD, n = 3).

negative controls showed activity on *Schistosoma* as well, but they were also toxic against human cancer cells in culture. In contrast, selective *Sm*Sirt2 inhibitors did not show toxicity in mammalian cells, further supporting the use of *Sm*Sirt2 as a valuable drug target in schistosomes.

RESULTS

Short-, Medium-, and Long-Chain Deacylation Activity of *Sm*Sirt2. To extend the biochemical characterization of *Sm*Sirt2 activity, we studied its ability to deacylate long-chain fatty acids from the ε-amino group of lysine substrates. We synthesized seven analogues of the *Sm*Sirt2 substrate (*Z*)-(Ac)Lys-AMC (ZMAL) **1**, i.e., **3a** ((*Z*)-(But)Lys-AMC), **3b** ((*Z*)-(Hex)Lys-AMC), **3c** ((*Z*)-(Oct)Lys-AMC), **3d** ((*Z*)-(Dec)Lys-AMC), **3e** ((*Z*)-(Lau)Lys-AMC), **3f** ((*Z*)-(Myr)-Lys-AMC), and **3g** ((*Z*)-(Pal)Lys-AMC, ZMML), by replacing its acetyl group with short, medium, and long acyl chains. Substrate **1** was synthesized according to published procedures.[46] For the preparation of **3a−g**, the appropriate acyl chlorides (commercially available for **3a−d** and **3g**, and synthesized for **3e** and **3f** by reaction of the corresponding lauric or myristic acid with thionyl chloride) were treated with (*Z*)-Lys-OH, leading to the formation of the ε-acyl-(*Z*)-Lys-OH **2a−g**, which were converted into the desired substrates **3a−g** by treatment with phosphorus oxychloride and 7-amino-4-methylcoumarin (AMC) (Scheme 1).

Then, we used the acyl-lysine substrates **3a−g**, in comparison to the acetylated **1**, in the homogeneous fluorescence-based assay,[43] to evaluate the ability of *Sm*Sirt2 to catalyze their conversion into free lysine substrate. Compounds **1** and **3a−g** were tested at 10.5 μM with one time point measurement, according to a published procedure for **1**.[43] As shown in Figure 1A (Table S1 in the Supporting Information), the measured substrate conversion increases with increasing chain length from acetyl to hexanoyl analogues (see **1**, **3a**, and **3b**), then exhibit an opposite trend from the octanoyl to the palmitoyl analogue (from **3c** to **3g**). When tested with hSirt2 (Figure 1B and Table S2), **1** and **3a−g** showed a somewhat discontinuous pattern of conversion, with **3a** (butyryl) and **3b** (hexanoyl) as the best substrates. Unfortunately, solubility issues did not allow the measurement of K_m values for any of the ZMAL analogues to obtain a more quantitative overview; however, we performed a quantitative analysis on peptidic substrates (see below).

Nicotinamide (NA) is a physiological sirtuin inhibitor, which, once released from NAD^+, stays in a subpocket of the enzyme (pocket C) and, by a rebound mechanism, can block the enzymatic activity.[47] In hSirt2, the lysine acyl chain pocket is in a close contact with the C pocket, determining the possibility for NA potency to be influenced by the substrate acyl chain length.[34] To study the effect of short-, medium-, and long-chain lysine substrates on the relative NA potency for *Sm*Sirt2 inhibition, we measured IC_{50} values for NA in the presence of our ZMAL analogues **1** and **3a−g**. As shown in Figure 2 (Table S3), the IC_{50} values of NA are similar using

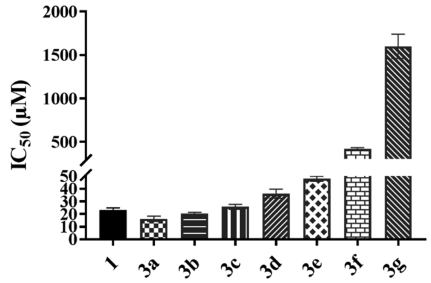

Figure 2. IC_{50} values of NA against *Sm*Sirt2 in the presence of the acetylated substrate **1** and the acylated ZMAL analogues **3a−g** (see Scheme 1). The errors are represented as standard error (SE) of the mean (SEM, n = 3). IC_{50} values are reported in Table S3 (Supporting Information).

substrates up to the decanoyl group (**3c**), after which they increase with the growth of the acyl chain length. Since an opposite trend has been published for acylated peptides and hSirt2,[34] we can hypothesize that, despite the structural identity[27,48] between the schistosome and the human Sirt2, these two enzymes are characterized by different kinetics. It could be possible that the putative structural differences in the active site/C pocket between hSirt2 and *Sm*Sirt2 can explain the obtained results, but due to a lack of structural data, this is yet speculative.

To gain a more quantitative insight into the interplay between *Sm*Sirt2 and its acylated substrates, we performed a kinetic analysis through the use of an high-performance liquid chromatography (HPLC)-based assay using more soluble peptides, not tagged with a fluorescent label to rule out potential artifactual effects. K_m, k_{cat}, and k_{cat}/K_m of *Sm*Sirt2 were measured in the presence of an acetylated (PSDKac) and a myristoylated peptide (PSDKmyr) derived from α-tubulin, which is a Sirt2 substrate.[49] As shown in Figure 3, the acyl chain elongation in PSDKmyr determined an increase of affinity for *Sm*Sirt2 without affecting the enzymatic turnover, with consequent 3-fold higher catalytic efficiency in the presence of PSDKmyr than with PSDKac (Table 1).

Moreover, since in hSirt2 the acylated substrate binds the enzyme before NAD^+,[50] the length of the acyl group could

DOI: 10.1021/acs.jmedchem.9b00638
J. Med. Chem. 2019, 62, 8733−8759

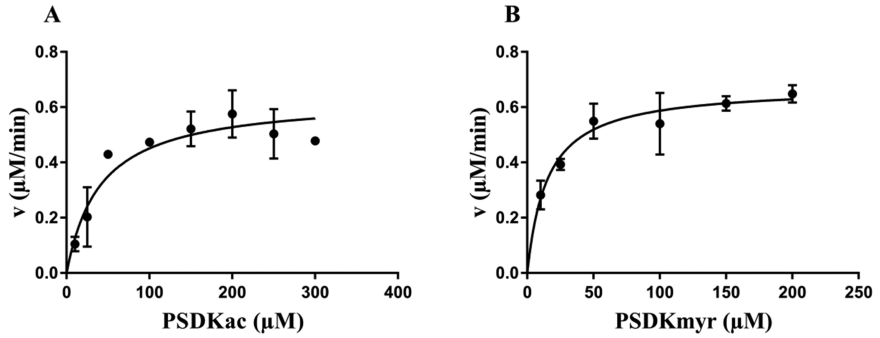

Figure 3. Michaelis–Menten plots for *Sm*Sirt2-dependent deacetylation (A) and demyristoylation (B). The error bars indicate standard error of the mean ($n \geq 2$).

Table 1. Kinetic Parameters of PSDKac, PSDKmyr, and NAD$^+$ for *Sm*Sirt2

	K_m (μM)[a]	k_{cat} (min^{-1})[a]	k_{cat}/K_m (s^{-1} M^{-1})[a]
PSDKac	40.9 ± 12.2	(31.8 ± 2.4) × 10^{-2}	(1.3 ± 0.3) × 10^2
PSDKmyr	15.1 ± 2.5	(33.8 ± 1.3) × 10^{-2}	(3.7 ± 0.9) × 10^2
NAD$^+$ (PSDKac)	33.9 ± 8.5	(10.3 ± 0.6) × 10^{-2}	(5.1 ± 1.8) × 10^1
NAD$^+$ (PSDKmyr)	13.3 ± 2.3	(32.3 ± 1.3) × 10^{-2}	(4.1 ± 0.9) × 10^2
ZMML	37.5 ± 12.7	(50.6 ± 4.9) × 10^{-4}	(1.3 ± 0.4) × 10^2
NAD$^+$ (ZMAL)	75.8 ± 8.1	(71.3 ± 3.2) × 10^{-4}	(9.4 ± 4.0) × 10^1
NAD$^+$ (ZMML)	9.3 ± 1.9	(51.8 ± 1.6) × 10^{-4}	(5.6 ± 0.9) × 10^2

[a]Reported as ±SE. K_m for ZMAL (59 μM) taken from ref 43.

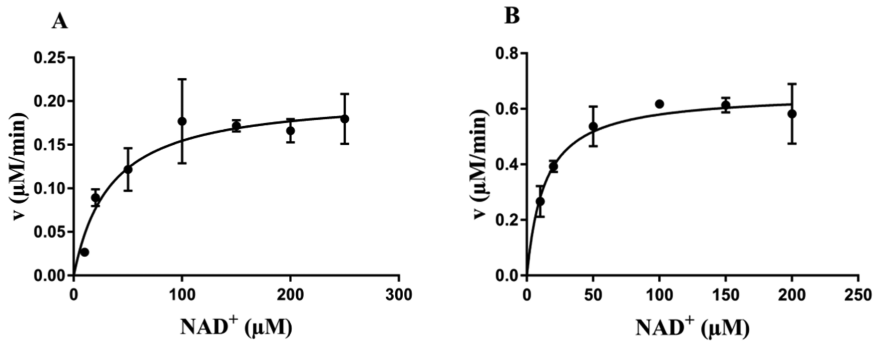

Figure 4. Michaelis–Menten plots for NAD$^+$ with PSDKac (A) and with PSDKmyr (B) in *Sm*Sirt2. The error bars indicate standard error of the mean ($n \geq 2$).

influence the NAD$^+$-binding affinity for *Sm*Sirt2 and have, more generally, an influence on the NAD$^+$ reaction. Consequently, the K_m values for NAD$^+$ were also analyzed in the presence of PSDKac and PSDKmyr. As shown in Figure 4, the extension of the peptide chain length increases the binding affinity of NAD$^+$ to *Sm*Sirt2 and the catalytic turnover. In fact, a 3-fold higher k_{cat} is the reason for a better catalytic efficiency in the presence of PSDKmyr than with PSDKac (Table 1). There was no inhibition of ZMAL conversion by PSDKac in a concentration of 300 μM (data not shown).

To further characterize the deacylation reactivity, we compared the potency of selected reference hSirt2 deacetylation inhibitors (NA, SirReal1 and 2,[51] AEM2[52]) with their ability to inhibit the demyristoylation reaction. As reported in Table 2, while in hSirt2, these compounds show higher inhibitory potency for deacetylation than for demyristoylation, they did not inhibit either reaction catalyzed by *Sm*Sirt2, with the only exception of NA.

***Sm*Sirt2 Inhibition.** Using the in vitro[43] assay described above, we initially screened the Food and Drug Administration-approved drugs library (provided by Enzo Life Sciences AG, Switzerland) that had already been tested on schistosomula and adult worms.[54,55] Idebenone (**4**) emerged as an overlapping compound that was known to block the growth of schistosomula and showed good *Sm*Sirt2 inhibition potency and selectivity over hSirt2[56] (Figure 5). Although Idebenone probably has a pleiotropic mode of action, this lent credence to our approach to identify druggable molecules from

Table 2. Activity of hSirt2 Standard Inhibitors with 1 or 3f as Substrates

	*Sm*Sirt2		hSirt2	
	IC_{50} (μM)[a] or % inhibition at 20 μM		IC_{50} (μM)[a] or % inhibition at 20 μM	
compound	1	3f	1	3f
NA	23.1 ± 1.8	420 ± 11.6	49.8 ± 4.6[b]	8.7 ± 0.5%
SirReal1	24.2 ± 0.8%	<15%	3.7 ± 0.8[c]	<15%
SirReal2	<15%	<15%	0.4 ± 0.1[c]	<15%
AEM2	<15%	<15%	2.5 ± 0.2[b]	42.8 ± 3.0%

[a]IC_{50} are reported as ±SEM (n = 3), for inhibition % ±SD (n = 3). [b]Ref 53. [c]Ref 51.

DOI: 10.1021/acs.jmedchem.9b00638
J. Med. Chem. 2019, 62, 8733–8759

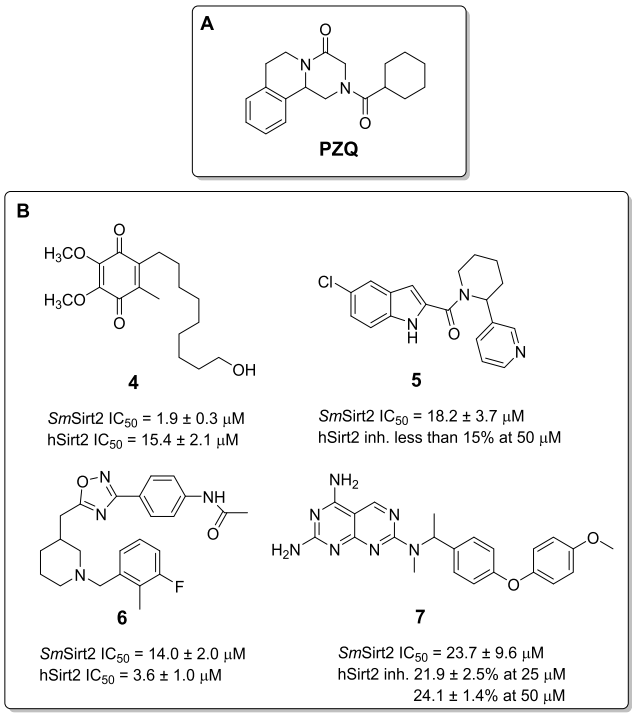

Figure 5. (A) Structure of antischistosomal treatment standard Praziquantel (PZQ). (B) Structures and in vitro data of idebenone (**4**) and hits from the Kinetobox library (**5**–**7**). For IC_{50} values, errors are represented as ±SEM (n = 3), while for inhibition % as ±SD (n = 3).

a diverse set of compounds that also show antischistosomal activity. We next proceeded with the GSK Kinetobox library, which was initially tested at the fixed assay concentration of 25 μM. Since we were looking for compounds with the IC_{50} value in the low micromolar range, we focused our attention only on compounds with inhibitory potency higher than 50% at that concentration. Furthermore, to test whether hits quench the AMC signal, inhibit the detection enzyme trypsin, or are autofluorescent compounds, all promising candidates were subjected to counteranalysis to exclude false positives and false negatives (data not shown). Compounds showing no assay interference and a dose-dependent activity were then tested on hSirt2 to evaluate their selectivity. Among the 592 tested compounds, we identified three hits characterized by potency in the low micromolar range: TCMDC-143159 (**5**), TCMDC-143362 (**6**), and TCMDC-143295 (**7**) (Figure 5). Due to reported toxicity of the anabasine ring,[57] present in **5**, we decided initially to resynthesize **6** and **7** to confirm their activity and to modify their structures to obtain analogues with improved activity and selectivity profiles. Since the inhibition of hSirt2 is an undesired feature in new antischistosomials, but might identify new scaffolds for optimization of human sirtuin inhibitors, we followed the lead of **6** as an unselective compound to some extent but focused mostly on the selective compound **7**.

Synthesis and Initial SAR of 1,2,4-Oxadiazolyl Compound 6. As previously cited, Feldman et al. have recently published the crystal structure of hSirt2 in complex with myristoylated peptides, showing the placement of the acyl chain in a hydrophobic pocket and the conservation of this localization during the entire catalytic reaction.[34,51] Since this could also be the case in *Sm*Sirt2, after establishing its synthesis, initial optimization of **6** was attempted with the replacement of the acetyl group with a longer fatty acyl group, such as an octanoyl (**11**) or a decanoyl (**12**) chain, to potentially address such a pocket. The synthesis of **6** and its analogues **11** and **12** is outlined in Scheme 2. A nucleophilic substitution between the commercially available 2-(piperidin-3-yl) acetic acid ethyl ester and 3-fluoro-2-methylbenzyl bromide was performed to obtain the intermediate **8**. The reaction between the requisite acyl chlorides and 4-amino-benzonitrile yielded the 4-cyanoanilides **9b** and **9c** which, together with the commercially available 4-cyanoacetanilide **9a**, were treated with hydroxylamine hydrochloride to give the benzamidoximes **10a**–**c**. Subsequent condensation between **10a**, **10b** and **8** afforded the required compounds **6** and **11**, and the reaction between **10c** and the acyl chloride of **8**, obtained by hydrolysis of the ethyl ester and subsequent chlorination, gave the final compound **12**.

When tested against *Sm*Sirt2 and hSirt2 at 25 μM, the hit **6** was confirmed to have inhibitory activity from the newly synthesized sample, whereas the octanoyl and decanoyl analogues **11** and **12** were practically inactive against both

Scheme 2. Synthesis of Compounds 6, 11, and 12[a]

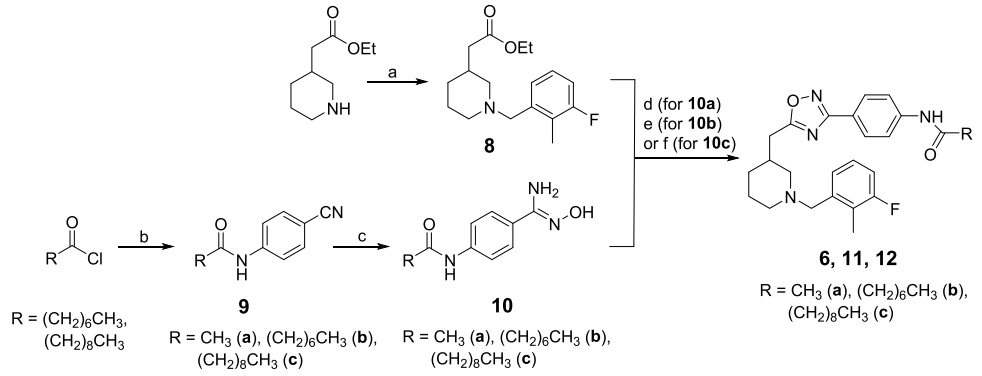

[a]Reagents and conditions: (a) 3-fluoro-2-methylbenzyl bromide, triethylamine, toluene, 0 °C → rt, 18 h; (b) 4-aminobenzonitrile, triethylamine, dry dichloromethane (DCM), 0 °C → rt, 2 h, N_2; (c) hydroxylamine hydrochloride, sodium carbonate, water/ethanol, reflux, 6–8 h; (d) **8**, **10a**, potassium carbonate, pyridine, reflux 8 h, then rt 72 h; (e) **8**, **10b**, potassium carbonate, pyridine, microwave, 180 °C, 10 min, 300 W, then reflux 43 h, and finally rt 12 h; (f) from **8**: (i) 1 M lithium hydroxide, ethanol, 20 h, rt; (ii) thionyl chloride, dimethylformamide (DMF), dry DCM, −15 °C → rt, 3 h, N_2; (iii) **10c**, triethylamine, DMF, dry DCM, rt, 22 h, then 150 °C 3 h, N_2.

DOI: 10.1021/acs.jmedchem.9b00638
J. Med. Chem. 2019, 62, 8733–8759

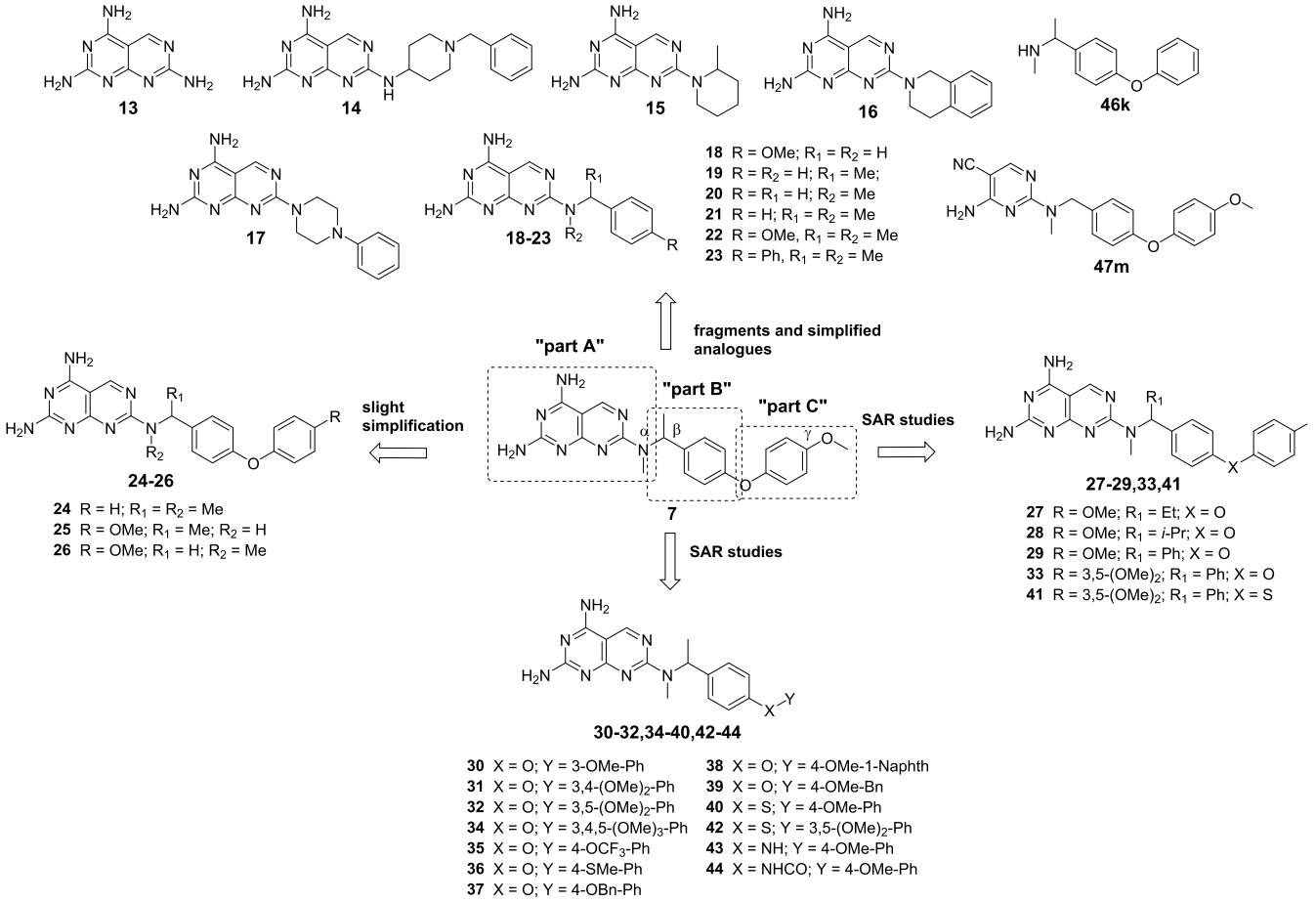

Figure 6. Overview of analogues of **7**: fragment-based approach and SAR studies.

parasite and human enzymes (**6**: *Sm*Sirt2 IC_{50} = 14.5 ± 0.6 μM; hSirt2 IC_{50} = 8.0 ± 1.1 μM; **11**: *Sm*Sirt2 inh. 30.5 ± 3.5%; hSirt2 inh. <15%. **12**: *Sm*Sirt2 inh. <15%; Sirt2 inh. <15%).

Synthesis and SAR of Pyrimidopyrimidine 7. To work on the structure of hit **7**, we started with a fragment-based approach with the development of analogues with a simplified structure, to identify the substructure(s) responsible for the inhibitory activity. In particular, since the 2,4,7-triaminopyrimidopyrimidine moiety of **7** ("part A", Figure 6) could mimic the adenosine part of NAD^+, we synthesized a first generation of analogues keeping this portion fixed and introducing several modifications at the Nα (Figure 6). More precisely, we purchased parent pyrimido[4,5-*d*]pyrimidine-2,4,7-triamine **13** and prepared derivatives where Nα is a secondary (**14**, **18**, and **19**), tertiary (**20**−**23**), or inserted in a cyclic amine (**15**−**17**). While **14**−**17** are characterized by small amine substitution at the C7 position, the N^7-benzylpyrimido[4,5-*d*]pyrimidine-2,4,7-triamines **18**−**23** represent the most substituted compounds of the series, with changes at the Nα, Cβ, and C4 benzyl positions ("part B", Figure 6).

As shown in Table 3 (see below), compounds **13**−**22** show complete loss of activity on *Sm*Sirt2 and remain inactive on the human enzyme. Among the simplified analogues, only **23**, bearing a large phenyl substituent on the right-hand side of the molecule (4-biphenyl portion; "part C", Figure 6), displayed low *Sm*Sirt2 inhibition. As a consequence, we designed a second generation of analogues in which small focused modifications were applied, without leading to an excessive alteration of the prototype structure, but maintaining a high similarity to it. Specifically, we focused on the Nα, Cβ, and Cγ positions of **7** (Figure 6) through the removal of the methyl or methoxy groups (**24**−**26**). We increased the steric hindrance of the Cβ substituent (part B, Figure 6), by replacing the methyl with an ethyl, isopropyl, or phenyl group (**27**−**29**, **33**, and **41**), and we explored the effect of replacement of the 4-methoxyphenoxy portion of **7** (part C, Figure 6) with other substituted phenoxy, 1-naphthyloxy, benzyloxy, phenylthio, aniline, and benzanilide moieties (**30**−**44**).

Chemistry. The pyrimido[4,5-*d*]pyrimidine-2,4,7-triamine **13** is commercially available. The final compounds **14**−**44** were prepared by reaction between the commercial 4-amino-2-bromopirimidine-5-carbonitrile and the appropriate amines **46** in anhydrous 2-methoxyethanol, in the presence of triethylamine at 80 °C. The obtained pyrimidine intermediates **47** were converted into the desired compounds **14**−**44** through condensation reactions performed at 150 °C with the guanidine free base in dry 2-methoxyethanol (Scheme 3). The amines **46a**−**h** used for the synthesis of the pyrimidine intermediates **47a**−**h** are commercially available and were purchased from vendors. The amines **46i**−**f′**, useful synthons for the synthesis of the final compounds **22**−**44**, were prepared by reaction of the corresponding phenyl ketones or aldehydes **45a**−**w** with 7 M ammonia (for secondary amines) or 2 M methylamine (for tertiary amines) solution in anhydrous methanol in the presence of titanium isopropoxide at room temperature, followed by the addition, after the formation of the imine intermediates, of the reducing agent sodium borohydride at 0 °C under nitrogen atmosphere (Scheme

DOI: 10.1021/acs.jmedchem.9b00638
J. Med. Chem. 2019, 62, 8733−8759

Table 3. In Vitro Inhibition of *Sm*Sirt2 and hSirt2 by 7, 13−44, 46k, and 47m

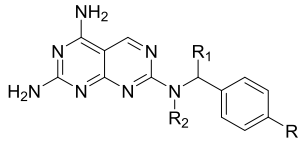

compd	R	R_1	R_2	*Sm*Sirt2[a] % inhibition at 25 μM or IC_{50} [μM]	hSirt2[a] % inhibition at 25 μM or IC_{50} [μM]
7	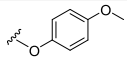	Me	Me	23.7 ± 9.6	21.9 ± 2.5%
13	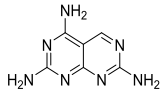			<15%	<15%
14	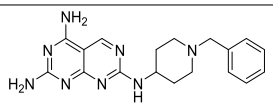			<15%	23.2 ± 0.8%
15	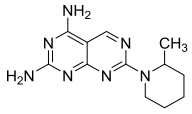			<15%	<15%
16	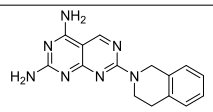			<15%	<15%
17	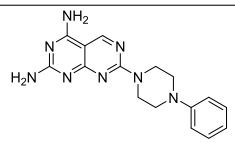			<15%	<15%
18	-OMe	H	H	<15%	<15%
19	H	Me	H	<15%	<15%
20	H	H	Me	<15%	<15%
21	H	Me	Me	<15%	<15%
22	-OMe	Me	Me	<15%	<15%
23	-Ph	Me	Me	24.8 ± 2.2%	<15%
24	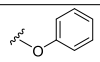	Me	Me	27.6 ± 2.8%	<15%
25	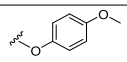	Me	H	37.5 ± 5.6%	21.0 ± 3.4%
26	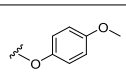	H	Me	<15%	<15%

DOI: 10.1021/acs.jmedchem.9b00638
J. Med. Chem. 2019, 62, 8733−8759

Table 3. continued

27	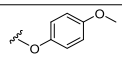	Et	Me	12.8 ± 0.8	36.7 ± 7.7
28	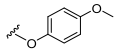	*i*-Pr	Me	27.7 ± 3.8	57.4 ± 5.2%
29	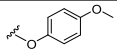	Ph	Me	2.34 ± 0.2[b]	22.1 ± 3.4%
30	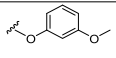	Me	Me	23.1 ± 1.4	33.8 ± 0.4%
31	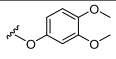	Me	Me	44.7 ± 4.4	35.3 ± 4.9%
32	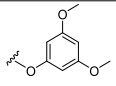	Me	Me	12.5 ± 1.1	7.4 ± 3.9%
33	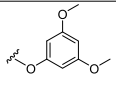	Ph	Me	3.3 ± 0.2	29.6 ± 1.9%
34	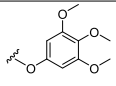	Me	Me	30.8 ± 3.0	29.2 ± 3.9%
35	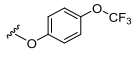	Me	Me	20.3 ± 2.1%	37.5 ± 4.8%
36	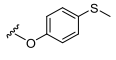	Me	Me	49± 1.1%	<15%
37	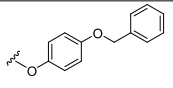	Me	Me	40.3 ± 5.2%	70.4± 4.2%
38	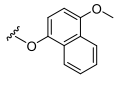	Me	Me	18.4 ± 0.9%	30.6 ± 0.2%
39	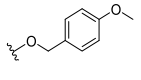	Me	Me	46.2 ± 4.3%	61.7± 5.3%
40	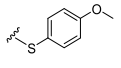	Me	Me	14.9 ± 0.9	13.3 ± 1.6
41	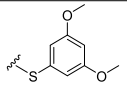	Me	Me	4.3 ± 0.4	27.9 ± 1.8 %
42	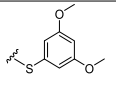	Ph	Me	2.0 ± 0.1	21.5 ± 3.1
43	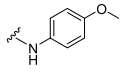	Me	Me	65.1 ± 7.2	40.8 ± 4.9%
44	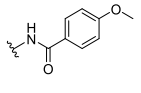	Me	Me	41.9 ± 2.2%	<15%

DOI: 10.1021/acs.jmedchem.9b00638
J. Med. Chem. 2019, 62, 8733−8759

Table 3. continued

44	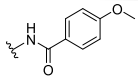	Me	Me	41.9 ± 2.2%	<15%
46k	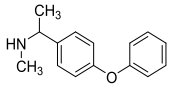			<15%	<15%
47m	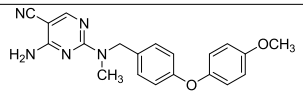			<15%	<15%

[a]IC_{50} ± SEM are reported (n = 3), while inhibition % are reported as ±SD (n = 3). [b]Maximum of observed inhibition: 60%.

Scheme 3. Synthesis of Compounds 7 and 14−44[a]

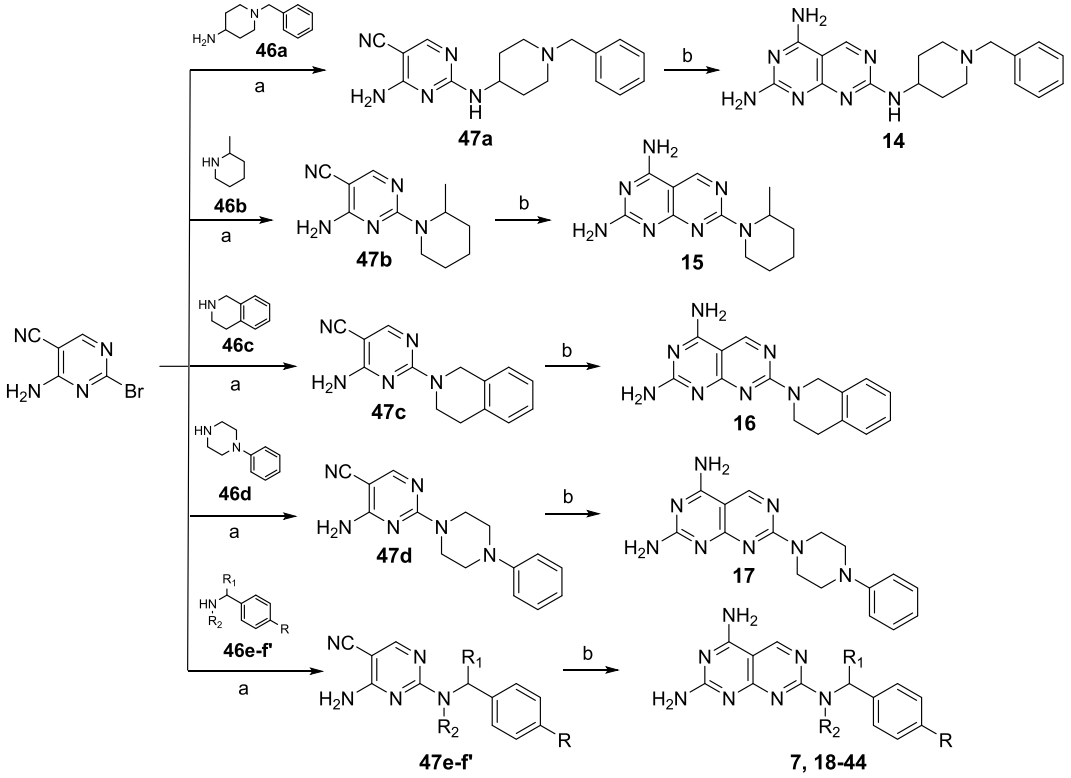

[a]Reagents and conditions: (a) triethylamine, dry 2-methoxyethanol, 80 °C, 2.5−8 h; (b) guanidine free base, dry 2-methoxyethanol, 150 °C, 1.5−4.5 h.

4A). The phenyl ketones/aldehydes **45a−e** are commercially available. The ketones **45f−q** and **45s−u** were synthesized by reaction between the appropriate aromatic alcohols or thiols and the 1-(4-fluorophenyl)ethan-1-one, -propan-1-one, -2-methylpropan-1-one, and -(phenyl)methanone in the presence of anhydrous potassium carbonate in dry DMF at 175 °C (Scheme 4B). The 1-(4-((4-methoxybenzyl)oxy)phenyl)-ethan-1-one **45r**,[58] the 1-(4-((4-methoxyphenyl)amino)-phenyl)ethan-1-one **45v**,[59] and the *N*-(4-acetylphenyl)-4-methoxybenzamide **45w**[60] were prepared according to the literature. For the structures of the intermediates **45** and **46**, see the Supporting Information (Table S4).

All of the above compounds were tested in vitro against *Sm*Sirt2[43] and hSirt2, to study their selectivity for the parasitic enzyme (Table 3).[56] An amine and a pyrimidine synthetic intermediates (**46k** and **47m**; see Figure 6 and Table 3 for their structures) were also included in the list, to confirm the importance of the intact pyrimido[4,5-*d*]pyrimidine-2,4,7-triamine scaffold for the inhibiting activity. The percentages of inhibition at 25 μM or the IC_{50} values of the new compounds tested against *Sm*Sirt2 as well as hSirt2 are reported in Table 3.

As stated above, none of the fragments or simplified molecules **13−22** showed inhibitory activity on either the parasite or human enzymes. Only the derivatives carrying the 1-([1,1′-biphenyl]-4-yl)ethyl (**23**) or 1-(4-phenoxyphenyl)-ethyl (**24**) substituent at Nα (Figure 6) partially retained inhibition against *Sm*Sirt2, demonstrating the crucial role of the substituted phenoxyphenyl or 1,1′-biphenyl portion on the right-hand side of the molecule (part C, Figure 6). The removal of the methyl group at either the 7 Nα (see **25**) or Cβ position (see **26**) (Figure 6) decreased or totally abolished the

DOI: 10.1021/acs.jmedchem.9b00638
J. Med. Chem. 2019, 62, 8733−8759

Scheme 4. Synthesis of the Intermediate Compounds 45 and 46[a]

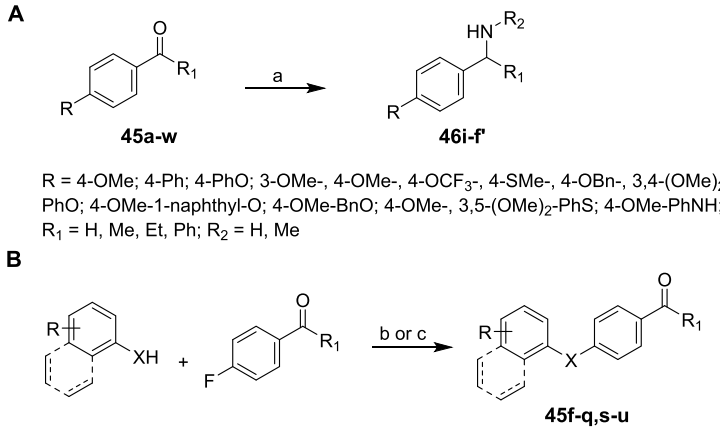

[a]Reagents and conditions: (a) 2 M methylamine in methanol, titanium isopropoxide, dry tetrahydrofuran (THF), N_2, 5−6 h, rt, then sodium borohydride, N_2, 2 h, rt; (b) 7 M ammonia in methanol, titanium isopropoxide, N_2, 5 h, rt, then sodium borohydride, N_2, 2 h, rt; (c) anhydrous potassium carbonate, dry DMF, 175 °C, 5 h.

*Sm*Sirt2 inhibitory activity, respectively. In contrast, the insertion at Cβ of groups bigger than methyl [ethyl (**27**), isopropyl (**28**), and phenyl (**29**)] generally improved the *Sm*Sirt2 inhibitory potency up to 10-fold, reaching with **29** the single-digit micromolar level (IC_{50} = 2.34 μM). Interestingly, **29** is more selective than **7** for *Sm*Sirt2 over hSirt2 as judged by IC_{50} values, but it reaches only a maximum of inhibition of 60%, which complicates the interpretation of the selectivity data. The isopropyl derivative **28** was an exception, displaying a similar inhibitory potency to **7** against *Sm*Sirt2 and higher potency against hSirt2.

At the part C of the molecule (4-methoxyphenoxy moiety, Figure 6), no particular increase in activity or selectivity was obtained with the shift of the methoxy group from para to meta position (**30**), and the introduction of 3,4-dimethoxy (**31**) or 3,4,5-trimethoxy (**34**) groups at the phenoxy portion, as well as the replacement of the 4-methoxy with a 4-trifluoromethoxy (**35**), 4-methylthio (**36**), or 4-benzyloxy (**37**) group reduced the inhibitory potency against *Sm*Sirt2. However, the insertion of two methoxy groups at the 3,5 position of the phenoxy moiety (**32**) led to 2-fold increase of potency against *Sm*Sirt2 and improved selectivity over hSirt2. In this last compound, the further replacement of the methyl group at Cβ with a phenyl ring (**33**) determined an additional increase of potency against *Sm*Sirt2 (IC_{50} = 3.3 μM, 7-fold higher potency compared to **7**), confirming the positive SAR about Cβ substitution with large groups. The replacement of the 4-methoxyphenoxy moiety of **7** with the larger 4-methoxy-1-naphthyloxy (**38**) or the longer 4-methoxybenzyloxy (**39**) group led to a decrease in potency against *Sm*Sirt2 and, in the case of **39**, improved hSirt2 inhibition. Again in the 4-methoxyphenoxy group, the isosteric change oxygen−sulfur atom led to the 4-methoxyphenylthio analogue **40**, which produced a 1.6-fold enhancement of *Sm*Sirt2 inhibition (IC_{50} = 14.9 μM), combined with improved inhibition of the human enzyme (IC_{50} = 13.3 μM). The further change from the 4-methoxy to the 3,5-dimethoxy substitution at the phenylthio moiety of **40** provided **41**, which showed improved potency and selectivity against *Sm*Sirt2 (*Sm*Sirt2 IC_{50} = 4.3 μM, hSirt2 inhibition = 27.9% at 25 μM). Moreover, the combination of the positive SAR of the series with the replacement of the Cβ methyl of **41** with the Cβ phenyl group gave **42**, the most potent compound of the series versus *Sm*Sirt2 (IC_{50} = 2 μM) and 10-fold selective over the human counterpart hSirt2 (IC_{50} = 21.5 μM).

The replacement of the 4-methoxyphenoxy portion with a 4-methoxyaniline (**43**) or 4-methoxybenzamide (**44**) group led to a decrease in potency against *Sm*Sirt2. Finally, the total absence of inhibitory activity against both parasitic and human enzymes by the intermediates **46k** and **47m** confirmed the importance of the intact pyrimido[4,5-*d*]pyrimidine-2,4,7-triamine scaffold (part A, Figure 6) for the inhibitory activity of such compounds. The inhibiting activity of selected compounds **33**, **36**, **41**, **42**, and **44** was also evaluated in the presence of the myristoylated substrate **3f** instead of the acetylated **1**. As reported in Table 4, in many cases, no significant inhibition was measured in the presence of *Sm*Sirt2 and hSirt2 with the exception of **33**, **41**, and **42**, which show an inhibitory potency for the hSirt2-catalyzed demyristoylation in the low micromolar range. This may present a new starting point for the development of human Sirtuin inhibitors with a selectivity for long-chain acyl removal, as so far a preference, if any, has been observed only for deacetylation.

Table 4. Inhibitory Activity of Selected Compounds 33, 36, 41, 42, and 44 against *Sm*Sirt2 and hSirt2 with Myristoylated 3f as Substrate

	*Sm*Sirt2 (**3f**)	hSirt2 (**3f**)
compound	IC_{50} (μM)[a] or % inhibition at 20 μM	IC_{50} (μM)[a] or % inhibition at 20 μM
7	16.8 ± 1.14[b]	<15%
33	<15%	13.1 ± 2.2
36	<15%	38.1 ± 5.2%
41	15%	25.1 ± 4.1
42	<15%	15.6 ± 1.9
44	<15%	<15%

[a]IC_{50} values are reported as ±SEM (n = 3), while inhibition % as ±SD (n = 3). [b]Maximum of inhibition: 45%.

DOI: 10.1021/acs.jmedchem.9b00638
J. Med. Chem. 2019, 62, 8733−8759

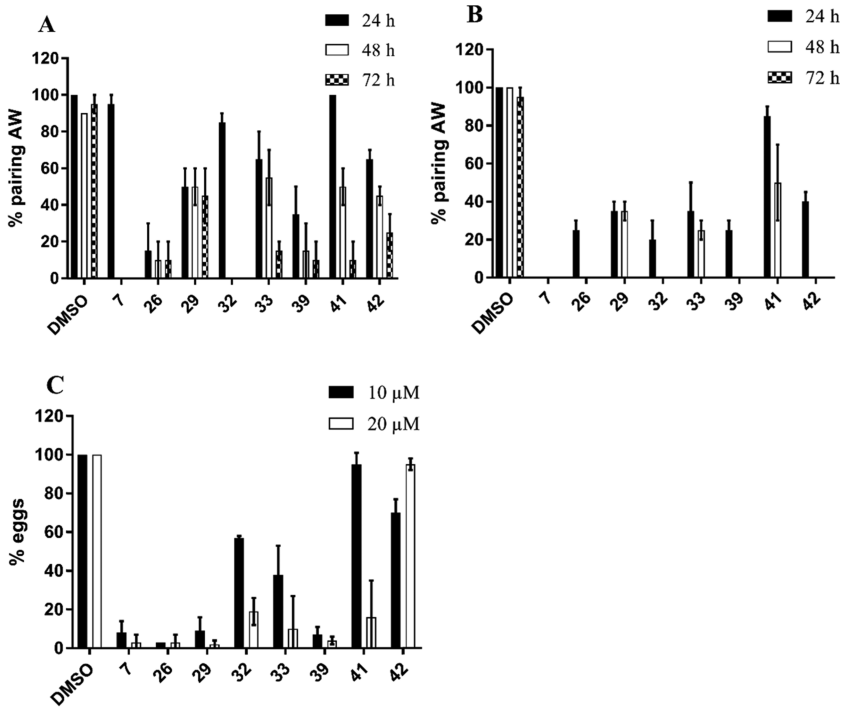

Figure 7. Effects of **7** and its analogues on adult worms (AWs) pairing at 10 and 20 μM ((A) and (B), respectively). Assay used: microscopy examination. Results after 24, 48, and 72 h are represented by the black, white, and checkered bars, respectively. Effect of these compounds on egg laying (C). Compounds **26** and **39** do not block *Sm*Sirt2 in vitro.

We also tested compounds **26**, **33**, **39**, and **41** on human isotypes Sirt1 and 3 regarding deacetylation. All compounds showed less than 15% inhibition at 25 μM (data not shown), while 500 μM of nicotinamide led to complete inhibition as expected.[51] Evenmore, hSirt2 is the closest human homologue to *Sm*Sirt2[48] (see also Table S5; data not shown for hSirt1, 3).

In Vitro Effects on Schistosomula and Adult Worms. To evaluate whether these optimized compounds have effects on the parasite, **29**, **32**, **33**, **41**, and **42** together with the prototype **7** were tested on schistosomula and adult worms. Two potential negative controls **26** and **39** were also included in the series. As shown in Table S6, all tested compounds reduce the viability of cultured schistosomula at 10 and 20 μM, including **26** and **39**, which show low or no activity on the recombinant enzyme (Table 3).

Experiments on adult worms report a similar trend (Figure 7), where again the *Sm*Sirt2 inhibitors as well as the potential negative controls reduce worm pairing and egg laying already after 24 h of culture. While the possibility that the enzyme inhibitors do exert their effects via inhibition of *Sm*Sirt2 cannot be ruled out, the strong effects that **26** and **39** also have on parasite viability and reproduction indicate that the effects of compounds shown in Figure 7 on the parasite may be at least in part due to the modulation of other targets (off-target effects).

To get some further insight, we measured selected compounds **7**, **26**, **29**, **32**, **33**, **39**, and **41** for toxicity on human cultured cancer cells using an 3-(4,5-dimethylthiazol-2-yl)-5-(3-carboxymethoxyphenyl)-2-(4-sulfophenyl)-2*H*-tetrazolium viability assay. In this assay, the compounds that are inactive on *Sm*Sirt2 but active on schistosomes also show toxicity on the human cells, while the *Sm*Sirt2 inhibitors with activity on the worms do not show this general toxicity (see Figure 8).

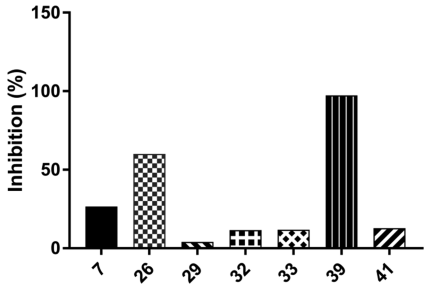

Figure 8. Growth inhibition of HL-60 acute myeloid leukemia cells by compound **7** and selected analogues at 10 μM assay concentration.

DISCUSSION AND CONCLUSIONS

The identification of a robust deacylase activity, supported by kinetic investigations, expands the range of possible biological activities relevant for *Sm*Sirt2. The high demyristoylation efficiency of this enzyme suggests the merit of undertaking future investigations on deacylation inhibition, in addition to deacetylation inhibition, as a new strategy to kill both schistosomula and adult worms. For inhibitors of hSirt2 with a thiomyristoylated lysine core (also called TM), it has been proposed that a dual deacetylase/demyristoylase activity is beneficial for cellular potency in cancer cells and selectivity over noncancer cells.[61]

With the aim of finding potent and selective inhibitors of *Sm*Sirt2, we performed screening of the GSK Kinetobox library, composed of 592 compounds with proven activity against cultured kinetoplastids, namely, *L. donovani*, *T. cruzi*, and *T. brucei*. From an initial test, we identified **5**−**7** as valuable hits for further optimization. As outlined above, we focused our attention on **6** and **7**. Regarding **6**, the attempt to potentially target the enzymatic (possibly extended) C pocket through an octanoylated and decanoylated analogue led to a

DOI: 10.1021/acs.jmedchem.9b00638
J. Med. Chem. 2019, 62, 8733−8759

loss in activity. Extensive SAR studies performed on **7** highlighted the crucial role of the presence of the intact pyrimido[4,5-*d*]pyrimidine-2,4,7-triamine (part A of the molecules), disubstituted at N7 (Nα in Figure 6) with a methyl and a substituted 1-phenylethyl moiety (part B), further carrying a substituted phenoxy/phenylthio group at its C4 position (part C), recognized as crucial to elicit *Sm*Sirt2 inhibitory potency and selectivity over hSirt2 (Figure 6). In particular, the presence at part C of the 4-methoxyphenoxy, 3,5-dimethoxyphenoxy, and 3,5-dimethoxyphenylthio portions, combined with the phenyl group at the Cβ position (part B), led to the most potent derivatives **29**, **33**, **41**, and **42** with IC_{50} values in the single-digit micromolar range for *Sm*Sirt2. Experiments with **7** and its analogues on schistosomula and adult worms showed strong activity, which was also present in enzymatically inactive compounds. However, while compounds **26** and **39**, inactive on *Sm*Sirt2, also showed unspecific toxicity to human cancer cells, the selective *Sm*Sirt2 inhibitors **7**, **29**, **32**, **33**, and **41** were nontoxic to human cancer cells. Generally, the compounds show good properties in terms of druglikeness, e.g., log *P* values are between 2.7 (**32**) and 4.6 (**42**) (see Table S7). Molecular weight is mostly above 400 but only up to 525 Da maximum.

Thus, for the first time, we can show that *Sm*Sirt2 can be drugged with selectivity over the human isotype (especially **29**, **33**, and **41**), and the inhibitors block *Schistosoma* growth without general toxicity to human cells. This can be used as starting point for further optimization studies. In addition, leads for new inhibitors of hSirt2 have been identified, interestingly some with a preference for demyristoylation over deacetylation.

EXPERIMENTAL SECTION

Recombinant Production and Purification of *Sm*Sirt2. Recombinant expression and purification of *Sm*Sirt2 were done as previously described.[43] Briefly, overexpression was carried out in *E. coli* BL21(DE3) cells in 2× Luria Broth medium. The cells were grown to OD_{600} of 1.2 at 37 °C; then, the culture was cooled down to 25 °C and induction of expression was done by adding 0.5 mM final isopropyl-1-thio-β-D-galactopyranoside (Euromedex), in the presence of 100 μM $ZnCl_2$. Harvested bacteria were resuspended in lysis buffer (400 mM NaCl, 10 mM Tris−HCl pH 8.0) and lysed by sonication. The lysate was clarified by centrifugation (17 000 rpm, JA-25.50 Beckman) for 1 h. The supernatant was loaded onto Talon Metal affinity resin (Clontech) preequilibrated with the lysis buffer. The 3C protease treatment was used to remove the His-tag from the recombinant protein, which was subsequently loaded onto HiLoad 16/60 Superdex 200 gel filtration column (Amersham Bioscience) equilibrated in 400 mM NaCl, 10 mM Tris−HCl pH 8.0, and 2 mM dithiothreitol (DTT). Finally, the protein was concentrated with an Amicon Ultra centrifugal filter unit (Millipore) to reach a final concentration of 1.5 mg/mL as assayed by the A280 measurement (NanoDrop).

Long-Chain Deacylation. Conversion in comparison to the theoretical maximal conversion (100% ZMAL conversion, obtained by measuring 10.5 μM AMC) of **3a−g** by *Sm*Sirt2 and hSirt2 and their inhibition were evaluated by homogeneous assay using 10.5 μM assay concentration of potential substrates (prepared from 12.6 mM stock solution in dimethyl sulfoxide (DMSO) and diluted with assay buffer) instead of ZMAL. Regarding hSirt2, 25 mM *N*-(2-hydroxyethyl)piperazine-*N*′-ethanesulfonic acid (HEPES), 137 mM NaCl, 2.7 mM KCl, 1 mM $MgCl_2$, 0.015% Triton X-100, pH = 8.0 were used as assay buffer. OriginPro 9.0 G and GraphPad 7.0 were used for the analysis of results.

Kinetic Analysis of PSDKac and PSDKmyr. Deacylation reactions were evaluated by reversed-phase HPLC (Kinetex XB-C18 column, 100 Å, 5 μm, 250 × 4.6 mm^2) by monitoring the formation of the deacylated product at 214 nm. Linear deacylation rates were determined by incubation of 47 μL of *Sm*Sirt2 solution (104 ng/μL; final assay concentration, 80 ng/μL) in assay buffer (25 mM HEPES, 137 mM NaCl, 2.7 mM KCl, 1 mM $MgCl_2$, 0.015% Triton X-100, pH = 8.0) with 3 μL of DMSO, 5 μL of PSDKac (Ac-Pro-Ser-Asp-Lys(acetyl)-Tyr-Ile-Gly-Gly-Trp-Trp-NH_2 custom synthesized by PSL, Heidelberg, Germany) or PSDKmyr (Ac-Pro-Ser-Asp-Lys-(myristoyl)-Tyr-Ile-Gly-Gly-Trp-Trp-NH_2 custom synthesized by PSL, Heidelberg, Germany) solution (prepared from 3.6 mM stocks in DMSO and diluted with assay buffer; concentration range, 10−300 μM), and 5 μL of NAD^+ (prepared from 6 mM stock in assay buffer and diluted in assay buffer; final assay concentration, 500 μM). At 0, 1, 3, 5, 10, 20, and 30 min, the deacylation was quenched with 6.7 μL of trifluoroacetyl (TFA) (10% in assay buffer; final assay concentration, 1%), incubated for 5 min at 37 °C and then centrifuged for 10 min at 14 000*g*. The supernatant (55 μL) were transferred into HPLC vials and analyzed. Each experiment was done twice in duplicate. The HPLC method was used to evaluate the deacylation: eluent A, H_2O + 0.05% TFA; eluent B, acetonitrile + 0.05% TFA; 0−4 min, linear increase from B = 10 to 40%; 4−10 min, linear increase to B = 60%; 10 min, linear increase to B = 100%; 10−14 min, B = 100%; 14−16 min, linear decrease to B = 10%; 16−25 min, B = 10% with a flow rate of 1 mL/min. The following method has been used to follow demyristoylation reactions: eluent A, H_2O + 0.05% TFA; eluent B, acetonitrile + 0.05% TFA; 0−5 min, linear increase from B = 10 to 40%; 5−8.5 min, linear increase to B = 80%; 8.5−9.5 min, linear increase to B = 90%; 9.5−10.5 min, linear increase to B = 100%; 10.5−15 min, B = 100%; 15 min, B = 100%; 15−18 min, linear decrease to B = 10% with a flow rate of 1 mL/min. The quantification of product peaks allowed the determination of deacylation rates, and the data have been fitted to the Michaelis−Menten equation. GraphPad Prism has been used to determine K_m, k_{cat}, and k_{cat}/K_m.

Kinetic Analysis of NAD_{PSDKac}^+ and $NAD_{PSDKmyr}^+$. Deacylation reactions were evaluated by reversed-phase HPLC (Kinetex XB-C18 column, 100 Å, 5 μm, 250 × 4.6 mm^2) by monitoring the formation of the deacylated product at 214 nm. Linear deacylation rates have been determined by incubation of 47 μL of *Sm*Sirt2 solution (104 ng/μL; final assay concentration, 80 ng/μL) in assay buffer (25 mM HEPES, 137 mM NaCl, 2.7 mM KCl, 1 mM $MgCl_2$, 0.015% Triton X-100, pH = 8.0) with 3 μL of DMSO, 5 μL of PSDKac or PSDKmyr (prepared, respectively, from 2.4 and 0.96 mM stock in DMSO and diluted with assay buffer, saturating assay concentrations), and 5 μL of NAD^+ (prepared from 6 mM stock in assay buffer and diluted with assay buffer; NAD^+ assay concentration range, 10−250 μM). At 0, 1, 3, 5, 10, 20, and 30 min, the deacylation was quenched with 6.7 μL of TFA (10% in assay buffer; final assay concentration, 1%), incubated for 5 min at 37 °C and then centrifuged for 10 min at 14 000*g*. The supernatant (55 μL) was transferred into HPLC vials and analyzed. Each experiment was done twice in duplicate. Deacetylation and demyristoylation were evaluated using the same HPLC methods described for PSDKac and PSDKmyr, respectively. The quantification of product peaks allowed the determination of deacylation rates, and the data have been fitted to the Michaelis−Menten equation. K_{m,NAD^+}, k_{cat,NAD^+}, and k_{cat}/K_m have been determined using GraphPhad Prism 7.0.

Kinetic Analysis of ZMML. Deacylation reactions were evaluated by a homogeneous fluorescence-based assay. *Sm*Sirt2 solution (14 μL, 104 ng/μL, final assay concentration 80 ng/μL) in assay buffer (25 mM Tris−HCl, 137 mM NaCl, 2.7 mM KCl, 1 mM $MgCl_2$, 0.5 mM DTT, 0.015% of Triton X-100, pH = 8.0) with 1 μL of DMSO, 2.5 μL of ZMML solution (prepared from 12.6 mM stocks in DMSO and diluted with assay buffer; concentration ranges, 10−250 μM), and 2.5 μL of NAD^+ (prepared from 4 mM stock in assay buffer and diluted in assay buffer; final assay concentration, 500 μM) was added to start the reaction. At 0, 1, 3, 5, 10, 20, and 30 min, the deacylation was quenched with 20 μL of stop solution (50 mM Tris, 100 mM NaCl, 6.7% (v/v) DMSO, trypsin 1 mg/mL, 8 mM nicotinamide, pH = 8.0). The plate was incubated for 20 min at 37 °C and 250 rpm, and the

DOI: 10.1021/acs.jmedchem.9b00638
J. Med. Chem. 2019, 62, 8733−8759

fluorescence intensity was measured in a microplate reader (λ_{ex} = 390 nm, λ_{em} = 460 nm, BMG POLARstar Optima, BMG Labtech, Germany). Each experiment was done in duplicate. Deacylation rates were evaluated in relation to theoretical maximal conversion (100% conversion of ZMML obtained by measuring respective concentration of AMC), and the data have been fitted to the Michaelis−Menten equation. Origin 9.0 G has been used to determine K_m, k_{cat}, and k_{cat}/K_m.

Kinetic Analysis of $NAD_{(ZMAL)}^+$ and $NAD_{(ZMML)}^+$. Deacylation reactions were evaluated by a homogeneous fluorescence-based assay. *Sm*Sirt2 solution (14 μL, 104 ng/μL; final assay concentration, 80 ng/μL) in assay buffer (25 mM Tris−HCl, 137 mM NaCl, 2.7 mM KCl, 1 mM $MgCl_2$, 0.5 mM DTT, 0.015% of Triton X-100, pH = 8.0) with 1 μL of DMSO, 2.5 μL of ZMAL or ZMML solution (prepared, respectively, from 12.6 mM stocks in DMSO and diluted with assay buffer, saturating assay concentrations), and 2.5 μL of NAD^+ (prepared from 4 mM stock in assay buffer and diluted in assay buffer; assay concentration range, 10−250 μM) was added to start the reaction. At 0, 1, 3, 5, 10, 20, and 30 min, the deacylation was quenched with 20 μL of stop solution (50 mM Tris, 100 mM NaCl, 6.7% (v/v) DMSO, trypsin 1 mg/mL, 8 mM nicotinamide, pH = 8.0). The plate was incubated for 20 min at 37 °C and 250 rpm, and the fluorescence intensity was measured in a microplate reader (λ_{ex} = 390 nm, λ_{em} = 460 nm, BMG POLARstar Optima, BMG Labtech, Germany). Each experiment was done in duplicate. Deacylation rates were evaluated in relation to theoretical maximal conversion (100% conversion of ZMAL or ZMML obtained by measuring respective concentration of AMC), and the data have been fitted to the Michaelis−Menten equation. Origin 9.0 G has been used to determine $K_{m,NAD}^+$, $k_{cat,NAD}^+$, and k_{cat}/K_m.

In Vitro Kinetobox Screening (*Sm*Sirt2). For the screening of the Kinetobox library, a homogeneous fluorescence-based assay, developed in our group, was used to determine *Sm*Sirt2[43] activity. OriginPro 9.0 G was employed to determine the IC_{50} values. The absence of eventual assay interference due to trypsin inhibition was confirmed according to the published procedures[43] (data not shown), while, to exclude any quenching of the AMC signal, 2.5 μL of an AMC solution (prepared from 12.6 mM stock solution in DMSO and diluted with assay buffer; final assay concentration, 10.5 μM) was used instead of ZMAL in the homogeneous assay. Active compounds were tested for known classes of assay interference compounds with the publicly available online tool "False Positive Remover" (www.cbligand.org). The only compound flagged to have Pan-assay interference compounds characteristics was the approved drug Idebenone (**4**), but none of our leads or analogues in the optimization campaign.

In Vitro Inhibition of hSirt2. The activity of potential hits on hSirt2 was measured according to the published procedures.[56] All compounds were initially tested at 25 μM and, for candidates that showed an hSirt2 inhibition equal to or higher than 50% at this concentration, IC_{50} values have been measured and determined using OriginPro 9.0 G.

General Chemistry Conditions. Reagents, starting materials, and solvents were used without further purification of the purchased form. All reactions were monitored by thin-layer chromatography (TLC) with Merck precoated silica gel 60 F_{254} plates and analyzed under UV light (254 nm) using different mobile phases. Microwave-assisted reactions were performed using a Discover S-1863 microwave system (CEM GmbH, Germany) and Biotage Initiator (Uppsala, Sweden) high-frequency microwave synthesizer working at 2.45 GHz, fitted with a magnetic stirrer and sample processor; reaction vessels were Biotage microwave glass vials sealed with applicable cap; temperature was controlled through the internal IR sensor of the microwave apparatus. Synthesized compounds were purified by flash column chromatography with a Biotage Isolera One automated flash purification system with a UV−vis detector. TELOS Flash-LL silica columns 60 M were used as stationary phase with a mobile phase as specified in the following description. Yields were not optimized. Proton (^{1}H), carbon (^{13}C), and fluorine (^{19}F) spectra were recorded on a Bruker Avance III HD spectrometer at 400, 100, and 376 MHz, respectively, in reference to the solvents reported in the description. Chemical shifts δ are given in parts per million (ppm), and the peak assignment was supported by correlation spectroscopy and heteronuclear multiple quantum correlation experiments. The purity of compounds **2**, **3**, **6**, **8**−**12** was determined by HPLC (UV detection at λ = 210 nm) and was found to be equal to or higher than 95% using the following conditions: eluent A, H_2O + 0.05% TFA; eluent B, acetonitrile + 0.05% TFA; linear gradient conditions (0−29 min, linear increase from A = 100% and B = 0% to A = 0% and B = 100%; 29−31 min, B = 100%; 31 min, decrease to B = 10%; 31−40 min B = 10%) with a flow rate of 1 mL/min; analytical column: Phenomenex Synergi 4 μm HYDRO-RP 80 Å, 250 mm × 4.6 mm for **3e**, **3f**, **3b**, **3c**, **3g**, and **11**; Phenomenex Kinetex 5 μm XB-C18 100 Å, 250 mm × 4.6 mm for **3a**, **3d**, **6**, and **12**. Low-resolution mass spectra of compounds **7** and **14**−**44** were recorded on an atmospheric pressure interface-time-of-flight Mariner by Perspective Biosystem (Stratford, Texas), and samples were injected by a Harvard pump at a flow rate of 5−10 μL/min, infused in the electrospray system. High-resolution mass spectrometry (HRMS) with electrospray ionization (ESI) analyses were performed using an Thermo Scientific Exactive mass spectrometer, and low-resolution mass spectrometry with electrospray ionization (ESI) analysis was performed using Advion expression compact mass spectrometer, with electron ionization on an Agilent Technologies 6890N Network GC-MS system. Elemental analysis was used to determine the purity of compounds **7** and **14**−**44** that was always >95%. Analytical results are within ±0.40% of the theoretical values. All chemicals were purchased from Sigma-Aldrich srl, Milan (Italy) or from TCI Europe NV, Zwijndrecht (Belgium), and were of the highest purity. As a rule, samples prepared for physical and biological studies were dried in high vacuum over phosphorus pentoxide for 20 h at temperatures ranging from 25 to 40 °C, depending on the sample melting point. General procedures and chemical, physical, and spectral data for the syntheses of the final compounds **7** and **14**−**44** and of all unknown compounds among intermediates **45**−**47** are described below

General Procedure for the Synthesis of 2-Benzyloxycarbonylamino-6-acylamino-hexanoic acid Compounds (2a−d and 2g). To an ice-cold solution of (*Z*)-lysine (1 equiv, 5.35−6.24 mmol, 1.50−1.75 g) in 5.35−6.24 mL of 1 M NaOH (1 equiv, 5.35−6.24 mmol) and water (8 equiv, 42.80−49.92 mmol, 42.80−49.92 mL), 1 equiv of acyl chloride (5.35−6.24 mmol, 0.57−1.19 g, 0.55−1.29 mL) in dry THF (1 equiv, 5.35−6.24 mmol, 5.35−6.24 mL) and 5.35−6.24 mL of 1 M NaOH (1 equiv, 5.35−6.24 mmol) were added dropwise. After 20−45 min, the reaction was saturated with $NaCl_{ss}$, cooled below 0 °C, and acidified to pH = 1.0 with 2 M HCl. The product was extracted with ethyl acetate (four times, 60 mL each), and the combined organic layers were extracted with 5% Na_2CO_3 (four times, 60 mL each). The bicarbonate solution was acidified with 2 M HCl to pH = 1.0 and extracted with ethyl acetate (four times, 60 mL each). The combined organic extracts were washed with $NaCl_{ss}$ and dried over Na_2SO_4 followed by evaporation of the solvent.

*2-Benzyloxycarbonylamino-6-butyrylamino-hexanoic Acid (**2a**).* The crude product was purified by flash column chromatography on SiO_2 gel with DCM−methanol (96−4%). Colorless oil; yield 5% (0.09 mmol, 31.7 mg); R_f = 0.09 (DCM−methanol 96−4%). ^{1}H NMR (400 MHz, $CDCl_3$): δ = 7.34 (s, 5H, C*H* aromatic ring), 5.82 (s, 1H, N*H* amide), 5.72 (s, 1H, N*H* amide), 5.10 (s, 2H, CH_2 benzyl), 4.38−4.33 (m, 1H, C*H*NH), 3.33−3.17 (m, 2H, CH_2NH), 2.15 (t, ^3J(H,H) = 7.5 Hz, 2H, $COCH_2$), 1.91−1.73 (m, 2H,CH_2CH), 1.61 (m, 2H, CH_2CH_3), 1.56−1.47 (m, 2H, CH_2CH_2), 1.39 (m, 2H, CH_2CH_2), 0.91 ppm (t, ^3J(H,H) = 7.4 Hz, 3H, CH_2CH_3). Mass spectrometry (MS) (ESI), *m*/*z*: 349.0 $[M - H]^-$.

*2-Benzyloxycarbonylamino-6-hexanoylamino-hexanoic Acid (**2b**).* The crude product was directly used for the next step without NMR.

*2-Benzyloxycarbonylamino-6-octanoylamino-hexanoic Acid (**2c**).* Yield 95% (5.93 mmol, 2.41 g) of crude viscous oil; R_f = 0.18 (DCM−methanol 96−4%). ^{1}H NMR (400 MHz, $CDCl_3$): δ = 7.37−7.28 (m, 5H, C*H* aromatic ring), 6.04 (s, 1H, N*H* amide), 5.67 (d,

DOI: 10.1021/acs.jmedchem.9b00638
J. Med. Chem. 2019, 62, 8733−8759

^3J(H,H) = 8.0 Hz, 1H, N*H* amide), 5.10 (s, 2H, CH_2 benzyl), 4.40–4.33 (m, 1H, C*H*NH), 3.29–3.18 (m, 2H, CH_2NH), 1.94–1.70 (m, 2H, CH_2CH), 1.65–1.58 (m, 2H, COCH_2), 1.55–1.48 (m, 2H, CH_2CH_2), 1.44–1.35 (m, 2H, CH_2CH_2), 1.30–1.24 (m, 10H, CH_2CH_2 octanoyl chain), 0.86 ppm (t, ^3J(H,H) = 6.4 Hz, 3H, CH$_2$CH_3). MS (ESI), *m*/*z*: 405.1 [M − H]$^-$.

*2-Benzyloxycarbonylamino-6-decanoylamino-hexanoic Acid (**2d**).* The crude product was purified by flash column chromatography on SiO_2 gel with DCM–methanol (methanol gradient from 1 to 10%). Colorless oil; yield 39% (2.31 mmol, 1.05 g); R_f = 0.60 (DCM–methanol 95–5%). ^{1}H NMR (400 MHz, $CDCl_3$): δ = 7.38–7.29 (m, 5H, C*H* aromatic ring), 5.85 (s, 1H, N*H* amide), 5.66 (s, 1H, N*H* amide), 5.10 (s, 2H, CH_2 benzyl), 4.40–4.36 (m, 1H, C*H*NH), 3.38–3.10 (m, 2H, CH_2NH), 2.18 (t, ^3J(H,H) = 7.6 Hz, 2H, COCH_2), 1.62–1.52 (m, 2H, CH_2CH), 1.63–1.58 (m, 2H, CH_2CH_2), 1.54–1.50 (m, 2H, CH_2CH_2), 1.47–1.35 (m, 2H, CH_2CH_2), 1.32–1.19 (m, 12H, CH_2CH_2 decanoyl chain), 0.87 ppm (t, ^3J(H,H) = 6.9 Hz, 3H, CH$_2$CH_3). MS (ESI), *m*/*z*: 433.3 [M − H]$^-$.

*2-Benzyloxycarbonylamino-6-palmitoylamino-hexanoic Acid (**2g**).* Yield 73% (4.59 mmol, 2.38 g) of crude product as colorless oil; R_f = 0.13 (DCM–acetonitrile 60–40%). ^{1}H NMR (400 MHz, $CDCl_3$): δ = 7.35–7.28 (m, 5H, C*H* aromatic ring), 5.94 (s, 1H, N*H* amide), 5.10 (s, 1H, N*H* amide), 4,54 (s, 2H, CH_2 benzyl), 4.41–4.33 (m, 1H, C*H*NH), 3.29–3.17 (m, 2H, CH_2NH), 1.92–1.70 (m, 2H, CH_2CH), 1.62–1.55 (m, 2H, COCH_2), 1.54–1.47 (m, 2H, CH_2CH_2), 1.44–1.35 (m, 2H, CH_2CH_2), 1.31–1.25 (m, 26H, CH_2CH_2 palmitoyl chain), 0.88 ppm (t, ^3J(H,H) = 6.9 Hz, 3H, CH$_2$CH_3). MS (ESI), *m*/*z*: 517.5 [M − H]$^-$.

General Procedure for the Synthesis of 2-Benzyloxycarbonylamino-6-acylamino-hexanoic Acid Compounds (2e and 2f). Myristc acid (3.50 mmol, 800 mg) or lauric acid (7.49 mmol, 1.5 g) (1 equiv) was dissolved in 1 mL of dry DCM. Then, 10 equiv of $SOCl_2$ (35.0–74.9 mmol, 4.16–8.91 g, 2.54–5.43 mL) were added. After 3 h at 90 °C, the reaction was cooled to rt and $SOCl_2$ was removed by evaporation. The crude product was then dissolved in 4 mL of DCM dry, and 1 equiv of (*Z*)-lysine (3.50–7.49 mmol, 0.981–2.01 g) was added at 0 °C with 2 equiv of 2 M NaOH (7.0–14.98 mmol, 280–599 mg, 0.26–0.55 mL). The reaction was left stirring for 20–72 h at rt. The reaction was then quenched by adding 2 N HCl to a pH of 2.0 and extracted three times with 20 mL of DCM. The combined organic phase was washed with $NaCl_{ss}$ and filtered over Na_2SO_4.

*2-Benzyloxycarbonylamino-6-lauroylamino-hexanoic Acid (**2e**).* The crude product was purified by flash chromatography on SiO_2 gel with DCM–acetonitrile (acetonitrile gradient from 1% to 40%). Yellow oil; yield 12.7% (0.95 mmol, 439 mg); R_f = 0.21 (DCM–acetonitrile 55–45%). ^{1}H NMR (400 MHz, $CDCl_3$): δ = 7.37–7.26 (m, 5H, C*H* aromatic ring), 5.81 (s, 1H, N*H* amide), 5.73 (d, ^3J(H,H) = 7.8 Hz, 1H, N*H* amide), 5.09 (s, 2H, CH_2 benzyl), 4.45–4.33 (m, 1H, C*H*NH), 3.30–3.12 (m, 2H, CH_2NH), 2.19–2.10 (m, 2H, COCH_2), 1.93–1.71 (m, 2H, CH_2CH), 1.63–1.55 (m, 2H, CH_2CH_2), 1.53–1.46 (m, 2H, CH_2CH $_2$), 1.45–1.36 (m, 2H, CH_2CH_2), 1.31–1.24 (m, 16H, CH_2CH_2 lauroyl chain), 0.88 ppm (t, ^3J(H,H) = 6.9 Hz, 3H, CH$_2$CH_3). MS (ESI$^-$): 461.2 [M − H]$^-$.

*2-Benzyloxycarbonylamino-6-myristoylamino-hexanoic Acid (**2f**).* A mixture of DCM–acetonitrile (acetonitrile gradient from 1 to 80%) was used to purify the crude product by flash chromatography on SiO_2 gel. Colorless oil; yield 13.4% (0.470 mmol, 231 mg); R_f = 0.35 (ethyl acetate–methanol 80–20%). ^{1}H NMR (400 MHz, $CDCl_3$): δ = 7.37–7.31 (m, 5H, C*H* aromatic ring), 5.91 (s, 1H, N*H* amide), 5.70 (d, ^3J(H,H) = 7.8 Hz, 1H, N*H* amide), 5.14 (s, 2H, CH_2 benzyl), 4.42–4.36 (m, 1H, C*H*NH), 3.34–3.14 (m, 2H, CH_2NH), 2.20 (t, 2H, ^3J(H,H) = 7.2 Hz, COCH_2), 1.96–1.73 (m, 2H, CH_2CH_2), 1.65–1.58 (m, 2H, CH_2CH_2), 1.56–1.51 (m, 2H, CH_2CH_2), 1.46–1.36 (m, 2H, CH_2CH_2), 1.32–1.27 (m, 20H, CH_2CH_2 myristoyl chain), 0.90 ppm (t, ^3J(H,H) = 6.9 Hz, 3H, CH$_2$CH_3). MS (ESI$^-$): 489.7 [M − H]$^-$.

General Procedure for the Synthesis of [5-Acylamino-1-(4-methyl-2-oxo-2*H*-chromen-7-ylcarbamoyl)pentyl]carbamic Acid Benzyl Esters (3a–g). **2a–g** (0.09–4.53 mmol, 0.03–1.72 g, 1 equiv) were dissolved in 52 equiv of dry pyridine (4.71–235 mmol, 0.372–18.62 g, 0.38–18.98 mL), and then 2.7 equiv of 7-amino,4-methylcoumarin (0.18–9.06 mmol, 0.03–1.60 g) was added at −15 °C. Then, 2.7 equiv (0.24–12.2 mmol, 0.04–1.90 g, 0.02–1.14 mL) of $POCl_3$ was added by a syringe, resulting in a red-orange solution. After 40 min to 3 h, the mixture was poured into a 10-fold volume of H_2O/ice and extracted with ethyl acetate (four times, 50 mL each). The combined organic layers were washed with $NaCl_{ss}$ (50 mL), 2 M HCl (50 mL), $NaCl_{ss}$ (50 mL), 5% $NaHCO_3$ (50 mL), and $NaCl_{ss}$ (30 mL). The organic phase was dried over Na_2SO_4, and the solvent was evaporated.

*[5-Butyrylamino-1-(4-methyl-2-oxo-2H-chromen-7-ylcarbamoyl)pentyl]carbamic Acid Benzyl Ester (**3a**).* The resulting product was purified by flash chromatography on SiO_2 gel with DCM–methanol 96–4%. White crystal; yield 44% (0.04 mmol, 20.1 mg); R_f = 0.22 (DCM–methanol 96–4%). ^{1}H NMR (400 MHz, $CDCl_3$): δ = 9.33 (s, 1H, N*H* amide), 7.67 (s, 1H, C*H* coumarin), 7.55 (d, ^3J(H,H) = 8.7 Hz, 1H, C*H* coumarin), 7.49 (d, ^3J(H,H) = 8.7 Hz, 1H, C*H* coumarin), 7.35 (s, 5H, C*H* benzyl), 6.18 (s, 1H, N*H* amide), 5.84 (s, 1H, N*H* amide), 5.82 (s, 1H, COC*H* coumarin), 5.13 (s, 2H, CH_2 benzyl), 4.37–4.33 (m, 1H, C*H*NH), 3.33–3.23 (m, 2H, CH_2NH), 2.41 (s, 3H, CH_3 coumarin), 2.15 (t, ^3J(H,H) = 7.5 Hz, 2H, COCH_2), 2.17–1.74 (m, 2H, CH_2CH$_2$), 1.65 (m, 2H, CH_2CH$_3$), 1.58 (quint, ^3J(H,H) = 6.1 Hz, 2H, CH_2CH$_2$), 1.46 (quint, ^3J(H,H) = 6.2 Hz, 2H, CH_2CH$_2$), 0.91 ppm (t, ^3J(H,H) = 7.4 Hz, 3H, CH$_2$CH_3). ^{13}C NMR (101 MHz, $CDCl_3$): δ = 173.8 (2C, *C*O amide), 170.9 (*C*O ester), 161.2 (*C*O carbamate), 154.0 (*C*CH$_3$ coumarin), 152.3 (*C*O coumarin), 141.5 (*C*NH coumarin), 136.0 (*C*CH$_2$ benzyl), 128.5 (2C, *C*H benzyl), 128.2 (*C*H benzyl), 128.0 (2C, *C*H benzyl), 125.0 (*C*H coumarin), 116.0 (*C*H coumarin), 115.7 (*C*CH coumarin), 113.3 (*C*H coumarin), 107.2 (*C*OCH coumarin), 67.2 (*C*H$_2$ benzyl), 55.3 (*C*HNH), 38.6 (*C*H$_2$NH), 37.9 (*C*OCH$_2$), 31.0 (*C*H$_2$CH), 28.6 (*C*H$_2$CH$_2$), 22.0 (*C*H$_2$CH$_2$), 19.0 (*C*CH$_3$), 18.5 (*C*H$_2$CH$_3$), 14.0 ppm (*C*H$_2$CH$_3$). HRMS (ESI): *m*/*z* calcd for $C_{28}H_{33}N_3O_6$ + H$^+$ [M + H]$^+$: 508.2442. Found: 508.2444. HPLC analysis: retention time = 19.496 min; peak area, 97%.

*[5-Hexanoylamino-1-(4-methyl-2-oxo-2H-chromen-7-ylcarbamoyl)pentyl]carbamic Acid Benzyl Ester (**3b**).* Purification of the resulting crude product by flash chromatography on SiO_2 gel with DCM–methanol 96–4%. Colorless powder; yield 7% (0.30 mmol, 162 mg); R_f = 0.25 (DCM–methanol 96–4%). ^{1}H NMR (400 MHz, $CDCl_3$): δ = 9.35 (s, 1H, N*H* amide), 7.68 (s, 1H, C*H* coumarin), 7.54 (d, ^3J(H,H) = 8.8 Hz, 1H, C*H* coumarin), 7.49 (d, ^3J(H,H) = 8.6 Hz, 1H, C*H* coumarin), 7.34 (s, 5H, C*H* benzyl), 6.18 (s, 1H, C*H* coumarin), 5.89 (s, 1H, COC*H*), 5.84 (d, ^3J(H,H) = 7.9 Hz, 1H, N*H* amide), 5.12 (s, 2H, CH_2 benzyl), 4.39–4.33 (m, 1H, C*H*NH), 3.36–3.19 (m, 2H, CH_2NH), 2.40 (s, 3H, CCH_3), 2.17 (t, ^3J(H,H) = 7.1 Hz, 2H, COCH_2), 2.12–1.99 (m, 2H, CH_2CH), 1.61–1.60 (m, 2H, CH_2CH$_2$), 1.60–1.57 (m, 2H, CH_2CH$_2$), 1.50–1.43 (m, 2H, CH_2CH$_2$), 1.34–1.21 (m, 4H, CH_2CH$_2$ and CH_2CH$_3$), 0.87 ppm (t, ^3J(H,H) = 6.9 Hz, 3H, CH$_2$CH_3). ^{13}C NMR (101 MHz, $CDCl_3$): δ = 174.1 (2C, *C*O amide), 171.1 (*C*O ester), 161.2 (*C*O carbamate), 154.0 (*C*CH$_3$ coumarin), 152.5 (*C*O coumarin), 141.5 (*C*NH coumarin), 136.0 (*C*CH$_2$ benzyl), 128.5 (2C, *C*H benzyl), 128.2 (*C*H benzyl), 127.9 (2C, *C*H benzyl), 125.0 (*C*H coumarin), 115.9 (*C*H coumarin), 115.8 (*C*CH coumarin), 113.2 (*C*H coumarin), 107.2 (*C*OCH coumarin), 67.1 (*C*H$_2$ benzyl), 55.3 (*C*HNH), 38.3 (*C*H$_2$NH), 36.6 (*C*OCH$_2$), 31.3 (2C, *C*H$_2$CH$_2$), 28.6 (*C*H$_2$CH$_2$), 25.4 (2C, *C*H$_2$CH$_2$), 22.3 (*C*H$_2$CH$_3$), 18.5 (*C*CH$_3$), 13.9 ppm (*C*H$_2$CH$_3$). HRMS (ESI): *m*/*z* calcd for $C_{30}H_{37}N_3O_6$ + H$^+$ [M + H]$^+$: 536.2755. Found: 536.2751. HPLC analysis: retention time = 22.108 min; peak area, 98%.

*[5-Octanoylamino-1-(4-methyl-2-oxo-2H-chromen-7-ylcarbamoyl)pentyl]carbamic Acid Benzyl Ester (**3c**).* Purification by flash chromatography on SiO_2 gel with DCM–methanol 96–4%. White crystal; yield 10% (0.39 mmol, 218 mg); R_f = 0.28 (DCM–methanol 96–4%). ^{1}H NMR (400 MHz, $CDCl_3$) δ = 9.41 (s, 1H, N*H* amide), 7.70 (s, 1H, C*H* coumarin), 7.54 (d, ^3J(H,H) = 8.3 Hz, 1H, C*H* coumarin), 7.49 (d, ^3J(H,H) = 8.3 Hz, 1H, C*H* cumarin), 7.34 (s,

DOI: 10.1021/acs.jmedchem.9b00638
J. Med. Chem. 2019, 62, 8733–8759

5H, C*H* benzyl), 6.18 (s, 1H, N*H* amide), 6.14 (s, 1H, COC*H* coumarin), 5.87 (s, 1H, N*H* amide), 5.12 (s, 2H, CH_2 benzyl), 4.41−4.33 (m, 1H, C*H*NH), 3.34−3.23 (m, 2H, CH_2NH), 2.40 (s, 3H, CCH_3), 2.20 (t, ^3J(H,H) = 7.1 Hz, 2H, COCH_2), 2.08−1.73 (m, 4H, CH_2CH$_2$ and CH_2CH), 1.60 (m, 2H, CH_2CH$_2$), 1.47 (quint, ^3J(H,H) = 7.2 Hz, 2H, CH_2CH$_2$), 1.25 (s, 8H, CH_2CH$_2$ octanoyl chain), 0.85 ppm (t, ^3J(H,H) = 6.8 Hz, 3H, CH$_2$CH_3). ^{13}C NMR (101 MHz, $CDCl_3$): δ = 174.2 (2C, *C*O amide), 171.2 (*C*O ester), 161.2 (*C*CH coumarin), 154.0 (*C*O coumarin), 152.5 (*C*CH$_3$ coumarin), 141.5 (*C*NH coumarin), 136.0 (*C*O carbamate), 128.5 (2C, *C*H benzyl), 128.2 (*C*H benzyl), 128.0 (2C, *C*H benzyl), 125.0 (*C*H coumarin), 115.9 (*C*H coumarin), 115.8 (*C*CH coumarin), 113.1 (*C*H coumarin), 107.1 (*C*OCH coumarin), 67.1 (*C*H$_2$ benzyl), 55.3 (*C*HNH), 38.3 (*C*H$_2$NH), 36.5 (*C*OCH$_2$), 31.6 (*C*H$_2$CH$_2$), 31.4 (*C*H$_2$CH$_2$), 29.2 (*C*H$_2$CH), 28.9 (*C*H$_2$CH$_2$), 28.6 (*C*H$_2$CH$_2$), 25.8 (*C*H$_2$CH$_2$), 22.5 (*C*H$_2$CH$_2$), 22.3 (*C*H$_2$CH$_3$), 18.5 (*C*CH$_3$), 14.0 ppm (CH$_2$*C*H$_3$). HRMS (ESI): *m*/*z* calcd for $C_{32}H_{41}N_3O_6$ + Na^+ [M + Na]$^+$: 563.2888. Found: 586.2885. HPLC analysis: retention time = 24.323 min; peak area, 99%.

*[5-Decanoylamino-1-(4-methyl-2-oxo-2H-chromen-7-ylcarbamoyl)pentyl]carbamic Acid Benzyl Ester (**3d**).* The crude product was purified by column chromatography on SiO_2 gel with DCM−methanol 96−4%. White powder; yield 5% (0.12 mmol, 69.40 mg); R_f = 0.33 (DCM−methanol 96−4%). ^{1}H NMR (400 MHz, $CDCl_3$): δ = 9.36 (s, 1H, N*H* amide), 7.69 (s, 1H, C*H* coumarin), 7.53 (d, ^3J(H,H) = 8.8 Hz, 1H, C*H* coumarin), 7.49 (d, ^3J(H,H) = 8.6 Hz, 1H, C*H* coumarin), 7.34 (s, 5H, C*H* benzyl), 6.18 (s, 1H, N*H* amide), 5.93 (s, 1H, COC*H* coumarin), 5.85 (s, 1H, N*H* amide), 5.13 (s, 2H, CH_2 benzyl), 4.38−4.34 (m, 1H, C*H*NH), 3.33−3.23 (m, 2H, CH_2NH), 2.40 (s, 3H, CCH_3), 2.18 (t, ^3J(H,H) = 7.7 Hz, 2H, COCH_2), 2.07−1.87 (m, 2H, CH_2CH), 1.81−1.72 (m, 2H, CH_2CH$_2$), 1.60 (quint, ^3J(H,H) = 7.2 Hz, 2H, CH_2CH$_2$), 1.47 (quint, ^3J(H,H) = 7.2 Hz, 2H, CH_2CH$_2$), 1.23 (s, 12H, CH_2CH$_2$ deacanoyl chain), 0.86 ppm (t, ^3J(H,H) = 6.9 Hz, 3H, CH$_2$CH_3). ^{13}C NMR (101 MHz, $CDCl_3$): δ = 207.1 (2C, *C*O amide), 174.1 (*C*O ester), 161.2 (*C*O carbamate), 154.0 (*C*CH$_3$ coumarin), 152.5 (*C*OCH coumarin), 141.5 (*C*NH coumarin), 136.0 (*C*CH$_2$ benzyl), 128.5 (2C, *C*H benzyl), 128.2 (*C*H benzyl), 128.0 (2C, *C*H benzyl), 125.0 (*C*H coumarin), 115.9 (*C*H coumarin), 115.8 (*C*CH coumarin), 113.2 (*C*H coumarin), 107.2 (*C*H coumarin), 67.1 (*C*H$_2$ benzyl), 55.3 (*C*HNH), 38.3 (*C*H$_2$NH), 36.7 (*C*OCH$_2$), 31.8 (*C*H$_2$CH$_2$), 30.9 (*C*H$_2$CH$_2$), 29.4 (*C*H$_2$CH), 29.3 (*C*H$_2$CH$_2$), 29.2 (*C*H$_2$CH$_2$), 29.2 (*C*H$_2$CH$_2$), 28.7 (*C*H$_2$CH$_2$), 25.7 (*C*H$_2$CH$_2$), 22.6 (*C*H$_2$CH$_2$), 22.3 (*C*H$_2$CH$_3$), 18.5 (*C*CH$_3$), 14.1 ppm (CH$_2$*C*H$_3$). HRMS (ESI): *m*/*z* calcd for $C_{34}H_{45}N_3O_6$ + Na^+ [M + Na]$^+$: 591.3201. Found: 614.3201. HPLC analysis: retention time = 26.061 min; peak area, 99%.

*[5-Lauroylamino-1-(4-methyl-2-oxo-2H-chromen-7-ylcarbamoyl)pentyl]carbamic Acid Benzyl Ester (**3e**).* Purification of crude product by flash column chromatography DCM−methanol (methanol gradient from 1 to 8%). White powder; yield 4% (0.04 mmol, 25 mg); R_f = 0.30 (DCM−methanol 96−4%). ^{1}H NMR (400 MHz, $CDCl_3$): δ = 9.29 (s, 1H, N*H* amide), 7.69 (s, 1H, C*H* coumarin), 7.54 (s, 1H, C*H* coumarin), 7.50 (s, 1H, C*H* coumarin), 7.35 (s, 5H, C*H* benzyl), 6.19 (s, 1H, N*H* amide), 5.80 (s, 2H, COC*H* coumarin and N*H* amide), 5.13 (s, 2H, CH_2 benzyl), 4.32−4.28 (m, 1H, C*H*NH), 3.40−3.17 (m, 2H, CH$_2$NH), 2.41 (s, 3H, CCH_3), 2.23−1.98 (m, 2H, CH_2CH), 1.79−1.70 (m, 4H, COCH_2 and CH_2CH$_2$), 1.61 (m, 4H, CH_2CH$_2$), 1.54−1.38 (m, 2H, CH_2CH$_2$), 1.24 (s, 14H, CH_2CH$_2$ lauroyl chain), 0.87 ppm (t, ^3J(H,H) = 6.8 Hz, 3H, CH$_2$CH_3). ^{13}C NMR (101 MHz, $CDCl_3$): δ = 171.3 (*C*O amide), 170.9 (*C*O amide), 161.2 (*C*O ester), 154.1 (*C*O carbamate), 152.3 (*C*NH coumarin), 141.4 (*C*O coumarin), 136.0 (*C*CH$_3$ coumarin), 128.5 (2C, *C*H benzyl), 128.2 (*C*H benzyl), 128.0 (2C, *C*H benzyl), 125.2 (*C*H coumarin), 125.1 (*C*CH coumarin), 120.6 (*C*CH$_2$ benzyl), 116.0 (*C*H coumarin), 113.3 (*C*H coumarin), 107.2 (*C*OCH coumarin), 70.04 (*C*H$_2$ benzyl), 67.3 (*C*HNH), 38.4 (*C*H$_2$NH), 37.3 (*C*OCH$_2$), 31.9 (*C*H$_2$CH$_2$), 31.4 (*C*H$_2$CH$_2$), 29.6 (*C*H$_2$CH$_2$), 29.5 (2C, *C*H$_2$CH$_2$), 29.4 (*C*H$_2$CH$_2$), 29.3 (*C*H$_2$CH$_2$), 28.8 (*C*H$_2$CH$_2$), 25.9 (*C*H$_2$CH$_2$), 22.6 (*C*H$_2$CH$_2$), 22.4 (*C*H$_2$CH$_3$), 18.6 (*C*H$_2$CH$_3$), 14.8 (*C*CH$_3$), 14.1 ppm (CH$_2$*C*H$_3$). HRMS (ESI): *m*/*z* calcd for $C_{36}H_{49}N_3O_6$ + Na^+ [M + Na]$^+$: 642.3514. Found: 642.3510. HPLC analysis: retention time = 25.175 min; peak area, 97%.

*[5-Myristoylamino-1-(4-methyl-2-oxo-2H-chromen-7-ylcarbamoyl)pentyl]carbamic Acid Benzyl Ester (**3f**).* Purification of crude product by flash column chromatography DCM−methanol (methanol gradient from 1 to 10%). White powder; yield 11% (0.05 mmol, 34 mg), R_f = 0.32 (DCM−methanol 96−4%). ^{1}H NMR (400 MHz, $CDCl_3$): δ = 9.56 (s, 1H, N*H* amide), 7.75 (s, 1H, C*H* coumarin), 7.57 (d, ^3J(H,H) = 8.3 Hz, 1H, C*H* coumarin), 7.50 (d, ^3J(H,H) = 8.6 Hz, 1H, C*H* coumarin), 7.35 (s, 5H, C*H* benzyl), 6.89 (s, 1H, N*H* amide), 6.20 (s, 1H, COC*H*), 6.01 (s, 1H, N*H* amide), 5.12 (s, 2H, CH_2 benzyl), 4.45−4.37 (m, 1H, C*H*NH), 3.41−3.24 (m, 2H, CH_2NH), 2.4 (s, 3H, CCH_3), 2.30 (t, ^3J(H,H) = 7.3 Hz, 2H, COCH_2), 2.12−1.64 (m, 2H, CH_2CH), 1.67−1.64 (m, 2H, CH_2CH$_2$), 1.62−1.58 (m, 2H, CH_2CH$_2$), 1.54−1.47 (m, 2H, CH_2CH$_2$), 1.33−1.23 (m, 20H, CH_2CH$_2$ myristoyl chain), 0.89 ppm (t, ^3J(H,H) = 6.9 Hz, 3H, CH$_2$CH_3). ^{13}C NMR (101 MHz, $(CD_3)_2SO$): δ = 172.4 (*C*O amide), 160.5 (*C*O amide), 156.6 (*C*O ester), 154.1 (*C*O carbamate), 153.6 (*C*CH$_3$ coumarin), 142.7 (*C*OCH coumarin), 128.8 (*C*NH coumarin), 128.3 (*C*CH$_2$ benzyl), 128.2 (2C, *C*H benzyl), 126.4 (*C*H benzyl), 115.7 (2C, *C*H benzyl), 115.5 (*C*H coumarin), 112.8 (*C*H coumarin), 106.1 (*C*CH coumarin), 65.9 (*C*H coumarin), 56.0 (*C*OCH coumarin), 38.5 (*C*H$_2$ benzyl), 35.9 (*C*HNH), 31.8 (*C*H$_2$NH), 29.5 (*C*OCH$_2$), 29.5 (*C*H$_2$CH), 29.4 (2C, *C*H$_2$CH$_2$), 29.3 (2C, *C*H$_2$CH$_2$), 29.2 (2C, *C*H$_2$CH$_2$), 29.2 (2C, *C*H$_2$CH$_2$), 29.1 (2C, *C*H$_2$CH$_2$), 25.8 (*C*H$_2$CH$_2$), 23.4 (*C*H$_2$CH$_2$), 22.6 (*C*H$_2$CH$_3$), 18.4 (*C*CH$_3$ coumarin), 14.4 ppm (CH$_2$*C*H$_3$). MS (ESI), *m*/*z*: 646.7 [M − H]$^-$. HPLC analysis: retention time = 30.424 min; peak area, 95%.

*[5-Palmitoylamino-1-(4-methyl-2-oxo-2H-chromen-7-ylcarbamoyl)pentyl]carbamic Acid Benzyl Ester (**3g**).* Purification of crude product by flash column chromatography DCM−methanol (methanol gradient from 1 to 8%). White powder; yield 10% (0.29 mmol, 200 mg); R_f = 0.60 (DCM−methanol 96−4%). ^{1}H NMR (400 MHz, $CDCl_3$): δ = 9.30 (s, 1H, N*H* amide), 7.68 (s, 1H, C*H* coumarin), 7.54 (d, ^3J(H,H) = 8.8 Hz, 1H, C*H* coumarin), 7.49 (d, ^3J = 8.6 Hz, 1H, C*H* coumarin), 7.35 (s, 5H, C*H* benzyl), 6.19 (s, 1H, N*H* amide), 5.79 (d, ^3J(H,H) = 8.8 Hz, 1H, N*H* amide), 5.75 (s, 1H, COC*H*), 5.13 (s, 2H, CH_2 benzyl), 4.38−4.30 (m, 1H, C*H*NH), 3.37−3.19 (m, 2H, CH_2NH), 2.41 (s, 3H, CCH_3), 2.16 (t, ^3J(H,H) = 7.1 Hz, 2H, COCH_2), 2.08−1.72 (m, 2H, CH_2CH$_2$), 1.64−1.60 (m, 2H, CH_2CH), 1.59−1.55 (m, 2H, CH_2CH$_2$), 1.50−1.42 (m, 2H, CH_2CH$_2$), 1.31−1.19 (m, 24H, CH_2CH$_2$ palmitoyl chain), 0.88 ppm (t, ^3J(H,H) = 6.9 Hz, 3H, CH$_2$CH_3). ^{13}C NMR (101 MHz, $CDCl_3$): δ = 174.0 (*C*O amide), 174.0 (*C*O amide), 171.0 (*C*O ester), 161.2 (*C*O carbamate), 154.0 (*C*CH$_3$ coumarin), 152.3 (*C*OCH coumarin), 141.5 (*C*NH coumarin), 136.0 (*C*CH$_2$ benzyl), 128.5 (2C, *C*H benzyl), 128.2 (*C*H benzyl), 127.9 (2C, *C*H benzyl), 125.0 (*C*H coumarin), 115.9 (*C*H coumarin), 115.7 (*C*CH coumarin), 113.2 (*C*H coumarin), 107.2 (*C*OCH), 67.2 (*C*H$_2$ benzyl), 65.8 (*C*HNH), 38.1 (*C*OCH$_2$), 36.7 (*C*H$_2$CH$_2$), 31.9 (*C*H$_2$CH$_2$), 31.2 (*C*H$_2$CH), 29.6 (2C, *C*H$_2$CH$_2$), 29.6 (2C, *C*H$_2$CH$_2$), 29.6 (*C*H$_2$CH$_2$), 29.5 (2C, *C*H$_2$CH$_2$), 29.3 (*C*H$_2$CH$_2$), 29.2 (*C*H$_2$CH$_2$), 28.6 (*C*H$_2$CH$_2$), 25.7 (*C*H$_2$CH$_2$), 22.6 (*C*H$_2$CH$_2$), 22.1 (*C*H$_2$CH$_2$), 18.5 (*C*H$_2$CH$_3$), 15.2 (*C*CH$_3$ coumarin), 14.1 ppm (CH$_2$*C*H$_3$). MS (ESI), *m*/*z*: 674.9 [M − H]$^-$. HPLC analysis: retention time = 26.635 min; peak area, 98%.

*Synthesis of N-(4-(5-((1-(3-Fluoro-2-methylbenzyl)piperidin-3-yl)methyl)-1,2,4-oxadiazol-3-yl)phenyl)acetamide (**6**).* Compound **8** (0.51 mmol, 150 mg, 1 equiv), **10a** (0.51 mmol, 98.8 mg, 1 equiv), and K_2CO_3 (1.89 mmol, 261.3 mg, 3.7 equiv) were mixed in 5.00 mL of pyridine and refluxed for 8 h. The reaction mixture was left for 72 h at rt and diluted with 15 mL of ethyl acetate; washed with H_2O (two times, 10 mL each), and $NaCl_{ss}$ (10 mL); and dried over Na_2SO_4. The solvent was evaporated, and the crude product purified by flash column chromatography on SiO_2 gel with DCM−methanol (98−2%). Yellow oil; yield 5% (0.03 mmol, 12 mg); R_f = 0.28 (DCM−methanol 95−5%). ^{1}H NMR (400 MHz, DMSO-d_6, 50 °C): δ = 10.12 (s, 1H, N*H* anilide), 7.88 (d, ^3J(H,H) = 8.8 Hz, 2H, C*H* anilide), 7.75 (d,

DOI: 10.1021/acs.jmedchem.9b00638
J. Med. Chem. 2019, 62, 8733−8759

^3J(H,H) = 8.8 Hz, 2H, C*H* anilide), 7.15−6.97 (m, 3H, C*H* benzyl), 3.44 (s, 2H, CH_2 benzyl), 3.00−2.92 (m, 2H, CHCH_2), 2.77−2.74 (m, 1H, C*H* piperidine), 2.63−2.56 (m, 1H, C*H* piperidine), 2.23 (s, 3H, CCH_3 benzyl), 2.15−2.13 (m, 1H, C*H* piperidine), 2.12−2.11 (m, 1H, C*H* piperidine), 2.09 (s, 3H, CH_3 amide), 2.00−1.92 (m, 1H, C*H* piperidine), 1.76−1.68 (m, 1H, C*H* piperidine), 1.67−1.61 (m, 1H, C*H* piperidine), 1.53−1.42 (m, 1H, C*H* piperidine), 1.21−1.11 ppm (m, 1H, C*H* piperidine). ^{13}C NMR (101 MHz, $(CD_3)_2SO$, 50 °C): δ = 179.4 (*C*ONH amide), 169.1 (*C*N oxadiazole), 167.6 (*C*O oxadiazole), 141.2 (d, ^1J(C,F) = 264.1 Hz, *C*F), 128.1 (*C*H anilide), 126.7 (*C*H benzyl), 125.8 (*C*H benzyl), 124.3 (2C, *C*CH anilide and *C*CH$_2$ benzyl), 124.1 (*C*NH anilide), 121.0 (*C*CH$_3$ benzyl), 120.6 (*C*CH anilide), 119.5 (2C, *C*H anilide), 113.7 (*C*H benzyl), 60.5 (NCH$_2$ benzyl), 58.7 (NCH$_2$ piperidine), 53.8 (NCH$_2$ piperidine), 34.50 (CH$_2$CH piperidine), 34.47 (CHCH$_2$ piperidine) 30.3 (CO*C*H$_3$), 30.1 (*C*H$_2$CH piperidine), 24.5 (*C*H$_2$CH$_2$ piperidine), 10.3 ppm (*C*CH$_3$ benzyl). ^{19}F (376 MHz, $(CD_3)_2SO$, 50 °C): δ = −117.73 ppm (s, *C*F). HRMS (ESI): *m*/*z* calcd for $C_{24}H_{27}FN_4O_2$ + H^+ [M + H]$^+$: 423.2191. Found: 423.2195. HPLC analysis: retention time = 16.559 min; peak area, 99%.

*Synthesis of N^7-(1-(4-(4-Methoxyphenoxy)phenyl)ethyl)-N^7-methylpyrimido[4,5-d]pyrimidine-2,4,7-triamine (**7**).* The substituted 4-aminopyrimidin-5-carbonitrile **47e′** (310 mg, 0.83 mmol) was stirred with 0.73 M free base guanidine solution in dry 2-methoxyethanol (3.5 equiv, 2.90 mmol, 3.97 mL) at 150 °C. After the completion of the reaction, the mixture was concentrated, quenched with water, and extracted with ethyl acetate. The organic phase was dried over anhydrous sodium sulfate, filtered, and evaporated giving a crude product purified by silica gel column chromatography eluting with a mixture of chloroform/methanol/ammonia (20/1/0.1, v/v/v) and then triturated with a mixture of petroleum ether/diethyl ether, which resulted in a white powder. It was then recrystallized from acetonitrile. Yield: 60.0%. mp: 181−184 °C. ^{1}H NMR (400 MHz, DMSO-d_6) δ ppm: 1.50−1.52 (d, 3H, CHCH_3), 2.82 (br s, 3H, NCH_3), 3.74 (s, 3H, OCH_3), 6.28 (br s, 1H, C*H*CH$_3$), 6.49 (br s, 2H, C$_2$−NH_2), 6.87−6.90 (d, 2H, C*H* benzene ring), 6.94−7.00 (m, 4H, C*H* benzene rings), 7.25−7.27 (d, 2H, C*H* benzene rings), 7.41 (br s, 2H, C$_4$−NH_2), 8.95 (s, 1H, C*H* pyrimidine ring). ^{13}C NMR (100 MHz, DMSO) δ 16.8, 29.2, 51.3, 55.9, 96.4, 115.5 (2C), 117.6 (2C), 121.1 (2C), 128.8 (2C), 136.3, 149.9, 156.0, 156.7, 157.3, 163.3, 163.4, 165.9, 166.0. MS (ESI), *m*/*z*: 418 [M + H]$^+$. Elemental anal. calcd (%) for $C_{22}H_{23}N_7O_2$: C 63.30, H 5.55, N 23.49. Found: C 63.38, H 5.57, N 23.41.

*Synthesis of Ethyl 2-(1-(3-fluoro-2-methylbenzyl)piperidin-3-yl)acetate (**8**).* 2-(Piperidin-3-yl) acetic acid ethyl ester (1 equiv, 5.84 mmol, 1 g) was dissolved in 2.5 mL of toluene, followed by the addition of 2.4 equiv of triethylamine (11.7 mmol, 1.62 mL) and 1 equiv of 3-fluoro-2-methylbenzyl bromide (5.84 mmol, 1.18 g) at 0 °C. After 10 min, the mixture was warmed up to room temperature. After 18 h, the precipitate was removed by filtration, washed with cyclohexane, and the filtrate was concentrated. The crude product was dried using a vacuum pump for 2−5 h and then purified by flash column chromatography on SiO_2 gel with DCM−methanol (99−1%). Colorless oil; yield 85−90% (2.45−2.89 mmol, 723−767 mg); R_f = 0.67 (DCM−methanol 95−5%). ^{1}H NMR (400 MHz, $CDCl_3$): δ = 7.10−7.0 (m, 2H, C*H* benzyl), 6.94−6.89 (m, 1H, C*H* benzyl), 4.15−4.03 (m, 2H, CH_2CH$_3$), 3.41 (s, 2H, CH_2 benzyl), 2.75−2.59 (m, 2H, CH_2COO), 2.25 (s, 3H, CH_3 benzyl), 2.24−2.22 (m, 1H, C*H* piperidine), 2.20−2.16 (m, 1H, C*H* piperidine), 2.13−1.99 (m, 1H, C*H* piperidine), 1.89−1.80 (m, 1H, C*H* piperidine), 1.76−1.74 (m, 1H, C*H* piperidine), 1.67−1.59 (m, 1H, C*H* piperidine), 1.59−1.50 (m, 2H, C*H* piperidine), 1.21 (t, ^3J(H,H) = 7.1 Hz, 3H, CH$_2$CH_3), 1.09−1.00 ppm (m, 1H, C*H* piperidine). MS (ESI), *m*/*z*: 294.32 [M + H]$^+$.

General Procedure for the Synthesis of *N*-(4-Cyanophenyl)-acylamide (9b and 9c). 4-Aminobenzonitrile (4.23 mmol, 500 mg, 1 equiv) was dissolved in 15 mL of dry DCM at 0 °C under nitrogen atmosphere, followed by addition of 7 equiv of triethylamine and 4 equiv of acyl chloride. After 2 h at rt, the reaction was quenched with water and extracted (three times, 15 mL of water each). Then, the organic phase was washed with 2 M HCl (once, 15 mL), $NaCl_{ss}$ (once, 15 mL), 5% Na_2CO_3 (once, 15 mL), $NaCl_{ss}$ (once, 15 mL), and dried over Na_2SO_4. The solvent was evaporated to dryness, and the crude product was purified by flash column chromatography on SiO_2 gel with DCM−methanol (98−2%).

*N-(4-Cyanophenyl)octanamide (**9b**).* White solid; yield 62−65% (2.60−2.73 mmol, 635−666 mg); R_f = 0.47 (DCM−methanol 98−2%). ^{1}H NMR (400 MHz, $CDCl_3$): δ = 7.67 (d, ^3J(H,H) = 8.8 Hz, 2H, C*H* aromatic ring), 7.61 (d, ^3J(H,H) = 8.8 Hz, 2H, C*H* aromatic ring), 7.38 (s, 1H, N*H* amide), 2.39 (t, ^3J(H,H) = 7.2 Hz, 2H, COCH_2), 1.73 (quint, ^3J(H,H) = 7.2 Hz, 2H, CH_2CH$_2$), 1.42−1.23 (m, 8H, CH_2CH$_2$), 0.88 ppm (t, ^3J(H,H) = 7.0 Hz, 3H, CH$_2$CH_3). MS (ESI), *m*/*z*: 243.3 [M − H]$^-$.

*N-(4-cyanophenyl)decanamide (**9c**).* Yellow solid; yield 71% (5.98 mmol, 1.63 g); R_f = 0.63 (DCM−methanol 99−1%). ^{1}H NMR (400 MHz, $CDCl_3$): δ = 7.67 (d, ^3J(H,H) = 8.9 Hz, 2H, C*H* aromatic ring), 7.61 (d, ^3J(H,H) = 8.9 Hz, 2H, C*H* aromatic ring), 7.35 (s, 1H, N*H* amide), 2.39 (t, ^3J(H,H)= 7.6 Hz, 2H, COCH_2), 1.73 (quint, ^3J(H,H) = 7.6 Hz, 2H, CH_2CH$_2$), 1.39−1.27 (m, 12H, CH_2CH$_2$), 0.88 ppm (t, ^3J(H,H) = 6.9 Hz, 3H, CH$_2$CH_3). MS (ESI), *m*/*z*: 271.4 [M − H]$^-$.

General Procedure for the Synthesis of (*Z*)-*N*-(4-(*N′*-Hydroxycarbamimidoyl)-phenyl)acylamide (10a−c). *N*-(4-Cyanophenyl)acylamide (3.74−5.98 mmol, 0.60−1.63 g, 1 equiv), NH_2OH·HCl (13.84−22.14 mmol, 0.96−1.50 g, 3.7 equiv), and Na_2CO_3 (6.36−10.17 mmol, 0.67−1.07 g, 1.7 equiv) were dissolved in a mixture of water and EtOH. After stirring for 6−8 h at reflux, the reaction was cooled on ice and a yellow-orange precipitate was formed. The precipitate was collected by filtration and dried under vacuum.

*N-(4-(N′-Hydroxycarbamimidoyl)phenyl)acetamide (**10a**).* The reaction was performed in a mixture of 5 mL of ethanol and 20 mL of water. **3a** was obtained as white crystal; yield 86% (4.03 mmol, 778 mg); R_f = 0.83 (DCM−methanol 80−20%). ^{1}H NMR (400 MHz, DMSO-d_6): δ = 10.04 (s, 1H, N*H* amide), 9.53 (s, 1H, NO*H*), 7.60 (d, ^3J(H,H) = 9.1 Hz, 2H, C*H* aromatic ring), 7.56 (d, ^3J(H,H) = 9.1 Hz, 2H, C*H* aromatic ring), 5.76 (s, 2H, CNH_2), 2.05 ppm (s, 3H, COCH_3). MS (ESI), *m*/*z*: 194.2 [M + H]$^+$.

*(Z)-N-(4-(N′-Hydroxycarbamimidoyl)phenyl)octanamide (**10b**).* A mixture of 15 mL of water and 45 mL of ethanol was used for the reaction. **3b** is a white crystal; yield 77% (4.04 mmol, 1.12 g); R_f = 0.07 (DCM−methanol 95−5%). ^{1}H NMR (400 MHz, DMSO-d_6): δ = 10.01 (s, 1H, N*H* amide), 9.54 (s, 1H, NO*H*), 7.86−7.23 (m, 4H, C*H* aromatic ring), 5.78 (s, 2H, CNH_2), 2.31 (t, ^3J(H,H) = 7.4 Hz, 2H, COCH_2), 1.65−1.52 (m, 2H, CH_2CH$_2$), 1.36−1.20 (m, 8H, CH_2CH$_2$), 0.86 ppm (t, ^3J(H,H) = 6.5 Hz, 3H, CH$_2$CH_3). MS (ESI), *m*/*z*: 278.2 [M + H]$^+$.

*(Z)-N-(4-(N′-Hydroxycarbamimidoyl)phenyl)decanamide (**10c**).* Water (20 mL) and ethanol (45 mL) were used in this case as reaction solvent. **3c** is a white crystal; yield 87% (5.17 mmol, 1.58 g); R_f = 0.07 (DCM−methanol 98−2%). ^{1}H NMR (400 MHz, DMSO-d_6): δ = 9.95 (s, 1H, N*H* amide), 9.52 (s, 1H, NO*H*), 7.85−7.26 (m, 4H, C*H* aromatic ring), 5.74 (s, 2H, CNH_2), 2.30 (t, ^3J(H,H) = 7.4 Hz, 2H, COCH_2), 1.62−1.55 (quint, ^3J(H,H) = 7.3 Hz, 2H, CH_2CH$_2$), 1.33−1.19 (m, 12H, CH_2CH$_2$), 0.86 ppm (t, ^3J(H,H) = 7.1 Hz, 3H, CH$_2$CH_3). MS (ESI), *m*/*z*: 306.4 [M + H]$^+$.

*Synthesis of N-(4-(5-((1-(3-Fluoro-2-methylbenzyl)piperidin-3-yl)methyl)-1,2,4-oxadiazol-3-yl)phenyl)octanamide (**11**).* Compound **8** (0.82 mmol, 240 mg, 1 equiv), **10b** (1.64 mmol, 453.5 mg, 2 equiv), and K_2CO_3 (3.27 mmol, 452 mg, 4 equiv) in 9 mL of pyridine were mixed, and the reaction was performed with microwaves (10 min, 180 °C, 300 W). Then, the mixture was refluxed at 160 °C for 43 h and stirred at rt for 12 h. After that, the pyridine was removed and the reaction mixture was dissolved in 40 mL of ethyl acetate, extracted with water (three times, 15 mL each), washed with $NaCl_{ss}$ (once, 15 mL), and dried over Na_2SO_4. The solvent was evaporated and the crude product was purified by flash column chromatography on SiO_2 gel with DCM−methanol (98−2%) and with DCM−methanol (95−5%) obtaining **11** as colorless oil. Yield 28.9% (0.02 mmol, 12 mg); R_f = 0.36 (DCM−methanol 95−

DOI: 10.1021/acs.jmedchem.9b00638
J. Med. Chem. 2019, 62, 8733−8759

5%). ^{1}H NMR (400 MHz, CD_3OD, 50 °C): δ = 10.06 (s, 1H, N*H* anilide), 7.93 (d, ^3J(H,H) = 8.6 Hz, 2H, C*H* anilide), 7.75 (d, ^3J(H,H) = 8.6 Hz, 2H, C*H* anilide), 7.24−6.97 (m, 3H, C*H* benzyl), 3.80−3.64 (m, 2H, CH_2CH), 3.13−3.02 (m, 1H, C*H* piperidine), 3.00−2.97 (m, 1H, C*H* piperidine), 2.95−2.92 (m, 1H, C*H* piperidine), 2.44−2.42 (m, 2H, $COCH_2$), 2.40−2.37 (m, 1H, C*H* piperidine), 2.30 (s, 3H, CCH_3 benzyl), 2.29−2.22 (m, 1H, C*H* piperidine), 2.18 (s, 2H, CH_2 benzyl), 1.89−1.84 (m, 1H, C*H* piperidine), 1.82−1.79 (m, 1H, C*H* piperidine), 1.78−1.76 (m, 2H, CH_2CH_2), 1.73−1.68 (m, 2H, CH_2CH_2), 1.67−1.60 (m, 1H, C*H* piperidine), 1.40−1.19 (m, 7H, C*H* piperidine and CH_2CH_2 octanoyl chain), 0.92 ppm (t, ^3J(H,H) = 6.4 Hz, 3H, CH_2CH_3). ^{13}C NMR (400 MHz, CD_3OD, 50 °C): δ = 178.7 (CONH amide), 173.6 (CN oxadiazole), 167.6 (CO oxadiazole), 141.5 (C*N*H anilide), 127.6 (2C, *C*H anilide), 126.3 (*C*H benzyl), 126.2 (2C, *C*CH anilide and CCH_2 benzyl), 126.0 (*C*H benzyl), 120.6 (d, ^1J(C−F) = 212.6 Hz, *C*F), 119.5 (2C, *C*H anilide), 114.2 (CCH_3 benzyl), 113.9 (*C*H benzyl), 100.0 (CH_2 benzyl), 59.5 (CH_2CH), 57.7 (NCH_2 piperidine), 53.5 (NCH_2 piperidine), 36.7 ($COCH_2$), 31.5 (CH_2CH_2), 29.9 ($CHCH_2$), 29.1 (CH_2CH piperidine), 28.9 (CH_2CH_2), 28.8 (CH_2CH_2), 25.4 (CH_2CH_2), 23.6 (CH_2CH_2 piperidine), 22.3 (CH_2CH_3), 13.0 (CH_2CH_3), 9.3 ppm (CCH_3). ^{19}F (376 MHz, $CDCl_3$, 50 °C): δ = −117.40 ppm (s, C*F*). HRMS (ESI): *m*/*z* calcd for $C_{30}H_{39}FN_4O_2$ + H^+ [M + H]$^+$: 507.3130. Found: 507.3129. HPLC analysis: retention time = 22.798 min; peak area, 96%.

*Synthesis of N-(4-(5-((1-(3-Fluoro-2-methylbenzyl)piperidin-3-yl)methyl)-1,2,4-oxadiazol-3-yl)phenyl)decanamide (**12**).* Compound **8** (3.41 mmol, 1 g, 1 equiv) was dissolved in 23 mL of ethanol, followed by dropwise addition of 4 equiv (13.63 mmol, 13.6 mL) of 1 M LiOH solution. The reaction mixture was stirred for 20 h at rt (TLC-control), acidified with 2 M HCl solution with consequent removal of water by evaporation. Under N_2 atmosphere, the previously formed carboxylic acid was dissolved in 200 μL of *N*,*N*-dimethylformamide and 2.5 mL of dry DCM. $SOCl_2$ (9.31 mmol, 1.1 g, 5 equiv) was added dropwise at −15 °C. The reaction mixture was stirred for 3 h (TLC-control) and then $SOCl_2$ was removed by a stream of N_2. Compound **10c** (2.42 mmol, 739 mg, 1.3 equiv), solubilized in 3 mL of *N*,*N*-dimethylformamide and 5 mL of dry DCM, was added to the acyl chloride, followed by 3 equiv of triethylamine (5.58 mmol, 0.77 mL). After 22 h, the solvent was evaporated and 5 mL of *N*,*N*-dimethylformamide was added. The mixture was heated at 150 °C for 3 h, basified with 2 M KOH, extracted with ethyl acetate (three times, 10 mL each), washed with $NaCl_{ss}$ (once, 10 mL), and dried over Na_2SO_4. The product was purified by flash chromatography DCM−methanol (methanol gradient from 2 to 25%), followed by preparative HPLC obtaining **12** as a white powder. Yield 2.3% (0.08 mmol, 41.8 mg); R_f = 0.33 (DCM−methanol 98−2%). ^{1}H NMR (400 MHz, CD_3OD, 50 °C): δ = 10.08 (s, 1H, N*H* amide), 7.90 (d, ^3J(H,H) = 8.3 Hz, 2H, C*H* anilide), 7.76 (d, ^3J(H,H) = 8.4 Hz, 2H, C*H* anilide), 7.36−7.20 (m, 3H, C*H* benzyl), 4.53−4.40 (m, 2H, $CHCH_2$), 3.87−3.79 (m, 1H, C*H* piperidine), 3.65−3.55 (m, 1H, C*H* piperidine), 3.16−3.12 (m, 1H, C*H* piperidine), 3.10−3.09 (m, 1H, C*H* piperidine), 3.03−3.01 (m, 1H, C*H* piperidine), 2.98−2.93 (m, 1H, C*H* piperidine), 2.49−2.43 (m, 2H, $COCH_2$), 2.40 (s, 3H, CCH_3 benzyl), 2.09−1.97 (m, 3H, C*H* piperidine and CH_2 benzyl), 1.95−1.85 (m, 1H, C*H* piperidine), 1.77−1.66 (quint, ^3J(H,H) = 7.8 Hz, 2H, CH_2CH_2), 1.52−1.32 (m, 13H, C*H* piperidine and CH_2CH_2 decanoyl chain), 0.91 ppm (t, ^3J(H,H) = 6.2 Hz, 3H, CH_2CH_3). ^{13}C NMR (400 MHz, CD_3OD, 50 °C): δ = 177.5 (CONH amide), 173.7 (*C*N oxadiazole), 167.6 (*C*O oxadiazole), 162.8 (*C*H benzyl), 141.6 (*C*NH anilide), 127.7 (CCH_3 benzyl), 127.6 (*C*H benzyl), 127.5 (2C, *C*CH anilide and CCH_2 benzyl), 120.6 (d, ^1J(C−F) = 188.1 Hz, *C*F), 119.5 (CH_2 benzyl), 119.5 (2C, *C*H anilide), 116.6 (2C, *C*H anilide), 116.3 (*C*H benzyl), 59.3 ($CHCH_2$), 55.7 (NCH_2 piperidine), 52.7 (NCH_2 piperidine), 36.8 ($COCH_2$), 32.4 (CH_2CH piperidine), 31.6 ($CHCH_2$ piperidine), 29.3 (CH_2CH_2), 29.2 (CH_2CH_2), 29.0 (CH_2CH_2 piperidine), 28.9 (CH_2CH_2 piperidine), 27.8 (CH_2CH_2), 25.4 (CH_2CH_2), 22.3 (CH_2CH_2), 22.2 (CH_2CH_3), 13.0 (CH_2CH_3), 9.8 ppm (CCH_3). ^{19}F (376 MHz, $CDCl_3$, 50 °C): δ = −112.65 ppm (s, C*F*). HRMS (ESI): *m*/*z* calcd for $C_{32}H_{43}FN_4O_2$ + H^+ [M + H]$^+$: 535.3443. Found: 535.3441. HPLC analysis: retention time = 13.378 min; peak area, 98%.

General Procedure for the Synthesis of the N^7-Substituted Pyrimido[4,5-*d*]pyrimidine-2,4,7-triamines (14−44). 2-Substituted-4-aminopyrimidin-5-carbonitriles **47** (1 equiv, 0.83 mmol) were stirred with 0.73 M free base guanidine solution in dry 2-methoxyethanol (3.5 equiv, 2.90 mmol, 3.97 mL) at 150 °C for 1.5−4.5 h. After the completion of the reaction, the mixture was concentrated, quenched with water, and extracted with ethyl acetate. The organic phase was dried over anhydrous sodium sulfate, filtered, and evaporated, giving a crude product purified by silica gel column chromatography eluting with a mixture of chloroform/methanol/ammonia and then triturated with a mixture of petroleum ether/diethyl ether to afford the final compounds **14**−**44** as a white powder.

*N^7-(1-Benzylpiperidin-4-yl)pyrimido[4,5-d]pyrimidine-2,4,7-triamine (**14**).* Recryst. solvent: acetonitrile/methanol. Yield: 75.3%. mp: 205−208 °C. ^{1}H NMR (400 MHz, DMSO-d_6) δ ppm: 1.46−1.54 (m, 2H, 2× C*H* piperidine ring), 1.82−1.85 (m, 2H, 2× C*H* piperidine ring), 1.99−2.04 (m, 2H, 2× C*H* piperidine ring), 2.79−2.81 (m, 2H, 2× C*H* piperidine ring), 3.46 (s, 2H, NCH_2Ph), 3.74 (br m, 1H, NHC_4−*H*-piperidine ring), 6.40 (br s, 2H, C_2−NH_2), 7.18−7.35 (m, 8H, C*H* benzene ring, N*H* and C_4−NH_2), 8.84 (s, 1H, C*H* pyrimidine ring). ^{13}C NMR (100 MHz, DMSO) δ 31.8 (2C), 48.2, 52.8 (2C), 62.7, 96.2, 127.3, 128.6 (2C), 129.2 (2C), 139.2, 157.0, 163.3, 163.4, 165.7, 166.2. MS (ESI), *m*/*z*: 351 [M + H]$^+$. Elemental anal. calcd (%) for $C_{18}H_{22}N_8$: C 61.70, H 6.33, N 31.98. Found: C 61.80, H 6.35, N 31.85.

*7-(2-Methylpiperidin-1-yl)pyrimido[4,5-d]pyrimidine-2,4-diamine (**15**).* Recryst. solvent: methanol. Yield: 52.8%. mp: >300 °C. ^{1}H NMR (400 MHz, DMSO) δ ppm: 1.12−1.14 (d, 3H, $CHCH_3$), 1.36 (m, 1H, C*H* piperidine ring), 1.58−1.70 (m, 5H, 5× C*H* piperidine ring), 2.85−2.92 (t, 1H, C*H* piperidine ring), 4.66−4.69 (m, 1H, C*H* piperidine ring), 5.10 (br s, 1H, C*H*−CH_3−piperidine ring), 6.43 (br s, 2H, C_2−NH_2), 7.34 (br s, 2H, C_4−NH_2), 8.90 (s, 1H, C*H* pyrimidine ring). ^{13}C NMR (100 MHz, DMSO) δ 15.4, 19.1, 25.9, 30.3, 38.3, 45.4, 96.1, 156.7, 162.6, 163.3, 165.9, 166.1. MS (ESI), *m*/*z*: 260 [M + H]$^+$. Elemental anal. calcd (%) for $C_{12}H_{17}N_7$: C 55.58, H 6.61, N 37.81. Found: C 55.68, H 6.63, N 37.69.

*7-(3,4-Dihydroisoquinolin-2(1H)-yl)pyrimido[4,5-d]pyrimidine-2,4-diamine (**16**).* Recryst. solvent: methanol. Yield: 70.6%. mp: 278−280 °C. ^{1}H NMR (400 MHz, DMSO-d_6) δ ppm: 2.85−2.88 (m, 2H, C*H* piperidine ring), 4.03 (m, 2H, C*H* piperidine ring), 4.92 (s, 2H, C*H* piperidine), 6.51 (br s, 2H, C_2−NH_2), 7.18−7.25 (m, 4H, C*H* isoquinoline ring), 7.43 (br s, 2H, C_4−NH_2), 8.97 (s, 1H, C*H* pyrimidine ring). ^{13}C NMR (100 MHz, DMSO-d_6) δ 28.6, 41.6, 46.1, 96.5, 126.5, 126.7, 126.8, 129.0, 134.7, 135.4, 156.8, 162.8, 163.4, 166.0, 166.1. MS (ESI), *m*/*z*: 294 [M + H]$^+$. Elemental anal. calcd (%) for $C_{15}H_{15}N_7$: C 61.42, H 5.15, N 33.43. Found: C 61.53, H 5.17, N 33.30.

*7-(4-Phenylpiperazin-1-yl)pyrimido[4,5-d]pyrimidine-2,4-diamine (**17**).* Recryst. solvent: methanol. Yield: 62.8%. mp: >300 °C. ^{1}H NMR (400 MHz, DMSO-d_6) δ ppm: 3.19 (m, 4H, 2× CH_2 piperazine ring), 3.95 (m, 4H, 2× CH_2 piperazine ring), 6.52 (br s, 2H, C_2−NH_2), 6.79.6.83 (t, 1H, C*H* benzene ring), 6.99−7.01 (m, 2H, C*H* benzene ring), 7.22−7.26 (m, 2H, C*H* benzene ring), 7.43 (br s, 2H, C_4−NH_2), 8.96 (s, 1H, C*H* pyrimidine ring). ^{13}C NMR (100 MHz, DMSO-d_6) δ 43.7 (2C), 48.9 (2C), 96.6, 116.3 (2C), 119.6, 129.4 (2C), 151.5, 156.8, 162.8, 163.4, 166.0, 166.1. MS (ESI), *m*/*z*: 323 [M + H]$^+$. Elemental anal. calcd (%) for $C_{16}H_{18}N_8$: C 59.61, H 5.63, N 34.76. Found: C 59.72, H 5.65, N 34.63.

*N^7-(4-Methoxybenzyl)pyrimido[4,5-d]pyrimidine-2,4,7-triamine (**18**).* Recryst. solvent: methanol. Yield: 82.7%. mp: >300 °C. ^{1}H NMR (400 MHz, DMSO-d_6) δ ppm: 3.71 (s, 3H, OCH_3), 4.42 (br m, 2H, $NHCH_2Ph$), 6.46 (br s, 2H, C_2−NH_2), 6.84−6.86 (d, 2H, C*H* benzene ring), 7.24−7.31 (br m, 4H, 2× C*H* benzene ring and C_4−NH_2), 7.66−7.76 (br m, 1H, $NHCH_2Ph$), 8.86 (s, 1H, C*H* pyrimidine ring). ^{13}C NMR (100 MHz, DMSO-d_6) δ 43.7, 55.5, 96.4, 113.9 (2C), 129.0 (2C), 132.8, 157.0, 158.5, 163.3, 164.1, 165.9, 166.3. MS

DOI: 10.1021/acs.jmedchem.9b00638
J. Med. Chem. 2019, 62, 8733−8759

(ESI), m/z: 298 $[M + H]^+$. Elemental anal. calcd (%) for $C_{14}H_{15}N_7O$: C 56.56, H 5.09, N 32.98. Found: C 56.67, H 5.11, N 32.85.

*N^7-(1-Phenylethyl)pyrimido[4,5-d]pyrimidine-2,4,7-triamine (**19**).* Recryst. solvent: methanol. Yield: 68.3%. mp: >300 °C. ^{1}H NMR (400 MHz, DMSO-d_6) δ ppm: 1.41−1.43 (d, 3H, $CHCH_3$), 5.14 (br s, 1H, $CHCH_3$), 6.44 (br s, 2H, C_2−NH_2), 7.16−7.19 (m, 1H, C*H* benzene ring), 7.27−7.39 (m, 6H, 4× C*H* benzene ring and C_4−NH_2), 7.79 (br m, 1H, N*H*), 8.85 (s, 1H, C*H* pyrimidine ring). ^{13}C NMR (100 MHz, DMSO-d_6) δ 23.4, 50.0, 96.4, 126.5 (2C), 126.8, 128.5 (2C), 146.2, 156.9, 163.3, 163.4, 165.9, 166.2. MS (ESI), m/z: 282 $[M + H]^+$. Elemental anal. calcd (%) for $C_{14}H_{15}N_7$: C 59.77, H 5.37, N 34.85. Found: C 59.89, H 5.38, N 34.73.

*N^7-Benzyl-N^7-methylpyrimido[4,5-d]pyrimidine-2,4,7-triamine (**20**).* Recryst. solvent: methanol. Yield: 65.2%. mp: 275−277 °C. ^{1}H NMR (400 MHz, DMSO-d_6) δ ppm: 3.09 (s, 3H, NCH_3), 4.89 (s, 2H, CH_2Ph), 6.49 (br s, 2H, C_2−NH_2), 6.24−7.33 (m, 7H, 5× C*H* benzene ring and C_4−NH_2), 8.94 (s, 1H, C*H* pyrimidine ring). ^{13}C NMR (100 MHz, DMSO-d_6) δ 35.1, 51.9, 96.4, 127.3 (2C), 127.7, 128.9 (2C), 139.0, 156.8, 163.4, 163.6, 166.0, 166.1. MS (ESI), m/z: 282 $[M + H]^+$. Elemental anal. calcd (%) for $C_{14}H_{15}N_7$: C 59.77, H 5.37, N 34.85. Found: C 59.87, H 5.39, N 34.74.

*N^7-Methyl-N^7-(1-phenylethyl)pyrimido[4,5-d]pyrimidine-2,4,7-triamine (**21**).* Recryst. solvent: acetonitrile/methanol. Yield: 76.8%. mp: 192−194 °C. ^{1}H NMR (400 MHz, DMSO-d_6) δ ppm: 1.53−1.55 (d, 3H, $CHCH_3$), 2.82 (s, 3H, NCH_3), 6.30 (br m, 1H, $CHCH_3$), 6.48 (br s, 2H, C_2−NH_2), 7.28−7.34 (m, 7H, 5× C*H* benzene ring and C_4−NH_2), 8.96 (s, 1H, C*H* pyrimidine ring). ^{13}C NMR (100 MHz, DMSO-d_6) δ 16.7, 29.3, 51.8, 96.4, 127.2 (2C), 127.3, 128.8 (2C), 142.2, 156.7, 163.4, 163.4, 165.9, 166.0. MS (ESI), m/z: 296 $[M + H]^+$. Elemental anal. calcd (%) for $C_{15}H_{17}N_7$: C 61.00, H 5.80, N 33.20. Found: C 61.11, H 5.82, N 33.07.

*N^7-(1-(4-Methoxyphenyl)ethyl)-N^7-methylpyrimido[4,5-d]pyrimidine-2,4,7-triamine (**22**).* Recryst. solvent: acetonitrile/methanol. Yield: 60.1%. mp: 184−187 °C. ^{1}H NMR (400 MHz, DMSO-d_6) δ ppm: 1.49 (d, 3H, $CHCH_3$), 2.78 (s, 3H, NCH_3), 3.73 (s, 3H, OCH_3), 6.26 (br s, 1H, $CHCH_3$), 6.48 (br s, 2H, C_2−NH_2), 6.88−6.90 (d, 2H, C*H* benzene ring), 7.20−7.22 (d, 2H, C*H* benzene ring), 7.39 (br s, 2H, C_4−NH_2), 8.95 (s, 1H, C*H* pyrimidine ring). ^{13}C NMR (100 MHz, DMSO-d_6) δ 16.8, 29.1, 51.2, 55.5, 96.4, 114.2 (2C), 128.4 (2C), 134.0, 156.7, 158.6, 163.3, 163.4, 166.0, 166.1. MS (ESI), m/z: 326 $[M + H]^+$. Elemental anal. calcd (%) for $C_{16}H_{19}N_7O$: C 59.06, H 5.89, N 30.13. Found: C 59.17, H 5.91, N 30.01.

*N^7-(1-([1,1′-Biphenyl]-4-yl)ethyl)-N^7-methylpyrimido[4,5-d]pyrimidine-2,4,7-triamine (**23**).* Recryst. solvent: methanol. Yield: 57.1%. mp: >300 °C. ^{1}H NMR (400 MHz, DMSO-d_6) δ ppm: 1.57−1.59 (d, 3H, $CHCH_3$), 2.87 (s, 3H, NCH_3), 6.35 (br s, 1H, $CHCH_3$), 6.51 (br s, 2H, C_2−NH_2), 7.34−7.48 (m, 7H, 5× C*H* benzene rings and C_4−NH_2), 7.63−7.66 (m, 4H, C*H* benzene rings), 8.97 (s, 1H, C*H* pyrimidine ring). ^{13}C NMR (100 MHz, DMSO-d_6) δ 16.9, 29.4, 51.7, 96.5, 127.0 (2C), 127.1 (2C), 127.8 (2C), 127.9, 129.4 (2C), 139.2, 140.3, 141.5, 156.7, 163.4, 163.4, 166.0, 166.1. MS (ESI), m/z: 372 $[M + H]^+$. Elemental anal. calcd (%) for $C_{21}H_{21}N_7$: C 67.90, H 5.70, N 26.40. Found: C 68.01, H 5.72, N 26.27.

*N^7-Methyl-N^7-(1-(4-phenoxyphenyl)ethyl)pyrimido[4,5-d]pyrimidine-2,4,7-triamine (**24**).* Recryst. solvent: acetonitrile/methanol. Yield: 41.9%. mp: 185−187 °C. ^{1}H NMR (400 MHz, DMSO-d_6) δ ppm: 1.52−1.54 (d, 3H, $CHCH_3$), 2.84 (s, 3H, NCH_3), 6.30 (br s, 1H, $CHCH_3$), 6.49 (br s, 2H, C_2−NH_2), 6.97−7.01 (m, 4H, C*H* benzene rings), 7.11−7.15 (t, 1H, C*H* benzene ring), 7.30−7.40 (m, 6H, C*H* benzene rings and C_4−NH_2), 8.96 (s, 1H, C*H* pyrimidine ring). ^{13}C NMR (100 MHz, DMSO-d_6) δ 16.8, 29.2, 51.4, 96.5, 118.9 (2C), 119.0 (2C), 123.8, 128.9 (2C), 130.5 (2C), 137.3, 155.9, 156.7, 157.2, 163.3, 163.4, 166.0, 166.1. MS (ESI), m/z: 388 $[M + H]^+$. Elemental anal. calcd (%) for $C_{21}H_{21}N_7O$: C 65.10, H 5.46, N 25.31. Found: C 65.20, H 5.48, N 25.20.

*N^7-(1-(4-(4-Methoxyphenoxy)phenyl)ethyl)pyrimido[4,5-d]pyrimidine-2,4,7-triamine (**25**).* Recryst. solvent: methanol. Yield: 82.5%. mp: >300 °C. ^{1}H NMR (400 MHz, DMSO-d_6) δ ppm: 1.40−1.42 (d, 3H, $CHCH_3$), 3.91 (s, 3H, OCH_3), 5.12 (br m, 1H, $CHCH_3$), 6.45 (br s, 2H, C_2−NH_2), 6.83−6.85 (m, 2H, C*H* benzene rings), 6.92−6.98 (m, 4H, C*H* benzene rings), 7.20−7.36 (m, 4H, C*H* benzene rings and C_4−NH_2), 7.76−7.78 (br m, 1H, N*H*), 8.85 (s, 1H, C*H* pyrimidine ring). ^{13}C NMR (100 MHz, DMSO-d_6) δ 23.3, 49.4, 55.9, 96.4, 115.5 (2C), 117.5 (2C), 121.0 (2C), 128.0 (2C), 140.4, 150.1, 155.9, 156.9, 157.0, 163.3, 163.6, 165.9, 166.2. MS (ESI), m/z: 404 $[M + H]^+$. Elemental anal. calcd (%) for $C_{21}H_{21}N_7O_2$: C 62.52, H 5.25, N 24.30. Found: C 62.62, H 5.27, N 24.20.

*N^7-(4-(4-Methoxyphenoxy)benzyl)-N^7-methylpyrimido[4,5-d]pyrimidine-2,4,7-triamine (**26**).* Recryst. solvent: methanol. Yield: 68.0%. mp: 244−247 °C. ^{1}H NMR (400 MHz, DMSO-d_6) δ ppm: 3.08 (br s, 3H, NCH_3), 3.74 (s, 3H, OCH_3), 4.85 (s, 2H, $N(CH_3)CH_2Ph$), 6.50 (br s, 2H, C_2−NH_2), 6.86−6.88 (d, 2H, C*H* benzene rings), 6.93−6.99 (m, 4H, C*H* benzene rings), 7.23 (br m, 2H, C*H* benzene rings), 7.41 (br s, 2H, C_4−NH_2), 8.94 (s, 1H, C*H* pyrimidine ring). ^{13}C NMR (100 MHz, DMSO-d_6) δ 35.0, 51.3, 55.9, 96.4, 115.5 (2C), 117.8 (2C), 121.0 (2C), 129.3 (2C), 133.2, 150.0, 156.0, 156.7, 157.4, 163.4, 163.5, 166.0, 166.1. MS (ESI), m/z: 404 $[M + H]^+$. Elemental anal. calcd (%) for $C_{21}H_{21}N_7O_2$: C 62.52, H 5.25, N 24.30. Found: C 62.63, H 5.26, N 24.19.

*N^7-(1-(4-(4-Methoxyphenoxy)phenyl)propyl)-N^7-methylpyrimido[4,5-d]pyrimidine-2,4,7-triamine (**27**).* Recryst. solvent: acetonitrile/methanol. Yield: 60.7%. mp: 186−190 °C. ^{1}H NMR (400 MHz, DMSO-d_6) δ ppm: 0.85 (t, 3H, CH_2CH_3), 1.90−2.07 (m, 2H, CH_2CH_3), 2.79−2.82 (br s, 3H, NCH_3), 3.74 (s, 3H, OCH_3), 6.10 (br m, 1H, $CHCH_3$), 6.48 (br s, 2H, C_2−NH_2), 6.86−6.88 (m, 2H, C*H* benzene rings), 6.93−7.00 (m, 4H, C*H* benzene rings), 7.20−7.38 (br m, 4H, C*H* benzene rings and C_4−NH_2), 8.94 (s, 1H, C*H* pyrimidine ring). ^{13}C NMR (100 MHz, DMSO-d_6) δ 11.5, 23.5, 28.9, 55.9, 57.2, 96.3, 115.5 (2C), 117.5 (2C), 121.1 (2C), 129.1 (2C), 135.6, 149.9, 156.1, 156.5, 157.4, 163.4, 164.0, 166.0, 166.1. MS (ESI), m/z: 432 $[M + H]^+$. Elemental anal. calcd (%) for $C_{23}H_{25}N_7O_2$: C 64.02, H 5.84, N 22.72. Found: C 64.12, H 5.86, N 22.60.

*N^7-(1-(4-(4-Methoxyphenoxy)phenyl)-2-methylpropyl)-N^7-methylpyrimido[4,5-d]pyrimidine-2,4,7-triamine (**28**).* Recryst. solvent: acetonitrile. Yield: 64.0%. mp: 162−165 °C. ^{1}H NMR (400 MHz, DMSO-d_6) (mixture of two rotamers 50:50) δ ppm: 0.83 and 0.89 (two d, 6H, $CH(CH_3)_2$), 2.51−2.58 (m, 1H, $CH(CH_3)_2$), 2.81 and 2.89 (two br s, 3H, NCH_3), 3.74 (s, 3H, OCH_3), 5.82−5.84 (m, 1H, $CHCH(CH_3)_2$), 6.46 (two br s, 2H, C_2−NH_2), 6.86−6.88 (m, 2H, C*H* benzene rings), 6.93−7.01 (m, 4H, C*H* benzene rings), 7.36−7.42 (m, 4H, 2× C*H* benzene rings and C_4−NH_2), 8.91 and 8.95 (two s, 1H, C*H* pyrimidine ring). ^{13}C NMR (100 MHz, DMSO-d_6) δ 20.0 (2C), 21.0, 27.6, 28.9, 55.9, 96.2, 115.5 (2C), 117.4 (2C), 121.3 (2C), 130.1 (2C), 134.4, 149.7, 156.1, 156.2, 156.8, 157.5, 163.3, 163.7, 166.0. MS (ESI), m/z: 446 $[M + H]^+$. Elemental anal. calcd (%) for $C_{24}H_{27}N_7O_2$: C 64.70, H 6.11, N 22.01. Found: C 64.81, H 6.13, N 21.89.

*N^7-((4-(4-Methoxyphenoxy)phenyl)(phenyl)methyl)-N^7-methylpyrimido[4,5-d]pyrimidine-2,4,7-triamine (**29**).* Recryst. solvent: methanol. Yield: 58.8%. mp: 248−250 °C. ^{1}H NMR (400 MHz, DMSO-d_6) δ ppm: 2.89 (br s, 3H, NCH_3), 3.93 (s, 3H, OCH_3), 6.52 (br s, 2H, C_2−NH_2), 6.91−7.04 (m, 6H, C*H* benzene rings), 7.13−7.18 (m, 4H, C*H* benzene rings), 7.28−7.43 (m, 6H, 4× C*H* benzene rings and C_4−NH_2), 8.97 (m, 1H, C*H* pyrimidine ring). ^{13}C NMR (100 MHz, DMSO-d_6) δ 32.0, 55.9, 61.2, 96.8, 115.6 (2C), 117.6 (2C), 121.3 (2C), 127.6, 128.7 (2C), 128.9 (2C), 130.5 (2C), 134.4, 140.5, 149.7, 156.2, 156.7, 157.6, 163.4, 163.6, 166.0, 166.1. MS (ESI), m/z: 480 $[M + H]^+$. Elemental anal. calcd (%) for $C_{27}H_{25}N_7O_2$: C 67.63, H 5.25, N 20.45. Found: C 67.74, H 5.27, N 20.34.

*N^7-(1-(4-(3-Methoxyphenoxy)phenyl)ethyl)-N^7-methylpyrimido-[4,5-d]pyrimidine-2,4,7-triamine (**30**).* Recryst. solvent: acetonitrile. Yield: 47.4%. mp: 152−154 °C. ^{1}H NMR (400 MHz, DMSO-d_6) δ ppm: 1.52−1.54 (d, 3H, $CHCH_3$), 2.83 (br s, 3H, NCH_3), 3.73 (s, 3H, OCH_3), 6.31 (br s, 1H, $CHCH_3$), 6.49−6.54 (br m, 3H, C*H* benzene rings and C_2−NH_2), 6.58 (t, 1H, C*H* benzene ring), 6.69−6.72 (dd, 1H, C*H* benzene ring), 6.98−7.00 (d, 2H, C*H* benzene rings), 7.25−7.32 (m, 3H, C*H* benzene rings), 7.40 (br s, 2H, C_4−NH_2), 8.96 (s, 1H, C*H* pyrimidine ring). ^{13}C NMR (100 MHz,

DOI: 10.1021/acs.jmedchem.9b00638
J. Med. Chem. 2019, 62, 8733−8759

DMSO-d_6) δ 16.8, 29.2, 51.4, 55.7, 96.5, 100.0, 105.0, 109.5, 110.8, 119.1 (2C), 128.9, 130.9 (2C), 137.4, 155.7, 156.7, 158.4, 161.2, 163.3, 163.4, 166.0. MS (ESI), m/z: 418 $[M + H]^+$. Elemental anal. calcd (%) for $C_{22}H_{23}N_7O_2$: C 63.30, H 5.55, N 23.49. Found: C 63.41, H 5.57, N 23.38.

*N^7-(1-(4-(3,4-Dimethoxyphenoxy)phenyl)ethyl)-N^7-methylpyrimido[4,5-d]pyrimidine-2,4,7-triamine (**31**).* Recryst. solvent: acetonitrile/methanol. Yield: 69.2%. mp: 185−188 °C. ^{1}H NMR (400 MHz, DMSO-d_6) δ ppm: 1.50−1.52 (d, 3H, $CHCH_3$), 2.82 (br s, 3H, NCH_3), 3.72 (s, 3H, OCH_3), 3.74 (s, 3H, OCH_3), 6.29 (br s, 1H, $CHCH_3$), 6.48−6.53 (br m, 3H, C*H* benzene ring and C_2-NH_2), 6.74 (d, 1H, C*H* benzene ring), 6.89−6.95 (m, 3H, C*H* benzene rings), 7.25−7.27 (m, 2H, C*H* benzene rings), 7.40 (br s, 2H, C_4-NH_2), 8.96 (s, 1H, C*H* pyrimidine ring). ^{13}C NMR (100 MHz, DMSO-d_6) δ 16.9, 29.2, 51.3, 56.1, 56.4, 96.5, 105.3, 110.9, 113.0, 117.6 (2C), 128.7 (2C), 136.3, 145.8, 150.1, 150.3, 156.7, 157.2, 163.3, 163.4, 166.0, 166.1. MS (ESI), m/z: 448 $[M + H]^+$. Elemental anal. calcd (%) for $C_{23}H_{25}N_7O_3$: C 61.73, H 5.63, N 21.91. Found: C 61.84, H 5.65, N 21.80.

*N^7-(1-(4-(3,5-Dimethoxyphenoxy)phenyl)ethyl)-N^7-methylpyrimido[4,5-d]pyrimidine-2,4,7-triamine (**32**).* Recryst. solvent: methanol. Yield: 75.6%. mp: 233−235 °C. ^{1}H NMR (400 MHz, DMSO-d_6) δ ppm: 1.52−1.54 (d, 3H, $CHCH_3$), 2.83 (br s, 3H, NCH_3), 3.70 (s, 6H, 2× OCH_3), 6.13 (m, 2H, C*H* benzene rings), 6.28 (m, 2H, $CHCH_3$ and C*H* benzene ring), 6.48 (br s, 2H, C_2-NH_2), 6.99 (d, 2H, C*H* benzene rings), 7.29−7.40 (m, 4H, 2× C*H* benzene rings and C_4-NH_2), 8.96 (s, 1H, C*H* pyrimidine ring). ^{13}C NMR (100 MHz, DMSO-d_6) δ 16.8, 29.2, 51.4, 55.8 (2C), 95.9, 96.5, 97.5 (2C), 119.2 (2C), 128.9 (2C), 137.5, 155.5, 156.7, 159.0, 161.8 (2C), 163.3, 163.4, 166.0, 166.1. MS (ESI), m/z: 448 $[M + H]^+$. Elemental anal. calcd (%) for $C_{23}H_{25}N_7O_3$: C 61.73, H 5.63, N 21.91. Found: C 61.82, H 5.64, N 21.82.

*N^7-((4-(3,5-Dimethoxyphenoxy)phenyl)(phenyl)methyl)-N^7-methylpyrimido[4,5-d]pyrimidine-2,4,7-triamine (**33**).* Recryst. solvent: acetonitrile. Yield: 58.2%. mp: 152−154 °C. ^{1}H NMR (400 MHz, DMSO-d_6) δ ppm: 2.91 (br s, 3H, NCH_3), 3.71 (s, 6H, 2× OCH_3), 6.17 (d, 2H, C*H* benzene rings), 6.30 (t, 1H, C*H* benzene rings), 6.52 (br s, 2H, C_2-NH_2), 7.02−7.04 (d, 2H, C*H* benzene rings), 7.17−7.20 (m, 4H, C*H* benzene rings), 7.29−7.46 (m, 6H, C*H* benzene rings, CHPh and C_4-NH_2), 8.98 (s, 1H, C*H* pyrimidine ring). ^{13}C NMR (100 MHz, DMSO-d_6) δ 32.0, 55.8 (2C), 61.2, 96.0, 97.8 (2C), 119.1 (2C), 119.1, 127.6, 128.7 (2C), 129.0 (2C), 130.5 (2C), 135.5, 140.5, 155.9, 156.8, 158.8, 161.9 (2C), 162.0, 163.4, 163.6, 166.1. MS (ESI), m/z: 510 $[M + H]^+$. Elemental anal. calcd (%) for $C_{28}H_{27}N_7O_3$: C 66.00, H 5.34, N 19.24. Found: C 66.10, H 5.35, N 19.14.

*N^7-(1-(4-(3,4,5-Trimethoxyphenoxy)phenyl)ethyl)-N^7-methylpyrimido[4,5-d]pyrimidine-2,4,7-triamine (**34**).* Recryst. solvent: acetonitrile. Yield: 67.1%. mp: 172−176 °C. ^{1}H NMR (400 MHz, DMSO-d_6) δ ppm: 1.51−1.53 (d, 3H, $CHCH_3$), 2.82 (br s, 3H, NCH_3), 3.64 (s, 3H, OCH_3), 3.71 (s, 6H, 2× OCH_3), 6.30 (br s, 1H, $CHCH_3$), 6.37 (s, 2H, C*H* benzene ring), 6.48 (br s, 2H, C_2-NH_2), 6.94−6.96 (d, 2H, C*H* benzene ring), 7.27−7.29 (d, 2H, C*H* benzene ring) 7.40 (br s, 2H, C_4-NH_2), 8.96 (s, 1H, C*H* pyrimidine ring). ^{13}C NMR (100 MHz, DMSO-d_6) δ 16.9, 29.2, 51.3, 56.4 (2C), 60.6, 96.5, 97.8 (2C), 117.9 (2C), 128.8 (2C), 134.4, 136.7, 152.6, 154.1, 156.6, 156.7 (2C), 163.3, 163.4, 166.0, 166.1. MS (ESI), m/z: 478 $[M + H]^+$. Elemental anal. calcd (%) for $C_{24}H_{27}N_7O_4$: C 60.37, H 5.70, N 20.53. Found: C 60.47, H 5.72, N 20.43.

*N^7-Methyl-N^7-(1-(4-(4-(trifluoromethoxy)phenoxy)phenyl)ethyl)-pyrimido[4,5-d]pyrimidine-2,4,7-triamine (**35**).* Recryst. solvent: toluene. Yield: 58.3%. mp: 140−143 °C. ^{1}H NMR (400 MHz, DMSO-d_6) δ ppm: 1.53−1.55 (d, 3H, $CHCH_3$), 2.85 (br s, 3H, NCH_3), 6.31 (br s, 1H, $CHCH_3$), 6.49 (br s, 2H, C_2-NH_2), 7.03−7.10 (m, 4H, C*H* benzene ring), 7.33−7.39 (m, 6H, C*H* benzene ring and C_4-NH_2), 8.96 (s, 1H, C*H* pyrimidine ring). ^{13}C NMR (100 MHz, DMSO-d_6) δ 16.9, 29.2, 51.4, 96.5, 119.5 (2C), 120.0 (2C), 120.6 (q OCF_3), 123.4 (2C), 129.1 (2C), 138.0, 144.0, 155.3, 156.3, 156.7, 163.3, 163.4, 166.0, 166.1. MS (ESI), m/z: 472 $[M + H]^+$. Elemental anal. calcd (%) for $C_{22}H_{20}F_3N_7O_2$: C 56.05, H 4.28, N 20.80. Found: C 56.15, H 4.30, N 20.70.

*N^7-Methyl-N^7-(1-(4-(4-(methylthio)phenoxy)phenyl)ethyl)-pyrimido[4,5-d]pyrimidine-2,4,7-triamine (**36**).* Recryst. solvent: toluene. Yield: 65.6%. mp: 145−146 °C. ^{1}H NMR (400 MHz, DMSO-d_6) δ ppm: 1.52−1.54 (d, 3H, $CHCH_3$), 2.46 (s, 3H, SCH_3), 2.83 (br s, 3H, NCH_3), 6.30 (br m, 1H, $CHCH_3$), 6.48 (br s, 2H, C_2-NH_2), 6.96−7.00 (m, 4H, C*H* benzene rings), 7.28−7.31 (m, 4H, C*H* benzene rings), 7.39 (br s, 2H C_4-NH_2), 8.95 (s, 1H, C*H* pyrimidine ring). ^{13}C NMR (100 MHz, DMSO-d_6) δ 16.2, 16.9, 29.2, 51.4, 96.5, 118.7 (2C), 119.9 (2C), 128.9 (2C), 128.9 (2C), 132.7, 137.2, 154.9, 156.0, 156.7, 163.3, 163.4, 166.0, 166.1. MS (ESI), m/z: 434 $[M + H]^+$. Elemental anal. calcd (%) for $C_{22}H_{23}N_7OS$: C 60.95, H 5.35, N 22.62, S 7.40. Found: C 61.06, H 5.36, N 22.52, S 7.37.

*N^7-(1-(4-(4-(Benzyloxy)phenoxy)phenyl)ethyl)-N^7-methylpyrimido[4,5-d]pyrimidine-2,4,7-triamine (**37**).* Recryst. solvent: cyclohexane. Yield: 77.8%. mp: 129−132 °C. ^{1}H NMR (400 MHz, DMSO-d_6) δ ppm: 1.50−1.52 (d, 3H, $CHCH_3$), 2.82 (br s, 3H, NCH_3), 5.08 (s, 2H, OCH_2Ph), 6.28 (br s, 1H, $CHCH_3$), 6.48 (br s, 2H, C_2-NH_2), 6.88−6.90 (d, 2H, CH benzene rings), 6.98−7.05 (m, 4H, C*H* benzene rings), 7.26−7.28 (d, 2H, C*H* benzene rings), 7.34−7.47 (m, 7H, 5× C*H* benzene rings and C_4-NH_2), 8.96 (s, 1H, C*H* pyrimidine ring). ^{13}C NMR (100 MHz, DMSO-d_6) δ 16.9, 29.2, 51.3, 70.1, 96.5, 116.5 (2C), 117.7 (2C), 121.0 (2C), 128.2 (2C), 128.3 (2C), 128.8, 128.9 (2C), 136.4, 137.5, 150.1, 155.1, 156.7, 157.2, 163.3, 163.4, 166.0, 166.1. MS (ESI), m/z: 494 $[M + H]^+$. Elemental anal. calcd (%) for $C_{28}H_{27}N_7O_2$: C 68.14, H 5.51, N 19.87. Found: C 68.25, H 5.53, N 19.77.

*N^7-(1-(4-((4-Methoxynaphthalen-1-yl)oxy)phenyl)ethyl)-N^7-methylpyrimido[4,5-d]pyrimidine-2,4,7-triamine (**38**).* Recryst. solvent: methanol. Yield: 71.9%. mp: >300 °C. ^{1}H NMR (400 MHz, DMSO-d_6) δ ppm: 1.49−1.51 (d, 3H, $CHCH_3$), 2.82 (br s, 3H, NCH_3), 3.98 (s, 3H, OCH_3), 6.28 (br s, 1H, $CHCH_3$), 6.46 (br s, 2H, C_2-NH_2), 6.89−6.96 (m, 3H, CH aromatic rings), 7.07−7.09 (d, 1H, C*H* naphthalene ring), 7.25−7.27 (d, 2H, C*H* aromatic rings), 7.38 (br s, 2H, C_4-NH_2), 7.53−7.58 (m, 2H, C*H* naphthalene ring), 7.89−7.91 (m, 1H, C*H* naphthalene ring), 8.19−8.21 (m, 1H, C*H* naphthalene ring), 8.95 (s, 1H, C*H* pyrimidine ring). ^{13}C NMR (100 MHz, DMSO-d_6) δ 16.9, 29.2, 51.3, 56.2, 96.4, 104.5, 116.3, 116.9 (2C), 121.9, 122.4, 126.3, 126.5, 127.4, 127.6, 128.8 (2C), 136.2, 144.9, 152.1, 156.7, 158.0, 163.3, 163.4, 166.0, 166.1. MS (ESI), m/z: 468 $[M + H]^+$. Elemental anal. calcd (%) for $C_{26}H_{25}N_7O_2$: C 66.79, H 5.39, N 20.97. Found: C 66.90, H 5.41, N 20.85.

*N^7-(1-(4-((4-Methoxybenzyl)oxy)phenyl)ethyl)-N^7-methylpyrimido[4,5-d]pyrimidine-2,4,7-triamine (**39**).* Recryst. solvent: methanol. Yield: 78.1%. mp: 225−228 °C. ^{1}H NMR (400 MHz, DMSO-d_6) δ ppm: 1.48−1.50 (d, 3H, $CHCH_3$), 2.79 (br s, 3H, NCH_3), 3.75 (s, 3H, OCH_3), 4.99 (s, 2H, OCH_2Ph), 6.26 (br s, 1H, $CHCH_3$), 6.47 (br s, 2H, C_2-NH_2), 6.93−6.97 (m, 4H, CH benzene rings), 7.20−7.22 (d, 2H, C*H* benzene rings), 7.36−7.38 (m, 4H, 2× C*H* benzene rings and C_4-NH_2), 8.95 (s, 1H, C*H* pyrimidine ring). ^{13}C NMR (100 MHz, DMSO-d_6) δ 16.8, 29.1, 51.2, 55.5, 69.4, 96.4, 114.3 (2C), 115.0 (2C), 128.4 (2C), 129.4, 129.9 (2C), 134.2, 156.7, 157.8, 159.4, 163.3, 163.4, 166.0, 166.1. MS (ESI), m/z: 432 $[M + H]^+$. Elemental anal. calcd (%) for $C_{23}H_{25}N_7O_2$: C 64.02, H 5.84, N 22.72. Found: C 64.13, H 5.85, N 22.61.

*N^7-(1-(4-((4-Methoxyphenyl)thio)phenyl)ethyl)-N^7-methylpyrimido[4,5-d]pyrimidine-2,4,7-triamine (**40**).* Recryst. solvent: acetonitrile. Yield: 72.9%. mp: 160−163 °C. ^{1}H NMR (400 MHz, DMSO-d_6) δ ppm: 1.48−1.50 (d, 3H, $CHCH_3$), 2.81 (br s, 3H, NCH_3), 3.77 (s, 3H, OCH_3), 6.24 (br s, 1H, $CHCH_3$), 6.49 (br s, 2H, C_2-NH_2), 6.98−7.01 (d, 2H, CH benzene rings), 7.10−7.12 (d, 2H, C*H* benzene rings), 7.21−7.41 (m, 6H, 4× C*H* benzene rings and C_4-NH_2), 8.94 (s, 1H, C*H* pyrimidine ring). ^{13}C NMR (100 MHz, DMSO-d_6) δ 16.8, 29.3, 51.5, 55.8, 96.5, 115.8 (2C), 123.8, 128.2 (2C), 128.6 (2C), 135.5 (2C), 136.4, 140.4, 156.7, 160.1, 163.3, 163.4, 166.0, 166.1. MS (ESI), m/z: 434 $[M + H]^+$. Elemental anal. calcd (%) for $C_{22}H_{23}N_7OS$: C 60.95, H 5.35, N 22.62, S 7.40. Found: C 61.06, H 5.36, N 22.51, S 7.37.

DOI: 10.1021/acs.jmedchem.9b00638
J. Med. Chem. 2019, 62, 8733−8759

*N^7-(1-(4-((3,5-Dimethoxyphenyl)thio)phenyl)ethyl)-N^7-methylpyrimido[4,5-d]pyrimidine-2,4,7-triamine (**41**).* Recryst. solvent: toluene. Yield: 64.0%. mp: 138−139 °C. ^{1}H NMR (400 MHz, DMSO-d_6) δ ppm: 1.53−1.55 (d, 3H, CHCH_3), 2.83 (br s, 3H, NCH_3), 3.69 (s, 6H, 2× OCH_3), 6.30 (br s, 1H, CHCH$_3$), 6.36 (m, 2H, CH benzene ring), 6.41 (m, 1H, CH benzene ring), 6.50 (br s, 2H, C$_2$−NH_2), 7.31−7.38 (m, 6H, 4× CH benzene ring and C$_4$−NH_2), 8.96 (s, 1H, CH pyrimidine ring). ^{13}C NMR (100 MHz, DMSO-d_6) δ 16.7, 29.4, 51.6, 55.8 (2C), 96.5, 99.4, 107.9 (2C), 128.5 (2C), 132.3, 132.3 (2C), 138.0, 142.4, 156.7, 161.3 (2C), 163.4, 166.0, 166.1, 166.2. MS (ESI), m/z: 464 [M + H]$^+$. Elemental anal. calcd (%) for $C_{23}H_{25}N_7O_2S$: C 59.59, H 5.44, N 21.15, S 6.92. Found: C 59.71, H 5.46, N 21.04, S 6.89.

*N^7-((4-((3,5-Dimethoxyphenyl)thio)phenyl)(phenyl)methyl)-N^7-methylpyrimido[4,5-d]pyrimidine-2,4,7-triamine (**42**).* Recryst. solvent: toluene. Yield: 76.2%. mp: 139−141 °C. ^{1}H NMR (400 MHz, DMSO-d_6) δ ppm: 2.90 (br s, 3H, NCH_3), 3.70 (s, 6H, 2× OCH_3), 6.42 (m, 3H, CH benzene rings), 6.53 (br s, 2H, C$_2$−NH_2), 7.17−7.21 (m, 4H, CH benzene rings), 7.30−7.34 (m, 1H, CH benzene ring), 7.37−7.46 (m, 7H, CH benzene rings, CHPh and C$_4$−NH_2), 8.97 (s, 1H, CH pyrimidine ring). ^{13}C NMR (100 MHz, DMSO-d_6) δ 32.1, 55.8 (2C), 61.5, 96.9, 99.7, 108.3 (2C), 127.8, 128.9 (2C), 129.0 (2C), 130.0 (2C), 132.0 (2C), 133.0, 137.5, 140.1, 140.3, 156.8, 161.4 (2C), 163.4, 163.5, 166.1, 166.2. MS (ESI), m/z: 526 [M + H]$^+$. Elemental anal. calcd (%) for $C_{28}H_{27}N_7O_2S$: C 63.98, H 5.18, N 18.65, S 6.10. Found: C 64.09, H 5.20, N 18.54, S 6.07.

*N^7-(1-(4-((4-Methoxyphenyl)amino)phenyl)ethyl)-N^7-methylpyrimido[4,5-d]pyrimidine-2,4,7-triamine (**43**).* Recryst. solvent: toluene. Yield: 52.1%. mp: 146−149 °C. ^{1}H NMR (400 MHz, DMSO-d_6) δ ppm: 1.46−1.48 (d, 3H, CHCH_3), 2.79 (br s, 3H, NCH_3), 3.71 (s, 3H, OCH_3), 6.23 (br s, 1H, CHCH$_3$), 6.46 (br s, 2H, C$_2$−NH_2), 6.84−6.90 (m, 4H, CH benzene rings), 7.01−7.03 (d, 2H, CH benzene rings), 7.09−7.11 (m, 2H, CH benzene rings), 7.38 (br s, 2H, C$_4$−NH_2), 7.83 (s, 1H, NHPh−OCH$_3$), 8.95 (s, 1H, CH pyrimidine ring). ^{13}C NMR (100 MHz, DMSO-d_6) δ 16.7, 29.1, 51.3, 55.7, 96.3, 115.0 (2C), 115.2 (2C), 120.6 (2C), 128.2 (2C), 131.7, 136.7, 144.4, 154.1, 156.7, 163.3, 163.4, 166.0, 166.1. MS (ESI), m/z: 417 [M + H]$^+$. Elemental anal. calcd (%) for $C_{22}H_{24}N_8O$: C 63.45, H 5.81, N 26.90. Found: C 63.56, H 5.83, N 26.79.

*N-(4-(1-((5,7-Diaminopyrimido[4,5-d]pyrimidin-2-yl)(methyl)amino)ethyl)phenyl)-4-methoxybenzamide (**44**).* Recryst. solvent: acetonitrile/methanol. Yield: 74.0%. mp: 196−198 °C. ^{1}H NMR (400 MHz, DMSO-d_6) δ ppm: 1.51−1.53 (d, 3H, CHCH_3), 2.81 (br s, 3H, NCH_3), 3.83 (s, 3H, OCH_3), 6.30 (br m, 1H, CHCH$_3$), 6.46 (br s, 2H, C$_2$−NH_2), 7.04−7.06 (d, 2H, CH benzene ring), 7.24−7.26 (d, 2H, CH benzene ring), 7.38 (br s, 2H, C$_4$−NH_2), 7.71−7.73 (d, 2H, CH benzene ring), 7.94−7.96 (d, 2H, CH benzene ring), 8.96 (s, 1H, CH pyrimidine ring), 10.08 (s, 1H, NHCO). ^{13}C NMR (100 MHz, DMSO-d_6) δ 16.7, 29.2, 51.5, 55.9, 96.4, 114.0 (2C), 120.7 (2C), 127.4, 127.5 (2C), 130.0 (2C), 137.1, 138.6, 156.7, 162.3, 163.3, 163.4, 165.3, 166.0, 166.1. MS (ESI), m/z: 445 [M + H]$^+$. Elemental anal. calcd (%) for $C_{23}H_{24}N_8O_2$: C 62.15, H 5.44, N 25.21. Found: C 62.25, H 5.46, N 25.10.

General Procedure for the Synthesis of the Intermediate Ketones 45f−q and 45s−u. A mixture of the appropriate alkyl/phenyl 4′-fluorophenyl ketone (1 equiv, 3 mmol), the properly substituted phenol, 1-naphthol or phenylthiol (1 equiv, 3 mmol), and anhydrous potassium carbonate (1.2 equiv, 3.6 mmol) in anhydrous DMF (3 mL) was stirred at 175 °C for 5 h. After the completion of the reaction, the medium was quenched with water (50 mL) and the product was extracted with ethyl acetate (3 × 25 mL). The organic phase was washed with saturated sodium chloride (2 × 50 mL), dried over anhydrous sodium sulfate, filtered, and concentrated under reduced pressure. The crude product was purified by silica gel column chromatography eluting with a mixture of ethyl acetate/*n*-hexane to obtain the pure ketones **45f−q** and **45s−u**.

*1-(4-(4-Methoxyphenoxy)phenyl)propan-1-one (**45f**).*[62] Yield: 83%. mp: 50−51 °C. ^{1}H NMR (400 MHz, CDCl$_3$) δ ppm: 1.14 (t, 3H, COCH$_2$CH_3), 2.87−2.89 (q, 2H, COCH_2CH$_3$), 3.75 (s, 3H, OCH_3), 6.86 (m, 4H, CH benzene rings), 6.95 (m, 2H, CH benzene ring), 7.85 (m, 2H, CH benzene ring).

*1-(4-(4-Methoxyphenoxy)phenyl)-2-methylpropan-1-one (**45g**).* Oil. Yield: 68%. ^{1}H NMR (400 MHz, CDCl$_3$) δ ppm: 1.13 (d, 6H, CH(CH_3)$_2$), 3.42−3.45 (m, 1H, CH(CH$_3$)$_2$), 3.76 (s, 3H, OCH_3), 6.86 (m, 4H, CH benzene rings), 6.95 (m, 2H, CH benzene ring), 7.85 (m, 2H, CH benzene ring).

*(4-(4-Methoxyphenoxy)phenyl)(phenyl)methanone (**45h**).*[63] Yield: 86%. mp: 107−108 °C. ^{1}H NMR (400 MHz, CDCl$_3$) δ ppm: 3.76 (s, 3H, OCH_3), 6.85−6.91 (m, 4H, CH benzene rings), 6.96−6.99 (m, 2H, CH benzene ring), 7.38−7.42 (m, 2H, CH ring), 7.48−7.50 (m, 1H, CH benzene ring), 7.68−7.74 (m, 4H, CH benzene rings).

*1-(4-(3-Methoxyphenoxy)phenyl)ethan-1-one (**45i**).*[64] Yield: 59%. mp: 65−67 °C. ^{1}H NMR (400 MHz, CDCl$_3$) δ ppm: 2.60 (s, 3H, COCH_3), 3.82 (s, 3H, OCH_3), 6.64−6.68 (m, 2H, CH benzene ring), 6.76−6.78 (m, 1H, CH benzene ring), 7.03−7.05 (m, 2H, CH benzene ring), 7.28−7.33 (m, 1H, CH benzene ring), 7.97 (m, 2H, CH benzene ring).

*1-(4-(3,4-Dimethoxyphenoxy)phenyl)ethan-1-one (**45j**).* Recryst. solvent: cyclohexane. Yield: 86%. mp: 99−101 °C. ^{1}H NMR (400 MHz, CDCl$_3$) δ ppm: 2.50 (s, 3H, COCH_3), 3.78 (s, 3H, OCH_3), 3.83 (s, 3H, OCH_3), 6.55−6.58 (m, 2H, CH benzene ring), 6.79−6.81 (d, 1H, CH benzene ring), 6.87−6.91 (m, 2H, CH benzene ring), 7.85−7.87 (m, 2H, CH benzene ring).

*1-(4-(3,5-Dimethoxyphenoxy)phenyl)ethan-1-one (**45k**).* Recryst. solvent: cyclohexane. Yield: 79%. mp: 85−87 °C. ^{1}H NMR (400 MHz, CDCl$_3$) δ ppm: 2.51 (s, 3H, COCH_3), 3.70 (s, 6H, 2× OCH_3), 6.15 (s, 2H, CH benzene ring), 6.23 (s, 1H, CH benzene ring), 6.96−6.98 (d, 2H, CH benzene ring), 7.86−7.88 (d, 2H, CH benzene ring).

*(4-(3,5-Dimethoxyphenoxy)phenyl)(phenyl)methanone (**45l**).* Oil. Yield: 92.0%. ^{1}H NMR (400 MHz, CDCl$_3$) δ ppm: 3.78 (s, 6H, 2× OCH_3), 6.25 (d, 2H, CH benzene ring), 6.30 (m, 1H, CH benzene ring), 7.07 (d, 2H, CH benzene ring), 7.46−7.50 (m, 2H, CH benzene ring), 7.56−7.60 (m, 1H, CH benzene ring), 7.77−7.79 (m, 4H, CH benzene rings).

*1-(4-(3,4,5-Trimethoxyphenoxy)phenyl)ethan-1-one (**45m**).* Recryst. solvent: cyclohexane. Yield: 66%. mp: 94−96 °C. ^{1}H NMR (400 MHz, CDCl$_3$) δ ppm: 2.60 (s, 3H, COCH_3), 3.83 (s, 6H, 3,5-(OCH_3)$_2$), 3.88 (s, 3H, 4-OCH_3), 6.34 (s, 2H, CH benzene ring), 7.02 (d, 2H, CH benzene ring), 7.96 (d, 2H, CH benzene ring).

*1-(4-(4-(Trifluoromethoxy)phenoxy)phenyl)ethan-1-one (**45n**).*[65] Oil. Yield: 95%. ^{1}H NMR (400 MHz, CDCl$_3$) δ ppm: 2.51 (s, 3H, COCH_3), 6.95 (d, 2H, CH benzene ring), 7.01 (d, 2H, CH benzene ring), 7.16−7.19 (d, 2H, CH benzene ring), 7.89 (d, 2H, CH benzene ring).

*1-(4-(4-(Methylthio)phenoxy)phenyl)ethan-1-one (**45o**).* Recryst. solvent: cyclohexane. Yield: 87%. mp: 83−84 °C. ^{1}H NMR (400 MHz, CDCl$_3$) δ ppm: 2.50 (s, 3H, SCH_3), 2.57 (s, 3H, COCH_3), 6.93−7.03 (m, 4H, CH benzene ring), 7.30 (m, 2H, CH benzene ring), 7.92−7.95 (m, 2H, CH benzene ring).

*1-(4-(4-(Benzyloxy)phenoxy)phenyl)ethan-1-one (**45p**).*[66] Yield: 70%. mp: 101−103 °C. ^{1}H NMR (400 MHz, CDCl$_3$) δ ppm: 2.49 (s, 3H, COCH_3), 5.00 (s, 2H, CH_2Ph), 6.86−6.89 (m, 2H, CH benzene ring), 6.94 (m, 4H, CH benzene rings), 7.27−7.39 (m, 5H, CH benzene rings), 7.83−7.85 (m, 2H, CH benzene ring).

*1-(4-((4-Methoxynaphthalen-1-yl)oxy)phenyl)ethan-1-one (**45q**).* Oil. Yield: 50%. ^{1}H NMR (400 MHz, CDCl$_3$) δ ppm: 2.48 (s, 3H, COCH_3), 3.96 (s, 3H, OCH_3), 6.70−6.72 (d, 1H, CH naphthalene ring), 6.87−6.89 (m, 2H, CH benzene ring), 7.02−7.04 (d, 1H, CH naphthalene ring), 7.38−7.47 (m, 2H, CH naphthalene ring), 7.77−7.79 (d, 1H, CH naphthalene ring), 7.82 (m, 2H, CH benzene ring), 8.22−8.24 (d, 1H, CH naphthalene ring).

*1-(4-((4-Methoxyphenyl)thio)phenyl)ethan-1-one (**45s**).*[58] Oil. Yield: 54%. ^{1}H NMR (400 MHz, CDCl$_3$) δ ppm: 2.47 (s, 3H, COCH_3), 3.79 (s, 3H, OCH_3), 6.88−6.90 (d, 2H, CH benzene ring), 7.01−7.04 (d, 2H, CH benzene ring), 7.41 (d, 2H, CH benzene ring), 7.72 (d, 2H, CH benzene ring).

*1-(4-((3,5-Dimethoxyphenyl)thio)phenyl)ethan-1-one (**45t**).* Recryst. solvent: cyclohexane. Yield: 72%. mp: 41−42 °C. ^{1}H NMR

DOI: 10.1021/acs.jmedchem.9b00638
J. Med. Chem. 2019, 62, 8733−8759

(400 MHz, $CDCl_3$) δ ppm: 2.56 (s, 3H, $COCH_3$), 3.77 (s, 6H, 2× OCH_3), 6.46 (m, 1H, C*H* benzene ring), 6.62 (m, 2H, C*H* benzene ring), 7.27 (d, 2H, C*H* benzene ring), 7.83 (d, 2H, C*H* benzene ring).

(4-((3,5-Dimethoxyphenyl)thio)phenyl)(phenyl)methanone (***45u***). Oil. Yield: 80%. ^{1}H NMR (400 MHz, $CDCl_3$) δ ppm: 3.71 (s, 6H, 2× OCH_3), 6.39 (m, 1H, C*H* benzene ring), 6.58 (m, 2H, C*H* benzene ring), 7.23 (d, 2H, C*H* benzene ring), 7.38−7.42 (m, 2H, C*H* benzene ring), 7.48−7.52 (m, 1H, C*H* benzene ring), 7.65 (d, 2H, C*H* benzene ring), 7.69−7.71 (m, 2H, C*H* benzene ring).

General Procedure for the Synthesis of the Intermediate Amines 46i−f′. A 2 M methylamine solution in methanol or, alternatively, a 7 M ammonia solution in methanol (3−6 equiv, 6−12 mmol) was added to a solution of titanium isopropoxide (1.3−2 equiv, 2.6−4 mmol) and the carbonyl compounds **45a−w** (1 equiv, 2 mmol) in THF (5 mL), and the reaction mixture was stirred under nitrogen atmosphere at room temperature. After 5−6 h, sodium borohydride (1.1 equiv, 2.2 mmol) was added portionwise at 0 °C, and the mixture was stirred for 2 h at room temperature. After completion, the reaction was quenched with distilled water (2 mL) and acidified at 0 °C with 1 M hydrochloric acid until pH was 1−2. The resulting suspension was filtered on celite and washed with a mixture of water (50 mL) and ethyl acetate (50 mL). The filtrate and the washings were combined, extracted with ethyl acetate (3 × 30 mL), basified with 10% w/w sodium hydroxide up to pH 10−12, and further extracted with ethyl acetate (3 × 30 mL). The organic phase was dried over anhydrous sodium sulfate, filtered, and concentrated under reduced pressure to give an oily crude product. This was finally purified by silica gel column chromatography eluting with a mixture of chloroform/methanol/ammonia or ethyl acetate/*n*-hexane, thus affording the pure amines **46i−f′**.

1-(4-Methoxyphenyl)-N-methylethan-1-amine (***46i***).[67] Oil. Yield: 87%. ^{1}H NMR (400 MHz, $CDCl_3$) δ ppm: 1.26 (d, 3H, $CHCH_3$), 2.22 (s, 3H, $NHCH_3$), 3.52 (m, 1H, $CHCH_3$), 3.73 (s, 3H, OCH_3), 6.81 (d, 2H, C*H* benzene ring), 7.15 (d, 2H, C*H* benzene ring).

1-([1,1′-Biphenyl]-4-yl)-N-methylethan-1-amine (***46j***). Oil. Yield: 55%. ^{1}H NMR (400 MHz, $CDCl_3$) δ ppm: 1.42 (d, 3H, $CHCH_3$), 2.37 (s, 3H, $NHCH_3$), 3.71−3.73 (m, 1H, $CHCH_3$), 7.35−7.41 (m, 3H, C*H* biphenyl ring), 7.44−7.47 (m, 2H, C*H* biphenyl ring), 7.58−7.62 (m, 4H, C*H* biphenyl ring).

N-Methyl-1-(4-phenoxyphenyl)ethan-1-amine (***46k***). Oil. Yield: 85%. ^{1}H NMR (400 MHz, $CDCl_3$) δ ppm: 1.39 (d, 3H, $CHCH_3$), 2.34 (s, 3H, $NHCH_3$), 3.65−3.70 (m, 1H, $CHCH_3$), 6.98−7.04 (m, 4H, C*H* benzene rings), 7.09−7.13 (m, 1H, C*H* benzene ring), 7.29−7.32 (m, 2H, C*H* benzene ring), 7.35−7.37 (m, 2H, C*H* benzene ring).

1-(4-(4-Methoxyphenoxy)phenyl)ethan-1-amine (***46l***). Oil. Yield: 34%. ^{1}H NMR (400 MHz, $CDCl_3$) δ ppm: 1.30 (d, 3H, $CHCH_3$), 3.73 (s, 3H, OCH_3), 4.03 (m, 1H, $CHCH_3$), 6.79−6.91 (m, 6H, C*H* benzene rings), 7.21 (m, 2H, C*H* benzene ring).

1-(4-(4-Methoxyphenoxy)phenyl)-N-methylmethanamine (***46m***). Oil. Yield: 78%. ^{1}H NMR (400 MHz, $CDCl_3$) δ ppm: 2.38 (s, 3H, $NHCH_3$), 3.63 (s, 2H, CH_2NHCH_3), 3.73 (s, 3H, OCH_3), 6.79−6.84 (m, 4H, C*H* benzene rings), 6.89−6.91 (d, 2H, C*H* benzene rings), 7.15−7.18 (m, 2H, C*H* benzene rings).

1-(4-(4-Methoxyphenoxy)phenyl)-N-methylethan-1-amine (***46n***). Oil. Yield: 73%. ^{1}H NMR (400 MHz, $CDCl_3$) δ ppm: 1.27 (d, 3H, $CHCH_3$), 2.24 (s, 3H, $NHCH_3$), 3.55 (m, 1H, $CHCH_3$), 3.73 (s, 3H, OCH_3), 6.79−6.84 (m, 4H, C*H* benzene rings), 6.89−6.92 (m, 2H, C*H* benzene ring), 7.14−7.16 (m, 2H, C*H* benzene ring).

1-(4-(4-Methoxyphenoxy)phenyl)-N-methylpropan-1-amine (***46o***). Oil. Yield: 83%. ^{1}H NMR (400 MHz, $CDCl_3$) δ ppm: 0.72−0.75 (t, 3H, $CHCH_2CH_3$), 1.51−1.58 (m, 1H, $CHCHHCH_3$), 1.63−1.71 (m, 1H, $CHCHHCH_3$), 2.21 (s, 3H, $NHCH_3$), 3.24−3.28 (m, 1H, $CHCH_2CH_3$), 3.74 (s, 3H, OCH_3), 6.79−6.84 (m, 4H, C*H* benzene rings), 6.90−6.92 (m, 2H, C*H* benzene ring), 7.1 (m, 2H, C*H* benzene ring).

1-(4-(4-Methoxyphenoxy)phenyl)-N,2-dimethylpropan-1-amine (***46p***). Oil. Yield: 62%. ^{1}H NMR (400 MHz, $CDCl_3$) δ ppm: 0.66−0.68 (d, 3H, $CHCH_3(CH_3)$), 0.88−0.90 (d, 3H, $CHCH_3(CH_3)$), 1.73−1.81 (m, 1H, $CH(CH_3)_2$), 2.16 (s, 3H, $NHCH_3$), 3.08−3.10 (m, 1H, $CHCH(CH_3)_2$), 3.73 (s, 3H, OCH_3), 6.79−6.83 (m, 4H, C*H* benzene rings), 6.89−6.94 (m, 2H, C*H* benzene ring), 7.07−7.10 (m, 2H, C*H* benzene ring).

1-(4-(4-Methoxyphenoxy)phenyl)-N-methyl-1-phenylmethanamine (***46q***). Oil. Yield: 60%. ^{1}H NMR (400 MHz, $CDCl_3$) δ ppm: 2.33 (s, 3H, $NHCH_3$), 3.72 (s, 3H, OCH_3), 4.59 (m, 1H, $CHPh$), 6.77−6.80 (m, 4H, C*H* benzene rings), 6.86−6.89 (m, 2H, C*H* benzene ring), 7.14−7.16 (m, 1H, C*H* benzene ring), 7.22−7.25 (m, 4H, C*H* benzene rings), 7.29−7.31 (m, 2H, C*H* benzene ring).

1-(4-(3-Methoxyphenoxy)phenyl)-N-methylethan-1-amine (***46r***). Oil. Yield: 79%. ^{1}H NMR (400 MHz, $CDCl_3$) δ ppm: 1.29 (d, 3H, $CHCH_3$), 2.25 (s, 3H, $NHCH_3$), 3.56−3.59 (m, 1H, $CHCH_3$), 3.71 (s, 3H, OCH_3), 6.50−6.52 (d, 2H, C*H* benzene ring), 6.56−6.58 (d, 1H, C*H* benzene ring), 6.90−6.92 (d, 2H, C*H* benzene ring), 7.12−7.20 (m, 3H, C*H* benzene rings).

1-(4-(3,4-Dimethoxyphenoxy)phenyl)-N-methylethan-1-amine (***46s***). Oil. Yield: 84%. ^{1}H NMR (400 MHz, $CDCl_3$) δ ppm: 1.27 (d, 3H, $CHCH_3$), 2.24 (s, 3H, $NHCH_3$), 3.54−3.56 (m, 1H, $CHCH_3$), 3.77 (s, 3H, OCH_3), 3.80 (s, 3H, OCH_3), 6.47−6.50 (d, 1H, C*H* benzene ring), 6.59 (s, 1H, C*H* benzene ring), 6.74−6.76 (d, 1H, C*H* benzene ring), 6.84−6.86 (d, 2H, C*H* benzene ring), 7.15−7.18 (m, 2H, C*H* benzene ring).

1-(4-(3,5-Dimethoxyphenoxy)phenyl)-N-methylethan-1-amine (***46t***). Oil. Yield: 72%. ^{1}H NMR (400 MHz, $CDCl_3$) δ ppm: 1.8 (d, 3H, $CHCH_3$), 2.25 (s, 3H, $NHCH_3$), 3.54−3.59 (m, 1H, $CHCH_3$), 3.68 (s, 6H, 2× OCH_3), 6.09 (m, 2H, C*H* benzene ring), 6.13 (m, 1H, C*H* benzene ring), 6.91−6.93 (d, 2H, C*H* benzene ring), 7.18−7.20 (d, 2H, C*H* benzene ring).

1-(4-(3,5-Dimethoxyphenoxy)phenyl)-N-methyl-1-phenylmethanamine (***46u***). Oil. Yield: 46%. ^{1}H NMR (400 MHz, $CDCl_3$) δ ppm: 2.41 (s, 3H, $NHCH_3$), 3.73 (s, 6H, 3,5-$(OCH_3)_2$), 4.68 (s, 1H, $NHCHPh$), 6.19 (m, 2H, C*H* benzene ring), 6.34 (m, 1H, C*H* benzene ring), 6.94−6.96 (d, 2H, C*H* benzene ring), 7.21−7.26 (m, 1H, C*H* benzene ring), 7.31−7.35 (m, 6H, C*H* phenyl rings).

N-Methyl-1-(4-(3,4,5-trimethoxyphenoxy)phenyl)ethan-1-amine (***46v***). Oil. Yield: 82%. ^{1}H NMR (400 MHz, $CDCl_3$) δ ppm: 1.27−1.29 (d, 3H, $CHCH_3$), 2.25 (s, 3H, $NHCH_3$), 3.55−3.57 (m, 1H, $CHCH_3$), 3.72 (s, 6H, 3,5-$(OCH_3)_2$), 3.76 (s, 3H, 4-OCH_3), 6.20 (s, 2H, C*H* benzene ring), 6.88−6.90 (m, 2H, C*H* benzene ring), 7.18−7.20 (m, 2H, C*H* benzene ring).

N-Methyl-1-(4-(4-(trifluoromethoxy)phenoxy)phenyl)ethan-1-amine (***46w***). Oil. Yield: 77%. ^{1}H NMR (400 MHz, $CDCl_3$) δ ppm: 1.28−1.30 (d, 3H, $CHCH_3$), 2.25 (s, 3H, $NHCH_3$), 3.57−3.59 (m, 1H, $CHCH_3$), 6.89−6.93 (m, 4H, C*H* benzene rings), 7.09 (m, 2H, C*H* benzene ring), 7.21−7.23 (m, 2H, C*H* benzene ring).

N-Methyl-1-(4-(4-(methylthio)phenoxy)phenyl)ethan-1-amine (***46x***). Oil. Yield: 84%. ^{1}H NMR (400 MHz, $CDCl_3$) δ ppm: 1.27−1.29 (d, 3H, $CHCH_3$), 2.25 (s, 3H, SCH_3), 2.40 (s, 3H, $NHCH_3$), 3.54−3.58 (m, 1H, $CHCH_3$), 6.87−6.89 (m, 4H, C*H* benzene rings), 7.18−7.20 (m, 4H, C*H* benzene rings).

1-(4-(4-(Benzyloxy)phenoxy)phenyl)-N-methylethan-1-amine (***46y***). Recryst. solvent: cyclohexane. Yield: 77%. mp: 90−91 °C. ^{1}H NMR (400 MHz, $CDCl_3$) δ ppm: 1.26−1.28 (d, 3H, $CHCH_3$), 2.24 (s, 3H, $NHCH_3$), 3.54−3.56 (m, 1H, $CHCH_3$), 4.98 (s, 2H, OCH_2Ph), 6.83−6.92 (m, 6H, C*H* benzene ring), 7.14−7.17 (m, 2H, C*H* benzene ring), 7.26−7.28 (m, 1H, C*H* benzene ring), 7.30−7.38 (m, 4H, C*H* benzene rings).

1-(4-((4-Methoxynaphthalen-1-yl)oxy)phenyl)-N-methylethan-1-amine (***46z***). Oil. Yield: 84%. ^{1}H NMR (400 MHz, $CDCl_3$) δ ppm: 1.26−1.28 (d, 3H, $CHCH_3$), 2.24 (s, 3H, $NHCH_3$), 3.52−3.57 (m, 1H, $CHCH_3$), 3.93 (s, 3H, OCH_3), 6.65−6.67 (d, 1H, C*H* naphthalene ring), 6.84−6.86 (d, 2H, C*H* naphthalene ring), 6.91−6.93 (d, 1H, C*H* naphthalene ring), 7.13−7.15 (m, 2H, C*H* benzene ring), 7.39−7.46 (m, 2H, C*H* benzene ring), 7.96−7.98 (d, 1H, C*H* naphthalene ring), 8.19−8.22 (d, 1H, C*H* naphthalene ring).

1-(4-((4-Methoxybenzyl)oxy)phenyl)-N-methylethan-1-amine (***46a′***). Recryst. solvent: cyclohexane. Yield: 70%. mp: 99−100 °C. ^{1}H NMR (400 MHz, $CDCl_3$) δ ppm: 1.25−1.27 (d, 3H, $CHCH_3$), 2.23 (s, 3H, $NHCH_3$), 3.50−3.55 (m, 1H, $CHCH_3$), 3.75 (s, 3H, OCH_3), 4.90 (s, 2H, OCH_2Ph), 6.84−6.88 (m, 4H, C*H* benzene rings), 7.13−

DOI: 10.1021/acs.jmedchem.9b00638
J. Med. Chem. 2019, 62, 8733−8759

7.15 (m, 2H, C*H* benzene ring), 7.28−7.30 (m, 2H, C*H* benzene ring).

*1-(4-((4-Methoxyphenyl)thio)phenyl)-N-methylethan-1-amine (**46b′**).* Oil. Yield: 80%. ^{1}H NMR (400 MHz, $CDCl_3$) δ ppm: 1.23−1.25 (d, 3H, CHCH_3), 2.22 (s, 3H, NHCH_3), 3.50−3.52 (m, 1H, C*H*CH$_3$), 3.75 (s, 3H, OCH_3), 6.81−6.83 (d, 2H, C*H* benzene ring), 7.06−7.12 (m, 4H, C*H* benzene rings), 7.32−7.34 (m, 2H, C*H* benzene ring).

*1-(4-((3,5-Dimethoxyphenyl)thio)phenyl)-N-methylethan-1-amine (**46c′**).* Oil. Yield: 78%. ^{1}H NMR (400 MHz, $CDCl_3$) δ ppm: 1.26−1.28 (d, 3H, CHCH_3), 2.24 (s, 3H, NHCH_3), 3.54−3.59 (m, 1H, C*H*CH$_3$), 3.66 (s, 6H, 3,5-(OCH_3)$_2$), 6.24 (m, 1H, C*H* benzene ring), 6.36 (m, 2H, C*H* benzene ring), 7.19−7.21 (d, 2H, C*H* benzene ring), 7.29−7.31 (d, 2H, C*H* benzene ring).

*1-(4-((3,5-Dimethoxyphenyl)thio)phenyl)-N-methyl-1-phenylmethanamine (**46d′**).* Oil. Yield: 30%. ^{1}H NMR (400 MHz, $CDCl_3$) δ ppm: 2.34 (s, 3H, NHCH_3), 3.64 (s, 6H, 2× OCH_3), 4.61 (s, 1H, NHC*H*Ph), 6.23 (m, 1H, C*H* benzene ring), 6.35 (m, 2H, C*H* benzene ring), 7.14−7.16 (m, 1H, C*H* benzene ring), 7.23−7.26 (m, 8H, C*H* benzene rings).

*4-Methoxy-N-(4-(1-(methylamino)ethyl)phenyl)aniline (**46e′**).* Oil. Yield: 57%. ^{1}H NMR (400 MHz, $CDCl_3$) δ ppm: 1.26−1.28 (d, 3H, CHCH_3), 2.25 (s, 3H, NHCH_3), 3.47−3.54 (m, 1H, C*H*CH$_3$), 3.73 (s, 3H, OCH_3), 5.34 (s, 1H, PhN*H*Ph−OCH$_3$), 6.75−6.83 (m, 4H, C*H* benzene rings), 6.98−7.00 (d, 2H, C*H* benzene ring), 7.06−7.08 (d, 2H, C*H* benzene ring).

*4-Methoxy-N-(4-(1-(methylamino)ethyl)phenyl)benzamide (**46f′**).* Recryst. solvent: methanol. Yield: 88%. mp: 220−221 °C. ^{1}H NMR (400 MHz, DMSO-d_6) δ ppm: 1.21−1.23 (d, 3H, CHCH_3), 2.12 (s, 3H, NHCH_3), 3.51−3.53 (m, 1H, C*H*CH$_3$), 3.84 (s, 3H, OCH_3), 7.05−7.07 (s, 2H, C*H* benzene ring), 7.25−7.27 (d, 2H, C*H* benzene ring), 7.67−7.69 (d, 2H, C*H* benzene ring), 7.94−7.96 (d, 2H, C*H* benzene ring), 10.02 (s, 1H, CON*H*).

General Procedure for the Synthesis of the 2-Substituted 4-Aminopyrimidin-5-Carbonitriles (47a−f′). 4-Amino-2-bromopyrimidine-5-carbonitrile (1 equiv, 1 mmol) and triethylamine (1.6 equiv, 1.6 mmol) were added to a solution of amines **46** (1 equiv, 1 mmol) in dry 2-methoxyetanol. After stirring at room temperature for 2.5 h, the reaction was stopped and the solvent was evaporated. The residue was diluted with ethyl acetate and washed two times with potassium hydrogen sulfate 0.1 N. The aqueous layer was counter-extracted with ethyl acetate, and the combined organic phases were dried over sodium sulfate, filtered, and evaporated under reduced pressure. The crude residue was finally purified by silica gel column chromatography eluting with a mixture of chloroform and *n*-hexane to afford the desired intermediate compounds **47** as white solids.

*4-Amino-2-((1-benzylpiperidin-4-yl)amino)pyrimidine-5-carbonitrile (**47a**).* Recryst. solvent: acetonitrile/methanol. Yield: 83%. mp: 205−208 °C. ^{1}H NMR (400 MHz, DMSO-d_6) δ ppm: 1.44−1.53 (m, 2H, 2× C*H* piperidine ring), 1.74 (m, 2H, 2× C*H* piperidine ring), 1.93−1.99 (m, 2H, 2× C*H* piperidine ring), 2.77−2.79 (m, 2H, 2× C*H* piperidine ring), 3.43−3.45 (m, 2H, NCH_2Ph), 3.72 (br m, 1H, NHC$_4$−*H*-piperidine ring), 7.02−7.49 (m, 8H, C*H* benzene ring, NH_2 and N*H*), 8.13 and 8.23 (two s, 1H, C*H* pyrimidine ring of two tautomers).

*4-Amino-2-(2-methylpiperidin-1-yl)pyrimidine-5-carbonitrile (**47b**).* Recryst. solvent: methanol. Yield: 82%. mp: 157−161 °C. ^{1}H NMR (400 MHz, DMSO-d_6) δ ppm: 1.07−1.09 (d, 3H, CH_3), 1.27−1.31 (m, 1H, C*H* piperidine ring), 1.54−1.68 (m, 5H, 5× C*H* piperidine ring), 2.84−2.92 (t, 1H, C*H* piperidine ring), 4.57−4.60 (m, 1H, C*H* piperidine ring), 5.02−5.04 (m, 1H, C*H* piperidine ring), 7.17 (br s, 2H, NH_2), 8.24 (s, 1H, C*H* pyrimidine ring).

*4-Amino-2-(3,4-dihydroisoquinolin-2(1H)-yl)pyrimidine-5-carbonitrile (**47c**).* Recryst. solvent: acetonitrile. Yield: 88%. mp: 186−189 °C. ^{1}H NMR (400 MHz, DMSO-d_6) δ ppm: 2.83−2.86 (m, 2H, CH_2 tetrahydroisoquinoline ring), 3.97 (m, 2H, CH_2 tetrahydroisoquinoline ring), 4.87 (s, 2H, CH_2 tetrahydroisoquinoline ring), 7.19 (m, 4H, C*H* tetrahydroisoquinoline ring), 7.33 (br s, 2H, NH_2), 8.31 (s, 1H, C*H* pyrimidine ring).

*4-Amino-2-(4-phenylpiperazin-1-yl)pyrimidine-5-carbonitrile (**47d**).* Recryst. solvent: methanol. Yield: 78%. mp: 272−277 °C. ^{1}H NMR (400 MHz, DMSO-d_6) δ ppm: 3.16−3.18 (m, 4H, 2× CH_2 piperazine ring), 3.89 (m, 4H, 2× CH_2 piperazine ring), 6.79−6.87 (m, 1H, C*H* benzene ring), 6.97−6.99 (m, 2H, C*H* benzene ring), 7.22−7.25 (m, 2H, C*H* benzene ring), 7.32 (br s, 2H, NH_2), 8.30 (s, 1H, C*H* pyrimidine ring).

*4-Amino-2-((4-methoxybenzyl)amino)pyrimidine-5-carbonitrile (**47e**).* Recryst. solvent: methanol. Yield: 62%. mp: 228−230 °C. ^{1}H NMR (400 MHz, DMSO-d_6) (mixture of two tautomers 60:40) δ ppm: 3.72 (s, 3H, OCH_3), 4.37−4.42 (m, 2H, NHCH_2Ph−OCH$_3$), 6.85−6.87 (m, 2H, C*H* benzene ring), 7.12−7.24 (m, 4H, C*H* benzene ring and NH_2), 7.81 and 7.97 (two t, 1H, N*H*CH$_2$), 8.17 and 8.24 (two s, 1H, C*H* pyrimidine ring).

*4-Amino-2-((1-phenylethyl)amino)pyrimidine-5-carbonitrile (**47f**).* Recryst. solvent: toluene. Yield: 94%. mp: 130−132 °C. ^{1}H NMR (400 MHz, DMSO-d_6) (mixture of two tautomers 60:40) δ ppm: 1.41 (d, 3H, CHCH_3), 5.12−5.16 (m, 1H, C*H*CH$_3$), 7.20−7.36 (m, 7H, C*H* benzene ring and NH_2), 7.81 and 8.05 (two d, 1H, N*H*), 8.16 (s, 1H, C*H* pyrimidine ring).

*4-Amino-2-(benzyl(methyl)amino)pyrimidine-5-carbonitrile (**47g**).* Recryst. solvent: acetonitrile. Yield: 91%. mp: 187−187 °C. ^{1}H NMR (400 MHz, DMSO-d_6) δ ppm: 3.04 (br s, 3H, NCH_3), 4.84 (s, 2H, NCH_2Ph), 7.21−7.34 (m, 7H, C*H* benzene ring and NH_2), 8.29 (s, 1H, C*H* pyrimidine ring).

*4-Amino-2-(methyl(1-phenylethyl)amino)pyrimidine-5-carbonitrile (**47h**).* Recryst. solvent: acetonitrile. Yield: 86%. mp: 189−191 °C. ^{1}H NMR (400 MHz, DMSO-d_6) δ ppm: 1.51 (d, 3H, CHCH_3), 2.77 (s, 3H, NCH_3), 6.21 (br m, 1H, C*H*CH$_3$), 7.26−7.35 (m, 7H, C*H* benzene ring and NH_2), 8.30 (s, 1H, C*H* pyrimidine ring).

*4-Amino-2-((1-(4-methoxyphenyl)ethyl)(methyl)amino)-pyrimidine-5-carbonitrile (**47i**).* Recryst. solvent: acetonitrile. Yield: 91%. mp: 153−154 °C. ^{1}H NMR (400 MHz, DMSO-d_6) δ ppm: 1.47 (d, 3H, CHCH_3), 2.74 (s, 3H, NCH_3), 3.73 (s, 3H, OCH_3), 6.16 (br m, 1H, C*H*CH$_3$), 6.89−6.91 (d, 2H, C*H* benzene ring), 7.19−7.26 (m, 4H, C*H* benzene ring and NH_2), 8.30 (s, 1H, C*H* pyrimidine ring).

*2-((1-([1,1′-Biphenyl]-4-yl)ethyl)(methyl)amino)-4-aminopyrimidine-5-carbonitrile (**47j**).* Recryst. solvent: acetonitrile. Yield: 89%. mp: 148−156 °C. ^{1}H NMR (400 MHz, DMSO-d_6) δ ppm: 1.56 (d, 3H, CHCH_3), 2.83 (s, 3H, NCH_3), 6.25 (br m, 1H, C*H*CH$_3$), 7.29−7.38 (m, 5H, C*H* biphenyl ring and NH_2), 7.44−7.48 (m, 2H, C*H* biphenyl ring), 7.63−7.66 (m, 4H, C*H* biphenyl ring), 8.32 (s, 1H, C*H* pyrimidine ring).

*4-Amino-2-(methyl(1-(4-phenoxyphenyl)ethyl)amino)-pyrimidine-5-carbonitrile (**47k**).* Recryst. solvent: toluene. Yield: 85%. mp: 147−150 °C. ^{1}H NMR (400 MHz, DMSO-d_6) δ ppm: 1.50 (d, 3H, CHCH_3), 2.79 (s, 3H, NCH_3), 6.20 (br m, 1H, C*H*CH$_3$), 6.97−7.01 (m, 4H, C*H* benzene rings), 7.13 (m, 1H, C*H* benzene ring), 7.28 (m, 4H, C*H* benzene rings and NH_2), 7.36−7.40 (m, 2H, C*H* benzene rings), 8.30 (s, 1H, C*H* pyrimidine ring).

*4-Amino-2-((1-(4-(4-methoxyphenoxy)phenyl)ethyl)amino)-pyrimidine-5-carbonitrile (**47l**).* Recryst. solvent: acetonitrile/methanol. Yield: 75%. mp: 193−196 °C. ^{1}H NMR (400 MHz, DMSO-d_6) (mixture of two tautomers 60:40) δ ppm: 1.39−1.41 (d, 3H, CHCH_3), 3.74 (s, 3H, OCH_3), 5.08−5.14 (two m, 1H, C*H*CH$_3$), 6.84−6.86 (m, 2H, C*H* benzene ring), 6.93−6.99 (m, 4H, C*H* benzene ring), 7.05 and 7.18 (two br s, 2H, NH_2), 7.29−7.34 (m, 2H, C*H* benzene ring), 7.82 and 8.02 (two br m, 1H, N*H*CHCH$_3$), 8.16 and 8.20 (two s, 1H, C*H* pyrimidine ring).

*4-Amino-2-((4-(4-methoxyphenoxy)benzyl)(methyl)amino)-pyrimidine-5-carbonitrile (**47m**).* Recryst. solvent: acetonitrile. Yield: 80%. mp: 188−189 °C. ^{1}H NMR (400 MHz, DMSO-d_6) (mixture of two rotamers 50:50) δ ppm: 3.02 and 3.05 (two s, 3H, NCH_3), 3.74 (s, 3H, OCH_3), 4.77 and 4.81 (two s, 2H, NCH_2Ph), 6.86−6.88 (d, 2H, C*H* benzene ring), 6.94−7.00 (m, 4H, C*H* benzene rings), 7.18−7.26 (m, 4H, C*H* benzene ring and NH_2), 8.29 (s, 1H, C*H* pyrimidine ring).

*4-Amino-2-((1-(4-(4-methoxyphenoxy)phenyl)ethyl)(methyl)-amino)pyrimidine-5-carbonitrile (**47n**).* Recryst. solvent: toluene. Yield: 81%. mp: 145−149 °C. ^{1}H NMR (400 MHz, DMSO-d_6) δ ppm: 1.49 (d, 3H, CHCH_3), 2.77 (br s, 3H, NCH_3), 3.75 (s, 3H, OCH_3), 6.17 (br m, 1H, C*H*CH$_3$), 6.88−6.90 (d, 2H, C*H* benzene

DOI: 10.1021/acs.jmedchem.9b00638
J. Med. Chem. 2019, 62, 8733−8759

ring), 6.94−7.00 (m, 4H, C*H* benzene rings), 7.26−7.31 (m, 4H, C*H* benzene ring and NH_2), 8.32 (s, 1H, C*H* pyrimidine ring).

*4-Amino-2-((1-(4-(4-methoxyphenoxy)phenyl)propyl)(methyl)-amino)pyrimidine-5-carbonitrile (**47o**).* Recryst. solvent: cyclohexane. Yield: 53%. mp: 55−58 °C. ^{1}H NMR (400 MHz, DMSO-d_6) (mixture of two rotamers 50:50) δ ppm: 0.82−0.86 (t, 3H, $CHCH_2CH_3$), 1.91 and 2.06 (two br m, 2H, $CHCH_2CH_3$), 2.75 and 2.81 (two br s, 3H, NCH_3), 3.75 (s, 3H, OCH_3), 5.93 and 6.01 (two br m, 1H, $CHCH_2CH_3$), 6.86−6.88 (d, 2H, C*H* benzene ring), 6.94−7.00 (m, 4H, C*H* benzene rings), 7.26−7.34 (m, 4H, C*H* benzene ring and NH_2), 8.30 (s, 1H, C*H* pyrimidine ring).

*4-Amino-2-((1-(4-(4-methoxyphenoxy)phenyl)-2-methylpropyl)-(methyl)amino)pyrimidine-5-carbonitrile (**47p**).* Recryst. solvent: cyclohexane. Yield: 37%. mp: 58−65 °C. ^{1}H NMR (400 MHz, DMSO-d_6) (mixture of two rotamers 50:50) δ ppm: 0.80 and 0.89 (two m, 6H, $CHCH(CH_3)_2$), 1.09 and 1.24 (two br m, 1H, $CHCH(CH_3)_2$), 2.79 and 2.86 (two br s, 3H, NCH_3), 3.92 (s, 3H, OCH_3), 5.58 and 5.73 (two br m, 1H, C*H* $CH(CH_3)_2$), 6.86−6.88 (m, 2H, C*H* benzene ring), 6.94−7.01 (m, 4H, C*H* benzene rings), 7.22 (br m, 2H, NH_2), 7.34 and 7.43 (two m, 2H, C*H* benzene ring), 8.24 and 8.32 (two s, 1H, C*H* pyrimidine ring).

*4-Amino-2-(((4-(4-methoxyphenoxy)phenyl)(phenyl)methyl)-(methyl)amino)pyrimidine-5-carbonitrile (**47q**).* Recryst. solvent: cyclohexane. Yield: 45%. mp: 60−66 °C. ^{1}H NMR (400 MHz, DMSO-d_6) δ ppm: 2.84 (s, 3H, NCH_3), 3.75 (s, 3H, OCH_3), 6.91−6.93 (m, 2H, C*H* benzene ring), 6.96−6.99 (m, 2H, C*H* benzene ring), 7.01−7.04 (m, 2H, C*H* benzene ring), 7.14−7.16 (m, 4H, C*H* benzene rings and NH_2), 7.31−7.40 (m, 6H, C*H* benzene rings and C*H*Ph), 8.32 (s, 1H, C*H* pyrimidine ring).

*4-Amino-2-((1-(4-(3-methoxyphenoxy)phenyl)ethyl)(methyl)-amino)pyrimidine-5-carbonitrile (**47r**).* Recryst. solvent: cyclohexane. Yield: 86%. mp: 45−41 °C. ^{1}H NMR (400 MHz, DMSO-d_6) δ ppm: 1.50−1.52 (d, 3H, $CHCH_3$), 2.79 (s, 3H, NCH_3), 3.73 (s, 3H, OCH_3), 6.20 (br m, 1H, $CHCH_3$), 6.51−6.58 (m, 2H, C*H* benzene ring), 6.70−6.73 (m, 1H, C*H* benzene ring), 6.98−7.00 (m, 2H, C*H* benzene ring), 7.25−7.29 (m, 5H, C*H* benzene rings and NH_2), 8.31 (s, 1H, C*H* pyrimidine ring).

*4-Amino-2-((1-(4-(3,4-dimethoxyphenoxy)phenyl)ethyl)-(methyl)amino)pyrimidine-5-carbonitrile (**47s**).* Recryst. solvent: cyclohexane. Yield: 90%. mp: 61−63 °C. ^{1}H NMR (400 MHz, DMSO-d_6) δ ppm: 1.48−1.50 (d, 3H, $CHCH_3$), 2.77 (br s, 3H, NCH_3), 3.72 (s, 3H, OCH_3), 3.74 (s, 3H, OCH_3), 6.17 (br m, 1H, $CHCH_3$), 6.50−6.53 (m, 1H, C*H* benzene ring), 6.74 (s, 1H, C*H* benzene ring), 6.89−6.95 (m, 3H, C*H* benzene rings), 7.25 (m, 4H, C*H* benzene rings and NH_2), 8.30 (s, 1H, C*H* pyrimidine ring).

*4-Amino-2-((1-(4-(3,5-dimethoxyphenoxy)phenyl)ethyl)-(methyl)amino)pyrimidine-5-carbonitrile (**47t**).* Recryst. solvent: cyclohexane. Yield: 65%. mp: 60−63 °C. ^{1}H NMR (400 MHz, DMSO-d_6) δ ppm: 1.51 (d, 3H, $CHCH_3$), 2.79 (br s, 3H, NCH_3), 3.70 (s, 6H, 3,5-$(OCH_3)_2$), 6.12−6.29 (m, 4H, C*H* benzene ring and $CHCH_3$), 6.99−7.01 (m, 2H, C*H* benzene ring), 7.28 (m, 4H, C*H* benzene ring and NH_2), 8.30 (s, 1H, C*H* pyrimidine ring).

*4-Amino-2-(((4-(3,5-dimethoxyphenoxy)phenyl)(phenyl)methyl)-(methyl)amino)pyrimidine-5-carbonitrile (**47u**).* Recryst. solvent: cyclohexane. Yield: 54%. mp: 54−58 °C. ^{1}H NMR (400 MHz, DMSO-d_6) δ ppm: 2.85 (s, 3H, NCH_3), 3.71 (s, 6H, 3,5-$(OCH_3)_2$), 6.16 (s, 2H, C*H* benzene ring), 6.30 (t, 1H, C*H* benzene ring), 7.01−7.03 (m, 2H, C*H* benzene ring), 7.16 (m, 4H, C*H* benzene rings and NH_2), 7.32−7.40 (m, 6H, C*H* benzene rings and C*H*Ph), 8.31 (s, 1H, C*H* pyrimidine ring).

*4-Amino-2-(methyl(1-(4-(3,4,5-trimethoxyphenoxy)phenyl)-ethyl)amino)pyrimidine-5-carbonitrile (**47v**).* Recryst. solvent: cyclohexane. Yield: 56%. mp: 65−67 °C. ^{1}H NMR (400 MHz, DMSO-d_6) δ ppm: 1.50 (d, 3H, $CHCH_3$), 2.77 (s, 3H, NCH_3), 3.64 (s, 3H, 4-OCH_3), 3.71 (s, 6H, 3,5-$(OCH_3)_2$), 6.17 (br m, 1H, $CHCH_3$), 6.37 (s, 2H, C*H* benzene ring), 6.94−6.96 (m, 2H, C*H* benzene ring), 7.27 (m, 4H, C*H* benzene ring and NH_2), 8.30 (s, 1H, C*H* pyrimidine ring).

*4-Amino-2-(methyl(1-(4-(4-(trifluoromethoxy)phenoxy)phenyl)-ethyl)amino)pyrimidine-5-carbonitrile (**47w**).* Recryst. solvent: cyclohexane. Yield: 65%. mp: 97−98 °C. ^{1}H NMR (400 MHz, DMSO-d_6) δ ppm: 1.51−1.53 (d, 3H, $CHCH_3$), 2.80 (br s, 3H, NCH_3), 6.21 (br m, 1H, $CHCH_3$), 7.03−7.05 (d, 2H, C*H* benzene ring), 7.08−7.10 (d, 2H, C*H* benzene ring), 7.31 (m, 4H, C*H* benzene ring and NH_2), 7.37−7.39 (d, 2H, C*H* benzene ring), 8.31 (s, 1H, C*H* pyrimidine ring).

*4-Amino-2-(methyl(1-(4-(4-(methylthio)phenoxy)phenyl)ethyl)-amino)pyrimidine-5-carbonitrile (**47x**).* Recryst. solvent: cyclohexane. Yield: 84%. mp: 48−50 °C. ^{1}H NMR (400 MHz, DMSO-d_6) δ ppm: 1.49−1.51 (d, 3H, $CHCH_3$), 2.45 (s, 3H, SCH_3), 2.78 (br s, 3H, NCH_3), 6.19 (br m, 1H, $CHCH_3$), 6.95−6.98 (m, 4H, C*H* benzene rings), 7.27−7.30 (m, 6H, C*H* benzene rings and NH_2), 8.30 (s, 1H, C*H* pyrimidine ring).

*4-Amino-2-((1-(4-(4-(benzyloxy)phenoxy)phenyl)ethyl)(methyl)-amino)pyrimidine-5-carbonitrile (**47y**).* Recryst. solvent: cyclohexane/toluene. Yield: 51%. mp: 109−110 °C. ^{1}H NMR (400 MHz, DMSO-d_6) δ ppm: 1.49 (d, 3H, $CHCH_3$), 2.77 (br s, 3H, NCH_3), 5.08 (s, 2H, OCH_2Ph), 6.18 (br m, 1H, $CHCH_3$), 6.88−6.90 (d, 2H, C*H* benzene ring), 6.97−7.05 (m, 4H, C*H* benzene rings), 7.26 (m, 4H, C*H* benzene ring and NH_2), 7.32−7.47 (m, 5H, C*H* benzene ring), 8.30 (s, 1H, C*H* pyrimidine ring).

*4-Amino-2-((1-(4-((4-methoxynaphthalen-1-yl)oxy)phenyl)-ethyl)(methyl)amino)pyrimidine-5-carbonitrile (**47z**).* Recryst. solvent: cyclohexane. Yield: 49%. mp: 82−83 °C. ^{1}H NMR (400 MHz, DMSO-d_6) δ ppm: 1.54 (d, 3H, $CHCH_3$), 2.84 (br s, 3H, NCH_3), 4.04 (s, 3H, OCH_3), 6.22 (br m, 1H, $CHCH_3$), 6.95−6.97 (d, 2H, CH naphthalene ring), 7.00−7.02 (m, 1H, C*H* naphthalene ring), 7.13−7.15 (m, 1H, C*H* naphthalene ring), 7.30 (br m, 4H, C*H* benzene ring and NH_2), 7.59−7.64 (m, 2H, C*H* benzene ring), 7.93−7.95 (m, 1H, C*H* naphthalene ring), 8.24−8.27 (m, 1H, C*H* naphthalene ring), 8.35 (s, 1H, CH pyrimidine ring).

*4-Amino-2-((1-(4-((4-methoxybenzyl)oxy)phenyl)ethyl)(methyl)-amino)pyrimidine-5-carbonitrile (**47a′**).* Recryst. solvent: acetonitrile/methanol. Yield: 52%. mp: 193−194 °C. ^{1}H NMR (400 MHz, DMSO-d_6) δ ppm: 1.46−1.48 (d, 3H, $CHCH_3$), 2.74 (br s, 3H, NCH_3), 3.75 (s, 3H, OCH_3), 4.99 (s, 2H, OCH_2Ph), 6.15 (br m, 1H, $CHCH_3$), 6.93−6.97 (m, 4H, C*H* benzene rings), 7.18 (m, 4H, C*H* benzene ring and NH_2), 7.36−7.38 (m, 2H, C*H* benzene ring), 8.30 (s, 1H, C*H* pyrimidine ring).

*4-Amino-2-((1-(4-((4-methoxyphenyl)thio)phenyl)ethyl)(methyl)-amino)pyrimidine-5-carbonitrile (**47b′**).* Recryst. solvent: acetonitrile. Yield: 91%. mp: 167−168 °C. ^{1}H NMR (400 MHz, DMSO-d_6) δ ppm: 1.46−1.48 (d, 3H, $CHCH_3$), 2.76 (br s, 3H, NCH_3), 3.78 (s, 3H, OCH_3), 6.13 (br m, 1H, $CHCH_3$), 6.98−7.02 (d, 2H, C*H* benzene ring), 7.10−7.12 (m, 2H, C*H* benzene ring), 7.26 (m, 4H, C*H* benzene ring and NH_2), 7.38−7.42 (m, 2H, C*H* benzene ring), 8.29 (s, 1H, C*H* pyrimidine ring).

*4-Amino-2-((1-(4-((3,5-dimethoxyphenyl)thio)phenyl)ethyl)-(methyl)amino)pyrimidine-5-carbonitrile (**47c′**).* Recryst. solvent: cyclohexane. Yield: 81%. mp: 48−50 °C. ^{1}H NMR (400 MHz, DMSO-d_6) δ ppm: 1.52 (d, 3H, $CHCH_3$), 2.79 (br s, 3H, NCH_3), 3.79 (s, 6H, 3,5-$(OCH_3)_2$), 6.19 (br m, 1H, $CHCH_3$), 6.37 (s, 2H, C*H* benzene ring), 6.41 (s, 1H, C*H* benzene ring), 7.29−7.31 (br m, 4H, C*H* benzene ring and NH_2), 7.35−7.38 (m, 2H, C*H* benzene ring), 8.30 (s, 1H, C*H* pyrimidine ring).

*4-Amino-2-(((4-((3,5-dimethoxyphenyl)thio)phenyl)(phenyl)-methyl)(methyl)amino)pyrimidine-5-carbonitrile (**47d′**).* Recryst. solvent: cyclohexane. Yield: 63%. mp: 84−87 °C. ^{1}H NMR (400 MHz, DMSO-d_6) δ ppm: 2.85 (br s, 3H, NCH_3), 3.71 (s, 6H, 3,5-$(OCH_3)_2$), 6.43 (m, 3H, C*H* benzene ring), 7.17−7.19 (m, 4H, C*H* benzene ring and NH_2), 7.31−7.41 (m, 8H, C*H* benzene rings and $CHCH_3$), 8.32 (br s, 1H, C*H* pyrimidine ring).

*4-Amino-2-((1-(4-((4-methoxyphenyl)amino)phenyl)ethyl)-(methyl)amino)pyrimidine-5-carbonitrile (**47e′**).* Recryst. solvent: cyclohexane. Yield: 65%. mp: 52−55 °C. ^{1}H NMR (400 MHz, DMSO-d_6) δ ppm: 1. 45 (d, 3H, $CHCH_3$), 2.74−2.76 (br s, 3H, NCH_3), 3.71 (s, 3H, 4-OCH_3), 6.12 (br m, 1H, $CHCH_3$), 6.84−7.89 (m, 4H, C*H* benzene rings), 7.00−7.07 (m, 4H, C*H* benzene ring and NH_2), 7.24 (m, 2H, C*H* benzene ring), 7.85 (s, 1H, N*H*), 8.29 (s, 1H, C*H* pyrimidine ring).

*N-(4-(1-((4-Amino-5-cyanopyrimidin-2-yl)(methyl)amino)ethyl)-phenyl)-4-methoxybenzamide (**47f′**).* Recryst. solvent: acetonitrile.

DOI: 10.1021/acs.jmedchem.9b00638
J. Med. Chem. 2019, 62, 8733−8759

Yield: 50%. mp: 164−165 °C. ^{1}H NMR (400 MHz, DMSO-d_6) δ ppm: 1.50 (d, 3H, CHCH_3), 2.67 (br s, 3H, NCH_3), 3.84 (s, 3H, 4-OCH_3), 6.18−6.20 (br m, 1H, CHCH$_3$), 7.05−7.07 (d, 2H, CH benzene ring), 7.25 (m, 4H, CH benzene ring and NH_2), 7.73−7.75 (d, 2H, CH benzene ring), 7.94−7.96 (d, 2H, CH benzene ring), 8.31 (s, 1H, CH pyrimidine ring), 10.11 (s, 1H, NHCO).

In Vitro Antischistosomal Effects of *Sm*Sirt2 Inhibitors. *Parasite Material and Ethics Statement.* A Puerto Rican strain of *S. mansoni* is maintained in the laboratory using albino *Biomphalaria glabrata* snails as intermediate host and *Mesocricetus auratus* (golden hamsters) as definitive host. Cercaria were released from infested snails and harvested on ice, as described previously.[68] Schistosomula were prepared in vitro by mechanical transformation;[68] 8 weeks post infestation, *S. mansoni* adult worms were recovered from the hamster hepatic system by whole-body perfusion with saline solution pumped through a perfusing needle placed in the left ventricle of the heart.[69] All animal experimentation was conducted in accordance with the European Convention for the Protection of Vertebrate Animals used for Experimental and other Scientific Purposes (ETS No 123, revised Appendix A) and was approved by the committee for ethics in animal experimentation of the Nord-Pas de Calais region (Authorization No. APAFIS#8289-2016122015127050V3) and the Pasteur Institute of Lille (Agreement No. B59-350009).

Schistosomula Viability. A total of 500 schistosomula were incubated at 37 °C under a humid atmosphere containing 5% CO_2 for 72 h in a 24-well plate containing 1 mL of complete medium (M199 medium, Invitrogen) supplemented with penicillin (50 U/mL), streptomycin (50 μg/mL), gentamycin (15 μg/mL), rifampicin (60 μg/mL), and 10% fetal calf serum (Gibco). Parasite death was evaluated by visual examination under a microscope for 72 h after the beginning of treatment using three major criteria: absence of motility, tegument defects, and granular appearance. For each condition, we observed a minimum of 300 larvae to determine the ratio of dead larvae to total larvae. Moreover, for each condition, two different assays were perfomed and two independent batches of schistosomula (biological replicates) were used. *Sm*Sirt2 inhibitors were dissolved in DMSO, and two different concentrations (10 and 20 μM) were used (single dose at D0).

Adult Worm Pairing Stability and Egg Laying. Ten pairs of *S. mansoni* adult worms were maintained in culture for 72 h in a 5% CO_2 atmosphere at 37 °C in a six-well plate containing 4 mL of complete medium in the presence of *Sm*Sirt2 inhibitors at 10 and 20 μM final concentration. Every day, the number of paired couples was evaluated by visual examination. At the end of the experiement, medium containing eggs was harvested and the total number of eggs was determined after centrifugation by microscopy. Two different assays were performed for each condition and repeated with two independent biological replicates.

Cell Proliferation Assay. HL-60 cells (grown in Roswell Park Memorial Institute 1640 supplemented with 10% fetal bovine serum) were incubated in 96-well tissue culture plates (density of 5000 per well) with *Sm*Sirt2 inhibitors at 10 μM final concentration or DMSO vehicle as control, in a total volume of 100 μL for 72 h at 37 °C; three replicates per concentration were used. Growth inhibition was determined using the CellTiter 96 AQueous Non-Radioactive Cell Proliferation Assay according to the manufacturer's instructions. Data were plotted as absorbance units against compound concentration using GraphPad Prism 7.0.

Calculation of Molecular Properties. Data in Table S7 were calculated using DataWarrior (version 5.0, http://www.openmolecules.org/datawarrior/).[70]

■ ASSOCIATED CONTENT

Supporting Information

The Supporting Information is available free of charge on the ACS Publications website at DOI: 10.1021/acs.jmedchem.9b00638.

Additional data for **1** and **3a−g** conversion by *Sm*Sirt2 and hSirt; IC_{50} of NA with **1** and **3a−g** as substrates; source of intermediate compounds **45a−e**, **r**, **v**, **w**, and **46a−h**; microscopy images of the effects of **7** and its analogues on schistosomula viability; molecular properties of selected compounds; and HPLC data (PDF)

Molecular formula strings for the synthesized compounds (CSV)

■ AUTHOR INFORMATION

Corresponding Authors

*E-mail: dante.rotili@uniroma1.it (D.R.).
*E-mail: antonello.mai@uniroma1.it (A.M.).
*E-mail: manfred.jung@pharmazie.uni-freiburg.de (M.J.).

ORCID

Martin Marek: 0000-0001-7220-5644
Christophe Romier: 0000-0002-3680-935X
Antonello Mai: 0000-0001-9176-2382
Manfred Jung: 0000-0002-6361-7716

Notes

The authors declare no competing financial interest.

■ ACKNOWLEDGMENTS

This work was supported by Deutsche Forschungsgemeinschaft (DFG, GRK1976, to D.M., N.W., and M.J., testing on human Sirtuins Ju295/14-1), Italian PRIN 2015 (prot. 20152TE5PK to A.M.), AIRC 2016 (n. 19162 to A.M.), Progetto Ateneo Sapienza 2017 (to D.R.), and the A-ParaDDisE program funded under the European Union's Seventh Framework Programme (grant agreement no. 602080 to M.J., C.R., R.J.P., A.M.) It was also supported by the grant ANR-10-LABX-0030-INRT, a French State fund managed by the Agence Nationale de la Recherche under the frame program Investissements d'Avenir ANR-10-IDEX-0002-02 to C.R., M.M., and E.R.-M. J.L. and R.J.P. are supported by institutional funds from the Centre National de la Recherche Scientifique (CNRS), the Institut National de la Sante et de la Recherche, Medicale (INSERM), the Institut Pasteur de Lille, and the Universite de Lille. The authors acknowledge GSK for kindly donating the Kineto Boxes compounds (aka TCKAS) for biological testing and the COST action CM1406 (Epigenetic Chemical Biology) for support.

■ ABBREVIATIONS

AMC, 7-amino-4-methylcoumarin; NA, nicotinamide; (*Z*)-Lys-OH, benzyloxycarbonyl lysine

■ REFERENCES

(1) Gray, D. J.; Ross, A. G.; Li, Y. S.; McManus, D. P. Diagnosis and Management of Schistosomiasis. *Br. Med. J.* **2011**, *342*, No. d2651.

(2) Cioli, D.; Pica-Mattoccia, L.; Basso, A.; Guidi, A. Schistosomiasis Control: Praziquantel Forever? *Mol. Biochem. Parasitol.* **2014**, *195*, 23−29.

(3) Fenwick, A.; Webster, J. P.; Bosque-Oliva, E.; Blair, L.; Fleming, F. M.; Zhang, Y.; Garba, A.; Stothard, J. R.; Gabrielli, A. F.; Clements, A. C. A.; Kabatereine, N. B.; Toure, S.; Dembele, R.; Nyandindi, U.; Mwansa, J.; Koukounari, A. The Schistosomiasis Control Initiative (SCI): Rationale, Development and Implementation from 2002−2008. *Parasitology* **2009**, *136*, 1719−1730.

(4) Webster, J. P.; Molyneux, D. H.; Hotez, P. J.; Fenwick, A. The Contribution of Mass Drug Administration to Global Health: Past, Present and Future. *Philos. Trans. R. Soc., B* **2014**, *369*, No. 20130434.

(5) Cleland, C. R.; Tukahebwa, E. M.; Fenwick, A.; Blair, L. Mass Drug Administration with Praziquantel Reduces the Prevalence of *Schistosoma mansoni* and Improves Liver Morbidity in Untreated

DOI: 10.1021/acs.jmedchem.9b00638
J. Med. Chem. 2019, 62, 8733−8759

Preschool Children. *Trans. R. Soc. Trop. Med. Hyg.* **2014**, *108*, 575−581.
(6) Vale, N.; Gouveia, M. J.; Rinaldi, G.; Brindley, P. J.; Gärtner, F.; da Costa, J. M. C. Praziquantel for Schistosomiasis: Single-Drug Metabolism Revisited, Mode of Action, and Resistance. *Antimicrob. Agents Chemother.* **2017**, *61*, No. e02582.
(7) Da Silva, V. B. R.; Campos, B. R. K. L.; De Oliveira, J. F.; Decout, J. L.; Alves de Lima, M. D. C. Medicinal Chemistry of Antischistosomal Drugs: Praziquantel and Oxamniquine. *Bioorg. Med. Chem.* **2017**, *25*, 3259−3277.
(8) Siqueira, L. D. P.; Fontes, D. A. F.; Aguilera, C. S. B.; Timóteo, T. R. R.; Ângelos, M. A.; Silva, L. C. P. B. B.; De Melo, C. G.; Rolim, L. A.; Da Silva, R. M. F.; Neto, P. J. R. Schistosomiasis: Drugs Used and Treatment Strategies. *Acta Trop.* **2017**, *176*, 179−187.
(9) Pica-Mattoccia, L.; Doenhoff, M. J.; Valle, C.; Basso, A.; Troiani, A. R.; Liberti, P.; Festucci, A.; Guidi, A.; Cioli, D. Genetic Analysis of Decreased Praziquantel Sensitivity in a Laboratory Strain of *Schistosoma mansoni*. *Acta Trop.* **2009**, *111*, 82−85.
(10) Pierce, R. J.; Dubois-Abdesselem, F.; Caby, S.; Trolet, J.; Lancelot, J.; Oger, F.; Bertheaume, N.; Roger, E. Chromatin Regulation in Schistosomes and Histone Modifying Enzymes as Drug Targets. *Mem. Inst. Oswaldo Cruz* **2011**, *106*, 794−801.
(11) Noël, F.; Mendonça-Silva, D. L.; Thibaut, J. P. B.; Lopes, D. V. S. Characterization of Two Classes of Benzodiazepine Binding Sites in *Schistosoma mansoni*. *Parasitology* **2007**, *134*, 1003−1012.
(12) Berriman, M.; Haas, B. J.; Loverde, P. T.; Wilson, R. A.; Dillon, G. P.; Cerqueira, G. C.; Mashiyama, S. T.; Al-Lazikani, B.; Andrade, L. F.; Ashton, P. D.; Aslett, M. A.; Bartholomeu, D. C.; Blandin, G.; Caffrey, C. R.; Coghlan, A.; Coulson, R.; Day, T. A.; Delcher, A.; De Marco, R.; Djikeng, A.; Eyre, T.; Gamble, J. A.; Ghedin, E.; Gu, Y.; Hertz-Fowler, C.; Hirai, H.; Hirai, Y.; Houston, R.; Ivens, A.; Johnston, D. A.; Lacerda, D.; Macedo, C. D.; Mc Veigh, P.; Ning, Z.; Oliveira, G.; Overington, J. P.; Parkhill, J.; Pertea, M.; Pierce, R. J.; Protasio, A. V.; Quail, M. A.; Rajandream, M. A.; Rogers, J.; Sajid, M.; Salzberg, S. L.; Stanke, M.; Tivey, A. R.; White, O.; Williams, D. L.; Wortman, J.; Wu, W.; Zamanian, M.; Zerlotini, A.; Fraser-Liggett, C. M.; Barrell, B. G.; El-Sayed, N. M. The Genome of the Blood Fluke *Schistosoma mansoni*. *Nature* **2009**, *460*, 352−358.
(13) Dissous, C.; Grevelding, C. G. Piggy-Backing the Concept of Cancer Drugs for Schistosomiasis Treatment: A Tangible Perspective? *Trends Parasitol.* **2011**, *27*, 59−66.
(14) Pierce, R. J.; Dubois-Abdesselem, F.; Lancelot, J.; Andrade, L.; Oliveira, G. Targeting Schistosome Histone Modifying Enzymes for Drug Development. *Curr. Pharm. Des.* **2012**, *18*, 3567−3578.
(15) Hailu, G.; Robaa, D.; Forgione, M.; Sippl, W.; Rotili, D.; Mai, A. Lysine Deacetylase Inhibitors in Parasites: Past, Present, and Future Perspectives. *J. Med. Chem.* **2017**, *60*, 4780−4804.
(16) Stolfa, D. A.; Marek, M.; Lancelot, J.; Hauser, A. T.; Walter, A.; Leproult, E.; Melesina, J.; Rumpf, T.; Wurtz, J. M.; Cavarelli, J.; Sippl, W.; Pierce, R. J.; Romier, C.; Jung, M. Molecular Basis for the Antiparasitic Activity of a Mercaptoacetamide Derivative That Inhibits Histone Deacetylase 8 (HDAC8) from the Human Pathogen *Schistosoma mansoni*. *J. Mol. Biol.* **2014**, *426*, 3442−3453.
(17) Simoben, C. V.; Robaa, D.; Chakrabarti, A.; Schmidtkunz, K.; Marek, M.; Lancelot, J.; Kannan, S.; Melesina, J.; Shaik, T. B.; Pierce, R. J.; Romier, C.; Jung, M.; Sippl, W. A Novel Class of *Schistosoma mansoni* Histone Deacetylase 8 (HDAC8) Inhibitors Identified by Structure-Based Virtual Screening and in Vitro Testing. *Molecules* **2018**, *23*, No. 566.
(18) Heimburg, T.; Chakrabarti, A.; Lancelot, J.; Marek, M.; Melesina, J.; Hauser, A. T.; Shaik, T. B.; Duclaud, S.; Robaa, D.; Erdmann, F.; Schmidt, M.; Romier, C.; Pierce, R. J.; Jung, M.; Sippl, W. Structure-Based Design and Synthesis of Novel Inhibitors Targeting HDAC8 from *Schistosoma mansoni* for the Treatment of Schistosomiasis. *J. Med. Chem.* **2016**, *59*, 2423−2435.
(19) Peck, B.; Chen, C. Y.; Ho, K. K.; Di Fruscia, P.; Myatt, S. S.; Coombes, R. C.; Fuchter, M. J.; Hsiao, C. D.; Lam, E. W. F. SIRT Inhibitors Induce Cell Death and P53 Acetylation through Targeting Both SIRT1 and SIRT2. *Mol. Cancer Ther.* **2010**, *9*, 844−855.
(20) Chakrabarty, S. P.; Saikumari, Y. K.; Bopanna, M. P.; Balaram, H. Biochemical Characterization of *Plasmodium falciparum* Sir2, a NAD+-Dependent Deacetylase. *Mol. Biochem. Parasitol.* **2008**, *158*, 139−151.
(21) Tonkin, C. J.; Carret, C. K.; Duraisingh, M. T.; Voss, T. S.; Ralph, S. A.; Hommel, M.; Duffy, M. F.; Da Silva, L. M.; Scherf, A.; Ivens, A.; Speed; Terence, P.; Beeson, J. G.; Cowman, A. F. Sir2 Paralogues Cooperate to Regulate Virulence Genes and Antigenic Variation in *Plasmodium falciparum*. *PLoS Biol.* **2009**, *7*, No. e1000084.
(22) Moretti, N. S.; Augusto, L. D. S.; Clemente, T. M.; Antunes, R. P. P.; Yoshida, N.; Torrecilhas, A. C.; Cano, M. I. N.; Schenkman, S. Characterization of *Trypanosoma cruzi* Sirtuins as Possible Drug Targets for Chagas Disease. *Antimicrob. Agents Chemother.* **2015**, *59*, 4669−4679.
(23) Ritagliati, C.; Alonso, V. L.; Manarin, R.; Cribb, P.; Serra, E. C. Overexpression of Cytoplasmic TcSIR2RP1 and Mitochondrial TcSIR2RP3 Impacts on *Trypanosoma cruzi* Growth and Cell Invasion. *PLoS Neglected Trop. Dis.* **2015**, *9*, No. e0003725.
(24) Yahiaoui, B.; Taibi, A.; Ouaissi, A. A Leishmania Major Protein with Extensive Homology to Silent Information Regulator 2 of Saccharomyces Cerevisiae. *Gene* **1996**, *169*, 115−118.
(25) Vergnes, B.; Sereno, D.; Madjidian-Sereno, N.; Lemesre, J. L.; Ouaissi, A. Cytoplasmic SIR2 Homologue Overexpression Promotes Survival of Leishmania Parasites by Preventing Programmed Cell Death. *Gene* **2002**, *296*, 139−150.
(26) Tavares, J.; Ouaissi, A.; Silva, A. M.; Lin, P. K. T.; Roy, N.; Cordeiro-da-Silva, A. Anti-Leishmanial Activity of the Bisnaphthalimidopropyl Derivatives. *Parasitol. Int.* **2012**, *61*, 360−363.
(27) Lancelot, J.; Caby, S.; Dubois-Abdesselem, F.; Vanderstraete, M.; Trolet, J.; Oliveira, G.; Bracher, F.; Jung, M.; Pierce, R. J. *Schistosoma mansoni* Sirtuins: Characterization and Potential as Chemotherapeutic Targets. *PLoS Neglected Trop. Dis.* **2013**, *7*, No. e2428.
(28) Grozinger, C. M.; Chao, E. D.; Blackwell, H. E.; Moazed, D.; Schreiber, S. L. Identification of a Class of Small Molecule Inhibitors of the Sirtuin Family of NAD-Dependent Deacetylases by Phenotypic Screening. *J. Biol. Chem.* **2001**, *276*, 38837−38843.
(29) Lara, E.; Mai, A.; Calvanese, V.; Altucci, L.; Lopez-Nieva, P.; Martinez-Chantar, M. L.; Varela-Rey, M.; Rotili, D.; Nebbioso, A.; Ropero, S.; Montoya, G.; Oyarzabal, J.; Velasco, S.; Serrano, M.; Witt, M.; Villar-Garea, A.; Inhof, A.; Mato, J. M.; Esteller, M.; Fraga, M. F. Salermide, a Sirtuin Inhibitor with a Strong Cancer-Specific Proapoptotic Effect. *Oncogene* **2009**, *28*, 781−791.
(30) Rotili, D.; Tarantino, D.; Nebbioso, A.; Paolini, C.; Huidobro, C.; Lara, E.; Mellini, P.; Lenoci, A.; Pezzi, R.; Botta, G.; Lahtela-Kakkonen, M.; Poso, A.; Steinkühler, C.; Gallinari, P.; De Maria, R.; Fraga, M.; Esteller, M.; Altucci, L.; Mai, A. Discovery of Salermide-Related Sirtuin Inhibitors: Binding Mode Studies and Antiproliferative Effects in Cancer Cells Including Cancer Stem Cells. *J. Med. Chem.* **2012**, *55*, 10937−10947.
(31) Wang, J.; Kim, T. H.; Ahn, M. Y.; Lee, J.; Jung, J. H.; Choi, W. S.; Lee, B. M.; Yoon, K. S.; Yoon, S.; Kim, H. S. Sirtinol, a Class III HDAC Inhibitor, Induces Apoptotic and Autophagic Cell Death in MCF-7 Human Breast Cancer Cells. *Int. J. Oncol.* **2012**, *41*, 1101−1109.
(32) Pasco, M. Y.; Rotili, D.; Altucci, L.; Farina, F.; Rouleau, G. A.; Mai, A.; Néri, C. Characterization of Sirtuin Inhibitors in Nematodes Expressing a Muscular Dystrophy Protein Reveals Muscle Cell and Behavioral Protection by Specific Sirtinol Analogues. *J. Med. Chem.* **2010**, *53*, 1407−1411.
(33) Du, J.; Zhou, Y.; Su, X.; Yu, J. J.; Khan, S.; Jiang, H.; Kim, J.; Woo, J.; Kim, J. H.; Choi, B. H.; He, B.; Chen, W.; Zhang, S.; Cerione, R. A.; Auwerx, J.; Hao, Q.; Lin, H. Sirt5 Is a NAD-Dependent Protein Lysine Demalonylase and Desuccinylase. *Science* **2011**, *334*, 806−809.
(34) Feldman, J. L.; Dittenhafer-Reed, K. E.; Kudo, N.; Thelen, J. N.; Ito, A.; Yoshida, M.; Denu, J. M. Kinetic and Structural Basis for

DOI: 10.1021/acs.jmedchem.9b00638
J. Med. Chem. 2019, 62, 8733−8759

Acyl-Group Selectivity and NAD + Dependence in Sirtuin-Catalyzed Deacylation. *Biochemistry* **2015**, *54*, 3037−3050.
(35) Jiang, H.; Khan, S.; Wang, Y.; Charron, G.; He, B.; Sebastian, C.; Du, J.; Kim, R.; Ge, E.; Mostoslavsky, R.; Hang, H. C.; Hao, Q.; Lin, H. SIRT6 Regulates TNF-α Secretion through Hydrolysis of Long-Chain Fatty Acyl Lysine. *Nature* **2013**, *496*, 110−113.
(36) Olsen, C. A. An Update on Lysine Deacylases Targeting the Expanding "Acylome". *ChemMedChem* **2014**, *9*, 434−437.
(37) Bao, X.; Wang, Y.; Li, X.; Li, X. M.; Liu, Z.; Yang, T.; Wong, C. F.; Zhang, J.; Hao, Q.; Li, X. D. Identification of "erasers" for Lysine Crotonylated Histone Marks Using a Chemical Proteomics Approach. *Elife* **2014**, *3*, No. e02999.
(38) Tan, M.; Peng, C.; Anderson, K. A.; Chhoy, P.; Xie, Z.; Dai, L.; Park, J.; Chen, Y.; Huang, H.; Zhang, Y.; Ro, J.; Gregory, R.; Green, M. F.; Madsen, A. S.; Schmiesing, J.; Brett, S.; Xu, G.; Ilkayeva, O. R.; Muehlbauer, M. J.; Braulke, T.; Mühlhausen, C.; Backos, D. S.; Olsen, C. A.; Mcguire, P. J.; Scott, D.; Lombard, D. B.; Hirschey, M. D.; Zhao, Y. Lysine Glutarylation Is a Protein Posttranslational Modification Regulated by SIRT5. *Cell Metab.* **2014**, *19*, 605−617.
(39) Anderson, K. A.; Huynh, F. K.; Fisher-Wellman, K.; Stuart, J. D.; Peterson, B. S.; Douros, J. D.; Wagner, G. R.; Thompson, J. W.; Madsen, A. S.; Green, M. F.; Sivley, R. M.; Ilkayeva, O. R.; Stevens, R. D.; Backos, D. S.; Capra, J. A.; Olsen, C. A.; Campbell, J. A.; Muoio, D. M.; Grimsrud, P. A.; Hirschey, M. D. SIRT4 Is a Lysine Deacylase That Controls Leucine Metabolism and Insulin Secretion. *Cell Metab.* **2017**, *25*, 838.e15−855.e15.
(40) Lin, H.; Su, X.; He, B. Protein Lysine Acylation and Cysteine Succination by Intermediates of Energy Metabolism. *Chem. Biol.* **2012**, *7*, 947−960.
(41) Feldman, J. L.; Baeza, J.; Denu, J. M. Activation of the Protein Deacetylase SIRT6 by Long-Chain Fatty Acids and Widespread Deacylation by Mammalian Sirtuins. *J. Biol. Chem.* **2013**, *288*, 31350−31356.
(42) Zhu, A. Y.; Zhou, Y.; Kahn, S.; Deitsch, K. W.; Hao, Q.; Lin, H. *Plasmodium falciparum* Sir2A Preferentially Hydrolyzes Medium and Long Chain Fatty Acyl Lysine. *ACS Chem. Biol.* **2012**, *7*, 155−159.
(43) Schiedel, M.; Marek, M.; Lancelot, J.; Karaman, B.; Almlöf, I.; Schultz, J.; Sippl, W.; Pierce, R. J.; Romier, C.; Jung, M. Fluorescence-Based Screening Assays for the NAD+-Dependent Histone Deacetylase SmSirt2 from *Schistosoma mansoni*. *J. Biomol. Screening* **2015**, *20*, 112−121.
(44) Peña, I.; Pilar Manzano, M.; Cantizani, J.; Kessler, A.; Alonso-Padilla, J.; Bardera, A. I.; Alvarez, E.; Colmenarejo, G.; Cotillo, I.; Roquero, I.; De Dios-Anton, F.; Barroso, V.; Rodriguez, A.; Gray, D. W.; Navarro, M.; Kumar, V.; Sherstnev, A.; Drewry, D. H.; Brown, J. R.; Fiandor, J. M.; Julio Martin, J. New Compound Sets Identified from High Throughput Phenotypic Screening against Three Kinetoplastid Parasites: An Open Resource. *Sci. Rep.* **2015**, *5*, No. 8771.
(45) Roquis, D.; Lepesant, J. M. J.; Picard, M. A. L.; Freitag, M.; Parrinello, H.; Groth, M.; Emans, R.; Cosseau, C.; Grunau, C. The Epigenome of *Schistosoma mansoni* Provides Insight about How Cercariae Poise Transcription until Infection. *PLoS Neglected Trop. Dis.* **2015**, *9*, No. e0003853.
(46) Heltweg, B.; Trapp, J.; Jung, M. In Vitro Assays for the Determination of Histone Deacetylase Activity. *Methods* **2005**, *36*, 332−337.
(47) Sauve, A. A.; Youn, D. Y. Sirtuins: NAD+-Dependent Deacetylase Mechanism and Regulation. *Curr. Opin. Chem. Biol.* **2012**, *16*, 535−543.
(48) Lancelot, J.; Cabezas-Cruz, A.; Caby, S.; Marek, M.; Schultz, J.; Romier, C.; Sippl, W.; Jung, M.; Pierce, R. J. Schistosome Sirtuins as Drug Targets. *Future Med. Chem.* **2015**, *7*, 765−782.
(49) North, B. J.; Marshall, B. L.; Borra, M. T.; Denu, J. M.; Verdin, E. The Human Sir2 Ortholog, SIRT2, Is an NAD+-Dependent Tubulin Deacetylase. *Mol. Cell* **2003**, *11*, 437−444.
(50) Borra, M. T.; Langer, M. R.; Slama, J. T.; Denu, J. M. Substrate Specificity and Kinetic Mechanism of the Sir2 Family of NAD +-Dependent Histone/Protein Deacetylases. *Biochemistry* **2004**, *43*, 9877−9887.
(51) Rumpf, T.; Schiedel, M.; Karaman, B.; Roessler, C.; North, B. J.; Lehotzky, A.; Olàh, J.; Ladwein, K. I.; Schmidtkunz, K.; Gajer, M.; Pannek, M.; Steegborn, C.; Sinclair, D. A.; Gerhardt, S.; Ovàdi, J.; Schutkowski, M.; Sippl, W.; Einsle, O.; Jung, M. Selective Sirt2 Inhibition by Ligand-Induced Rearrangement of the Active Site. *Nat. Commun.* **2015**, *6*, No. 6263.
(52) Hoffmann, G.; Breitenbücher, F.; Schuler, M.; Ehrenhofer-Murray, A. E. A Novel Sirtuin 2 (SIRT2) Inhibitor with P53-Dependent pro-Apoptotic Activity in Non-Small Cell Lung Cancer. *J. Biol. Chem.* **2014**, *289*, 5208−5216.
(53) Swyter, S.; Schiedel, M.; Monaldi, D.; Sippl, W.; Lehotzky, A.; Rumpf, T.; Ovàdi, J.; Jung, M. New Chemical Tools for Probing Activity and Inhibition of the NAD+-Dependent Lysine Deacylase Sirtuin 2. *Philos. Trans. R. Soc., B* **2018**, *373*, No. 20170083.
(54) Panic, G.; Vargas, M.; Scandale, I.; Keiser, J. Activity Profile of an FDA-Approved Compound Library against *Schistosoma mansoni*. *PLoS Neglected Trop. Dis.* **2015**, *9*, No. e0003962.
(55) Abdulla, M. H.; Ruelas, D. S.; Wolff, B.; Snedecor, J.; Lim, K. C.; Xu, F.; Renslo, A. R.; Williams, J.; McKerrow, J. H.; Caffrey, C. R. Drug Discovery for Schistosomiasis: Hit and Lead Compounds Identified in a Library of Known Drugs by Medium-Throughput Phenotypic Screening. *PLoS Neglected Trop. Dis.* **2009**, *3*, No. e478.
(56) Schiedel, M.; Rumpf, T.; Karaman, B.; Lehotzky, A.; Oláh, J.; Gerhardt, S.; Ovádi, J.; Sippl, W.; Einsle, O.; Jung, M. Aminothiazoles as Potent and Selective Sirt2 Inhibitors: A Structure-Activity Relationship Study. *J. Med. Chem.* **2016**, *59*, 1599−1612.
(57) Green, B. T.; Lee, S. T.; Welch, K. D.; Panter, K. E. Plant Alkaloids That Cause Developmental Defects through the Disruption of Cholinergic Neurotransmission. *Birth Defects Res., Part C* **2013**, *99*, 235−246.
(58) Barradas, S.; Hern, G.; Urbano, A.; Carre, M. C. Total Synthesis of Natural p-Quinol Cochinchinenone. *Org. Lett.* **2012**, *14*, 5952−5955.
(59) Biscoe, M. R.; Fors, B. P.; Buchwald, S. L. A New Class of Easily Activated Palladium Precatalysts for Facile C−N Cross-Coupling Reactions and the Low Temperature Oxidative Addition of Aryl Chlorides. *J. Am. Chem. Soc.* **2008**, *130*, 6686−6687.
(60) Vicker, N.; Xiangdong, S.; Ganeshapillai, D.; Purhoit, A.; Reed, M. J.; Potter, B. Phenyl Carboxamide and Sulfonamide Derivatives for Use as 11-Beta-Hydroxysteroid Dehydrogenase. WO2005042513A1, 2005.
(61) Spiegelman, N. A.; Price, I. R.; Jing, H.; Wang, M.; Yang, M.; Cao, J.; Hong, J. Y.; Zhang, X.; Aramsangtienchai, P.; Sadhukhan, S.; Hening, L. Direct Comparison of SIRT2 Inhibitors: Potency, Specificity, Activity-Dependent Inhibition, and On-Target Anticancer Activities. *ChemMedChem* **2018**, *13*, 1890−1894.
(62) Hamid, M. H. S. A.; Allen, C. L.; Gareth, W.; Maytum, H. C.; Maxwell, A. C.; Watson, A. J. A.; Williams, J. M. J. Ruthenium-Catalyzed N-Alkylation of Amines and Sulfonamides Using Borrowing Hydrogen Methodology. *J. Am. Chem. Soc.* **2009**, *131*, 1766−1774.
(63) Lovering, J. R.; Ridd, J. H.; Parker, D. G.; Rose, J. B. Polymerisation and Related Reactions Involving Nucleophilic Aromatic Substitution. Part 2.' The Rates of Reaction of Substituted 4-Halogenobenzophenones with the Salts of Substituted Hydroquinones. *J. Chem. Soc., Perkin Trans. 2* **1988**, 1735−1738.
(64) Zhao, Y.; Wang, Y.; Sun, H.; Li, L.; Zhang, H. Ullmann Reaction in Tetraethyl Orthosilicate: A Novel Synthesis of Triarylamines and Diaryl Ethers. *Chem. Commun.* **2007**, 3186−3188.
(65) Yang, Y.; Yu, Y.; Li, X.; Li, J.; Wu, Y.; Yu, J.; Ge, J.; Huang, Z.; Jiang, L.; Rao, Y.; Yang, M. Target Elucidation by Co-Crystal Structures of NADH-Ubiquinone Oxidoreductase of *Plasmodium falciparum* (Pf NDH2) with Small Molecule to Eliminate Drug-Resistant Malaria. *J. Med. Chem.* **2017**, *60*, 1994−2005.
(66) Breyoltz, H.-J.; Schäfers, M.; Wagner, S.; Höltke, C.; Faust, A.; Rabeneck, H.; Levkau, B.; Schober, O.; Kopka, K. C-5-Disubstituted

DOI: 10.1021/acs.jmedchem.9b00638
J. Med. Chem. 2019, 62, 8733−8759

Barbiturates as Potential Molecular Probes for Noninvasive Matrix Metalloproteinase Imaging. *J. Med. Chem.* **2005**, *48*, 3400−3409.
(67) Wakchaure, V. N.; Kaib, P. S. J.; Leutzsch, M.; List, B. Disulfonimide-Catalyzed Asymmetric Reduction of *N*-Alkyl Imines. *Angew. Chem., Int. Ed.* **2015**, *54*, 11852−11856.
(68) Ramalho-Pinto, F. J.; Gazzinelli, G.; Howells, R. E.; Mota-Santos, T. A.; Figueiredo, E. A.; Pellegrino, J. *Schistosoma mansoni*: Defined System for Stepwise Transformation of Cercaria to Schistosomule in Vitro. *Exp. Parasitol.* **1974**, *36*, 360−372.
(69) Smithers, S. R.; Terry, R. J. The Infection of Laboratory Hosts with Cercariae of *Schistosoma mansoni* and the Recovery of the Adult Worms. *Parasitology* **1965**, *55*, 695−700.
(70) Sander, T.; Freyss, J.; von Korff, M.; Rufener, C. DataWarrior: An Open-Source Program For Chemistry Aware Data Visualization And Analysis. *J. Chem. Inf. Model.* **2015**, *55*, 460−473.

DOI: 10.1021/acs.jmedchem.9b00638
J. Med. Chem. 2019, 62, 8733−8759

Article 5

Design, synthesis, and biological evaluation of dual targeting inhibitors of histone deacetylase 6/8 and bromodomain BRPF1

European Journal of Medicinal Chemistry 200 (2020) 112338

Contents lists available at ScienceDirect

European Journal of Medicinal Chemistry

journal homepage: http://www.elsevier.com/locate/ejmech

Research paper

Design, synthesis, and biological evaluation of dual targeting inhibitors of histone deacetylase 6/8 and bromodomain BRPF1

Ehab Ghazy [a], Patrik Zeyen [a], Daniel Herp [b], Martin Hügle [b], Karin Schmidtkunz [b], Frank Erdmann [a], Dina Robaa [a], Matthias Schmidt [a], Elizabeth R. Morales [c], Christophe Romier [c], Stefan Günther [b], Manfred Jung [b], Wolfgang Sippl [a, *]

[a] Institute of Pharmacy, Martin-Luther University of Halle-Wittenberg, 06120, Halle/Saale, Germany
[b] Institute of Pharmaceutical Sciences, University of Freiburg, 79104, Freiburg, Germany
[c] Département de Biologie Structurale Intégrative, Institut de Génétique et Biologie Moléculaire et Cellulaire (IGBMC), Université de Strasbourg, CNRS, INSERM, 67404, Illkirch Cedex, France

ARTICLE INFO

Article history:
Received 17 February 2020
Received in revised form
9 April 2020
Accepted 13 April 2020
Available online 18 May 2020

Keywords:
Epigenetics
Dual targeting inhibitors
HDAC6
HDAC8
Bromodomain
BRPF1
Hydroxamic acids
Acute myeloid leukemia

ABSTRACT

Histone modifying proteins, specifically histone deacetylases (HDACs) and bromodomains, have emerged as novel promising targets for anticancer therapy. In the current work, based on available crystal structures and docking studies, we designed dual inhibitors of both HDAC6/8 and the bromodomain and PHD finger containing protein 1 (BRPF1). Biochemical and biophysical tests showed that compounds **23a,b** and **37** are nanomolar inhibitors of both target proteins. Detailed structure-activity relationships were deduced for the synthesized inhibitors which were supported by extensive docking and molecular dynamics studies. Cellular testing in acute myeloid leukemia (AML) cells showed only a weak effect, most probably because of the poor permeability of the inhibitors. We also aimed to analyse the target engagement and the cellular activity of the novel inhibitors by determining the protein acetylation levels in cells by western blotting (tubulin vs histone acetylation), and by assessing their effects on various cancer cell lines.

1. Introduction

Post-translational modifications (PTMs) of histones, along with DNA methylation, are the most extensively studied pathways of epigenetic control of gene expression [1]. Histones are subject to various PTMs that include acylation, acetylation, methylation, phosphorylation, and ubiquitination. Acetylation of lysine residues of histones is a dynamic process which results in opening up the chromatin structure. This leads to an increase in the accessibility of the DNA by the transcription machinery and is usually associated with increased gene expression [2–4]. The state of histone acetylation is controlled by different regulators, namely writer proteins; (histone acetyltransferases (HATs)), reader proteins; (bromodomains (BRDs)), and eraser proteins; (histone deacetylases (HDACs)). Deregulation of these key players, and consequently abnormal acetylation levels, is linked to several pathologies such as inflammatory, metabolic, and cardiovascular diseases, and more clearly cancer [5–10].

Bromodomains usually occur as an integral part of larger protein complexes. Due to their ability to specifically recognize ε-*N*-acetylated lysine residues, they are generally responsible - together with other epigenetic readers - for the recruitment of transcription factors to chromatin. The human proteome contains 61 bromodomains, which are present within 46 different proteins and are classified into eight distinct families [11,12]. Due to their relation to different malignancies and their druggability, they have emerged as promising targets for anticancer therapy. Many inhibitors showed notable potency and selectivity in biochemical and biophysical assays against different bromodomain classes, together with significant in vitro activity against various tumor cell lines (reviewed in Ref. [13,14]). The bromodomain and PHD finger containing protein (BRPF) family has recently received increasing interest to

* Corresponding author. Wolfgang-Langenbeck-Str. 4, 06120, Halle (Saale), Germany.
E-mail address: Wolfgang.sippl@pharmazie.uni-halle.de (W. Sippl).

https://doi.org/10.1016/j.ejmech.2020.112338
0223-5234/

elucidate its physiological role and pathological functions. BRPFs have multiple reader domains, including a bromodomain, and act as a scaffold for the recruitment and assembly of the histone acetyltransferases of the MYST family. Normal activity of these HATs is essential for different physiological processes, whereas their deregulation is associated with overexpression of oncogenes and development of different tumors, more notably leukemia [15–17]. Several BRPF inhibitors containing a 1,3-dimethyl benzimidazolone scaffold were reported (Fig. 1; compound I), which not only showed high potency and selectivity against the BRPF family, but in some cases also subtype selectivity for BRPF1 [18,19]. This scaffold was also utilized to design dual targeting inhibitors of BRPF1 and the transcription factor TRIM24 (e.g. compound II, Fig. 1) as well as dual inhibitors of BRPF and other bromodomains [20–23]. Another group reported a pan BRPF inhibitor containing a 1,3-dimethylquinolin-2-one scaffold (e.g. compound III; Fig. 1) that showed low nanomolar potency against BRPFs and excellent selectivity [24,25]. Recently, a hit-to-lead campaign identified a 1,4-dimethyl-2,3-dioxo-quinoxaline (e.g. compound IV; Fig. 1) and 2,4-dimethyloxazole derivatives as low micromolar probes for BRPF1 with good selectivity [26,27].

HDACs are a group of enzymes responsible for the removal of acyl groups from acylated lysine residues in histones and non-histone proteins. HDACs comprise 18 isoforms categorized into 4 classes differing in size, cellular distribution, substrate, and mechanism of catalytic activity. The deacetylase activity of classical HDACs (class I, II and IV) is mediated through zinc ion, while sirtuins (class III) depend on nicotinamide adenine dinucleotide (NAD^+) for their action [28,29]. Given the large variation of their substrates, HDACs regulate diverse physiological processes, in addition to their epigenetic role. Their aberrant activity is linked to different pathologies such as cardiac hypertrophy [30,31], neurodegenerative diseases [32,33], viral infections [34,35], and cancer [36,37]. As a result, a lot of effort has been devoted to the development of HDAC inhibitors (HDACi) to fully reveal their physiological role. This work has already resulted in a large number of promising probes and some candidates in clinical trials (either as single agents or in combination therapy). Four drugs for the treatment of specific hematological malignancies have been approved by the FDA [38]. However, currently FDA approved drugs are pan HDAC inhibitors, with several side effects such as cardiotoxicity. This necessitates the design of selective HDAC inhibitors for disease-related isoforms [39–41].

The quest for selective HDAC6 and 8 inhibitors is of high importance given their specific role in different disorders and limited side effects that observed from their inhibition or knockdown studies. HDAC6 is a class IIb isoform that localizes in the cytoplasm, and deacetylates mainly non-histone proteins including α-tubulin, cortactin and heat-shock protein 90 (Hsp90) [42,43]. Over the last decade, a variety of HDAC6 selective inhibitors (in vitro) were reported ([44–50] and reviewed [51]) showing nanomolar inhibitory activity, good in vitro selectivity over other isoforms in biochemical assays (Fig. 2), and some also exhibited promising in vitro activity against various cancer cell lines. Additionally HDAC6 deregulation is associated with different neurodegenerative disorders, inflammatory and rare diseases [52–55], and its selective inhibitors could represent a valuable tool to study the mechanisms underlying these diseases and/or a potential therapeutic tool to treat them. Recently published studies have however shown that selective HDAC6 inhibition in cells is not sufficient for an anti-cancer effect and that the observed anti-cancer effect of reported HDAC6 inhibitors might be the result of inhibiting other HDACs or other off-targets [56,57]. Class I member HDAC8 localizes to either the nucleus or the cytoplasm, and therefore can interact with non-histone proteins such as cortactin, SMC3, ERRα and p53. HDAC8 is associated with a wide variety of tumors, and recent evidence suggests a potential therapeutic benefit from its inhibition [58,59]. Recent research also revealed some unique structural features in this isoform, which distinguish it from other HDACs and which can be utilized to design selective inhibitors [60]. As a result, a variety of probes emerged (Fig. 3) that showed preferential in vitro inhibition of HDAC8 compared to other isoforms ([61–66], reviewed in Ref. [67,68]).

Several studies suggest that combination therapies of epigenetic modulators could achieve better clinical results than a monotherapy, especially against solid and resistant tumors (reviewed in Ref. [69]). As a result, the polypharmacology concept was extended to the epigenetics field, assuming that a multi-target inhibitor could be more effective than single agents. Moreover, such an inhibitor is postulated to show higher therapeutic efficacy, better predictable pharmacokinetic profile, and improved patient compliance as compared to a combination therapy. In this context, several dual acting HDACi were designed to interact with a second target such as kinases, metalloproteinases, topoisomerases, and others (reviewed in details in Ref. [70]). Bromodomains received also some interest in this regard, as some dual bromodomain/kinase inhibitors were investigated [71–74]. Of particular relevance to the current work are the attempts to design dual HDAC/BRD epigenetic inhibitors [75–79]. In all of the reported studies, the rationale was to change the cap group of HDACi, mostly SAHA, to a reported BRD4 inhibiting pharmacophore. Indeed, the authors were not only able to achieve dual inhibitory activity for some compounds (Fig. 4), but also promising in vitro activity against some cancer cell lines. However, the results failed to show superior activity over the original HDAC or BRD inhibitors. Additionally, little information was given regarding the selectivity of these dual inhibitors on different HDAC isoforms.

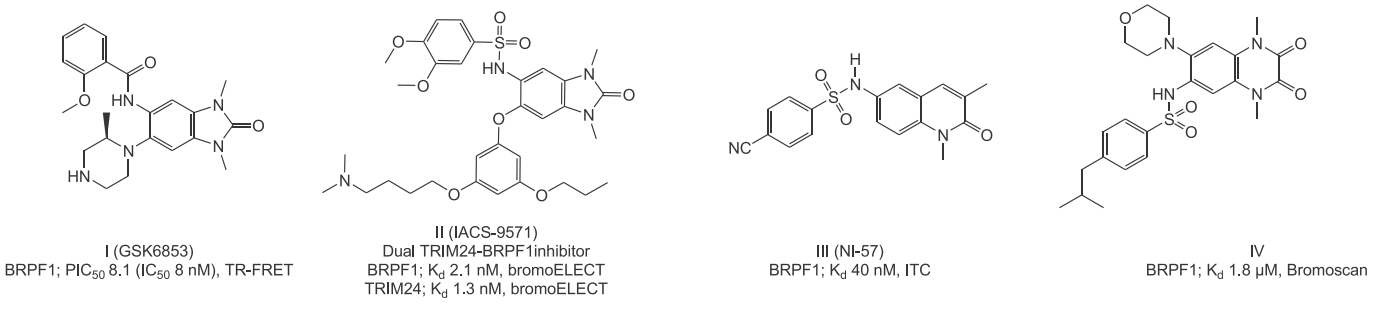

Fig. 1. Examples of previously reported BRPF bromodomain inhibitors.

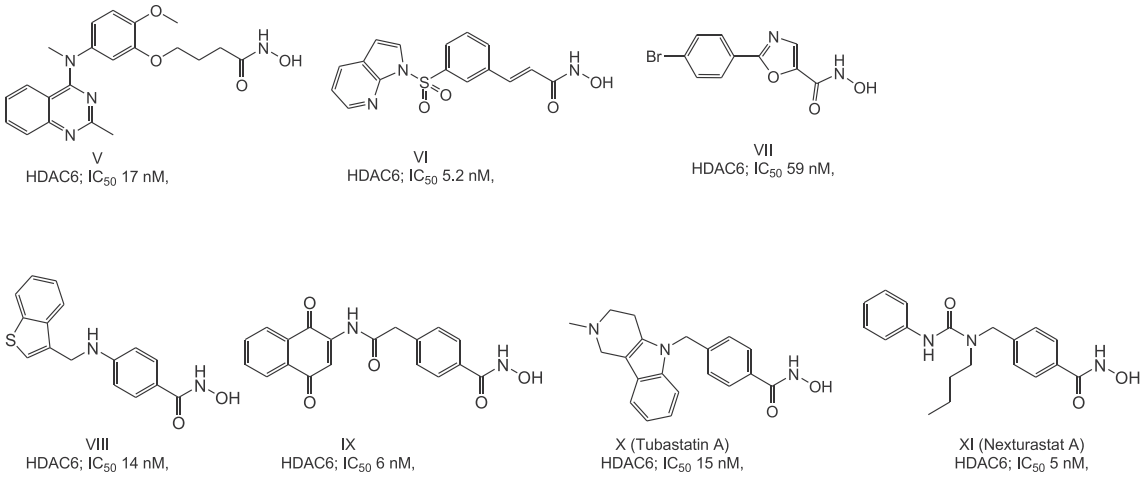

Fig. 2. Examples of previously reported HDAC6 inhibitors.

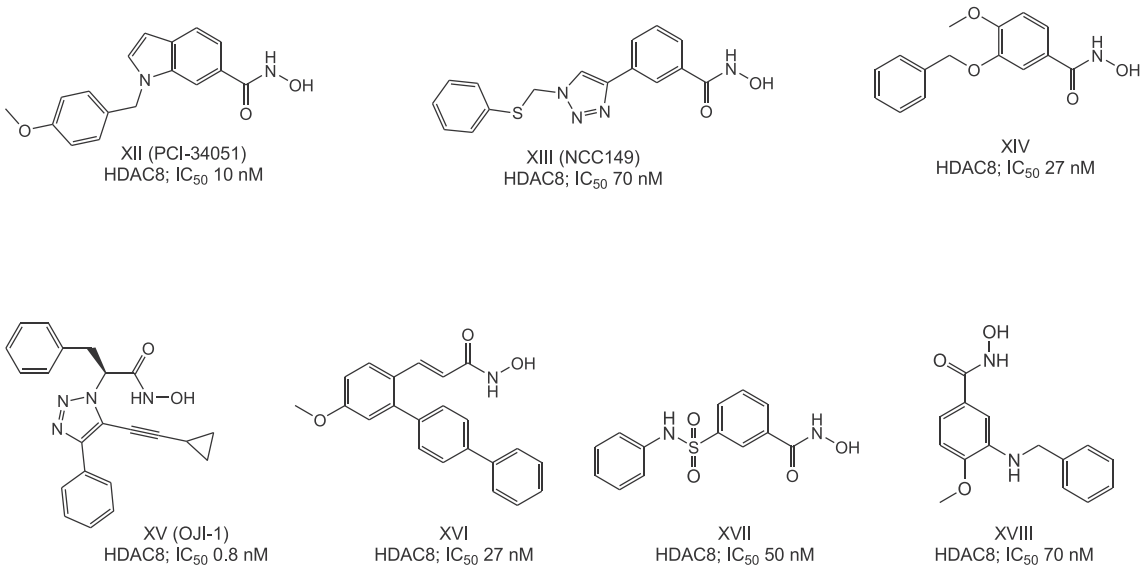

Fig. 3. Examples of previously reported HDAC8 inhibitors.

Therefore we wanted to focus on the design of dual targeting inhibitors based on isoform selective HDACi. We have previously reported the structural guided design, optimization and synthesis of benzhydroxamic acids as potent and selective HDAC8 inhibitors [64,80]. These inhibitors were used as starting point, as we set to modify their structure by including a bromodomain inhibiting scaffold. We decided to target the BRPF1 bromodomain rather than the extensively studied BRD4 from the bromodomain and extra-terminal motif (BET) family. BRPF1 was chosen in the current study due to the reported activity of BRPF1 inhibitors against several cancer cell lines as well as due to the availability of crystal structures in complex with inhibitors. In addition, some BRPF1 inhibitors were reported to selectively inhibit it over other bromodomains and BRPF isoforms. Guided by molecular modelling studies, the essential structural features for binding to both targets were merged to come up with dual targeting inhibitors for HDAC8 and BRPF1. Moreover, we extended the scope of our dual targeting inhibitors to selectively target HDAC6 and BRPF1. We report on the synthesis and in vitro testing of dual targeting inhibitors against specific HDAC isoforms and non-BET bromodomains.

2. Results and discussion

2.1. HDAC8/BRPF1 inhibitors

Our previously reported HDAC8 inhibitors were designed, so that the benzhydroxamic acid moiety, which occupies the lysine tunnel and chelates the zinc ion, is linked to an aromatic cap group through amine, amide, inverse amide and ether moieties. These two-atom linkers provided additional interactions with the enzyme, and together with the *meta*-substitution pattern contributed to the HDAC8 selectivity [64]. According to our experience with HDAC8 inhibitors, *meta*-substitution of the cap group with respect to the benzhydroxamic acid moiety is important for selective inhibition. These findings were also supported by other groups [61,81]. In the current work, we first maintained this substitution pattern and chose the 1,3-dimethylquinolin-2-one to serve as a cap group and BRPF targeting scaffold. This moiety was selected as it contains the essential features to bind BRPF1, namely the *N*-methyl and carbonyl groups to fit in the acetyllysine binding pocket, and the 3-methyl substituent to increase the hydrophobic interactions

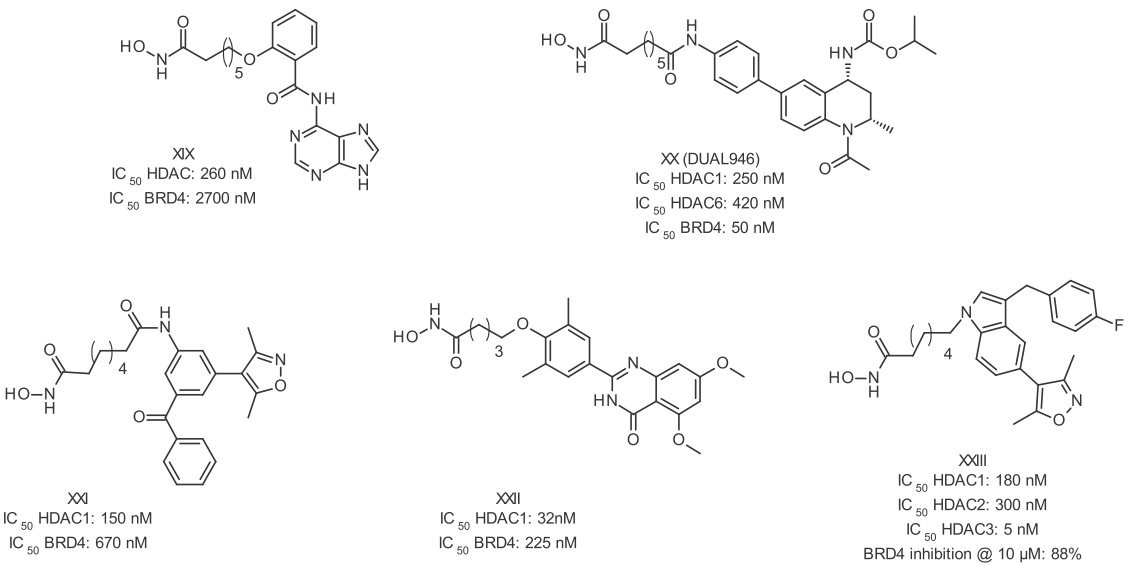

Fig. 4. Previously reported dual HDAC/BRD inhibitors.

with the bromodomain [24]. This ring is also chemically advantageous since it can be easily synthesized and functionalized with an amino group at position 6 to attach the benzhydroxamic acid moiety. Finally, BRDi containing this scaffold showed nanomolar potency against BRPF1, and excellent selectivity over other bromodomains [24,25]. Compounds **17a,b** and **20a,b** were generated (Fig. 5) by retaining the amine and inverse amide two-atom linkers as found in our original HDAC8i. Meanwhile in compounds **23a,b**, we introduced a sulfamoyl linker [61] to retain the bent conformation of the original BRPF1 inhibitor [24]. The previous compounds are designed to block either of the targets. We then designed a structurally different dual HDAC8/BRPF1 inhibitor **32**. The idea here was not to modify the cap group of our previously reported selective HDAC8i **XVIII** but rather to attach it as an intact unit through a relatively longer linker to the 1,3-dimethylquinolin-2-one scaffold (Fig. 5).

We determined the activity of compounds **17a,b**, **20a,b** and **23a,b** on human recombinant HDAC8 (Table 1). As expected, all the compounds showed a good inhibitory activity, with the amide derivatives **17a** and **17b** showing the lowest IC_{50} values (113 and 65 nM). This was in accordance with our previous observation that this orientation of the amide bond is favorable for the interaction with HDAC8 [64]. Compounds **20a,b**, bearing an amine linker, showed lower activity, while the sulfonamides **23a,b** displayed the lowest inhibitory activity, albeit IC_{50} values still remained in the submicromolar range. As expected, docking studies of these *meta*-substituted derivatives in HDAC8 show the capping group, i.e. the 1,3-dimethylquinolin-2-one scaffold, accommodated in the HDAC8-specific side pocket where it undergoes π-π stacking interactions with Tyr306 (Fig. 6).

The most active compound on hHDAC8 **17a** and the sulfonamide derivatives **23a,b** were then selected for the BRPF1 binding assay,

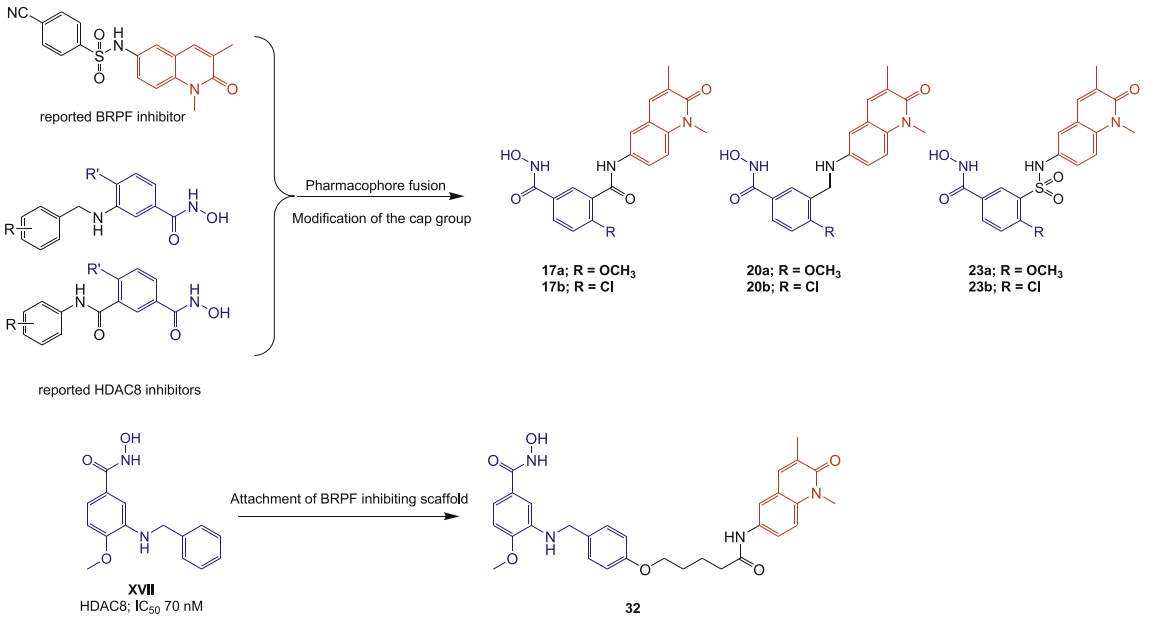

Fig. 5. Design of dual targeting HDAC8/BRPF1 inhibitors.

Table 1
Inhibitory activity of the HDAC8/BRPF1 inhibitors against different human HDACs and BRPF1. Recombinant HDAC1,6,8 and fluorogenic peptide substrates (HDAC1,6: ZMAL (Z (Ac)Lys-AMC), HDAC8: Fluor-de-Lys) were used for enzymatic testing. BRPF1 binding was measured by isothermal titration calorimetry.

Compound	IC_{50} (nM)/% inhibition HDAC1	IC_{50} (nM)/% inhibition HDAC6	IC_{50} (nM) HDAC8	K_d BRPF1 (nM)	$P99_{K_d}$(nM)
17a	6900 ± 500	709 ± 174	65 ± 7	857	690 - 1065
17b	n.d.	n.d.	113 ± 9	n.d.	n.d.
20a	0 @ 1 μM 31 @10 μM[a]	40 @ 1 μM 68 @ 10 μM[a]	555 ± 169	n.d.	n.d.
20b	0 @ 1 μM 20 @10 μM[a]	28 @ 1 μM 84 @ 10 μM[a]	3193 ± 660	n.d.	n.d.
23a	6 @ 1 μM 38 @ 10 μM[b]	21 @ 1 μM 64 @ 10 μM[b]	443 ± 23	67	55–82
23b	13 @ 1 μM 31 @ 10 μM	13 @ 1 μM 59 @10 μM	560 ± 42	234	198–275
32	5200 ± 1100	50 @ 1 μM 68 @ 10 μM[b]	956 ± 74	4080	2544 - 6022

n.d.: not determined. For K_d BRPF1 the *P99* interval is given.
[a] Self-fluorescence of the compounds hindered measurements at concentrations above 10 μM.
[b] Solubility problems at higher concentration hindered IC_{50} value determination.

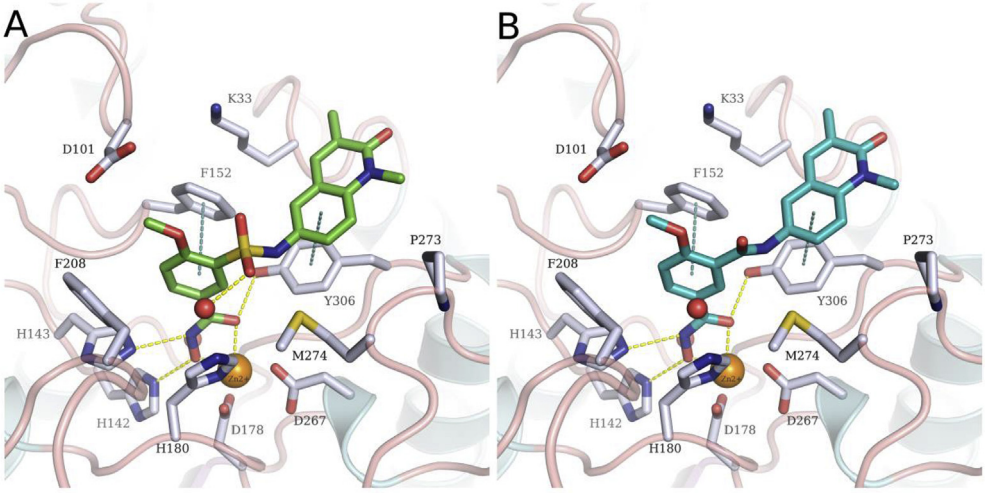

Fig. 6. A. Predicted binding mode of **23a** (green sticks) in HDAC8 (PDB ID 2V5X). **B**. Predicted binding mode of **17a** (cyan sticks) in HDAC8 (PDB ID 2V5X). The ligands are shown as cyan sticks, side chains of binding site residues as white sticks, water molecules as red spheres and the catalytic zinc ion as orange sphere. Yellow-dashed lines indicate hydrogen bond interactions or metal-coordination, while cyan-dashed lines depict π-π stacking interactions. (For interpretation of the references to colour in this figure legend, the reader is referred to the Web version of this article.)

where the amide derivative **17a** showed only a modest affinity. Interestingly, the sulfonamides **23a,b** had a much better affinity with K_d values in the nanomolar range. In order to rationalize the difference in the activities between the sulfonamide and amide derivatives (**23a** and **17a**, respectively), docking studies were performed into the crystal structure of BRPF1 in complex with **NI-57** (PDB ID 5MYG) using Glide (Schrödinger LLC, NEW York, USA). Our docking studies revealed that compounds bearing a sulfonamide linker, as exemplified by **23a** in (Fig. 7A), could adopt a highly similar binding conformation as the co-crystallized ligand. The quinolinone ring of **23a** is embedded in the acetyllysine site, showing the conserved hydrogen bond interaction with Asn708 and a water molecule mediated hydrogen bond with Tyr665. In addition, two π-π stacking interactions between the side chain of Phe714 and the quinolone ring on the one hand and the phenyl ring on the other hand, were observed. Meanwhile, the amide linker in **17a** prevents the compound from adopting the bent conformation observed in compounds bearing a sulfonamide linker. The predicted binding mode shows that the benzhydroxamic acid moiety is solvent-exposed (Fig. 7B) which explains its significantly decreased activity.

We then tested the activity of the most promising compounds on the class I member HDAC1 and class IIb HDAC6, where they generally showed weak inhibition (Table 1). From this series, we were able to identify compounds **23a,b** as nanomolar inhibitors of both HDAC8 and BRPF1, which showed low in vitro activity against HDAC1 and 6.

Compound **32** showed only a modest activity against hHDAC8 and only weak micromolar activity against BRPF1.

2.2. HDAC6/BRPF1 inhibitors

In order to target HDAC6, we took advantage of the common structure characteristics of selective HDAC6 inhibitors [81]. They are usually aromatic hydroxamic acids with a cap group located in the *para* position. The linker consists of one to three atoms often including a methylene group. As we already have the bulky 1,3-dimethylquinolin-2-one as a cap group, we hypothesized that shifting it to the *para*-position would shift the activity to HDAC6, and hence dual HDAC6/BRPF1 inhibitors could be obtained (Fig. 8). For this series, we generally retained the sulfamoyl linker since the compounds containing this linker **23a,b** from the HDAC8/BRPF1 series showed the highest affinity for BRPF1 bromodomain. While in compound **37** we retained the two-atom sulfamoyl bridge, we incorporated an additional methylene group in compounds **44a,b**.

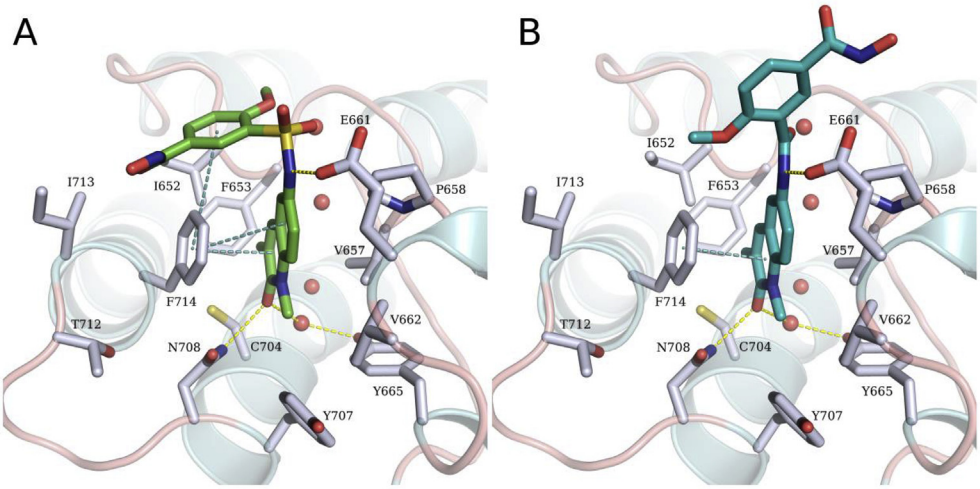

Fig. 7. A. Predicted binding mode of **23a** (green sticks) in BRPF1. **B**. Predicted binding mode of **17a** (cyan sticks) in BRPF1. The ligands are shown as green sticks, side chains of binding site residues as white sticks, and water molecules as red spheres. Yellow-dashed lines indicate hydrogen bond interactions and cyan-dashed lines π-π stacking interactions. (For interpretation of the references to colour in this figure legend, the reader is referred to the Web version of this article.)

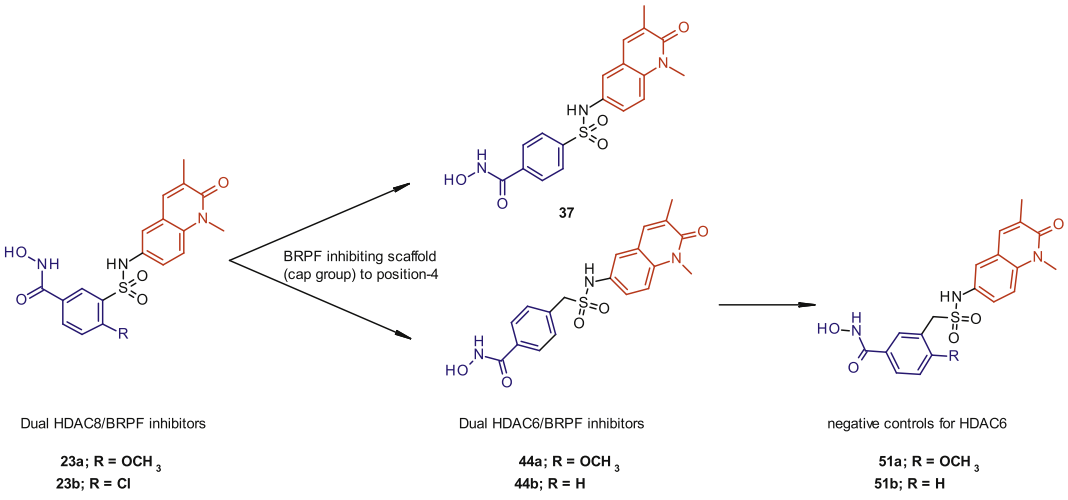

Fig. 8. Design of dual HDAC6/BRPF1 inhibitors.

To further prove the effect of the substitution pattern on HDAC isoform selectivity, compounds with *meta* substitution pattern **51a,b** were synthesized as negative controls for HDAC6 inhibition (isomers of **44a,b** respectively).

These five compounds were first tested in vitro for HDAC inhibition, where the *para* substituted compounds **37** and **44b** showed, as expected, IC_{50} values in the nanomolar range (Table 2). However, both compounds did not show pronounced selectivity and inhibited HDAC1, 6 and 8 in submicromolar concentrations. The observed HDAC6 inhibitory activity could be strongly attributed to the 4-substitution pattern of the cap group, as the *meta* substituted compounds from the first series **23a,b** and the control compound

Table 2
Inhibitory activity of the HDAC6/BRPF1 inhibitors against different human HDACs and BRPF1. Recombinant HDAC1,6,8 and fluorogenic peptide substrates (HDAC1,6: ZMAL (Z(Ac)Lys-AMC), HDAC8: Fluor-de-Lys) were used for enzymatic testing. BRPF1 binding was measured by isothermal titration calorimetry.

Compound	IC_{50} (nM)/% inhibition HDAC1	IC_{50} (nM)/% inhibition HDAC6	IC_{50} (nM) HDAC8	K_d BRPF1 (nM)	$P99_{K_d}$ (nM)
37	797 ± 282 nM	344 ± 41	908 ± 274	175.2	160–193
44a	11 @ 1 μM	15 @ 1 μM	231 ± 24	1582	1402–1609
	29 @ 10 μM[a]	46 @ 10 μM[a]			
44b	545 ± 59 nM	152 ± 13	360 ± 44	1497	1358–1652
51a	4 @ 1 μM	14 @ 1 μM	158 ± 21	n.d.	n.d.
	29 @ 10 μM	63 @ 10 μM			
51b	2 @ 1 μM	3 @ 1 μM	465 ± 72	n.d.	n.d.
	26 @ 10 μM	33 @ 10 μM			

n.d.: not determined. For K_d BRPF1 the *P99* interval is given.
[a] Solubility problems at higher concentration hindered IC_{50} value determination.

51b showed only a very weak HDAC6 inhibitory activity. Interestingly, compound **44a** did not show the expected HDAC6 activity, despite the 4-substitution pattern of the cap group, suggesting that the introduction of an *ortho* methoxy group (with respect to the cap group) has a negative effect on the activity against HDAC6. Docking of **37** and **44b** into HDAC6 showed that both compounds adopt a highly similar binding mode (Fig. 9), where the hydroxamic acid group is able to chelate the catalytic zinc ion in a monodentate fashion and undergo a hydrogen bond interaction with the side chain of Tyr 782 in addition to a water mediated interaction. Meanwhile the quinolone capping group is embedded in a hydrophobic region lined with Phe620 and His500 and undergoes and additional hydrogen bond interaction with Asn494. An additional *ortho* methoxy substitution, as found in **44a**, would lead in this case to a steric clash with the side chain of Leu749, which might explain the loss of HDAC6 inhibitory activity.

The *para*-substituted compounds **37** and **44a,b** were also tested in the BRPF1 binding assay (Table 2), where only **37** showed a nanomolar K_d value. The introduction of the additional methylene group in the linker of **44a,b** remarkably decreased the BRPF1 affinity (almost 9fold decrease for **44b** compared to **37**). In order to comprehend the observed negative effect of an additional methylene group in the linker on the BRPF1 affinity, we first performed docking into the crystal structure of BRPF1 as previously described. Compound **37** could maintain the same binding conformation as the co-crystallized ligand, where the quinolinone ring shows the conserved hydrogen bond interaction with Asn708 and a water mediated hydrogen bond with Tyr665, in addition to π-π stacking interactions between the side chain of Phe714 (Fig. 10A). Moreover, the benzhydroxamic moiety is placed in a perpendicular T-shaped orientation to the side chain of Phe714 where it can undergo π-π stacking interactions. Meanwhile, the docking pose of compound **44b** shows that it similarly adopts a bent conformation, where the benzhydroxamic moiety is still placed in the vicinity of Phe714 (Fig. 10B). Notably, the predicted binding mode compound **37** perfectly overlaps with the cocrystallized analogue **NI-57**, while in **44b** the benzhydroxamic group shows a strong deviation (Fig. 10C). We postulated that, owing to the flexibility of the methylene-sulfamoyl linker in **44b**, the predicted binding mode is not stable. In order to investigate this hypothesis, molecular dynamics (MD) simulations of the predicted complexes of BRPF1 with **37** and **44b** were performed using Amber16. These revealed that, as expected, the predicted binding mode of **37** in BRPF1 is highly stable with the ligand having a root mean square deviation (RMSD) below 2.5 Å throughout the 100 ns MD simulation (Fig. 10D and Video 1 suppl.). Meanwhile, the binding mode of **44b** is highly unstable (Fig. 10E) and the benzhydroxamic moiety becomes majorly solvent-exposed (Video 2 suppl.). The applied MD simulation setup was also validated using the cocrystal structure of BRPF1 with **NI-57** (Fig. S7, Supporting Information).

Supplementary video related to this article can be found at https://doi.org/10.1016/j.ejmech.2020.112338

We then tested the activity of the most promising compounds on HDAC1 where they generally showed no or low inhibition (Table 2). Testing on HDAC8 showed that compound **44a** has a good inhibitory activity against HDAC8 with an IC_{50} value in the low nanomolar range.

Among this group of inhibitors, compound **37** appeared to be the best HDAC6/BRPF1 dual inhibitor showing a nanomolar in vitro inhibitory activity against both targets, and in vitro selectivity over HDAC1 and 8.

In addition we synthesized several control compounds including a dimeric BRPF1i compound **38** (Scheme 3) and carboxylic esters **21**, **35** and **42b** (analogs of **23a**, **37** and **44b**) lacking the hydroxamic acid functionality.

2.3. Cellular assay

The first objective of our cellular assays was to determine the potential toxicity of our compounds on normal cells. Therefore, the compounds were tested in a human epithelial kidney cell line (HEK293). We also incorporated some of the intermediate carboxylic acids and esters in the assay as negative controls. The majority of the compounds showed no effect on HEK 293 cells, except for **32** which displayed only 15% viability of the cells. It is also worth mentioning that some esters showed more toxic effects compared to their corresponding hydroxamic acids, such as **21** and **23a**. Viability of HEK293 cells upon treatment with our compounds is provided in supporting information, **S5**.

Our second objective was to assess the potential anti-proliferative effects on cancer cell lines. As previously mentioned, HDAC and BRD are interesting targets for the anticancer therapy,

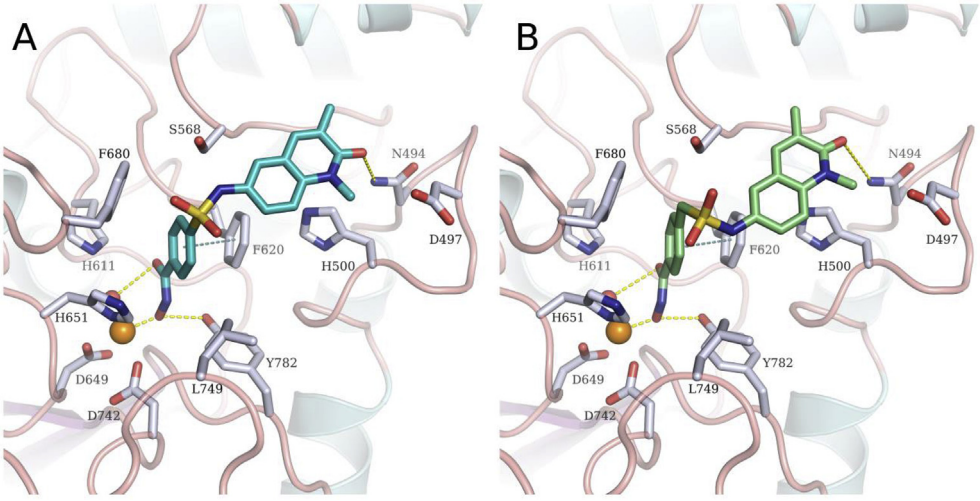

Fig. 9. A. Predicted binding mode of **37** (cyan sticks) in HDAC6 (PDB ID 5EDU). **B**. Predicted binding mode of **44b** (green sticks) in HDAC6. The ligands are shown as green sticks, side chains of binding site residues as white sticks, and water molecules as red spheres. Yellow-dashed lines indicate hydrogen bond interactions or metal coordination and cyan-dashed lines π-π stacking interactions. (For interpretation of the references to colour in this figure legend, the reader is referred to the Web version of this article.)

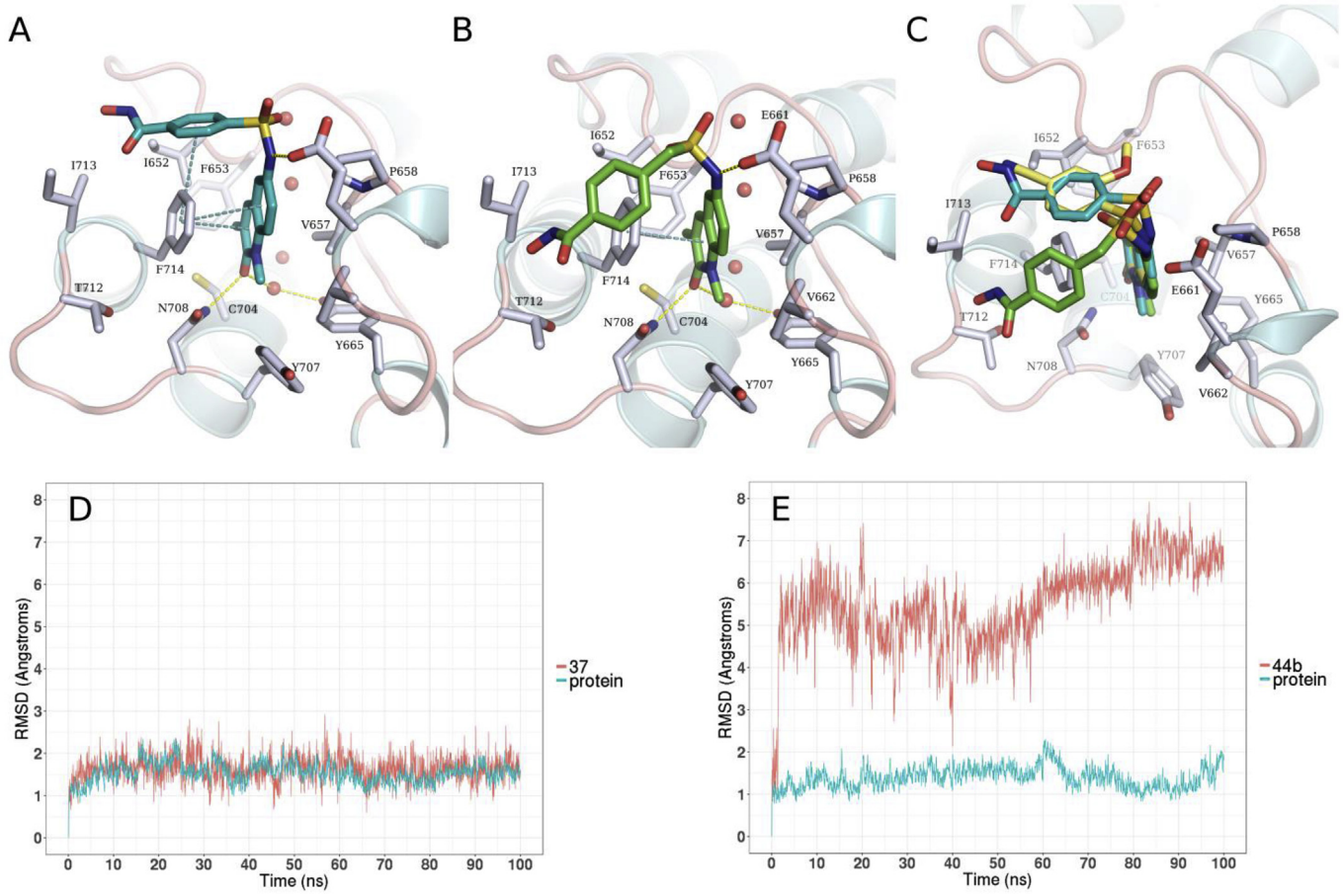

Fig. 10. **A**. Predicted binding mode of **37** (cyan stick) in BRPF1. **B**. Predicted binding mode of **44b** (green sticks) in BRPF1. **C**. Overlay of the predicted binding mode of **37** (cyan stick) and **44b** (green sticks) with the cocrystallized ligand **NI-57** (yellow sticks). Side chains of binding site residues are depicted as white sticks, and water molecules as red spheres. Yellow-dashed lines indicate hydrogen bond interactions and cyan-dashed lines π-π stacking interactions. **D**. RMSD plot of the MD simulation of **37** in BRPF1. **E**. RMSD plot of the MD simulation of **44b** in BRPF1. (For interpretation of the references to colour in this figure legend, the reader is referred to the Web version of this article.)

and their inhibitors showed cytotoxic activity against different tumors. Our main focus was acute myeloid leukemia (AML) cell lines (THP-1 and HL60) based on some previous reports showing evidence of significance of HDAC6 [82] and HDAC8 [83,84] as well as BRPF [15–17] inhibition in these cells. We tested our most promising compounds **23a,b** (HDAC8/BRPF1), **37** and **44b** (HDAC6/BRPF1) -together with their esters as negative controls-on THP-1 and HL60 cell lines to investigate if the compounds in vitro inhibitory activity could be translated into cellular anticancer activity (Table 3).

Although all the hydroxamic acids showed no or weak growth inhibition on the cells, a much stronger inhibition was generally observed for the esters, and the GI_{50} value of **21** was determined to be around 5.5 μM. The activity of the esters could be attributed to the BRPF1 inhibiting scaffold. In fact, both **21** and the potent BRPF1 inhibitor **13-d** [24] have almost the same GI_{50} value on THP-1 cells. The corresponding hydroxamic acids, however, did not show an inhibition, despite their bromodomain inhibitory scaffold. We assumed that since the esters are more lipophilic than the hydroxamic acids (log P value for **21** is 1.83 compared to 1.09 for **23a,** calculated with ChemDraw Ultra 8), they should have better cell permeability, and consequently better cellular activity than the hydroxamic acids.

To get insight into the cellular activity of our hydroxamic acids, western blotting experiments were performed with our best HDAC6 inhibitor **44b** (IC_{50} value: 152 nM, Table 2) in the two cell lines THP-1 and HL60. The cells were incubated with **44b** or SAHA (reference compound), and then cell lysates were blotted against acetylated-α-tubulin (HDAC6 substrate), acetylated-histone H3 (HDAC1 substrate), and glyceraldehyde 3-phosphate dehydrogenase (GAPDH) as a loading control (Fig. 11). At lower concentrations, **44b** showed negligible or no induction of tubulin acetylation in both cell lines, whereas some degree of acetylation was observed at 10 μM. The lack of hyperacetylation at lower concentrations is in line with the antiproliferative assays, where the compound showed inhibition only at a high concentration of 100 μM. The western blots were quantified by determining the ratio of acetylated tubulin or acetylated histone 3 versus GAPDH (Table 4). These results further supported our postulation that our hydroxamic acids have poor permeability and therefore did not show remarkable cellular activity. It is worth mentioning that the dimeric compound **38** (Scheme 3 and later discussed in 2.5.2.) showed a promising growth inhibition on THP-1 cells at 1 μM. However, its relatively poor solubility hindered further testing at higher concentrations and consequently GI_{50} determination.

Based on these findings, we then aimed to modify some of our hydroxamic acids in order to acquire better cellular permeability. To achieve that, we masked the hydroxamic acid functionality in **23a** and **44b** by synthesizing the corresponding benzyl and *para*-acetoxy-benzyl ester prodrugs of hydroxamic acids **59a,b** and **60b** (Fig. 12) as prodrugs. Masking hydroxamic acids was recently reported as an approach to overcome problems like fast elimination,

Table 3
Antiproliferative activity on acute myeloid leukemia cells THP-1 and HL60. Growth inhibition was determined using the CellTiter 96AQueous Non-Radioactive Cell Proliferation Assay.

Class	Structure	Compound	THP-1			HL60		
			Primary testing		GI_{50}	Primary testing		GI_{50}
			Conc. [μM]	Inhibition [%]		Conc. [μM]	Inhibition [%]	
Hydroxamic acids	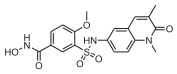	**23a**	100 20 4	43 32 0	n.d.	100 20 4	39 10 25	n.d.
	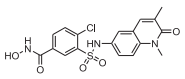	**23b**	100 20 4	21 8 16	n.d.	100 20 4	33 32 29	n.d.
	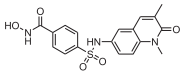	**37**	100 10 1	78 0 0	n.d.	100 10 1	34 6 3	n.d.
	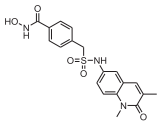	**44b**	100 10 1	89 8 0	n.d.	100 10 1	27 0 5	n.d.
Masked hydroxamic acids	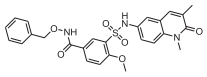	**59a**	100 10 1	0 20 0	n.d	100 10 1	13 13 2	n.d
	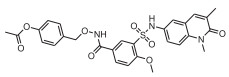	**59b**	100 10 1	27 3 0	n.d	100 10 1	95 0 0	n.d
	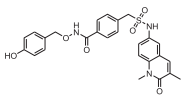	**60a**	100 10 1	91 1 0	n.d	n.d		
	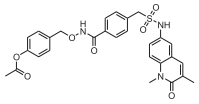	**60b**	100 10 1	91 1 4	n.d	100 10 1	97 0 3	n.d
Esters	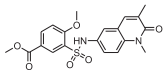	**21**	100 20 4	102 101 40	5.5 μM	100 20 4	66 44 39	n.d.
	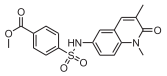	**35**	100 10 1	95 85 0	n.d	100 10 1	68 22 5	n.d
	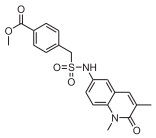	**42b**	100 10 1	93 9 0	n.d	100 10 1	78 14 15	n.d
BRPF1i-dimer	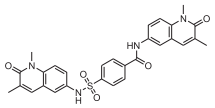	**38**	50 10 1	73 84 0	n.d	50 10 1	48 55 20	n.d
Reference		**SAHA**	100 10 1	98 97 84	n.d	100 10 1	95 98 55	n.d

decreased cellular uptake and poor tissue penetration caused by the highly polar hydroxamic acid group [85–90]. In addition, para-acetoxybenzyl-based prodrugs were shown to be completely converted to the parent hydroxamic acid in plasma [91]. Unfortunately, even these masked hydroxamic acids **59a,b** and **60b** (log P values ranging from 2.51 to 3.08, calculated with ChemDraw Ultra 8) did not show an improvement in the activity against either THP-1 or HL60 cell lines. Compounds **60a,b** showed only promising inhibition at 100 μM, but not at lower concentrations.

2.4. Stability analysis

Stability stress tests were carried out to investigate the stability of the synthesized hydroxamic acids, and to see if the masked derivatives are hydrolyzed to release the free hydroxamic acid under assay conditions. We used the hydroxamic acid **44b** and the derivative **60b** as representatives. For this purpose, the compounds were subjected to standard cellular assay conditions (Dulbecco's Modified Eagle's Medium, DMEM) and also to buffer (in vitro assay)

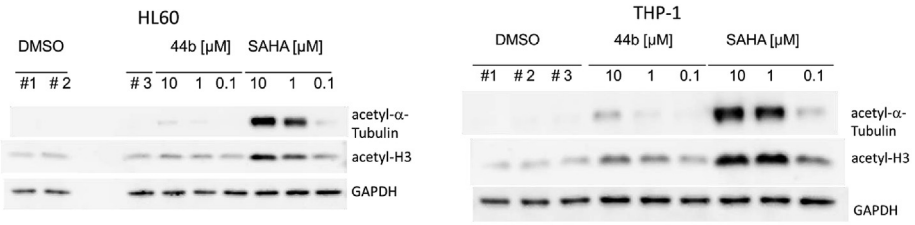

Fig. 11. Western blots of acetyl-α-tubulin, acetyl-H3, and GAPDH after treatment of HL60 and THP-1 cells with SAHA and **44b**. GAPDH and DMSO were used as loading and negative controls.

Table 4
Quantification of western blots in THP-1 and HL60 cells.

Compound	THP-1		HL60	
	Ac-tubulin/GAPDH	Ac-H3/GAPDH	Ac-tubulin/GAPDH	Ac-H3/GAPDH
DMSO	1.00	1.00	1.00	1.00
44b 10 μM	7.67	2.63	7.36	1.38
44b 1 μM	2.51	1.98	4.96	1.66
44b 0.1 μM	2.64	1.53	1.36	0.90
SAHA 10 μM	78.80	8.78	309.78	5.73
SAHA 1 μM	68.15	10.09	146.10	2.57
SAHA 0.1 μM	6.21	2.78	8.36	1.12

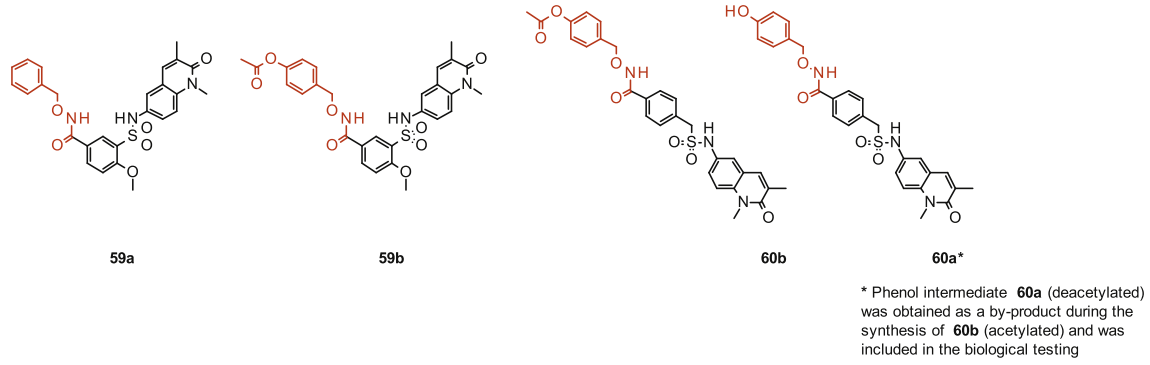

Fig. 12. Benzyl and *para*-acetoxy-benzyl ester prodrugs of hydroxamic acids synthesized in the current work.

conditions (Phosphate-Buffered Saline, PBS pH 7.4). After incubation at 37 °C for different time intervals, the original compounds and potential hydrolysis products were detected and quantified via HPLC.

We observed that the free hydroxamic acid **44b** showed acceptable stability over 4 days for both in cellular assay and in vitro conditions. The prodrg **60b** was relatively stable under buffer conditions (70%) and showed only a 15% release of **44b** as hydrolysis product after 12 h. After 96 h several non-identified degradation products could be detected. However, under cellular assay conditions **60b** was rapidly hydrolyzed (50% after 4 h) showing **44b** as the major degradation product. After 24 h, we could only detect **44b** without any traces of **60b**. The data clearly showed that the masked prodrug was indeed hydrolyzed to release the active hydroxamic acid under cellular assay conditions. However, this also suggested that the rapid hydrolysis might be responsible that the required concentration of the masked hydroxamic acid couldn't be delivered to cells, where the hydrolysis is supposed to occur. Experimental details and graphs are provided in the supplementary information (Fig. S6, Supporting Information).

2.5. Chemistry

2.5.1. Synthesis of HDAC8/BRPF1 inhibitors

Synthesis of the 6-amino-1,3-dimethylquinolin-2-(*1H*)-one (**5**), the common starting material for the compounds, was achieved using the procedure reported by Igoe et al. [24] with some modifications (Scheme S1.1, supporting information). Briefly, 3-methylquinoline (**1**) was converted to 3-methylquinolin-2(*1H*)-one (**2**) in two steps using 3-chloroperbenzoic acid then benzoyl chloride. Methylation with iodomethane afforded the *N*-methyl derivative (**3**), which was then nitrated to yield 1,3-dimethyl-6-nitroquinolin-2-(*1H*)-one (**4**). Our main modification to the procedure was the conversion of the latter compound to the targeted amine **5** using a microwave assisted reduction protocol [92]. This enabled a much faster, more efficient, and easier reduction process than the reported stannous chloride based procedure. To synthesize the first dual HDAC8/BRBF inhibitors **17a,b**, **20a,b** and **23a,b**, the required starting materials were prepared as reported in the literature (Scheme S1.1, supporting information) [93–95]. The synthesis of the target compounds is illustrated in Scheme 1.

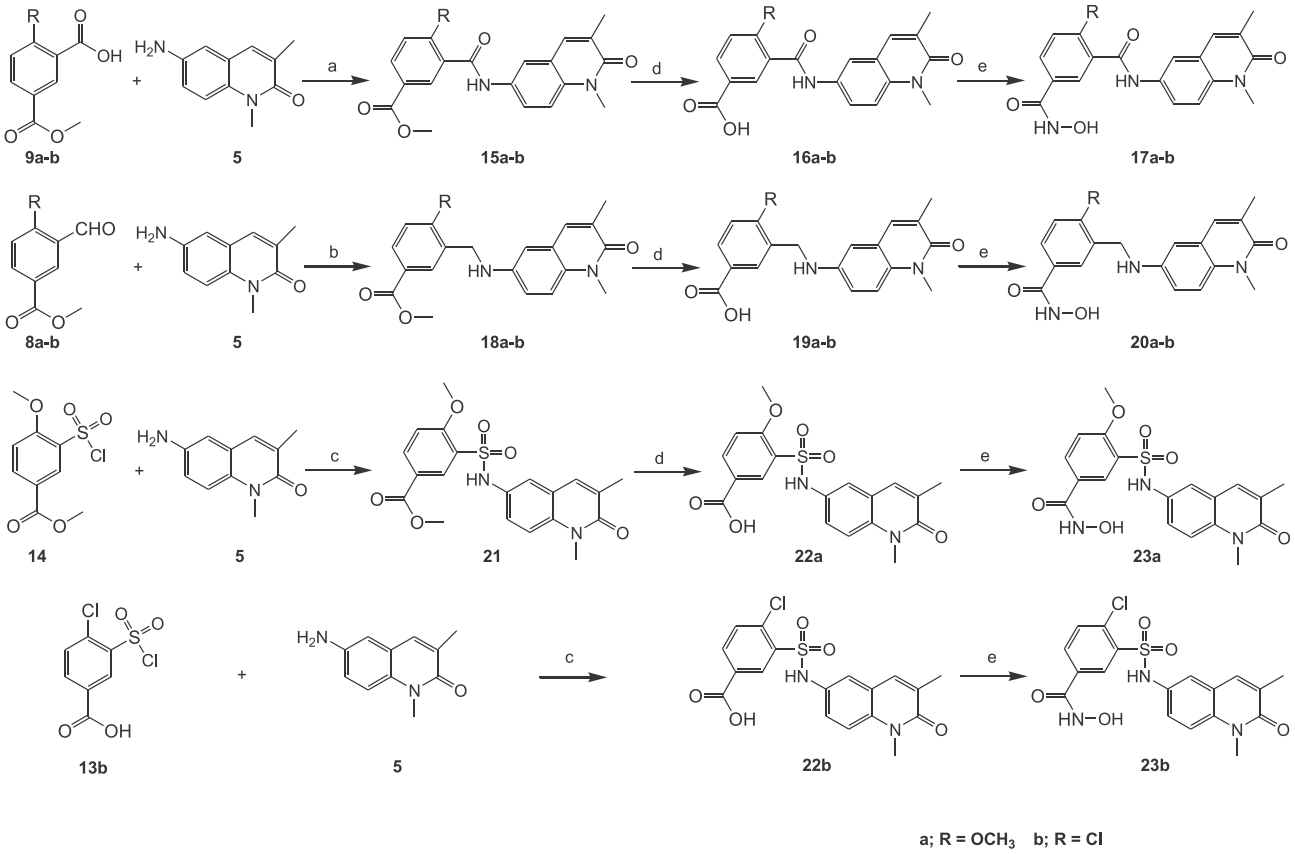

Scheme 1. Synthesis of dual HDAC8/BRPF1 inhibitors **17a,b, 20a,b and 23a,b**. Reagents and conditions: (a) i) oxalyl chloride, cat. DMF, CH_2Cl_2, ii) DIPEA, CH_2Cl_2; (b) $Na(AcO)_3BH$, CH_3COOH, THF; (c) pyridine; (d) i) aqu. NaOH, MeOH, reflux, ii) c. HCl; (e) i) PyBOP, DIPEA, H_2NOTHP, THF, ii) cat. HCl, THF.

Briefly, compounds **17a,b** were prepared starting from the 5-methoxycarbonyl-2-substitutedbenzoic acids (**9a,b**) which were first activated using oxalyl chloride, and then coupled to 6-amino-1,3-dimethylquinolin-2-(*1H*)-one (**5**) to give methyl 3-[(1,3-dimethyl-2-oxo-1,2-dihydroquinolin-6-yl)carbamoyl]-4-substitutedbenzoates (**15a,b**). These were finally hydrolyzed to yield the corresponding carboxylic acids **16a,b**. For inhibitors **20a,b**, sodium triacetoxyborohydride was utilized for the reductive amination of aldehydes **8a,b** and amine **5** to synthesize the esters **18a,b**, again followed by hydrolysis to afford the 3-[(1,3-dimethyl-2-oxo-1,2-dihydroquinolin-6-ylamino)methyl]-4-substitutedbenzoic acids (**19a,b**). Carboxylic acid **22b** was prepared directly from the aromatic sulfonyl chloride **13b** and amine **5** using pyridine as a base. The same protocol for the synthesis of intermediate **22a** afforded a major byproduct (which was extremely insoluble in common solvents, and unfortunately could not be characterized). This necessitated an alternative route, where compound **5** was reacted with the ester derivative **14** to first give methyl 3-[(1,3-dimethyl-2-oxo-1,2-dihydroquinolin-6-yl)sulfamoyl]-4-methoxybenzoate (**21**), which was further hydrolyzed to yield the carboxylic acid **22a**. The desired hydroxamic acids **17a,b**, **20a,b** and **23a,b** were finally obtained from the corresponding carboxylic acids **16a,b**, **19a,b** and **22a,b** using PyBOP as an activating agent and *O*-(tetrahydro-*2H*-pyran-2-yl)hydroxylamine followed by cleavage of the protecting group [65]. We adopted this method rather than the classical one (reaction with hydroxylamine hydrochloride and a strong base like KOH), as this method facilitated the purification of the final hydroxamic acids.

In the case of synthesis of compound **32**, it was quiet challenging to find the optimal synthetic sequence. As shown in Scheme 2, the 4-hydroxybenzaldehyde (**26**) was first alkylated with 5-bromovalerate (**25**) to give the ester **27**, which was then hydrolyzed to the corresponding acid **28**. Again oxalyl chloride served as an activating agent and the resulting acid chloride was reacted with **5** to give *N*-(1,3-dimethyl-2-oxo-1,2-dihydroquinolin-6-yl)-5-(4-formylphenoxy)pentanamide (**29**). The previously mentioned conditions of reductive amination were not successful for the reaction of **29** with 3-amino-4-methoxybenzoic acid (**30**), and required a modification by adding trifluoroacetic acid (TFA) [96] to obtain the carboxylic acid **31**, which was finally converted to the target compound **32** using the above mentioned protocol.

2.5.2. Synthesis of HDAC6/BRPF1 inhibitors

The starting materials for the dual HDAC6/BRPF1 inhibitors were the appropriate sulfonyl chlorides. Trials to directly synthesize the carboxylic acid **36** from the commercially available 4-(chlorosulfonyl)benzoic acid (**33**) again afforded a major byproduct. This product had a reasonable solubility and was identified as 4-[(1,3-dimethyl-2-oxo-1,2-dihydroquinolin-6-yl)sulfamoyl]-*N*-(1,3-dimethyl-2-oxo-1,2-dihydroquinolin-6-yl)benzamide **38** (Scheme 3). In case of **34**, **41a,b** and **48a,b** we decided to start with the sulfonyl chloride esters. Reaction of the corresponding alkyl bromides **40a,b** and **47a,b** with sodium sulphite and phosphorus pentachloride yielded the aliphatic sulfonyl chlorides **41a,b** and **48a,b** (Scheme S1.2., supporting information). Again reaction of these sulfonyl chlorides with **5** in pyridine afforded the esters **35**, **42a,b** and **49a,b**, which were hydrolyzed to the carboxylic acids and finally converted to the desired hydroxamic acids **37**, **44a,b** and **51a,b** as previously discussed (Scheme 4).

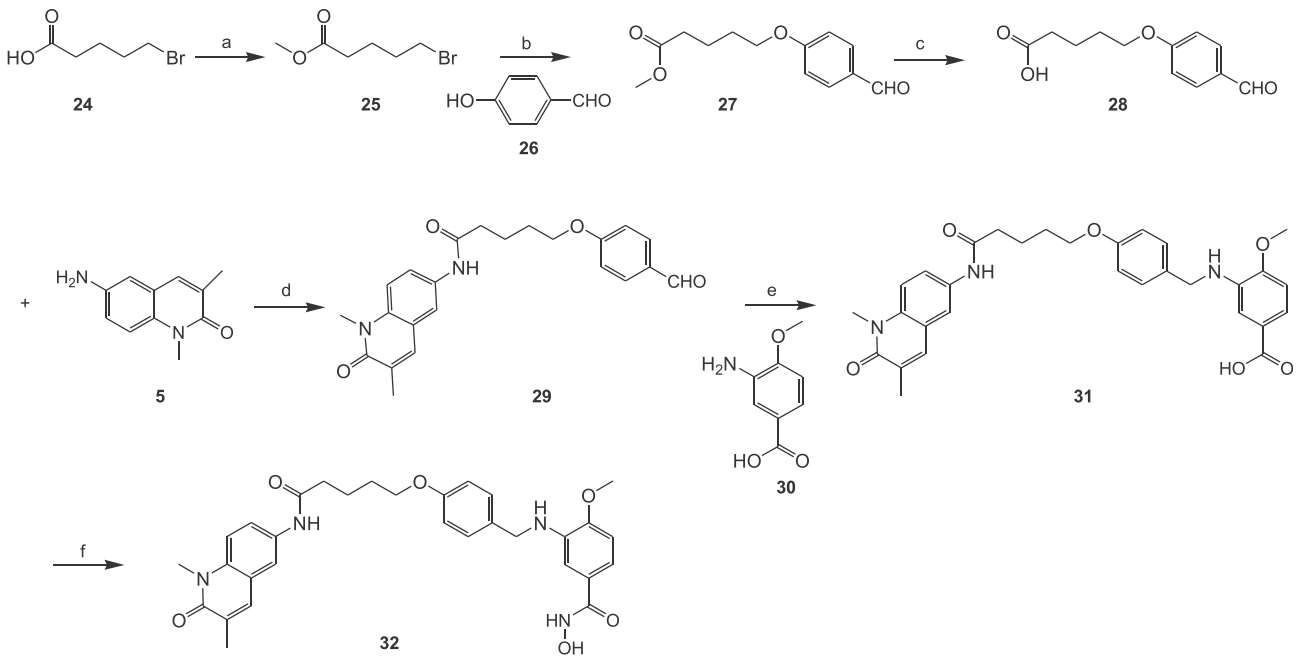

Scheme 2. Synthesis of dual HDAC8/BRPF1 inhibitor **32.** Reagents and conditions: (a) p-toluenesulfonic acid, CH_3OH; (b) K_2CO_3, acetone, reflux; (c) $LiOH.H_2O$, THF, H2O; (d) i) oxalyl chloride, cat. DMF, CH_2Cl_2, ii) DIPEA, CH_2Cl_2; (e) $Na(AcO)_3BH$, CF_3COOH, THF; (f) i) PyBOP, DIPEA, H_2NOTHP, THF, ii) cat. HCl, THF.

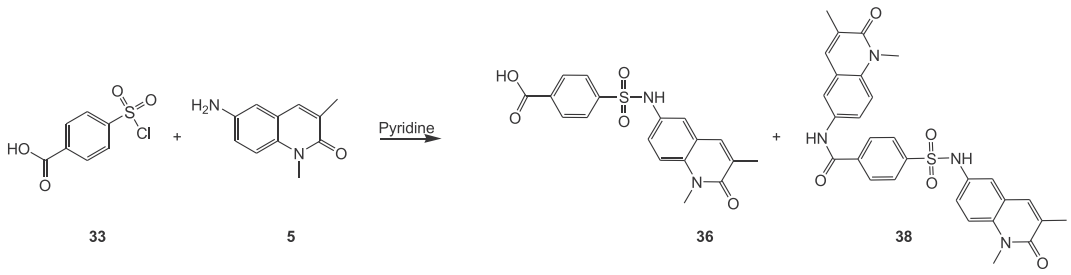

Scheme 3. Synthesis of dimeric BRPF1i **38**.

2.5.3. Synthesis of masked hydroxamic acids

Compounds **59a,b** and **60a,b** were synthesized as shown in Scheme 5 from the corresponding carboxylic acids **22a** and **43b**, respectively. Whereas intermediate **58a** was commercially available, intermediate **58b** was synthesized following the procedure reported by Rais et al. [91] with some modifications (Scheme S1.3., supporting information). Unlike the protocol for hydroxamic acid synthesis (Schemes 1, 2 and 4), activation of the carboxylic acids using PyBOP to synthesize the masked hydroxamic acid was not optimal and complicated the purification process. Instead, we used HATU as an activating agent, since its traces and side products could be efficiently removed by aqueous workup which facilitated purification. It is also worth mentioning that compound **60a** was obtained as a deacetylated side product of compound **60b** (probably during the hydrazinolysis process due to slightly increased reaction time). It was then purified, characterized, identified and incorporated in our cellular assays.

3. Conclusion

HDACs and bromodomains represent interesting epigenetic targets whose deregulation is linked to different disorders. The current work was initiated based on promising results of the combination therapy of HDAC and bromodomain inhibitors, assuming that a dual target inhibitor could achieve superior activity to the single agents. We used previously developed selective HDAC8 inhibitors as starting points and modified the cap group to achieve simultaneous HDAC8 and BRPF1 inhibition. Two dual HDAC8/BRPF1 nanomolar inhibitors (**23a,b**) were identified. In vitro assays and modelling studies showed that small modifications of the linker are not tolerated, especially for the BRPF1 inhibition. Since HDAC6 is in the scope of this work, we took advantage of the structural differences between different HDAC isoforms to achieve the dual HDAC6/BRPF1 inhibitor **37**. Further attempts to enhance HDAC6 activity abolished the BRPF1 activity emphasizing the limited available space to optimize these dual inhibitors. The promising in vitro enzymatic results of the developed dual target inhibitors were not translated into cellular activity against AML cell lines, while the corresponding esters, which served as HDAC negative controls with only BRPF1 activity, showed a modest effect. Therefore, we assumed that the poor permeability of the hydroxamic acid is the reason for the lack of cellular activity. Indeed, Western blot experiments showed a very weak acetylation of α-tubulin, substantiating the lack of cellular HDAC6 activity of the tested compounds. In an attempt to enhance the cellular effect of the dual target inhibitors, some masked hydroxamic acids were synthesized as potential prodrugs. However, no improvement in the antiproliferative effect could be observed. Reasons for that

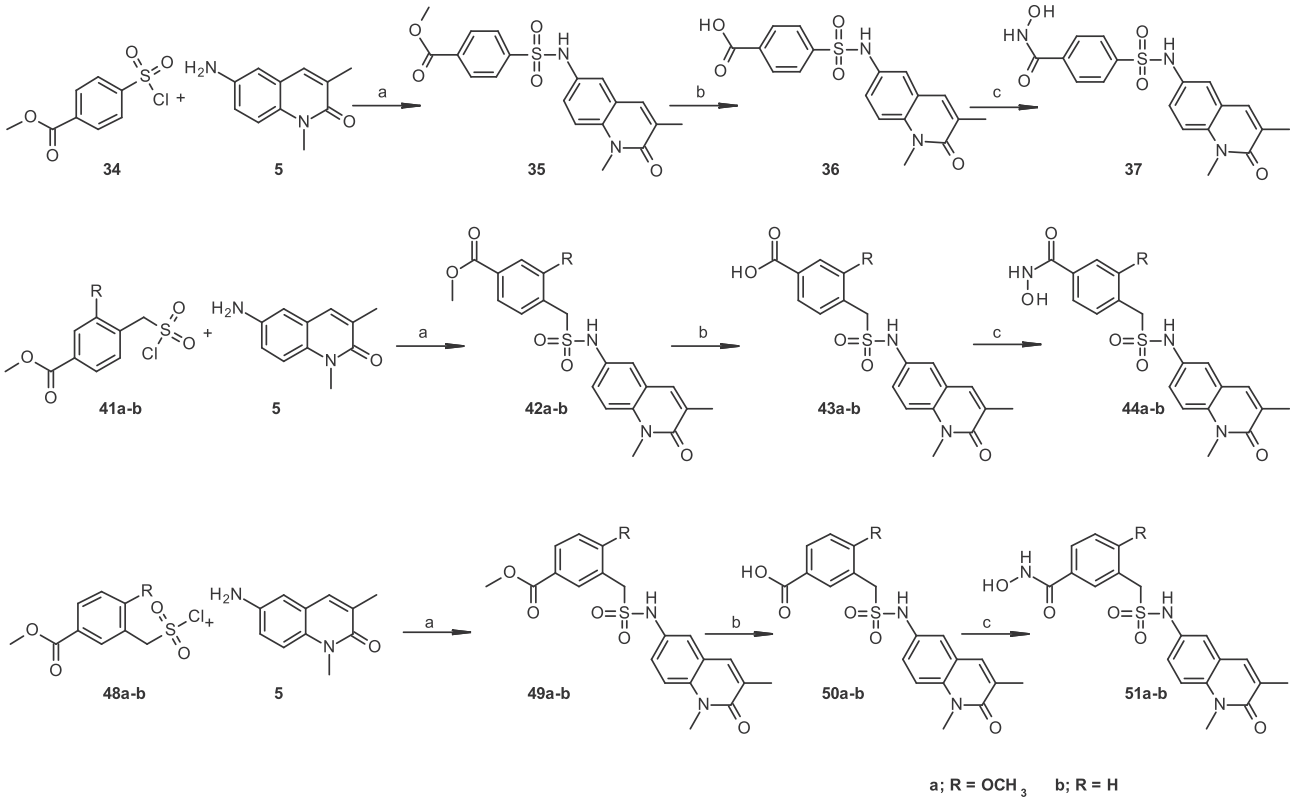

Scheme 4. Synthesis of dual HDAC6/BRPF1 inhibitors **37, 44a,b and 51a,b**. Reagents and conditions: (a) pyridne; (b) i) aqu. NaOH, CH_3OH, reflux, ii) c. HCl; (c) i) PyBOP, DIPEA, H_2NOTHP, THF, ii) cat. HCl, THF.

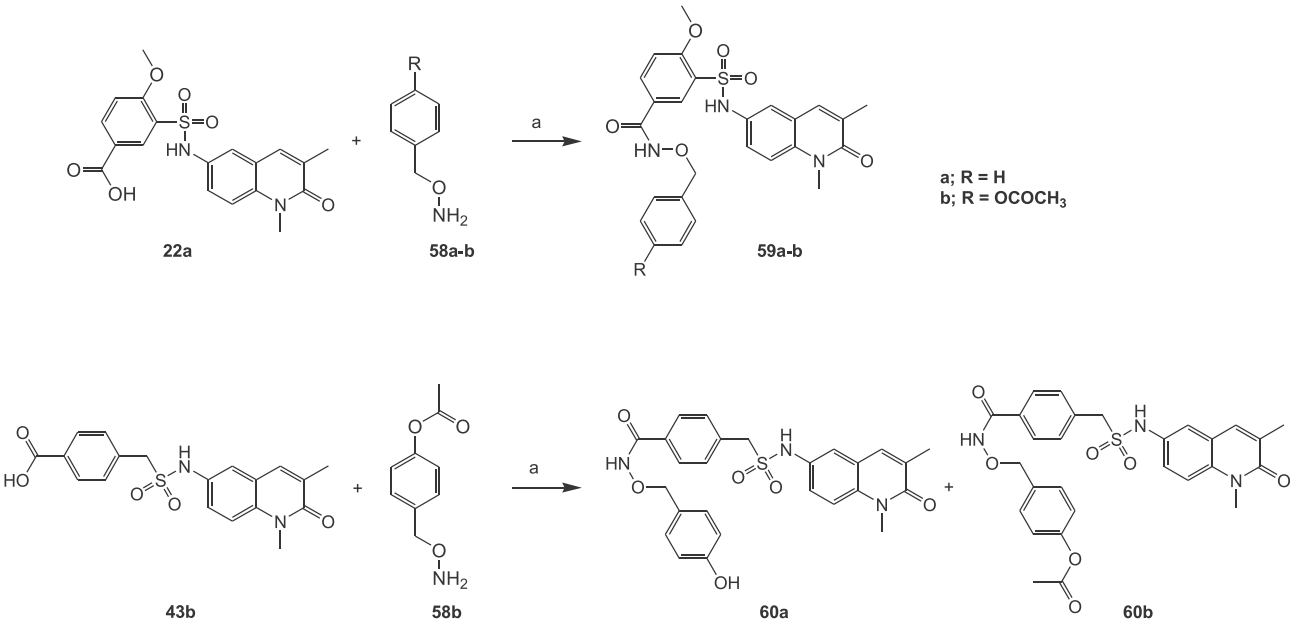

Scheme 5. Synthesis of masked hydroxamic acids 59a,b and 60a,b. Reagents and conditions: (a) HATU, DIPEA, THF, DMF.

could be the known limited cell permeability and short half-life of hydroxamic acids due to fast metabolization. One prospective modification of the developed dual inhibitors could be a replacement of the hydroxamic acid moiety by more stable and permeable zinc binding groups. It would be interesting to investigate if this modification could achieve a balance between activities on both targets and confer cellular activity.

4. Experimental protocols

4.1. Chemistry

4.1.1. General

All materials and reagents were purchased from Sigma-Aldrich Co. Ltd. and abcr GmbH. All solvents were analytically pure and

dried before use. Thin layer chromatography was carried out on aluminum sheets coated with silica gel 60 F254 (Merck, Darmstadt, Germany). For column chromatography under normal pressure silica gel 60 (0.036–0.200 mm) was used.

Final compounds were confirmed to be of >95% purity based on HPLC. Purity was measured by UV absorbance at 254 nm. The HPLC consists of an XTerra RP18 column (3.5 μm, 3.9 mm × 100 mm) from the manufacturer Waters (Milford, MA, USA) and two LC-10AD pumps, a SPD-M10A VP PDA detector, and a SIL-HT auto-sampler, all from the manufacturer Shimadzu (Kyoto, Japan). For preparative tasks a XTerra RP18 column (7 μm, 19 mm × 150 mm) from the manufacturer Waters (Milford, MA, USA) and two LC-20AD pumps were used. The mobile phase was in all cases a gradient of methanol/water (starting at 95% water going to 5% water).

Mass spectrometry analyses were performed with a Finnigan MAT710C (Thermo Separation Products, San Jose, CA, USA) for the ESIMS spectra and with a LTQ (linear ion trap) Orbitrap XL hybrid mass spectrometer (Thermo Fisher Scientific, Bremen, Germany) for the HRMS-ESI (high resolution mass spectrometry) spectra. For the HRMS analyses the signal for the isotopes with the highest prevalence was given and calculated (^{35}Cl, ^{79}Br).

^{1}H NMR and ^{13}C NMR spectra were taken on a Varian Inova 500 using deuterated chloroform and deuterated DMSO as solvent. Chemical shifts are referenced to the residual solvent signals. The following abbreviations and formulas for solvents and reagents were used: ethyl acetate (EtOAc), dimethylformamide (DMF), dimethylsulfoxide (DMSO), methanol (MeOH), tetrahydrofuran (THF), chloroform ($CHCl_3$), water (H_2O), dichloromethane (CH_2Cl_2), *N*,*N*-diisopropylethylamine (DIPEA), trimethylamine (TEA), hydrochloric acid (HCl) and trifluoroacetic acid (TFA).

*4.1.2. General method for the synthesis of methyl 3-[(1,3-dimethyl-2-oxo-1,2-dihydroquinolin-6-yl)carbamoyl]-4-substitutedbenzoates (**15a-b**)*

The appropriate 5-methoxycarbonyl-2-substitutedbenzoic acid **9a-b** (3 mmol), DMF (one drop) and oxalyl chloride (4 mmol) were stirred in CH_2Cl_2 at room temperature for 3 h. The mixture was then added dropwise to a solution of 6-amino-1,3-dimethylquinolin-2-(1*H*)-one (**5**; 3 mmol) and DIPEA (8 mmol) in CH_2Cl_2, and stirring was continued for another 2 h at room temperature. The reaction mixture was washed with a saturated aqueous solution of ammonium chloride and brine. The organic layer was dried over anhydrous sodium sulfate, filtered, and concentrated in vacuo. The residue was purified using column chromatography ($CHCl_3$: MeOH, 100:0–99:1).

Detailed characterization data of the compounds are provided in the supporting information.

*4.1.3. General method for the synthesis of methyl 3-[(1,3-dimethyl-2-oxo-1,2-dihydroquinolin-6-ylamino)methyl]-4-substitutedbenzoates (**18a-b**)*

A mixture of the appropriate 4-substituted-3-formylbenzoate **8a-b** (1.2 mmol) and 6-amino-1,3-dimethylquinolin-2-(1*H*)-one (**5**; 1 mmol) was dissolved in toluene, and the reaction mixture was refluxed for 2 h using a dean stark apparatus. The solvent was then evaporated under reduced pressure, and the crude product was dissolved in CH_2Cl_2 and cooled to 0 °C. Then sodium triacetoxyborohydride (4 mmol) was added and the reaction mixture was stirred overnight at room temperature. The reaction was quenched by adding H_2O, and the pH was adjusted to 5 with aqueous potassium bicarbonate solution. The mixture was extracted with EtOAc, and the organic layer was evaporated under vacuum. The products were purified by column chromatography ($CHCl_3$: MeOH, 100:0–99:1).

Detailed characterization data of the compounds are provided in the supporting information.

*4.1.4. General method for the ~~of~~ synthesis of methyl 3(or 4)-[(1,3-dimethyl-2-oxo-1,2-dihydroquinolin-6-yl)sulfamoyl]-4-substitutedbenzoates (**21 and 35**) and methyl 3(or 4)-{[(1,3-dimethyl-2-oxo-1,2-dihydroquinolin-6-yl)sulfamoyl]methyl}-4-substitutedbenzoates (**42a-b**) and (**49a-b**)*

To a solution of 6-amino-1,3-dimethylquinolin-2-(1*H*)-one (**5**; 1 mmol) in pyridine was added the appropriate methyl chlorosulfonylbenzoate or methyl (chlorosulfonylmethyl)benzoate **14**, **34**, **14a-b** or **48a-b** (1 mmol), and the reaction was stirred at room temperature overnight. The solvent was then removed under vacuum, and the residue obtained was dissolved in EtOAc and washed successively with aqueous 1M HCl, 1M copper sulfate and brine solutions. The organic layer was dried over anhydrous sodium sulfate, filtered, and concentrated in vacuo. The residue was purified using column chromatography ($CHCl_3$: MeOH, 100:0–99:1).

Detailed characterization data of the compounds are provided in the supporting information.

*4.1.5. General method for the synthesis of carboxylic acids **16a-b**, **19a-b**, **22a-b**, **36**, **43a-b** and **50a-b***

The appropriate methyl esters **15a-b**, **18a-b**, **21**, **35**, **42a-b** or **49a-b** (1 mmol) was dissolved in MeOH followed by the addition of aqueous solution of sodium carbonate (10 mmol) and the mixture was stirred under reflux for 2–4 h until complete hydrolysis of the ester. MeOH was then evaporated and the reaction was neutralized with aqueous solution of 1M HCl until pH 6. The liberated free acid was extracted with a mixture of EtOAc and THF, and the extract was dried over sodium sulfate and evaporated under reduced pressure. The product required no further purification.

Compound **22b** was prepared directly from 6-amino-1,3-dimethylquinolin-2-(1*H*)-one and methyl 4-chloro-3-chlorosulfonylbenzoate using the procedure described in 4.1.4.

Detailed characterization data of the compounds are provided in the supporting information.

*4.1.6. General method for the of synthesis of hydroxamic acids **17a-b**, **20a-b**, **23a-b**, **37**, **44a-b** and **51a-b***

The appropriate carboxylic acid **16a-b**, **19a-b**, **22a-b**, **36**, **43a-b and 50a-b** (1 mmol) was dissolved in dry THF, followed by the addition of PyBOP (1.5 mmol) and DIPEA (3 mmol). The mixture was stirred for 15 min, then NH_2OTHP (1.2 mmol) was added and the reaction mixture was stirred at room temperature for 2–4 h. The solvent was evaporated under vacuum and the mixture was dissolved in EtOAc (50 ml) and washed with 1M sodium carbonate solution and brine. The organic layer was evaporated under vacuum and the product was purified by column chromatography ($CHCl_3$/MeOH/TEA, 99:0.95:0.05).

The obtained product was dissolved in THF and a catalytic amount of diluted HCl was added. The mixture was stirred at room temperature overnight. The reaction was controlled by TLC. After that the solvent was evaporated under vacuum and the hydroxamic acid product was purified by column chromatography ($CHCl_3$: MeOH, TEA 95:4.95:0.05).

Detailed characterization data of the compounds are provided in the supporting information.

*4.1.7. Synthesis of 3-{4-[5-(1,3-dimethyl-2-oxo-1,2-dihydroquinolin-6-ylamino)-5-oxopentyloxy]benzylamino}-N-hydroxy-4-methoxybenzamide (**32**)*

Detailed synthesis of intermediates **25**–**28** are provided in the supporting information.

*4.1.7.1. N-(1,3-dimethyl-2-oxo-1,2-dihydroquinolin-6-yl)-5-(4-formylphenoxy)pentanamide (**29**).*

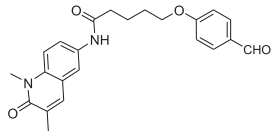

5-(4-Formylphenoxy)pentanoic acid (**28**; 3 mmol), DMF (one drop) and oxalyl chloride (4 mmol) were stirred in CH_2Cl_2 at room temperature for 3 h. The mixture was then added dropwise to a solution of 6-amino-1,3-dimethylquinolin-2-(1*H*)-one (**5**; 3 mmol) and DIPEA (8 mmol) in CH_2Cl_2, and stirring was continued for another 2 h at room temperature. The reaction mixture was washed with saturated aqueous solution of ammonium chloride and brine. The organic layer was dried over anhydrous sodium sulfate, filtered, and concentrated in vacuo. The residue was purified using column chromatography ($CHCl_3$: MeOH, 100:0–98:2).

MS *m*/*z*: 393.20 $[M+H]^+$

Yield: 74%

^{1}H NMR (400 MHz, DMSO) δ 10.00 (s, 1H, −CO−N***H***-Ar), 9.84 (s, 1H, -C***H***O), 7.91 (d, *J* = 2.4 Hz, 1H, Ar−***H***), 7.86–7.80 (m, 2H, Ar−***H***), 7.70 (s, 1H, Ar−***H***), 7.65 (dd, *J* = 9.1, 2.4 Hz, 1H, Ar−***H***), 7.42 (d, *J* = 9.1 Hz, 1H, Ar−***H***), 7.14–7.07 (m, 2H, Ar−***H***), 4.11 (t, *J* = 5.9 Hz, 2H, -C***H*****$_2$**-O-), 3.60 (s, 3H, -NC***H*****$_3$**), 2.39 (t, *J* = 6.9 Hz, 2H, -C***H*****$_2$**CO-), 2.10 (d, *J* = 1.0 Hz, 3H, Ar-C***H*****$_3$**), 1.84–1.71 (m, 4H, $-CH_2-C_2$***H*****$_4$**$-CH_2-$).

*4.1.7.2. 3-{4-[5-(1,3-Dimethyl-2-oxo-1,2-dihydroquinolin-6-ylamino)-5-oxopentyloxy]-benzylamino}-4-methoxybenzoic acid (**31**).*

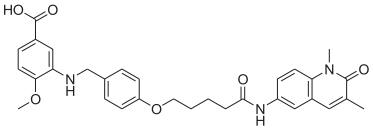

A mixture of *N*-(1,3-dimethyl-2-oxo-1,2-dihydroquinolin-6-yl)-5-(4-formylphenoxy)pentanamide (**29**; 1.1 mmol), 3-amino-4-methoxybenzoic acid (**30**; 1 mmol) and TFA (2 mmol) in a (1:1) mixture of THF and EtOAc was cooled to 0 °C, then sodium triacetoxyborohydride (4 mmol) was added and the reaction mixture was stirred overnight at room temperature. The reaction was quenched by adding H_2O, and the pH was adjusted to 5 with aqueous potassium bicarbonate solution. The organic layer was separated and the aqueous layer was extracted with EtOAc. The organic layers were collected, dried over anhydrous sodium sulfate, filtered, and concentrated in vacuo. The residue was purified using column chromatography ($CHCl_3$: MeOH, 100:0–97:3).

MS *m*/*z*: 542.82 $[M-H]^-$

Yield: 81%

^{1}H NMR (400 MHz, DMSO) δ 12.26 (s, 1H, -COO***H***), 9.98 (s, 1H, −CO−N***H***-Ar), 7.91 (d, *J* = 2.2 Hz, 1H, Ar−***H***), 7.71 (s, 1H, Ar−***H***), 7.65 (dd, *J* = 9.1, 2.3 Hz, 1H, Ar−***H***), 7.42 (d, *J* = 9.1 Hz, 1H, Ar−***H***), 7.25–7.16 (m, 3H, Ar−***H***), 6.95 (d, *J* = 2.0 Hz, 1H, Ar−***H***), 6.89–6.82 (m, 3H, Ar−***H***), 5.59 (t, *J* = 6.0 Hz, 1H, $-CH_2-$N***H***-Ar), 4.24 (d, *J* = 5.6 Hz, 2H, -C***H*****$_2$**-NH-Ar), 3.98–3.91 (m, 2H, -C***H*****$_2$**-O-), 3.85 (s, 3H, -OC***H*****$_3$**), 3.60 (s, 3H, -NC***H*****$_3$**), 2.40–2.34 (m, 2H, -C***H*****$_2$**CO-), 2.10 (3H, Ar-C***H*****$_3$**), 1.74 (m, 4H, $-CH_2-C_2$***H*****$_4$**$-CH_2-$).

*4.1.7.3. 3-{4-[5-(1,3-Dimethyl-2-oxo-1,2-dihydroquinolin-6-ylamino)-5-oxopentyloxy]-benzylamino}-N-hydroxy-4-methoxybenzamide (**32**).* This compound was prepared from 3-{4-[5-(1,3-dimethyl-2-oxo-1,2-dihydroquinolin-6-ylamino)-5-oxopentyloxy]-benzylamino}-4-methoxybenzoic acid (**31**) according to the method described in 4.1.6.

Detailed characterization data of the compound are provided in the supporting information.

*4.1.8. General method for the synthesis of masked hydroxamic acids **59a-b** and **60a-b***

The appropriate carboxylic acids **23a** or **44b** (1 mmol) were dissolved in dry THF, followed by the addition of HATU (1.2 mmol) and DIPEA (3 mmol). The mixture was stirred for 15 min, then the appropriate *O*-substitutedhydroxylamine **58a-b** (1.2 mmol) was added and the reaction mixture was stirred at room temperature for 2 h. The solvent was evaporated under vacuum and the mixture was dissolved in EtOAc and washed with aqueous sodium bicarbonate and ammonium chloride solutions then brine. The organic layer was separated, dried over anhydrous sodium sulfate, filtered and concentrated in vacuo. The residue was purified by column chromatography ($CHCl_3$: MeOH, 100:0–99:1).

Detailed characterization data of the compounds are provided in the supporting information.

4.2. In vitro HDAC inhibitory activity

Recombinant human HDAC1 and -6 were purchased from BPS Biosciences. Enzyme inhibition was determined by using a published homogenous fluorescence assay [97]. The enzymes were incubated for 90 min at 37 °C, with the fluorogenic substrate ZMAL (Z-(Ac)Lys-AMC) in a concentration of 10.5 μM and increasing concentrations of inhibitors. Fluorescence intensity was measured at an excitation wavelength of 390 nm and an emission wavelength of 460 nm in a microtiter plate reader (BMG Polarstar).

Recombinant hHDAC8 was produced by Romier et al. in Strasbourg [60]. The HDAC8 activity assay was performed according to the commercial HDAC8 Fluorometric Drug Discovery Kit [Fluor de Lys®-HDAC8, BML-KI178] corresponding to the manufacturer's instructions as described earlier [98]. The substrate was a synthesized tetrapeptide bound to aminomethylcoumarine (AMC) H_2N-Arg-His-Lys(Ac)-Lys(Ac)-AMC. The enzyme was incubated for 90 min at 37 °C, with a substrate concentration of 50 μM and increasing concentrations of inhibitors. The Stop-solution containing Trichostatin A (TSA), to stop the hHDAC8 activity, and Trypsin, to release the AMC, was added. The solution was incubated for 20 min at 37 °C to develop the assay. Fluorescence intensity was measured at an excitation wavelength of 355 nm and an emission wavelength of 460 nm in a microtiter plate reader (BMG Polarstar). Detailed synthesis and characterization of the substrate are provided in the supporting information.

4.3. Isothermal titration calorimetry (ITC)

ITC experiments were carried out and processed as described previously [99–101] using Microcal Origin for experiment setups, NITPIC [102,103] and SEDPHAT [104] for data evaluation, and GUSSI [105] for plotting. Ligand concentrations were between 20 and 40 μM in the sample cell and BRPF1 concentrations between 200 and 400 μM in the injection syringe. Images and calculations are provided in the supporting information. For the final K_d BRPF1 value the *P99* interval was determined.

4.4. Cellular assays

4.4.1. Viability of human HEK293 cells

HEK293 cells (DSMZ Braunschweig, ACC305) were incubated at 37 °C in a humidified incubator with 5% CO_2 in Dulbecco's modified Eagle's medium (DMEM) supplemented with 10% FCS and 5 mM glutamine. Cells were seeded at 1.5×10^3 cells per well in a 96-well cell culture plate (TPP, Switzerland). The compounds were added immediately to the medium at 50 μM to determine the percentage viability. After 24 h, AlamarBlue® reagent (Invitrogen, CA, USA) was added according to the manufacturer's instructions and incubated again for 21 h before samples were analyzed. Detection of viable cells that convert the resazurin reagent into the highly fluorescent resorufin was performed by using a FLUOstarOPTIMA microplate reader (BMG Labtec) with the following filter set: Ex 560 nm/Em 590 nm. All measurements were performed in triplicates over three independent experiments.

4.4.2. Antiproliferative activity on acute myeloid leukemia cells THP-1 and HL60

HL60 or THP-1 cells were diluted in 96-well tissue culture plates at a density of 5000 per well and immediately incubated with inhibitors or DMSO vehicle to a total volume of 100 μL. Compounds were diluted from 200x stock solutions in DMSO and were compared to DMSO vehicle only. Three replicates per concentration were used. Growth inhibition was determined using the CellTiter 96AQueous Non-Radioactive Cell Proliferation Assay according to the manufacturer's instructions. Data was plotted as absorbance units against compound concentration for pretest results or against logarithm of compound concentration using OriginPro 9. 50% Growth inhibition (GI_{50}) was determined as compound concentration required to reduce the number of metabolically active cells by 50% compared to DMSO control. The assay was already described for MCF7 [106].

4.4.3. Western blot assay in THP-1 and HL60

HL60 or THP-1 cells were seeded in a 12-well plate at a density of 2.5×10^5 cells per well, and immediately incubated with different concentrations of test compounds for 4 h. After incubation, cells were collected in Eppendorf tubes and centrifuged with 500 g for 5 min at room temperature. Cells were washed with phosphate-buffered saline and lysed in 90 μL of sodium dodecyl sulfate (SDS) sample buffer (cell signaling, 62.5 mM Tris hydrochloride (pH 6.8 at 25 °C), 2% w/v SDS, 10% v/v glycerol, 50 mM dithiothreitol, 0.01% bromophenol blue). After sonicating for 5 min, to shear DNA and reduce sample viscosity, the samples were heated to 95 °C for 1 min. Cell extracts were used directly for SDS polyacrylamide gel electrophoresis (PAGE) or kept frozen at −20 °C until usage. For the SDS-PAGE, an amount of 7 μL of cell extracts was loaded onto a 12.5% SDS gel and run at 160 V followed by the transfer to a nitrocellulose membrane via western blotting for antibody-based detection. After transfer, the nonspecific binding was blocked by incubating the membrane in 25 mL of blocking buffer [5% nonfat dry milk in Tris buffered saline with 0.1% Tween 20 (TBS-T)] for 1 h at room temperature or at 4 °C overnight. After washing the membrane three times for 5 min with TBS-T, the primary antibody [antiacetylated α-tubulin (Sigma-Aldrich T7451-200UL, 1:1000)] was added in 3% milk in TBS-T for 3 h at room temperature or overnight at 4 °C. Before exposing the membrane with the secondary antibody, it was washed again three times for 5 min with TBS-T to remove an unbound primary antibody. The secondary antibody antimouse-IgG-HRP (Sigma-Aldrich, 1:2000) was added in 3% milk in TBS-T at room temperature for 1 h. Afterward, the membrane was washed again. The detection was performed via enhanced chemiluminescence (ECL Prime) after incubation for 5 min in the dark with a FUSION-SL (PEQLAB) and the FUSION-CAPT software. After detection of acetylated tubulin, the whole procedure was repeated with the primary antibody antiacetyl-histone H3 (Millipore 06.599, 1:2000) and the secondary antibody anti-rabbit IgG-HRP (Sigma-Aldrich, 1:5000) to detect the acetylation of histone H3 and again with the primary antibody antiGAPDH (Sigma-Aldrich 69545-200UL, 1:5000) and the secondary antibody antirabbit IgGHRP (Sigma-Aldrich, 1:10 000) to control the loading amount.

4.5. Docking and molecular dynamics simulations

4.5.1. Docking into HDAC8

The crystal structure of an HDAC8/inhibitor complex (PDB ID 2V5X) was downloaded from Protein Data Bank [107] and only chain A was retained. Protein preparation was done using Schrödinger's Protein Preparation Wizard (Schrödinger Suite 2017−1: Protein Preparation Wizard; Epik, Schrödinger, LLC, New York, NY, 2016; Impact, Schrödinger, LLC, New York, NY, 2016; Prime, Schrödinger, LLC, New York, NY, 2017) by adding hydrogen atoms, assigning protonation states and minimizing the protein. Solvent molecules were removed except for two conserved water molecules: HOH2061 and HOH2152. Hydrogen bond networks, amino acid residues protonation states and tautomers were optimized, and the complex was finally subjected to energy minimization using the OPLS-2005 force field using the default settings. Receptor grids were generated using default settings by assigning the cocrystallized ligand as the center of the grid.

Ligands were first prepared using LigPrep (Schrödinger Release 2017−1: LigPrep, Schrödinger, LLC, New York, NY, 2017) were the hydroxamic acids were kept in the neutral forms and energy minimized using the OPLS2005 force field. Twenty conformers for each ligand were subsequently generated using ConfGen (Schrödinger Release 2017−1: ConfGen, Schrödinger, LLC, New York, NY, 2017).

Molecular docking was performed using Glide (Schrödinger Release 2017−1: Glide, Schrödinger, LLC, New York, NY, 2017) in the Standard Precision mode. Default settings without any constraints were used, the number of docking poses for post-docking minimization per ligand was increased to 20 and the maximal number of output poses per ligand was set to 2.

4.5.2. Docking into HDAC6

The crystal structure HDAC6/trichostatin A complex (PDB ID 5EDU) was downloaded from the Protein Data Bank and only chain A was kept. Since the crystal structure was resolved without water molecules in the binding site, we chose to insert the crucial water molecules by superposing with the crystal structures of the homologous DrHDAC6 in complex with HPOB (PDB ID 5EF7). Altogether, four water molecules (HOH 921, 990, 999, and 1011) together with the cocrystallized ligand HPOP were taken from chain A of the crystal structure of DrHDAC6 (PDB ID 5EF7). Further protein preparation was performed as described for HDAC8; the ligand was however kept in the deprotonated hydroxamate form. Ligands were generated in the hydroxamate form and further prepared using Ligprep and ConfGen as previously described.

Molecular docking was performed using Glide in the Standard Precision mode using the same settings as with HDAC8.

4.5.3. Docking into BRPF1

The crystal structure BRPF1/**NI-57** complex (PDB ID 5MYG) was downloaded from the Protein Data Bank, and only chain C together with the ligand and four water molecules (HOH 906, 907, 910, and 911) were kept. The complex was prepared using Schrödinger's Protein Preparation Wizard as described for HDAC8. Ligands were

prepared using LigPrep and 20 conformers were generated using ConfGen as previously described. Docking was finally performed using Glide in the Standard Precision mode using the same setting as described for HDAC8. The applied setting was able to reproduce the binding mode of **NI-57** in BRPF1 (RMSD < 1 Å).

4.5.4. Molecular dynamics simulation

Initial coordinates of the BRPF1/ligand complexes were taken from the obtained docking poses described above. MD simulations were performed using Amber16 package (AMBER 2016, UCSF, San Francisco, California, USA, 2016). Force field parameters for the ligands were assigned using the Antechamber package and AM1-BCC atomic charges [108,109]. The complex structure was combined using the TLeap module, where the ff14SB force field [110,111] and the General Amber Force Field (GAFF2) [112] were used for the parameterization of protein residues and ligand, respectively. The complex structures were solvated in an octahedral periodic box of SPC/E water molecules [113] at a margin of 10 Å and the system was neutralized using Na^+ counter ions.

The system was first subjected to two steps of minimization: The first step involved the minimization of only the solvent atoms in 3000 iterations (first 1000 steepest descent and then 2000 conjugate gradient), while restraining the protein, ligand and conserved water molecules to their initial coordinates with a force constant of 10 kcal*mol^{-1}*Å^{-2}. In the second step, the whole system was minimized with no restraints using 4000 iterations (first 2000 steepest descent and then 2000 conjugate gradient). The system was subsequently heated to the production temperature (300 K) through 100 ps of MD simulation, while keeping the complex atoms (protein, ligand and conserved water molecules) restrained with a force constant of 10 kcal*mol^{-1}*Å^{-2}. Constant volume periodic boundary was set to equilibrate the temperature of the system by Langevin thermostat using a collision frequency of 2 ps^{-1}. The system was subsequently subjected to a pressure equilibration routine for 100 ps at 300 K, where a constant pressure of 1 bar was applied.

Finally, a production run of 100 ns with a time step of 2 fs was simulated at a constant temperature of 300 K using Langevin thermostat with a collision frequency of 2 ps^{-1}. Constant pressure periodic boundary was used to maintain the pressure of the system at 1 bar using isotropic position scaling with a relaxation time of 2 ps. A non-bonded cut-off distance of 10.0 Å for long-range electrostatic interactions was used by applying the Particle Mesh Ewald (PME) [114] method during the temperature equilibration and MD routines. The SHAKE algorithm [115] was applied to constrain all bonds involving hydrogen. All simulations were run using PMEMD.cuda implementation in Amber16 on CUDA-enabled NVIDIA graphics processing units (GPUs).

RMSD analysis of the trajectories was performed using the CPPTRAJ module of Amber16. Plots were generated using the R package, and the videos using PYMOL.

4.5.5. PAINS filter

All the herein described compounds were filtered for pan-assay interference compounds (PAINS) [116]. For this purpose, PAINS1, PAINS2 and PAINS3 filters, as implemented in Schrödinger's Canvas program, were employed. None of the compounds was flagged as PAINS.

Author contribution

Ehab Ghazy: Synthesis of all inhibitors, preparation of manuscript.

Patrik Zeyen: Carried out HDAC8 in vitro assays.

Daniel Herp: Carried out HDAC1 and 6 in vitro assays.

Karin Schmidtkunz: AML cellular assays and Western blot.

Martin Hügle: Produced the recombinant BRPF1 protein and ran the ITC assay.

Frank Erdmann: Carried out cytotoxicity tests on HEK293 cells.

Dina Robaa: Did all modelling studies, preparation of manuscript.

Matthias Schmidt: Did compound analytics, supervision of organic synthesis.

Elizabeth R. Morales: Produced the recombinant HDAC8 protein for in vitro testing.

Christophe Romier: Coordination of protein expression and preparation of manuscript.

Stefan Günther: Coordination of ITC assays, preparation of manuscript.

Manfred Jung: Coordination of HDAC1&6, AML cellular assays and Western blot, preparation of manuscript.

Wolfgang Sippl: Study design, research planning, preparation of manuscript.

Declaration of competing interest

The authors declare that they have no known competing financial interests or personal relationships that could have appeared to influence the work reported in this paper.

Acknowledgment

E.G. received his scholarship through the GERLS program from the German Academic Exchange Service (DAAD) and Ministry of higher education, Egypt. W.S. and M.J. acknowledge the funding from Deutsche Forschungsgemeinschaft (DFG Grants Ju 295/13−1, Si 846/13−1)). This work was supported by the European Regional Development Fund of the European Commission.

Appendix A. Supplementary data

Supplementary data to this article can be found online at https://doi.org/10.1016/j.ejmech.2020.112338.

Abbreviations

HDAC	Histone Deacetylase
BRD	Bromodomain
PTMs	Post-Translational Modification
DNA	Deoxyribonucleic Acid
HAT	Histone Acetyltransferase
BRPF	Bromodomain and PHD Finger-Containing Protein
FDA	U.S. Food and Drug Administration
HSP 90	Heat Shock Protein 90
BET	Bromodomain and Extra-Terminal Motif
PDB	Protein Data Bank
RMSD	Root-Mean-Square Deviation
MD	Molecular Dynamics
AML	Acute Myeloid Leukemia
GAPDH	Glyceraldehyde 3-Phosphate Dehydrogenase
Ac	Acetylated
DMSO	Dimethyl Sulfoxide
TFA	Trifluoroacetic Acid
PyBOP	Benzotriazol-1-Yl-Oxytripyrrolidinophosphonium Hexafluorophosphate
HATU	Hexafluorophosphate Azabenzotriazole Tetramethyl Uronium
HPLC	High-Performance Liquid Chromatography
UV	Ultraviolet
ESI-MS	Electrospray Ionization Mass Spectrometry

HRMS-ESI	High Resolution Mass Spectroscopy- Electrospray Ionization
EtOAc	Ethyl Acetate
DMF	Dimethylformamide
MeOH	Methanol
THF	Tetrahydrofuran
$CHCl_3$	Chloroform
H_2O	Water
CH_2Cl_2	Dichloromethane
DIPEA	*N*,*N*-Diisopropylethylamine
HCl	Hydrochloric Acid
TEA	Triethylamine
h	Hour
TLC	Thin Layer Chromatography
mmol	Millimole
Min	Minute
TSA	Trichostatin A
AMC	Aminomethylcoumarin
ITC	Isothermal Titration Calorimetry
DMEM	Dulbecco's Modified Eagle's Medium
SDS	Sodium Dodecyl Sulfate
PAGE	Polyacrylamide Gel Electrophoresis
TBS-T	Tris Buffered Saline With 0.1% Tween 20
ECL	Enhanced Chemiluminescence
GAFF2	General Amber Force Field
Ps	Picosecond
Gpus	Graphics Processing Units
HEK	Human Embryonic Kidney
n.d.	Not Determined

References

[1] G. Zhang, S. Pradhan, Mammalian epigenetic mechanisms, IUBMB Life 66 (2014) 240–256.
[2] J. Fan, K.A. Krautkramer, J.L. Feldman, J.M. Denu, Metabolic regulation of histone post-translational modifications, ACS Chem. Biol. 10 (2015) 95–108.
[3] A.M. Arnaudo, B.A. Garcia, Proteomic characterization of novel histone post-translational modifications, Epigenet. Chromatin 6 (2013) 24.
[4] R. Sanchez, J. Meslamani, M.M. Zhou, The bromodomain: from epigenome reader to druggable target, Biochim. Biophys. Acta 1839 (2014) 676–685.
[5] A. Spyropoulou, C. Piperi, C. Adamopoulos, A.G. Papavassiliou, Deregulated chromatin remodeling in the pathobiology of brain tumors, NeuroMolecular Med. 15 (2013) 1–24.
[6] F. Miao, I.G. Gonzalo, L. Lanting, R. Natarajan, In vivo chromatin remodeling events leading to inflammatory gene transcription under diabetic conditions, J. Biol. Chem. 279 (2004) 18091–18097.
[7] B.R. Selvi, D.V. Mohankrishna, Y.B. Ostwal, T.K. Kundu, Small molecule modulators of histone acetylation and methylation: a disease perspective, Biochim. Biophys. Acta 1799 (2010) 810–828.
[8] S.N. Khan, A.U. Khan, Role of histone acetylation in cell physiology and diseases: an update, Clin. Chim. Acta 411 (2010) 1401–1411.
[9] S. Timmermann, H. Lehrmann, A. Polesskaya, A. Harel-Bellan, Histone acetylation and disease, Cell. Mol. Life Sci. 58 (2001) 728–736.
[10] G.A. Josling, S.A. Selvarajah, M. Petter, M.F. Duffy, The role of bromodomain proteins in regulating gene expression, Genes 3 (2012) 320–343.
[11] E. Ferri, C. Petosa, C.E. McKenna, Bromodomains: structure, function and pharmacology of inhibition, Biochem. Pharmacol. 106 (2016) 1–18.
[12] P. Filippakopoulos, S. Knapp, Targeting bromodomains: epigenetic readers of lysine acetylation, Nat. Rev. Drug Discov. 13 (2014) 337–356.
[13] F.A. Romero, A.M. Taylor, T.D. Crawford, V. Tsui, A. Cote, S. Magnuson, Disrupting acetyl-lysine recognition: progress in the development of bromodomain inhibitors, J. Med. Chem. 59 (2016) 1271–1298.
[14] S.G. Smith, M.M. Zhou, The bromodomain: a New target in emerging epigenetic medicine, ACS Chem. Biol. 11 (2016) 598–608.
[15] B.J. Klein, M.E. Lalonde, J. Cote, X.J. Yang, T.G. Kutateladze, Crosstalk between epigenetic readers regulates the MOZ/MORF HAT complexes, Epigenetics 9 (2014) 186–193.
[16] A. Poplawski, K. Hu, W. Lee, S. Natesan, D. Peng, S. Carlson, X. Shi, S. Balaz, J.L. Markley, K.C. Glass, Molecular insights into the recognition of N-terminal histone modifications by the BRPF1 bromodomain, J. Mol. Biol. 426 (2014) 1661–1676.
[17] H. Shima, K. Yamagata, Y. Aikawa, M. Shino, H. Koseki, H. Shimada, I. Kitabayashi, Bromodomain-PHD finger protein 1 is critical for leukemogenesis associated with MOZ-TIF2 fusion, Int. J. Hematol. 99 (2014) 21–31.
[18] E.H. Demont, P. Bamborough, C.W. Chung, P.D. Craggs, D. Fallon, L.J. Gordon, P. Grandi, C.I. Hobbs, J. Hussain, E.J. Jones, A. Le Gall, A.M. Michon, D.J. Mitchell, R.K. Prinjha, A.D. Roberts, R.J. Sheppard, R.J. Watson, 1,3-Dimethyl benzimidazolones are potent, selective inhibitors of the BRPF1 bromodomain, ACS Med. Chem. Lett. 5 (2014) 1190–1195.
[19] P. Bamborough, H.A. Barnett, I. Becher, M.J. Bird, C.W. Chung, P.D. Craggs, E.H. Demont, H. Diallo, D.J. Fallon, L.J. Gordon, P. Grandi, C.I. Hobbs, E. Hooper-Greenhill, E.J. Jones, R.P. Law, A. Le Gall, D. Lugo, A.M. Michon, D.J. Mitchell, R.K. Prinjha, R.J. Sheppard, A.J. Watson, R.J. Watson, GSK6853, a chemical probe for inhibition of the BRPF1 bromodomain, ACS Med. Chem. Lett. 7 (2016) 552–557.
[20] W.S. Palmer, Development of small molecule inhibitors of BRPF1 and TRIM24 bromodomains, Drug Discov. Today Technol. 19 (2016) 65–71.
[21] W.S. Palmer, G. Poncet-Montange, G. Liu, A. Petrocchi, N. Reyna, G. Subramanian, J. Theroff, A. Yau, M. Kost-Alimova, J.P. Bardenhagen, E. Leo, H.E. Shepard, T.N. Tieu, X. Shi, Y. Zhan, S. Zhao, M.C. Barton, G. Draetta, C. Toniatti, P. Jones, M. Geck Do, J.N. Andersen, Structure-guided design of IACS-9571, a selective high-affinity dual TRIM24-BRPF1 bromodomain inhibitor, J. Med. Chem. 59 (2016) 1440–1454.
[22] J. Bennett, O. Fedorov, C. Tallant, O. Monteiro, J. Meier, V. Gamble, P. Savitsky, G.A. Nunez-Alonso, B. Haendler, C. Rogers, P.E. Brennan, S. Muller, S. Knapp, Discovery of a chemical tool inhibitor targeting the bromodomains of TRIM24 and BRPF, J. Med. Chem. 59 (2016) 1642–1647.
[23] L. Bouche, C.D. Christ, S. Siegel, A.E. Fernandez-Montalvan, S.J. Holton, O. Fedorov, A. Ter Laak, T. Sugawara, D. Stockigt, C. Tallant, J. Bennett, O. Monteiro, L. Diaz-Saez, P. Siejka, J. Meier, V. Putter, J. Weiske, S. Muller, K.V.M. Huber, I.V. Hartung, B. Haendler, Benzoisoquinolinediones as potent and selective inhibitors of BRPF2 and TAF1/TAF1L bromodomains, J. Med. Chem. 60 (2017) 4002–4022.
[24] N. Igoe, E.D. Bayle, O. Fedorov, C. Tallant, P. Savitsky, C. Rogers, D.R. Owen, G. Deb, T.C. Somervaille, D.M. Andrews, N. Jones, A. Cheasty, H. Ryder, P.E. Brennan, S. Muller, S. Knapp, P.V. Fish, Design of a biased potent small molecule inhibitor of the bromodomain and PHD finger-containing (BRPF) proteins suitable for cellular and in vivo studies, J. Med. Chem. 60 (2017) 668–680.
[25] N. Igoe, E.D. Bayle, C. Tallant, O. Fedorov, J.C. Meier, P. Savitsky, C. Rogers, Y. Morias, S. Scholze, H. Boyd, D. Cunoosamy, D.M. Andrews, A. Cheasty, P.E. Brennan, S. Muller, S. Knapp, P.V. Fish, Design of a chemical probe for the bromodomain and plant homeodomain finger-containing (BRPF) family of proteins, J. Med. Chem. 60 (2017) 6998–7011.
[26] J. Zhu, A. Caflisch, Twenty crystal structures of bromodomain and PHD finger containing protein 1 (BRPF1)/Ligand complexes reveal conserved binding motifs and rare interactions, J. Med. Chem. 59 (2016) 5555–5561.
[27] J. Zhu, C. Zhou, A. Caflisch, Structure-based discovery of selective BRPF1 bromodomain inhibitors, Eur. J. Med. Chem. 155 (2018) 337–352.
[28] P. Bertrand, Inside HDAC with HDAC inhibitors, Eur. J. Med. Chem. 45 (2010) 2095–2116.
[29] L. Zhang, J. Zhang, Q. Jiang, L. Zhang, W. Song, Zinc binding groups for histone deacetylase inhibitors, J. Enzym. Inhib. Med. Chem. 33 (2018) 714–721.
[30] P. Gallo, M.V. Latronico, P. Gallo, S. Grimaldi, F. Borgia, M. Todaro, P. Jones, P. Gallinari, R. De Francesco, G. Ciliberto, C. Steinkuhler, G. Esposito, G. Condorelli, Inhibition of class I histone deacetylase with an apicidin derivative prevents cardiac hypertrophy and failure, Cardiovasc. Res. 80 (2008) 416–424.
[31] H. Kook, J.J. Lepore, A.D. Gitler, M.M. Lu, W. Wing-Man Yung, J. Mackay, R. Zhou, V. Ferrari, P. Gruber, J.A. Epstein, Cardiac hypertrophy and histone deacetylase-dependent transcriptional repression mediated by the atypical homeodomain protein Hop, J. Clin. Invest. 112 (2003) 863–871.
[32] A. Mai, D. Rotili, S. Valente, A.G. Kazantsev, Histone deacetylase inhibitors and neurodegenerative disorders: holding the promise, Curr. Pharmaceut. Des. 15 (2009) 3940–3957.
[33] E. Soragni, C. Xu, A. Cooper, H.L. Plasterer, J.R. Rusche, J.M. Gottesfeld, Evaluation of histone deacetylase inhibitors as therapeutics for neurodegenerative diseases, Methods Mol. Biol. 793 (2011) 495–508.
[34] Y. Zhou, Q. Wang, Q. Yang, J. Tang, C. Xu, D. Gai, X. Chen, J. Chen, Histone deacetylase 3 inhibitor suppresses hepatitis C virus replication by regulating apo-A1 and LEAP-1 expression, Virol. Sin. 33 (2018) 418–428.
[35] T.D. Zaikos, M.M. Painter, N.T. Sebastian Kettinger, V.H. Terry, K.L. Collins, Class 1-selective histone deacetylase (HDAC) inhibitors enhance HIV latency reversal while preserving the activity of HDAC isoforms necessary for maximal HIV gene expression, J. Virol. 92 (2018).
[36] Y. Imai, Y. Maru, J. Tanaka, Action mechanisms of histone deacetylase inhibitors in the treatment of hematological malignancies, Canc. Sci. 107 (2016) 1543–1549.
[37] A.C. West, R.W. Johnstone, New and emerging HDAC inhibitors for cancer treatment, J. Clin. Invest. 124 (2014) 30–39.
[38] A. Suraweera, K.J. O'Byrne, D.J. Richard, Combination therapy with histone deacetylase inhibitors (HDACi) for the treatment of cancer: achieving the full therapeutic potential of HDACi, Front. Oncol. 8 (2018) 92.
[39] I. Kopljar, D.J. Gallacher, A. De Bondt, L. Cougnaud, E. Vlaminckx, I. Van den Wyngaert, H.R. Lu, Functional and transcriptional characterization of histone deacetylase inhibitor-mediated cardiac adverse effects in human induced pluripotent stem cell-derived cardiomyocytes, Stem Cells Transl. Med. 5 (2016) 602–612.
[40] J. Roche, P. Bertrand, Inside HDACs with more selective HDAC inhibitors, Eur. J. Med. Chem. 121 (2016) 451–483.

[41] J. Fraczek, T. Vanhaecke, V. Rogiers, Toxicological and metabolic considerations for histone deacetylase inhibitors, Expet Opin. Drug Metabol. Toxicol. 9 (2013) 441–457.
[42] S. Dallavalle, C. Pisano, F. Zunino, Development and therapeutic impact of HDAC6-selective inhibitors, Biochem. Pharmacol. 84 (2012) 756–765.
[43] G.I. Aldana-Masangkay, K.M. Sakamoto, The role of HDAC6 in cancer, J. Biomed. Biotechnol. 2011 (2011) 875824.
[44] K.V. Butler, J. Kalin, C. Brochier, G. Vistoli, B. Langley, A.P. Kozikowski, Rational design and simple chemistry yield a superior, neuroprotective HDAC6 inhibitor, tubastatin A, J. Am. Chem. Soc. 132 (2010) 10842–10846.
[45] C. Zhang, C.J. Chou, Metal-free direct amidation of naphthoquinones using hydroxamic acids as an amide source: application in the synthesis of an HDAC6 inhibitor, Org. Lett. 18 (2016) 5512–5515.
[46] R. De Vreese, N. Van Steen, T. Verhaeghe, T. Desmet, N. Bougarne, K. De Bosscher, V. Benoy, W. Haeck, L. Van Den Bosch, M. D'Hooghe, Synthesis of benzothiophene-based hydroxamic acids as potent and selective HDAC6 inhibitors, Chem. Commun. 51 (2015) 9868–9871.
[47] J. Senger, J. Melesina, M. Marek, C. Romier, I. Oehme, O. Witt, W. Sippl, M. Jung, Synthesis and biological investigation of oxazole hydroxamates as highly selective histone deacetylase 6 (HDAC6) inhibitors, J. Med. Chem. 59 (2016) 1545–1555.
[48] H.-Y. Lee, A.-C. Tsai, M.-C. Chen, P.-J. Shen, Y.-C. Cheng, C.-C. Kuo, S.-L. Pan, Y.-M. Liu, J.-F. Liu, T.-K. Yeh, J.-C. Wang, C.-Y. Chang, J.-Y. Chang, J.-P. Liou, Azaindolylsulfonamides, with a more selective inhibitory effect on histone deacetylase 6 activity, exhibit antitumor activity in colorectal cancer HCT116 cells, J. Med. Chem. 57 (2014) 4009–4022.
[49] Z. Yang, T. Wang, F. Wang, T. Niu, Z. Liu, X. Chen, C. Long, M. Tang, D. Cao, X. Wang, W. Xiang, Y. Yi, L. Ma, J. You, L. Chen, Discovery of selective histone deacetylase 6 inhibitors using the quinazoline as the cap for the treatment of cancer, J. Med. Chem. 59 (2016) 1455–1470.
[50] S. Shen, M. Hadley, K. Ustinova, J. Pavlíček, T. Knox, S. Noonepalle, M.T. Tavares, C.A. Zimprich, G. Zhang, M.B. Robers, C. Barinka, A. Kozikowski, A. Villagra, Discovery of a New isoxazole-3-hydroxamate based histone deacetylase 6 inhibitor SS-208 with anti-tumor activity in syngeneic melanoma mouse models, J. Med. Chem. 62 (18) (2019) 8557–8577.
[51] X.X. Wang, R.Z. Wan, Z.P. Liu, Recent advances in the discovery of potent and selective HDAC6 inhibitors, Eur. J. Med. Chem. 143 (2018) 1406–1418.
[52] C. Simões-Pires, V. Zwick, A. Nurisso, E. Schenker, P.-A. Carrupt, M. Cuendet, HDAC6 as a target for neurodegenerative diseases: what makes it different from the other HDACs? Mol. Neurodegener. 8 (2013) 7.
[53] G. Li, H. Jiang, M. Chang, H. Xie, L. Hu, HDAC6 α-tubulin deacetylase: a potential therapeutic target in neurodegenerative diseases, J. Neurol. Sci. 304 (2011) 1–8.
[54] Y. Li, D. Shin, S.H. Kwon, Histone deacetylase 6 plays a role as a distinct regulator of diverse cellular processes, FEBS J. 280 (2013) 775–793.
[55] M. Brindisi, A.P. Saraswati, S. Brogi, S. Gemma, S. Butini, G. Campiani, Old but gold: tracking the New guise of histone deacetylase 6 (HDAC6) enzyme as a biomarker and therapeutic target in rare diseases, J. Med. Chem. 63 (1) (2019) 23–39.
[56] Y. Depetter, S. Geurs, R. De Vreese, S. Goethals, E. Vandoorn, A. Laevens, J. Steenbrugge, E. Meyer, P. de Tullio, M. Bracke, M. D'Hooghe, O. De Wever, Selective pharmacological inhibitors of HDAC6 reveal biochemical activity but functional tolerance in cancer models, Int. J. Canc. 145 (3) (2019) 735–747.
[57] K. Vogerl, N. Ong, J. Senger, D. Herp, K. Schmidtkunz, M. Marek, M. Muller, K. Bartel, T.B. Shaik, N.J. Porter, D. Robaa, D.W. Christianson, C. Romier, W. Sippl, M. Jung, F. Bracher, Synthesis and biological investigation of phenothiazine-based benzhydroxamic acids as selective histone deacetylase 6 inhibitors, J. Med. Chem. 62 (2019) 1138–1166.
[58] J. Li, S. Chen, R.A. Cleary, R. Wang, O.J. Gannon, E. Seto, D.D. Tang, Histone deacetylase 8 regulates cortactin deacetylation and contraction in smooth muscle tissues, Am. J. Physiol. Cell Physiol. 307 (2014) C288–C295.
[59] A. Chakrabarti, I. Oehme, O. Witt, G. Oliveira, W. Sippl, C. Romier, R.J. Pierce, M. Jung, HDAC8: a multifaceted target for therapeutic interventions, Trends Pharmacol. Sci. 36 (2015) 481–492.
[60] M. Marek, T.B. Shaik, T. Heimburg, A. Chakrabarti, J. Lancelot, E. Ramos-Morales, C. Da Veiga, D. Kalinin, J. Melesina, D. Robaa, K. Schmidtkunz, T. Suzuki, R. Holl, E. Ennifar, R.J. Pierce, M. Jung, W. Sippl, C. Romier, Characterization of histone deacetylase 8 (HDAC8) selective inhibition reveals specific active site structural and functional determinants, J. Med. Chem. 61 (2018) 10000–10016.
[61] C. Zhao, J. Zang, Q. Ding, E.S. Inks, W. Xu, C.J. Chou, Y. Zhang, Discovery of meta-sulfamoyl N-hydroxybenzamides as HDAC8 selective inhibitors, Eur. J. Med. Chem. 150 (2018) 282–291.
[62] W.J. Huang, Y.C. Wang, S.W. Chao, C.Y. Yang, L.C. Chen, M.H. Lin, W.C. Hou, M.Y. Chen, T.L. Lee, P. Yang, C.I. Chang, Synthesis and biological evaluation of ortho-aryl N-hydroxycinnamides as potent histone deacetylase (HDAC) 8 isoform-selective inhibitors, ChemMedChem 7 (2012) 1815–1824.
[63] O.J. Ingham, R.M. Paranal, W.B. Smith, R.A. Escobar, H. Yueh, T. Snyder, J.A. Porco Jr., J.E. Bradner, A.B. Beeler, Development of a potent and selective HDAC8 inhibitor, ACS Med. Chem. Lett. 7 (2016) 929–932.
[64] T. Heimburg, F.R. Kolbinger, P. Zeyen, E. Ghazy, D. Herp, K. Schmidtkunz, J. Melesina, T.B. Shaik, F. Erdmann, M. Schmidt, C. Romier, D. Robaa, O. Witt, I. Oehme, M. Jung, W. Sippl, Structure-based design and biological characterization of selective histone deacetylase 8 (HDAC8) inhibitors with anti-neuroblastoma activity, J. Med. Chem. 60 (2017) 10188–10204.
[65] T. Suzuki, Y. Ota, M. Ri, M. Bando, A. Gotoh, Y. Itoh, H. Tsumoto, P.R. Tatum, T. Mizukami, H. Nakagawa, S. Iida, R. Ueda, K. Shirahige, N. Miyata, Rapid discovery of highly potent and selective inhibitors of histone deacetylase 8 using click chemistry to generate candidate libraries, J. Med. Chem. 55 (2012) 9562–9575.
[66] S. Balasubramanian, J. Ramos, W. Luo, M. Sirisawad, E. Verner, J.J. Buggy, A novel histone deacetylase 8 (HDAC8)-specific inhibitor PCI-34051 induces apoptosis in T-cell lymphomas, Leukemia 22 (2008) 1026–1034.
[67] S.A. Amin, N. Adhikari, T. Jha, Structure-activity relationships of HDAC8 inhibitors: non-hydroxamates as anticancer agents, Pharmacol. Res. 131 (2018) 128–142.
[68] S. Banerjee, N. Adhikari, S.A. Amin, T. Jha, Histone deacetylase 8 (HDAC8) and its inhibitors with selectivity to other isoforms: an overview, Eur. J. Med. Chem. 164 (2019) 214–240.
[69] A.R. de Lera, A. Ganesan, Epigenetic polypharmacology: from combination therapy to multitargeted drugs, Clin. Epigenet. 8 (2016) 105.
[70] R. Schobert, B. Biersack, Multimodal HDAC inhibitors with improved anticancer activity, Curr. Cancer Drug Targets 18 (2018) 39–56.
[71] P. Ciceri, S. Muller, A. O'Mahony, O. Fedorov, P. Filippakopoulos, J.P. Hunt, E.A. Lasater, G. Pallares, S. Picaud, C. Wells, S. Martin, L.M. Wodicka, N.P. Shah, D.K. Treiber, S. Knapp, Dual kinase-bromodomain inhibitors for rationally designed polypharmacology, Nat. Chem. Biol. 10 (2014) 305–312.
[72] L. Chen, J.L. Yap, M. Yoshioka, M.E. Lanning, R.N. Fountain, M. Raje, J.A. Scheenstra, J.W. Strovel, S. Fletcher, BRD4 structure-activity relationships of dual PLK1 kinase/BRD4 bromodomain inhibitor BI-2536, ACS Med. Chem. Lett. 6 (2015) 764–769.
[73] S. Liu, H.O. Yosief, L. Dai, H. Huang, G. Dhawan, X. Zhang, A.M. Muthengi, J. Roberts, D.L. Buckley, J.A. Perry, L. Wu, J.E. Bradner, J. Qi, W. Zhang, Structure-guided design and development of potent and selective dual bromodomain 4 (BRD4)/Polo-like kinase 1 (PLK1) inhibitors, J. Med. Chem. 61 (2018) 7785–7795.
[74] J. Wang, T. Erazo, F.M. Ferguson, D.L. Buckley, N. Gomez, P. Munoz-Guardiola, N. Dieguez-Martinez, X. Deng, M. Hao, W. Massefski, O. Fedorov, N.K. Offei-Addo, P.M. Park, L. Dai, A. DiBona, K. Becht, N.D. Kim, M.R. McKeown, J.M. Roberts, J. Zhang, T. Sim, D.R. Alessi, J.E. Bradner, J.M. Lizcano, S.C. Blacklow, J. Qi, X. Xu, N.S. Gray, Structural and atropisomeric factors governing the selectivity of pyrimido-benzodiazipinones as inhibitors of kinases and bromodomains, ACS Chem. Biol. 13 (2018) 2438–2448.
[75] S.J. Atkinson, P.E. Soden, D.C. Angell, M. Bantscheff, C.W. Chung, K.A. Giblin, N. Smithers, R.C. Furze, L. Gordon, G. Drewes, I. Rioja, J. Witherington, N.J. Parr, R.K. Prinjha, The structure based design of dual HDAC/BET inhibitors as novel epigenetic probes, Medchemcomm 5 (2014) 342–351.
[76] Z. Zhang, S. Hou, H. Chen, T. Ran, F. Jiang, Y. Bian, D. Zhang, Y. Zhi, L. Wang, L. Zhang, H. Li, Y. Zhang, W. Tang, T. Lu, Y. Chen, Targeting epigenetic reader and eraser: rational design, synthesis and in vitro evaluation of dimethylisoxazoles derivatives as BRD4/HDAC dual inhibitors, Bioorg. Med. Chem. Lett 26 (2016) 2931–2935.
[77] S. Amemiya, T. Yamaguchi, Y. Hashimoto, T. Noguchi-Yachide, Synthesis and evaluation of novel dual BRD4/HDAC inhibitors, Bioorg. Med. Chem. 25 (2017) 3677–3684.
[78] M. Shao, L. He, L. Zheng, L. Huang, Y. Zhou, T. Wang, Y. Chen, M. Shen, F. Wang, Z. Yang, L. Chen, Structure-based design, synthesis and in vitro antiproliferative effects studies of novel dual BRD4/HDAC inhibitors, Bioorg. Med. Chem. Lett 27 (2017) 4051–4055.
[79] G. Cheng, Z. Wang, J. Yang, Y. Bao, Q. Xu, L. Zhao, D. Liu, Design, synthesis and biological evaluation of novel indole derivatives as potential HDAC/BRD4 dual inhibitors and anti-leukemia agents, Bioorg. Chem. 84 (2019) 410–417.
[80] T. Heimburg, A. Chakrabarti, J. Lancelot, M. Marek, J. Melesina, A.T. Hauser, T.B. Shaik, S. Duclaud, D. Robaa, F. Erdmann, M. Schmidt, C. Romier, R.J. Pierce, M. Jung, W. Sippl, Structure-based design and synthesis of novel inhibitors targeting HDAC8 from schistosoma mansoni for the treatment of schistosomiasis, J. Med. Chem. 59 (2016) 2423–2435.
[81] R. De Vreese, M. D'Hooghe, Synthesis and applications of benzohydroxamic acid-based histone deacetylase inhibitors, Eur. J. Med. Chem. 135 (2017) 174–195.
[82] B. Hackanson, L. Rimmele, M. Benkisser, M. Abdelkarim, M. Fliegauf, M. Jung, M. Lubbert, HDAC6 as a target for antileukemic drugs in acute myeloid leukemia, Leuk. Res. 36 (2012) 1055–1062.
[83] K.L. Durst, B. Lutterbach, T. Kummalue, A.D. Friedman, S.W. Hiebert, The inv(16) fusion protein associates with corepressors via a smooth muscle myosin heavy-chain domain, Mol. Cell Biol. 23 (2003) 607–619.
[84] J. Qi, S. Singh, W.K. Hua, Q. Cai, S.W. Chao, L. Li, H. Liu, Y. Ho, T. McDonald, A. Lin, G. Marcucci, R. Bhatia, W.J. Huang, C.I. Chang, Y.H. Kuo, HDAC8 inhibition specifically targets inv(16) acute myeloid leukemic stem cells by restoring p53 acetylation, Cell stem cell 17 (2015) 597–610.
[85] K. King, A.T. Hauser, J. Melesina, W. Sippl, M. Jung, Carbamates as potential prodrugs and a New warhead for HDAC inhibition, Molecules 23 (2018) 321.
[86] S. Zheng, S. Guo, Q. Zhong, C. Zhang, J. Liu, L. Yang, Q. Zhang, G. Wang, Biocompatible boron-containing prodrugs of belinostat for the potential treatment of solid tumors, ACS Med. Chem. Lett. 9 (2018) 149–154.
[87] S. Schlimme, A.T. Hauser, V. Carafa, R. Heinke, S. Kannan, D.A. Stolfa, S. Cellamare, A. Carotti, L. Altucci, M. Jung, W. Sippl, Carbamate prodrug concept for hydroxamate HDAC inhibitors, ChemMedChem 6 (2011) 1193–1198.

[88] H. Seki, S. Pellett, P. Silhar, G.N. Stowe, B. Blanco, M.A. Lardy, E.A. Johnson, K.D. Janda, Synthesis/biological evaluation of hydroxamic acids and their prodrugs as inhibitors for Botulinum neurotoxin A light chain, Bioorg. Med. Chem. 22 (2014) 1208–1217.
[89] P. Silhar, L.M. Eubanks, H. Seki, S. Pellett, S. Javor, W.H. Tepp, E.A. Johnson, K.D. Janda, Targeting botulinum A cellular toxicity: a prodrug approach, J. Med. Chem. 56 (2013) 7870–7879.
[90] Y. Liao, L. Xu, S. Ou, H. Edwards, D. Luedtke, Y. Ge, Z. Qin, H2O2/Peroxynitrite-Activated hydroxamic acid HDAC inhibitor prodrugs show antileukemic activities against AML cells, ACS Med. Chem. Lett. 9 (2018) 635–640.
[91] R. Rais, J. Vavra, T. Tichy, R.P. Dash, A.J. Gadiano, L. Tenora, L. Monincova, C. Barinka, J. Alt, S.C. Zimmermann, C.E. Slusher, Y. Wu, K. Wozniak, P. Majer, T. Tsukamoto, B.S. Slusher, Discovery of a para-Acetoxy-benzyl ester prodrug of a hydroxamate-based glutamate carboxypeptidase II inhibitor as oral therapy for neuropathic pain, J. Med. Chem. 60 (2017) 7799–7809.
[92] D. Cantillo, M.M. Moghaddam, C.O. Kappe, Hydrazine-mediated reduction of nitro and azide functionalities catalyzed by highly active and reusable magnetic iron oxide nanocrystals, J. Org. Chem. 78 (2013) 4530–4542.
[93] K. Hada, A. Suda, K. Asoh, T. Tsukuda, M. Hasegawa, Y. Sato, K. Ogawa, S. Kuramoto, Y. Aoki, N. Shimma, T. Ishikawa, H. Koyano, Angiogenesis inhibitors identified by cell-based high-throughput screening: synthesis, structure-activity relationships and biological evaluation of 3-[(E)-styryl] benzamides that specifically inhibit endothelial cell proliferation, Bioorg. Med. Chem. 20 (2012) 1442–1460.
[94] Y. Jiao, B.T. Xin, Y. Zhang, J. Wu, X. Lu, Y. Zheng, W. Tang, X. Zhou, Design, synthesis and evaluation of novel 2-(1H-imidazol-2-yl) pyridine Sorafenib derivatives as potential BRAF inhibitors and anti-tumor agents, Eur. J. Med. Chem. 90 (2015) 170–183.
[95] Organikum, Organisch-Chemisches Grundpraktikum, VEB Deutscher Verlag der Wissenschaften, 1986.
[96] M. McLaughlin, M. Palucki, I.W. Davies, Efficient access to azaindoles and indoles, Org. Lett. 8 (2006) 3307–3310.
[97] D.A. Stolfa, A. Stefanachi, J.M. Gajer, A. Nebbioso, L. Altucci, S. Cellamare, M. Jung, A. Carotti, Design, synthesis, and biological evaluation of 2-aminobenzanilide derivatives as potent and selective HDAC inhibitors, ChemMedChem 7 (2012) 1256–1266.
[98] M. Marek, S. Kannan, A.T. Hauser, M. Moraes Mourao, S. Caby, V. Cura, D.A. Stolfa, K. Schmidtkunz, J. Lancelot, L. Andrade, J.P. Renaud, G. Oliveira, W. Sippl, M. Jung, J. Cavarelli, R.J. Pierce, C. Romier, Structural basis for the inhibition of histone deacetylase 8 (HDAC8), a key epigenetic player in the blood fluke Schistosoma mansoni, PLoS Pathog. 9 (2013), e1003645.
[99] X. Lucas, D. Wohlwend, M. Hugle, K. Schmidtkunz, S. Gerhardt, R. Schule, M. Jung, O. Einsle, S. Gunther, 4-Acyl pyrroles: mimicking acetylated lysines in histone code reading, Angew Chem. Int. Ed. Engl. 52 (2013) 14055–14059.
[100] M. Hugle, X. Lucas, G. Weitzel, D. Ostrovskyi, B. Breit, S. Gerhardt, O. Einsle, S. Gunther, D. Wohlwend, 4-Acyl pyrrole derivatives yield novel vectors for designing inhibitors of the acetyl-lysine recognition site of BRD4(1), J. Med. Chem. 59 (2016) 1518–1530.
[101] M. Hugle, X. Lucas, D. Ostrovskyi, P. Regenass, S. Gerhardt, O. Einsle, M. Hau, M. Jung, B. Breit, S. Gunther, D. Wohlwend, Beyond the BET family: targeting CBP/p300 with 4-acyl pyrroles, Angew Chem. Int. Ed. Engl. 56 (2017) 12476–12480.
[102] S. Keller, C. Vargas, H. Zhao, G. Piszczek, C.A. Brautigam, P. Schuck, High-precision isothermal titration calorimetry with automated peak-shape analysis, Anal. Chem. 84 (2012) 5066–5073.
[103] C.A. Brautigam, H.Y. Zhao, C. Vargas, S. Keller, P. Schuck, Integration and global analysis of isothermal titration calorimetry data for studying macromolecular interactions, Nat. Protoc. 11 (2016) 882–894.
[104] J.C. Houtman, P.H. Brown, B. Bowden, H. Yamaguchi, E. Appella, L.E. Samelson, P. Schuck, Studying multisite binary and ternary protein interactions by global analysis of isothermal titration calorimetry data in SEDPHAT: application to adaptor protein complexes in cell signaling, Protein Sci. 16 (2007) 30–42.
[105] C.A. Brautigam, Chapter five - calculations and publication-quality illustrations for analytical ultracentrifugation data, in: J.L. Cole (Ed.), Methods Enzymol., Academic Press, 2015, pp. 109–133.
[106] S.D. Furdas, S. Shekfeh, E.M. Bissinger, J.M. Wagner, S. Schlimme, V. Valkov, M. Hendzel, M. Jung, W. Sippl, Synthesis and biological testing of novel pyridoisothiazolones as histone acetyltransferase inhibitors, Bioorg. Med. Chem. 19 (2011) 3678–3689.
[107] H.M. Berman, J. Westbrook, Z. Feng, G. Gilliland, T.N. Bhat, H. Weissig, I.N. Shindyalov, P.E. Bourne, The protein Data Bank, Nucleic Acids Res. 28 (2000) 235–242.
[108] A. Jakalian, B.L. Bush, D.B. Jack, C.I. Bayly, Fast, efficient generation of high-quality atomic Charges. AM1-BCC model: I. Method, J. Comput. Chem. 21 (2000) 132–146.
[109] A. Jakalian, D.B. Jack, C.I. Bayly, Fast, efficient generation of high-quality atomic charges. AM1-BCC model: II. Parameterization and validation, J. Comput. Chem. 23 (2002) 1623–1641.
[110] V. Hornak, R. Abel, A. Okur, B. Strockbine, A. Roitberg, C. Simmerling, Comparison of multiple Amber force fields and development of improved protein backbone parameters, Proteins 65 (2006) 712–725.
[111] J.A. Maier, C. Martinez, K. Kasavajhala, L. Wickstrom, K.E. Hauser, C. Simmerling, ff14SB: improving the accuracy of protein side chain and backbone parameters from ff99SB, J. Chem. Theor. Comput. 11 (2015) 3696–3713.
[112] J.M. Wang, R.M. Wolf, J.W. Caldwell, P.A. Kollman, D.A. Case, Development and testing of a general amber force field, J. Comput. Chem. 25 (2004) 1157–1174.
[113] H.J.C. Berendsen, J.R. Grigera, T.P. Straatsma, The missing term in effective pair potentials, J. Phys. Chem. 91 (1987) 6269–6271.
[114] T. Darden, D. York, L. Pedersen, Particle Mesh Ewald - an N.log(N) method for Ewald sums in large systems, J. Chem. Phys. 98 (1993) 10089–10092.
[115] J.P. Ryckaert, G. Ciccotti, H.J.C. Berendsen, Numerical-integration of cartesian equations of motion of a system with constraints - molecular-dynamics of N-alkanes, J. Comput. Phys. 23 (1977) 327–341.
[116] J.B. Baell, G.A. Holloway, New substructure filters for removal of pan assay interference compounds (PAINS) from screening libraries and for their exclusion in bioassays, J. Med. Chem. 53 (2010) 2719–2740.

Résumé de thèse en Français

Etudes biochimiques, biophysiques et structurales des protéines associées aux maladies humaines : tcDAC2 et le complexe ADAT

Introduction

Au cours de ma thèse, j'ai travaillé sur des enzymes associées aux maladies humaines : tcDAC2 et ADAT. TcDAC2 est une protéine essentielle du parasite *Trypanosoma cruzi* qui cause la maladie de Chagas. TcDAC2 est une enzyme épigénétique, appartenant à la famille des histones désacétylases. Ainsi, le ciblage de l'épigénome de T. cruzi, en inhibant tcDAC2, représente un traitement potentiel de la maladie de Chagas. Dans ce projet, j'ai résolu la structure de tcDAC2 pour guider le développement d'inhibiteurs spécifiques de tcDAC2. Dans mon deuxième projet, j'ai étudié le mécanisme par lequel une mutation dans le complexe ADAT, formé de deux sous-unités, ADAT2 et ADAT3, déclenche un trouble neurodéveloppemental caractérisé par une déficience intellectuelle, de la microcéphalie, du strabisme et de l'épilepsie. ADAT est une enzyme qui transforme l'adénosine en position 34 des ARNt en inosine. ADAT est donc une enzyme appartenant au domaine épitranscriptomique.

Les mondes de l'épigénétique et de l'épitranscriptomique

L'épigénétique et l'épitranscriptomique sont deux domaines caractérisés par la réversibilité des modifications chimiques dans deux substrats différents : (i) l'ADN et les protéines histones et (ii) les ARN, respectivement. Ces deux domaines participent à la régulation de l'expression des gènes et des différentes voies de signalisation dans le noyau dans le cas de l'épigénétique et dans les compartiments du noyau et du cytoplasme dans le cas de l'épitranscriptomique. Si le domaine de l'épigénétique est désormais bien établi, le domaine de l'épitranscriptomique reçoit de plus en plus d'attention. Les effecteurs de ces deux domaines contrôlent la différenciation et le développement cellulaire, et leur dérégulation provoque de nombreuses maladies dont le cancer, des troubles neurologiques, cardiovasculaires, immunitaires et métaboliques. Ces domaines attirent donc beaucoup d'attention pour développer de nouvelles approches thérapeutiques. Au cours de mon doctorat, j'ai développé des projets de recherche scientifique dans ces deux domaines, obtenant des informations importantes dans chacun d'entre eux.

Mécanismes épigénétiques, maladies associées et médicaments épigénétiques

Afin de s'intégrer dans le noyau eucaryote, le génome des eucaryotes est compacté en une structure spécifique appelée chromatine. L'unité de base de la chromatine est le nucléosome qui est composé de deux paires d'histones H2A/H2B et de deux paires d'histones H3/H4 qui forment un octamère d'histones, enveloppant environ 147 paires de pb d'ADN (Luger et al. 1997). Les nucléosomes peuvent interagir les uns avec les autres pour former des structures plus compactes qui vont de la fibre de 30 nm aux boucles de chromatine, jusqu'au compactage le plus élevé dans les chromosomes mitotiques (Baldi, Korber et Becker 2020).

La structure de la chromatine forme une barrière et un élément régulateur pour l'accès à l'information génétique des autres effecteurs nucléaires. La régulation de la structure de la chromatine par les mécanismes épigénétiques fournit en outre un moyen aux cellules de réguler les mécanismes nucléaires, avec une implication directe sur l'homéostasie cellulaire, le développement, mais aussi sur la maladie (Allis et Jenuwein 2016). Notamment, les mécanismes épigénétiques jouent un rôle majeur dans la régulation de l'expression des gènes par le biais de changements dans la structure de la chromatine (Day et Sweatt 2011 ; Goldberg, Allis et Bernstein 2007).

Les cellules utilisent cinq mécanismes épigénétiques majeurs pour moduler la structure de la chromatine. Ceux-ci incluent : (i) les variants d'histones et leurs chaperons associés, (ii) les complexes de remodelage de la chromatine dépendant de l'ATP, (iii) la régulation médiée par les ARN longs non-codants (iv) la méthylation de l'ADN et (v) les modifications des histones (Kouzarides 2007). Au cours de ma thèse, je me suis focalisée sur la modification par acétylation, et plus particulièrement sur la désacétylation. La marque d'acétylation est une marque de régulation majeure en épigénétique, mais aussi dans de nombreux autres processus cellulaires.

Acétylation et histone désacétylases (HDACs et Sirtuines)

La queue amino-terminale des histones est principalement ciblée par des modifications telles que la méthylation, la phosphorylation, l'acétylation et autres. L'acétylation des histones est généralement associée à une activation transcriptionnelle. Les niveaux d'acétylation des lysines des histones et des protéines non-histones sont régulés par l'interaction entre les lysines acétyltransférases (KATs) et les histones désacétylases (HDACs). Les KATs déposent les marques d'acétylation sur le groupe ε-amino des résidus lysine et sont connues sous le nom

de dépositaire (writer) de l'acétylation. Les HDACs enlèvent la marque acétyle et sont connues sous le nom d'effaceur (eraser) de l'acétylation.

18 HDACs ont été identifiés dans les cellules de mammifères. Ils sont répartis en quatre classes (I-IV) : Classe I (HDAC 1, 2, 3, 8), classe IIa (HDAC 4, 5, 7, 9), classe IIb (HDAC 6 et 10), classe III (Sirtuine 1-7) et classe IV (HDAC 11). Les HDACs peuvent être divisés en deux familles basées sur leur domaine désacétylase et leur dépendance aux cofacteurs : la famille des histones désacétylases et la famille des sirtuines. Les classes I, II et IV forment la famille des histones désacétylases qui dépendent de l'ion Zn^{2+} pour leur activité catalytique. La classe III forme la famille Sirtuine qui dépend du NAD^{+} pour son activité catalytique (Gregoretti, Lee et Goodson 2004).

Les HDACs de classe I sont exprimés de manière ubiquitaire et principalement localisés dans le noyau. HDAC1 et HDAC2 font partie des complexes répresseurs SIN3, MiDAC, NuRD et CoREST (Laherty et al. 1997 ; Xue et al. 1998 ; Ballas et al. 2001 ; Bantscheff et al. 2011). HDAC3 fait partie des complexes co-répresseurs NCOR1 et SMRT1 (Matthew G. Guenther et al. 2000 ; M. G. Guenther, Barak et Lazar 2001). En revanche, HDAC8 ne fait pas partie d'un complexe (Gregoretti, Lee et Goodson 2004). Les HDACs de classe II se trouvent principalement dans le cytoplasme et leur domaine désacétylase est situé à leur extrémité C-terminale. Les HDACs de classe IIa ont à leur extrémité N-terminale un site de liaison pour le facteur de transcription de liaison à l'ADN MEF2. Ils possèdent également des sites de phosphorylation pour la liaison des protéines 14-3-3 (X.-J. Yang et Grégoire 2005 ; Parra et Verdin 2010). Les HDACs de classe IIa font également partie du complexe de co-répresseurs NCOR1 et SMRT1 (Fischle et al. 2002). En raison d'une substitution dans les HDACs de classe IIa de la tyrosine catalytique en histidine, ces HDACs présentent une activité catalytique très faible et sont plutôt supposées avoir un rôle d'échafaudage (Fischle et al. 2002). Les HDACs de classe IIb ont conservé une tyrosine catalytique et présentent une extension à leur extrémité C-terminale connue sous le nom de domaine de queue. Notamment, HDAC6 présente deux domaines désacétylases et un domaine à doigt de zinc pour la reconnaissance de l'ubiquitine à son extrémité C-terminale qui est important pour le transport des protéines mal repliées vers l'aggresome (Kawaguchi et al. 2003). HDAC10 présente un domaine désacétylase et un domaine répété riche en leucine à son extrémité C-terminale. HDAC10 est une acétylpolyamine désacétylase (Hai et al. 2017). Les HDACs de classe IV sont composées de HDAC11 qui a une activité désacylase des groupes acyle gras à longue chaîne (Gao et al. 2002; J. Cao et al. 2019).

Les HDACs de classe III sont des sirtuines localisées dans différents compartiments, tels que le nucléole (SIRT7), le noyau (SIRT1 et SIRT6), le cytoplasme (SIRT2) et dans les mitochondries (SIRT3, SIRT4 et SIRT5) (Houtkooper, Pirinen et Auwerx 2012). SIRT4, SIRT5 et SIRT6 ont une activité de désacylation plutôt qu'une activité de désacétylation. SIRT4 élimine les fractions acyle des méthylglutaryl-, hydroxyméthylglutaryl- et 3-méthylglutaconyl-lysine (K. A. Anderson et al. 2017). SIRT5 est une desuccinylase, une démalonylase et une déglutarylase (C. Peng et al. 2011 ; J. Park et al. 2013 ; M. Tan et al. 2014). SIRT6 élimine les groupes acyle gras à longue chaîne des résidus lysine (Jiang et al. 2013).

Mécanisme catalytique des HDACs dépendantes du zinc

Le mécanisme catalytique proposé pour les HDACs dépendantes du zinc est basé sur des études structurales et biochimiques de HDAC8. Au sein du site actif de HDAC8, un ion catalytique Zn^{2+} est coordonné par une histidine (H180), deux aspartates (D178 et D267) et deux molécules d'eau (Vannini et al. 2004 ; Somoza et al. 2004). Lors de la liaison au substrat, le groupement acétyl du substrat de lysine acétylée remplace une molécule d'eau, se coordonne au Zn^{2+} et accepte une liaison hydrogène de la tyrosine catalytique (Y306) (Vannini et al. 2007). Il est possible que Y306 change d'une conformation orientée vers l'extérieur du site actif à une conformation orientée vers l'intérieur du site actif pour s'adapter à la liaison au substrat (Decroos et al. 2015). L'histidine 143 (H143) agit comme une base générale, pour aider le Zn^{2+} à activer la molécule d'eau ; tandis que His142 reste protoné tout au long du cycle catalytique (Gantt et al. 2016). H142 et His143 lient l'hydrogène de la molécule d'eau liée au zinc pour positionner correctement cette molécule d'eau pour une attaque nucléophile. Ensuite, le groupe carbonyle de la lysine acétylée subit une attaque nucléophile par la molécule d'eau liée au zinc, conduisant à la formation d'un intermédiaire tétraédrique (Porter et Christianson 2017). Lors du transfert de protons de H143 (agissant comme un acide général) au groupe amino partant, l'intermédiaire tétraédrique disparaît en produisant une lysine et un acétate (Gantt et al. 2016).

Inhibiteurs des HDACs

La dérégulation de l'acétylation des lysines est associée aux troubles neurologiques, au cancer, et aux maladies cardiovasculaires (P. Li, Ge et Li 2020 ; Falkenberg et Johnstone 2014). Plusieurs inhibiteurs des histones désacétylaces (HDACi) ont été approuvés par la FDA pour le traitement du cancer (Cappellacci et al. 2020). Le Vorinostat (Saha) et la Romidepsine sont

utilisés pour le traitement du lymphome cutané à cellules T (Duvic et al. 2018 ; Marks et Breslow 2007). Le Belinostat et le Chidamide (ce dernier approuvé en Chine uniquement) sont utilisés pour le traitement du lymphome périphérique à cellules T (Poole 2014 ; Chan, Tse et Kwong 2017). Le Panobinostat, un inhibiteur non sélectif (pan-inhibiteur) utilisé pour le traitement du myélome multiple (Prince, Bishton et Johnstone 2009). De plus, deux HDACi sont approuvées par la FDA pour le traitement des troubles neurologiques : l'acide valproïque et le butyrate de sodium. Le Vorinostat, le Belinostat et le Panobinostat sont des acides hydroxamiques qui chélatent le Zn^{2+} dans les HDAC (Richon 2006; Cappellacci et al. 2020). La Romidepsine est un depsipeptide cyclique qui, sous forme réduite, possède un groupe thiol qui coordonne le Zn^{2+} (Nakajima et al. 1998).

Le traitement des maladies négligées et le ciblage de smHDAC8

La schistosomiase est une maladie infectieuse causée par des vers plats parasites du genre Schistosoma. Environ 240 millions de personnes sont infectées dans le monde et la schistosomiase cause 300 000 décès par an. Le seul médicament disponible pour le traitement de la schistosomiase, le Praziquantel, est utilisé pour le traitement de masse, ce qui soulève le risque de la possibilité d'apparition de résistance (Doenhoff et al. 2002). Par conséquent, il est urgent de développer de nouveaux médicaments contre la schistosomiase. Le génome de *Schistosoma mansoni* possède trois HDAC de classe I, qui sont des orthologues des HDAC mammifères HDAC1, HDAC3 et HDAC8 (Oger et al. 2008). Les ARNm de ces trois HDAC sont exprimés à tous les stades du cycle de vie de *S. mansoni*, mais *S. mansoni* HDAC8 (smHDAC8) possède le transcrit le plus abondant parmi les HDAC de classe I à tous les stades de la vie du parasite. En revanche, dans les tissus humains, *HDAC8* est le plus faible transcrit exprimé à partir des HDAC de classe I (E. Hu et al. 2000). Cela suggère que *smHDAC8* doit avoir des fonctions vitales pour *S.mansoni*. smHDAC8 constitue donc une cible potentielle pour le développement de médicaments pour traiter la schistosomiase.

Étant donné que le développement de nouveaux médicaments est un processus long et coûteux, une stratégie appelée Piggyback a été appliquée par mon équipe d'accueil en collaboration avec de nombreux autres groupes européens et brésiliens au sein de deux grands projets européens FP7 (SETTReND, Schistosoma Epigenetics – Targets, Regulation, New Drugs et A-ParaDDisE, Anti-Parasitic Drug Discovery in Epigenetics). Cette stratégie implique la modification des inhibiteurs de HDAC (épidrogues) approuvés par la FDA et utilisés dans les traitements contre le cancer (Falkenberg et Johnstone 2014) pour être utilisés

dans le traitement des maladies infectieuses. Ces épidrogues servent d'échafaudages pour le développement d'inhibiteurs spécifiques ciblant les HDACs parasitaires.

La stratégie Piggyback combine des méthodes de criblage à haut débit et de la conception de médicaments basées sur la structure 3D des protéines. Cette seconde approche est utilisée pour résoudre le problème de sélectivité inhérent au fait que les enzymes HDAC8 humaines et de schistosomes ont de fortes similitudes dans leur site actif et qui pourraient provoquer des effets secondaires en essayant d'inhiber smHDAC8. Par conséquent, une conception de médicament basée sur la structure a pour objectif de rendre un médicament aussi spécifique que possible pour l'enzyme du Schistosome. La structure du smHDAC8 a cependant montré qu'il existe quelques différences par rapport aux HDAC humaines (Marek et al. 2013). Par exemple, smHDAC8 a une poche de site actif plus large que son orthologue HDAC8 humain, ce qui est dû à la conformation différente du résidu F152 dans smHDAC8. De plus, M274 dans HDAC8 humain est remplacé par H292 dans smHDAC8. Ces caractéristiques spécifiques de smHDAC8 ont été utilisées pour le développement d'inhibiteurs spécifiques de smHDAC8 (Marek et al. 2015).

Un criblage virtuel *in silico* utilisant une bibliothèque d'un demi-million de composés chélateurs du zinc et la structure de smHDAC8 a été mené, aboutissant à l'identification de deux composés volumineux, J1038 et J1075 (Kannan et al. 2014). Des tests *in vitro* de l'activité d'inhibition ont montré que ces composés ont une sélectivité pour les enzymes HDAC8 (smHDAC8 et hHDAC8) par rapport aux autres HDAC (HDAC1, HDAC2, HDAC3 and HDAC6) en comparaison avec le médicament anti-HDAC commercial Voristonat, qui inhibe sans sélectivité toutes les HDACs de classe I (HDAC1, HDAC2, HDAC3 et HDAC8) et de classe IIb HDAC6 (Marek et al. 2013). J1038 a été sélectionné pour des optimisations car il s'agit d'un composé plus volumineux conformément au site actif plus large de smHDAC8. Sur la base du hit J1038, plusieurs composés ont été développés. Des tests *in vitro* de leur capacité d'inhibition contre smHDAC8 et HDAC8 humain ont montré que ces composés ont une valeur IC_{50} dans la gamme nanomolaire basse, et certains de ces composés sont également sélectifs pour smHDAC8 par rapport à son homologue humain (Heimburg et al. 2016).

Néanmoins, cette étude a révélé la difficulté à concevoir des médicaments ne montrant une sélectivité que pour les HDAC des parasites lorsque ceux-ci sont similaires à leurs homologues humains, soulevant la question de savoir comment améliorer la sélectivité.

Cependant, cette preuve de concept selon laquelle la machinerie épigénétique des agents pathogènes peut être ciblée par la stratégie Piggyback a ouvert de nouvelles voies pour cibler d'autres maladies infectieuses où les agents pathogènes ont des HDAC qui présentent une divergence significative par rapport aux HDAC humains. Au cours de ma thèse, j'ai abordé ces deux questions en (i) participant à la caractérisation moléculaire précise de l'inhibition sélective de HDAC8 (Article 1) et (ii) en étudiant l'inhibition sélective des HDAC parasites divergents, notamment DAC2 de *Trypanosoma cruzi* (tcDAC2) (article 2).

Le monde de l'ARN et l'épitranscriptome

Pendant des décennies, notre vision du monde des acides ribonucléiques (ARN) s'est principalement limitée à l'ARN messager (ARNm), qui est une « photocopie » de nos gènes, à l'ARN ribosomique (ARNr), le composant en acide nucléique structurant les ribosomes, et à l'ARN de transfert (ARNt), la molécule adaptatrice entre les mondes de l'ARN et des protéines. Depuis quelques décennies, cependant, cette vision initiale du monde de l'ARN est devenue beaucoup plus complexe, avec la découverte de beaucoup plus d'espèces d'ARN, telles que les petits ARN nucléaires (snRNA), les petits ARN nucléolaires (snoRNA), les longs ARN non codants. (lncRNA), les micro ARN (miRNA), les ARN enhancer (eRNA), les ARN vault (VTRNA) et les ARN circulaires (circRNA) (Statello et al. 2021b). Ces différentes espèces d'ARN participent fonctionnellement, avec les ARNm, les ARNr, les ARNt et les autres effecteurs cellulaires, au développement et à l'homéostasie des cellules et des organismes (Cech et Steitz 2014).

Outre la grande variété d'espèces d’ARN, il a été montré que la plupart de ces espèces peuvent subir un grand nombre de modifications (X. Li, Xiong et Yi 2017). Plus d'une centaine de modifications d'ARN ont été identifiées à ce jour dans tous les types de molécules d'ARN, y compris des modifications du ribose et des nucléobases (Boccaletto et al. 2018). La découverte que certaines de ces modifications d'ARN sont déposées, lues et supprimées en réponse à des stimuli cellulaires internes ou externes, montre que les modifications d'ARN peuvent être réversibles et dynamiques, comme observé dans le domaine épigénétique. Ceci a donné naissance au domaine émergent de l'épitranscriptomique qui reflète le domaine établi de l'épigénétique (McMahon, Forester et Buffenstein 2021 ; Livneh et al. 2020 ; Wiener et Schwartz 2021 ; Barbieri et Kouzarides 2020).

Notamment, les modifications de l'ARN peuvent réguler l'expression des gènes, modulant ainsi un grand nombre de processus cellulaires, l'homéostasie cellulaire et le développement

(Roundtree, Evans, et al. 2017 ; Frye et al. 2018 ; Barbieri et Kouzarides 2020 ; Chujo et Tomizawa 2021). Il n'est donc pas surprenant que la dérégulation des modifications de l'ARN soit impliquée dans diverses maladies. Notamment, des mutations dans la moitié des enzymes de modification de l'ARN sont associées à des maladies humaines (Tsutomu Suzuki 2021 ; Jonkhout et al. 2017). Il s'agit notamment de cancers et de maladies cardiovasculaires, immunitaires, métaboliques, liées aux mitochondries et neurologiques. Curieusement, les maladies les plus fréquentes associées à la dérégulation de la modification de l'ARN sont représentées par les troubles neurologiques, ce qui concorde avec le fait que de nombreuses modifications de l'ARN sont enrichies dans le cerveau (Jonkhout et al. 2017 ; Chi et Delgado-Olguín 2013).

Parmi les espèces d'ARN, les ARNt sont les macromolécules d'ARN les plus modifiées, contenant environ 120 modifications. Chaque molécule d'ARNt contient en moyenne 13 modifications situées dans ses différents bras où elles jouent des rôles très différents dans le repliement, la stabilisation et le décodage des ARNt (Paul F. Agris et al. 2018 ; Tsutomu Suzuki 2021 ; Schimmel 2018 ; Kirchner et Ignatova 2014). Là encore, des mutations et une expression altérée de 72 % des enzymes de modification des ARNt sont associées à des maladies humaines, 50 % de ces maladies étant des troubles neurologiques, notamment des Troubles Neurodéveloppementaux (NDD) (Chujo et Tomizawa 2021).

Il y a donc un intérêt croissant pour comprendre dans les détails moléculaires les voies de modification de l'ARN, les rôles biologiques de ces modifications, et comment le dérèglement de ces voies (i) conduit à un déséquilibre des modifications, (ii) influence le métabolisme de l'ARN et l'expression des gènes, et (iii) comment ces perturbations conduisent à la maladie. Plus précisément, la grande implication des ARNt dans le développement du cerveau, évaluée par les dérèglements de ses modifications à l'origine des NDD, suscite un fort regain d'intérêt pour ces molécules effectrices essentielles.

Modifications des ARNt, leurs rôles et leur implication dans les maladies neurologiques

Les ARNt sont les macromolécules d'ARN les plus modifiées (Tsutomu Suzuki 2021). Les modifications peuvent concerner le sucre ou la base des nucléosides et sont réparties à divers endroits le long de l'ARNt. Il s'agit notamment de la tige acceptrice, de la tige-boucle D, de la tige-boucle anticodon (ASL), de la boucle variable (VL) et de la tige-boucle T.

Les modifications ont différents rôles, notamment le repliement, la stabilisation structurale et la flexibilité des ARNt. De plus, certaines modifications sont déterminantes pour une

aminoacylation correcte, tandis que d'autres peuvent empêcher le clivage enzymatique de l'ARNt (Tsutomu Suzuki 2021). De plus, les modifications de l'ARNt au sein de l'ASL sont importantes pour le décodage correct des codons et le maintien du cadre de lecture. Il est important de noter que des mutations dans les enzymes modifiant l'ARNt ont été associées à plusieurs maladies, les plus fréquentes étant les troubles neurologiques, révélant l'importance de ces modifications et ravivant l'intérêt pour les ARNt en tant que molécules effectrices (Chujo et Tomizawa 2021). Parmi les modifications de l'ARN, une modification ubiquitaire et essentielle et l'édition d'adénosine en inosine (A-en-I) (Srinivasan, Torres, et Ribas de Pouplana 2021).

Édition A-en-I de l'adénosine en position wobble de l'ARNt-Arg (ACG) chez les procaryotes par l'homodimère TadA

Chez les bactéries, un homodimère de la protéine TadA catalyse la réaction de désamination hydrolytique qui convertit A34 en I34 dans un seul isotype d'ARNt, l'ARNt-Arg(ACG) (Wolf, Gerber et Keller 2002). TadA appartient à la grande famille des cytidine désaminases (CDA) (A. P. Gerber et Keller 2001). TadA a un repliement global formé d'un feuillet β central flanquée d'hélices. Les hélices α1, α5 sont opposées à l'interface du dimère tandis que les hélices α2 à α4 sont situées à l'interface dimère (J. Kim et al. 2006 ; Kuratani et al. 2005 ; Losey, Ruthenburg et Verdine 2006). Les hélices α2-α4 et leurs boucles forment le site actif de TadA, chaque monomère contribuant cependant aux deux sites actifs du complexe. Le site actif de TadA contient un ion zinc qui est coordonné par His53, Cys83, Cys86 et une molécule d'eau qui participe à la catalyse (Losey, Ruthenburg et Verdine 2006). De plus, le résidu conservé Glu55 participe au transfert de protons pendant la catalyse, la mutation de ce glutamate conservé en alanine produisant une enzyme catalytiquement inactive (Elias et Huang 2005). Il a été proposé que le mécanisme catalytique de l'édition A-en-I soit similaire à celui des cytidine désaminases (Betts et al. 1994; S. J. Chung, Fromme et Verdine 2005). Glu55 agit comme une navette de protons, qui à la fois extrait un proton de la molécule d'eau liée au zinc pour produire un ion hydroxyde, et protone le N^1 de l'adénosine 34. Ainsi, Glu55 réduit la double liaison entre les atomes N^1 et C^6 de l'adénosine, ce qui rend le C^6 plus sensible à l'attaque de l'ion hydroxyde, pour former l'intermédiaire tétraédrique. Ensuite, le clivage de la liaison C^6-$NH_2{}^6$ est médié par le transfert de proton de OH^6 à $NH_2{}^6$, ce proton est ensuite extrait par Glu55. L'intermédiaire tétraédrique disparaît après abstraction de ce proton par Glu55 et le transfert de ce proton à l'amine sortante, pour produire l'inosine et l'ammoniac

(Wilson, Rudolph et Quiocho 1991 ; Kinoshita et al. 2003 ; Hall et al. 2011 ; T.-P. Ko et al. 2003 ; Sh et al. 2004).

La structure de TadA en complexe avec l'ASL de son substrat, l'ARNt-Arg-ACG, a montré qu'à l'entrée du site actif de TadA, plusieurs poches sont formées par les deux monomères de TadA et qui interagissent avec l'ASL, notamment la boucle de l'anticodon. Ces poches accueillent les bases 33 à 37. Il n'y a pas de poches pour la paire de base 32-38, mais cette paire interagit également avec TadA (Losey, Ruthenburg et Verdine 2006). Des résidus de l'hélice alpha C-terminale de TadA ont été proposés comme interagissant avec l'ARNt, et il a été démontré que des mutations de ces résidus affectent l'activité de TadA (Elias et Huang 2005). En effet, la structure de TadA/ASL montre que les résidus formant l'hélice C-terminale de TadA interagissent avec l'ASL. Par exemple, F144 et F145 forment des interactions d'empilement avec C35 et G36 respectivement, R149 interagit avec le phosphate de U33 et forme deux liaisons hydrogènes avec la base G36 (Losey, Ruthenburg et Verdine 2006). De façon intéressante, en l'absence de substrat, cette hélice alpha n'est que partiellement observée ou n'est pas du tout présente dans la densité électronique, montrant qu'elle peut s'adapter pour reconnaître le substrat ASL (Elias et Huang 2005).

Édition A-en-I de la position wobble des ARNt chez les eucaryotes par l'hétérodimère ADAT

L'édition A-en-I chez les eucaryotes est médiée par l'Adénosine Désaminase Agissant sur les ARNt (ADAT). Il existe trois types de protéine ADAT : ADAT1, ADAT2 et ADAT3. Toutes possèdent un domaine désaminase similaire à celui des cytidine désaminases (Schaub et Keller 2002). ADAT1 médie l'édition A-en-I en position 37 dans l'ARNt-Ala et en position 57 dans les ARNt archéens (H. Grosjean et al. 1996; A. Gerber et al. 1998). ADAT2 et ADAT3 (ADAT2/3) forment un complexe dans le noyau pour effectuer l'édition A-en-I à la position 34 sur les ARNt (Torres et al. 2015). Contrairement au substrat unique du procaryote TadA, le complexe eucaryote ADAT2/3 possède jusqu'à huit isotypes d'ARNt comme substrats selon l'espèce considéré. Ces substrats contiennent tous une adénosine en position 34 : ARNt-Ala-AGC, -Pro-AGG, -Thr-AGT, -Val-AAC, -Ser-AGA, -Arg-ACG, -Ile-AAT et Leu-AAG.

Les acides aminés Ala, Pro, Thr et Val sont codés par quatre codons différents, c'est-à-dire qu'ils sont quadruplements dégénérés. Ile est codé par trois codons différents, triplement dégénéré. Arg, Ser et Leu sont sextuples dégénérés (M. Nirenberg et al. 1965; Paul F. Agris, Vendeix et Graham 2007). Contrairement à la protéine bactérienne TadA qui est capable de

désaminer A34 à partir d'une ASL seule, le complexe ADAT2/3 nécessite un ARNt complet pour désaminer A34 (Auxilien et al. 1996 ; Roura Frigolé et al. 2019). Les substrats ADAT2/3 ne nécessitent pas pour l'édition A-to-I d'avoir un leader 5', une terminaison 3', le 3'-CCA, ou une autre modification dans une autre base de l'ARNt (Torres et al. 2015; Roura Frigolé et al. 2019).

Bien que ADAT2 et ADAT3 aient un domaine désaminase, seul ADAT2 est la sous-unité catalytiquement active. ADAT3 a été proposé comme étant inactif puisque le glutamate conservé participant à la catalyse comme navette de protons est muté en valine dans cette protéine (A. P. Gerber et Keller 1999). Néanmoins, ADAT2 nécessite la présence d'ADAT3 pour effectuer la réaction de désamination. La façon dont ADAT3 contribue à l'édition A-to-I est inconnue. La comparaison de séquences de TadA et d'ADAT2/3 de souris montre que ADAT2 de souris a une similarité de séquence de 49,7 % avec *E. coli* TadA. De manière surprenante, lorsque l'on compare TadA et ADAT3, on observe que seule la partie C-terminale d'ADAT3 (résidus 177-349) a 45% de similarité de séquence avec *E. coli* TadA. Le domaine N-terminal d'ADAT3 est un domaine supplémentaire, caractéristique d'ADAT3, qui n'est présent ni dans *E. coli* TadA, ni dans ADAT2 eucaryote.

Mutations en ADAT et association à la maladie

Plusieurs mutations du gène *ADAT3* ont été identifiées chez des patients atteints d'un trouble neurodéveloppemental. Ce trouble est caractérisé par une déficience intellectuelle (DI), du strabisme, de la microcéphalie, l'épilepsie, l'hypotonie, un retard de la parole et un retard de croissance. Il a été démontré que 41 patients sont porteurs de la mutation faux-sens homozygote c.382G > A dans le gène *ADAT3*, qui conduit au remplacement de la valine 128 en méthionine dans la protéine ADAT3 (Sharkia et al. 2019 ; Alazami et al. 2013 ; El- Hattab et al. 2016). Il a été démontré que deux autres patients étaient porteurs d'une mutation faux-sens hétérozygote composée d'*ADAT3*, où chaque allèle code pour un variant différent d'ADAT3, c'est-à-dire Val196Ala et Val196Leu (Thomas et al. 2019). De plus, un patient a présenté une duplication homozygote de 8 pb dans le gène *ADAT3* conduisant à une troncature N-terminale dans ADAT3 (Salehi Chaleshtori et al. 2018).

Questions associées

Si le mécanisme et les propriétés de reconnaissance de l'ARNt de TadA procaryote ont été étudiés en profondeur, il reste beaucoup à comprendre sur ADAT. Notamment, plusieurs questions restent sans réponse. Premièrement, quel est le rôle d'ADAT3 dans ADAT ?

Deuxièmement, quel est le rôle du domaine N-terminal spécifique d'ADAT3 ? Troisièmement, contrairement aux procaryotes où un homodimère de TadA est suffisant pour l'édition A-en-I, pourquoi les eucaryotes ont-ils besoin d'un complexe hétérodimérique pour accomplir le même objectif ? Quatrièmement, comment ADAT2/3 parvient-il à reconnaître les ARNt contenant A34 ? Cinquièmement, comment le mutant V128M d'ADAT2/3, qui est cause de maladie, affecte-t-il les niveaux d'inosine des ARNt ? Sixièmement, l'affinité du mutant maladie ADAT2/3 pour les ARNt est-elle réduite par rapport à celle du complexe de type sauvage (WT) ? Enfin, septièmement, l'activité du mutant d'ADAT2/3 causant la maladie est-elle diminuée par rapport à celle du complexe WT ?

Objectifs de la thèse

Je m'intéresse tout particulièrement à la compréhension des maladies humaines et à la manière dont elles peuvent être soignées. Les deux principaux projets que j'ai menés au cours de ma thèse ont abordé ces questions, en examinant la mécanistique des protéines et des complexes protéiques impliqués dans des processus essentiels et qui pourraient être ciblés afin d'aider à développer les interventions thérapeutiques, le diagnostic et les soins aux patients. Notamment, mes projets ont abordé des projets dans les domaines en pleine expansion de l'épigénétique et de l'épitranscriptomique, où l'on sait que de nombreux effecteurs sont impliqués dans l'apparition et/ou la progression des maladies.

Les objectifs de ma thèse sont donc en adéquation avec mes intérêts scientifiques et répondent aux questions suivantes :

Concernant tcDAC2 :

- Résoudre la structure de tcDAC2 pour déterminer ses caractéristiques qui la différencient des HDACs humaines.

- Résoudre la structure de tcDAC2 en complexe avec des inhibiteurs pour comprendre comment développer de nouveaux médicaments anti-parasitaires.

Concernant le complexe ADAT2/ADAT3 :

- Résoudre la structure des complexes de souris ADAT2/ADAT3-WT et mutants pour étudier le mécanisme par lequel la mutation la plus courante V128M dans ADAT3 déclenche le phénotype de la maladie.

- Étudier le rôle d'ADAT3, notamment du domaine ADAT3 N-terminal.

- Caractériser l'activité et l'affinité de liaison des complexes ADAT2/3 WT et du mutant maladie aux tRNAs.

Résultats

Article 1

La caractérisation de l'inhibition sélective de l'histone désacétylase 8 (HDAC8) révèle des déterminants structurels et fonctionnels spécifiques de son site actif (publié)

Il a été démontré que HDAC8 est surexprimée dans différentes tumeurs, y compris le neuroblastome, et le traitement d'un modèle cellulaire de neuroblastome avec des inhibiteurs sélectifs de HDAC8 a entraîné une différenciation cellulaire et un arrêt de la croissance. Néanmoins, le mode de liaison de ces inhibiteurs spécifiques de HDAC8 n'est pas connu. En outre, étant donné que les inhibiteurs spécifiques de HDAC8 humains PCI-34051 et NCC-149 (ci-après dénommés PCI et NCC) inhibent également l'enzyme HDAC8 du schistosome *in vitro* et *in vivo*, ceux-ci ont été aussi utilisés pour étudier les déterminants structuraux de l'inhibition sélective des enzymes HDAC8 en utilisant smHDAC8 comme modèle. De plus, plusieurs composés ciblant sélectivement smHDAC8 par rapport aux HDACs humaines ont été développés précédemment dans les équipes de nos collaborateurs pour lutter contre la schistosomiase. Ainsi, pour connaître le mode de liaison de ces différents inhibiteurs sélectifs d'HDAC8, mon équipe les a co-cristallisés en complexe avec l'enzyme smHDAC8.

La structure de smHDAC8 en complexe avec ces inhibiteurs sélectifs de HDAC8 a montré que la partie hydroxamique des inhibiteurs coordonne le zinc catalytique et établit des liaisons hydrogène avec Tyr341, H141 et H142. De plus, la forme en L de ces inhibiteurs permet à leur coiffe d'interagir avec Tyr341 et les résidus de la boucle L6 (P291 et H292). Nous avons ainsi pu mettre en évidence une poche spécifique dans les enzymes HDAC8 où se fixent les inhibiteurs spécifiques de cette enzyme. Cette poche, dénommée « poche de sélectivité », est formée par des résidus de différentes boucles. La base de la poche est formée par Tyr 341 (boucle L7) qui participe à la catalyse, tandis que les parois de la poche sont formées par des résidus des boucles L1 et L6. La coiffe des inhibiteurs spécifiques d'HDAC8 interagit avec la tyrosine catalytique. D'autres HDACs ne présentent pas cette poche. Par exemple, dans les HDAC1, 2, 3, 6 et 10, cette poche est couverte par des résidus des boucles L1 et L6 empêchant l'accessibilité à cette poche, ce que nous avons dénommé « verrou L1-L6 ». Dans

les HDAC de classe IIa, la poche n'existe pas puisque la tyrosine catalytique est remplacée par une histidine.

D'autres expériences de mutagenèse ont montré que le remplacement des boucles L6 de hHDAC8 par celles de la boucle L6 de HDAC1 humaine ne modifiait pas la conformation globale de cette boucle, comme observé dans HDAC8, mais entraînait une diminution de l'activité de HDAC8 et une augmentation des valeurs IC_{50} de PCI et de NCC pour HDAC8. Ces résultats ont démontré l'importance de la poche de sélectivité de HDAC8 pour la liaison des inhibiteurs sélectifs de HDAC8. D'une part, nous avons pu déterminer pourquoi les inhibiteurs développés par nos collaborateurs sont puissants et sont des inhibiteurs sélectifs de smHDAC8 par rapport aux HDAC humaines. D'autre part, nous avons montré comment ces inhibiteurs peuvent être utilisés comme pistes de médicaments pour combattre la schistosomiase. Enfin, la découverte de la poche de sélectivité de HDAC8 permettra de guider le développement d'inhibiteurs de HDAC8 humains plus puissants et plus sélectifs pour le traitement du cancer.

J'ai rejoint ce projet en tant qu'étudiante en master et j'ai réalisé l'analyse structurale de la HDAC8 humaine dont la boucle L6 a été remplacée par celle de la HDAC1 humaine. J'ai notamment résolu la structure de ce mutant de HDAC humaine en complexe avec l'inhibiteur pan-HDAC Quisinostat(QSN).

Article 2

La structure atypique et la modularité du site actif de l'histone désacétylase essentielle DAC2 de *Trypanosoma cruzi* comme cible d'inhibition (soumis)

La maladie de Chagas est causée par infection par le parasite *Trypanosoma cruzi*. Environ 7 millions de personnes sont infectées dans le monde par ce parasite qui cause des dizaines de milliers de décès chaque année. Le traitement de la phase aiguë n'est efficace que dans 70% des cas. De plus, la phase aiguë n'est pas facilement détectée, ce qui conduit à une infection chronique qui ne peut être traitée par aucun médicament jusqu'à présent. La phase chronique se caractérise par des symptômes compliqués affectant le cœur, le cerveau et le système digestif, aucun traitement n'est disponible à ce stade et peut également provoquer une mort subite.

Il a été démontré que l'histone désacétylase 2 de *Trypanosome cruzi* (tcDAC2) est essentielle à la viabilité de *T. cruzi*. Par conséquent, tcDAC2 représente une cible pour le développement

de médicaments contre la maladie de Chagas. La stratégie piggyback, qui combine le criblage à haut débit et le développement de médicaments basés sur la structure, s'est déjà avérée efficace pour développer plusieurs inhibiteurs pouvant servir de piste de médicaments dans la lutte contre la schistosomiase. Par conséquent, pour développer des inhibiteurs ciblant tcDAC2, la stratégie piggyback a également été appliquée à cette enzyme. J'ai rejoint ce projet en tant qu'étudiante de master et l'ai poursuivi pendant mon doctorat. J'ai notamment été impliquée dans toutes les étapes d'ingénierie de tcDAC2 et j'ai développé sa stabilisation par des inhibiteurs, ce qui m'a ensuite permis de déterminer la structure et d'en faire la caractérisation poussée de cette enzyme.

Plus précisément, j'ai rationalisé les composés inhibiteurs à utiliser en complexe avec tcDAC2 pour les expériences de cristallisation en effectuant des essais de stabilisation thermique de cette enzyme. Ces expériences ont montré que le Quisinostat (QSN), TB56 et TB75 augmentaient la stabilité thermique de tcDAC2. Ces inhibiteurs ont donc été utilisés pour les essais de cristallisation. J'ai pu cristalliser et résoudre la structure de tcDAC2 en complexe avec deux inhibiteurs, QSN et TB56 qui ont révélé les caractéristiques spécifiques de tcDAC2 par rapport aux HDACs humaines. Notamment, la plupart des boucles formant le site catalytique de tcDAC2 sont comme celles de la HDAC8 humaine, mais la boucle 6 est comme celle de la HDAC1-3 humaine. Ces caractéristiques entraînent une interaction partielle entre les boucles L1 et L6 de tcDAC2, ce qui est différent des HDAC humaines.

De plus, mes travaux ont révélé que tcDAC2 possède une poche spécifique dans son site actif. Cette poche est formée entre les boucles L5 et L6 du site actif et son existence est due au remplacement de résidus plus volumineux Phe/Tyr et Lysine dans les HDACs humaines par des résidus plus petits Ile266 et Ala261, respectivement, dans tcDAC2. De plus, tcDAC2 possède une poche située au pied de son site actif. Cette poche chez tcDAC2 est plus petite par rapport à celle des HDAC1-3 humaines, la taille de cette poche chez la HDAC8 humaine dépendant de la conformation de W141. Ce dernier résidu est remplacé par un résidu Leu dans HDAC1-3 et par R196 dans tcDAC2, ce qui montre que cette poche chez tcDAC2 possède des propriétés physico-chimiques différentes. Par conséquent, de nombreuses caractéristiques spécifiques de tcDAC2 peuvent être exploitées pour le développement d'inhibiteurs sélectifs ciblant tcDAC2, en combinant un développement de médicaments basé sur la structure et des stratégies à haut débit. Cette dernière stratégie a été appliquée en utilisant le programme European Lead Factory (ELF) qui nous a permis de tester tcDAC2 avec un demi-million de composés provenant de 7 grandes sociétés pharmaceutiques. Les

résultats de ce criblage sont en cours d'utilisation pour la conception de médicaments sélectifs contre tcDAC2.

Article 3

La structure du complexe ADAT2/ADAT3 de la souris révèle les bases moléculaires de la désamination de l'adénosine en inosine de l'ARNt des mammifères (Publié)

L'édition de l'adénosine en inosine (A-to-I) en position 34 dans les ARNt est importante pour étendre la capacité de décodage des ARNt, puisque l'inosine 34 peut reconnaître l'uridine, la cytosine et l'adénosine en troisième position du codon, contrairement à l'adénosine 34 qui ne peut s'apparier qu'à l'uridine en troisième position du codon. Chez les procaryotes, l'édition A-en-I est réalisée par le complexe homodimèrique de TadA sur son substrat unique, l'ARNt-Arg(AGC). Chez les eucaryotes, l'édition A-en-I est réalisée par le complexe hétérodimérique ADAT2/ADAT3 sur jusqu'à huit isotypes d'ARNt, ADAT2 étant la sous-unité active et ADAT3 étant considérée comme la sous-unité inactive au rôle inconnu. De plus, la comparaison de la séquence de TadA procaryote avec ADAT2 eucaryote a montré 50 % de similarité et avec le domaine C-terminal d'ADAT3 45 % de similarité. Il est intéressant de noter que le domaine N-terminal de l'ADAT3 est une extension qui n'est pas présente dans le TadA procaryote. De plus, la mutation de la valine 128 en méthionine localisée dans le domaine N-terminal de la sous-unité ADAT3 provoque un trouble neurodéveloppemental caractérisé par une déficience intellectuelle, une microcéphalie, un strabisme, une épilepsie.

Plusieurs questions sont soulevées par ces connaissances. Par exemple, pourquoi les eucaryotes ont-ils besoin d'un complexe hétérodimérique pour l'édition A-en-I des ARNt ? Quel est le rôle du domaine N-terminal de la sous-unité ADAT3 eucaryote ? Pourquoi ADAT3 est-elle la sous-unité inactive ? Le mutant V128M de l'ADAT est-il toujours capable de lier les ARNt ? Pour répondre à ces questions, la structure du complexe ADAT des mammifères était nécessaire. Ce projet a représenté une grande partie de mon travail de thèse. J'ai pu purifier, cristalliser et résoudre la structure du premier complexe ADAT de mammifère, qui révèle des informations importantes. Premièrement, le domaine N-terminal de l'ADAT3 est essentiel pour la reconnaissance des ARNt, ce que j'ai notamment démontré par des tests de liaison. Deuxièmement, la sous-unité ADAT3 est inactivée par le coiffage de son site de liaison au zinc par les résidus C-terminaux d'ADAT3, ce qui bloquerait le site d'entrée de l'adénosine 34, ce que j'ai également confirmé par des tests enzymatiques. De plus, la structure d'ADAT confirme que dans le site de liaison au zinc d'ADAT3, V225 remplace

un glutamate qui participe à la catalyse observée dans le site actif d'ADAT2. Troisièmement, le mutant V128M d'ADAT peut lier les ARNt, mais son activité catalytique est compromise par rapport à l'enzyme sauvage.

De l'ensemble de mes travaux, il apparaît que le domaine N-terminal de ADAT3 va reconnaître spécifiquement la structure 3D des ARNt sans distinguer cependant s'ils peuvent être substrats ou non. La rotation de ce domaine par rapport au domaine catalytique de ADAT va permettre de positionner correctement la boucle de l'anticodon des ARNt dans le site actif de ADAT2. Les ANRt possédant une adénosine en position 34 seront alors modifiés, transformant I34 en I34. Ce mécanisme m'a permis d'émettre l'hypothèse que le niveau réduit d'inosine dans les ARNt chez les patients atteints par la maladie suite à la mutation V128M pourrait provenir d'une présentation incorrecte du substrat ARNt par le domaine N-terminal d'ADAT3 dans le site actif de l'ADAT2, entraînant une activité catalytique réduite.

Conclusions et perspectives

Pendant ma thèse de doctorat, j'ai travaillé sur des enzymes associées à des maladies humaines : tcDAC2 et le complexe ADAT. tcDAC2 est une protéine essentielle du parasite *T. cruzi* qui cause la maladie de Chagas. tcDAC2 représente donc une cible potentielle pour le traitement de la maladie de Chagas. Dans mon deuxième projet, j'ai étudié le mécanisme par lequel une mutation dans le complexe ADAT déclenche un trouble neurodéveloppemental caractérisé par une déficience intellectuelle, de la microcéphalie, du strabisme et l'épilepsie.

Plusieurs pistes d'inhibiteurs puissants et spécifiques ciblant smHDAC8, pour traiter la schistosomiase, ont été développées précédemment dans l'équipe en utilisant la stratégie Piggyback, qui combine le criblage à haut débit et la conception de médicaments basée sur la structure. Le travail de lutte contre la schistosomiase a également permis de découvrir une poche spécifique dans les enzymes HDAC8 où se fixent les inhibiteurs spécifiques de HDAC8. La base de cette poche est formée par une tyrosine catalytique et les parois par les boucles L1 et L6. Une telle poche n'est pas présente dans les autres HDACs, car elle est bloquée par des interactions entre les résidus de ces deux boucles. La poche spécifique d'HDAC8 guidera le développement d'inhibiteurs d'HDAC8 humains plus puissants et spécifiques pour le traitement de cancers, par exemple le neuroblastome où HDAC8 est surexprimée.

Une stratégie similaire à celle utilisée pour cibler smHDAC8 a été appliquée pour cibler tcDAC2, puisque la déplétion de *tcDAC2* affecte la viabilité de *T. cruzi*. Au cours de ma

thèse, j'ai pu résoudre la structure de tcDAC2 en complexe avec deux inhibiteurs non spécifiques. Ces structures ont révélé des caractéristiques spécifiques de tcDAC2. Par exemple, tcDAC2 possède des caractéristiques similaires à son orthologue hHDAC8 mais aussi à d'autres HDACs humaines (hHDAC1-3). De plus, tcDAC2 possède une poche spécifique dans son site actif, ce qui n'est pas observé dans les HDACs humaines. En outre, tcDAC2 présente une composition différente de résidus dans sa poche au pied de son site actif. Par conséquent, toutes ces caractéristiques spécifiques de tcDAC2 seront utilisées pour guider le développement d'inhibiteurs puissants et sélectifs de tcDAC2 en combinant le criblage à haut débit et la conception de médicaments basée sur la structure.

En ce qui concerne mon deuxième projet, le complexe ADAT est formé de deux sous-unités, ADAT2 et ADAT3. J'ai pu déterminer l'importance du domaine N-terminal de l'ADAT3, caractéristique des eucaryotes, dans la sélection et la liaison des molécules d'ARNt. J'ai pu déterminer la première structure du complexe ADAT des mammifères, qui révèle que le recouvrement du site de liaison au zinc d'ADAT3 est couvert par les résidus C-terminaux d'ADAT3, ce qui contribue à l'inactivité de l'ADAT3 en bloquant l'entrée de l'ARNt-adénosine 34. Des tests enzymatiques *in vitro* ont également confirmé l'inactivité d'ADAT3. En outre, le complexe ADAT mutant de la maladie qui contient la mutation V128M dans le domaine N-terminal d'ADAT3 est toujours capable de lier les ARNt. Par conséquent, j'émets l'hypothèse que la diminution des niveaux d'inosine observée dans les ARNt des patients porteurs de la mutation V128M d'ADAT pourrait provenir de la présentation incorrecte de l'ARNt substrat par ADAT3 dans le site actif d'ADAT2, provoquant ainsi une activité inefficace de l'ADAT sur les ARNt.

Mes travaux sur le complexe ADAT permettent de mieux comprendre le mécanisme de ce complexe et le mécanisme à l'origine du trouble neurodéveloppemental causé par l'ADAT mutante. Cependant, d'autres études sont nécessaires pour comprendre les implications du complexe ADAT sur le trouble neurodéveloppemental. Par exemple, les structures d'ADAT en complexe avec differents ARNt dans le contexte de l'ADAT sauvage et de l'ADAT mutant de la maladie révéleront les déterminants structurals qui déclenchent le processus de la maladie. Il sera également important d'étudier l'ADAT avec des ARNt portant une longue boucle variable, puisqu'il semble que le mutant V128M ait une affinité plus faible pour ces types d'ARNt.

References

Abbasi-Moheb, Lia, Sara Mertel, Melanie Gonsior, Leyla Nouri-Vahid, Kimia Kahrizi, Sebahattin Cirak, Dagmar Wieczorek, et al. 2012. "Mutations in NSUN2 Cause Autosomal- Recessive Intellectual Disability." *The American Journal of Human Genetics* 90 (5): 847–55. https://doi.org/10.1016/j.ajhg.2012.03.021.

Agris, P. F. 1996. "The Importance of Being Modified: Roles of Modified Nucleosides and Mg2+ in RNA Structure and Function." *Progress in Nucleic Acid Research and Molecular Biology* 53: 79–129. https://doi.org/10.1016/s0079-6603(08)60143-9.

Agris, P. F., H. Sierzputowska-Gracz, and C. Smith. 1986. "Transfer RNA Contains Sites of Localized Positive Charge: Carbon NMR Studies of [13C]Methyl-Enriched Escherichia Coli and Yeast TRNAPhe." *Biochemistry* 25 (18): 5126–31. https://doi.org/10.1021/bi00366a022.

Agris, Paul F., Emily R. Eruysal, Amithi Narendran, Ville Y. P. Väre, Sweta Vangaveti, and Srivathsan V. Ranganathan. 2018. "Celebrating Wobble Decoding: Half a Century and Still Much Is New." *RNA Biology* 15 (4–5): 537–53. https://doi.org/10.1080/15476286.2017.1356562.

Agris, Paul F., Franck A.P. Vendeix, and William D. Graham. 2007. "TRNA's Wobble Decoding of the Genome: 40 Years of Modification." *Journal of Molecular Biology* 366 (1): 1–13. https://doi.org/10.1016/j.jmb.2006.11.046.

Aguilo, Francesca, SiDe Li, Natarajan Balasubramaniyan, Ana Sancho, Sabina Benko, Fan Zhang, Ajay Vashisht, et al. 2016. "Deposition of 5-Methylcytosine on Enhancer RNAs Enables the Coactivator Function of PGC-1α." *Cell Reports* 14 (3): 479–92. https://doi.org/10.1016/j.celrep.2015.12.043.

Akella, Jyothi S., Dorota Wloga, Jihyun Kim, Natalia G. Starostina, Sally Lyons-Abbott, Naomi S. Morrissette, Scott T. Dougan, Edward T. Kipreos, and Jacek Gaertig. 2010. "MEC-17 Is an α-Tubulin Acetyltransferase." *Nature* 467 (7312): 218–22. https://doi.org/10.1038/nature09324.

Alarcón, Claudio R., Hyeseung Lee, Hani Goodarzi, Nils Halberg, and Sohail F. Tavazoie. 2015. "N 6 -Methyladenosine Marks Primary MicroRNAs for Processing." *Nature* 519 (7544): 482–85. https://doi.org/10.1038/nature14281.

Alazami, Anas M., Hadia Hijazi, Mohammed S. Al-Dosari, Ranad Shaheen, Amal Hashem, Mohammed A. Aldahmesh, Jawahir Y. Mohamed, et al. 2013. "Mutation in ADAT3, Encoding Adenosine Deaminase Acting on Transfer RNA, Causes Intellectual Disability and Strabismus." *Journal of Medical Genetics* 50 (7): 425–30. https://doi.org/10.1136/jmedgenet-2012-101378.

Alekseyenko, Artyom A., Andrey A. Gorchakov, Peter V. Kharchenko, and Mitzi I. Kuroda. 2014. "Reciprocal Interactions of Human C10orf12 and C17orf96 with PRC2 Revealed by BioTAP-XL Cross-Linking and Affinity Purification." *Proceedings of the National Academy of Sciences of the United States of America* 111 (7): 2488–93. https://doi.org/10.1073/pnas.1400648111.

Alexandrov, Andrei, Mark R. Martzen, and Eric M. Phizicky. 2002. "Two Proteins That Form a Complex Are Required for 7-Methylguanosine Modification of Yeast TRNA." *RNA (New York, N.Y.)* 8 (10): 1253–66. https://doi.org/10.1017/s1355838202024019.

Ali, Aamir, and Shweta Tyagi. 2017. "Diverse Roles of WDR5-RbBP5-ASH2L-DPY30 (WRAD) Complex in the Functions of the SET1 Histone Methyltransferase Family." *Journal of Biosciences* 42 (1): 155–59. https://doi.org/10.1007/s12038-017-9666-9.

Allis, C. David, and Thomas Jenuwein. 2016. “The Molecular Hallmarks of Epigenetic Control.” *Nature Reviews Genetics* 17 (8): 487–500. https://doi.org/10.1038/nrg.2016.59.

Allshire, Robin C., and Hiten D. Madhani. 2018. “Ten Principles of Heterochromatin Formation and Function.” *Nature Reviews Molecular Cell Biology* 19 (4): 229–44. https://doi.org/10.1038/nrm.2017.119.

Altaf, Mohammed, Andréanne Auger, Julie Monnet-Saksouk, Joëlle Brodeur, Sandra Piquet, Myriam Cramet, Nathalie Bouchard, et al. 2010. “NuA4-Dependent Acetylation of Nucleosomal Histones H4 and H2A Directly Stimulates Incorporation of H2A.Z by the SWR1 Complex*.” *Journal of Biological Chemistry* 285 (21): 15966–77. https://doi.org/10.1074/jbc.M110.117069.

Amin, Elianna M., Yuan Liu, Su Deng, Kay See Tan, Neel Chudgar, Marty W. Mayo, Francisco Sanchez-Vega, Prasad S. Adusumilli, Nikolaus Schultz, and David R. Jones. 2017. “The RNA-Editing Enzyme ADAR Promotes Lung Adenocarcinoma Migration and Invasion by Stabilizing FAK.” *Science Signaling* 10 (497). https://doi.org/10.1126/scisignal.aah3941.

Amort, Thomas, Dietmar Rieder, Alexandra Wille, Daria Khokhlova-Cubberley, Christian Riml, Lukas Trixl, Xi-Yu Jia, Ronald Micura, and Alexandra Lusser. 2017. “Distinct 5-Methylcytosine Profiles in Poly(A) RNA from Mouse Embryonic Stem Cells and Brain.” *Genome Biology* 18 (1): 1. https://doi.org/10.1186/s13059-016-1139-1.

Anderson, Kelly M., Douglas M. Anderson, John R. McAnally, John M. Shelton, Rhonda Bassel-Duby, and Eric N. Olson. 2016. “Transcription of the Non-Coding RNA Upperhand Controls Hand2 Expression and Heart Development.” *Nature* 539 (7629): 433–36. https://doi.org/10.1038/nature20128.

Anderson, Kristin A., Frank K. Huynh, Kelsey Fisher-Wellman, J. Darren Stuart, Brett S. Peterson, Jonathan D. Douros, Gregory R. Wagner, et al. 2017. “SIRT4 Is a Lysine Deacylase That Controls Leucine Metabolism and Insulin Secretion.” *Cell Metabolism* 25 (4): 838-855.e15. https://doi.org/10.1016/j.cmet.2017.03.003.

Andreu-Vieyra, Claudia V., Ruihong Chen, Julio E. Agno, Stefan Glaser, Konstantinos Anastassiadis, A. Francis Stewart, and Martin M. Matzuk. 2010. “MLL2 Is Required in Oocytes for Bulk Histone 3 Lysine 4 Trimethylation and Transcriptional Silencing.” *PLoS Biology* 8 (8): e1000453. https://doi.org/10.1371/journal.pbio.1000453.

Arab, Khelifa, Emil Karaulanov, Michael Musheev, Philipp Trnka, Andrea Schäfer, Ingrid Grummt, and Christof Niehrs. 2019. “GADD45A Binds R-Loops and Recruits TET1 to CpG Island Promoters.” *Nature Genetics* 51 (2): 217–23. https://doi.org/10.1038/s41588-018-0306-6.

Aravin, Alexei A., Ravi Sachidanandam, Deborah Bourc’his, Christopher Schaefer, Dubravka Pezic, Katalin Fejes Toth, Timothy Bestor, and Gregory J. Hannon. 2008. “A PiRNA Pathway Primed by Individual Transposons Is Linked to De Novo DNA Methylation in Mice.” *Molecular Cell* 31 (6): 785–99. https://doi.org/10.1016/j.molcel.2008.09.003.

Armache, Anja, Shuang Yang, Alexia Martínez de Paz, Lexi E. Robbins, Ceyda Durmaz, Jin Q. Cheong, Arjun Ravishankar, et al. 2020. “Histone H3.3 Phosphorylation Amplifies Stimulation-Induced Transcription.” *Nature* 583 (7818): 852–57. https://doi.org/10.1038/s41586-020-2533-0.

Auxilien, Sylvie, Pamela F. Crain, Ronald W. Trewyn, and Henri Grosjean. 1996. “Mechanism, Specificity and General Properties of the Yeast Enzyme Catalysing the Formation of Inosine 34 in the Anticodon of Transfer RNA.” *Journal of Molecular Biology* 262 (4): 437–58. https://doi.org/10.1006/jmbi.1996.0527.

Bagchi, Dia N., Anna M. Battenhouse, Daechan Park, and Vishwanath R. Iyer. 2020. "The Histone Variant H2A.Z in Yeast Is Almost Exclusively Incorporated into the +1 Nucleosome in the Direction of Transcription." *Nucleic Acids Research* 48 (1): 157–70. https://doi.org/10.1093/nar/gkz1075.

Bahar Halpern, Keren, Tal Vana, and Michael D. Walker. 2014. "Paradoxical Role of DNA Methylation in Activation of FoxA2 Gene Expression during Endoderm Development*." *Journal of Biological Chemistry* 289 (34): 23882–92. https://doi.org/10.1074/jbc.M114.573469.

Baldi, Sandro, Philipp Korber, and Peter B. Becker. 2020. "Beads on a String—Nucleosome Array Arrangements and Folding of the Chromatin Fiber." *Nature Structural & Molecular Biology* 27 (2): 109–18. https://doi.org/10.1038/s41594-019-0368-x.

Ballaré, Cecilia, Martin Lange, Audrone Lapinaite, Gloria Mas Martin, Lluis Morey, Gloria Pascual, Robert Liefke, et al. 2012. "Phf19 Links Methylated Lys36 of Histone H3 to Regulation of Polycomb Activity." *Nature Structural & Molecular Biology* 19 (12): 1257–65. https://doi.org/10.1038/nsmb.2434.

Ballas, Nurit, Elena Battaglioli, Fouad Atouf, Maria E. Andres, Josh Chenoweth, Mary E. Anderson, Corinna Burger, et al. 2001. "Regulation of Neuronal Traits by a Novel Transcriptional Complex." *Neuron* 31 (3): 353–65. https://doi.org/10.1016/S0896-6273(01)00371-3.

Bannister, Andrew J., Robert Schneider, Fiona A. Myers, Alan W. Thorne, Colyn Crane-Robinson, and Tony Kouzarides. 2005. "Spatial Distribution of Di- and Tri-Methyl Lysine 36 of Histone H3 at Active Genes*." *Journal of Biological Chemistry* 280 (18): 17732–36. https://doi.org/10.1074/jbc.M500796200.

Bantis, A., A. Giannopoulos, M. Gonidi, A. Liossi, E. Aggelonidou, E. Petrakakou, P. Athanassiades, and P. Athanassiadou. 2004. "Expression of P120, Ki-67 and PCNA as Proliferation Biomarkers in Imprint Smears of Prostate Carcinoma and Their Prognostic Value." *Cytopathology* 15 (1): 25–31. https://doi.org/10.1046/j.0956-5507.2003.00090.x.

Bantscheff, Marcus, Carsten Hopf, Mikhail M. Savitski, Antje Dittmann, Paola Grandi, Anne-Marie Michon, Judith Schlegl, et al. 2011. "Chemoproteomics Profiling of HDAC Inhibitors Reveals Selective Targeting of HDAC Complexes." *Nature Biotechnology* 29 (3): 255–65. https://doi.org/10.1038/nbt.1759.

Barau, Joan, Aurélie Teissandier, Natasha Zamudio, Stéphanie Roy, Valérie Nalesso, Yann Hérault, Florian Guillou, and Déborah Bourc'his. 2016. "The DNA Methyltransferase DNMT3C Protects Male Germ Cells from Transposon Activity." *Science* 354 (6314): 909–12. https://doi.org/10.1126/science.aah5143.

Barbieri, Isaia, and Tony Kouzarides. 2020. "Role of RNA Modifications in Cancer." *Nature Reviews Cancer* 20 (6): 303–22. https://doi.org/10.1038/s41568-020-0253-2.

Barski, Artem, Suresh Cuddapah, Kairong Cui, Tae-Young Roh, Dustin E. Schones, Zhibin Wang, Gang Wei, Iouri Chepelev, and Keji Zhao. 2007. "High-Resolution Profiling of Histone Methylations in the Human Genome." *Cell* 129 (4): 823–37. https://doi.org/10.1016/j.cell.2007.05.009.

Bartholomew, Blaine. 2014. "Regulating the Chromatin Landscape: Structural and Mechanistic Perspectives." *Annual Review of Biochemistry* 83 (1): 671–96. https://doi.org/10.1146/annurev-biochem-051810-093157.

Baubec, Tuncay, Robert Ivánek, Florian Lienert, and Dirk Schübeler. 2013. "Methylation-Dependent and -Independent Genomic Targeting Principles of the MBD Protein Family." *Cell* 153 (2): 480–92. https://doi.org/10.1016/j.cell.2013.03.011.

Bayliss, Jill, Piali Mukherjee, Chao Lu, Siddhant U. Jain, Chan Chung, Daniel Martinez, Benjamin Sabari, et al. 2016. “Lowered H3K27me3 and DNA Hypomethylation Define Poorly Prognostic Pediatric Posterior Fossa Ependymomas.” *Science Translational Medicine* 8 (366): 366ra161. https://doi.org/10.1126/scitranslmed.aah6904.

Beckedorff, Felipe C., Ana C. Ayupe, Renan Crocci-Souza, Murilo S. Amaral, Helder I. Nakaya, Daniela T. Soltys, Carlos F. M. Menck, Eduardo M. Reis, and Sergio Verjovski-Almeida. 2013. “The Intronic Long Noncoding RNA ANRASSF1 Recruits PRC2 to the RASSF1A Promoter, Reducing the Expression of RASSF1A and Increasing Cell Proliferation.” *PLoS Genetics* 9 (8): e1003705. https://doi.org/10.1371/journal.pgen.1003705.

Becker, Peter B., and Jerry L. Workman. 2013. “Nucleosome Remodeling and Epigenetics.” *Cold Spring Harbor Perspectives in Biology* 5 (9): a017905. https://doi.org/10.1101/cshperspect.a017905.

Behjati, Sam, Patrick S. Tarpey, Nadège Presneau, Susanne Scheipl, Nischalan Pillay, Peter Van Loo, David C. Wedge, et al. 2013. “Distinct H3F3A and H3F3B Driver Mutations Define Chondroblastoma and Giant Cell Tumor of Bone.” *Nature Genetics* 45 (12): 1479–82. https://doi.org/10.1038/ng.2814.

Bellodi, Cristian, Olya Krasnykh, Nikesha Haynes, Marily Theodoropoulou, Guang Peng, Lorenzo Montanaro, and Davide Ruggero. 2010. “Loss of Function of the Tumor Suppressor DKC1 Perturbs P27 Translation Control and Contributes to Pituitary Tumorigenesis.” *Cancer Research* 70 (14): 6026–35. https://doi.org/10.1158/0008-5472.CAN-09-4730.

Ben-Shahar, T. R., S. Heeger, C. Lehane, P. East, H. Flynn, M. Skehel, and F. Uhlmann. 2008. “Eco1-Dependent Cohesin Acetylation During Establishment of Sister Chromatid Cohesion.” *Science* 321 (5888): 563–66. https://doi.org/10.1126/science.1157774.

Bernstein, Bradley E., Michael Kamal, Kerstin Lindblad-Toh, Stefan Bekiranov, Dione K. Bailey, Dana J. Huebert, Scott McMahon, et al. 2005. “Genomic Maps and Comparative Analysis of Histone Modifications in Human and Mouse.” *Cell* 120 (2): 169–81. https://doi.org/10.1016/j.cell.2005.01.001.

Bernstein, Bradley E., Tarjei S. Mikkelsen, Xiaohui Xie, Michael Kamal, Dana J. Huebert, James Cuff, Ben Fry, et al. 2006. “A Bivalent Chromatin Structure Marks Key Developmental Genes in Embryonic Stem Cells.” *Cell* 125 (2): 315–26. https://doi.org/10.1016/j.cell.2006.02.041.

Betts, Laurie, Shibin Xiang, Steven A. Short, Richard Wolfenden, and Charles W. Carter. 1994. “Cytidine Deaminase. The 2·3 Å Crystal Structure of an Enzyme: Transition-State Analog Complex.” *Journal of Molecular Biology* 235 (2): 635–56. https://doi.org/10.1006/jmbi.1994.1018.

Bhalla, Tarun, Joshua J. C. Rosenthal, Miguel Holmgren, and Robert Reenan. 2004. “Control of Human Potassium Channel Inactivation by Editing of a Small MRNA Hairpin.” *Nature Structural & Molecular Biology* 11 (10): 950–56. https://doi.org/10.1038/nsmb825.

Black, Ben E., and Don W. Cleveland. 2011. “Epigenetic Centromere Propagation and the Nature of CENP-A Nucleosomes.” *Cell* 144 (4): 471–79. https://doi.org/10.1016/j.cell.2011.02.002.

Blanco, Sandra, Sabine Dietmann, Joana V Flores, Shobbir Hussain, Claudia Kutter, Peter Humphreys, Margus Lukk, et al. 2014. “Aberrant Methylation of TRNAs Links Cellular Stress to Neuro-Developmental Disorders.” *The EMBO Journal* 33 (18): 2020–39. https://doi.org/10.15252/embj.201489282.

Blewitt, Marnie E., Anne-Valerie Gendrel, Zhenyi Pang, Duncan B. Sparrow, Nadia Whitelaw, Jeffrey M. Craig, Anwyn Apedaile, et al. 2008. “SmcHD1, Containing a Structural-Maintenance-of-Chromosomes Hinge Domain, Has a Critical Role in X Inactivation.” *Nature Genetics* 40 (5): 663–69. https://doi.org/10.1038/ng.142.

Boccaletto, Pietro, Magdalena A Machnicka, Elzbieta Purta, Paweł Piątkowski, Błażej Bagiński, Tomasz K Wirecki, Valérie de Crécy-Lagard, et al. 2018. “MODOMICS: A Database of RNA Modification Pathways. 2017 Update.” *Nucleic Acids Research* 46 (D1): D303–7. https://doi.org/10.1093/nar/gkx1030.

Boeger, Hinrich, Joachim Griesenbeck, J. Seth Strattan, and Roger D Kornberg. 2004. “Removal of Promoter Nucleosomes by Disassembly Rather Than Sliding In Vivo.” *Molecular Cell* 14 (5): 667–73. https://doi.org/10.1016/j.molcel.2004.05.013.

Bohnsack, Markus T., and Katherine E. Sloan. 2018. “Modifications in Small Nuclear RNAs and Their Roles in Spliceosome Assembly and Function.” *Biological Chemistry* 399 (11): 1265–76. https://doi.org/10.1515/hsz-2018-0205.

Bonaldi, Tiziana, Fabio Talamo, Paola Scaffidi, Denise Ferrera, Annalisa Porto, Angela Bachi, Anna Rubartelli, Alessandra Agresti, and Marco E. Bianchi. 2003. “Monocytic Cells Hyperacetylate Chromatin Protein HMGB1 to Redirect It towards Secretion.” *The EMBO Journal* 22 (20): 5551–60. https://doi.org/10.1093/emboj/cdg516.

Boque-Sastre, Raquel, Marta Soler, Cristina Oliveira-Mateos, Anna Portela, Catia Moutinho, Sergi Sayols, Alberto Villanueva, Manel Esteller, and Sonia Guil. 2015. “Head-to-Head Antisense Transcription and R-Loop Formation Promotes Transcriptional Activation.” *Proceedings of the National Academy of Sciences of the United States of America* 112 (18): 5785–90. https://doi.org/10.1073/pnas.1421197112.

Bose, Daniel A., Greg Donahue, Danny Reinberg, Ramin Shiekhattar, Roberto Bonasio, and Shelley L. Berger. 2017. “RNA Binding to CBP Stimulates Histone Acetylation and Transcription.” *Cell* 168 (1): 135-149.e22. https://doi.org/10.1016/j.cell.2016.12.020.

Bostick, Magnolia, Jong Kyong Kim, Pierre-Olivier Estève, Amander Clark, Sriharsa Pradhan, and Steven E. Jacobsen. 2007. “UHRF1 Plays a Role in Maintaining DNA Methylation in Mammalian Cells.” *Science* 317 (5845): 1760–64. https://doi.org/10.1126/science.1147939.

Bourc’his, Déborah, Guo-Liang Xu, Chyuan-Sheng Lin, Brooke Bollman, and Timothy H. Bestor. 2001. “Dnmt3L and the Establishment of Maternal Genomic Imprints.” *Science* 294 (5551): 2536–39. https://doi.org/10.1126/science.1065848.

Brien, Gerard L., Guillermo Gambero, David J. O’Connell, Emilia Jerman, Siobhán A. Turner, Chris M. Egan, Eiseart J. Dunne, et al. 2012. “Polycomb PHF19 Binds H3K36me3 and Recruits PRC2 and Demethylase NO66 to Embryonic Stem Cell Genes during Differentiation.” *Nature Structural & Molecular Biology* 19 (12): 1273–81. https://doi.org/10.1038/nsmb.2449.

Burns, Colleen M., Hsin Chu, Susan M. Rueter, Linda K. Hutchinson, Hervé Canton, Elaine Sanders-Bush, and Ronald B. Emeson. 1997. “Regulation of Serotonin-2C Receptor G-Protein Coupling by RNA Editing.” *Nature* 387 (6630): 303–8. https://doi.org/10.1038/387303a0.

Buschbeck, Marcus, Iris Uribesalgo, Indra Wibowo, Pau Rué, David Martin, Arantxa Gutierrez, Lluís Morey, Roderic Guigó, Hernán López-Schier, and Luciano Di Croce. 2009. “The Histone Variant MacroH2A Is an Epigenetic Regulator of Key Developmental Genes.” *Nature Structural & Molecular Biology* 16 (10): 1074–79. https://doi.org/10.1038/nsmb.1665.

Cabello-Villegas, Javier, Malcolm E. Winkler, and Edward P. Nikonowicz. 2002. “Solution Conformations of Unmodified and A(37)N(6)-Dimethylallyl Modified Anticodon Stem-Loops of Escherichia Coli TRNA(Phe).” *Journal of Molecular Biology* 319 (5): 1015–34. https://doi.org/10.1016/S0022-2836(02)00382-0.

Cai, Mingbo, Zhenhua Hu, Juanjuan Liu, Jian Gao, Mingzi Tan, Danye Zhang, Liancheng Zhu, Shuice Liu, Rui Hou, and Bei Lin. 2015. “Expression of HMOF in Different Ovarian Tissues and Its Effects on Ovarian Cancer Prognosis.” *Oncology Reports* 33 (2): 685–92. https://doi.org/10.3892/or.2014.3649.

Cámara, Yolanda, Jorge Asin-Cayuela, Chan Bae Park, Metodi D. Metodiev, Yonghong Shi, Benedetta Ruzzenente, Christian Kukat, et al. 2011. “MTERF4 Regulates Translation by Targeting the Methyltransferase NSUN4 to the Mammalian Mitochondrial Ribosome.” *Cell Metabolism* 13 (5): 527–39. https://doi.org/10.1016/j.cmet.2011.04.002.

Cantara, William A., Yann Bilbille, Jia Kim, Rob Kaiser, Grażyna Leszczyńska, Andrzej Malkiewicz, and Paul F. Agris. 2012. “Modifications Modulate Anticodon Loop Dynamics and Codon Recognition of E. Coli TRNA(Arg1,2).” *Journal of Molecular Biology* 416 (4): 579–97. https://doi.org/10.1016/j.jmb.2011.12.054.

Cao, Ji, Lei Sun, Pornpun Aramsangtienchai, Nicole A. Spiegelman, Xiaoyu Zhang, Weishan Huang, Edward Seto, and Hening Lin. 2019. “HDAC11 Regulates Type I Interferon Signaling through Defatty-Acylation of SHMT2.” *Proceedings of the National Academy of Sciences of the United States of America* 116 (12): 5487–92. https://doi.org/10.1073/pnas.1815365116.

Cao, Lingling, Lin Zhu, Jiaxing Yang, Jiaming Su, Jinsong Ni, Yujun Du, Da Liu, et al. 2014. “Correlation of Low Expression of HMOF with Clinicopathological Features of Colorectal Carcinoma, Gastric Cancer and Renal Cell Carcinoma.” *International Journal of Oncology* 44 (4): 1207–14. https://doi.org/10.3892/ijo.2014.2266.

Cao, Ru, and Yi Zhang. 2004. “SUZ12 Is Required for Both the Histone Methyltransferase Activity and the Silencing Function of the EED-EZH2 Complex.” *Molecular Cell* 15 (1): 57–67. https://doi.org/10.1016/j.molcel.2004.06.020.

Cao, Wangsen, Clare Bao, Elizaveta Padalko, and Charles J. Lowenstein. 2008. “Acetylation of Mitogen-Activated Protein Kinase Phosphatase-1 Inhibits Toll-like Receptor Signaling.” *Journal of Experimental Medicine* 205 (6): 1491–1503. https://doi.org/10.1084/jem.20071728.

Cappellacci, Loredana, Diego R. Perinelli, Filippo Maggi, Mario Grifantini, and Riccardo Petrelli. 2020. “Recent Progress in Histone Deacetylase Inhibitors as Anticancer Agents.” *Current Medicinal Chemistry* 27 (15): 2449–93. https://doi.org/10.2174/0929867325666181016163110.

Cech, Thomas R., and Joan A. Steitz. 2014. “The Noncoding RNA Revolution—Trashing Old Rules to Forge New Ones.” *Cell* 157 (1): 77–94. https://doi.org/10.1016/j.cell.2014.03.008.

Cenci, Caterina, Rita Barzotti, Federica Galeano, Sandro Corbelli, Rossella Rota, Luca Massimi, Concezio Di Rocco, Mary A. O’Connell, and Angela Gallo. 2008. “Down-Regulation of RNA Editing in Pediatric Astrocytomas: Adar2 Editing Activity Inhibits Cell Migration And Proliferation*.” *Journal of Biological Chemistry* 283 (11): 7251–60. https://doi.org/10.1074/jbc.M708316200.

Cenik, Bercin K., and Ali Shilatifard. 2021. “COMPASS and SWI/SNF Complexes in Development and Disease.” *Nature Reviews Genetics* 22 (1): 38–58. https://doi.org/10.1038/s41576-020-0278-0.

Cesarini, Valeriana, Domenico A Silvestris, Valentina Tassinari, Sara Tomaselli, Shahar Alon, Eli Eisenberg, Franco Locatelli, and Angela Gallo. 2018. "ADAR2/MiR-589-3p Axis Controls Glioblastoma Cell Migration/Invasion." *Nucleic Acids Research* 46 (4): 2045–59. https://doi.org/10.1093/nar/gkx1257.

Chan, Thomas S., Eric Tse, and Yok-Lam Kwong. 2017. "Chidamide in the Treatment of Peripheral T-Cell Lymphoma." *OncoTargets and Therapy* 10: 347–52. https://doi.org/10.2147/OTT.S93528.

Chatterjee, Nilanjana, Divya Sinha, Mekonnen Lemma-Dechassa, Song Tan, Michael A. Shogren-Knaak, and Blaine Bartholomew. 2011. "Histone H3 Tail Acetylation Modulates ATP-Dependent Remodeling through Multiple Mechanisms." *Nucleic Acids Research* 39 (19): 8378–91. https://doi.org/10.1093/nar/gkr535.

Chen, Leilei, Yan Li, Chi Ho Lin, Tim Hon Man Chan, Raymond Kwok Kei Chow, Yangyang Song, Ming Liu, et al. 2013. "Recoding RNA Editing of AZIN1 Predisposes to Hepatocellular Carcinoma." *Nature Medicine* 19 (2): 209–16. https://doi.org/10.1038/nm.3043.

Chen, Ling-Ling, and Gordon G. Carmichael. 2009. "Altered Nuclear Retention of MRNAs Containing Inverted Repeats in Human Embryonic Stem Cells: Functional Role of a Nuclear Noncoding RNA." *Molecular Cell* 35 (4): 467–78. https://doi.org/10.1016/j.molcel.2009.06.027.

Chen, Xin, Ang Li, Bao-Fa Sun, Ying Yang, Ya-Nan Han, Xun Yuan, Ri-Xin Chen, et al. 2019. "5-Methylcytosine Promotes Pathogenesis of Bladder Cancer through Stabilizing MRNAs." *Nature Cell Biology* 21 (8): 978–90. https://doi.org/10.1038/s41556-019-0361-y.

Chen, Xuechai, Chunyu Yu, Minjun Guo, Xiaotong Zheng, Sakhawat Ali, Hua Huang, Lihua Zhang, et al. 2019. "Down-Regulation of M6A MRNA Methylation Is Involved in Dopaminergic Neuronal Death." *ACS Chemical Neuroscience* 10 (5): 2355–63. https://doi.org/10.1021/acschemneuro.8b00657.

Chen, Yue, Robert Sprung, Yi Tang, Haydn Ball, Bhavani Sangras, Sung Chan Kim, John R. Falck, Junmin Peng, Wei Gu, and Yingming Zhao. 2007. "Lysine Propionylation and Butyrylation Are Novel Post-Translational Modifications in Histones." *Molecular & Cellular Proteomics: MCP* 6 (5): 812–19. https://doi.org/10.1074/mcp.M700021-MCP200.

Chevillard-Briet, Martine, Muriel Quaranta, Aude Grézy, Lise Mattera, Céline Courilleau, Magali Philippe, Pascale Mercier, et al. 2014. "Interplay between Chromatin-Modifying Enzymes Controls Colon Cancer Progression through Wnt Signaling." *Human Molecular Genetics* 23 (8): 2120–31. https://doi.org/10.1093/hmg/ddt604.

Chi, Lijun, and Paul Delgado-Olguín. 2013. "Expression of NOL1/NOP2/Sun Domain (Nsun) RNA Methyltransferase Family Genes in Early Mouse Embryogenesis." *Gene Expression Patterns* 13 (8): 319–27. https://doi.org/10.1016/j.gep.2013.06.003.

Cho, Dan-Sung C., Weidong Yang, Joshua T. Lee, Ramin Shiekhattar, John M. Murray, and Kazuko Nishikura. 2003. "Requirement of Dimerization for RNA Editing Activity of Adenosine Deaminases Acting on RNA*." *Journal of Biological Chemistry* 278 (19): 17093–102. https://doi.org/10.1074/jbc.M213127200.

Cho, Hyo Je, Hao Li, Brian M. Linhares, EunGi Kim, Juliano Ndoj, Hongzhi Miao, Jolanta Grembecka, and Tomasz Cierpicki. 2018. "GAS41 Recognizes Diacetylated Histone H3 through a Bivalent Binding Mode." *ACS Chemical Biology* 13 (9): 2739–46. https://doi.org/10.1021/acschembio.8b00674.

Choi, Junhong, Ka-Weng Ieong, Hasan Demirci, Jin Chen, Alexey Petrov, Arjun Prabhakar, Seán E. O'Leary, et al. 2016. "N 6 -Methyladenosine in MRNA Disrupts TRNA Selection and Translation-Elongation Dynamics." *Nature Structural & Molecular Biology* 23 (2): 110–15. https://doi.org/10.1038/nsmb.3148.

Choudhury, Yukti, Felix Chang Tay, Dang Hoang Lam, Edwin Sandanaraj, Carol Tang, Beng-Ti Ang, and Shu Wang. 2012. "Attenuated Adenosine-to-Inosine Editing of MicroRNA-376a* Promotes Invasiveness of Glioblastoma Cells." *The Journal of Clinical Investigation* 122 (11): 4059–76. https://doi.org/10.1172/JCI62925.

Chujo, Takeshi, and Kazuhito Tomizawa. 2021. "Human Transfer RNA Modopathies: Diseases Caused by Aberrations in Transfer RNA Modifications." *The FEBS Journal*, January. https://doi.org/10.1111/febs.15736.

Chung, Hachung, Jorg J. A. Calis, Xianfang Wu, Tony Sun, Yingpu Yu, Stephanie L. Sarbanes, Viet Loan Dao Thi, et al. 2018. "Human ADAR1 Prevents Endogenous RNA from Triggering Translational Shutdown." *Cell* 172 (4): 811-824.e14. https://doi.org/10.1016/j.cell.2017.12.038.

Chung, Sang J., J. Christopher Fromme, and Gregory L. Verdine. 2005. "Structure of Human Cytidine Deaminase Bound to a Potent Inhibitor." *Journal of Medicinal Chemistry* 48 (3): 658–60. https://doi.org/10.1021/jm0496279.

Clapier, C. R., G. Längst, D. F. Corona, P. B. Becker, and K. P. Nightingale. 2001. "Critical Role for the Histone H4 N Terminus in Nucleosome Remodeling by ISWI." *Molecular and Cellular Biology* 21 (3): 875–83. https://doi.org/10.1128/MCB.21.3.875-883.2001.

Clapier, Cedric R., and Bradley R. Cairns. 2009. "The Biology of Chromatin Remodeling Complexes." *Annual Review of Biochemistry* 78: 273–304. https://doi.org/10.1146/annurev.biochem.77.062706.153223.

Clapier, Cedric R., Janet Iwasa, Bradley R. Cairns, and Craig L. Peterson. 2017. "Mechanisms of Action and Regulation of ATP-Dependent Chromatin-Remodelling Complexes." *Nature Reviews Molecular Cell Biology* 18 (7): 407–22. https://doi.org/10.1038/nrm.2017.26.

Clapier, Cedric R., Karl P. Nightingale, and Peter B. Becker. 2002. "A Critical Epitope for Substrate Recognition by the Nucleosome Remodeling ATPase ISWI." *Nucleic Acids Research* 30 (3): 649–55. https://doi.org/10.1093/nar/30.3.649.

Clayton-Smith, Jill, James O'Sullivan, Sarah Daly, Sanjeev Bhaskar, Ruth Day, Beverley Anderson, Anne K. Voss, et al. 2011. "Whole-Exome-Sequencing Identifies Mutations in Histone Acetyltransferase Gene KAT6B in Individuals with the Say-Barber-Biesecker Variant of Ohdo Syndrome." *The American Journal of Human Genetics* 89 (5): 675–81. https://doi.org/10.1016/j.ajhg.2011.10.008.

Cocciadiferro, Dario, Bartolomeo Augello, Pasquelena De Nittis, Jiyuan Zhang, Barbara Mandriani, Natascia Malerba, Gabriella M Squeo, et al. 2018. "Dissecting KMT2D Missense Mutations in Kabuki Syndrome Patients." *Human Molecular Genetics* 27 (21): 3651–68. https://doi.org/10.1093/hmg/ddy241.

Cohen, Todd J., Jing L. Guo, David E. Hurtado, Linda K. Kwong, Ian P. Mills, John Q. Trojanowski, and Virginia M. Y. Lee. 2011. "The Acetylation of Tau Inhibits Its Function and Promotes Pathological Tau Aggregation." *Nature Communications* 2 (1): 252. https://doi.org/10.1038/ncomms1255.

Cohen, Todd J., Andrew W. Hwang, Clark R. Restrepo, Chao-Xing Yuan, John Q. Trojanowski, and Virginia M. Y. Lee. 2015. "An Acetylation Switch Controls TDP-43 Function and Aggregation Propensity." *Nature Communications* 6 (1): 5845. https://doi.org/10.1038/ncomms6845.

Comerford, Sarah A., Zhiguang Huang, Xinlin Du, Yun Wang, Ling Cai, Agnes K. Witkiewicz, Holly Walters, et al. 2014. “Acetate Dependence of Tumors.” *Cell* 159 (7): 1591–1602. https://doi.org/10.1016/j.cell.2014.11.020.

Cook, Casey, Yari Carlomagno, Tania F. Gendron, Judy Dunmore, Kristyn Scheffel, Caroline Stetler, Mary Davis, et al. 2014. “Acetylation of the KXGS Motifs in Tau Is a Critical Determinant in Modulation of Tau Aggregation and Clearance.” *Human Molecular Genetics* 23 (1): 104–16. https://doi.org/10.1093/hmg/ddt402.

Corona, Davide F. V, Gernot Längst, Cedric R Clapier, Edgar J Bonte, Simona Ferrari, John W Tamkun, and Peter B Becker. 1999. “ISWI Is an ATP-Dependent Nucleosome Remodeling Factor.” *Molecular Cell* 3 (2): 239–45. https://doi.org/10.1016/S1097-2765(00)80314-7.

Crécy-Lagard, Valérie de, Céline Brochier-Armanet, Jaunius Urbonavicius, Bernard Fernandez, Gabriela Phillips, Benjamin Lyons, Akiko Noma, et al. 2010. “Biosynthesis of Wyosine Derivatives in TRNA: An Ancient and Highly Diverse Pathway in Archaea.” *Molecular Biology and Evolution* 27 (9): 2062–77. https://doi.org/10.1093/molbev/msq096.

Creyghton, Menno P., Styliani Markoulaki, Stuart S. Levine, Jacob Hanna, Michael A. Lodato, Ky Sha, Richard A. Young, Rudolf Jaenisch, and Laurie A. Boyer. 2008. “H2AZ Is Enriched at Polycomb Complex Target Genes in ES Cells and Is Necessary for Lineage Commitment.” *Cell* 135 (4): 649–61. https://doi.org/10.1016/j.cell.2008.09.056.

Crick, F. H. C., Leslie Barnett, S. Brenner, and R. J. Watts-Tobin. 1961. “General Nature of the Genetic Code for Proteins.” *Nature* 192 (4809): 1227–32. https://doi.org/10.1038/1921227a0.

Crick, F. H. 1966. “Codon--Anticodon Pairing: The Wobble Hypothesis.” *Journal of Molecular Biology* 19 (2): 548–55. https://doi.org/10.1016/s0022-2836(66)80022-0.

Cs, Yarian, Basti Mm, Cain Rj, Ansari G, Guenther Rh, Sochacka E, Czerwinska G, Malkiewicz A, and Agris Pf. 1999. “Structural and Functional Roles of the N1- and N3-Protons of Psi at TRNA’s Position 39.” *Nucleic Acids Research* 27 (17): 3543–49. https://doi.org/10.1093/nar/27.17.3543.

Dalluge, J J, T Hashizume, A E Sopchik, J A McCloskey, and D R Davis. 1996. “Conformational Flexibility in RNA: The Role of Dihydrouridine.” *Nucleic Acids Research* 24 (6): 1073–79.

Daniel Ricketts, M., Brian Frederick, Henry Hoff, Yong Tang, David C. Schultz, Taranjit Singh Rai, Maria Grazia Vizioli, Peter D. Adams, and Ronen Marmorstein. 2015. “Ubinuclein-1 Confers Histone H3.3-Specific-Binding by the HIRA Histone Chaperone Complex.” *Nature Communications* 6 (1): 7711. https://doi.org/10.1038/ncomms8711.

Dao, Lan T. M., Ariel O. Galindo-Albarrán, Jaime A. Castro-Mondragon, Charlotte Andrieu-Soler, Alejandra Medina-Rivera, Charbel Souaid, Guillaume Charbonnier, et al. 2017. “Genome-Wide Characterization of Mammalian Promoters with Distal Enhancer Functions.” *Nature Genetics* 49 (7): 1073–81. https://doi.org/10.1038/ng.3884.

Davis, D. R. 1995. “Stabilization of RNA Stacking by Pseudouridine.” *Nucleic Acids Research* 23 (24): 5020–26. https://doi.org/10.1093/nar/23.24.5020.

Davis, Darrell R. 1998. “Biophysical and Conformational Properties of Modified Nucleosides in RNA (Nuclear Magnetic Resonance Studies).” In *Modification and Editing of RNA*, 85–102. John Wiley & Sons, Ltd. https://doi.org/10.1128/9781555818296.ch5.

Day, Jeremy J., and J. David Sweatt. 2011. “Epigenetic Mechanisms in Cognition.” *Neuron* 70 (5): 813–29. https://doi.org/10.1016/j.neuron.2011.05.019.

De Rubeis, Silvia, Xin He, Arthur P. Goldberg, Christopher S. Poultney, Kaitlin Samocha, A. Ercument Cicek, Yan Kou, et al. 2014. “Synaptic, Transcriptional and Chromatin Genes Disrupted in Autism.” *Nature* 515 (7526): 209–15. https://doi.org/10.1038/nature13772.

Deardorff, Matthew A., Masashige Bando, Ryuichiro Nakato, Erwan Watrin, Takehiko Itoh, Masashi Minamino, Katsuya Saitoh, et al. 2012. “HDAC8 Mutations in Cornelia de Lange Syndrome Affect the Cohesin Acetylation Cycle.” *Nature* 489 (7415): 313–17. https://doi.org/10.1038/nature11316.

Decroos, Christophe, Nicolas H. Christianson, Laura E. Gullett, Christine M. Bowman, Karen E. Christianson, Matthew A. Deardorff, and David W. Christianson. 2015. “Biochemical and Structural Characterization of HDAC8 Mutants Associated with Cornelia de Lange Syndrome Spectrum Disorders.” *Biochemistry* 54 (42): 6501–13. https://doi.org/10.1021/acs.biochem.5b00881.

Dennis, K., T. Fan, T. Geiman, Q. Yan, and K. Muegge. 2001. “Lsh, a Member of the SNF2 Family, Is Required for Genome-Wide Methylation.” *Genes & Development* 15 (22): 2940–44. https://doi.org/10.1101/gad.929101.

Dhayalan, Arunkumar, Arumugam Rajavelu, Philipp Rathert, Raluca Tamas, Renata Z. Jurkowska, Sergey Ragozin, and Albert Jeltsch. 2010. “The Dnmt3a PWWP Domain Reads Histone 3 Lysine 36 Trimethylation and Guides DNA Methylation*.” *Journal of Biological Chemistry* 285 (34): 26114–20. https://doi.org/10.1074/jbc.M109.089433.

Doenhoff, Michael J., John R. Kusel, Gerald C. Coles, and Donato Cioli. 2002. “Resistance of Schistosoma Mansoni to Praziquantel: Is There a Problem?” *Transactions of the Royal Society of Tropical Medicine and Hygiene* 96 (5): 465–69. https://doi.org/10.1016/s0035-9203(02)90405-0.

Dominissini, Dan, Sharon Moshitch-Moshkovitz, Schraga Schwartz, Mali Salmon-Divon, Lior Ungar, Sivan Osenberg, Karen Cesarkas, et al. 2012. “Topology of the Human and Mouse m 6 A RNA Methylomes Revealed by m 6 A-Seq.” *Nature* 485 (7397): 201–6. https://doi.org/10.1038/nature11112.

Dorn Lisa E., Lasman Lior, Chen Jing, Xu Xianyao, Hund Thomas J., Medvedovic Mario, Hanna Jacob H., van Berlo Jop H., and Accornero Federica. 2019. “The N6-Methyladenosine MRNA Methylase METTL3 Controls Cardiac Homeostasis and Hypertrophy.” *Circulation* 139 (4): 533–45. https://doi.org/10.1161/CIRCULATIONAHA.118.036146.

Dou, Yali, Thomas A. Milne, Alan J. Tackett, Edwin R. Smith, Aya Fukuda, Joanna Wysocka, C. David Allis, Brian T. Chait, Jay L. Hess, and Robert G. Roeder. 2005. “Physical Association and Coordinate Function of the H3 K4 Methyltransferase MLL1 and the H4 K16 Acetyltransferase MOF.” *Cell* 121 (6): 873–85. https://doi.org/10.1016/j.cell.2005.04.031.

Douet, Julien, David Corujo, Roberto Malinverni, Justine Renauld, Viola Sansoni, Melanija Posavec Marjanović, Neus Cantariño, et al. 2017. “MacroH2A Histone Variants Maintain Nuclear Organization and Heterochromatin Architecture.” *Journal of Cell Science* 130 (9): 1570–82. https://doi.org/10.1242/jcs.199216.

Draker, Ryan, Elizabeth Sarcinella, and Peter Cheung. 2011. “USP10 Deubiquitylates the Histone Variant H2A.Z and Both Are Required for Androgen Receptor-Mediated Gene Activation.” *Nucleic Acids Research* 39 (9): 3529–42. https://doi.org/10.1093/nar/gkq1352.

Drané, Pascal, Khalid Ouararhni, Arnaud Depaux, Muhammad Shuaib, and Ali Hamiche. 2010. “The Death-Associated Protein DAXX Is a Novel Histone Chaperone Involved in the Replication-Independent Deposition of H3.3.” *Genes & Development* 24 (12): 1253–65. https://doi.org/10.1101/gad.566910.

Dryhurst, Deanna, Toyotaka Ishibashi, Kristie L. Rose, José M. Eirín-López, Darin McDonald, Begonia Silva-Moreno, Nik Veldhoen, et al. 2009. “Characterization of the Histone H2A.Z-1 and H2A.Z-2 Isoforms in Vertebrates.” *BMC Biology* 7 (1): 1–16. https://doi.org/10.1186/1741-7007-7-86.

Du, Tingfu, Shuquan Rao, Lin Wu, Ning Ye, Zeyue Liu, Huiling Hu, Jianbo Xiu, Yan Shen, and Qi Xu. 2015. “An Association Study of the M6A Genes with Major Depressive Disorder in Chinese Han Population.” *Journal of Affective Disorders* 183 (September): 279–86. https://doi.org/10.1016/j.jad.2015.05.025.

Du, Zhanwen, Jing Song, Yong Wang, Yiqing Zhao, Kishore Guda, Shuming Yang, Hung-Ying Kao, et al. 2010. “DNMT1 Stability Is Regulated by Proteins Coordinating Deubiquitination and Acetylation-Driven Ubiquitination.” *Science Signaling* 3 (146): ra80–ra80. https://doi.org/10.1126/scisignal.2001462.

Dunleavy, Elaine M., Geneviève Almouzni, and Gary H. Karpen. 2011. “H3.3 Is Deposited at Centromeres in S Phase as a Placeholder for Newly Assembled CENP-A in G_1 Phase.” *Nucleus (Austin, Tex.)* 2 (2): 146–57. https://doi.org/10.4161/nucl.2.2.15211.

Dunleavy, Elaine M., Danièle Roche, Hideaki Tagami, Nicolas Lacoste, Dominique Ray-Gallet, Yusuke Nakamura, Yataro Daigo, Yoshihiro Nakatani, and Geneviève Almouzni-Pettinotti. 2009. “HJURP Is a Cell-Cycle-Dependent Maintenance and Deposition Factor of CENP-A at Centromeres.” *Cell* 137 (3): 485–97. https://doi.org/10.1016/j.cell.2009.02.040.

Durant, Philippe C., Ashok C. Bajji, Mallikarjun Sundaram, Raju K. Kumar, and Darrell R. Davis. 2005. “Structural Effects of Hypermodified Nucleosides in the Escherichia Coli and Human TRNALys Anticodon Loop: The Effect of Nucleosides S2U, Mcm5U, Mcm5s2U, Mnm5s2U, T6A, and Ms2t6A.” *Biochemistry* 44 (22): 8078–89. https://doi.org/10.1021/bi050343f.

Duvic, Madeleine, Susan E. Bates, Richard Piekarz, Robin Eisch, Youn H. Kim, Adam Lerner, Tadeusz Robak, et al. 2018. “Responses to Romidepsin in Patients with Cutaneous T-Cell Lymphoma and Prior Treatment with Systemic Chemotherapy.” *Leukemia & Lymphoma* 59 (4): 880–87. https://doi.org/10.1080/10428194.2017.1361022.

El-Hattab, Ayman W., Mohammed A. Saleh, Amal Hashem, Mohammed Al-Owain, Ali Al Asmari, Hala Rabei, Hanem Abdelraouf, et al. 2016. “ADAT3-Related Intellectual Disability: Further Delineation of the Phenotype.” *American Journal of Medical Genetics. Part A* 170A (5): 1142–47. https://doi.org/10.1002/ajmg.a.37578.

Elias, Youssef, and Raven H. Huang. 2005. “Biochemical and Structural Studies of A-to-I Editing by TRNA:A34 Deaminases at the Wobble Position of Transfer RNA.” *Biochemistry* 44 (36): 12057–65. https://doi.org/10.1021/bi050499f.

Ellmeier, Wilfried, and Christian Seiser. 2018. “Histone Deacetylase Function in CD4 + T Cells.” *Nature Reviews Immunology* 18 (10): 617–34. https://doi.org/10.1038/s41577-018-0037-z.

Elsässer, Simon J., Kyung-Min Noh, Nichole Diaz, C. David Allis, and Laura A. Banaszynski. 2015. “Histone H3.3 Is Required for Endogenous Retroviral Element Silencing in Embryonic Stem Cells.” *Nature* 522 (7555): 240–44. https://doi.org/10.1038/nature14345.

Endoh, Mitsuhiro, Takaho A. Endo, Jun Shinga, Katsuhiko Hayashi, Anca Farcas, Kit-Wan Ma, Shinsuke Ito, et al. 2017. “PCGF6-PRC1 Suppresses Premature Differentiation of Mouse Embryonic Stem Cells by Regulating Germ Cell-Related Genes.” *ELife* 6 (March): e21064. https://doi.org/10.7554/eLife.21064.

Engreitz, Jesse M., Jenna E. Haines, Elizabeth M. Perez, Glen Munson, Jenny Chen, Michael Kane, Patrick E. McDonel, Mitchell Guttman, and Eric S. Lander. 2016. “Local Regulation of Gene Expression by LncRNA Promoters, Transcription and Splicing.” *Nature* 539 (7629): 452–55. https://doi.org/10.1038/nature20149.

Ernst, Patricia, and Christopher R. Vakoc. 2012. “WRAD: Enabler of the SET1-Family of H3K4 Methyltransferases.” *Briefings in Functional Genomics* 11 (3): 217–26. https://doi.org/10.1093/bfgp/els017.

Faghihi, Mohammad Ali, Ming Zhang, Jia Huang, Farzaneh Modarresi, Marcel P. Van der Brug, Michael A. Nalls, Mark R. Cookson, Georges St-Laurent, and Claes Wahlestedt. 2010. “Evidence for Natural Antisense Transcript-Mediated Inhibition of MicroRNA Function.” *Genome Biology* 11 (5): R56. https://doi.org/10.1186/gb-2010-11-5-r56.

Falkenberg, Katrina J., and Ricky W. Johnstone. 2014. “Histone Deacetylases and Their Inhibitors in Cancer, Neurological Diseases and Immune Disorders.” *Nature Reviews Drug Discovery* 13 (9): 673–91. https://doi.org/10.1038/nrd4360.

Fan, Jun Y., Faye Gordon, Karolin Luger, Jeffrey C. Hansen, and David John Tremethick. 2002. “The Essential Histone Variant H2A.Z Regulates the Equilibrium between Different Chromatin Conformational States.” *Nature Structural Biology* 9 (3): 172–76. https://doi.org/10.1038/nsb767.

Fan, Wei, and Jianyuan Luo. 2010. “SIRT1 Regulates UV-Induced DNA Repair through Deacetylating XPA.” *Molecular Cell* 39 (2): 247–58. https://doi.org/10.1016/j.molcel.2010.07.006.

Fang, Dong, Haiyun Gan, Jeong-Heon Lee, Jing Han, Zhiquan Wang, Scott M. Riester, Long Jin, et al. 2016. “The Histone H3.3K36M Mutation Reprograms the Epigenome of Chondroblastomas.” *Science* 352 (6291): 1344–48. https://doi.org/10.1126/science.aae0065.

Fang, Lan, Jun Zhang, Hui Zhang, Xiaoqin Yang, Xueling Jin, Ling Zhang, David G. Skalnik, et al. 2016. “H3K4 Methyltransferase Set1a Is A Key Oct4 Coactivator Essential for Generation of Oct4 Positive Inner Cell Mass.” *STEM CELLS* 34 (3): 565–80. https://doi.org/10.1002/stem.2250.

Farooq, Zeenat, Ehsaan Abdullah, Shahid Banday, Shabir Ahmad Ganai, Romana Rashid, Arjamand Mushtaq, Samia Rashid, and Mohammad Altaf. 2019. “Vigilin Protein Vgl1 Is Required for Heterochromatin-Mediated Gene Silencing in Schizosaccharomyces Pombe.” *Journal of Biological Chemistry* 294 (48): 18029–40. https://doi.org/10.1074/jbc.RA119.009262.

Fei, Jia, Sharon E. Torigoe, Christopher R. Brown, Mai T. Khuong, George A. Kassavetis, Hinrich Boeger, and James T. Kadonaga. 2015. “The Prenucleosome, a Stable Conformational Isomer of the Nucleosome.” *Genes & Development* 29 (24): 2563–75. https://doi.org/10.1101/gad.272633.115.

Feng, Qin, Hengbin Wang, Huck Hui Ng, Hediye Erdjument-Bromage, Paul Tempst, Kevin Struhl, and Yi Zhang. 2002. “Methylation of H3-Lysine 79 Is Mediated by a New Family of HMTases without a SET Domain.” *Current Biology* 12 (12): 1052–58. https://doi.org/10.1016/S0960-9822(02)00901-6.

Feng, Yi, Christopher L. Sansam, Minati Singh, and Ronald B. Emeson. 2006. “Altered RNA Editing in Mice Lacking ADAR2 Autoregulation.” *Molecular and Cellular Biology* 26 (2): 480–88. https://doi.org/10.1128/MCB.26.2.480-488.2006.

Fischer, Adrian, Wignand W. D. Mühlhäuser, Bettina Warscheid, and Gerald Radziwill. 2017. “Membrane Localization of Acetylated CNK1 Mediates a Positive Feedback on RAF/ERK Signaling.” *Science Advances* 3 (8): e1700475. https://doi.org/10.1126/sciadv.1700475.

Fischle, Wolfgang, Franck Dequiedt, Michael J Hendzel, Matthew G Guenther, Mitchell A Lazar, Wolfgang Voelter, and Eric Verdin. 2002. “Enzymatic Activity Associated with Class II HDACs Is Dependent on a Multiprotein Complex Containing HDAC3 and SMRT/N-CoR.” *Molecular Cell* 9 (1): 45–57. https://doi.org/10.1016/S1097-2765(01)00429-4.

Foltz, Daniel R., Lars E. T. Jansen, Aaron O. Bailey, John R. Yates, Emily A. Bassett, Stacey Wood, Ben E. Black, and Don W. Cleveland. 2009. “Centromere-Specific Assembly of CENP-A Nucleosomes Is Mediated by HJURP.” *Cell* 137 (3): 472–84. https://doi.org/10.1016/j.cell.2009.02.039.

Frye, Michaela, Bryan T. Harada, Mikaela Behm, and Chuan He. 2018. “RNA Modifications Modulate Gene Expression during Development.” *Science* 361 (6409): 1346–49. https://doi.org/10.1126/science.aau1646.

Fujino, Takahiro, Jun Kondo, Momoyo Ishikawa, Kosuke Morikawa, and Tokuo T. Yamamoto. 2001. “Acetyl-CoA Synthetase 2, a Mitochondrial Matrix Enzyme Involved in the Oxidation of Acetate*.” *Journal of Biological Chemistry* 276 (14): 11420–26. https://doi.org/10.1074/jbc.M008782200.

Fuks, F., W. A. Burgers, N. Godin, M. Kasai, and T. Kouzarides. 2001. “Dnmt3a Binds Deacetylases and Is Recruited by a Sequence-Specific Repressor to Silence Transcription.” *The EMBO Journal* 20 (10): 2536–44. https://doi.org/10.1093/emboj/20.10.2536.

Funderburk, Sarah F., Qing Jun Wang, and Zhenyu Yue. 2010. “The Beclin 1–VPS34 Complex – at the Crossroads of Autophagy and Beyond.” *Trends in Cell Biology* 20 (6): 355–62. https://doi.org/10.1016/j.tcb.2010.03.002.

Gantt, Sister M. Lucy, Christophe Decroos, Matthew S. Lee, Laura E. Gullett, Christine M. Bowman, David W. Christianson, and Carol A. Fierke. 2016. “General Base–General Acid Catalysis in Human Histone Deacetylase 8.” *Biochemistry* 55 (5): 820–32. https://doi.org/10.1021/acs.biochem.5b01327.

Gao, Lin, Maria A. Cueto, Fred Asselbergs, and Peter Atadja. 2002. “Cloning and Functional Characterization of HDAC11, a Novel Member of the Human Histone Deacetylase Family*.” *Journal of Biological Chemistry* 277 (28): 25748–55. https://doi.org/10.1074/jbc.M111871200.

Gelfman, Sahar, Noa Cohen, Ahuvi Yearim, and Gil Ast. 2013. “DNA-Methylation Effect on Cotranscriptional Splicing Is Dependent on GC Architecture of the Exon-Intron Structure.” *Genome Research* 23 (5): 789–99. https://doi.org/10.1101/gr.143503.112.

Gendrel, Anne-Valerie, Anwyn Apedaile, Heather Coker, Ausma Termanis, Ilona Zvetkova, Jonathan Godwin, Y. Amy Tang, et al. 2012. “Smchd1-Dependent and -Independent Pathways Determine Developmental Dynamics of CpG Island Methylation on the Inactive X Chromosome.” *Developmental Cell* 23 (2): 265–79. https://doi.org/10.1016/j.devcel.2012.06.011.

Gerber, A. P., and W. Keller. 1999. “An Adenosine Deaminase That Generates Inosine at the Wobble Position of TRNAs.” *Science (New York, N.Y.)* 286 (5442): 1146–49. https://doi.org/10.1126/science.286.5442.1146.

Gerber, A. P., and W. Keller. 2001. “RNA Editing by Base Deamination: More Enzymes, More Targets, New Mysteries.” *Trends in Biochemical Sciences* 26 (6): 376–84. https://doi.org/10.1016/s0968-0004(01)01827-8.

Gerber, André, Henri Grosjean, Thorsten Melcher, and Walter Keller. 1998. “Tad1p, a Yeast TRNA-Specific Adenosine Deaminase, Is Related to the Mammalian Pre-MRNA Editing Enzymes ADAR1 and ADAR2.” *The EMBO Journal* 17 (16): 4780–89. https://doi.org/10.1093/emboj/17.16.4780.

Geula, Shay, Sharon Moshitch-Moshkovitz, Dan Dominissini, Abed AlFatah Mansour, Nitzan Kol, Mali Salmon-Divon, Vera Hershkovitz, et al. 2015. “M6A MRNA Methylation Facilitates Resolution of Naïve Pluripotency toward Differentiation.” *Science* 347 (6225): 1002–6. https://doi.org/10.1126/science.1261417.

Ghanim, George E., Adam J. Fountain, Anne-Marie M. van Roon, Ramya Rangan, Rhiju Das, Kathleen Collins, and Thi Hoang Duong Nguyen. 2021. “Structure of Human Telomerase Holoenzyme with Bound Telomeric DNA.” *Nature*, April, 1–5. https://doi.org/10.1038/s41586-021-03415-4.

Ghiraldini, Flávia G., Dan Filipescu, and Emily Bernstein. 2021. “Solid Tumours Hijack the Histone Variant Network.” *Nature Reviews Cancer* 21 (4): 257–75. https://doi.org/10.1038/s41568-020-00330-0.

Gibbons, Hunter R., Guzel Shaginurova, Laura C. Kim, Nathaniel Chapman, Charles F. Spurlock, and Thomas M. Aune. 2018. “Divergent LncRNA GATA3-AS1 Regulates GATA3 Transcription in T-Helper 2 Cells.” *Frontiers in Immunology* 9: 2512. https://doi.org/10.3389/fimmu.2018.02512.

Glaser, Stefan, Sandra Lubitz, Kate L. Loveland, Kazu Ohbo, Lorraine Robb, Frieder Schwenk, Jost Seibler, et al. 2009. “The Histone 3 Lysine 4 Methyltransferase, Mll2, Is Only Required Briefly in Development and Spermatogenesis.” *Epigenetics & Chromatin* 2 (1): 5. https://doi.org/10.1186/1756-8935-2-5.

Glaser, Stefan, Julia Schaft, Sandra Lubitz, Kristina Vintersten, Frank van der Hoeven, Katharina R. Tufteland, Rein Aasland, Konstantinos Anastassiadis, Siew-Lan Ang, and A. Francis Stewart. 2006. “Multiple Epigenetic Maintenance Factors Implicated by the Loss of Mll2 in Mouse Development.” *Development (Cambridge, England)* 133 (8): 1423–32. https://doi.org/10.1242/dev.02302.

Goldberg, Aaron D., C. David Allis, and Emily Bernstein. 2007. “Epigenetics: A Landscape Takes Shape.” *Cell* 128 (4): 635–38. https://doi.org/10.1016/j.cell.2007.02.006.

Goldberg, Aaron D., Laura A. Banaszynski, Kyung-Min Noh, Peter W. Lewis, Simon J. Elsaesser, Sonja Stadler, Scott Dewell, et al. 2010. “Distinct Factors Control Histone Variant H3.3 Localization at Specific Genomic Regions.” *Cell* 140 (5): 678–91. https://doi.org/10.1016/j.cell.2010.01.003.

Goldman, Joseph A., Joseph D. Garlick, and Robert E. Kingston. 2010. “Chromatin Remodeling by Imitation Switch (ISWI) Class ATP-Dependent Remodelers Is Stimulated by Histone Variant H2A.Z.” *Journal of Biological Chemistry* 285 (7): 4645–51. https://doi.org/10.1074/jbc.M109.072348.

Goll, Mary Grace, Finn Kirpekar, Keith A. Maggert, Jeffrey A. Yoder, Chih-Lin Hsieh, Xiaoyu Zhang, Kent G. Golic, Steven E. Jacobsen, and Timothy H. Bestor. 2006. “Methylation of TRNAAsp by the DNA Methyltransferase Homolog Dnmt2.” *Science* 311 (5759): 395–98. https://doi.org/10.1126/science.1120976.

Gorrini, Chiara, Massimo Squatrito, Chiara Luise, Nelofer Syed, Daniele Perna, Landon Wark, Francesca Martinato, et al. 2007. “Tip60 Is a Haplo-Insufficient Tumour Suppressor Required for an Oncogene-Induced DNA Damage Response.” *Nature* 448 (7157): 1063–67. https://doi.org/10.1038/nature06055.

Govind, Chhabi K., Fan Zhang, Hongfang Qiu, Kimberly Hofmeyer, and Alan G. Hinnebusch. 2007. “Gcn5 Promotes Acetylation, Eviction, and Methylation of Nucleosomes in Transcribed Coding Regions.” *Molecular Cell* 25 (1): 31–42. https://doi.org/10.1016/j.molcel.2006.11.020.

Grant, Mark, Maurizio Zuccotti, and Marilyn Monk. 1992. “Methylation of CpG Sites of Two X–Linked Genes Coincides with X–Inactivation in the Female Mouse Embryo but Not in the Germ Line.” *Nature Genetics* 2 (2): 161–66. https://doi.org/10.1038/ng1092-161.

Greenberg, Maxim V. C., and Deborah Bourc’his. 2019. “The Diverse Roles of DNA Methylation in Mammalian Development and Disease.” *Nature Reviews Molecular Cell Biology* 20 (10): 590–607. https://doi.org/10.1038/s41580-019-0159-6.

Greenberg, Maxim V. C., Juliane Glaser, Máté Borsos, Fatima El Marjou, Marius Walter, Aurélie Teissandier, and Déborah Bourc’his. 2017. “Transient Transcription in the Early Embryo Sets an Epigenetic State That Programs Postnatal Growth.” *Nature Genetics* 49 (1): 110–18. https://doi.org/10.1038/ng.3718.

Gregoretti, IvanV, Yun-Mi Lee, and Holly V Goodson. 2004. “Molecular Evolution of the Histone Deacetylase Family: Functional Implications of Phylogenetic Analysis.” *Journal of Molecular Biology* 338 (1): 17–31. https://doi.org/10.1016/j.jmb.2004.02.006.

Grewal, Shiv I. S., and Songtao Jia. 2007. “Heterochromatin Revisited.” *Nature Reviews Genetics* 8 (1): 35–46. https://doi.org/10.1038/nrg2008.

Grijzenhout, Anne, Jonathan Godwin, Haruhiko Koseki, Michal Ryszard Gdula, Dorota Szumska, Joanna F. McGouran, Shoumo Bhattacharya, Benedikt M. Kessler, Neil Brockdorff, and Sarah Cooper. 2016. “Functional Analysis of AEBP2, a PRC2 Polycomb Protein, Reveals a Trithorax Phenotype in Embryonic Development and in ESCs.” *Development (Cambridge, England)* 143 (15): 2716–23. https://doi.org/10.1242/dev.123935.

Groff, Abigail F., Diana B. Sanchez-Gomez, Marcela M. L. Soruco, Chiara Gerhardinger, A. Rasim Barutcu, Eric Li, Lara Elcavage, et al. 2016. “In Vivo Characterization of Linc-P21 Reveals Functional Cis-Regulatory DNA Elements.” *Cell Reports* 16 (8): 2178–86. https://doi.org/10.1016/j.celrep.2016.07.050.

Grönroos, Eva, Ulf Hellman, Carl-Henrik Heldin, and Johan Ericsson. 2002. “Control of Smad7 Stability by Competition between Acetylation and Ubiquitination.” *Molecular Cell* 10 (3): 483–93. https://doi.org/10.1016/S1097-2765(02)00639-1.

Grosjean, H., S. Auxilien, F. Constantinesco, C. Simon, Y. Corda, H. F. Becker, D. Foiret, et al. 1996. “Enzymatic Conversion of Adenosine to Inosine and to N1-Methylinosine in Transfer RNAs: A Review.” *Biochimie* 78 (6): 488–501. https://doi.org/10.1016/0300-9084(96)84755-9.

Grosjean, Henri, and Glenn R. Björk. 2004. “Enzymatic Conversion of Cytidine to Lysidine in Anticodon of Bacterial Isoleucyl-TRNA--an Alternative Way of RNA Editing.” *Trends in Biochemical Sciences* 29 (4): 165–68. https://doi.org/10.1016/j.tibs.2004.02.009.

Grossi, Elena, Ivan Raimondi, Enrique Goñi, Jovanna González, Francesco P. Marchese, Vicente Chapaprieta, José I. Martín-Subero, Shuling Guo, and Maite Huarte. 2020. “A LncRNA-SWI/SNF Complex Crosstalk Controls Transcriptional Activation at Specific Promoter Regions.” *Nature Communications* 11 (1): 936. https://doi.org/10.1038/s41467-020-14623-3.

Gu, Tian-Peng, Fan Guo, Hui Yang, Hai-Ping Wu, Gui-Fang Xu, Wei Liu, Zhi-Guo Xie, et al. 2011. “The Role of Tet3 DNA Dioxygenase in Epigenetic Reprogramming by Oocytes.” *Nature* 477 (7366): 606–10. https://doi.org/10.1038/nature10443.

Guenther, M. G., O. Barak, and M. A. Lazar. 2001. “The SMRT and N-CoR Corepressors Are Activating Cofactors for Histone Deacetylase 3.” *Molecular and Cellular Biology* 21 (18): 6091–6101. https://doi.org/10.1128/MCB.21.18.6091-6101.2001.

Guenther, Matthew G., William S. Lane, Wolfgang Fischle, Eric Verdin, Mitchell A. Lazar, and Ramin Shiekhattar. 2000. “A Core SMRT Corepressor Complex Containing HDAC3 and TBL1, a WD40-Repeat Protein Linked to Deafness.” *Genes & Development* 14 (9): 1048–57. https://doi.org/10.1101/gad.14.9.1048.

Guibert, Sylvain, Thierry Forné, and Michael Weber. 2012. “Global Profiling of DNA Methylation Erasure in Mouse Primordial Germ Cells.” *Genome Research* 22 (4): 633–41. https://doi.org/10.1101/gr.130997.111.

Guo, Rui, Lijuan Zheng, Juw Won Park, Ruitu Lv, Hao Chen, Fangfang Jiao, Wenqi Xu, et al. 2014. “BS69/ZMYND11 Reads and Connects Histone H3.3 Lysine 36 Trimethylation-Decorated Chromatin to Regulated Pre-MRNA Processing.” *Molecular Cell* 56 (2): 298–310. https://doi.org/10.1016/j.molcel.2014.08.022.

Guo, Xue, Ling Wang, Jie Li, Zhanyu Ding, Jianxiong Xiao, Xiaotong Yin, Shuang He, et al. 2015. “Structural Insight into Autoinhibition and Histone H3-Induced Activation of DNMT3A.” *Nature* 517 (7536): 640–44. https://doi.org/10.1038/nature13899.

Gurard-Levin, Zachary A., Jean-Pierre Quivy, and Geneviève Almouzni. 2014. “Histone Chaperones: Assisting Histone Traffic and Nucleosome Dynamics.” *Annual Review of Biochemistry* 83 (1): 487–517. https://doi.org/10.1146/annurev-biochem-060713-035536.

Haag, Sara, Jens Kretschmer, and Markus T. Bohnsack. 2015. “WBSCR22/Merm1 Is Required for Late Nuclear Pre-Ribosomal RNA Processing and Mediates N7-Methylation of G1639 in Human 18S RRNA.” *RNA (New York, N.Y.)* 21 (2): 180–87. https://doi.org/10.1261/rna.047910.114.

Haag, Sara, Katherine E. Sloan, Namit Ranjan, Ahmed S. Warda, Jens Kretschmer, Charlotte Blessing, Benedikt Hübner, et al. 2016. “NSUN3 and ABH1 Modify the Wobble Position of Mt-TRNAMet to Expand Codon Recognition in Mitochondrial Translation.” *The EMBO Journal* 35 (19): 2104–19. https://doi.org/10.15252/embj.201694885.

Haag, Sara, Ahmed S. Warda, Jens Kretschmer, Manuel A. Günnigmann, Claudia Höbartner, and Markus T. Bohnsack. 2015. “NSUN6 Is a Human RNA Methyltransferase That Catalyzes Formation of M5C72 in Specific TRNAs.” *RNA* 21 (9): 1532–43. https://doi.org/10.1261/rna.051524.115.

Hackett, Jamie A., Roopsha Sengupta, Jan J. Zylicz, Kazuhiro Murakami, Caroline Lee, Thomas A. Down, and M. Azim Surani. 2013. “Germline DNA Demethylation Dynamics and Imprint Erasure Through 5-Hydroxymethylcytosine.” *Science* 339 (6118): 448–52. https://doi.org/10.1126/science.1229277.

Hai, Yang, Stephen A. Shinsky, Nicholas J. Porter, and David W. Christianson. 2017. “Histone Deacetylase 10 Structure and Molecular Function as a Polyamine Deacetylase.” *Nature Communications* 8 (1): 15368. https://doi.org/10.1038/ncomms15368.

Hake, Sandra B., Benjamin A. Garcia, Monika Kauer, Stephen P. Baker, Jeffrey Shabanowitz, Donald F. Hunt, and C. David Allis. 2005. “Serine 31 Phosphorylation of Histone Variant H3.3 Is Specific to Regions Bordering Centromeres in Metaphase Chromosomes.” *Proceedings of the National Academy of Sciences of the United States of America* 102 (18): 6344–49. https://doi.org/10.1073/pnas.0502413102.

Hall, Richard S., Alexander A. Fedorov, Chengfu Xu, Elena V. Fedorov, Steven C. Almo, and Frank M. Raushel. 2011. “The Three-Dimensional Structure and Catalytic Mechanism of Cytosine Deaminase.” *Biochemistry* 50 (22): 5077–85. https://doi.org/10.1021/bi200483k.

Hallows, William C., Susan Lee, and John M. Denu. 2006. “Sirtuins Deacetylate and Activate Mammalian Acetyl-CoA Synthetases.” *Proceedings of the National Academy of Sciences* 103 (27): 10230–35. https://doi.org/10.1073/pnas.0604392103.

Hamiche, A., J. G. Kang, C. Dennis, H. Xiao, and C. Wu. 2001. “Histone Tails Modulate Nucleosome Mobility and Regulate ATP-Dependent Nucleosome Sliding by NURF.” *Proceedings of the National Academy of Sciences of the United States of America* 98 (25): 14316–21. https://doi.org/10.1073/pnas.251421398.

Han, Zhen, Hong Wu, Sunjoo Kim, Xiangkun Yang, Qianjin Li, He Huang, Houjian Cai, et al. 2018. “Revealing the Protein Propionylation Activity of the Histone Acetyltransferase MOF (Males Absent on the First).” *Journal of Biological Chemistry* 293 (9): 3410–20. https://doi.org/10.1074/jbc.RA117.000529.

Hanson, R. D., J. L. Hess, B. D. Yu, P. Ernst, M. van Lohuizen, A. Berns, N. M. van der Lugt, et al. 1999. “Mammalian Trithorax and Polycomb-Group Homologues Are Antagonistic Regulators of Homeotic Development.” *Proceedings of the National Academy of Sciences of the United States of America* 96 (25): 14372–77. https://doi.org/10.1073/pnas.96.25.14372.

Hargreaves, Diana C., and Gerald R. Crabtree. 2011. “ATP-Dependent Chromatin Remodeling: Genetics, Genomics and Mechanisms.” *Cell Research* 21 (3): 396–420. https://doi.org/10.1038/cr.2011.32.

He, Quanyuan, Hyeung Kim, Rui Huang, Weisi Lu, Mengfan Tang, Fengtao Shi, Dong Yang, et al. 2015. “The Daxx/Atrx Complex Protects Tandem Repetitive Elements during DNA Hypomethylation by Promoting H3K9 Trimethylation.” *Cell Stem Cell* 17 (3): 273–86. https://doi.org/10.1016/j.stem.2015.07.022.

He, Yu-Fei, Bin-Zhong Li, Zheng Li, Peng Liu, Yang Wang, Qingyu Tang, Jianping Ding, et al. 2011. “Tet-Mediated Formation of 5-Carboxylcytosine and Its Excision by TDG in Mammalian DNA.” *Science* 333 (6047): 1303–7. https://doi.org/10.1126/science.1210944.

Heaphy, Christopher M., Roeland F. de Wilde, Yuchen Jiao, Alison P. Klein, Barish H. Edil, Chanjuan Shi, Chetan Bettegowda, et al. 2011. “Altered Telomeres in Tumors with ATRX and DAXX Mutations.” *Science* 333 (6041): 425–425. https://doi.org/10.1126/science.1207313.

Heimburg, Tino, Alokta Chakrabarti, Julien Lancelot, Martin Marek, Jelena Melesina, Alexander-Thomas Hauser, Tajith B. Shaik, et al. 2016. “Structure-Based Design and Synthesis of Novel Inhibitors Targeting HDAC8 from Schistosoma Mansoni for the Treatment of Schistosomiasis.” *Journal of Medicinal Chemistry* 59 (6): 2423–35. https://doi.org/10.1021/acs.jmedchem.5b01478.

Heintzman, Nathaniel D., Gary C. Hon, R. David Hawkins, Pouya Kheradpour, Alexander Stark, Lindsey F. Harp, Zhen Ye, et al. 2009. “Histone Modifications at Human Enhancers Reflect Global Cell-Type-Specific Gene Expression.” *Nature* 459 (7243): 108–12. https://doi.org/10.1038/nature07829.

Heintzman, Nathaniel D., Rhona K. Stuart, Gary Hon, Yutao Fu, Christina W. Ching, R. David Hawkins, Leah O. Barrera, et al. 2007. “Distinct and Predictive Chromatin Signatures of Transcriptional Promoters and Enhancers in the Human Genome.” *Nature Genetics* 39 (3): 311–18. https://doi.org/10.1038/ng1966.

Heissenberger, Clemens, Lisa Liendl, Fabian Nagelreiter, Yulia Gonskikh, Guohuan Yang, Elena M Stelzer, Teresa L Krammer, et al. 2019. “Loss of the Ribosomal RNA Methyltransferase NSUN5 Impairs Global Protein Synthesis and Normal Growth.” *Nucleic Acids Research* 47 (22): 11807–25. https://doi.org/10.1093/nar/gkz1043.

Helm, M, H Brulé, F Degoul, C Cepanec, J P Leroux, R Giegé, and C Florentz. 1998. “The Presence of Modified Nucleotides Is Required for Cloverleaf Folding of a Human Mitochondrial TRNA.” *Nucleic Acids Research* 26 (7): 1636–43.

Helm, M., R. Giegé, and C. Florentz. 1999. “A Watson-Crick Base-Pair-Disrupting Methyl Group (M1A9) Is Sufficient for Cloverleaf Folding of Human Mitochondrial TRNALys.” *Biochemistry* 38 (40): 13338–46. https://doi.org/10.1021/bi991061g.

Herbert, Alan. 2019. “ADAR and Immune Silencing in Cancer.” *Trends in Cancer* 5 (5): 272–82. https://doi.org/10.1016/j.trecan.2019.03.004.

Hess, Martin E., Simon Hess, Kate D. Meyer, Linda A. W. Verhagen, Linda Koch, Hella S. Brönneke, Marcelo O. Dietrich, et al. 2013. “The Fat Mass and Obesity Associated Gene (Fto) Regulates Activity of the Dopaminergic Midbrain Circuitry.” *Nature Neuroscience* 16 (8): 1042–48. https://doi.org/10.1038/nn.3449.

Heyn, Patricia, Clare V. Logan, Adeline Fluteau, Rachel C. Challis, Tatsiana Auchynnikava, Carol-Anne Martin, Joseph A. Marsh, et al. 2019. “Gain-of-Function DNMT3A Mutations Cause Microcephalic Dwarfism and Hypermethylation of Polycomb-Regulated Regions.” *Nature Genetics* 51 (1): 96–105. https://doi.org/10.1038/s41588-018-0274-x.

Higuchi, M., F. N. Single, M. Köhler, B. Sommer, R. Sprengel, and P. H. Seeburg. 1993. “RNA Editing of AMPA Receptor Subunit GluR-B: A Base-Paired Intron-Exon Structure Determines Position and Efficiency.” *Cell* 75 (7): 1361–70. https://doi.org/10.1016/0092-8674(93)90622-w.

Hiraide, Takuya, Mitsuko Nakashima, Kaori Yamoto, Tokiko Fukuda, Mitsuhiro Kato, Hiroko Ikeda, Yoko Sugie, et al. 2018. “De Novo Variants in SETD1B Are Associated with Intellectual Disability, Epilepsy and Autism.” *Human Genetics* 137 (1): 95–104. https://doi.org/10.1007/s00439-017-1863-y.

Hnisz, Denes, Brian J. Abraham, Tong Ihn Lee, Ashley Lau, Violaine Saint-André, Alla A. Sigova, Heather A. Hoke, and Richard A. Young. 2013. “Super-Enhancers in the Control of Cell Identity and Disease.” *Cell* 155 (4): 934–47. https://doi.org/10.1016/j.cell.2013.09.053.

Hoelper, Dominik, Hongda Huang, Aayushi Y. Jain, Dinshaw J. Patel, and Peter W. Lewis. 2017. “Structural and Mechanistic Insights into ATRX-Dependent and -Independent Functions of the Histone Chaperone DAXX.” *Nature Communications* 8 (1): 1193. https://doi.org/10.1038/s41467-017-01206-y.

Holdt, Lesca M., Steve Hoffmann, Kristina Sass, David Langenberger, Markus Scholz, Knut Krohn, Knut Finstermeier, et al. 2013. “Alu Elements in ANRIL Non-Coding RNA at Chromosome 9p21 Modulate Atherogenic Cell Functions through Trans-Regulation of Gene Networks.” *PLoS Genetics* 9 (7): e1003588. https://doi.org/10.1371/journal.pgen.1003588.

Hopkins, Benjamin D., Cindy Hodakoski, Douglas Barrows, Sarah M. Mense, and Ramon E. Parsons. 2014. “PTEN Function: The Long and the Short of It.” *Trends in Biochemical Sciences* 39 (4): 183–90. https://doi.org/10.1016/j.tibs.2014.02.006.

Hori, Hiroyuki. 2014. “Methylated Nucleosides in TRNA and TRNA Methyltransferases.” *Frontiers in Genetics* 5. https://doi.org/10.3389/fgene.2014.00144.

Hou, Fajian, and Hui Zou. 2005. “Two Human Orthologues of Eco1/Ctf7 Acetyltransferases Are Both Required for Proper Sister-Chromatid Cohesion.” *Molecular Biology of the Cell* 16 (8): 3908–18. https://doi.org/10.1091/mbc.e04-12-1063.

Houtkooper, Riekelt H., Eija Pirinen, and Johan Auwerx. 2012. “Sirtuins as Regulators of Metabolism and Healthspan.” *Nature Reviews Molecular Cell Biology* 13 (4): 225–38. https://doi.org/10.1038/nrm3293.

Howell, Carina Y., Timothy H. Bestor, Feng Ding, Keith E. Latham, Carmen Mertineit, Jacquetta M. Trasler, and J. Richard Chaillet. 2001. “Genomic Imprinting Disrupted by a Maternal Effect Mutation in the Dnmt1 Gene.” *Cell* 104 (6): 829–38. https://doi.org/10.1016/S0092-8674(01)00280-X.

Hsu, Chih-Chao, Jiejun Shi, Chao Yuan, Dan Zhao, Shiming Jiang, Jie Lyu, Xiaolu Wang, et al. 2018. “Recognition of Histone Acetylation by the GAS41 YEATS Domain Promotes H2A.Z Deposition in Non-Small Cell Lung Cancer.” *Genes & Development* 32 (1): 58–69. https://doi.org/10.1101/gad.303784.117.

Hu, Baohong, Qianli Wang, Yueju Wang, Jian Chen, Peng Li, and Mingyong Han. 2017. “Holliday Junction-Recognizing Protein Promotes Cell Proliferation and Correlates with Unfavorable Clinical Outcome of Hepatocellular Carcinoma.” *OncoTargets and Therapy* 10: 2601–7. https://doi.org/10.2147/OTT.S127738.

Hu, Deqing, Xin Gao, Marc A. Morgan, Hans-Martin Herz, Edwin R. Smith, and Ali Shilatifard. 2013. “The MLL3/MLL4 Branches of the COMPASS Family Function as Major Histone H3K4 Monomethylases at Enhancers.” *Molecular and Cellular Biology* 33 (23): 4745–54. https://doi.org/10.1128/MCB.01181-13.

Hu, Deqing, Alexander S. Garruss, Xin Gao, Marc A. Morgan, Malcolm Cook, Edwin R. Smith, and Ali Shilatifard. 2013. “The Mll2 Branch of the COMPASS Family Regulates Bivalent Promoters in Mouse Embryonic Stem Cells.” *Nature Structural & Molecular Biology* 20 (9): 1093–97. https://doi.org/10.1038/nsmb.2653.

Hu, Erding, Zunxuan Chen, Todd Fredrickson, Yuan Zhu, Robert Kirkpatrick, Gui-Feng Zhang, Kyung Johanson, Chiu-Mei Sung, Ronggang Liu, and James Winkler. 2000. “Cloning and Characterization of a Novel Human Class I Histone Deacetylase That Functions as a Transcription Repressor*.” *Journal of Biological Chemistry* 275 (20): 15254–64. https://doi.org/10.1074/jbc.M908988199.

Hu, Gangqing, Kairong Cui, Daniel Northrup, Chengyu Liu, Chaochen Wang, Qingsong Tang, Kai Ge, David Levens, Colyn Crane-Robinson, and Keji Zhao. 2013. “H2A.Z Facilitates Access of Active and Repressive Complexes to Chromatin in Embryonic Stem Cell Self-Renewal and Differentiation.” *Cell Stem Cell* 12 (2): 180–92. https://doi.org/10.1016/j.stem.2012.11.003.

Hu, Hao, Yang Liu, Mingzhu Wang, Junnan Fang, Hongda Huang, Na Yang, Yanbo Li, et al. 2011. “Structure of a CENP-A-Histone H4 Heterodimer in Complex with Chaperone HJURP.” *Genes & Development* 25 (9): 901–6. https://doi.org/10.1101/gad.2045111.

Hu, Shaohui, Jun Wan, Yijing Su, Qifeng Song, Yaxue Zeng, Ha Nam Nguyen, Jaehoon Shin, et al. 2013. “DNA Methylation Presents Distinct Binding Sites for Human Transcription Factors.” *ELife* 2 (September): e00726. https://doi.org/10.7554/eLife.00726.

Hua, Sujun, Caleb B. Kallen, Ruby Dhar, Maria T. Baquero, Christopher E. Mason, Beth A. Russell, Parantu K. Shah, et al. 2008. “Genomic Analysis of Estrogen Cascade Reveals Histone Variant H2A.Z Associated with Breast Cancer Progression.” *Molecular Systems Biology* 4: 188. https://doi.org/10.1038/msb.2008.25.

Huang, Hua, Bao Zhen Tan, Yiru Shen, Jin Tao, Fengli Jiang, Ying Ying Sung, Choon Keow Ng, et al. 2012. “RNA Editing of the IQ Domain in Cav1.3 Channels Modulates Their Ca2+-Dependent Inactivation.” *Neuron* 73 (2): 304–16. https://doi.org/10.1016/j.neuron.2011.11.022.

Huang, Huilin, Hengyou Weng, and Jianjun Chen. 2020. “M6A Modification in Coding and Non-Coding RNAs: Roles and Therapeutic Implications in Cancer.” *Cancer Cell* 37 (3): 270–88. https://doi.org/10.1016/j.ccell.2020.02.004.

Huang, Rui, Yinfeng Xu, Wei Wan, Xin Shou, Jiali Qian, Zhiyuan You, Bo Liu, et al. 2015. "Deacetylation of Nuclear LC3 Drives Autophagy Initiation under Starvation." *Molecular Cell* 57 (3): 456–66. https://doi.org/10.1016/j.molcel.2014.12.013.

Huarte, Maite, Mitchell Guttman, David Feldser, Manuel Garber, Magdalena J. Koziol, Daniela Kenzelmann-Broz, Ahmad M. Khalil, et al. 2010. "A Large Intergenic Noncoding RNA Induced by P53 Mediates Global Gene Repression in the P53 Response." *Cell* 142 (3): 409–19. https://doi.org/10.1016/j.cell.2010.06.040.

Hubbert, Charlotte, Amaris Guardiola, Rong Shao, Yoshiharu Kawaguchi, Akihiro Ito, Andrew Nixon, Minoru Yoshida, Xiao-Fan Wang, and Tso-Pang Yao. 2002. "HDAC6 Is a Microtubule-Associated Deacetylase." *Nature* 417 (6887): 455–58. https://doi.org/10.1038/417455a.

Hung, Tiffany, Yulei Wang, Michael F. Lin, Ashley K. Koegel, Yojiro Kotake, Gavin D. Grant, Hugo M. Horlings, et al. 2011. "Extensive and Coordinated Transcription of Noncoding RNAs within Cell-Cycle Promoters." *Nature Genetics* 43 (7): 621–29. https://doi.org/10.1038/ng.848.

Huntly, Brian J. P., Hirokazu Shigematsu, Kenji Deguchi, Benjamin H. Lee, Shinichi Mizuno, Nicky Duclos, Rebecca Rowan, et al. 2004. "MOZ-TIF2, but Not BCR-ABL, Confers Properties of Leukemic Stem Cells to Committed Murine Hematopoietic Progenitors." *Cancer Cell* 6 (6): 587–96. https://doi.org/10.1016/j.ccr.2004.10.015.

Hussain, Shobbir, Abdulrahim A. Sajini, Sandra Blanco, Sabine Dietmann, Patrick Lombard, Yoichiro Sugimoto, Maike Paramor, et al. 2013. "NSun2-Mediated Cytosine-5 Methylation of Vault Noncoding RNA Determines Its Processing into Regulatory Small RNAs." *Cell Reports* 4 (2): 255–61. https://doi.org/10.1016/j.celrep.2013.06.029.

Iizasa, Hisashi, Bjorn-Erik Wulff, Nageswara R. Alla, Manolis Maragkakis, Molly Megraw, Artemis Hatzigeorgiou, Dai Iwakiri, et al. 2010. "Editing of Epstein-Barr Virus-Encoded BART6 MicroRNAs Controls Their Dicer Targeting and Consequently Affects Viral Latency*,." *Journal of Biological Chemistry* 285 (43): 33358–70. https://doi.org/10.1074/jbc.M110.138362.

Iqbal, Khursheed, Seung-Gi Jin, Gerd P. Pfeifer, and Piroska E. Szabó. 2011. "Reprogramming of the Paternal Genome upon Fertilization Involves Genome-Wide Oxidation of 5-Methylcytosine." *Proceedings of the National Academy of Sciences of the United States of America* 108 (9): 3642–47. https://doi.org/10.1073/pnas.1014033108.

Ishiyama, Satoshi, Atsuya Nishiyama, Yasushi Saeki, Kei Moritsugu, Daichi Morimoto, Luna Yamaguchi, Naoko Arai, et al. 2017. "Structure of the Dnmt1 Reader Module Complexed with a Unique Two-Mono-Ubiquitin Mark on Histone H3 Reveals the Basis for DNA Methylation Maintenance." *Molecular Cell* 68 (2): 350-360.e7. https://doi.org/10.1016/j.molcel.2017.09.037.

Ito, Akihiro, Tadahiro Shimazu, Satoko Maeda, Asad Ali Shah, Tatsuhiko Tsunoda, Shun-ichiro Iemura, Toru Natsume, et al. 2015. "The Subcellular Localization and Activity of Cortactin Is Regulated by Acetylation and Interaction with Keap1." *Science Signaling* 8 (404): ra120–ra120. https://doi.org/10.1126/scisignal.aad0667.

Ito, Shinsuke, Li Shen, Qing Dai, Susan C. Wu, Leonard B. Collins, James A. Swenberg, Chuan He, and Yi Zhang. 2011. "Tet Proteins Can Convert 5-Methylcytosine to 5-Formylcytosine and 5-Carboxylcytosine." *Science* 333 (6047): 1300–1303. https://doi.org/10.1126/science.1210597.

Ito, Takashi, Michael Bulger, Michael J Pazin, Ryuji Kobayashi, and James T Kadonaga. 1997. “ACF, an ISWI-Containing and ATP-Utilizing Chromatin Assembly and Remodeling Factor.” *Cell* 90 (1): 145–55. https://doi.org/10.1016/S0092-8674(00)80321-9.

Iwafuchi-Doi, Makiko, Greg Donahue, Akshay Kakumanu, Jason A. Watts, Shaun Mahony, B. Franklin Pugh, Dolim Lee, Klaus H. Kaestner, and Kenneth S. Zaret. 2016. “The Pioneer Transcription Factor FoxA Maintains an Accessible Nucleosome Configuration at Enhancers for Tissue-Specific Gene Activation.” *Molecular Cell* 62 (1): 79–91. https://doi.org/10.1016/j.molcel.2016.03.001.

Jain, Abhinav K., Yuanxin Xi, Ryan McCarthy, Kendra Allton, Kadir C. Akdemir, Lalit R. Patel, Bruce Aronow, et al. 2016. “LncPRESS1 Is a P53-Regulated LncRNA That Safeguards Pluripotency by Disrupting SIRT6-Mediated De-Acetylation of Histone H3K56.” *Molecular Cell* 64 (5): 967–81. https://doi.org/10.1016/j.molcel.2016.10.039.

Janin, Maxime, Vanessa Ortiz-Barahona, Manuel Castro de Moura, Anna Martínez-Cardús, Pere Llinàs-Arias, Marta Soler, Daphna Nachmani, et al. 2019. “Epigenetic Loss of RNA-Methyltransferase NSUN5 in Glioma Targets Ribosomes to Drive a Stress Adaptive Translational Program.” *Acta Neuropathologica* 138 (6): 1053–74. https://doi.org/10.1007/s00401-019-02062-4.

Jia, Guifang, Ye Fu, Xu Zhao, Qing Dai, Guanqun Zheng, Ying Yang, Chengqi Yi, et al. 2011. “N 6-Methyladenosine in Nuclear RNA Is a Major Substrate of the Obesity-Associated FTO.” *Nature Chemical Biology* 7 (12): 885–87. https://doi.org/10.1038/nchembio.687.

Jiang, Hong, Saba Khan, Yi Wang, Guillaume Charron, Bin He, Carlos Sebastian, Jintang Du, et al. 2013. “SIRT6 Regulates TNF-α Secretion through Hydrolysis of Long-Chain Fatty Acyl Lysine.” *Nature* 496 (7443): 110–13. https://doi.org/10.1038/nature12038.

Jiao, Wanju, Yajun Chen, Huajie Song, Dan Li, Hong Mei, Feng Yang, Erhu Fang, et al. 2018. “HPSE Enhancer RNA Promotes Cancer Progression through Driving Chromatin Looping and Regulating HnRNPU/P300/EGR1/HPSE Axis.” *Oncogene* 37 (20): 2728–45. https://doi.org/10.1038/s41388-018-0128-0.

Jiao, Yuchen, Chanjuan Shi, Barish H. Edil, Roeland F. de Wilde, David S. Klimstra, Anirban Maitra, Richard D. Schulick, et al. 2011. “DAXX/ATRX, MEN1, and MTOR Pathway Genes Are Frequently Altered in Pancreatic Neuroendocrine Tumors.” *Science* 331 (6021): 1199–1203. https://doi.org/10.1126/science.1200609.

Jin, Chunyuan, and Gary Felsenfeld. 2007. “Nucleosome Stability Mediated by Histone Variants H3.3 and H2A.Z.” *Genes & Development* 21 (12): 1519–29. https://doi.org/10.1101/gad.1547707.

Jin, Chunyuan, Chongzhi Zang, Gang Wei, Kairong Cui, Weiqun Peng, Keji Zhao, and Gary Felsenfeld. 2009. “H3.3/H2A.Z Double Variant–Containing Nucleosomes Mark ‘nucleosome-Free Regions’ of Active Promoters and Other Regulatory Regions.” *Nature Genetics* 41 (8): 941–45. https://doi.org/10.1038/ng.409.

Jonkhout, Nicky, Julia Tran, Martin A. Smith, Nicole Schonrock, John S. Mattick, and Eva Maria Novoa. 2017. “The RNA Modification Landscape in Human Disease.” *RNA (New York, N.Y.)* 23 (12): 1754–69. https://doi.org/10.1261/rna.063503.117.

Kagey, Michael H., Jamie J. Newman, Steve Bilodeau, Ye Zhan, David A. Orlando, Nynke L. van Berkum, Christopher C. Ebmeier, et al. 2010. “Mediator and Cohesin Connect Gene Expression and Chromatin Architecture.” *Nature* 467 (7314): 430–35. https://doi.org/10.1038/nature09380.

Kannan, Srinivasaraghavan, Jelena Melesina, Alexander-Thomas Hauser, Alokta Chakrabarti, Tino Heimburg, Karin Schmidtkunz, Alexandra Walter, et al. 2014. “Discovery of Inhibitors of Schistosoma Mansoni HDAC8 by Combining Homology Modeling, Virtual Screening, and in Vitro Validation.” *Journal of Chemical Information and Modeling* 54 (10): 3005–19. https://doi.org/10.1021/ci5004653.

Karras, Georgios I., Georg Kustatscher, Heeran R. Buhecha, Mark D. Allen, Céline Pugieux, Fiona Sait, Mark Bycroft, and Andreas G. Ladurner. 2005. “The Macro Domain Is an ADP-Ribose Binding Module.” *The EMBO Journal* 24 (11): 1911–20. https://doi.org/10.1038/sj.emboj.7600664.

Kato, Tatsuya, Nagato Sato, Satoshi Hayama, Takumi Yamabuki, Tomoo Ito, Masaki Miyamoto, Satoshi Kondo, Yusuke Nakamura, and Yataro Daigo. 2007. “Activation of Holliday Junction–Recognizing Protein Involved in the Chromosomal Stability and Immortality of Cancer Cells.” *Cancer Research* 67 (18): 8544–53. https://doi.org/10.1158/0008-5472.CAN-07-1307.

Kawaguchi, Yoshiharu, Jeffrey J Kovacs, Adam McLaurin, Jeffery M Vance, Akihiro Ito, and Tso-Pang Yao. 2003. “The Deacetylase HDAC6 Regulates Aggresome Formation and Cell Viability in Response to Misfolded Protein Stress.” *Cell* 115 (6): 727–38. https://doi.org/10.1016/S0092-8674(03)00939-5.

Kawahara, Yukio, Molly Megraw, Edward Kreider, Hisashi Iizasa, Louis Valente, Artemis G. Hatzigeorgiou, and Kazuko Nishikura. 2008. “Frequency and Fate of MicroRNA Editing in Human Brain.” *Nucleic Acids Research* 36 (16): 5270–80. https://doi.org/10.1093/nar/gkn479.

Kawahara, Yukio, Boris Zinshteyn, Thimmaiah P Chendrimada, Ramin Shiekhattar, and Kazuko Nishikura. 2007. “RNA Editing of the MicroRNA-151 Precursor Blocks Cleavage by the Dicer–TRBP Complex.” *EMBO Reports* 8 (8): 763–69. https://doi.org/10.1038/sj.embor.7401011.

Kawahara, Yukio, Boris Zinshteyn, Praveen Sethupathy, Hisashi Iizasa, Artemis G. Hatzigeorgiou, and Kazuko Nishikura. 2007. “Redirection of Silencing Targets by Adenosine-to-Inosine Editing of MiRNAs.” *Science* 315 (5815): 1137–40. https://doi.org/10.1126/science.1138050.

Kawai, G., H. Ue, M. Yasuda, K. Sakamoto, T. Hashizume, J. A. McCloskey, T. Miyazawa, and S. Yokoyama. 1991. “Relation between Functions and Conformational Characteristics of Modified Nucleosides Found in TRNAs.” *Nucleic Acids Symposium Series*, no. 25: 49–50.

Kawai, G., Y. Yamamoto, T. Kamimura, T. Masegi, M. Sekine, T. Hata, T. Iimori, T. Watanabe, T. Miyazawa, and S. Yokoyama. 1992. “Conformational Rigidity of Specific Pyrimidine Residues in TRNA Arises from Posttranscriptional Modifications That Enhance Steric Interaction between the Base and the 2’-Hydroxyl Group.” *Biochemistry* 31 (4): 1040–46. https://doi.org/10.1021/bi00119a012.

Kemper, Jongsook Kim, Zhen Xiao, Bhaskar Ponugoti, Ji Miao, Sungsoon Fang, Deepthi Kanamaluru, Stephanie Tsang, Shwu-Yuan Wu, Cheng-Ming Chiang, and Timothy D. Veenstra. 2009. “FXR Acetylation Is Normally Dynamically Regulated by P300 and SIRT1 but Constitutively Elevated in Metabolic Disease States.” *Cell Metabolism* 10 (5): 392–404. https://doi.org/10.1016/j.cmet.2009.09.009.

Khan, Muzammil Ahmad, Muhammad Arshad Rafiq, Abdul Noor, Shobbir Hussain, Joana V. Flores, Verena Rupp, Akshita K. Vincent, et al. 2012. “Mutation in NSUN2, Which Encodes an RNA Methyltransferase, Causes Autosomal-Recessive Intellectual Disability.” *American Journal of Human Genetics* 90 (5): 856–63. https://doi.org/10.1016/j.ajhg.2012.03.023.

Khermesh, Khen, Anna Maria D'Erchia, Michal Barak, Anita Annese, Chaim Wachtel, Erez Y. Levanon, Ernesto Picardi, and Eli Eisenberg. 2016. "Reduced Levels of Protein Recoding by A-to-I RNA Editing in Alzheimer's Disease." *RNA* 22 (2): 290–302. https://doi.org/10.1261/rna.054627.115.

Khoddami, Vahid, and Bradley R. Cairns. 2013. "Identification of Direct Targets and Modified Bases of RNA Cytosine Methyltransferases." *Nature Biotechnology* 31 (5): 458–64. https://doi.org/10.1038/nbt.2566.

Kierzek, Elzbieta, Magdalena Malgowska, Jolanta Lisowiec, Douglas H. Turner, Zofia Gdaniec, and Ryszard Kierzek. 2014. "The Contribution of Pseudouridine to Stabilities and Structure of RNAs." *Nucleic Acids Research* 42 (5): 3492–3501. https://doi.org/10.1093/nar/gkt1330.

Kim, Jungwook, Vladimir Malashkevich, Setu Roday, Michael Lisbin, Vern L. Schramm, and Steven C. Almo. 2006. "Structural and Kinetic Characterization of Escherichia Coli TadA, the Wobble-Specific TRNA Deaminase." *Biochemistry* 45 (20): 6407–16. https://doi.org/10.1021/bi0522394.

Kim, S. H., F. L. Suddath, G. J. Quigley, A. McPherson, J. L. Sussman, A. H. J. Wang, N. C. Seeman, and Alexander Rich. 1974. "Three-Dimensional Tertiary Structure of Yeast Phenylalanine Transfer RNA." *Science* 185 (4149): 435–40. https://doi.org/10.1126/science.185.4149.435.

King, Thomas H., Ben Liu, Ryan R. McCully, and Maurille J. Fournier. 2003. "Ribosome Structure and Activity Are Altered in Cells Lacking SnoRNPs That Form Pseudouridines in the Peptidyl Transferase Center." *Molecular Cell* 11 (2): 425–35. https://doi.org/10.1016/S1097-2765(03)00040-6.

Kinoshita, T., N. Nishio, I. Nakanishi, A. Sato, and T. Fujii. 2003. "Structure of Bovine Adenosine Deaminase Complexed with 6-Hydroxy-1,6-Dihydropurine Riboside." *Acta Crystallographica Section D: Biological Crystallography* 59 (2): 299–303. https://doi.org/10.1107/S090744490202190X.

Kirchner, Sebastian, and Zoya Ignatova. 2014. "Emerging Roles of TRNA in Adaptive Translation, Signalling Dynamics and Disease." *Nature Reviews Genetics* 16: 98. https://doi.org/10.1038/nrg3861.

Kirwan, M., and I. Dokal. 2008. "Dyskeratosis Congenita: A Genetic Disorder of Many Faces." *Clinical Genetics* 73 (2): 103–12. https://doi.org/10.1111/j.1399-0004.2007.00923.x.

Kleefstra, Tjitske, Jamie M. Kramer, Kornelia Neveling, Marjolein H. Willemsen, Tom S. Koemans, Lisenka E. L. M. Vissers, Willemijn Wissink-Lindhout, et al. 2012. "Disruption of an EHMT1-Associated Chromatin-Modification Module Causes Intellectual Disability." *The American Journal of Human Genetics* 91 (1): 73–82. https://doi.org/10.1016/j.ajhg.2012.05.003.

Klein, Christopher J., Maria-Victoria Botuyan, Yanhong Wu, Christopher J. Ward, Garth A. Nicholson, Simon Hammans, Kaori Hojo, et al. 2011. "Mutations in DNMT1 Cause Hereditary Sensory Neuropathy with Dementia and Hearing Loss." *Nature Genetics* 43 (6): 595–600. https://doi.org/10.1038/ng.830.

Klose, Robert J., Kenichi Yamane, Yangjin Bae, Dianzheng Zhang, Hediye Erdjument-Bromage, Paul Tempst, Jiemin Wong, and Yi Zhang. 2006. "The Transcriptional Repressor JHDM3A Demethylates Trimethyl Histone H3 Lysine 9 and Lysine 36." *Nature* 442 (7100): 312–16. https://doi.org/10.1038/nature04853.

Ko, Myunggon, Yun Huang, Anna M. Jankowska, Utz J. Pape, Mamta Tahiliani, Hozefa S. Bandukwala, Jungeun An, et al. 2010. "Impaired Hydroxylation of 5-Methylcytosine in Myeloid Cancers with Mutant TET2." *Nature* 468 (7325): 839–43. https://doi.org/10.1038/nature09586.

Ko, Tzu-Ping, Jing-Jer Lin, Chih-Yung Hu, Yi-Hsin Hsu, Andrew H.-J. Wang, and Shwu-Huey Liaw. 2003. "Crystal Structure of Yeast Cytosine Deaminase. Insights into Enzyme Mechanism and Evolution." *The Journal of Biological Chemistry* 278 (21): 19111–17. https://doi.org/10.1074/jbc.M300874200.

Kobayashi, Hisato, Takayuki Sakurai, Misaki Imai, Nozomi Takahashi, Atsushi Fukuda, Obata Yayoi, Shun Sato, et al. 2012. "Contribution of Intragenic DNA Methylation in Mouse Gametic DNA Methylomes to Establish Oocyte-Specific Heritable Marks." *PLoS Genetics* 8 (1): e1002440. https://doi.org/10.1371/journal.pgen.1002440.

Kondo, Yutaka, and Jean-Pierre J. Issa. 2003. "Enrichment for Histone H3 Lysine 9 Methylation at Alu Repeats in Human Cells *." *Journal of Biological Chemistry* 278 (30): 27658–62. https://doi.org/10.1074/jbc.M304072200.

Konen, Lyndsey M., Amanda L. Wright, Gordon A. Royle, Gary P. Morris, Benjamin K. Lau, Patrick W. Seow, Raphael Zinn, Luke T. Milham, Christopher W. Vaughan, and Bryce Vissel. 2020. "A New Mouse Line with Reduced GluA2 Q/R Site RNA Editing Exhibits Loss of Dendritic Spines, Hippocampal CA1-Neuron Loss, Learning and Memory Impairments and NMDA Receptor-Independent Seizure Vulnerability." *Molecular Brain* 13 (1): 27. https://doi.org/10.1186/s13041-020-0545-1.

Kouzarides, Tony. 2007. "Chromatin Modifications and Their Function." *Cell* 128 (4): 693–705. https://doi.org/10.1016/j.cell.2007.02.005.

Kozlowski, Marek, David Corujo, Michael Hothorn, Iva Guberovic, Imke K. Mandemaker, Charlotte Blessing, Judith Sporn, et al. 2018. "MacroH2A Histone Variants Limit Chromatin Plasticity through Two Distinct Mechanisms." *EMBO Reports* 19 (10): e44445. https://doi.org/10.15252/embr.201744445.

Kretschmer, Jens, Harita Rao, Philipp Hackert, Katherine E. Sloan, Claudia Höbartner, and Markus T. Bohnsack. 2018. "The M6A Reader Protein YTHDC2 Interacts with the Small Ribosomal Subunit and the 5'-3' Exoribonuclease XRN1." *RNA (New York, N.Y.)* 24 (10): 1339–50. https://doi.org/10.1261/rna.064238.117.

Kriaucionis, Skirmantas, and Nathaniel Heintz. 2009. "The Nuclear DNA Base 5-Hydroxymethylcytosine Is Present in Purkinje Neurons and the Brain." *Science* 324 (5929): 929–30. https://doi.org/10.1126/science.1169786.

Krogan, Nevan J., Jim Dover, Shahram Khorrami, Jack F. Greenblatt, Jessica Schneider, Mark Johnston, and Ali Shilatifard. 2002. "COMPASS, a Histone H3 (Lysine 4) Methyltransferase Required for Telomeric Silencing of Gene Expression*." *Journal of Biological Chemistry* 277 (13): 10753–55. https://doi.org/10.1074/jbc.C200023200.

Krogan, Nevan J., Minkyu Kim, Amy Tong, Ashkan Golshani, Gerard Cagney, Veronica Canadien, Dawn P. Richards, et al. 2003. "Methylation of Histone H3 by Set2 in Saccharomyces Cerevisiae Is Linked to Transcriptional Elongation by RNA Polymerase II." *Molecular and Cellular Biology* 23 (12): 4207–18. https://doi.org/10.1128/MCB.23.12.4207-4218.2003.

Ku, Manching, Jacob D. Jaffe, Richard P. Koche, Esther Rheinbay, Mitsuhiro Endoh, Haruhiko Koseki, Steven A. Carr, and Bradley E. Bernstein. 2012. "H2A.Z Landscapes and Dual Modifications in Pluripotent and Multipotent Stem Cells Underlie Complex Genome Regulatory Functions." *Genome Biology* 13 (10): R85. https://doi.org/10.1186/gb-2012-13-10-r85.

Kueh, Andrew J., Mathew P. Dixon, Anne K. Voss, and Tim Thomas. 2011. "HBO1 Is Required for H3K14 Acetylation and Normal Transcriptional Activity during Embryonic Development." *Molecular and Cellular Biology* 31 (4): 845–60. https://doi.org/10.1128/MCB.00159-10.

Kuratani, Mitsuo, Ryohei Ishii, Yoshitaka Bessho, Ryuya Fukunaga, Toru Sengoku, Mikako Shirouzu, Shun-ichi Sekine, and Shigeyuki Yokoyama. 2005. "Crystal Structure of TRNA Adenosine Deaminase (TadA) from Aquifex Aeolicus*." *Journal of Biological Chemistry* 280 (16): 16002–8. https://doi.org/10.1074/jbc.M414541200.

Kustatscher, Georg, Michael Hothorn, Céline Pugieux, Klaus Scheffzek, and Andreas G Ladurner. 2005. "Splicing Regulates NAD Metabolite Binding to Histone MacroH2A." *Nature Structural & Molecular Biology* 12 (7): 624–25. https://doi.org/10.1038/nsmb956.

Laherty, Carol D, Wen-Ming Yang, Jian-Min Sun, James R Davie, Edward Seto, and Robert N Eisenman. 1997. "Histone Deacetylases Associated with the MSin3 Corepressor Mediate Mad Transcriptional Repression." *Cell* 89 (3): 349–56. https://doi.org/10.1016/S0092-8674(00)80215-9.

Lane, Natasha, Wendy Dean, Sylvia Erhardt, Petra Hajkova, Azim Surani, Jörn Walter, and Wolf Reik. 2003. "Resistance of IAPs to Methylation Reprogramming May Provide a Mechanism for Epigenetic Inheritance in the Mouse." *Genesis* 35 (2): 88–93. https://doi.org/10.1002/gene.10168.

Langemeijer, Saskia M C, Roland P Kuiper, Marieke Berends, Ruth Knops, Mariam G Aslanyan, Marion Massop, Ellen Stevens-Linders, et al. 2009. "Acquired Mutations in TET2 Are Common in Myelodysplastic Syndromes." *Nature Genetics* 41 (7): 838–42. https://doi.org/10.1038/ng.391.

Largeot, Anne, Flor Maria Perez-Campo, Elli Marinopoulou, Michael Lie-a-Ling, Valerie Kouskoff, and Georges Lacaud. 2016. "Expression of the MOZ-TIF2 Oncoprotein in Mice Represses Senescence." *Experimental Hematology* 44 (4): 231-237.e4. https://doi.org/10.1016/j.exphem.2015.12.006.

Larsen, F., G. Gundersen, R. Lopez, and H. Prydz. 1992. "CpG Islands as Gene Markers in the Human Genome." *Genomics* 13 (4): 1095–1107. https://doi.org/10.1016/0888-7543(92)90024-m.

Latos, Paulina A., Florian M. Pauler, Martha V. Koerner, H. Başak Şenergin, Quanah J. Hudson, Roman R. Stocsits, Wolfgang Allhoff, et al. 2012. "Airn Transcriptional Overlap, But Not Its LncRNA Products, Induces Imprinted Igf2r Silencing." *Science* 338 (6113): 1469–72. https://doi.org/10.1126/science.1228110.

Lawrence, Michael S., Petar Stojanov, Craig H. Mermel, James T. Robinson, Levi A. Garraway, Todd R. Golub, Matthew Meyerson, Stacey B. Gabriel, Eric S. Lander, and Gad Getz. 2014. "Discovery and Saturation Analysis of Cancer Genes across 21 Tumour Types." *Nature* 505 (7484): 495–501. https://doi.org/10.1038/nature12912.

Laxminarayana, Dama, Islam U Khan, and Gary M Kammer. 2002. "Transcript Mutations of the α Regulatory Subunit of Protein Kinase A and Up-Regulation of the RNA-Editing Gene Transcript in Lupus T Lymphocytes." *The Lancet* 360 (9336): 842–49. https://doi.org/10.1016/S0140-6736(02)09966-X.

Lee, In Hye, Liu Cao, Raul Mostoslavsky, David B. Lombard, Jie Liu, Nicholas E. Bruns, Maria Tsokos, Frederick W. Alt, and Toren Finkel. 2008. "A Role for the NAD-Dependent Deacetylase Sirt1 in the Regulation of Autophagy." *Proceedings of the National Academy of Sciences* 105 (9): 3374–79. https://doi.org/10.1073/pnas.0712145105.

Lee, In Hye, and Toren Finkel. 2009. "Regulation of Autophagy by the P300 Acetyltransferase*." *Journal of Biological Chemistry* 284 (10): 6322–28. https://doi.org/10.1074/jbc.M807135200.

Lee, Jeong-Heon, and David G. Skalnik. 2005. “CpG-Binding Protein (CXXC Finger Protein 1) Is a Component of the Mammalian Set1 Histone H3-Lys4 Methyltransferase Complex, the Analogue of the Yeast Set1/COMPASS Complex*.” *Journal of Biological Chemistry* 280 (50): 41725–31. https://doi.org/10.1074/jbc.M508312200.

Lee, Jeong-Heon, Courtney M. Tate, Jin-Sam You, and David G. Skalnik. 2007. “Identification and Characterization of the Human Set1B Histone H3-Lys4 Methyltransferase Complex*.” *Journal of Biological Chemistry* 282 (18): 13419–28. https://doi.org/10.1074/jbc.M609809200.

Lee, Ji-Eun, Chaochen Wang, Shiliyang Xu, Young-Wook Cho, Lifeng Wang, Xuesong Feng, Anne Baldridge, et al. 2013. “H3K4 Mono- and Di-Methyltransferase MLL4 Is Required for Enhancer Activation during Cell Differentiation.” *ELife* 2 (December): e01503. https://doi.org/10.7554/eLife.01503.

Lee, William, Sewit Teckie, Thomas Wiesner, Leili Ran, Carlos N. Prieto Granada, Mingyan Lin, Sinan Zhu, et al. 2014. “PRC2 Is Recurrently Inactivated through EED or SUZ12 Loss in Malignant Peripheral Nerve Sheath Tumors.” *Nature Genetics* 46 (11): 1227–32. https://doi.org/10.1038/ng.3095.

Leemhuis, Hans, Len C. Packman, Karl P. Nightingale, and Florian Hollfelder. 2008. “The Human Histone Acetyltransferase P/CAF Is a Promiscuous Histone Propionyltransferase.” *ChemBioChem* 9 (4): 499–503. https://doi.org/10.1002/cbic.200700556.

Leeuwen, Fred van, Philip R. Gafken, and Daniel E. Gottschling. 2002. “Dot1p Modulates Silencing in Yeast by Methylation of the Nucleosome Core.” *Cell* 109 (6): 745–56. https://doi.org/10.1016/S0092-8674(02)00759-6.

Lerin, Carles, Joseph T. Rodgers, Dario E. Kalume, Seung-hee Kim, Akhilesh Pandey, and Pere Puigserver. 2006. “GCN5 Acetyltransferase Complex Controls Glucose Metabolism through Transcriptional Repression of PGC-1α.” *Cell Metabolism* 3 (6): 429–38. https://doi.org/10.1016/j.cmet.2006.04.013.

Levanon, Erez Y., Eli Eisenberg, Rodrigo Yelin, Sergey Nemzer, Martina Hallegger, Ronen Shemesh, Zipora Y. Fligelman, et al. 2004. “Systematic Identification of Abundant A-to-I Editing Sites in the Human Transcriptome.” *Nature Biotechnology* 22 (8): 1001–5. https://doi.org/10.1038/nbt996.

Levitt, Michael. 1969. “Detailed Molecular Model for Transfer Ribonucleic Acid.” *Nature* 224 (5221): 759–63. https://doi.org/10.1038/224759a0.

Lev-Maor, Galit, Rotem Sorek, Erez Y. Levanon, Nurit Paz, Eli Eisenberg, and Gil Ast. 2007. “RNA-Editing-Mediated Exon Evolution.” *Genome Biology* 8 (2): R29. https://doi.org/10.1186/gb-2007-8-2-r29.

Lewis, Peter W., Simon J. Elsaesser, Kyung-Min Noh, Sonja C. Stadler, and C. David Allis. 2010. “Daxx Is an H3.3-Specific Histone Chaperone and Cooperates with ATRX in Replication-Independent Chromatin Assembly at Telomeres.” *Proceedings of the National Academy of Sciences of the United States of America* 107 (32): 14075–80. https://doi.org/10.1073/pnas.1008850107.

Lewis, Peter W., Manuel M. Müller, Matthew S. Koletsky, Francisco Cordero, Shu Lin, Laura A. Banaszynski, Benjamin A. Garcia, Tom W. Muir, Oren J. Becher, and C. David Allis. 2013. “Inhibition of PRC2 Activity by a Gain-of-Function H3 Mutation Found in Pediatric Glioblastoma.” *Science* 340 (6134): 857–61. https://doi.org/10.1126/science.1232245.

Li, Haitao, Serge Ilin, Wooikoon Wang, Elizabeth M. Duncan, Joanna Wysocka, C. David Allis, and Dinshaw J. Patel. 2006. “Molecular Basis for Site-Specific Read-out of Histone H3K4me3 by the BPTF PHD Finger of NURF.” *Nature* 442 (7098): 91–95. https://doi.org/10.1038/nature04802.

Li, Haojie, Robert Liefke, Junyi Jiang, Jesse Vigoda Kurland, Wei Tian, Pujuan Deng, Weidi Zhang, et al. 2017. “Polycomb-like Proteins Link the PRC2 Complex to CpG Islands.” *Nature* 549 (7671): 287–91. https://doi.org/10.1038/nature23881.

Li, Huajie, Yi Ren, Keshi Mao, Fei Hua, Yilin Yang, Ning Wei, Chunxian Yue, Dawen Li, and Hao Zhang. 2018. “FTO Is Involved in Alzheimer’s Disease by Targeting TSC1-MTOR-Tau Signaling.” *Biochemical and Biophysical Research Communications* 498 (1): 234–39. https://doi.org/10.1016/j.bbrc.2018.02.201.

Li, Lin, Xiaoli Li, Qin Meng, Abdul Qadir Khan, and Xiaomei Chen. 2018. “Increased Expression of Holliday Junction-Recognizing Protein (HJURP) as an Independent Prognostic Biomarker in Advanced-Stage Serous Ovarian Carcinoma.” *Medical Science Monitor: International Medical Journal of Experimental and Clinical Research* 24 (May): 3050–55. https://doi.org/10.12659/MSM.906647.

Li, Liping, Liqun Zang, Feiran Zhang, Junchen Chen, Hui Shen, Liqi Shu, Feng Liang, et al. 2017. “Fat Mass and Obesity-Associated (FTO) Protein Regulates Adult Neurogenesis.” *Human Molecular Genetics* 26 (13): 2398–2411. https://doi.org/10.1093/hmg/ddx128.

Li, Peng, Junbo Ge, and Hua Li. 2020. “Lysine Acetyltransferases and Lysine Deacetylases as Targets for Cardiovascular Disease.” *Nature Reviews Cardiology* 17 (2): 96–115. https://doi.org/10.1038/s41569-019-0235-9.

Li, Tuo, Benjamin A. Diner, Jin Chen, and Ileana M. Cristea. 2012. “Acetylation Modulates Cellular Distribution and DNA Sensing Ability of Interferon-Inducible Protein IFI16.” *Proceedings of the National Academy of Sciences of the United States of America* 109 (26): 10558–63. https://doi.org/10.1073/pnas.1203447109.

Li, Wenbo, Dimple Notani, Qi Ma, Bogdan Tanasa, Esperanza Nunez, Aaron Yun Chen, Daria Merkurjev, et al. 2013. “Functional Roles of Enhancer RNAs for Oestrogen-Dependent Transcriptional Activation.” *Nature* 498 (7455): 516–20. https://doi.org/10.1038/nature12210.

Li, Xiaoyu, Xushen Xiong, and Chengqi Yi. 2017. “Epitranscriptome Sequencing Technologies: Decoding RNA Modifications.” *Nature Methods* 14 (1): 23–31. https://doi.org/10.1038/nmeth.4110.

Li, Ying, Wei Xu, Michael W. McBurney, and Valter D. Longo. 2008. “SirT1 Inhibition Reduces IGF-I/IRS-2/Ras/ERK1/2 Signaling and Protects Neurons.” *Cell Metabolism* 8 (1): 38–48. https://doi.org/10.1016/j.cmet.2008.05.004.

Li, Yingfeng, Zhuqiang Zhang, Jiayu Chen, Wenqiang Liu, Weiyi Lai, Baodong Liu, Xiang Li, et al. 2018. “Stella Safeguards the Oocyte Methylome by Preventing de Novo Methylation Mediated by DNMT1.” *Nature* 564 (7734): 136–40. https://doi.org/10.1038/s41586-018-0751-5.

Li, Yize, Shuvojit Banerjee, Stephen A Goldstein, Beihua Dong, Christina Gaughan, Sneha Rath, Jesse Donovan, Alexei Korennykh, Robert H Silverman, and Susan R Weiss. 2017. “Ribonuclease L Mediates the Cell-Lethal Phenotype of Double-Stranded RNA Editing Enzyme ADAR1 Deficiency in a Human Cell Line.” Edited by Timothy W Nilsen. *ELife* 6 (March): e25687. https://doi.org/10.7554/eLife.25687.

Li, Yongmei, Zhi Zhu, Shuhui Zhang, Danghui Yu, Hongyu Yu, Lina Liu, Xiaozhe Cao, Li Wang, Hengjun Gao, and Minghua Zhu. 2011. “ShRNA-Targeted Centromere Protein A Inhibits Hepatocellular Carcinoma Growth.” *PloS One* 6 (3): e17794. https://doi.org/10.1371/journal.pone.0017794.

Li, Yuanyuan, Hui Zheng, Qiujun Wang, Chen Zhou, Lei Wei, Xuehui Liu, Wenhao Zhang, et al. 2018. “Genome-Wide Analyses Reveal a Role of Polycomb in Promoting Hypomethylation of DNA Methylation Valleys.” *Genome Biology* 19 (February): 18. https://doi.org/10.1186/s13059-018-1390-8.

Liang, Xiaoping, Shan Shan, Lu Pan, Jicheng Zhao, Anand Ranjan, Feng Wang, Zhuqiang Zhang, et al. 2016. “Structural Basis of H2A.Z Recognition by SRCAP Chromatin-Remodeling Subunit YL1.” *Nature Structural & Molecular Biology* 23 (4): 317–23. https://doi.org/10.1038/nsmb.3190.

Liang, Xue-hai, Qing Liu, and Maurille J. Fournier. 2007. “RRNA Modifications in an Intersubunit Bridge of the Ribosome Strongly Affect Both Ribosome Biogenesis and Activity.” *Molecular Cell* 28 (6): 965–77. https://doi.org/10.1016/j.molcel.2007.10.012.

Liang, Xue-hai, Qing Liu, and Maurille J. Fournier. 2009. “Loss of RRNA Modifications in the Decoding Center of the Ribosome Impairs Translation and Strongly Delays Pre-RRNA Processing.” *RNA* 15 (9): 1716–28. https://doi.org/10.1261/rna.1724409.

Liddicoat, Brian J., Robert Piskol, Alistair M. Chalk, Gokul Ramaswami, Miyoko Higuchi, Jochen C. Hartner, Jin Billy Li, Peter H. Seeburg, and Carl R. Walkley. 2015. “RNA Editing by ADAR1 Prevents MDA5 Sensing of Endogenous DsRNA as Nonself.” *Science* 349 (6252): 1115–20. https://doi.org/10.1126/science.aac7049.

Lin, Shuibin, Qi Liu, Victor S. Lelyveld, Junho Choe, Jack W. Szostak, and Richard I. Gregory. 2018. “Mettl1/Wdr4-Mediated M7G TRNA Methylome Is Required for Normal MRNA Translation and Embryonic Stem Cell Self-Renewal and Differentiation.” *Molecular Cell* 71 (2): 244-255.e5. https://doi.org/10.1016/j.molcel.2018.06.001.

Lin, Shu-Yong, Terytty Yang Li, Qing Liu, Cixiong Zhang, Xiaotong Li, Yan Chen, Shi-Meng Zhang, et al. 2012. “GSK3-TIP60-ULK1 Signaling Pathway Links Growth Factor Deprivation to Autophagy.” *Science* 336 (6080): 477–81. https://doi.org/10.1126/science.1217032.

Lin, Wenchu, Zhijing Zhang, Chih-Hsin Chen, Richard R. Behringer, and Sharon Y. R. Dent. 2008. “Proper Gcn5 Histone Acetyltransferase Expression Is Required for Normal Anteroposterior Patterning of the Mouse Skeleton.” *Development, Growth & Differentiation* 50 (5): 321–30. https://doi.org/10.1111/j.1440-169X.2008.01041.x.

Lister, Ryan, Mattia Pelizzola, Robert H. Dowen, R. David Hawkins, Gary Hon, Julian Tonti-Filippini, Joseph R. Nery, et al. 2009. “Human DNA Methylomes at Base Resolution Show Widespread Epigenomic Differences.” *Nature* 462 (7271): 315–22. https://doi.org/10.1038/nature08514.

Liu, Jianzhao, Yanan Yue, Dali Han, Xiao Wang, Ye Fu, Liang Zhang, Guifang Jia, et al. 2014. “A METTL3–METTL14 Complex Mediates Mammalian Nuclear RNA N 6 -Adenosine Methylation.” *Nature Chemical Biology* 10 (2): 93–95. https://doi.org/10.1038/nchembio.1432.

Liu, Jun, Xiaoyang Dou, Chuanyuan Chen, Chuan Chen, Chang Liu, Meng Michelle Xu, Siqi Zhao, et al. 2020. “N6-Methyladenosine of Chromosome-Associated Regulatory RNA Regulates Chromatin State and Transcription.” *Science* 367 (6477): 580–86. https://doi.org/10.1126/science.aay6018.

Liu, Nian, Qing Dai, Guanqun Zheng, Chuan He, Marc Parisien, and Tao Pan. 2015. “N 6 -Methyladenosine-Dependent RNA Structural Switches Regulate RNA–Protein Interactions.” *Nature* 518 (7540): 560–64. https://doi.org/10.1038/nature14234.

Liu, Xiaoguang, Wei Wei, Yuting Liu, Xueli Yang, Jian Wu, Yang Zhang, Qiao Zhang, et al. 2017. “MOF as an Evolutionarily Conserved Histone Crotonyltransferase and Transcriptional Activation by Histone Acetyltransferase-Deficient and Crotonyltransferase-Competent CBP/P300.” *Cell Discovery* 3 (1): 1–17. https://doi.org/10.1038/celldisc.2017.16.

Liu, Xiaoxi, Takafumi Shimada, Takeshi Otowa, Yu-Yu Wu, Yoshiya Kawamura, Mamoru Tochigi, Yasuhide Iwata, et al. 2016. “Genome-Wide Association Study of Autism Spectrum Disorder in the East Asian Populations.” *Autism Research: Official Journal of the International Society for Autism Research* 9 (3): 340–49. https://doi.org/10.1002/aur.1536.

Liu, Yang, Yusheng Zhang, Qiang Chi, Zhen Wang, and Boshi Sun. 2020. “Methyltransferase-like 1 (METTL1) Served as a Tumor Suppressor in Colon Cancer by Activating 7-Methyguanosine (M7G) Regulated Let-7e MiRNA/HMGA2 Axis.” *Life Sciences* 249 (May): 117480. https://doi.org/10.1016/j.lfs.2020.117480.

Liu, Yi, Renaud Dentin, Danica Chen, Susan Hedrick, Kim Ravnskjaer, Simon Schenk, Jill Milne, et al. 2008. “A Fasting Inducible Switch Modulates Gluconeogenesis via Activator/Coactivator Exchange.” *Nature* 456 (7219): 269–73. https://doi.org/10.1038/nature07349.

Livneh, Ido, Sharon Moshitch-Moshkovitz, Ninette Amariglio, Gideon Rechavi, and Dan Dominissini. 2020. “The m 6 A Epitranscriptome: Transcriptome Plasticity in Brain Development and Function.” *Nature Reviews Neuroscience* 21 (1): 36–51. https://doi.org/10.1038/s41583-019-0244-z.

Lonsdale, John, Jeffrey Thomas, Mike Salvatore, Rebecca Phillips, Edmund Lo, Saboor Shad, Richard Hasz, et al. 2013. “The Genotype-Tissue Expression (GTEx) Project.” *Nature Genetics* 45 (6): 580–85. https://doi.org/10.1038/ng.2653.

Losey, Heather C., Alexander J. Ruthenburg, and Gregory L. Verdine. 2006. “Crystal Structure of Staphylococcus Aureus TRNA Adenosine Deaminase TadA in Complex with RNA.” *Nature Structural & Molecular Biology* 13 (2): 153–59. https://doi.org/10.1038/nsmb1047.

Loyola, Alejandra, Hideaki Tagami, Tiziana Bonaldi, Danièle Roche, Jean Pierre Quivy, Axel Imhof, Yoshihiro Nakatani, Sharon Y. R. Dent, and Geneviève Almouzni. 2009. “The HP1alpha-CAF1-SetDB1-Containing Complex Provides H3K9me1 for Suv39-Mediated K9me3 in Pericentric Heterochromatin.” *EMBO Reports* 10 (7): 769–75. https://doi.org/10.1038/embor.2009.90.

Lu, Chao, Siddhant U. Jain, Dominik Hoelper, Denise Bechet, Rosalynn C. Molden, Leili Ran, Devan Murphy, et al. 2016. “Histone H3K36 Mutations Promote Sarcomagenesis through Altered Histone Methylation Landscape.” *Science* 352 (6287): 844–49. https://doi.org/10.1126/science.aac7272.

Luger, Karolin, Armin W. Mäder, Robin K. Richmond, David F. Sargent, and Timothy J. Richmond. 1997. “Crystal Structure of the Nucleosome Core Particle at 2.8 Å Resolution.” *Nature* 389 (6648): 251–60. https://doi.org/10.1038/38444.

Luk, Ed, Anand Ranjan, Peter C. FitzGerald, Gaku Mizuguchi, Yingzi Huang, Debbie Wei, and Carl Wu. 2010. “Stepwise Histone Replacement by SWR1 Requires Dual Activation with Histone H2A.Z and Canonical Nucleosome.” *Cell* 143 (5): 725–36. https://doi.org/10.1016/j.cell.2010.10.019.

Luo, Huacheng, Ganqian Zhu, Jianfeng Xu, Qian Lai, Bowen Yan, Ying Guo, Tsz Kan Fung, et al. 2019. “HOTTIP LncRNA Promotes Hematopoietic Stem Cell Self-Renewal Leading to AML-like Disease in Mice.” *Cancer Cell* 36 (6): 645-659.e8. https://doi.org/10.1016/j.ccell.2019.10.011.

Ma, Chunhui, Mengqi Chang, Hongyi Lv, Zhi-Wei Zhang, Weilong Zhang, Xue He, Gaolang Wu, et al. 2018. “RNA M6A Methylation Participates in Regulation of Postnatal Development of the Mouse Cerebellum.” *Genome Biology* 19 (1): 68. https://doi.org/10.1186/s13059-018-1435-z.

Ma, Honghui, Xiaoyun Wang, Jiabin Cai, Qing Dai, S. Kundhavai Natchiar, Ruitu Lv, Kai Chen, et al. 2019. “N 6 -Methyladenosine Methyltransferase ZCCHC4 Mediates Ribosomal RNA Methylation.” *Nature Chemical Biology* 15 (1): 88–94. https://doi.org/10.1038/s41589-018-0184-3.

Maas, Stefan, and Willemijn M. Gommans. 2009. “Identification of a Selective Nuclear Import Signal in Adenosine Deaminases Acting on RNA.” *Nucleic Acids Research* 37 (17): 5822–29. https://doi.org/10.1093/nar/gkp599.

Maden, B. E. 1986. “Identification of the Locations of the Methyl Groups in 18 S Ribosomal RNA from Xenopus Laevis and Man.” *Journal of Molecular Biology* 189 (4): 681–99. https://doi.org/10.1016/0022-2836(86)90498-5.

Maden, B. E. H. 1988. “Locations of Methyl Groups in 28 S RRNA of Xenopus Laevis and Man: Clustering in the Conserved Core of Molecule.” *Journal of Molecular Biology* 201 (2): 289–314. https://doi.org/10.1016/0022-2836(88)90139-8.

Maiti, Atanu, and Alexander C. Drohat. 2011. “Thymine DNA Glycosylase Can Rapidly Excise 5-Formylcytosine and 5-Carboxylcytosine: POTENTIAL IMPLICATIONS FOR ACTIVE DEMETHYLATION OF CpG SITES*.” *Journal of Biological Chemistry* 286 (41): 35334–38. https://doi.org/10.1074/jbc.C111.284620.

Malbec, Lionel, Ting Zhang, Yu-Sheng Chen, Ying Zhang, Bao-Fa Sun, Bo-Yang Shi, Yong-Liang Zhao, Ying Yang, and Yun-Gui Yang. 2019. “Dynamic Methylome of Internal MRNA N 7 -Methylguanosine and Its Regulatory Role in Translation.” *Cell Research* 29 (11): 927–41. https://doi.org/10.1038/s41422-019-0230-z.

Mandal, Debabrata, Caroline Köhrer, Dan Su, Susan P. Russell, Kady Krivos, Colette M. Castleberry, Paul Blum, Patrick A. Limbach, Dieter Söll, and Uttam L. RajBhandary. 2010. “Agmatidine, a Modified Cytidine in the Anticodon of Archaeal TRNA(Ile), Base Pairs with Adenosine but Not with Guanosine.” *Proceedings of the National Academy of Sciences of the United States of America* 107 (7): 2872–77. https://doi.org/10.1073/pnas.0914869107.

Mao, Zhuo, Lu Pan, Weixiang Wang, Jian Sun, Shan Shan, Qiang Dong, Xiaoping Liang, et al. 2014. “Anp32e, a Higher Eukaryotic Histone Chaperone Directs Preferential Recognition for H2A.Z.” *Cell Research* 24 (4): 389–99. https://doi.org/10.1038/cr.2014.30.

Marasca, Federica, Beatrice Bodega, and Valerio Orlando. 2018. “How Polycomb-Mediated Cell Memory Deals With a Changing Environment: Variations in PcG Complexes and Proteins Assortment Convey Plasticity to Epigenetic Regulation as a Response to Environment.” *BioEssays: News and Reviews in Molecular, Cellular and Developmental Biology* 40 (4): e1700137. https://doi.org/10.1002/bies.201700137.

Marek, Martin, Srinivasaraghavan Kannan, Alexander-Thomas Hauser, Marina Moraes Mourão, Stéphanie Caby, Vincent Cura, Diana A. Stolfa, et al. 2013. “Structural Basis for the Inhibition of Histone Deacetylase 8 (HDAC8), a Key Epigenetic Player in the Blood Fluke Schistosoma Mansoni.” *PLoS Pathogens* 9 (9): e1003645. https://doi.org/10.1371/journal.ppat.1003645.

Marek, Martin, Guilherme Oliveira, Raymond J. Pierce, Manfred Jung, Wolfgang Sippl, and Christophe Romier. 2015. “Drugging the Schistosome Zinc-Dependent HDACs: Current Progress and Future Perspectives.” *Future Medicinal Chemistry* 7 (6): 783–800. https://doi.org/10.4155/fmc.15.25.

Mariño, Guillermo, Federico Pietrocola, Tobias Eisenberg, Yongli Kong, Shoaib Ahmad Malik, Aleksandra Andryushkova, Sabrina Schroeder, et al. 2014. “Regulation of Autophagy by Cytosolic Acetyl-Coenzyme A.” *Molecular Cell* 53 (5): 710–25. https://doi.org/10.1016/j.molcel.2014.01.016.

Marks, Paul A., and Ronald Breslow. 2007. “Dimethyl Sulfoxide to Vorinostat: Development of This Histone Deacetylase Inhibitor as an Anticancer Drug.” *Nature Biotechnology* 25 (1): 84–90. https://doi.org/10.1038/nbt1272.

Martinez, Fernando Jose, Jeong Ho Lee, Ji Eun Lee, Sandra Blanco, Elizabeth Nickerson, Stacey Gabriel, Michaela Frye, Lihadh Al-Gazali, and Joseph G. Gleeson. 2012. “Whole Exome Sequencing Identifies a Splicing Mutation in NSUN2 as a Cause of a Dubowitz-like Syndrome.” *Journal of Medical Genetics* 49 (6): 380–85. https://doi.org/10.1136/jmedgenet-2011-100686.

Martire, Sara, and Laura A. Banaszynski. 2020. “The Roles of Histone Variants in Fine-Tuning Chromatin Organization and Function.” *Nature Reviews Molecular Cell Biology* 21 (9): 522–41. https://doi.org/10.1038/s41580-020-0262-8.

Martire, Sara, Aishwarya A. Gogate, Amanda Whitmill, Amanuel Tafessu, Jennifer Nguyen, Yu-Ching Teng, Melodi Tastemel, and Laura A. Banaszynski. 2019. “Phosphorylation of Histone H3.3 at Serine 31 Promotes P300 Activity and Enhancer Acetylation.” *Nature Genetics* 51 (6): 941–46. https://doi.org/10.1038/s41588-019-0428-5.

Mateo, Francesca, Miriam Vidal-Laliena, Núria Canela, Annalisa Zecchin, Marian Martínez-Balbás, Neus Agell, Mauro Giacca, María Jesús Pujol, and Oriol Bachs. 2009. “The Transcriptional Co-Activator PCAF Regulates Cdk2 Activity.” *Nucleic Acids Research* 37 (21): 7072–84. https://doi.org/10.1093/nar/gkp777.

Mathiyalagan Prabhu, Adamiak Marta, Mayourian Joshua, Sassi Yassine, Liang Yaxuan, Agarwal Neha, Jha Divya, et al. 2019. “FTO-Dependent N6-Methyladenosine Regulates Cardiac Function During Remodeling and Repair.” *Circulation* 139 (4): 518–32. https://doi.org/10.1161/CIRCULATIONAHA.118.033794.

Matsuda, Ryo, Tetsuya Hori, Hiroshi Kitamura, Kozo Takeuchi, Tatsuo Fukagawa, and Masahiko Harata. 2010. “Identification and Characterization of the Two Isoforms of the Vertebrate H2A.Z Histone Variant.” *Nucleic Acids Research* 38 (13): 4263–73. https://doi.org/10.1093/nar/gkq171.

Mattera, L, F Escaffit, M-J Pillaire, J Selves, S Tyteca, J-S Hoffmann, P-A Gourraud, M Chevillard-Briet, C Cazaux, and D Trouche. 2009. “The P400/Tip60 Ratio Is Critical for Colorectal Cancer Cell Proliferation through DNA Damage Response Pathways.” *Oncogene* 28 (12): 1506–17. https://doi.org/10.1038/onc.2008.499.

Maunakea, Alika K, Iouri Chepelev, Kairong Cui, and Keji Zhao. 2013. “Intragenic DNA Methylation Modulates Alternative Splicing by Recruiting MeCP2 to Promote Exon Recognition.” *Cell Research* 23 (11): 1256–69. https://doi.org/10.1038/cr.2013.110.

Maunakea, Alika K., Raman P. Nagarajan, Mikhail Bilenky, Tracy J. Ballinger, Cletus D’Souza, Shaun D. Fouse, Brett E. Johnson, et al. 2010. “Conserved Role of Intragenic DNA Methylation in Regulating Alternative Promoters.” *Nature* 466 (7303): 253–57. https://doi.org/10.1038/nature09165.

McCullough, Cheryl E., and Ronen Marmorstein. 2016. “Molecular Basis for Histone Acetyltransferase Regulation by Binding Partners, Associated Domains, and Autoacetylation.” *ACS Chemical Biology* 11 (3): 632–42. https://doi.org/10.1021/acschembio.5b00841.

McGovern, Susan L., Yuan Qi, Lajos Pusztai, William F. Symmans, and Thomas A. Buchholz. 2012. “Centromere Protein-A, an Essential Centromere Protein, Is a Prognostic Marker for Relapse in Estrogen Receptor-Positive Breast Cancer.” *Breast Cancer Research: BCR* 14 (3): R72. https://doi.org/10.1186/bcr3181.

McMahon, Mary, Craig Forester, and Rochelle Buffenstein. 2021. “Aging through an Epitranscriptomic Lens.” *Nature Aging* 1 (4): 335–46. https://doi.org/10.1038/s43587-021-00058-y.

Melo, Carlos A., Jarno Drost, Patrick J. Wijchers, Harmen van de Werken, Elzo de Wit, Joachim A. F. Oude Vrielink, Ran Elkon, et al. 2013. “ERNAs Are Required for P53-Dependent Enhancer Activity and Gene Transcription.” *Molecular Cell* 49 (3): 524–35. https://doi.org/10.1016/j.molcel.2012.11.021.

Mendiratta, Shweta, Alberto Gatto, and Genevieve Almouzni. 2018. “Histone Supply: Multitiered Regulation Ensures Chromatin Dynamics throughout the Cell Cycle.” *Journal of Cell Biology* 218 (1): 39–54. https://doi.org/10.1083/jcb.201807179.

Messerschmidt, D. M., W. de Vries, M. Ito, D. Solter, A. Ferguson-Smith, and B. B. Knowles. 2012. “Trim28 Is Required for Epigenetic Stability During Mouse Oocyte to Embryo Transition.” *Science* 335 (6075): 1499–1502. https://doi.org/10.1126/science.1216154.

Metodiev, Metodi Dimitrov, Henrik Spåhr, Paola Loguercio Polosa, Caroline Meharg, Christian Becker, Janine Altmueller, Bianca Habermann, Nils-Göran Larsson, and Benedetta Ruzzenente. 2014. “NSUN4 Is a Dual Function Mitochondrial Protein Required for Both Methylation of 12S RRNA and Coordination of Mitoribosomal Assembly.” *PLOS Genetics* 10 (2): e1004110. https://doi.org/10.1371/journal.pgen.1004110.

Metzger, Eric, Melanie Wissmann, Na Yin, Judith M. Müller, Robert Schneider, Antoine H. F. M. Peters, Thomas Günther, Reinhard Buettner, and Roland Schüle. 2005. “LSD1 Demethylates Repressive Histone Marks to Promote Androgen-Receptor-Dependent Transcription.” *Nature* 437 (7057): 436–39. https://doi.org/10.1038/nature04020.

Mews, Philipp, Greg Donahue, Adam M. Drake, Vincent Luczak, Ted Abel, and Shelley L. Berger. 2017. “Acetyl-CoA Synthetase Regulates Histone Acetylation and Hippocampal Memory.” *Nature* 546 (7658): 381–86. https://doi.org/10.1038/nature22405.

Meyer, Esther, Keren J. Carss, Julia Rankin, John M. E. Nichols, Detelina Grozeva, Agnel P. Joseph, Niccolo E. Mencacci, et al. 2017. “Mutations in the Histone Methyltransferase Gene KMT2B Cause Complex Early-Onset Dystonia.” *Nature Genetics* 49 (2): 223–37. https://doi.org/10.1038/ng.3740.

Meyer, Kate D., Yogesh Saletore, Paul Zumbo, Olivier Elemento, Christopher E. Mason, and Samie R. Jaffrey. 2012. “Comprehensive Analysis of MRNA Methylation Reveals Enrichment in 3′ UTRs and near Stop Codons.” *Cell* 149 (7): 1635–46. https://doi.org/10.1016/j.cell.2012.05.003.

Meyer, Kate D., Deepak P. Patil, Jun Zhou, Alexandra Zinoviev, Maxim A. Skabkin, Olivier Elemento, Tatyana V. Pestova, Shu-Bing Qian, and Samie R. Jaffrey. 2015. “5′ UTR M6A Promotes Cap-Independent Translation.” *Cell* 163 (4): 999–1010. https://doi.org/10.1016/j.cell.2015.10.012.

Mierlo, Guido van, Gert Jan C. Veenstra, Michiel Vermeulen, and Hendrik Marks. 2019. “The Complexity of PRC2 Subcomplexes.” *Trends in Cell Biology* 29 (8): 660–71. https://doi.org/10.1016/j.tcb.2019.05.004.

Mikkelsen, Tarjei S., Manching Ku, David B. Jaffe, Biju Issac, Erez Lieberman, Georgia Giannoukos, Pablo Alvarez, et al. 2007. “Genome-Wide Maps of Chromatin State in Pluripotent and Lineage-Committed Cells.” *Nature* 448 (7153): 553–60. https://doi.org/10.1038/nature06008.

Miller, Trissa, Nevan J. Krogan, Jim Dover, H. Erdjument-Bromage, Paul Tempst, Mark Johnston, Jack F. Greenblatt, and Ali Shilatifard. 2001. “COMPASS: A Complex of Proteins Associated with a Trithorax-Related SET Domain Protein.” *Proceedings of the National Academy of Sciences of the United States of America* 98 (23): 12902–7. https://doi.org/10.1073/pnas.231473398.

Mohan, Man, Chengqi Lin, Erin Guest, and Ali Shilatifard. 2010. “Licensed to Elongate: A Molecular Mechanism for MLL-Based Leukaemogenesis.” *Nature Reviews. Cancer* 10 (10): 721–28. https://doi.org/10.1038/nrc2915.

Montanaro, Lorenzo, Maria Calienni, Sara Bertoni, Laura Rocchi, Pasquale Sansone, Gianluca Storci, Donatella Santini, et al. 2010. “Novel Dyskerin-Mediated Mechanism of P53 Inactivation through Defective MRNA Translation.” *Cancer Research* 70 (11): 4767–77. https://doi.org/10.1158/0008-5472.CAN-09-4024.

Montes de Oca, Rocío, Zachary A. Gurard-Levin, Frédérique Berger, Haniya Rehman, Elise Martel, Armelle Corpet, Leanne de Koning, et al. 2015. “The Histone Chaperone HJURP Is a New Independent Prognostic Marker for Luminal A Breast Carcinoma.” *Molecular Oncology* 9 (3): 657–74. https://doi.org/10.1016/j.molonc.2014.11.002.

Morin, Ryan D., Nathalie A. Johnson, Tesa M. Severson, Andrew J. Mungall, Jianghong An, Rodrigo Goya, Jessica E. Paul, et al. 2010. “Somatic Mutations Altering EZH2 (Tyr641) in Follicular and Diffuse Large B-Cell Lymphomas of Germinal-Center Origin.” *Nature Genetics* 42 (2): 181–85. https://doi.org/10.1038/ng.518.

Morin, Ryan D., Maria Mendez-Lago, Andrew J. Mungall, Rodrigo Goya, Karen L. Mungall, Richard D. Corbett, Nathalie A. Johnson, et al. 2011. “Frequent Mutation of Histone-Modifying Genes in Non-Hodgkin Lymphoma.” *Nature* 476 (7360): 298–303. https://doi.org/10.1038/nature10351.

Morita, Yoko, Toshihiro Shibutani, Nozomi Nakanishi, Kazuko Nishikura, Shigenori Iwai, and Isao Kuraoka. 2013. “Human Endonuclease V Is a Ribonuclease Specific for Inosine-Containing RNA.” *Nature Communications* 4 (1): 2273. https://doi.org/10.1038/ncomms3273.

Morris, Rana C., Kenneth G. Brown, and Mark S. Elliott. 1999. “The Effect of Queuosine on TRNA Structure and Function.” *Journal of Biomolecular Structure and Dynamics* 16 (4): 757–74. https://doi.org/10.1080/07391102.1999.10508291.

Mujtaba, Shiraz, Yan He, Lei Zeng, Sherry Yan, Olga Plotnikova, Sachchidanand, Roberto Sanchez, Nancy J Zeleznik-Le, Ze’ev Ronai, and Ming-Ming Zhou. 2004. “Structural Mechanism of the Bromodomain of the Coactivator CBP in P53 Transcriptional Activation.” *Molecular Cell* 13 (2): 251–63. https://doi.org/10.1016/S1097-2765(03)00528-8.

Mullighan, Charles G., Jinghui Zhang, Lawryn H. Kasper, Stephanie Lerach, Debbie Payne-Turner, Letha A. Phillips, Sue L. Heatley, et al. 2011. “CREBBP Mutations in Relapsed Acute Lymphoblastic Leukaemia.” *Nature* 471 (7337): 235–39. https://doi.org/10.1038/nature09727.

Muntean, Andrew G., Jiaying Tan, Kajal Sitwala, Yongsheng Huang, Joel Bronstein, James A. Connelly, Venkatesha Basrur, Kojo S. J. Elenitoba-Johnson, and Jay L. Hess. 2010. “The PAF Complex Synergizes with MLL Fusion Proteins at HOX Loci to Promote Leukemogenesis.” *Cancer Cell* 17 (6): 609–21. https://doi.org/10.1016/j.ccr.2010.04.012.

Muramatsu, Tomonari, Kazuya Nishikawa, Fumiko Nemoto, Yoshiyuki Kuchino, Susumu Nishimura, Tatsuo Miyazawa, and Shigeyuki Yokoyama. 1988. “Codon and Amino-Acid Specificities of a Transfer RNA Are Both Converted by a Single Post-Transcriptional Modification.” *Nature* 336 (6195): 179–81. https://doi.org/10.1038/336179a0.

Murphy, Frank V., and V. Ramakrishnan. 2004. “Structure of a Purine-Purine Wobble Base Pair in the Decoding Center of the Ribosome.” *Nature Structural & Molecular Biology* 11 (12): 1251–52. https://doi.org/10.1038/nsmb866.

Murphy, Frank V., Venki Ramakrishnan, Andrzej Malkiewicz, and Paul F. Agris. 2004. “The Role of Modifications in Codon Discrimination by TRNA Lys UUU.” *Nature Structural & Molecular Biology* 11 (12): 1186–91. https://doi.org/10.1038/nsmb861.

Musacchio, Andrea, and Arshad Desai. 2017. “A Molecular View of Kinetochore Assembly and Function.” *Biology* 6 (1): 5. https://doi.org/10.3390/biology6010005.

Myant, Kevin, Ausma Termanis, Arvind Y. M. Sundaram, Tristin Boe, Chao Li, Cara Merusi, Joe Burrage, Jose I. de Las Heras, and Irina Stancheva. 2011. “LSH and G9a/GLP Complex Are Required for Developmentally Programmed DNA Methylation.” *Genome Research* 21 (1): 83–94. https://doi.org/10.1101/gr.108498.110.

Nakajima, Hidenori, Young Bae Kim, Hiroshi Terano, Minoru Yoshida, and Sueharu Horinouchi. 1998. “FR901228, a Potent Antitumor Antibiotic, Is a Novel Histone Deacetylase Inhibitor.” *Experimental Cell Research* 241 (1): 126–33. https://doi.org/10.1006/excr.1998.4027.

Nakano, Saori, Takeo Suzuki, Layla Kawarada, Hiroyoshi Iwata, Kana Asano, and Tsutomu Suzuki. 2016. “NSUN3 Methylase Initiates 5-Formylcytidine Biogenesis in Human Mitochondrial TRNA Met.” *Nature Chemical Biology* 12 (7): 546–51. https://doi.org/10.1038/nchembio.2099.

Nan, Xinsheng, Huck-Hui Ng, Colin A. Johnson, Carol D. Laherty, Bryan M. Turner, Robert N. Eisenman, and Adrian Bird. 1998. “Transcriptional Repression by the Methyl-CpG-Binding Protein MeCP2 Involves a Histone Deacetylase Complex.” *Nature* 393 (6683): 386–89. https://doi.org/10.1038/30764.

Narita, Takeo, Brian T. Weinert, and Chunaram Choudhary. 2019. “Functions and Mechanisms of Non-Histone Protein Acetylation.” *Nature Reviews Molecular Cell Biology* 20 (3): 156–74. https://doi.org/10.1038/s41580-018-0081-3.

Narlikar, Geeta J., Ramasubramanian Sundaramoorthy, and Tom Owen-Hughes. 2013. “Mechanisms and Functions of ATP-Dependent Chromatin-Remodeling Enzymes.” *Cell* 154 (3): 490–503. https://doi.org/10.1016/j.cell.2013.07.011.

Nasvall, S. Joakim, Peng Chen, and Glenn R. Bjork. 2004. “The Modified Wobble Nucleoside Uridine-5-Oxyacetic Acid in TRNAPro(Cmo5UGG) Promotes Reading of All Four Proline Codons in Vivo.” *RNA (New York, N.Y.)* 10 (10): 1662–73. https://doi.org/10.1261/rna.7106404.

Näsvall, S. Joakim, Peng Chen, and Glenn R. Björk. 2007. “The Wobble Hypothesis Revisited: Uridine-5-Oxyacetic Acid Is Critical for Reading of G-Ending Codons.” *RNA (New York, N.Y.)* 13 (12): 2151–64. https://doi.org/10.1261/rna.731007.

Neri, Francesco, Stefania Rapelli, Anna Krepelova, Danny Incarnato, Caterina Parlato, Giulia Basile, Mara Maldotti, Francesca Anselmi, and Salvatore Oliviero. 2017. “Intragenic DNA Methylation Prevents Spurious Transcription Initiation.” *Nature* 543 (7643): 72–77. https://doi.org/10.1038/nature21373.

Neumann, Heinz, Susan M. Hancock, Ruth Buning, Andrew Routh, Lynda Chapman, Joanna Somers, Tom Owen-Hughes, John van Noort, Daniela Rhodes, and Jason W. Chin. 2009. “A Method for Genetically Installing Site-Specific Acetylation in Recombinant Histones Defines the Effects of H3 K56 Acetylation.” *Molecular Cell* 36 (1): 153–63. https://doi.org/10.1016/j.molcel.2009.07.027.

Newman, Dane M., Shinya Sakaguchi, Aaron Lun, Simon Preston, Marc Pellegrini, Kseniya Khamina, Andreas Bergthaler, et al. 2016. “Acetylation of the Cd8 Locus by KAT6A Determines Memory T Cell Diversity.” *Cell Reports* 16 (12): 3311–21. https://doi.org/10.1016/j.celrep.2016.08.056.

Ng, Huck-Hui, Yi Zhang, Brian Hendrich, Colin A. Johnson, Bryan M. Turner, Hediye Erdjument-Bromage, Paul Tempst, Danny Reinberg, and Adrian Bird. 1999. "MBD2 Is a Transcriptional Repressor Belonging to the MeCP1 Histone Deacetylase Complex." *Nature Genetics* 23 (1): 58–61. https://doi.org/10.1038/12659.

Ng, Sarah B., Abigail W. Bigham, Kati J. Buckingham, Mark C. Hannibal, Margaret J. McMillin, Heidi I. Gildersleeve, Anita E. Beck, et al. 2010. "Exome Sequencing Identifies MLL2 Mutations as a Cause of Kabuki Syndrome." *Nature Genetics* 42 (9): 790–93. https://doi.org/10.1038/ng.646.

Nihira, Naoe T., Kohei Ogura, Kouhei Shimizu, Brian J. North, Jinfang Zhang, Daming Gao, Hiroyuki Inuzuka, and Wenyi Wei. 2017. "Acetylation-Dependent Regulation of MDM2 E3 Ligase Activity Dictates Its Oncogenic Function." *Science Signaling* 10 (466). https://doi.org/10.1126/scisignal.aai8026.

Nirenberg, Marshall W., and J. Heinrich Matthaei. 1961. "The Dependence of Cell- free Protein Synthesis in *E. coli* upon Naturally Occurring or Synthetic Polyribonucleotides." *Proceedings of the National Academy of Sciences of the United States of America* 47 (10): 1588–1602.

Nirenberg, M, P Leder, M Bernfield, R Brimacombe, J Trupin, F Rottman, and C O'Neal. 1965. "RNA Codewords and Protein Synthesis, VII. On the General Nature of the RNA Code." *Proceedings of the National Academy of Sciences of the United States of America* 53 (5): 1161–68.

Nishikura, Kazuko. 2010. "Functions and Regulation of RNA Editing by ADAR Deaminases." *Annual Review of Biochemistry* 79 (1): 321–49. https://doi.org/10.1146/annurev-biochem-060208-105251.

Nishikura, Kazuko. 2016. "A-to-I Editing of Coding and Non-Coding RNAs by ADARs." *Nature Reviews Molecular Cell Biology* 17 (2): 83–96. https://doi.org/10.1038/nrm.2015.4.

Nishiyama, Atsuya, Luna Yamaguchi, Jafar Sharif, Yoshikazu Johmura, Takeshi Kawamura, Keiko Nakanishi, Shintaro Shimamura, et al. 2013. "Uhrf1-Dependent H3K23 Ubiquitylation Couples Maintenance DNA Methylation and Replication." *Nature* 502 (7470): 249–53. https://doi.org/10.1038/nature12488.

Novikov, Leonid, Jong Woo Park, Hongshan Chen, Hadassa Klerman, Abubakar S. Jalloh, and Matthew J. Gamble. 2011. "QKI-Mediated Alternative Splicing of the Histone Variant MacroH2A1 Regulates Cancer Cell Proliferation." *Molecular and Cellular Biology* 31 (20): 4244–55. https://doi.org/10.1128/MCB.05244-11.

Oakes, Eimile, Ashley Anderson, Aaron Cohen-Gadol, and Heather A. Hundley. 2017. "Adenosine Deaminase That Acts on RNA 3 (ADAR3) Binding to Glutamate Receptor Subunit B Pre-MRNA Inhibits RNA Editing in Glioblastoma*." *Journal of Biological Chemistry* 292 (10): 4326–35. https://doi.org/10.1074/jbc.M117.779868.

Obara, Keisuke, Takeshi Noda, Kaori Niimi, and Yoshinori Ohsumi. 2008. "Transport of Phosphatidylinositol 3-Phosphate into the Vacuole via Autophagic Membranes in Saccharomyces Cerevisiae." *Genes to Cells: Devoted to Molecular & Cellular Mechanisms* 13 (6): 537–47. https://doi.org/10.1111/j.1365-2443.2008.01188.x.

Obri, Arnaud, Khalid Ouararhni, Christophe Papin, Marie-Laure Diebold, Kiran Padmanabhan, Martin Marek, Isabelle Stoll, et al. 2014. "ANP32E Is a Histone Chaperone That Removes H2A.Z from Chromatin." *Nature* 505 (7485): 648–53. https://doi.org/10.1038/nature12922.

O'Carroll, D., S. Erhardt, M. Pagani, S. C. Barton, M. A. Surani, and T. Jenuwein. 2001. "The Polycomb-Group Gene Ezh2 Is Required for Early Mouse Development." *Molecular and Cellular Biology* 21 (13): 4330–36. https://doi.org/10.1128/MCB.21.13.4330-4336.2001.

Oger, Frédérik, Florence Dubois, Stéphanie Caby, Christophe Noël, Jocelyne Cornette, Benjamin Bertin, Monique Capron, and Raymond J. Pierce. 2008. "The Class I Histone Deacetylases of the Platyhelminth Parasite Schistosoma Mansoni." *Biochemical and Biophysical Research Communications* 377 (4): 1079–84. https://doi.org/10.1016/j.bbrc.2008.10.090.

Ohlson, Johan, Jakob Skou Pedersen, David Haussler, and Marie Ohman. 2007. "Editing Modifies the GABA(A) Receptor Subunit Alpha3." *RNA (New York, N.Y.)* 13 (5): 698–703. https://doi.org/10.1261/rna.349107.

Okano, Masaki, Daphne W Bell, Daniel A Haber, and En Li. 1999. "DNA Methyltransferases Dnmt3a and Dnmt3b Are Essential for De Novo Methylation and Mammalian Development." *Cell* 99 (3): 247–57. https://doi.org/10.1016/S0092-8674(00)81656-6.

Okano, Masaki, Shaoping Xie, and En Li. 1998. "Cloning and Characterization of a Family of Novel Mammalian DNA (Cytosine-5) Methyltransferases." *Nature Genetics* 19 (3): 219–20. https://doi.org/10.1038/890.

Olejniczak, Mikołaj, and Olke C. Uhlenbeck. 2006. "TRNA Residues That Have Coevolved with Their Anticodon to Ensure Uniform and Accurate Codon Recognition." *Biochimie* 88 (8): 943–50. https://doi.org/10.1016/j.biochi.2006.06.005.

Ooi, Steen K. T., Chen Qiu, Emily Bernstein, Keqin Li, Da Jia, Zhe Yang, Hediye Erdjument-Bromage, et al. 2007. "DNMT3L Connects Unmethylated Lysine 4 of Histone H3 to de Novo Methylation of DNA." *Nature* 448 (7154): 714–17. https://doi.org/10.1038/nature05987.

Ota, Hiromitsu, Masayuki Sakurai, Ravi Gupta, Louis Valente, Bjorn-Erik Wulff, Kentaro Ariyoshi, Hisashi Iizasa, Ramana V. Davuluri, and Kazuko Nishikura. 2013. "ADAR1 Forms a Complex with Dicer to Promote MicroRNA Processing and RNA-Induced Gene Silencing." *Cell* 153 (3): 575–89. https://doi.org/10.1016/j.cell.2013.03.024.

Paggetti, J., A. Largeot, R. Aucagne, A. Jacquel, B. Lagrange, X.-J. Yang, E. Solary, J.-N. Bastie, and L. Delva. 2010. "Crosstalk between Leukemia-Associated Proteins MOZ and MLL Regulates HOX Gene Expression in Human Cord Blood CD34+ Cells." *Oncogene* 29 (36): 5019–31. https://doi.org/10.1038/onc.2010.254.

Pajtler, Kristian W., Ji Wen, Martin Sill, Tong Lin, Wilda Orisme, Bo Tang, Jens-Martin Hübner, et al. 2018. "Molecular Heterogeneity and CXorf67 Alterations in Posterior Fossa Group A (PFA) Ependymomas." *Acta Neuropathologica* 136 (2): 211–26. https://doi.org/10.1007/s00401-018-1877-0.

Pandolfini, Luca, Isaia Barbieri, Andrew J. Bannister, Alan Hendrick, Byron Andrews, Natalie Webster, Pierre Murat, et al. 2019. "METTL1 Promotes Let-7 MicroRNA Processing via M7G Methylation." *Molecular Cell* 74 (6): 1278-1290.e9. https://doi.org/10.1016/j.molcel.2019.03.040.

Papamichos-Chronakis, Manolis, Shinya Watanabe, Oliver J. Rando, and Craig L. Peterson. 2011. "Global Regulation of H2A.Z Localization by the INO80 Chromatin-Remodeling Enzyme Is Essential for Genome Integrity." *Cell* 144 (2): 200–213. https://doi.org/10.1016/j.cell.2010.12.021.

Paralkar, Vikram R., Cristian C. Taborda, Peng Huang, Yu Yao, Andrew V. Kossenkov, Rishi Prasad, Jing Luan, et al. 2016. "Unlinking an LncRNA from Its Associated Cis Element." *Molecular Cell* 62 (1): 104–10. https://doi.org/10.1016/j.molcel.2016.02.029.

Park, Jeongsoon, Yue Chen, Daniel X. Tishkoff, Chao Peng, Minjia Tan, Lunzhai Dai, Zhongyu Xie, et al. 2013. "SIRT5-Mediated Lysine Desuccinylation Impacts Diverse Metabolic Pathways." *Molecular Cell* 50 (6): 919–30. https://doi.org/10.1016/j.molcel.2013.06.001.

Park, Young-Jun, Pamela N. Dyer, David J. Tremethick, and Karolin Luger. 2004. “A New Fluorescence Resonance Energy Transfer Approach Demonstrates That the Histone Variant H2AZ Stabilizes the Histone Octamer within the Nucleosome*.” *Journal of Biological Chemistry* 279 (23): 24274–82. https://doi.org/10.1074/jbc.M313152200.

Parra, Maribel, and Eric Verdin. 2010. “Regulatory Signal Transduction Pathways for Class IIa Histone Deacetylases.” *Current Opinion in Pharmacology*, Cancer/Immunomodulation, 10 (4): 454–60. https://doi.org/10.1016/j.coph.2010.04.004.

Pasini, Diego, Adrian P. Bracken, Michael R. Jensen, Eros Lazzerini Denchi, and Kristian Helin. 2004. “Suz12 Is Essential for Mouse Development and for EZH2 Histone Methyltransferase Activity.” *The EMBO Journal* 23 (20): 4061–71. https://doi.org/10.1038/sj.emboj.7600402.

Patil, Deepak P., Chun-Kan Chen, Brian F. Pickering, Amy Chow, Constanza Jackson, Mitchell Guttman, and Samie R. Jaffrey. 2016. “M6A RNA Methylation Promotes XIST-Mediated Transcriptional Repression.” *Nature* 537 (7620): 369–73. https://doi.org/10.1038/nature19342.

Paul, Deepanjan, Ashis Narayan Sinha, Arjun Ray, Megha Lal, Subhashree Nayak, Anchal Sharma, Bharati Mehani, et al. 2017. “A-to-I Editing in Human MiRNAs Is Enriched in Seed Sequence, Influenced by Sequence Contexts and Significantly Hypoedited in Glioblastoma Multiforme.” *Scientific Reports* 7 (1): 2466. https://doi.org/10.1038/s41598-017-02397-6.

Peifer, Martin, Lynnette Fernández-Cuesta, Martin L. Sos, Julie George, Danila Seidel, Lawryn H. Kasper, Dennis Plenker, et al. 2012. “Integrative Genome Analyses Identify Key Somatic Driver Mutations of Small-Cell Lung Cancer.” *Nature Genetics* 44 (10): 1104–10. https://doi.org/10.1038/ng.2396.

Peña, Pedro V., Foteini Davrazou, Xiaobing Shi, Kay L. Walter, Vladislav V. Verkhusha, Or Gozani, Rui Zhao, and Tatiana G. Kutateladze. 2006. “Molecular Mechanism of Histone H3K4me3 Recognition by Plant Homeodomain of ING2.” *Nature* 442 (7098): 100–103. https://doi.org/10.1038/nature04814.

Pendleton, Kathryn E., Beibei Chen, Kuanqing Liu, Olga V. Hunter, Yang Xie, Benjamin P. Tu, and Nicholas K. Conrad. 2017. “The U6 SnRNA M6A Methyltransferase METTL16 Regulates SAM Synthetase Intron Retention.” *Cell* 169 (5): 824-835.e14. https://doi.org/10.1016/j.cell.2017.05.003.

Peng, Chao, Zhike Lu, Zhongyu Xie, Zhongyi Cheng, Yue Chen, Minjia Tan, Hao Luo, et al. 2011. “The First Identification of Lysine Malonylation Substrates and Its Regulatory Enzyme.” *Molecular & Cellular Proteomics: MCP* 10 (12): M111.012658. https://doi.org/10.1074/mcp.M111.012658.

Peng, Peter L., Xiafen Zhong, Weihong Tu, Mangala M. Soundarapandian, Peter Molner, Dongya Zhu, Lorraine Lau, Shuhong Liu, Fang Liu, and YouMing Lu. 2006. “ADAR2-Dependent RNA Editing of AMPA Receptor Subunit GluR2 Determines Vulnerability of Neurons in Forebrain Ischemia.” *Neuron* 49 (5): 719–33. https://doi.org/10.1016/j.neuron.2006.01.025.

Penzo, Marianna, Ania N. Guerrieri, Federico Zacchini, Davide Treré, and Lorenzo Montanaro. 2017. “RNA Pseudouridylation in Physiology and Medicine: For Better and for Worse.” *Genes* 8 (11): 301. https://doi.org/10.3390/genes8110301.

Penzo, Marianna, Vienna Ludovini, Davide Trerè, Annamaria Siggillino, Jacopo Vannucci, Guido Bellezza, Lucio Crinò, and Lorenzo Montanaro. 2015. “Dyskerin and TERC Expression May Condition Survival in Lung Cancer Patients.” *Oncotarget* 6 (25): 21755–60. https://doi.org/10.18632/oncotarget.4580.

Penzo, Marianna, and Lorenzo Montanaro. 2018. “Turning Uridines around: Role of RRNA Pseudouridylation in Ribosome Biogenesis and Ribosomal Function.” *Biomolecules* 8 (2): 38. https://doi.org/10.3390/biom8020038.

Pestal, Kathleen, Cory C. Funk, Jessica M. Snyder, Nathan D. Price, Piper M. Treuting, and Daniel B. Stetson. 2015. “Isoforms of RNA-Editing Enzyme ADAR1 Independently Control Nucleic Acid Sensor MDA5-Driven Autoimmunity and Multi-Organ Development.” *Immunity* 43 (5): 933–44. https://doi.org/10.1016/j.immuni.2015.11.001.

Peters, Antoine H. F. M., Stefan Kubicek, Karl Mechtler, Roderick J. O’Sullivan, Alwin A. H. A. Derijck, Laura Perez-Burgos, Alexander Kohlmaier, et al. 2003. “Partitioning and Plasticity of Repressive Histone Methylation States in Mammalian Chromatin.” *Molecular Cell* 12 (6): 1577–89. https://doi.org/10.1016/S1097-2765(03)00477-5.

Peters, Antoine H. F. M., Dónal O’Carroll, Harry Scherthan, Karl Mechtler, Stephan Sauer, Christian Schöfer, Klara Weipoltshammer, et al. 2001. “Loss of the Suv39h Histone Methyltransferases Impairs Mammalian Heterochromatin and Genome Stability.” *Cell* 107 (3): 323–37. https://doi.org/10.1016/S0092-8674(01)00542-6.

Petrif, Fred, Rachel H. Giles, Hans G. Dauwerse, Jasper J. Saris, Raoul C. M. Hennekam, Mitsuo Masuno, Niels Tommerup, et al. 1995. “Rubinstein-Taybi Syndrome Caused by Mutations in the Transcriptional Co-Activator CBP.” *Nature* 376 (6538): 348–51. https://doi.org/10.1038/376348a0.

Pfister, Stefan, Stephen Rea, Mikko Taipale, Frank Mendrzyk, Beate Straub, Carina Ittrich, Olaf Thuerigen, Hans Peter Sinn, Asifa Akhtar, and Peter Lichter. 2008. “The Histone Acetyltransferase HMOF Is Frequently Downregulated in Primary Breast Carcinoma and Medulloblastoma and Constitutes a Biomarker for Clinical Outcome in Medulloblastoma.” *International Journal of Cancer* 122 (6): 1207–13. https://doi.org/10.1002/ijc.23283.

Phelps, Steven S., Andrzej Malkiewicz, Paul F. Agris, and Simpson Joseph. 2004. “Modified Nucleotides in TRNALys and TRNAVal Are Important for Translocation.” *Journal of Molecular Biology* 338 (3): 439–44. https://doi.org/10.1016/j.jmb.2004.02.070.

Piekna-Przybylska, Dorota, Piotr Przybylski, Agnès Baudin-Baillieu, Jean-Pierre Rousset, and Maurille J. Fournier. 2008. “Ribosome Performance Is Enhanced by a Rich Cluster of Pseudouridines in the A-Site Finger Region of the Large Subunit.” *The Journal of Biological Chemistry* 283 (38): 26026–36. https://doi.org/10.1074/jbc.M803049200.

Pietrocola, Federico, Lorenzo Galluzzi, José Manuel Bravo-San Pedro, Frank Madeo, and Guido Kroemer. 2015. “Acetyl Coenzyme A: A Central Metabolite and Second Messenger.” *Cell Metabolism* 21 (6): 805–21. https://doi.org/10.1016/j.cmet.2015.05.014.

Pillai, Vinodkumar B., Nagalingam R. Sundaresan, Sadhana A. Samant, Don Wolfgeher, Chinmay M. Trivedi, and Mahesh P. Gupta. 2011. “Acetylation of a Conserved Lysine Residue in the ATP Binding Pocket of P38 Augments Its Kinase Activity during Hypertrophy of Cardiomyocytes.” *Molecular and Cellular Biology* 31 (11): 2349–63. https://doi.org/10.1128/MCB.01205-10.

Ping, Yanyan, Yulan Deng, Li Wang, Hongyi Zhang, Yong Zhang, Chaohan Xu, Hongying Zhao, et al. 2015. “Identifying Core Gene Modules in Glioblastoma Based on Multilayer Factor-Mediated Dysfunctional Regulatory Networks through Integrating Multi-Dimensional Genomic Data.” *Nucleic Acids Research* 43 (4): 1997–2007. https://doi.org/10.1093/nar/gkv074.

Piquet, Sandra, Florent Le Parc, Siau-Kun Bai, Odile Chevallier, Salomé Adam, and Sophie E. Polo. 2018. “The Histone Chaperone FACT Coordinates H2A.X-Dependent Signaling and Repair of DNA Damage.” *Molecular Cell* 72 (5): 888-901.e7. https://doi.org/10.1016/j.molcel.2018.09.010.

Piunti, Andrea, and Ali Shilatifard. 2016. “Epigenetic Balance of Gene Expression by Polycomb and COMPASS Families.” *Science* 352 (6290): aad9780. https://doi.org/10.1126/science.aad9780.

Piunti, Andrea, and Ali Shilatifard. 2021. “The Roles of Polycomb Repressive Complexes in Mammalian Development and Cancer.” *Nature Reviews Molecular Cell Biology* 22 (5): 326–45. https://doi.org/10.1038/s41580-021-00341-1.

Piunti, Andrea, Edwin R. Smith, Marc A. J. Morgan, Michal Ugarenko, Natalia Khaltyan, Kathryn A. Helmin, Caila A. Ryan, et al. 2019. “CATACOMB: An Endogenous Inducible Gene That Antagonizes H3K27 Methylation Activity of Polycomb Repressive Complex 2 via an H3K27M-like Mechanism.” *Science Advances* 5 (7): eaax2887. https://doi.org/10.1126/sciadv.aax2887.

Pober, Barbara R. 2010. “Williams–Beuren Syndrome.” *New England Journal of Medicine* 362 (3): 239–52. https://doi.org/10.1056/NEJMra0903074.

Poole, Raewyn M. 2014. “Belinostat: First Global Approval.” *Drugs* 74 (13): 1543–54. https://doi.org/10.1007/s40265-014-0275-8.

Porter, Nicholas J., and David W. Christianson. 2017. “Binding of the Microbial Cyclic Tetrapeptide Trapoxin A to the Class I Histone Deacetylase HDAC8.” *ACS Chemical Biology* 12 (9): 2281–86. https://doi.org/10.1021/acschembio.7b00330.

Porter, Nicholas J, and David W Christianson. 2019. “Structure, Mechanism, and Inhibition of the Zinc-Dependent Histone Deacetylases.” *Current Opinion in Structural Biology*, Catalysis and Regulation ● Protein Nucleic Interactions, 59 (December): 9–18. https://doi.org/10.1016/j.sbi.2019.01.004.

Prasanth, Kannanganattu V., Supriya G. Prasanth, Zhenyu Xuan, Stephen Hearn, Susan M. Freier, C. Frank Bennett, Michael Q. Zhang, and David L. Spector. 2005. “Regulating Gene Expression through RNA Nuclear Retention.” *Cell* 123 (2): 249–63. https://doi.org/10.1016/j.cell.2005.08.033.

Pratt, Drew, Martha Quezado, Zied Abdullaev, Debra Hawes, Fusheng Yang, Hugh J. L. Garton, Alexander R. Judkins, et al. 2020. “Diffuse Intrinsic Pontine Glioma-like Tumor with EZHIP Expression and Molecular Features of PFA Ependymoma.” *Acta Neuropathologica Communications* 8 (1): 37. https://doi.org/10.1186/s40478-020-00905-w.

Prince, H. Miles, Mark J. Bishton, and Ricky W. Johnstone. 2009. “Panobinostat (LBH589): A Potent Pan-Deacetylase Inhibitor with Promising Activity against Hematologic and Solid Tumors.” *Future Oncology (London, England)* 5 (5): 601–12. https://doi.org/10.2217/fon.09.36.

Proudhon, Charlotte, Rachel Duffié, Sophie Ajjan, Michael Cowley, Julian Iranzo, Guillermo Carbajosa, Heba Saadeh, et al. 2012. “Protection against De Novo Methylation Is Instrumental in Maintaining Parent-of-Origin Methylation Inherited from the Gametes.” *Molecular Cell* 47 (6): 909–20. https://doi.org/10.1016/j.molcel.2012.07.010.

Qin, Weihua, Patricia Wolf, Nan Liu, Stephanie Link, Martha Smets, Federica La Mastra, Ignasi Forné, et al. 2015. “DNA Methylation Requires a DNMT1 Ubiquitin Interacting Motif (UIM) and Histone Ubiquitination.” *Cell Research* 25 (8): 911–29. https://doi.org/10.1038/cr.2015.72.

Qiu, Jun-Jun, Jun-Jie Guo, Tian-Jiao Lv, Hong-Yan Jin, Jing-Xin Ding, Wei-Wei Feng, Ying Zhang, and Ke-Qin Hua. 2013. “Prognostic Value of Centromere Protein-A Expression in Patients with Epithelial Ovarian Cancer.” *Tumor Biology* 34 (5): 2971–75. https://doi.org/10.1007/s13277-013-0860-6.

Quenneville, Simon, Gaetano Verde, Andrea Corsinotti, Adamandia Kapopoulou, Johan Jakobsson, Sandra Offner, Ilaria Baglivo, et al. 2011. “In Embryonic Stem Cells, ZFP57/KAP1 Recognize a Methylated Hexanucleotide to Affect Chromatin and DNA Methylation of Imprinting Control Regions.” *Molecular Cell* 44 (3): 361–72. https://doi.org/10.1016/j.molcel.2011.08.032.

Quivy, Jean-Pierre, Danièle Roche, Doris Kirschner, Hideaki Tagami, Yoshihiro Nakatani, and Geneviève Almouzni. 2004. “A CAF-1 Dependent Pool of HP1 during Heterochromatin Duplication.” *The EMBO Journal* 23 (17): 3516–26. https://doi.org/10.1038/sj.emboj.7600362.

Raddatz, Günter, Paloma M. Guzzardo, Nelly Olova, Marcelo Rosado Fantappié, Markus Rampp, Matthias Schaefer, Wolf Reik, Gregory J. Hannon, and Frank Lyko. 2013. “Dnmt2-Dependent Methylomes Lack Defined DNA Methylation Patterns.” *Proceedings of the National Academy of Sciences of the United States of America* 110 (21): 8627–31. https://doi.org/10.1073/pnas.1306723110.

Rajagopal, Nisha, Jason Ernst, Pradipta Ray, Jie Wu, Michael Zhang, Manolis Kellis, and Bing Ren. 2014. “Distinct and Predictive Histone Lysine Acetylation Patterns at Promoters, Enhancers, and Gene Bodies.” *G3 (Bethesda, Md.)* 4 (11): 2051–63. https://doi.org/10.1534/g3.114.013565.

Ramanathan, Anand, G. Brett Robb, and Siu-Hong Chan. 2016. “MRNA Capping: Biological Functions and Applications.” *Nucleic Acids Research* 44 (16): 7511–26. https://doi.org/10.1093/nar/gkw551.

Rasmussen, Kasper D., Guangshuai Jia, Jens V. Johansen, Marianne T. Pedersen, Nicolas Rapin, Frederik O. Bagger, Bo T. Porse, Olivier A. Bernard, Jesper Christensen, and Kristian Helin. 2015. “Loss of TET2 in Hematopoietic Cells Leads to DNA Hypermethylation of Active Enhancers and Induction of Leukemogenesis.” *Genes & Development* 29 (9): 910–22. https://doi.org/10.1101/gad.260174.115.

Ravens, Sarina, Marjorie Fournier, Tao Ye, Matthieu Stierle, Doulaye Dembele, Virginie Chavant, and Làszlò Tora. 2014. “Mof-Associated Complexes Have Overlapping and Unique Roles in Regulating Pluripotency in Embryonic Stem Cells and during Differentiation.” *ELife* 3 (June). https://doi.org/10.7554/eLife.02104.

Reed, Sara M., and Dawn E. Quelle. 2015. “P53 Acetylation: Regulation and Consequences.” *Cancers* 7 (1): 30–69. https://doi.org/10.3390/cancers7010030.

Rehwinkel, Jan, and Michaela U. Gack. 2020. “RIG-I-like Receptors: Their Regulation and Roles in RNA Sensing.” *Nature Reviews Immunology* 20 (9): 537–51. https://doi.org/10.1038/s41577-020-0288-3.

Ren, Wendan, Jiuwei Lu, Mengjiang Huang, Linfeng Gao, Dongxu Li, Gang Greg Wang, and Jikui Song. 2019. “Structure and Regulation of ZCCHC4 in m 6 A-Methylation of 28S RRNA.” *Nature Communications* 10 (1): 5042. https://doi.org/10.1038/s41467-019-12923-x.

Rice, Gillian I., Paul R. Kasher, Gabriella M. A. Forte, Niamh M. Mannion, Sam M. Greenwood, Marcin Szynkiewicz, Jonathan E. Dickerson, et al. 2012. “Mutations in ADAR1 Cause Aicardi-Goutières Syndrome Associated with a Type I Interferon Signature.” *Nature Genetics* 44 (11): 1243–48. https://doi.org/10.1038/ng.2414.

Rice, Judd C., Scott D. Briggs, Beatrix Ueberheide, Cynthia M. Barber, Jeffrey Shabanowitz, Donald F. Hunt, Yoichi Shinkai, and C. David Allis. 2003. "Histone Methyltransferases Direct Different Degrees of Methylation to Define Distinct Chromatin Domains." *Molecular Cell* 12 (6): 1591–98. https://doi.org/10.1016/S1097-2765(03)00479-9.

Richon, V M. 2006. "Cancer Biology: Mechanism of Antitumour Action of Vorinostat (Suberoylanilide Hydroxamic Acid), a Novel Histone Deacetylase Inhibitor." *British Journal of Cancer* 95 (Suppl 1): S2–6. https://doi.org/10.1038/sj.bjc.6603463.

Rickels, Ryan, Deqing Hu, Clayton K. Collings, Ashley R. Woodfin, Andrea Piunti, Man Mohan, Hans-Martin Herz, Evgeny Kvon, and Ali Shilatifard. 2016. "An Evolutionary Conserved Epigenetic Mark of Polycomb Response Elements Implemented by Trx/MLL/COMPASS." *Molecular Cell* 63 (2): 318–28. https://doi.org/10.1016/j.molcel.2016.06.018.

Rintala-Dempsey, Anne C., and Ute Kothe. 2017. "Eukaryotic Stand-Alone Pseudouridine Synthases - RNA Modifying Enzymes and Emerging Regulators of Gene Expression?" *RNA Biology* 14 (9): 1185–96. https://doi.org/10.1080/15476286.2016.1276150.

Rishi, Vikas, Paramita Bhattacharya, Raghunath Chatterjee, Julian Rozenberg, Jianfei Zhao, Kimberly Glass, Peter Fitzgerald, and Charles Vinson. 2010. "CpG Methylation of Half-CRE Sequences Creates C/EBPalpha Binding Sites That Activate Some Tissue-Specific Genes." *Proceedings of the National Academy of Sciences of the United States of America* 107 (47): 20311–16. https://doi.org/10.1073/pnas.1008688107.

Ritter, Nicole, Tamer Ali, Nina Kopitchinski, Peggy Schuster, Arica Beisaw, David A. Hendrix, Marcel H. Schulz, Michaela Müller-McNicoll, Stefanie Dimmeler, and Phillip Grote. 2019. "The LncRNA Locus Handsdown Regulates Cardiac Gene Programs and Is Essential for Early Mouse Development." *Developmental Cell* 50 (5): 644-657.e8. https://doi.org/10.1016/j.devcel.2019.07.013.

Rocchi, Laura, Annalisa Pacilli, Rajni Sethi, Marianna Penzo, Robert J. Schneider, Davide Treré, Maurizio Brigotti, and Lorenzo Montanaro. 2013. "Dyskerin Depletion Increases VEGF MRNA Internal Ribosome Entry Site-Mediated Translation." *Nucleic Acids Research* 41 (17): 8308–18. https://doi.org/10.1093/nar/gkt587.

Roelfsema, Jeroen H., Stefan J. White, Yavuz Ariyürek, Deborah Bartholdi, Dunja Niedrist, Francesco Papadia, Carlos A. Bacino, et al. 2005. "Genetic Heterogeneity in Rubinstein-Taybi Syndrome: Mutations in Both the CBP and EP300 Genes Cause Disease." *The American Journal of Human Genetics* 76 (4): 572–80. https://doi.org/10.1086/429130.

Rohrer, D. C., and M. Sundaralingam. 1970. "Stereochemistry of Nucleic Acids and Their Constituents. VI. The Crystal Structure and Conformation of Dihydrouracil: A Minor Base of Transfer-Ribonucleic Acid." *Acta Crystallographica. Section B: Structural Crystallography and Crystal Chemistry* 26 (5): 546–53. https://doi.org/10.1107/s0567740870002789.

Roundtree, Ian A., Molly E. Evans, Tao Pan, and Chuan He. 2017. "Dynamic RNA Modifications in Gene Expression Regulation." *Cell* 169 (7): 1187–1200. https://doi.org/10.1016/j.cell.2017.05.045.

Roundtree, Ian A, Guan-Zheng Luo, Zijie Zhang, Xiao Wang, Tao Zhou, Yiquang Cui, Jiahao Sha, et al. 2017. "YTHDC1 Mediates Nuclear Export of N6-Methyladenosine Methylated MRNAs." Edited by Nick J Proudfoot. *ELife* 6 (October): e31311. https://doi.org/10.7554/eLife.31311.

Roura Frigolé, Helena, Noelia Camacho, Maria Castellví Coma, Carla Fernández-Lozano, Jorge García-Lema, Àlbert Rafels-Ybern, Albert Canals, Miquel Coll, and Lluís Ribas de Pouplana. 2019. "TRNA Deamination by ADAT Requires Substrate-Specific Recognition Mechanisms and Can Be Inhibited by TRFs." *RNA (New York, N.Y.)* 25 (5): 607–19. https://doi.org/10.1261/rna.068189.118.

Rowley, Janet D. 1998. "The Critical Role of Chromosome Translocations in Human Leukemias." *Annual Review of Genetics* 32 (1): 495–519. https://doi.org/10.1146/annurev.genet.32.1.495.

Ruhl, Donald D., Jingji Jin, Yong Cai, Selene Swanson, Laurence Florens, Michael P. Washburn, Ronald C. Conaway, Joan Weliky Conaway, and John C. Chrivia. 2006. "Purification of a Human SRCAP Complex That Remodels Chromatin by Incorporating the Histone Variant H2A.Z into Nucleosomes." *Biochemistry* 45 (17): 5671–77. https://doi.org/10.1021/bi060043d.

Russler-Germain, David A., David H. Spencer, Margaret A. Young, Tamara L. Lamprecht, Christopher A. Miller, Robert Fulton, Matthew R. Meyer, et al. 2014. "The R882H DNMT3A Mutation Associated with AML Dominantly Inhibits Wild-Type DNMT3A by Blocking Its Ability to Form Active Tetramers." *Cancer Cell* 25 (4): 442–54. https://doi.org/10.1016/j.ccr.2014.02.010.

Ryan, Daniel P., and David J. Tremethick. 2018. "The Interplay between H2A.Z and H3K9 Methylation in Regulating HP1α Binding to Linker Histone-Containing Chromatin." *Nucleic Acids Research* 46 (18): 9353–66. https://doi.org/10.1093/nar/gky632.

Sabari, Benjamin R., Zhanyun Tang, He Huang, Vladimir Yong-Gonzalez, Henrik Molina, Ha Eun Kong, Lunzhi Dai, et al. 2015. "Intracellular Crotonyl-CoA Stimulates Transcription through P300-Catalyzed Histone Crotonylation." *Molecular Cell* 58 (2): 203–15. https://doi.org/10.1016/j.molcel.2015.02.029.

Sadoul, Karin, Jin Wang, Boubou Diagouraga, and Saadi Khochbin. 2011. "The Tale of Protein Lysine Acetylation in the Cytoplasm." *Journal of Biomedicine & Biotechnology* 2011: 970382. https://doi.org/10.1155/2011/970382.

Saijo, Y., G. Sato, K. Usui, M. Sato, M. Sagawa, T. Kondo, Y. Minami, and T. Nukiwa. 2001. "Expression of Nucleolar Protein P120 Predicts Poor Prognosis in Patients with Stage I Lung Adenocarcinoma." *Annals of Oncology: Official Journal of the European Society for Medical Oncology* 12 (8): 1121–25. https://doi.org/10.1023/a:1011617707999.

Sajini, Abdulrahim A., Nila Roy Choudhury, Rebecca E. Wagner, Susanne Bornelöv, Tommaso Selmi, Christos Spanos, Sabine Dietmann, Juri Rappsilber, Gracjan Michlewski, and Michaela Frye. 2019. "Loss of 5-Methylcytosine Alters the Biogenesis of Vault-Derived Small RNAs to Coordinate Epidermal Differentiation." *Nature Communications* 10 (1): 1–13. https://doi.org/10.1038/s41467-019-10020-7.

Saksouk, Nehmé, Nikita Avvakumov, Karen S. Champagne, Tiffany Hung, Yannick Doyon, Christelle Cayrou, Eric Paquet, et al. 2009. "HBO1 HAT Complexes Target Chromatin throughout Gene Coding Regions via Multiple PHD Finger Interactions with Histone H3 Tail." *Molecular Cell* 33 (2): 257–65. https://doi.org/10.1016/j.molcel.2009.01.007.

Salehi Chaleshtori, Ahmad Reza, Noriko Miyake, Mohammad Ahmadvand, Oranous Bashti, Naomichi Matsumoto, and Mehrdad Noruzinia. 2018. "A Novel 8-Bp Duplication in ADAT3 Causes Mild Intellectual Disability." *Human Genome Variation* 5 (1): 1–3. https://doi.org/10.1038/s41439-018-0007-9.

Santos-Rosa, Helena, Robert Schneider, Bradley E. Bernstein, Nickoletta Karabetsou, Antonin Morillon, Christoph Weise, Stuart L. Schreiber, Jane Mellor, and Tony Kouzarides. 2003. "Methylation of Histone H3 K4 Mediates Association of the Isw1p ATPase with Chromatin." *Molecular Cell* 12 (5): 1325–32. https://doi.org/10.1016/S1097-2765(03)00438-6.

Sanulli, S., M. J. Trnka, V. Dharmarajan, R. W. Tibble, B. D. Pascal, A. L. Burlingame, P. R. Griffin, J. D. Gross, and G. J. Narlikar. 2019. "HP1 Reshapes Nucleosome Core to Promote Phase Separation of Heterochromatin." *Nature* 575 (7782): 390–94. https://doi.org/10.1038/s41586-019-1669-2.

Sarcinella, Elizabeth, Philip C. Zuzarte, Priscilla N. I. Lau, Ryan Draker, and Peter Cheung. 2007. "Monoubiquitylation of H2A.Z Distinguishes Its Association with Euchromatin or Facultative Heterochromatin." *Molecular and Cellular Biology* 27 (18): 6457–68. https://doi.org/10.1128/MCB.00241-07.

Sardina, Jose Luis, Samuel Collombet, Tian V. Tian, Antonio Gómez, Bruno Di Stefano, Clara Berenguer, Justin Brumbaugh, et al. 2018. "Transcription Factors Drive Tet2-Mediated Enhancer Demethylation to Reprogram Cell Fate." *Cell Stem Cell* 23 (5): 727-741.e9. https://doi.org/10.1016/j.stem.2018.08.016.

Sauer, Paul V, Yajie Gu, Wallace H Liu, Francesca Mattiroli, Daniel Panne, Karolin Luger, and Mair EA Churchill. 2018. "Mechanistic Insights into Histone Deposition and Nucleosome Assembly by the Chromatin Assembly Factor-1." *Nucleic Acids Research* 46 (19): 9907–17. https://doi.org/10.1093/nar/gky823.

Schaefer, Matthias, Tim Pollex, Katharina Hanna, Francesca Tuorto, Madeleine Meusburger, Mark Helm, and Frank Lyko. 2010. "RNA Methylation by Dnmt2 Protects Transfer RNAs against Stress-Induced Cleavage." *Genes & Development* 24 (15): 1590–95. https://doi.org/10.1101/gad.586710.

Schaub, Myriam, and Walter Keller. 2002. "RNA Editing by Adenosine Deaminases Generates RNA and Protein Diversity." *Biochimie* 84 (8): 791–803. https://doi.org/10.1016/s0300-9084(02)01446-3.

Schertzer, Megan D., Keean C. A. Braceros, Joshua Starmer, Rachel E. Cherney, David M. Lee, Gabriela Salazar, Megan Justice, et al. 2019. "LncRNA-Induced Spread of Polycomb Controlled by Genome Architecture, RNA Abundance, and CpG Island DNA." *Molecular Cell* 75 (3): 523-537.e10. https://doi.org/10.1016/j.molcel.2019.05.028.

Schimmel, Paul. 2018. "The Emerging Complexity of the TRNA World: Mammalian TRNAs beyond Protein Synthesis." *Nature Reviews Molecular Cell Biology* 19 (1): 45–58. https://doi.org/10.1038/nrm.2017.77.

Schmitt, Adam M., Julia T. Garcia, Tiffany Hung, Ryan A. Flynn, Ying Shen, Kun Qu, Alexander Y. Payumo, et al. 2016. "An Inducible Long Noncoding RNA Amplifies DNA Damage Signaling." *Nature Genetics* 48 (11): 1370–76. https://doi.org/10.1038/ng.3673.

Schneider, William M., Meike Dittmann Chevillotte, and Charles M. Rice. 2014. "Interferon-Stimulated Genes: A Complex Web of Host Defenses." *Annual Review of Immunology* 32 (1): 513–45. https://doi.org/10.1146/annurev-immunol-032713-120231.

Schöller, Eva, Franziska Weichmann, Thomas Treiber, Sam Ringle, Nora Treiber, Andrew Flatley, Regina Feederle, Astrid Bruckmann, and Gunter Meister. 2018. "Interactions, Localization, and Phosphorylation of the M6A Generating METTL3-METTL14-WTAP Complex." *RNA (New York, N.Y.)* 24 (4): 499–512. https://doi.org/10.1261/rna.064063.117.

Schuettengruber, Bernd, Henri-Marc Bourbon, Luciano Di Croce, and Giacomo Cavalli. 2017. “Genome Regulation by Polycomb and Trithorax: 70 Years and Counting.” *Cell* 171 (1): 34–57. https://doi.org/10.1016/j.cell.2017.08.002.

Schug, Zachary T., Barrie Peck, Dylan T. Jones, Qifeng Zhang, Shaun Grosskurth, Israt S. Alam, Louise M. Goodwin, et al. 2015. “Acetyl-CoA Synthetase 2 Promotes Acetate Utilization and Maintains Cancer Cell Growth under Metabolic Stress.” *Cancer Cell* 27 (1): 57–71. https://doi.org/10.1016/j.ccell.2014.12.002.

Schumacher, Armin, Cynthia Faust, and Terry Magnuson. 1996. “Positional Cloning of a Global Regulator of Anterior–Posterior Patterning in Mice.” *Nature* 383 (6597): 250–53. https://doi.org/10.1038/383250a0.

Schwartz, Schraga, Douglas A. Bernstein, Maxwell R. Mumbach, Marko Jovanovic, Rebecca H. Herbst, Brian X. León-Ricardo, Jesse M. Engreitz, et al. 2014. “Transcriptome-Wide Mapping Reveals Widespread Dynamic-Regulated Pseudouridylation of NcRNA and MRNA.” *Cell* 159 (1): 148–62. https://doi.org/10.1016/j.cell.2014.08.028.

Schwartzentruber, Jeremy, Andrey Korshunov, Xiao-Yang Liu, David T. W. Jones, Elke Pfaff, Karine Jacob, Dominik Sturm, et al. 2012. “Driver Mutations in Histone H3.3 and Chromatin Remodelling Genes in Paediatric Glioblastoma.” *Nature* 482 (7384): 226–31. https://doi.org/10.1038/nature10833.

Schwer, Bjoern, Jakob Bunkenborg, Regis O. Verdin, Jens S. Andersen, and Eric Verdin. 2006. “Reversible Lysine Acetylation Controls the Activity of the Mitochondrial Enzyme Acetyl-CoA Synthetase 2.” *Proceedings of the National Academy of Sciences* 103 (27): 10224–29. https://doi.org/10.1073/pnas.0603968103.

Semer, M., B. Bidon, A. Larnicol, G. Caliskan, P. Catez, J. M. Egly, F. Coin, and N. Le May. 2019. “DNA Repair Complex Licenses Acetylation of H2A.Z.1 by KAT2A during Transcription.” *Nature Chemical Biology* 15 (10): 992–1000. https://doi.org/10.1038/s41589-019-0354-y.

Senger, B., S. Auxilien, U. Englisch, F. Cramer, and F. Fasiolo. 1997. “The Modified Wobble Base Inosine in Yeast TRNAIle Is a Positive Determinant for Aminoacylation by Isoleucyl-TRNA Synthetase.” *Biochemistry* 36 (27): 8269–75. https://doi.org/10.1021/bi970206l.

Sh, Liaw, Chang Yj, Lai Ct, Chang Hc, and Chang Gg. 2004. “Crystal Structure of Bacillus Subtilis Guanine Deaminase: The First Domain-Swapped Structure in the Cytidine Deaminase Superfamily.” *The Journal of Biological Chemistry* 279 (34): 35479–85. https://doi.org/10.1074/jbc.m405304200.

Sharif, Jafar, Masahiro Muto, Shin-ichiro Takebayashi, Isao Suetake, Akihiro Iwamatsu, Takaho A. Endo, Jun Shinga, et al. 2007. “The SRA Protein Np95 Mediates Epigenetic Inheritance by Recruiting Dnmt1 to Methylated DNA.” *Nature* 450 (7171): 908–12. https://doi.org/10.1038/nature06397.

Sharkia, Rajech, Abdelnaser Zalan, Azhar Jabareen-Masri, Hazar Zahalka, and Muhammad Mahajnah. 2019. “A New Case Confirming and Expanding the Phenotype Spectrum of ADAT3-Related Intellectual Disability Syndrome.” *European Journal of Medical Genetics* 62 (11): 103549. https://doi.org/10.1016/j.ejmg.2018.10.001.

Sharma, Sahil, Fabian Poetz, Marius Bruer, Thi Bach Nga Ly-Hartig, Johanna Schott, Bertrand Séraphin, and Georg Stoecklin. 2016. “Acetylation-Dependent Control of Global Poly(A) RNA Degradation by CBP/P300 and HDAC1/2.” *Molecular Cell* 63 (6): 927–38. https://doi.org/10.1016/j.molcel.2016.08.030.

Sheikh, Bilal N., and Asifa Akhtar. 2019. “The Many Lives of KATs — Detectors, Integrators and Modulators of the Cellular Environment.” *Nature Reviews Genetics* 20 (1): 7–23. https://doi.org/10.1038/s41576-018-0072-4.

Sheikh, Bilal N., Stanley C. W. Lee, Farrah El-Saafin, Hannah K. Vanyai, Yifang Hu, Swee Heng Milon Pang, Stephanie Grabow, et al. 2015. "MOZ Regulates B-Cell Progenitors and, Consequently, Moz Haploinsufficiency Dramatically Retards MYC-Induced Lymphoma Development." *Blood* 125 (12): 1910–21. https://doi.org/10.1182/blood-2014-08-594655.

Shen, Qicong, Qian Zhang, Yang Shi, Qingzhu Shi, Yanyan Jiang, Yan Gu, Zhiqing Li, et al. 2018. "Tet2 Promotes Pathogen Infection-Induced Myelopoiesis through MRNA Oxidation." *Nature* 554 (7690): 123–27. https://doi.org/10.1038/nature25434.

Shi, Hailing, Xiao Wang, Zhike Lu, Boxuan S. Zhao, Honghui Ma, Phillip J. Hsu, Chang Liu, and Chuan He. 2017. "YTHDF3 Facilitates Translation and Decay of N 6 -Methyladenosine-Modified RNA." *Cell Research* 27 (3): 315–28. https://doi.org/10.1038/cr.2017.15.

Shi, Jian, Yifan Wang, Lei Zeng, Yadi Wu, Jiong Deng, Qiang Zhang, Yiwei Lin, et al. 2014. "Disrupting the Interaction of BRD4 with Diacetylated Twist Suppresses Tumorigenesis in Basal-like Breast Cancer." *Cancer Cell* 25 (2): 210–25. https://doi.org/10.1016/j.ccr.2014.01.028.

Shi, Yujiang, Fei Lan, Caitlin Matson, Peter Mulligan, Johnathan R. Whetstine, Philip A. Cole, Robert A. Casero, and Yang Shi. 2004. "Histone Demethylation Mediated by the Nuclear Amine Oxidase Homolog LSD1." *Cell* 119 (7): 941–53. https://doi.org/10.1016/j.cell.2004.12.012.

Shida, Toshinobu, Juan G. Cueva, Zhenjie Xu, Miriam B. Goodman, and Maxence V. Nachury. 2010. "The Major Alpha-Tubulin K40 Acetyltransferase AlphaTAT1 Promotes Rapid Ciliogenesis and Efficient Mechanosensation." *Proceedings of the National Academy of Sciences of the United States of America* 107 (50): 21517–22. https://doi.org/10.1073/pnas.1013728107.

Shimazu, Tadahiro, Sueharu Horinouchi, and Minoru Yoshida. 2007. "Multiple Histone Deacetylases and the CREB-Binding Protein Regulate Pre-MRNA 3′-End Processing*." *Journal of Biological Chemistry* 282 (7): 4470–78. https://doi.org/10.1074/jbc.M609745200.

Shoshan, Einav, Aaron K. Mobley, Russell R. Braeuer, Takafumi Kamiya, Li Huang, Mayra E. Vasquez, Ahmad Salameh, et al. 2015. "Reduced Adenosine-to-Inosine MiR-455-5p Editing Promotes Melanoma Growth and Metastasis." *Nature Cell Biology* 17 (3): 311–21. https://doi.org/10.1038/ncb3110.

Shukla, Sanjeev, Ersen Kavak, Melissa Gregory, Masahiko Imashimizu, Bojan Shutinoski, Mikhail Kashlev, Philipp Oberdoerffer, Rickard Sandberg, and Shalini Oberdoerffer. 2011. "CTCF-Promoted RNA Polymerase II Pausing Links DNA Methylation to Splicing." *Nature* 479 (7371): 74–79. https://doi.org/10.1038/nature10442.

Sieron, P., C. Hader, J. Hatina, R. Engers, A. Wlazlinski, M. Müller, and W. A. Schulz. 2009. "DKC1 Overexpression Associated with Prostate Cancer Progression." *British Journal of Cancer* 101 (8): 1410–16. https://doi.org/10.1038/sj.bjc.6605299.

Sims, Robert J., Chi-Fu Chen, Helena Santos-Rosa, Tony Kouzarides, Smita S. Patel, and Danny Reinberg. 2005. "Human but Not Yeast CHD1 Binds Directly and Selectively to Histone H3 Methylated at Lysine 4 via Its Tandem Chromodomains*." *Journal of Biological Chemistry* 280 (51): 41789–92. https://doi.org/10.1074/jbc.C500395200.

Sitbon, David, Ekaterina Boyarchuk, Florent Dingli, Damarys Loew, and Geneviève Almouzni. 2020. "Histone Variant H3.3 Residue S31 Is Essential for Xenopus Gastrulation Regardless of the Deposition Pathway." *Nature Communications* 11 (1): 1256. https://doi.org/10.1038/s41467-020-15084-4.

Sleutels, Frank, Ronald Zwart, and Denise P. Barlow. 2002. “The Non-Coding Air RNA Is Required for Silencing Autosomal Imprinted Genes.” *Nature* 415 (6873): 810–13. https://doi.org/10.1038/415810a.

Sloan, Katherine E., Ahmed S. Warda, Sunny Sharma, Karl-Dieter Entian, Denis L. J. Lafontaine, and Markus T. Bohnsack. 2017. “Tuning the Ribosome: The Influence of RRNA Modification on Eukaryotic Ribosome Biogenesis and Function.” *RNA Biology* 14 (9): 1138–52. https://doi.org/10.1080/15476286.2016.1259781.

Slupianek, Artur, Smitha Yerrum, Fayez F. Safadi, and M. Alexandra Monroy. 2010. “The Chromatin Remodeling Factor SRCAP Modulates Expression of Prostate Specific Antigen and Cellular Proliferation in Prostate Cancer Cells.” *Journal of Cellular Physiology* 224 (2): 369–75. https://doi.org/10.1002/jcp.22132.

Smallwood, Sébastien A., Shin-ichi Tomizawa, Felix Krueger, Nico Ruf, Natasha Carli, Anne Segonds-Pichon, Shun Sato, Kenichiro Hata, Simon R. Andrews, and Gavin Kelsey. 2011. “Dynamic CpG Island Methylation Landscape in Oocytes and Preimplantation Embryos.” *Nature Genetics* 43 (8): 811–14. https://doi.org/10.1038/ng.864.

Smith, Susan, and Bruce Stillman. 1989. “Purification and Characterization of CAF-I, a Human Cell Factor Required for Chromatin Assembly during DNA Replication in Vitro.” *Cell* 58 (1): 15–25. https://doi.org/10.1016/0092-8674(89)90398-X.

Smolle, Michaela, Swaminathan Venkatesh, Madelaine M. Gogol, Hua Li, Ying Zhang, Laurence Florens, Michael P. Washburn, and Jerry L. Workman. 2012. “Chromatin Remodelers Isw1 and Chd1 Maintain Chromatin Structure during Transcription by Preventing Histone Exchange.” *Nature Structural & Molecular Biology* 19 (9): 884–92. https://doi.org/10.1038/nsmb.2312.

Sneeringer, Christopher J., Margaret Porter Scott, Kevin W. Kuntz, Sarah K. Knutson, Roy M. Pollock, Victoria M. Richon, and Robert A. Copeland. 2010. “Coordinated Activities of Wild-Type plus Mutant EZH2 Drive Tumor-Associated Hypertrimethylation of Lysine 27 on Histone H3 (H3K27) in Human B-Cell Lymphomas.” *Proceedings of the National Academy of Sciences of the United States of America* 107 (49): 20980–85. https://doi.org/10.1073/pnas.1012525107.

Somoza, John R, Robert J Skene, Bradley A Katz, Clifford Mol, Joseph D Ho, Andy J Jennings, Christine Luong, et al. 2004. “Structural Snapshots of Human HDAC8 Provide Insights into the Class I Histone Deacetylases.” *Structure* 12 (7): 1325–34. https://doi.org/10.1016/j.str.2004.04.012.

Song, Jikui, Olga Rechkoblit, Timothy H. Bestor, and Dinshaw J. Patel. 2011. “Structure of DNMT1-DNA Complex Reveals a Role for Autoinhibition in Maintenance DNA Methylation.” *Science* 331 (6020): 1036–40. https://doi.org/10.1126/science.1195380.

Soukup, G. A., and R. R. Breaker. 1999. “Relationship between Internucleotide Linkage Geometry and the Stability of RNA.” *RNA (New York, N.Y.)* 5 (10): 1308–25. https://doi.org/10.1017/s1355838299990891.

Soutoglou, Evi, Nitsa Katrakili, and Iannis Talianidis. 2000. “Acetylation Regulates Transcription Factor Activity at Multiple Levels.” *Molecular Cell* 5 (4): 745–51. https://doi.org/10.1016/S1097-2765(00)80253-1.

Spenkuch, Felix, Yuri Motorin, and Mark Helm. 2014. “Pseudouridine: Still Mysterious, but Never a Fake (Uridine)!” *RNA Biology* 11 (12): 1540–54. https://doi.org/10.4161/15476286.2014.992278.

Sporn, J. C., G. Kustatscher, T. Hothorn, M. Collado, M. Serrano, T. Muley, P. Schnabel, and A. G. Ladurner. 2009. “Histone MacroH2A Isoforms Predict the Risk of Lung Cancer Recurrence.” *Oncogene* 28 (38): 3423–28. https://doi.org/10.1038/onc.2009.26.

Srinivasan, Sundaramoorthy, Adrian Gabriel Torres, and Lluís Ribas de Pouplana. 2021. "Inosine in Biology and Disease." *Genes* 12 (4): 600. https://doi.org/10.3390/genes12040600.

Stangeland, Biljana, Awais A. Mughal, Zanina Grieg, Cecilie Jonsgar Sandberg, Mrinal Joel, Ståle Nygård, Torstein Meling, Wayne Murrell, Einar O. Vik Mo, and Iver A. Langmoen. 2015. "Combined Expressional Analysis, Bioinformatics and Targeted Proteomics Identify New Potential Therapeutic Targets in Glioblastoma Stem Cells." *Oncotarget* 6 (28): 26192–215. https://doi.org/10.18632/oncotarget.4613.

Statello, Luisa, Chun-Jie Guo, Ling-Ling Chen, and Maite Huarte. 2021a. "Gene Regulation by Long Non-Coding RNAs and Its Biological Functions." *Nature Reviews Molecular Cell Biology* 22 (2): 96–118. https://doi.org/10.1038/s41580-020-00315-9.

Statello, Luisa, Chun-Jie Guo, Ling-Ling Chen, and Maite Huarte. 2021b. "Gene Regulation by Long Non-Coding RNAs and Its Biological Functions." *Nature Reviews Molecular Cell Biology* 22 (2): 96–118. https://doi.org/10.1038/s41580-020-00315-9.

Statham, Aaron L., Mark D. Robinson, Jenny Z. Song, Marcel W. Coolen, Clare Stirzaker, and Susan J. Clark. 2012. "Bisulfite Sequencing of Chromatin Immunoprecipitated DNA (BisChIP-Seq) Directly Informs Methylation Status of Histone-Modified DNA." *Genome Research* 22 (6): 1120–27. https://doi.org/10.1101/gr.132076.111.

Steinberg, S, and R Cedergren. 1995. "A Correlation between N2-Dimethylguanosine Presence and Alternate TRNA Conformers." *RNA* 1 (9): 886–91.

Stielow, Bastian, Florian Finkernagel, Thorsten Stiewe, Andrea Nist, and Guntram Suske. 2018. "MGA, L3MBTL2 and E2F6 Determine Genomic Binding of the Non-Canonical Polycomb Repressive Complex PRC1.6." *PLoS Genetics* 14 (1): e1007193. https://doi.org/10.1371/journal.pgen.1007193.

Stoeckli, Esther T. 2018. "Understanding Axon Guidance: Are We Nearly There Yet?" *Development* 145 (10). https://doi.org/10.1242/dev.151415.

Strom, Samuel P., Reymundo Lozano, Hane Lee, Naghmeh Dorrani, John Mann, Patricia F. O'Lague, Nicole Mans, et al. 2014. "De Novo Variants in the KMT2A (MLL) Gene Causing Atypical Wiedemann-Steiner Syndrome in Two Unrelated Individuals Identified by Clinical Exome Sequencing." *BMC Medical Genetics* 15 (1): 1–8. https://doi.org/10.1186/1471-2350-15-49.

Stuart, J. W., Z. Gdaniec, R. Guenther, M. Marszalek, E. Sochacka, A. Malkiewicz, and P. F. Agris. 2000. "Functional Anticodon Architecture of Human TRNALys3 Includes Disruption of Intraloop Hydrogen Bonding by the Naturally Occurring Amino Acid Modification, T6A." *Biochemistry* 39 (44): 13396–404. https://doi.org/10.1021/bi0013039.

Suganuma, Tamaki, and Jerry L. Workman. 2011. "Signals and Combinatorial Functions of Histone Modifications." *Annual Review of Biochemistry* 80: 473–99. https://doi.org/10.1146/annurev-biochem-061809-175347.

Sullivan, K F, M Hechenberger, and K Masri. 1994. "Human CENP-A Contains a Histone H3 Related Histone Fold Domain That Is Required for Targeting to the Centromere." *Journal of Cell Biology* 127 (3): 581–92. https://doi.org/10.1083/jcb.127.3.581.

Sun, Ting, Xuan Li, Peng Zhang, Wen-Dan Chen, Hai-liang Zhang, Dan-Dan Li, Rong Deng, et al. 2015. "Acetylation of Beclin 1 Inhibits Autophagosome Maturation and Promotes Tumour Growth." *Nature Communications* 6 (1): 7215. https://doi.org/10.1038/ncomms8215.

Sun, Xiao-Jian, Ju Wei, Xin-Yan Wu, Ming Hu, Lan Wang, Hai-Hong Wang, Qing-Hua Zhang, Sai-Juan Chen, Qiu-Hua Huang, and Zhu Chen. 2005. "Identification and Characterization of a Novel Human Histone H3 Lysine 36-Specific

Methyltransferase*." *Journal of Biological Chemistry* 280 (42): 35261–71. https://doi.org/10.1074/jbc.M504012200.

Sun, Zhen, and Emily Bernstein. 2019. "Histone Variant MacroH2A: From Chromatin Deposition to Molecular Function." *Essays in Biochemistry* 63 (1): 59–74. https://doi.org/10.1042/EBC20180062.

Sun, Zhen, Dan Filipescu, Joshua Andrade, Alexandre Gaspar-Maia, Beatrix Ueberheide, and Emily Bernstein. 2018. "Transcription-Associated Histone Pruning Demarcates MacroH2A Chromatin Domains." *Nature Structural & Molecular Biology* 25 (10): 958–70. https://doi.org/10.1038/s41594-018-0134-5.

Sundaresan, N. R., V. B. Pillai, D. Wolfgeher, S. Samant, P. Vasudevan, V. Parekh, H. Raghuraman, J. M. Cunningham, M. Gupta, and M. P. Gupta. 2011. "The Deacetylase SIRT1 Promotes Membrane Localization and Activation of Akt and PDK1 During Tumorigenesis and Cardiac Hypertrophy." *Science Signaling* 4 (182): ra46–ra46. https://doi.org/10.1126/scisignal.2001465.

Sutendra, Gopinath, Adam Kinnaird, Peter Dromparis, Roxane Paulin, Trevor H. Stenson, Alois Haromy, Kyoko Hashimoto, Nancy Zhang, Eric Flaim, and Evangelos D. Michelakis. 2014. "A Nuclear Pyruvate Dehydrogenase Complex Is Important for the Generation of Acetyl-CoA and Histone Acetylation." *Cell* 158 (1): 84–97. https://doi.org/10.1016/j.cell.2014.04.046.

Suto, Robert K., Michael J. Clarkson, David J. Tremethick, and Karolin Luger. 2000. "Crystal Structure of a Nucleosome Core Particle Containing the Variant Histone H2A.Z." *Nature Structural Biology* 7 (12): 1121–24. https://doi.org/10.1038/81971.

Suzuki, Takeo, and Tsutomu Suzuki. 2014. "A Complete Landscape of Post-Transcriptional Modifications in Mammalian Mitochondrial TRNAs." *Nucleic Acids Research* 42 (11): 7346–57. https://doi.org/10.1093/nar/gku390.

Suzuki, Tsutomu. 2021. "The Expanding World of TRNA Modifications and Their Disease Relevance." *Nature Reviews Molecular Cell Biology*, March, 1–18. https://doi.org/10.1038/s41580-021-00342-0.

Tachiwana, Hiroaki, Wataru Kagawa, Tatsuya Shiga, Akihisa Osakabe, Yuta Miya, Kengo Saito, Yoko Hayashi-Takanaka, et al. 2011. "Crystal Structure of the Human Centromeric Nucleosome Containing CENP-A." *Nature* 476 (7359): 232–35. https://doi.org/10.1038/nature10258.

Tagami, Hideaki, Dominique Ray-Gallet, Geneviève Almouzni, and Yoshihiro Nakatani. 2004. "Histone H3.1 and H3.3 Complexes Mediate Nucleosome Assembly Pathways Dependent or Independent of DNA Synthesis." *Cell* 116 (1): 51–61. https://doi.org/10.1016/S0092-8674(03)01064-X.

Tahiliani, Mamta, Kian Peng Koh, Yinghua Shen, William A. Pastor, Hozefa Bandukwala, Yevgeny Brudno, Suneet Agarwal, et al. 2009. "Conversion of 5-Methylcytosine to 5-Hydroxymethylcytosine in Mammalian DNA by MLL Partner TET1." *Science* 324 (5929): 930–35. https://doi.org/10.1126/science.1170116.

Takata, Atsushi, Bin Xu, Iuliana Ionita-Laza, J. Louw Roos, Joseph A. Gogos, and Maria Karayiorgou. 2014. "Loss-of-Function Variants in Schizophrenia Risk and SETD1A as a Candidate Susceptibility Gene." *Neuron* 82 (4): 773–80. https://doi.org/10.1016/j.neuron.2014.04.043.

Takemoto, Chie, Linda L. Spremulli, Lisa A. Benkowski, Takuya Ueda, Takashi Yokogawa, and Kimitsuna Watanabe. 2009. "Unconventional Decoding of the AUA Codon as Methionine by Mitochondrial TRNA Met with the Anticodon f 5 CAU as Revealed with a Mitochondrial in Vitro Translation System." *Nucleic Acids Research* 37 (5): 1616–27. https://doi.org/10.1093/nar/gkp001.

Takeshita, Kohei, Isao Suetake, Eiki Yamashita, Michihiro Suga, Hirotaka Narita, Atsushi Nakagawa, and Shoji Tajima. 2011. “Structural Insight into Maintenance Methylation by Mouse DNA Methyltransferase 1 (Dnmt1).” *Proceedings of the National Academy of Sciences of the United States of America* 108 (22): 9055–59. https://doi.org/10.1073/pnas.1019629108.

Tan, Meng How, Qin Li, Raghuvaran Shanmugam, Robert Piskol, Jennefer Kohler, Amy N. Young, Kaiwen Ivy Liu, et al. 2017. “Dynamic Landscape and Regulation of RNA Editing in Mammals.” *Nature* 550 (7675): 249–54. https://doi.org/10.1038/nature24041.

Tan, Minjia, Chao Peng, Kristin A. Anderson, Peter Chhoy, Zhongyu Xie, Lunzhi Dai, Jeongsoon Park, et al. 2014. “Lysine Glutarylation Is a Protein Posttranslational Modification Regulated by SIRT5.” *Cell Metabolism* 19 (4): 605–17. https://doi.org/10.1016/j.cmet.2014.03.014.

Tang, Zhanyun, Wei-Yi Chen, Miho Shimada, Uyen T. T. Nguyen, Jaehoon Kim, Xiao-Jian Sun, Toru Sengoku, et al. 2013. “SET1 and P300 Act Synergistically, through Coupled Histone Modifications, in Transcriptional Activation by P53.” *Cell* 154 (2): 297–310. https://doi.org/10.1016/j.cell.2013.06.027.

Tao, Yongguang, Sichuan Xi, Jigui Shan, Alika Maunakea, Anney Che, Victorino Briones, Eunice Y. Lee, et al. 2011. “Lsh, Chromatin Remodeling Family Member, Modulates Genome-Wide Cytosine Methylation Patterns at Nonrepeat Sequences.” *Proceedings of the National Academy of Sciences of the United States of America* 108 (14): 5626–31. https://doi.org/10.1073/pnas.1017000108.

Tatton-Brown, Katrina, Anne Murray, Sandra Hanks, Jenny Douglas, Ruth Armstrong, Siddharth Banka, Lynne M. Bird, et al. 2013. “Weaver Syndrome and EZH2 Mutations: Clarifying the Clinical Phenotype.” *American Journal of Medical Genetics. Part A* 161A (12): 2972–80. https://doi.org/10.1002/ajmg.a.36229.

Tatton-Brown, Katrina, Sheila Seal, Elise Ruark, Jenny Harmer, Emma Ramsay, Silvana del Vecchio Duarte, Anna Zachariou, et al. 2014. “Mutations in the DNA Methyltransferase Gene DNMT3A Cause an Overgrowth Syndrome with Intellectual Disability.” *Nature Genetics* 46 (4): 385–88. https://doi.org/10.1038/ng.2917.

Tayrac, Marie de, Stephan Saikali, Marc Aubry, Pascale Bellaud, Rachel Boniface, Véronique Quillien, and Jean Mosser. 2013. “Prognostic Significance of EDN/RB, HJURP, P60/CAF-1 and PDLI4, Four New Markers in High-Grade Gliomas.” *PloS One* 8 (9): e73332. https://doi.org/10.1371/journal.pone.0073332.

Terranova, Rémi, Hanane Agherbi, Annie Boned, Stéphane Meresse, and Malek Djabali. 2006. “Histone and DNA Methylation Defects at Hox Genes in Mice Expressing a SET Domain-Truncated Form of Mll.” *Proceedings of the National Academy of Sciences of the United States of America* 103 (17): 6629–34. https://doi.org/10.1073/pnas.0507425103.

Tham, Emma, Anna Lindstrand, Avni Santani, Helena Malmgren, Addie Nesbitt, Holly A. Dubbs, Elaine H. Zackai, et al. 2015. “Dominant Mutations in KAT6A Cause Intellectual Disability with Recognizable Syndromic Features.” *The American Journal of Human Genetics* 96 (3): 507–13. https://doi.org/10.1016/j.ajhg.2015.01.016.

Thomas, Elizabeth, Andrea M. Lewis, Yaping Yang, Sirisak Chanprasert, Lorraine Potocki, and Daryl A. Scott. 2019. “Novel Missense Variants in ADAT3 as a Cause of Syndromic Intellectual Disability.” *Journal of Pediatric Genetics* 8 (4): 244–51. https://doi.org/10.1055/s-0039-1693151.

Thompson, Paul R., Dongxia Wang, Ling Wang, Marcella Fulco, Natalia Pediconi, Dianzheng Zhang, Woojin An, et al. 2004. “Regulation of the P300 HAT Domain via a Novel Activation Loop.” *Nature Structural & Molecular Biology* 11 (4): 308–15. https://doi.org/10.1038/nsmb740.

Thuy-Boun, Alexander S., Justin M. Thomas, Herra L. Grajo, Cody M. Palumbo, SeHee Park, Luan T. Nguyen, Andrew J. Fisher, and Peter A. Beal. 2020. “Asymmetric Dimerization of Adenosine Deaminase Acting on RNA Facilitates Substrate Recognition.” *Nucleic Acids Research* 48 (14): 7958–72. https://doi.org/10.1093/nar/gkaa532.

Tian, Qiu-Hong, Mei-Fang Zhang, Jin-Sheng Zeng, Rong-Guang Luo, Yang Wen, Jun Chen, Liu-Gen Gan, and Jian-Ping Xiong. 2019. “METTL1 Overexpression Is Correlated with Poor Prognosis and Promotes Hepatocellular Carcinoma via PTEN.” *Journal of Molecular Medicine (Berlin, Germany)* 97 (11): 1535–45. https://doi.org/10.1007/s00109-019-01830-9.

Timinszky, Gyula, Susanne Till, Paul O. Hassa, Michael Hothorn, Georg Kustatscher, Bianca Nijmeijer, Julien Colombelli, et al. 2009. “A Macrodomain-Containing Histone Rearranges Chromatin upon Sensing PARP1 Activation.” *Nature Structural & Molecular Biology* 16 (9): 923–29. https://doi.org/10.1038/nsmb.1664.

Tomikawa, Chie. 2018. “7-Methylguanosine Modifications in Transfer RNA (TRNA).” *International Journal of Molecular Sciences* 19 (12): 4080. https://doi.org/10.3390/ijms19124080.

Torigoe, Sharon E., Debra L. Urwin, Haruhiko Ishii, Douglas E. Smith, and James T. Kadonaga. 2011. “Identification of a Rapidly Formed Nonnucleosomal Histone-DNA Intermediate That Is Converted into Chromatin by ACF.” *Molecular Cell* 43 (4): 638–48. https://doi.org/10.1016/j.molcel.2011.07.017.

Torres, Adrian Gabriel, David Piñeyro, Marta Rodríguez-Escribà, Noelia Camacho, Oscar Reina, Adélaïde Saint-Léger, Liudmila Filonava, Eduard Batlle, and Lluís Ribas de Pouplana. 2015. “Inosine Modifications in Human TRNAs Are Incorporated at the Precursor TRNA Level.” *Nucleic Acids Research* 43 (10): 5145–57. https://doi.org/10.1093/nar/gkv277.

Tsukada, Yu-ichi, Jia Fang, Hediye Erdjument-Bromage, Maria E. Warren, Christoph H. Borchers, Paul Tempst, and Yi Zhang. 2006. “Histone Demethylation by a Family of JmjC Domain-Containing Proteins.” *Nature* 439 (7078): 811–16. https://doi.org/10.1038/nature04433.

Tuorto, Francesca, Reinhard Liebers, Tanja Musch, Matthias Schaefer, Sarah Hofmann, Stefanie Kellner, Michaela Frye, Mark Helm, Georg Stoecklin, and Frank Lyko. 2012. “RNA Cytosine Methylation by Dnmt2 and NSun2 Promotes TRNA Stability and Protein Synthesis.” *Nature Structural & Molecular Biology* 19 (9): 900–905. https://doi.org/10.1038/nsmb.2357.

Udugama, Maheshi, Fiona T. M Chang, F. Lyn Chan, Michelle C. Tang, Hilda A. Pickett, James D. R McGhie, Lynne Mayne, Philippe Collas, Jeffrey R. Mann, and Lee H. Wong. 2015. “Histone Variant H3.3 Provides the Heterochromatic H3 Lysine 9 Tri-Methylation Mark at Telomeres.” *Nucleic Acids Research* 43 (21): 10227–37. https://doi.org/10.1093/nar/gkv847.

Ueda, Yoshihide, Masaki Okano, Christine Williams, Taiping Chen, Katia Georgopoulos, and En Li. 2006. “Roles for Dnmt3b in Mammalian Development: A Mouse Model for the ICF Syndrome.” *Development (Cambridge, England)* 133 (6): 1183–92. https://doi.org/10.1242/dev.02293.

Ünal, Elçin, Jill M. Heidinger-Pauli, Woong Kim, Vincent Guacci, Itay Onn, Steven P. Gygi, and Douglas E. Koshland. 2008. “A Molecular Determinant for the Establishment of Sister Chromatid Cohesion.” *Science* 321 (5888): 566–69. https://doi.org/10.1126/science.1157880.

Urbonavicius, Jaunius, Jean Armengaud, and Henri Grosjean. 2006. “Identity Elements Required for Enzymatic Formation of N2,N2-Dimethylguanosine from N2-Monomethylated Derivative and Its Possible Role in Avoiding Alternative Conformations in Archaeal TRNA.” *Journal of Molecular Biology* 357 (2): 387–99. https://doi.org/10.1016/j.jmb.2005.12.087.

Urbonavicius, Jaunius, Guillaume Stahl, Jérôme M. B. Durand, Samia N. Ben Salem, Qiang Qian, Philip J. Farabaugh, and Glenn R. Björk. 2003. “Transfer RNA Modifications That Alter +1 Frameshifting in General Fail to Affect -1 Frameshifting.” *RNA (New York, N.Y.)* 9 (6): 760–68. https://doi.org/10.1261/rna.5210803.

Valdés-Mora, Fátima, Cathryn M. Gould, Yolanda Colino-Sanguino, Wenjia Qu, Jenny Z. Song, Kylie M. Taylor, Fabian A. Buske, et al. 2017. “Acetylated Histone Variant H2A.Z Is Involved in the Activation of Neo-Enhancers in Prostate Cancer.” *Nature Communications* 8 (1): 1346. https://doi.org/10.1038/s41467-017-01393-8.

Valdés-Mora, Fátima, Jenny Z. Song, Aaron L. Statham, Dario Strbenac, Mark D. Robinson, Shalima S. Nair, Kate I. Patterson, David J. Tremethick, Clare Stirzaker, and Susan J. Clark. 2012. “Acetylation of H2A.Z Is a Key Epigenetic Modification Associated with Gene Deregulation and Epigenetic Remodeling in Cancer.” *Genome Research* 22 (2): 307–21. https://doi.org/10.1101/gr.118919.110.

Valente, Valeria, Rodolfo Bortolozo Serafim, Leonardo Cesar de Oliveira, Fernando Soares Adorni, Raul Torrieri, Daniela Pretti da Cunha Tirapelli, Enilza Maria Espreafico, et al. 2013. “Modulation of HJURP (Holliday Junction-Recognizing Protein) Levels Is Correlated with Glioblastoma Cells Survival.” *PloS One* 8 (4): e62200. https://doi.org/10.1371/journal.pone.0062200.

Van Haute, Lindsey, Sabine Dietmann, Laura Kremer, Shobbir Hussain, Sarah F. Pearce, Christopher A. Powell, Joanna Rorbach, et al. 2016. “Deficient Methylation and Formylation of Mt-TRNA Met Wobble Cytosine in a Patient Carrying Mutations in NSUN3.” *Nature Communications* 7 (1): 12039. https://doi.org/10.1038/ncomms12039.

Vannini, Alessandro, Cinzia Volpari, Gessica Filocamo, Elena Caroli Casavola, Mirko Brunetti, Debora Renzoni, Prasun Chakravarty, et al. 2004. “Crystal Structure of a Eukaryotic Zinc-Dependent Histone Deacetylase, Human HDAC8, Complexed with a Hydroxamic Acid Inhibitor.” *Proceedings of the National Academy of Sciences of the United States of America* 101 (42): 15064–69. https://doi.org/10.1073/pnas.0404603101.

Vannini, Alessandro, Cinzia Volpari, Paola Gallinari, Philip Jones, Marco Mattu, Andrea Carfí, Raffaele De Francesco, Christian Steinkühler, and Stefania Di Marco. 2007. “Substrate Binding to Histone Deacetylases as Shown by the Crystal Structure of the HDAC8-Substrate Complex.” *EMBO Reports* 8 (9): 879–84. https://doi.org/10.1038/sj.embor.7401047.

van Tran, Nhan, Felix G M Ernst, Ben R Hawley, Christiane Zorbas, Nathalie Ulryck, Philipp Hackert, Katherine E Bohnsack, et al. 2019. “The Human 18S RRNA M6A Methyltransferase METTL5 Is Stabilized by TRMT112.” *Nucleic Acids Research* 47 (15): 7719–33. https://doi.org/10.1093/nar/gkz619.

Vardabasso, Chiara, Alexandre Gaspar-Maia, Dan Hasson, Sebastian Pünzeler, David Valle-Garcia, Tobias Straub, Eva C. Keilhauer, et al. 2015. “Histone Variant H2A.Z.2 Mediates Proliferation and Drug Sensitivity of Malignant Melanoma.” *Molecular Cell* 59 (1): 75–88. https://doi.org/10.1016/j.molcel.2015.05.009.

Väre, Ville Y. P., Emily R. Eruysal, Amithi Narendran, Kathryn L. Sarachan, and Paul F. Agris. 2017. “Chemical and Conformational Diversity of Modified Nucleosides Affects TRNA Structure and Function.” *Biomolecules* 7 (1). https://doi.org/10.3390/biom7010029.

Vega, Hugo, Quinten Waisfisz, Miriam Gordillo, Norio Sakai, Itaru Yanagihara, Minoru Yamada, Djoke van Gosliga, et al. 2005. “Roberts Syndrome Is Caused by Mutations in ESCO2 , a Human Homolog of Yeast ECO1 That Is Essential for the Establishment of Sister Chromatid Cohesion.” *Nature Genetics* 37 (5): 468–70. https://doi.org/10.1038/ng1548.

Velasco, Guillaume, Florent Hubé, Jérôme Rollin, Damien Neuillet, Cathy Philippe, Haniaa Bouzinba-Segard, Angélique Galvani, Evani Viegas-Péquignot, and Claire Francastel. 2010. “Dnmt3b Recruitment through E2F6 Transcriptional Repressor Mediates Germ-Line Gene Silencing in Murine Somatic Tissues.” *Proceedings of the National Academy of Sciences of the United States of America* 107 (20): 9281–86. https://doi.org/10.1073/pnas.1000473107.

Vendeix, Franck A. P., Agnieszka Dziergowska, Estella M. Gustilo, William D. Graham, Brian Sproat, Andrzej Malkiewicz, and Paul F. Agris. 2008. “Anticodon Domain Modifications Contribute Order to TRNA for Ribosome-Mediated Codon Binding.” *Biochemistry* 47 (23): 6117–29. https://doi.org/10.1021/bi702356j.

Vikram, Ajit, Christopher M. Lewarchik, Jin-Young Yoon, Asma Naqvi, Santosh Kumar, Gina M. Morgan, Julia S. Jacobs, et al. 2017. “Sirtuin 1 Regulates Cardiac Electrical Activity by Deacetylating the Cardiac Sodium Channel.” *Nature Medicine* 23 (3): 361–67. https://doi.org/10.1038/nm.4284.

Vincent, John J., Yun Huang, Pao-Yang Chen, Suhua Feng, Joseph H. Calvopiña, Kevin Nee, Serena A. Lee, et al. 2013. “Stage-Specific Roles for Tet1 and Tet2 in DNA Demethylation in Primordial Germ Cells.” *Cell Stem Cell* 12 (4): 470–78. https://doi.org/10.1016/j.stem.2013.01.016.

Visel, Axel, Matthew J. Blow, Zirong Li, Tao Zhang, Jennifer A. Akiyama, Amy Holt, Ingrid Plajzer-Frick, et al. 2009. “ChIP-Seq Accurately Predicts Tissue-Specific Activity of Enhancers.” *Nature* 457 (7231): 854–58. https://doi.org/10.1038/nature07730.

Vitali, Patrice, and Tamás Kiss. 2019. “Cooperative 2’-O-Methylation of the Wobble Cytidine of Human Elongator TRNAMet(CAT) by a Nucleolar and a Cajal Body-Specific Box C/D RNP.” *Genes & Development* 33 (13–14): 741–46. https://doi.org/10.1101/gad.326363.119.

Vlachogiannis, Nikolaos I., Aikaterini Gatsiou, Domenico Alessandro Silvestris, Kimon Stamatelopoulos, Maria G. Tektonidou, Angela Gallo, Petros P. Sfikakis, and Konstantinos Stellos. 2020. “Increased Adenosine-to-Inosine RNA Editing in Rheumatoid Arthritis.” *Journal of Autoimmunity* 106 (January): 102329. https://doi.org/10.1016/j.jaut.2019.102329.

Voorhees, Rebecca M., Debabrata Mandal, Cajetan Neubauer, Caroline Köhrer, Uttam L. RajBhandary, and V. Ramakrishnan. 2013. “The Structural Basis for Specific Decoding of AUA by Isoleucine TRNA on the Ribosome.” *Nature Structural & Molecular Biology* 20 (5): 641–43. https://doi.org/10.1038/nsmb.2545.

Voss, Anne K., Caitlin Collin, Mathew P. Dixon, and Tim Thomas. 2009. “Moz and Retinoic Acid Coordinately Regulate H3K9 Acetylation, Hox Gene Expression, and Segment Identity.” *Developmental Cell* 17 (5): 674–86. https://doi.org/10.1016/j.devcel.2009.10.006.

Voss, Anne K., Hannah K. Vanyai, Caitlin Collin, Mathew P. Dixon, Tamara J. McLennan, Bilal N. Sheikh, Peter Scambler, and Tim Thomas. 2012. “MOZ Regulates the Tbx1 Locus, and Moz Mutation Partially Phenocopies DiGeorge Syndrome.” *Developmental Cell* 23 (3): 652–63. https://doi.org/10.1016/j.devcel.2012.07.010.

Waas, William F., Zhanna Druzina, Melanie Hanan, and Paul Schimmel. 2007. “Role of a TRNA Base Modification and Its Precursors in Frameshifting in Eukaryotes.” *The Journal of Biological Chemistry* 282 (36): 26026–34. https://doi.org/10.1074/jbc.M703391200.

Wan, Wei, Zhiyuan You, Yinfeng Xu, Li Zhou, Zhunlv Guan, Chao Peng, Catherine C. L. Wong, et al. 2017. “MTORC1 Phosphorylates Acetyltransferase P300 to Regulate Autophagy and Lipogenesis.” *Molecular Cell* 68 (2): 323-335.e6. https://doi.org/10.1016/j.molcel.2017.09.020.

Wang, Chen-Xin, Guan-Shen Cui, Xiuying Liu, Kai Xu, Meng Wang, Xin-Xin Zhang, Li-Yuan Jiang, et al. 2018. “METTL3-Mediated M6A Modification Is Required for Cerebellar Development.” *PLOS Biology* 16 (6): e2004880. https://doi.org/10.1371/journal.pbio.2004880.

Wang, Kevin C., Yul W. Yang, Bo Liu, Amartya Sanyal, Ryan Corces-Zimmerman, Yong Chen, Bryan R. Lajoie, et al. 2011. “A Long Noncoding RNA Maintains Active Chromatin to Coordinate Homeotic Gene Expression.” *Nature* 472 (7341): 120–24. https://doi.org/10.1038/nature09819.

Wang, Liang, Yifei Gao, Xiangdong Zheng, Cuifang Liu, Shuangshuang Dong, Ru Li, Guanwei Zhang, et al. 2019. “Histone Modifications Regulate Chromatin Compartmentalization by Contributing to a Phase Separation Mechanism.” *Molecular Cell* 76 (4): 646-659.e6. https://doi.org/10.1016/j.molcel.2019.08.019.

Wang, Lu, Clayton K. Collings, Zibo Zhao, Kira Alia Cozzolino, Quanhong Ma, Kaiwei Liang, Stacy A. Marshall, et al. 2017. “A Cytoplasmic COMPASS Is Necessary for Cell Survival and Triple-Negative Breast Cancer Pathogenesis by Regulating Metabolism.” *Genes & Development* 31 (20): 2056–66. https://doi.org/10.1101/gad.306092.117.

Wang, Lu, Jun Zhang, Jialei Duan, Xinxing Gao, Wei Zhu, Xingyu Lu, Lu Yang, et al. 2014. “Programming and Inheritance of Parental DNA Methylomes in Mammals.” *Cell* 157 (4): 979–91. https://doi.org/10.1016/j.cell.2014.04.017.

Wang, Pengfei, Chengqi Lin, Edwin R. Smith, Hong Guo, Brian W. Sanderson, Min Wu, Madelaine Gogol, et al. 2009. “Global Analysis of H3K4 Methylation Defines MLL Family Member Targets and Points to a Role for MLL1-Mediated H3K4 Methylation in the Regulation of Transcriptional Initiation by RNA Polymerase II.” *Molecular and Cellular Biology* 29 (22): 6074–85. https://doi.org/10.1128/MCB.00924-09.

Wang, Qiaoqiao, Zuo Zhang, Katherine Blackwell, and Gordon G. Carmichael. 2005. “Vigilins Bind to Promiscuously A-to-I-Edited RNAs and Are Involved in the Formation of Heterochromatin.” *Current Biology* 15 (4): 384–91. https://doi.org/10.1016/j.cub.2005.01.046.

Wang, Xiao, Zhike Lu, Adrian Gomez, Gary C. Hon, Yanan Yue, Dali Han, Ye Fu, et al. 2014. “N 6 -Methyladenosine-Dependent Regulation of Messenger RNA Stability.” *Nature* 505 (7481): 117–20. https://doi.org/10.1038/nature12730.

Wang, Xiao, Boxuan Simen Zhao, Ian A. Roundtree, Zhike Lu, Dali Han, Honghui Ma, Xiaocheng Weng, Kai Chen, Hailing Shi, and Chuan He. 2015. "N6-Methyladenosine Modulates Messenger RNA Translation Efficiency." *Cell* 161 (6): 1388–99. https://doi.org/10.1016/j.cell.2015.05.014.

Wang, Xiaoyun, Zaneta Matuszek, Yong Huang, Marc Parisien, Qing Dai, Wesley Clark, Michael H. Schwartz, and Tao Pan. 2018. "Queuosine Modification Protects Cognate TRNAs against Ribonuclease Cleavage." *RNA (New York, N.Y.)* 24 (10): 1305–13. https://doi.org/10.1261/rna.067033.118.

Wang, Yan, Haizhen Long, Juan Yu, Liping Dong, Michel Wassef, Baowen Zhuo, Xia Li, et al. 2018. "Histone Variants H2A.Z and H3.3 Coordinately Regulate PRC2-Dependent H3K27me3 Deposition and Gene Expression Regulation in MES Cells." *BMC Biology* 16 (1): 1–18. https://doi.org/10.1186/s12915-018-0568-6.

Wang, Yi-Ping, Li-Sha Zhou, Yu-Zheng Zhao, Shi-Wen Wang, Lei-Lei Chen, Li-Xia Liu, Zhi-Qiang Ling, et al. 2014. "Regulation of G6PD Acetylation by SIRT2 and KAT9 Modulates NADPH Homeostasis and Cell Survival during Oxidative Stress." *The EMBO Journal* 33 (12): 1304–20. https://doi.org/10.1002/embj.201387224.

Wang, Yugang, Yusong R. Guo, Ke Liu, Zheng Yin, Rui Liu, Yan Xia, Lin Tan, et al. 2017. "KAT2A Coupled with the α-KGDH Complex Acts as a Histone H3 Succinyltransferase." *Nature* 552 (7684): 273–77. https://doi.org/10.1038/nature25003.

Wang, Zhibin, Chongzhi Zang, Jeffrey A. Rosenfeld, Dustin E. Schones, Artem Barski, Suresh Cuddapah, Kairong Cui, et al. 2008. "Combinatorial Patterns of Histone Acetylations and Methylations in the Human Genome." *Nature Genetics* 40 (7): 897–903. https://doi.org/10.1038/ng.154.

Watanabe, Shinya, Marta Radman-Livaja, Oliver J. Rando, and Craig L. Peterson. 2013. "A Histone Acetylation Switch Regulates H2A.Z Deposition by the SWR-C Remodeling Enzyme." *Science* 340 (6129): 195–99. https://doi.org/10.1126/science.1229758.

Watanabe, Shinya, Dongyan Tan, Mahadevan Lakshminarasimhan, Michael P. Washburn, Eun-Jin Erica Hong, Thomas Walz, and Craig L. Peterson. 2015. "Structural Analyses of the Chromatin Remodelling Enzymes INO80-C and SWR-C." *Nature Communications* 6 (1): 7108. https://doi.org/10.1038/ncomms8108.

Weber, Alain R., Claudia Krawczyk, Adam B. Robertson, Anna Kuśnierczyk, Cathrine B. Vågbø, David Schuermann, Arne Klungland, and Primo Schär. 2016. "Biochemical Reconstitution of TET1–TDG–BER-Dependent Active DNA Demethylation Reveals a Highly Coordinated Mechanism." *Nature Communications* 7 (1): 10806. https://doi.org/10.1038/ncomms10806.

Weber, Michael, Ines Hellmann, Michael B. Stadler, Liliana Ramos, Svante Pääbo, Michael Rebhan, and Dirk Schübeler. 2007. "Distribution, Silencing Potential and Evolutionary Impact of Promoter DNA Methylation in the Human Genome." *Nature Genetics* 39 (4): 457–66. https://doi.org/10.1038/ng1990.

Wei, Chang-Wei, Ting Luo, Shan-Shan Zou, and An-Shi Wu. 2018. "The Role of Long Noncoding RNAs in Central Nervous System and Neurodegenerative Diseases." *Frontiers in Behavioral Neuroscience* 12. https://doi.org/10.3389/fnbeh.2018.00175.

Wei, Jun, Zhaohui Li, Chao Du, Bin Qi, Xingli Zhao, Liping Wang, Lirong Bi, et al. 2014. "Abnormal Expression of an ADAR2 Alternative Splicing Variant in Gliomas Downregulates Adenosine-to-Inosine RNA Editing." *Acta Neurochirurgica* 156 (6): 1135–42. https://doi.org/10.1007/s00701-014-2004-1.

Weixlbaumer, Albert, Frank V. Murphy, Agnieszka Dziergowska, Andrzej Malkiewicz, Franck A. P. Vendeix, Paul F. Agris, and V. Ramakrishnan. 2007. “Mechanism for Expanding the Decoding Capacity of Transfer RNAs by Modification of Uridines.” *Nature Structural & Molecular Biology* 14 (6): 498–502. https://doi.org/10.1038/nsmb1242.

Wellen, Kathryn E., Georgia Hatzivassiliou, Uma M. Sachdeva, Thi V. Bui, Justin R. Cross, and Craig B. Thompson. 2009. “ATP-Citrate Lyase Links Cellular Metabolism to Histone Acetylation.” *Science* 324 (5930): 1076–80. https://doi.org/10.1126/science.1164097.

Wen, Hong, Yuanyuan Li, Yuanxin Xi, Shiming Jiang, Sabrina Stratton, Danni Peng, Kaori Tanaka, et al. 2014. “ZMYND11 Links Histone H3.3K36me3 to Transcription Elongation and Tumour Suppression.” *Nature* 508 (7495): 263–68. https://doi.org/10.1038/nature13045.

Whetstine, Johnathan R., Amanda Nottke, Fei Lan, Maite Huarte, Sarit Smolikov, Zhongzhou Chen, Eric Spooner, et al. 2006. “Reversal of Histone Lysine Trimethylation by the JMJD2 Family of Histone Demethylases.” *Cell* 125 (3): 467–81. https://doi.org/10.1016/j.cell.2006.03.028.

Wiener, David, and Schraga Schwartz. 2021. “The Epitranscriptome beyond m 6 A.” *Nature Reviews Genetics* 22 (2): 119–31. https://doi.org/10.1038/s41576-020-00295-8.

Wilde, Jonathan J., Julie A. Siegenthaler, Sharon Y. R. Dent, and Lee A. Niswander. 2017. “Diencephalic Size Is Restricted by a Novel Interplay Between GCN5 Acetyltransferase Activity and Retinoic Acid Signaling.” *The Journal of Neuroscience: The Official Journal of the Society for Neuroscience* 37 (10): 2565–79. https://doi.org/10.1523/JNEUROSCI.2121-16.2017.

Wilson, D. K., F. B. Rudolph, and F. A. Quiocho. 1991. “Atomic Structure of Adenosine Deaminase Complexed with a Transition-State Analog: Understanding Catalysis and Immunodeficiency Mutations.” *Science* 252 (5010): 1278–84. https://doi.org/10.1126/science.1925539.

Winkelmann, Juliane, Ling Lin, Barbara Schormair, Birgitte R. Kornum, Juliette Faraco, Giuseppe Plazzi, Atle Melberg, et al. 2012. “Mutations in DNMT1 Cause Autosomal Dominant Cerebellar Ataxia, Deafness and Narcolepsy.” *Human Molecular Genetics* 21 (10): 2205–10. https://doi.org/10.1093/hmg/dds035.

Wolf, J., A. P. Gerber, and W. Keller. 2002. “TadA, an Essential TRNA-Specific Adenosine Deaminase from Escherichia Coli.” *EMBO J* 21 (14): 3841–51. https://doi.org/10.1093/emboj/cdf362.

Wong, Lee H., James D. McGhie, Marcus Sim, Melissa A. Anderson, Soyeon Ahn, Ross D. Hannan, Amee J. George, Kylie A. Morgan, Jeffrey R. Mann, and K.H. Andy Choo. 2010. “ATRX Interacts with H3.3 in Maintaining Telomere Structural Integrity in Pluripotent Embryonic Stem Cells.” *Genome Research* 20 (3): 351–60. https://doi.org/10.1101/gr.101477.109.

Wong, Madeline M., Linda K. Cox, and John C. Chrivia. 2007. “The Chromatin Remodeling Protein, SRCAP, Is Critical for Deposition of the Histone Variant H2A.Z at Promoters*.” *Journal of Biological Chemistry* 282 (36): 26132–39. https://doi.org/10.1074/jbc.M703418200.

Wu, Hao, Volkan Coskun, Jifang Tao, Wei Xie, Weihong Ge, Kazuaki Yoshikawa, En Li, Yi Zhang, and Yi Eve Sun. 2010. “Dnmt3a-Dependent Nonpromoter DNA Methylation Facilitates Transcription of Neurogenic Genes.” *Science (New York, N.Y.)* 329 (5990): 444–48. https://doi.org/10.1126/science.1190485.

Wu, Jinjun, Nadine L. Samara, Isao Kuraoka, and Wei Yang. 2019. “Evolution of Inosine-Specific Endonuclease V from Bacterial DNase to Eukaryotic RNase.” *Molecular Cell* 76 (1): 44-56.e3. https://doi.org/10.1016/j.molcel.2019.06.046.

Wu, Qing, Yi-Ming Qian, Xiang-Li Zhao, Shou-Mei Wang, Xiao-Jun Feng, Xin-Fang Chen, and Shu-Hui Zhang. 2012. “Expression and Prognostic Significance of Centromere Protein A in Human Lung Adenocarcinoma.” *Lung Cancer* 77 (2): 407–14. https://doi.org/10.1016/j.lungcan.2012.04.007.

Wysocka, Joanna, Tomek Swigut, Hua Xiao, Thomas A. Milne, So Yeon Kwon, Joe Landry, Monika Kauer, et al. 2006. “A PHD Finger of NURF Couples Histone H3 Lysine 4 Trimethylation with Chromatin Remodelling.” *Nature* 442 (7098): 86–90. https://doi.org/10.1038/nature04815.

Xiao, Wen, Samir Adhikari, Ujwal Dahal, Yu-Sheng Chen, Ya-Juan Hao, Bao-Fa Sun, Hui-Ying Sun, et al. 2016. “Nuclear M6A Reader YTHDC1 Regulates MRNA Splicing.” *Molecular Cell* 61 (4): 507–19. https://doi.org/10.1016/j.molcel.2016.01.012.

Xiong, Chaoyang, Zengqi Wen, Juan Yu, Jun Chen, Chao-Pei Liu, Xiaodong Zhang, Ping Chen, Rui-Ming Xu, and Guohong Li. 2018. “UBN1/2 of HIRA Complex Is Responsible for Recognition and Deposition of H3.3 at Cis-Regulatory Elements of Genes in Mouse ES Cells.” *BMC Biology* 16 (1): 110. https://doi.org/10.1186/s12915-018-0573-9.

Xiong, Xiaozhe, Tatyana Panchenko, Shuang Yang, Shuai Zhao, Peiqiang Yan, Wenhao Zhang, Wei Xie, et al. 2016. “Selective Recognition of Histone Crotonylation by Double PHD Fingers of MOZ and DPF2.” *Nature Chemical Biology* 12 (12): 1111–18. https://doi.org/10.1038/nchembio.2218.

Xu, Zhenjie, Laura Schaedel, Didier Portran, Andrea Aguilar, Jérémie Gaillard, M. Peter Marinkovich, Manuel Théry, and Maxence V. Nachury. 2017. “Microtubules Acquire Resistance from Mechanical Breakage through Intralumenal Acetylation.” *Science* 356 (6335): 328–32. https://doi.org/10.1126/science.aai8764.

Xue, Yutong, Jiemin Wong, G.Tony Moreno, Mary K. Young, Jacques Côté, and Weidong Wang. 1998. “NURD, a Novel Complex with Both ATP-Dependent Chromatin-Remodeling and Histone Deacetylase Activities.” *Molecular Cell* 2 (6): 851–61. https://doi.org/10.1016/S1097-2765(00)80299-3.

Yakubovskaya, Elena, Kip E. Guja, Edison Mejia, Steven Castano, Elena Hambardjieva, Woo Suk Choi, and Miguel Garcia-Diaz. 2012. “Structure of the Essential MTERF4:NSUN4 Protein Complex Reveals How an MTERF Protein Collaborates to Facilitate RRNA Modification.” *Structure* 20 (11): 1940–47. https://doi.org/10.1016/j.str.2012.08.027.

Yamamori, Tohru, Jeremy DeRicco, Asma Naqvi, Timothy A. Hoffman, Ilwola Mattagajasingh, Kenji Kasuno, Saet-Byel Jung, Cuk-Seong Kim, and Kaikobad Irani. 2010. “SIRT1 Deacetylates APE1 and Regulates Cellular Base Excision Repair.” *Nucleic Acids Research* 38 (3): 832–45. https://doi.org/10.1093/nar/gkp1039.

Yamasaki, Satoshi, Pavel Ivanov, Guo-Fu Hu, and Paul Anderson. 2009. “Angiogenin Cleaves TRNA and Promotes Stress-Induced Translational Repression.” *The Journal of Cell Biology* 185 (1): 35–42. https://doi.org/10.1083/jcb.200811106.

Yamashita, Takenari, Takuto Hideyama, Kosuke Hachiga, Sayaka Teramoto, Jiro Takano, Nobuhisa Iwata, Takaomi C. Saido, and Shin Kwak. 2012. “A Role for Calpain-Dependent Cleavage of TDP-43 in Amyotrophic Lateral Sclerosis Pathology.” *Nature Communications* 3 (1): 1307. https://doi.org/10.1038/ncomms2303.

Yang, Hee Doo, Pum-Joon Kim, Jung Woo Eun, Qingyu Shen, Hyung Seok Kim, Woo Chan Shin, Young Min Ahn, Won Sang Park, Jung Young Lee, and Suk Woo Nam. 2016. "Oncogenic Potential of Histone-Variant H2A.Z.1 and Its Regulatory Role in Cell Cycle and Epithelial-Mesenchymal Transition in Liver Cancer." *Oncotarget* 7 (10): 11412–23. https://doi.org/10.18632/oncotarget.7194.

Yang, Weidong, Thimmaiah P. Chendrimada, Qingde Wang, Miyoko Higuchi, Peter H. Seeburg, Ramin Shiekhattar, and Kazuko Nishikura. 2006. "Modulation of MicroRNA Processing and Expression through RNA Editing by ADAR Deaminases." *Nature Structural & Molecular Biology* 13 (1): 13–21. https://doi.org/10.1038/nsmb1041.

Yang, Xiang-Jiao, and Serge Grégoire. 2005. "Class II Histone Deacetylases: From Sequence to Function, Regulation, and Clinical Implication." *Molecular and Cellular Biology* 25 (8): 2873–84. https://doi.org/10.1128/MCB.25.8.2873-2884.2005.

Yang, Xin, Ying Yang, Bao-Fa Sun, Yu-Sheng Chen, Jia-Wei Xu, Wei-Yi Lai, Ang Li, et al. 2017. "5-Methylcytosine Promotes MRNA Export — NSUN2 as the Methyltransferase and ALYREF as an m 5 C Reader." *Cell Research* 27 (5): 606–25. https://doi.org/10.1038/cr.2017.55.

Yang, Ying, Lu Wang, Xiao Han, Wen-Lan Yang, Mengmeng Zhang, Hai-Li Ma, Bao-Fa Sun, et al. 2019. "RNA 5-Methylcytosine Facilitates the Maternal-to-Zygotic Transition by Preventing Maternal MRNA Decay." *Molecular Cell* 75 (6): 1188-1202.e11. https://doi.org/10.1016/j.molcel.2019.06.033.

Yap, Kyoko L., Side Li, Ana M. Muñoz-Cabello, Selina Raguz, Lei Zeng, Shiraz Mujtaba, Jesús Gil, Martin J. Walsh, and Ming-Ming Zhou. 2010. "Molecular Interplay of the Noncoding RNA ANRIL and Methylated Histone H3 Lysine 27 by Polycomb CBX7 in Transcriptional Silencing of INK4a." *Molecular Cell* 38 (5): 662–74. https://doi.org/10.1016/j.molcel.2010.03.021.

Yin, Yimeng, Ekaterina Morgunova, Arttu Jolma, Eevi Kaasinen, Biswajyoti Sahu, Syed Khund-Sayeed, Pratyush K. Das, et al. 2017. "Impact of Cytosine Methylation on DNA Binding Specificities of Human Transcription Factors." *Science* 356 (6337). https://doi.org/10.1126/science.aaj2239.

Yoder, J A, C P Walsh, and T H Bestor. 1997. "Cytosine Methylation and the Ecology of Intragenomic Parasites." *Trends in Genetics* 13 (8): 335–40. https://doi.org/10.1016/s0168-9525(97)01181-5.

Yoon, Andrew, Guang Peng, Yves Brandenburg, Ornella Zollo, Wei Xu, Eduardo Rego, and Davide Ruggero. 2006. "Impaired Control of IRES-Mediated Translation in X-Linked Dyskeratosis Congenita." *Science* 312 (5775): 902–6. https://doi.org/10.1126/science.1123835.

Yoon, Ki-Jun, Francisca Rojas Ringeling, Caroline Vissers, Fadi Jacob, Michael Pokrass, Dennisse Jimenez-Cyrus, Yijing Su, et al. 2017. "Temporal Control of Mammalian Cortical Neurogenesis by M6A Methylation." *Cell* 171 (4): 877-889.e17. https://doi.org/10.1016/j.cell.2017.09.003.

Yu, Futao, Yoshikazu Tanaka, Keitaro Yamashita, Takeo Suzuki, Akiyoshi Nakamura, Nagisa Hirano, Tsutomu Suzuki, Min Yao, and Isao Tanaka. 2011. "Molecular Basis of Dihydrouridine Formation on TRNA." *Proceedings of the National Academy of Sciences of the United States of America* 108 (49): 19593–98. https://doi.org/10.1073/pnas.1112352108.

Yu, Jun, Mengxian Chen, Haijiao Huang, Junda Zhu, Huixue Song, Jian Zhu, Jaewon Park, and Sheng-Jian Ji. 2018. "Dynamic M6A Modification Regulates Local Translation of MRNA in Axons." *Nucleic Acids Research* 46 (3): 1412–23. https://doi.org/10.1093/nar/gkx1182.

Zack, Travis I., Steven E. Schumacher, Scott L. Carter, Andrew D. Cherniack, Gordon Saksena, Barbara Tabak, Michael S. Lawrence, et al. 2013. “Pan-Cancer Patterns of Somatic Copy Number Alteration.” *Nature Genetics* 45 (10): 1134–40. https://doi.org/10.1038/ng.2760.

Zaidi, Nousheen, Johannes V. Swinnen, and Karine Smans. 2012. “ATP-Citrate Lyase: A Key Player in Cancer Metabolism.” *Cancer Research* 72 (15): 3709–14. https://doi.org/10.1158/0008-5472.CAN-11-4112.

Zaini, Mohamad A., Christine Müller, Tristan V. de Jong, Tobias Ackermann, Götz Hartleben, Gertrud Kortman, Karl-Heinz Gührs, et al. 2018. “A P300 and SIRT1 Regulated Acetylation Switch of C/EBPα Controls Mitochondrial Function.” *Cell Reports* 22 (2): 497–511. https://doi.org/10.1016/j.celrep.2017.12.061.

Zemach, Assaf, and Daniel Zilberman. 2010. “Evolution of Eukaryotic DNA Methylation and the Pursuit of Safer Sex.” *Current Biology* 20 (17): R780–85. https://doi.org/10.1016/j.cub.2010.07.007.

Zhang, Jin, Hui Liu, Hao Pan, Yuan Yang, Gang Huang, Yun Yang, Wei-Ping Zhou, and Ze-Ya Pan. 2014. “The Histone Acetyltransferase HMOF Suppresses Hepatocellular Carcinoma Growth.” *Biochemical and Biophysical Research Communications* 452 (3): 575–80. https://doi.org/10.1016/j.bbrc.2014.08.122.

Zhang, Li-Sheng, Chang Liu, Honghui Ma, Qing Dai, Hui-Lung Sun, Guanzheng Luo, Zijie Zhang, et al. 2019. “Transcriptome-Wide Mapping of Internal N7-Methylguanosine Methylome in Mammalian MRNA.” *Molecular Cell* 74 (6): 1304-1316.e8. https://doi.org/10.1016/j.molcel.2019.03.036.

Zhang, Xiaohong, Zhigang Yuan, Yingtao Zhang, Sarah Yong, Alexis Salas-Burgos, John Koomen, Nancy Olashaw, et al. 2007. “HDAC6 Modulates Cell Motility by Altering the Acetylation Level of Cortactin.” *Molecular Cell* 27 (2): 197–213. https://doi.org/10.1016/j.molcel.2007.05.033.

Zhang, Y., M. Zhang, H. Dong, S. Yong, X. Li, N. Olashaw, P. A. Kruk, et al. 2009. “Deacetylation of Cortactin by SIRT1 Promotes Cell Migration.” *Oncogene* 28 (3): 445–60. https://doi.org/10.1038/onc.2008.388.

Zhang, Yi, Younghoon Jang, Ji-Eun Lee, JaeWoo Ahn, Longxia Xu, Michael R. Holden, Evan M. Cornett, et al. 2019. “Selective Binding of the PHD6 Finger of MLL4 to Histone H4K16ac Links MLL4 and MOF.” *Nature Communications* 10 (1): 2314. https://doi.org/10.1038/s41467-019-10324-8.

Zhang, Yingying, Renata Jurkowska, Szabolcs Soeroes, Arumugam Rajavelu, Arunkumar Dhayalan, Ina Bock, Philipp Rathert, et al. 2010. “Chromatin Methylation Activity of Dnmt3a and Dnmt3a/3L Is Guided by Interaction of the ADD Domain with the Histone H3 Tail.” *Nucleic Acids Research* 38 (13): 4246–53. https://doi.org/10.1093/nar/gkq147.

Zhang, Zuo, and Gordon G. Carmichael. 2001. “The Fate of DsRNA in the Nucleus: A P54nrb-Containing Complex Mediates the Nuclear Retention of Promiscuously A-to-I Edited RNAs.” *Cell* 106 (4): 465–76. https://doi.org/10.1016/S0092-8674(01)00466-4.

Zhao, Meimei, Rui Geng, Xiang Guo, Ruoshi Yuan, Xiao Zhou, Yanyan Zhong, Yanfei Huo, et al. 2017. “PCAF/GCN5-Mediated Acetylation of RPA1 Promotes Nucleotide Excision Repair.” *Cell Reports* 20 (9): 1997–2009. https://doi.org/10.1016/j.celrep.2017.08.015.

Zhao, Xiansi, Jeffrey R. Patton, Shannon L. Davis, Brian Florence, Sarah J. Ames, and Remco A. Spanjaard. 2004. “Regulation of Nuclear Receptor Activity by a Pseudouridine Synthase through Posttranscriptional Modification of Steroid Receptor RNA Activator.” *Molecular Cell* 15 (4): 549–58. https://doi.org/10.1016/j.molcel.2004.06.044.

Zheng, Guanqun, John Arne Dahl, Yamei Niu, Peter Fedorcsak, Chun-Min Huang, Charles J. Li, Cathrine B. Vågbø, et al. 2013. "ALKBH5 Is a Mammalian RNA Demethylase That Impacts RNA Metabolism and Mouse Fertility." *Molecular Cell* 49 (1): 18–29. https://doi.org/10.1016/j.molcel.2012.10.015.

Zhong, Yun, Qing Jun Wang, Xianting Li, Ying Yan, Jonathan M. Backer, Brian T. Chait, Nathaniel Heintz, and Zhenyu Yue. 2009. "Distinct Regulation of Autophagic Activity by Atg14L and Rubicon Associated with Beclin 1–Phosphatidylinositol-3-Kinase Complex." *Nature Cell Biology* 11 (4): 468–76. https://doi.org/10.1038/ncb1854.

Zhou, Chan, Benoit Molinie, Kaveh Daneshvar, Joshua V. Pondick, Jinkai Wang, Nicholas Van Wittenberghe, Yi Xing, Cosmas C. Giallourakis, and Alan C. Mullen. 2017. "Genome-Wide Maps of M6A CircRNAs Identify Widespread and Cell-Type-Specific Methylation Patterns That Are Distinct from MRNAs." *Cell Reports* 20 (9): 2262–76. https://doi.org/10.1016/j.celrep.2017.08.027.

Zhou, Jing, Qiaoqiao Wang, Ling-Ling Chen, and Gordon G. Carmichael. 2008. "On the Mechanism of Induction of Heterochromatin by the RNA-Binding Protein Vigilin." *RNA* 14 (9): 1773–81. https://doi.org/10.1261/rna.1036308.

Zhou, Katherine I., Hailing Shi, Ruitu Lyu, Adam C. Wylder, Żaneta Matuszek, Jessica N. Pan, Chuan He, Marc Parisien, and Tao Pan. 2019. "Regulation of Co-Transcriptional Pre-MRNA Splicing by M6A through the Low-Complexity Protein HnRNPG." *Molecular Cell* 76 (1): 70-81.e9. https://doi.org/10.1016/j.molcel.2019.07.005.

Zhu, Lin, Jiaxing Yang, Linhong Zhao, Xue Yu, Lingyao Wang, Fei Wang, Yong Cai, and Jingji Jin. 2015. "Expression of HMOF, but Not HDAC4, Is Responsible for the Global Histone H4K16 Acetylation in Gastric Carcinoma." *International Journal of Oncology* 46 (6): 2535–45. https://doi.org/10.3892/ijo.2015.2956.

Zhuang, Mengru, Xinbei Li, Junda Zhu, Jian Zhang, Fugui Niu, Fanghao Liang, Mengxian Chen, Duo Li, Peng Han, and Sheng-Jian Ji. 2019. "The M6A Reader YTHDF1 Regulates Axon Guidance through Translational Control of Robo3.1 Expression." *Nucleic Acids Research* 47 (9): 4765–77. https://doi.org/10.1093/nar/gkz157.

Ziller, Michael J., Juan A. Ortega, Katharina A. Quinlan, David P. Santos, Hongcang Gu, Eric J. Martin, Christina Galonska, et al. 2018. "Dissecting the Functional Consequences of De Novo DNA Methylation Dynamics in Human Motor Neuron Differentiation and Physiology." *Cell Stem Cell* 22 (4): 559-574.e9. https://doi.org/10.1016/j.stem.2018.02.012.

Zipeto, Maria Anna, Angela C. Court, Anil Sadarangani, Nathaniel P. Delos Santos, Larisa Balaian, Hye-Jung Chun, Gabriel Pineda, et al. 2016. "ADAR1 Activation Drives Leukemia Stem Cell Self-Renewal by Impairing Let-7 Biogenesis." *Cell Stem Cell* 19 (2): 177–91. https://doi.org/10.1016/j.stem.2016.05.004.

Zou, Fan, Renjun Tu, Bo Duan, Zhenlin Yang, Zhaohua Ping, Xiaoqing Song, Shiyuan Chen, et al. 2020. "Drosophila YBX1 Homolog YPS Promotes Ovarian Germ Line Stem Cell Development by Preferentially Recognizing 5-Methylcytosine RNAs." *Proceedings of the National Academy of Sciences* 117 (7): 3603–9. https://doi.org/10.1073/pnas.1910862117.

Zoysa, Meemanage D. De, Guowei Wu, Raviv Katz, and Yi-Tao Yu. 2018. "Guide-Substrate Base-Pairing Requirement for Box H/ACA RNA-Guided RNA Pseudouridylation." *RNA* 24 (8): 1106–17. https://doi.org/10.1261/rna.066837.118.

Université de Strasbourg

Elizabeth RAMOS MORALES

Biochemical, biophysical and structural study of proteins associated to human diseases: tcDAC2 and ADAT complex

École Doctorale des Sciences de la Vie et de la Santé STRASBOURG

Résumé

Au cours de ma thèse, j'ai étudié deux protéines associées aux maladies humaines : tcDAC2 et le complexe ADAT.

TcDAC2 est une histone désacétylase du parasite *Typanosoma cruzi* qui cause la maladie de Chagas. *TcDAC2* est essentiel pour la viabilité de T. cruzi et représente donc une cible potentielle de médicament. J'ai résolu la structure tcDAC2 qui montre des différences majeures avec celles des HDAC humains. Notamment, je montre que tcDAC2 possède une poche de site actif spécifique et unique qui peut être ciblée par des inhibiteurs. Ces connaissances seront utilisées pour développer des pistes médicamenteuses puissantes et sélectives pour traiter la maladie de Chagas.

Le complexe eucaryote ADAT est une enzyme d'édition d'adénosine en inosine des ARNt en position 34. ADAT est composé de deux sous-unités : ADAT2, qui est la sous-unité catalytique, et ADAT3 de rôle inconnu. Notamment, ADAT3 possède un domaine N-terminal supplémentaire par rapport à son homologue procaryote, la mutation V128M dans ce domaine provoquant un trouble neurodéveloppemental. Au cours de ma thèse de doctorat, j'ai résolu la structure du complexe ADAT mammifère, ce qui donne un aperçu de son mode d'action. J'ai déterminé le rôle clé du domaine ADAT3-Nterminal dans la liaison de l'ARNt. Mes résultats montrent que le mutant ADAT3 V128M positionne de manière incorrecte le substrat d'ARNt dans le site catalytique ADAT2, provoquant ainsi une diminution des niveaux d'inosine dans les ARNt des patients affectés.

Mots clés : Histone désacétylases, adénosine désaminase des ARNt, Maladies neurodéveloppementales et parasitaires, Mécanismes moléculaires, Pistes de médicaments

Summary

During my PhD thesis, I studied two proteins associated to human diseases: tcDAC2 and the ADAT complex.

TcDAC2 is a histone deacetylase from the parasite *Typanosoma cruzi* which causes the Chagas disease. *TcDAC2* is essential for *T. cruzi* viability and represents therefore a potential drug target. I solved the tcDAC2 structure which shows major differences with those of human HDACs. Notably, I show that tcDAC2 has a specific and unique active site pocket that can be targeted by inhibitors. This knowledge will be used to develop potent and selective drug leads to treat Chagas disease.

The eukaryotic ADAT complex is an adenosine-to-inosine editing enzyme of tRNAs at position 34. ADAT is composed of two subunits: ADAT2, which is the catalytic subunit, and ADAT3 of unknown role. Notably, ADAT3 has an additional N-terminal domain compared to its prokaryotic homologue, the mutation V128M in this domain causing a neurodevelopmental disorder. During my PhD thesis, I solved the structure of the mammalian ADAT complex, which gives insights of its mode of action. I determined the key role of ADAT3-Nterminal domain in tRNA binding. My results show that the ADAT3 V128M mutant positions incorrectly the tRNA substrate in ADAT2 catalytic site, thereby causing a decrease of inosine levels in tRNAs of affected patients.

Key words: Histone deacetylases, tRNA adenosine deaminase, Neurodevelopmental and parasitic diseases, Molecular mechanisms, Drug leads